
Universidade de Aveiro
2007
Departamento de Electrónica Telecomunicações e Informática

Manuel de Jesus Ferreira Dinis

Desempenho de um Sistema Celular de Banda Larga na Faixa dos 40 GHz

Performance Evaluation of a 40 GHz Broadband Cellular System

Universidade de Aveiro
2007
Departamento de Electrónica Telecomunicações e Informática

Manuel de Jesus Ferreira Dinis

Desempenho de um Sistema Celular de Banda Larga na Faixa dos 40 GHz

Performance Evaluation of a 40 GHz Broadband Cellular System

Tese apresentada à Universidade de Aveiro para cumprimento dos requisitos necessários à obtenção do grau de Doutor em Engenharia Electrotécnica, realizada sob a orientação científica do Professor Doutor José Carlos da Silva Neves, Professor Catedrático do Departamento de Electrónica Telecomunicações e Informática da Universidade de Aveiro.

Apoio financeiro da FCT e do FSE no âmbito do III Quadro Comunitário de Apoio.

To my son Linton.

It is dangerous to put limits on wireless.
Guglielmo Marconi, 1932, physicist

All men by nature desire knowledge.
Aristotle (384 BC - 322 BC), Metaphysics

Something unknown is doing we don't know what.
Sir Arthur Eddington (1882 - 1944), Comment on the Uncertainty Principle in quantum physics, 1927

It does not matter how slowly you go so long as you do not stop.
Confucius, Chinese philosopher & reformer (551 BC - 479 BC)

Truth is what stands the test of experience.
Albert Einstein, US (German-born) physicist (1879 - 1955)

I would never die for my beliefs because I might be wrong.
Bertrand Russell, Mathematician & philosopher (1872 - 1970)

o júri

presidente

Doutor José Ferreira da Rocha
professor catedrático da Universidade de Aveiro

Doutor Rahim Tafazolli
full professor da Universidade de Surrey (UK)

Doutor José Carlos da Silva Neves
professor catedrático da Universidade de Aveiro

Doutor Nuno Miguel Gonçalves Borges de Carvalho
professor associado da Universidade de Aveiro

Doutor Francisco António Bucho Cercas
professor associado do Instituto Superior de Ciências do Trabalho e da Empresa

agradecimentos

Ao Prof. Doutor José Carlos da Silva Neves, meu orientador, pelo apoio e amizade que sempre demonstrou.

À Fundação para a Ciência e Tecnologia (FCT) pela concessão de uma bolsa sem a qual nunca teria escolhido este caminho.

Aos participantes no projecto europeu SAMBA por tudo aquilo que aprendi e facilidades concedidas.

Ao Eng. Vasco Lagarto pelo companheirismo durante os vários anos em que o projecto SAMBA decorreu.

Ao Eng. Paulo Nordeste pelo tempo livre que me concedeu sem o qual teria sido muito mais difícil ou mesmo impossível acabar este trabalho.

Aos Professores Barry Evans e Rahim Tafazolli da Universidade de Surrey, UK, pelo incentivo e apoio demonstrados.

Aos Professores John Gardiner e Ray Sheriff da Universidade de Bradford, UK, pela colaboração prestada no início desta longa caminhada.

Ao Prof. Doutor José Joaquim Gomes Fernandes, meu amigo e colega de longa data pelo incentivo e apoio que sempre me deu.

A todos os Bolseiros do Instituto de Telecomunicações e Alunos de Projecto da Licenciatura de Eng. Electrónica e Telecomunicações do Departamento de Electrónica Telecomunicações e Informática da Universidade de Aveiro, que trabalharam comigo durante todos estes anos e que contribuíram decisivamente para a realização deste trabalho, nomeadamente: José Garcia, Valdemar Monteiro, Nelson Oliveira, Susana Mota, Adão Silva, José Pires, Pedro Lopes, Nuno Oliveira, Filipe Matos, Paulo Silva, Paulo Jesus e Mario Rui Santos.

Ao Miguel Lacerda do Instituto de Telecomunicações pela sua constante disponibilidade.

Aos meus pais e irmã pelo apoio que sempre me deram.

À Natália e meu filho Linton pelo sofrimento que lhes causei que jamais vai ser possível compensar.

A todos que de uma forma ou outra me ajudaram.

palavras-chave

Comunicações Móveis Celulares, Banda Larga, 4G, Protótipo, Canal Rádio, 40 GHz, Transmissão, Simulação, Resposta Impulsiva, Ambientes Interiores, Ambientes Exteriores e Limite Inferior de Fleury.

resumo

O trabalho apresentado nesta tese enquadra-se na área das comunicações móveis celulares e tem subjacente a utilização de um protótipo de um sistema de comunicações móveis de banda larga desenvolvido no âmbito do projecto Europeu SAMBA. Este protótipo apresenta como principais características inovadoras as taxas de transmissão, a frequência de operação, a mobilidade e os protocolos de handover rádio. Inicialmente são descritos aspectos relacionados com a evolução das comunicações móveis ao longo do tempo e apresentados conceitos teóricos fundamentais para compreender o comportamento do canal rádio móvel e os mecanismos de propagação. São identificados os tipos de desvanecimento e descritos os vários parâmetros que permitem caracterizar o canal rádio. A descrição do impacto do desvanecimento e as formas de o mitigar são apresentadas para contextualizar o trabalho desenvolvido em termos da especificação do protótipo e as opções escolhidas. As características globais do protótipo são apresentadas o que inclui a descrição do interface rádio, da arquitectura, dos módulos de RF, dos módulos de processamento de banda base, protocolos e algoritmo de transferência rádio. O protótipo foi avaliado em vários cenários com diferentes características. No cenário exterior foi analisada uma rua urbana típica do tipo *canyon*. Em termos de configuração do sistema foram consideradas e analisadas várias alturas da Estação Base, anglos de inclinação das antenas, várias velocidades da Terminal Móvel, operação com e sem linha de vista e a penetração do sinal rádio em ruas transversais. No cenário interior foram realizados testes similares e medidas relativas às transferências que só foram executadas para este cenário por questões logísticas. Numa primeira abordagem foi analisada a cobertura oferecida por cada célula e posteriormente activada a funcionalidade de transferência. Foram também efectuados estudos com uma única Estação Base cobrindo toda a área. Em termos de caracterização do canal rádio em banda larga são apresentadas medidas da resposta impulsiva para dois cenários interiores e complementados por outros estudos via simulação utilizando uma ferramenta de *ray tracing*. Nas medidas foi utilizado um método de medição do canal no domínio da frequência. A relação entre o Espalhamento do Atraso e a Banda de Coerência em diferentes cenários foi analisada em detalhe e feita a verificação em termos da violação do limite teórico de Fleury. Como consequência dos tópicos abordados, esta tese apresenta um estudo abrangente de aspectos relacionados com o comportamento do canal rádio na faixa dos 40 GHz e a análise das opções técnicas do protótipo em termos do seu desempenho no âmbito dos sistemas de comunicações móveis 4G.

keywords

Mobile Cellular Communications, Broadband, 4G, Prototype, Radio Channel, 40 GHz, Transmission, Simulation, Impulsive Response, Indoor Environments, Outdoor Environments and Fleury Lower Bond.

abstract

The work presented in this thesis addresses the area of mobile cellular broadband communications and encompasses the utilization of a prototype developed in the framework of the European project SAMBA. This prototype has as main innovative characteristics the transmission rates, the frequency band of operation, the mobility and the radio handover protocols. Initially are described aspects related with the historical evolution of the mobile communications and presented fundamental theoretical concepts to understand the behaviour of the radio channel and the propagation mechanisms. The different types of fading are identified as well as the various parameters that allow the characterisation of the radio channel. The fading impact and its mitigation techniques are presented to contextualise the work developed in terms of the specification of the features implemented in the prototype and the options available. The global characteristic of the prototype are presented namely the radio interface, the architecture, the RF modules, the baseband modules, protocols and the algorithm for the radio handover. The prototype was evaluated in various scenarios with different characteristics. In the outdoor scenario a canyon type street was analysed. Several heights of the Base Station, antenna tilting angles, Mobile Terminal velocities, operation in line-of-sight and non line-of-sight and the penetration of the signal in a transversal street. In the indoor scenario similar measurements were performed. The handover feature was analysed just for this scenario due to logistic reasons. In a first phase the coverage provided by each Base Station was analysed and subsequently activated the handover functionality. Studies using a single Base Station to cover the whole pavilion were also performed. In terms of broadband analysis, channel impulse response measurements were performed using a frequency domain technique in two scenarios and complemented by others analysed only using a ray tracing simulation tool. The relationship between the radio channel Delay Spread and the Coherence Bandwidth was analysed in different scenarios and the possible violation of the Fleury lower bond checked. As a consequence of the several topics covered in this thesis, a deep study of the aspects related with the behaviour of the radio channel in the 40 GHz band and the performance of the technical options implemented in the prototype is presented in the framework of 4G mobile communication systems.

Table of Contents

Table of Figures

Table of Tables

List of Acronyms

1G	1st Generation
2G	2nd Generation
3G	3rd Generation
3GPP	3rd Generation Partnership Project
3GPP2	3rd Generation Partnership Project 2
4G	4th Generation
4MORE	4G MC-CDMA Multiple Antenna System on Chip for Radio Enhancements
AAL	ATM Adaptation Layer
AAL5	ATM Adaptation Layer Type 5
ACCORD	ACTS Broadband Communication Joint Trials and Demonstrations
ACK	Acknowledgement
ACM	ATM Cell Memory
ACTS	Advanced Communications Technologies and Services
ADSL	Asymmetric Digital Subscriber Loop
AFD	Average Fade Duration
AGC	Automatic Gain Control
AMC	Adaptive Modulation and Coding
AMPS	Advanced Mobile Phone System
AMS	ATM Mobility Server
ARQ	Automatic Repeat Request
ASCII	American Standard Code for Information Interchange
ASIC	Application-Specific Integrated Circuit
ASR-ARQ	Adaptive Selective Repeat – ARQ
ATM	Asynchronous Transfer Mode
AWACS	ATM Wireless Access Communication System
AWGN	Additive White Gaussian Noise
B3G	Beyond 3G
BBPU	BaseBand Processing Unit
BCH	Bose-Chadhuri-Hocquenghem
BER	Bit Error Rate
BH	Blackman-Harris
BIF	BBPU Interface Board
B-ISDN	Broadband Integrated Services Data Network
BRAHMS	Broadband Access High data rate Multimedia Satellite
BRAIN	Broadband Radio Access for IP based Networks
BRAN	Broadband Radio Access Network
BS	Base Station
BSC	Base Station Controller
BST	Base Station Transceiver
BW	Bandwidth

C&M	Controlling and Monitoring
CAPEX	Capital Expenditure
CB	Coherence Bandwidth
CBR	Constant Bit Rate
CC	Call Control
CDF	Cumulative Distribution Function
CDMA	Code Division Multiple Access
CDMA2000	3G multicarrier CDMA system
CI	Control Information
CIR	Channel Impulse Response
CPU	Central Processing Unit
CR	Code Redundancy
CU	Control Unit
CW	Continuous Wave
DAB	Digital Audio Broadcast
D-AMPS	Digital Advanced Mobile Phone System
DCA	Dynamic Channel Allocation
DECT	Digital European Cordless Telephone
DFE	Decision Feedback Equaliser
DFSE	Decision Feedback Sequence Estimation
DLC	Data Link Control
DMA	Direct Memory Access
DS	Delay Spread
DSA	Dynamic Slot Assignment
DSSS	Direct Sequence Spread Spectrum
DTMF	Dual Tone Multiple Frequency
DVB	Digital Video Broadcast
EC	European Commission
EDGE	Enhanced Data rates for GSM Evolution
ERI	ERror Information
Erl	Erlang
ETSI	European Telecommunications Standards Institute
FDD	Frequency Division Duplex
FDMA	Frequency Division Multiple Access
FEC	Forward Error Correction
FFT	Fast Fourier Transform
FIFO	First In First Out
FPGA	Field Programmable Gate Array
GBR	Gross Bit Rate
GF	Galois Field
GO	Geometric Optics
GoS	Grade of Service
GPRS	General Packet Radio Service
GSM	Global System for Mobile communications

GT	Guard Time
GTD	Geometrical Theory of Diffraction
HAL	Hardware Abstraction Layer
HARQ	Hybrid ARQ
HEMT	High Electron Mobility Transistors
HIPERACCESS	High Performance Radio Access
HIPERLAN	High Performance Local Area Network
HIPERMAN	High Performance Radio Metropolitan Area Network
HO	Handover
HSCSD	High-Speed Circuit-Switched Data
HSDPA	High Speed Downlink Packet Access
HSOPA	High-Speed OFDM Packet Access
HSUPA	High Speed Uplink Packet Access
ID	Identifier
IDFT	Inverse Discrete Fourier Transform
IEEE	Institute of Electrical and Electronic Engineers
IETF	Internet Engineering Task Force
IF	Intermediate Frequency
ILMI	Interim Local Management Interface
IMS	IP Multimedia Subsystem
IMT 2000	International Mobile Telecommunications 2000
IP	Internet Protocol
IS-95	Interim Standard 95
ISDN	Integrated Services Data Network
ISI	Inter Symbol Interference
IST	Information Society Technologies
IT	Instituto de Telecomunicações
ITU	International Telecommunications Union
JTACS	Japanese Total Access Communications Systems
LAN	Local Area Network
LCR	Level Crossing Rate
LIF	Line Interface
LLC	Logical Link Control
LO	Local Oscillator
LoS	Line-of-sight
LTE	Long Term Evolution
MAC	Medium Access Control
MAN	Metropolitan Area Network
MATRICE	MC-CDMA Transmission Techniques for Integrated Broadband Cellular System
MBMS	Multimedia Broadcast Multicast Service
MBS	Mobile Broadband System
MC	Multi-carrier
MC-CDMA	Multi-Carrier Code Division Multiple Access

MC-DS-CDMA	Multi-Carrier Direct Sequence Code Division Multiple Access
MH	Millimetrewave Head
MIMO	Multiple Input Multiple Output
MIND	Mobile IP based Network Developments
MISO	Multiple Input Single Output
mITF	Mobile IT Forum
MLSE	Maximum Likelihood Sequence Estimation
MM	Mobility Management
MMIC	Monolithic Millimetrewave Integrated Circuit
MRC	Maximal Ratio Combining
MRP	Mobility and Resource Management Protocol
MSB	Most Significant Bit
MSE	Mean Square Error
MSR	Mobility Server
MT	Mobile Terminal
MTA	Mobile Terminal Adapter
MWT	MillimeterWave Transceiver
NA	Network Analyser
NMT	Nordic Mobile Telephone
NNI	Network-to-Network Interface
NRP	Normalised Received Power
NRZ	Non Return to Zero
OBANET	Optically Beam-formed Antennas for adaptive broadband fixed and mobile wireless access NETworks
OFDM	Orthogonal Frequency-Division Multiplexing
OFDMA	Orthogonal Frequency Division Multiple Access
OPEX	Operational Expenditure
OQAM	Offset Quadrature Amplitude Modulation
OQPSK	Offset Quadrature Phase Shift Keying
P	Preamble
PASTORAL	Platform and Software for Terminals: Operationally Re-configurable
PC	Personal Computer
PCI	Peripheral Component Interconnect
PDC	Personal Digital Communications
PDP	Power Delay Profile
PDU	Packet Data Unit
PHY	Physical Layer
PL	Payload
PLL	Phase Lock Loop
PNNI	Private Network-to-Network Interface
ppm	parts per million
PSD	Power Spectral Density
PVC	Permanent Virtual Circuit
QoS	Quality of Service

RACE	Research and Development in Advanced Communications Technologies in Europe
RF	Radio Frequency
RRM	Radio Resource Management
RM	Resource Management
RNC	Radio Network Controller
RS	Reed-Solomon
RSSI	Received Signal Strength Indicator
RSVP	Resource Reservation Protocol
RTOS	Real Time Operating System
Rx	Receiver
SAAL	Signalling ATM Adaptation Layer
SAMBA	System for Advanced Mobile Broadband Applications
SAW	Surface Acoustic Wave
SC	Single Carrier
SDL	Specification and Description Language
SDW	Sliding Delay Window
SECOMS	Satellite EHF Communications for Mobile Multimedia
SIMO	Single Input Multiple Output
SIP	Session Initiation Protocol
SISO	Single Input Single Output
SNR	Signal to Noise Ratio
SS-MC-MA	Spread Spectrum-Multi Carrier-Multiple Access
SVC	Switched Virtual Channel
TACS	Total Access Communications Systems
TAXI	Transparent Asynchronous transmitting Interface
TB	Tail in the Beginning
TDD	Time Division Duplex
TDMA	Time Division Multiple Access
TD-SCDMA	Time Division-Synchronous CDMA
TE	Tail in the End
TF	Transfer Function
THRESH	Threshold
TISPAN	Telecoms & Internet converged Services & Protocols for Advanced Networks
TM	Tail in the Middle
TRUST	Transparently Re-configurable Ubiquitous Terminal
TS	Training Sequence
Ts	Time slot
Tx	Transmitter
UCIF	Universal Cell Interface
UMTS	Universal Mobile Telecommunications System
UNI	User-to-Network Interface
UNI sig.	UNI signalling

URL	Uniform Resource Locator
UTD	Uniform GTD
UWD	Unique Word Detection
VBR	Variable Bit Rate
VC	Virtual Channel
VCI	Virtual Channel Identifier
VME	Versa Module Euro (BUS)
VPI	Virtual Path Identifier
VSN	Virtual Slot Number
WAND	Wireless ATM Network Demonstrator
WCDMA	Wideband CDMA
WiFi	Wireless Fidelity
WiMAX	Worldwide Interoperability for Microwave Access
WIND-FLEX	Wireless Indoor Flexible High Bit rate Modem Architecture
WINNER	Wireless World Initiative New Radio
WLAN	Wireless LAN
WMAN	Wireless MAN
WSS	Wide-Sense Stationary
WSSUS	Wide-Sense Stationary Uncorrelated Scattering
WWRF	Wireless World Research Forum

List of Symbols

$\propto$	Proportional
$\times$	External vectors product
$\otimes$	Convolution
$\bullet$	Matrices product
ϕ	Phase
θ	Angle
ξ	Angle between two coordinate systems
δ	Phase difference between the θ and ϕ components of the electrical field
$\delta[.]$	Dirac function
Γ	Polarisation efficiency
ε	Permittivity
μ	Permeability
σ	Conductivity
η	Index of refraction
ρ	Reflection coefficient
$\rho_{\perp}$	Reflection coefficient for $E_{\perp}$
$\rho_{\parallel}$	Reflection coefficient for $E_{\parallel}$
Δ	Phase difference between the direct and ground reflected paths
υ	Doppler shift variable
λ	Wavelength
α	Angle or amplitude of a ray
τ	Delay
$\tau_{\perp}$	Transmission coefficient for $E_{\perp}$
$\tau_{\parallel}$	Transmission coefficient for $E_{\parallel}$
$\Delta\tau$	Delay separation
$\Gamma(.)$	Gamma function
$\mu[.]$	Centre of gravity
$\sigma[.]$	Delay spread
σ^2	Mean scattered signal power
Δf	Frequency separation
σh	Standard deviation of a surface roughness
θ_i	Angle of incidence
θm	Maximum angle of arrival
τ_{max}	Maximum delay
α_n	Amplitude of the n^{th} received ray
φ_n	Phase of the n^{th} received ray
γ	Propagation coefficient of the medium
τ_n	Excess delay of the n^{th} received ray

τ_p	Excess delay of ray p
$\overline{\tau}$	Mean time delay
η_p	NRP of ray p
θ_r	Angle of reflection
ε_r	Relative permittivity
θ_t	Angle of transmission
Δt	Time separation
*	Complex conjugate
${}_1F_1(.)$	Confluent hypergeometric function
A	Surface attenuation factor
$A_l(s',s)$	Spatial attenuation factor for the diffracted rays
$As(\xi_n)$	Polarisation loss factor
b	y-intercept in the straight line slop-intercept equation form
B	Bandwidth used for the frequency response measurements
Bd	Doppler spread
BitErrors	Number of bit errors in a frame before FEC
BW	Bandwidth
c	Correlation level
$C_{antenna\&radio\_channel}(k)$	Radio channel and antennas transfer function
CB	Coherence bandwidth
CI	Control information
c_n	Data sequence
CR	Code redundancy
Cw(k)	Waveguide transfer function
d	Distance
d_0	Distance that occurs the break-point in a two slop path loss model
Dc[.]	Coherence bandwidth at level c
D_l	Diffraction coefficient for the l^{th} diffracting edge
D_n	Bit sequence
DS	Delay spread
$e_\perp$	Direction vector perpendicular to **ri** and $e_\parallel$
$e_\parallel$	Direction vector perpendicular to **ri** and $e_\perp$
eθ	Direction vector parallel to the reference plane Vr
eϕ	Direction vector perpendicular to the reference plane Vr
$E[\ ]$	Mathematical expectation
$E[X^n]$	nth central moment of random variable X
Eθ	Electrical field in the direction of θ
Eϕ	Electrical field in the direction of ϕ
$Ei_\perp$	Perpendicular component of the incident electrical field
$Et_\perp$	Perpendicular component of the transmitted electrical field
$Er_\perp$	Perpendicular component of the reflected electrical field

$Ei_{\parallel}$	Parallel component of the incident electrical field
$Et_{\parallel}$	Parallel component of the transmitted electrical field
$Er_{\parallel}$	Parallel component of the reflected electrical field
$E_{\perp}$	Perpendicular polarised wave
$E_{\parallel}$	Parallel polarised wave
$E\theta_{Rxn}$	Amplitude of the n^{th} received ray in the θ direction
$E\phi_{Rxn}$	Amplitude of the n^{th} received ray in the ϕ direction
$E\theta_{Txn}$	Amplitude of the n^{th} transmitted ray in the θ direction
$E\phi_{Txn}$	Amplitude of the n^{th} transmitted ray in the ϕ direction
E_0	Reference electrical field
E_b	Bit energy
E_{dMT}	Electrical field strength at the MT receiving antenna due to the direct wave
Ei	Incident electrical field
E_{MT}	Electrical field strength at the MT receiving antenna
Er	Reflected electrical field
E_{rn}	Complex received electrical field for ray n
E_{Rxn}	Electrical field vector of the n^{th} received ray
Et	Transmitted electrical field
F	Receiver noise figure
f	Frequency
F(.)	Fourier transform
F(X)	Function to be searched for a local minimum
$F^{-1}(.)$	Inverse Fourier transform
f_c	Carrier frequency
f_D	Doppler shift
fm	Maximum Doppler shift
f_{rn}	Receiving antenna field radiation pattern in the direction of the n^{th} ray
f_{tn}	Transmitting antenna field radiation pattern in the direction of the n^{th} ray
G(θ)	Antenna gain in the θ direction
G(t,f)	Time variant transfer function
G(x)	WSS process with zero-mean
G_{BS}	Gain of the BS antenna
G_{MH}	Gain of the MH
G_{MT}	Gain of the MT antenna
G_{Rx}	Receiver antenna gain
G_{Tx}	Transmitter antenna gain
$Hi_{\parallel}$	Parallel component of the incident magnetic field
$Ht_{\parallel}$	Parallel component of the transmitted magnetic field

$Hr_{\parallel}$	Parallel component of the reflected magnetic field
$Hi_{\perp}$	Perpendicular component of the incident magnetic field
$Ht_{\perp}$	Perpendicular component of the transmitted magnetic field
$Hr_{\perp}$	Perpendicular component of the reflected magnetic field
H	MIMO radio channel function
h	height
H(f,υ)	Output Doppler-spread function
H(k)	Discrete transfer function
h(n)	Discrete impulse response
h(t,τ)	Input delay-spread function
$h_{antenna\&radio\_channel}(k)$	Impulse response of the radio channel and antennas
h_{BS}	Height of the BS antenna
$H_{MHx}(k)$	MH transfer function
h_{MT}	Height of the MT antenna
$H_{Other\_components}(k)$	Transfer function of cables, connectors and other small effects
$H_T(k)$	Fourier transform of $h_T(n)$
$h_T(n)$	Truncated impulse response
Hw(k)	System transfer function with the waveguide
$IFFT[.]$	Inverse Fast Fourier transform
$I_0(.)$	Modified zero-order Bessel function
$I_1(.)$	Modified first-order Bessel function
j	Wall number or square root of -1
k	Constant or total number of samples used for path loss modelling
K	Boltzman constant
K(.)	Complete elliptical integral of the first kind
K_{Rice}	Rice factor
L(d)	Path loss at distance d
le	Antenna effective length
$Ls(d_0)$	Average reference path loss at distance d_0
M	Number of terms of the Blackman-Harris window
min	Minimum
Mx	Mirror point x in the ray tracing algorithm
n	Normal vector to a plane
n	Straight line slop
N	Total number of rays or samples in the frequency domain
N_0	Noise spectral density
$\mathbf{n_r}$	Normal vector to the reference plane
p(θ)	pdf of the θ random variable
P_A	Power that reaches the BS antenna
P_{avg}	Average power
P_B	Power at the MH output
P_{BS}	Power received by the BS
P_h	Cross power spectral density of h(t,τ)

P_H	Cross power spectral density of H(f,υ)
PL	Payload
P_{MT}	Power received by the MT
P_r or P_{Rx}	Received power
P_S	Cross power spectral density of S(τ,υ)
P_t	Transmitted power
P_{Total}	Total power in a PDP
P_{Tx}	Transmitted power
P_x	Point number x
Pz(x)	pdf of random variable z
r_{coef}	Correlation coefficient
R(Δf)	Frequency correlation function
Rb	Bit rate
Re{.}	Real part of a complex number
RF	Rayleigh factor
R_h	Autocorrelation function of h(t,τ)
R_H	Autocorrelation function of H(f,υ)
ri	Vector that indicates the propagation direction
R_j	Reflection coefficient for the j^{th} reflector
r_{max}	Maximum value of r in a given interval
R_S	Autocorrelation function of S(τ,υ)
R_T	Autocorrelation function of T(f,t)
Rx1	Receiver channel 1
Rx2	Receiver channel 2
S	Intersection point
s	Amplitude of the LoS component in the Rice distribution
S(τ,υ)	Delay Doppler-spread function
s(t)	OQPSK signal complex envelop
S(y)	Delay scattering function
t	Time
T	Temperature in Kelvin
T(f,t)	Time-variant transfer function
tanδ	Losses tangent
Tb	Bit duration
Tc	Coherence time
tilting	BS antenna tilting angle
T_k	Transmission coefficient for the k^{th} transmitter
Tm	Maximum excess delay
TransAct	Number of slots with valid data
Ts	Symbol time duration
Tsamp	Sampling time
u,v	Direction vectors
V	Plane
v	velocity

Vb	Reflecting plane
Vi	Incidence plane
Vr	Reference plane
W(f)	Input signal spectrum
W(k)	Fourier transform of w(n)
w(k)	Truncation window
w(t)	Complex low-pass input signal
X	Vector in array format or application point of plane V
x	Abscissa
$\underline{x}$	Vector x
$X\sigma$	Zero-mean Gaussian random variable
x(.)	Modulation pulse
x(t)	Impulse signal at rate 1/Ts
X_0	Starting vector for the Nelder-Mead algorithm
y	Ordinate
Y(f)	Output signal spectrum
y(t)	Complex low pass output signal
$y_I(t)$	In-phase component of a complex low pass signal
$y_Q(t)$	Quadrature component of a complex low pass signal
Z	Medium impedance
z(t)	Envelop of a complex low pass signal

Mobile broadband system prototype in action, Rennes, France

1st Chapter

Introduction

Mobile communications play a very important role in the telecommunications sector and have been responsible for a tremendous change in society by altering the way people communicate, act and work. Strong research activities continue being developed in this area leading to new mobile network features and capabilities that will be exploited by the users in the short term future, catapulting new societal changes and paradigms.

The evolution of mobile communication is also made itself of changes in paradigms leading to various generations. Analogue, digital and multimedia are respectively the main keywords behind the 1st (1G), 2nd (2G) and 3rd generations (3G). Currently there are various designations for the next generation systems, namely B3G (Beyond 3G) or 4G (4th Generation) systems. 4G systems specifically operating in the millimetrewave frequency bands, where large bandwidths of spectrum are available for mobile

communication systems, are also known as mobile broadband systems[1]. This thesis addresses this type of systems.

This chapter starts with a review of the mobile communication systems evolution, back to its origins in 1887 up to nowadays (2007), where the so-called 3.5 generation systems are already in the market. In section 2, the most relevant and emblematic European projects belonging to various EC (European Commission) R&D (Research & Development) Frameworks are described to highlight the research activities most supported by the EC with emphasis on B3G as well as other activities carried out by other worldwide forum or bodies. Section 3 describes B3G systems main research challenges and applications/services. Finally the motivation, objectives, contents and main original contributions of this thesis are presented.

1. Mobile Telecommunications Evolution Path

It was back in 1820 that the French physician and mathematician André-Marie Ampère and the Danish physician Hans Christian Oersted discovered electricity and magnetism, respectively. But it was only in 1864 that the English physician James Clerk Maxwell, based on the studies undertaken for propagation of light and the derivation of his famous equations, has predicted the existence of radio waves that would also propagate in the atmosphere and would exhibit similar electromagnetic properties as light.

The human dream to communicate at long distances was made possible via the invention of the fixed telephone patented in 1876 by the American physician Alexander Graham Bell. Meanwhile the work has continued and between 1880 and 1887, the German physician Heinrich Rudolf Hertz succeeded to demonstrate the existence of the electromagnetic waves predicted by James Clerk Maxwell, leading the way to one of the major revolutions that humans have experienced.

In 1887, Guglielmo Marconi made a new and important step when he has patented the first wireless communication system – the radiotelegraph. Mobile radio

[1] In this thesis the terms B3G and 4G are used with the same meaning. Mobile Broadband Systems (MBS) are here considered a subset of the 4G or B3G systems that operate specifically in the millimetrewave frequency bands, being therefore affected by specific constrains and limitations.

telecommunications were born. In its initial stage the Morse code was used to transmit the information. Today the ability to use advanced applications and mass communicate in a user friendly way, while on the move, anywhere and anytime, makes of mobile communications a fundamental tool for people.

1.1 1G systems

The 1G systems could only transmit voice in a half duplex mode. These systems were directly related to military and police forces activities and used for the first time in 1921, Detroit, USA. Figure 1.1 shows one of the first MT (Mobile Terminal) prototypes under trials.

Figure 1.1: Early mobile telecommunications trials in 1924 [2]

The general public had access to mobile communications only a couple of decades latter, in 1946, just after the end of the Second World War, when the Bell Telephone Labs

[2] This photo was sourced at the Bell Labs Photo Gallery.

started operating this new service in St. Louis, USA. The system was operated manually, terminals were bulky and heavy and the coverage area relatively small, based on a single cell, leading rapidly to traffic congestion problems. In the subsequent years, mobile communication systems have evolved and more spectrum was also allocated. Latter they became automatic enabling the provision of a better GoS (Grade of Service).

It took the whole 20th century for the electronics technology to reach the current state of development and integration leading to the present miniaturized MTs [1]. Telecommunication systems have also evolved enormously allowing calls and connections to be established automatically virtually everywhere on earth in a full duplex mode. These new advances could also be incorporated in mobile telecommunication systems enabling the implementation of the cellular concept introduced by Bell Systems in 1971 (see Figure 1.2). The coverage area was divided in smaller areas – the cells – each served by different frequency carriers and antenna subsystems. The cellular concept enabled the re-utilisation of the frequency spectrum (in Figure 1.2 each colour shows a different carrier frequency set), leading directly to an increase on the systems capacity. One of the drawbacks of this approach was the necessity of having seamless handovers between two neighbouring cells, while the MT moves during a call.

The 1G mobile communication systems were based on analogue technology [2]. Voice was however the only service available in these mobile networks. Each country had its own system technology and, in some cases, two or more technologies coexisted. International roaming was not possible at all. Examples of 1G systems are: NMT-450 (Nordic Mobile Telephone) in the Nordic countries, AMPS (Advanced Mobile Phone System) in North America, C-450 in Portugal and Germany, TACS (Total Access Communications Systems) in UK and the Japanese JTACS (Total Access Communication Systems). The main problems of these systems were lack of capacity, leading easily to saturation and low QoS (Quality of Service).

Next subsections describe the main characteristics of 2G and 3G systems as well as currently available WLANs (Wireless Local Area Networks) and WMANs (Wireless Metropolitan Area Networks) systems.

1.2 2G systems

2G brought the digital technology and the first data services. An enormous effort was made at European level in terms of standardisation leading to one of the most ever successful mobile technologies – the GSM (Global System for Mobile communications). The high number of GSM subscribers worldwide (2,278 million in the 1st Quarter of 2007 – 80.5% of the worldwide market[3]) shows the large expansion of this technology, well beyond the European borders. International roaming is a built-in feature enabling the subscriber to carry its own terminal in many countries and accessing the GSM services locally, being charged at home. GSM also brought higher privacy and a set of services (data at 9.6 kbit/s, fax, SMS (Short Message Service) and supplementary services) not possible with the analogue technology. Since it is TDMA (Time Division Multiple Access) based it provides better spectrum efficiency and higher capacity than the former 1G systems FDMA (Frequency Division Multiple Access) based. GSM operates in three frequency bands: 900 MHz, 1800 MHz and 1900 MHz, but other bands are under consideration.

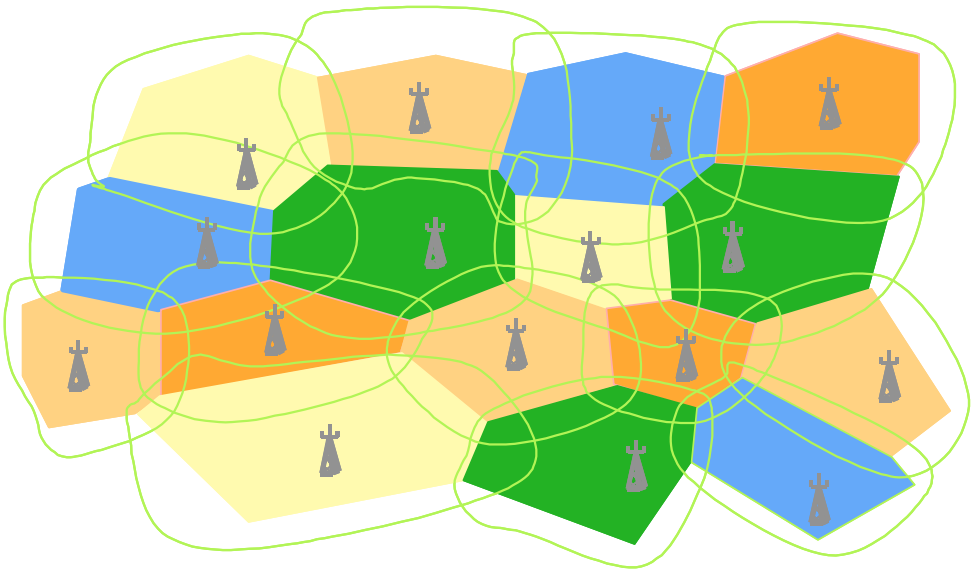

Figure 1.2: The cellular and frequency re-use concepts

In fact three more standards have played an important role in 2G, two of them originally from North America, namely the D-AMPS (Digital Advanced Mobile Phone System)

[3] Data sourced from Wireless Inteligence.

and the IS-95 (Interim Standard 95), the last based on CDMA (Code Division Multiple Access) technology. The Japanese have also developed a very successful standard based on the D-AMPS and called PDC (Personal Digital Communications).

Many mobile operators deployed 2.5G systems e.g. GPRS (General Packet Radio Service) [3] before moving to the 3G technology. The introduction of the GPRS technology enabled packet transmission via the mobile network in a much more efficient manner, opening the way to more efficient data service. Data rates up to 115 kbit/s are supported by using multiple time slots for a single terminal (user). A less successful technology aiming to enhance the circuit switch data transmission mode is the HSCSD (High-Speed Circuit-Switched Data). The utilisation of four time slots can provide a data transfer rate of 57.6 kbit/s (4 x 14.4 kbit/s).

1.3 3G systems

The paradigm behind 3G is the widespread provision of multimedia services and applications to users while on the move therefore adding to the "anytime and anywhere" concept a multimedia flavour.

At ITU (International Telecommunications Union) level, 3G is known as IMT 2000 (International Mobile Telecommunications 2000) and embraces a family of standards, namely UMTS (Universal Mobile Telecommunications System) FDD (Frequency Division Duplex) and TDD (Time Division Duplex), cdma2000 (a multicarrier CDMA system), EDGE (Enhanced Data rates for GSM Evolution) and a TDMA multicarrier system based on the DECT (Digital European Cordless Telephone) standard. Later a proposal from China and supported by 3GPP (3rd Generation Partnership Project) [4] was added being the Time-Division Synchronous CDMA (TD-SCDMA). cdma2000 is the technology supported by USA, standardised by 3GPP2 (3rd Generation Partnership Project 2) and is an evolution of the narrowband CDMA used in IS 95 [5]. In the next paragraphs only UMTS related aspects and the evolution of this technology, standardised by 3GPP, is presented since this is the system implemented in Portugal and Europe.

UMTS uses WCDMA (Wideband CDMA) technology on the air interface and brings multimedia to mobile terminals based on the fact that higher transmission data rates are

supported, ranging from 144 kbit/s in rural areas up to 2 Mbit/s in indoor environments as defined by Release '99 of 3GPP [5] [6]. In order to serve multimedia traffic, UMTS provides symmetric and asymmetric transmission. Furthermore, circuit and packet switching modes are also available. The radio interface operates in two modes: FDD and TDD. The MT must be able to support various services simultaneously allowing real multimedia sessions to be established. In its first deployment phase, UMTS will serve only densely populated areas, existing therefore in islands that are complemented with GSM coverage, therefore vertical handovers are required. Currently (1st Quarter of 2007) there exists in the market 114 millions terminals representing approximately 4% of the total market share.

Figure 1.3 illustrates a 3G UMTS network as defined by Release '99 [4] [5]. Two core domains are shown: circuit and packet switched. The first comes originally from GSM and the second from the lately added GPRS component (2.5G). The separation of these two domains is made at the BSC (Base Station Controller) for GSM and at the RNC (Radio Network Controller) for UMTS.

Several Releases of UMTS are now available being currently Release 07 and 08 under preparation by 3GPP. Features included in Releases 05 and 06 are commonly accepted to be part of 3.5G. Examples are HSDPA (High Speed Downlink Packet Access), HSUPA (High Speed Uplink Packet Access), MBMS (Multimedia Broadcast Multicast Service) and IMS (IP Multimedia Subsystem).

HSDPA is a cost-effective high-bandwidth and low-delay packet-oriented data service in the WCDMA downlink with data transmission up to 14 Mbit/s over a 5MHz bandwidth. The HSDPA concept introduces new adaptation and control mechanisms to enhance downlink peak data rates, spectral efficiency and QoS control for packet services. High trunking efficiency for bursty data services is obtained by employing code as well as time multiplexing. New features present in HSDPA are: AMC (Adaptive Modulation and Coding); HARQ (Hybrid Automatic Request); fast scheduling; and channel quality feedback. Compatibility with UMTS earlier releases was ensured being a straightforward enhancement of the UMTS Release '99 architecture, with the addition of a repetition/scheduling entity within the base station that resides below the Release '99 MAC (Medium Access Control) layer.

HSUPA technology is similar to HSDPA but to enhance the uplink transmission capabilities up to 5.8 Mbit/s.

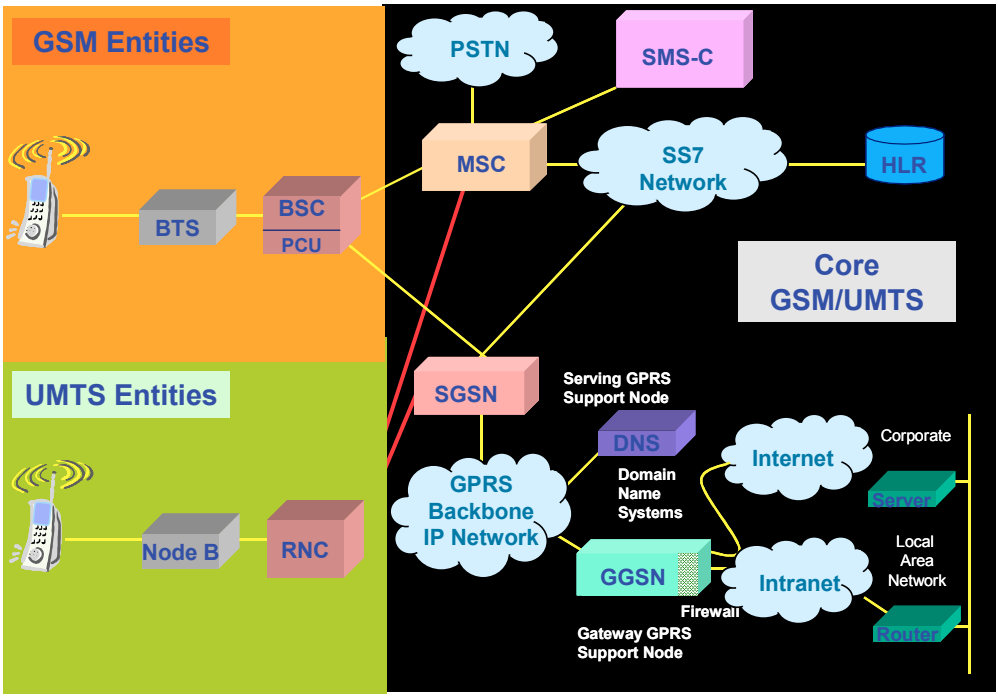

Figure 1.3: UMTS architecture – Release '99

IMS intends to efficiently support IP multimedia applications and services involving multiple media components as video, audio and tools like shared online whiteboards, with the possibility to add and drop components during the session. It was originally designed by 3GPP and is part of the vision for evolving mobile networks for delivering "Internet services". This vision was later updated by 3GPP, 3GPP2 and TISPAN by requiring support of other networks such as Wireless LAN, cdma2000 and fixed networks. To ease the integration with the Internet, IMS uses as far as possible IETF (Internet Engineering Task Force) protocols such as SIP (Session Initiation Protocol). IMS is not intended to standardise applications itself but to aid the access of multimedia and voice applications across wireless and wireline terminals, i.e. aid a form of fixed mobile convergence. This is done by having an horizontal control layer that isolates the access network from the service layer.

MBMS is a point-to-multipoint service where data is transmitted from a single source entity to multiple recipients, allowing network resources to be shared and enabling audiovisual broadcasting/multicasting over the UMTS network. The intention is to use

efficiently the mobile radio and network resources for Mobile TV like services where the data is transmitted over a common radio channel in the broadcast service area as defined by the network. In the multicast mode there is the possibility for the network to selectively transmit to cells within the multicast service area, which contain members of a multicast group. The network shall support service announcements in order to enable the user to be informed about the services available in the service area. For instance, users should be able to discover and monitor broadcast/multicast services availability by using an URL (Universal Resource Locator). Broadcast services are available to the users without any request to the network while multicast services require a specific request for activation of the service.

1.4 WiMAX, WiFi and HIPERLAN systems

WiMAX (Worldwide Interoperability for Microwave Access) system was standardised by IEEE (Institute of Electrical and Electronics Engineers). The IEEE 802.16 set of specifications define a wireless metropolitan-area network technology that provides interoperable broadband[4] wireless connectivity to fixed, portable and nomadic users without the need of a direct line-of-sight (LoS) to the BS (Base Station). This standard covers frequency bands between 2-11 GHz both licensed and unlicensed and from 10-66 GHz licensed. On the 1st of October 2004, all the standards related with the fixed component of WiMAX have been included in IEEE 802.16-2004 standard. In December 2002, the IEEE 802.16e Task Group was created to improve support for combined fixed and mobile operation in frequencies below 6 GHz enabling subscriber stations moving at vehicular speeds. This amendment was concluded in December 2005.

Wireless networking technologies offers a wide assortment of high-performance, feature-rich and cost effective solutions. The IEEE 802.11 local area networks, also known as WiFi, are implemented as part of private networks[5]. The service coverage area can be increased by using directional antennas or implementing WiFi-mesh topologies. The IEEE 802.11b extends the original IEEE 802.11 Direct Sequence Spread Spectrum (DSSS) standard to operate up to 11 Mbit/s in the 2.4 GHz band. The IEEE 802.11a

[4] Broadband is used to indicate transmission rates above 2 Mbit/s.

[5] WiFi technology is also available for public access via Network Operators.

standard provides data rates up to 54 Mbit/s in the 5 GHz band. IEEE 802.11g standard provides optional data rates of up to 54 Mbit/s and is backward compatible with IEEE 802.11b devices in the 2.4 GHz. The IEEE 802.11n was not yet published and adds the utilization of MIMO (Multiple Input Multiple Output) technology, enabling maximum data rates of 248 Mbit/s (with two streams) in the 2.4 and 5 GHz bands.

The European Telecommunications Standards Institute (ETSI) has also contributed to the development and standardization of wireless networks through its project BRAN (Broadband Radio Access Network), namely the specifications for the HIPERLAN/2 (High Performance Radio Local Area Network Type 2), HIPERACCESS (High Performance Radio Access) and HIPERMAN (High Performance Radio Metropolitan Area Network). HIPERLAN/2 offers high data rates (27 Mbit/s, 54Mbit/s) to different networks and operates in the 5 GHz frequency band. HIPERACCESS is a fixed-wireless point-to-multipoint architecture planned to offer access to residential area or company premises with typical data rates of 25 Mbit/s. HIPERMAN is a fixed wireless access system operating at radio frequencies between 2 GHz and 11 GHz for residences and small and medium enterprises and is capable of non-line-of-sight operation supporting point-to-multipoint and mesh network configurations.

Figure 1.4 and Table 1.1 summarise the main characteristics of all systems presented formerly. In the next section are presented briefly other worldwide initiatives that contributed definitively to the evolution of mobile and wireless systems.

2. The R&D Activities Worldwide

The need for mobile broadband communications was identified some years ago during the EC RACE I programme (from 1988 to 1992) in which the mobile broadband systems and UMTS concepts have emerged. During the subsequent years and for what concerns mobile broadband systems, further and more specific research was carried out in another project called MBS[6] (Mobile Broadband System) during the RACE II programme [7]. Since 1996, the research activities have increased enormously and are going on in various parts of the world namely Europe, USA and Japan [8]. In Europe various projects

[6] MBS was also the name of a project where these concepts were first investigated.

were partially funded by the EC under the ACTS and IST R&D programmes. Research continues now under the IST programme and it will continue in the FP7 (seventh Framework Programme) for the period of 2007-2013.

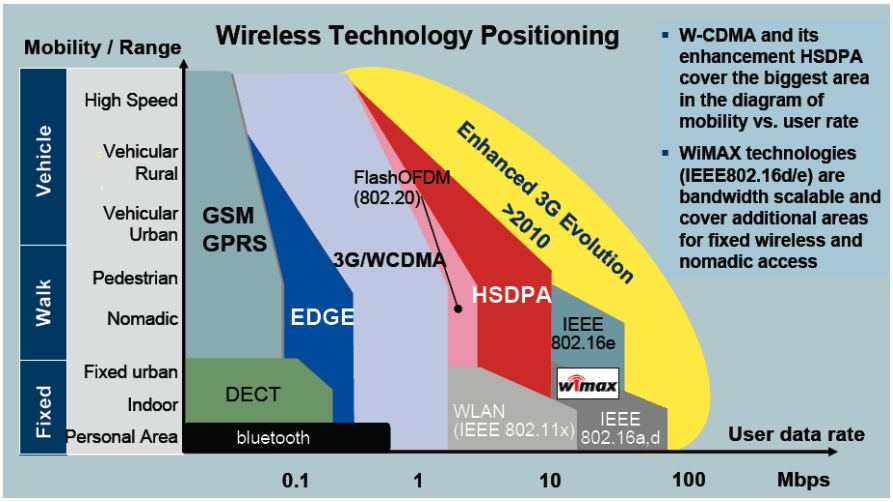

Figure 1.4: Mobility and data rates for current radio systems[7]

During the ACTS programme six main projects were accepted in this area, namely SAMBA (System for Advanced Mobile Broadband Applications), MEDIAN (Wireless Broadband CPN/LAN for Professional and Residential Multimedia), WAND (Wireless ATM Network Demonstrator), AWACS (ATM Wireless Access Communication System), ACCORD (ACTS Broadband Communication Joint Trials and Demonstrations) and SECOMS (Satellite EHF Communications for Mobile Multimedia). Out of the six projects, the first four addressed the mobile broadband systems terrestrial segments, the fifth the satellite component and the last one the possibility of integrating the terrestrial and satellite components.

For what concerns the terrestrial component of mobile broadband systems, MEDIAN objective was to evaluate and implement a high-speed WLAN supporting data rates up to 150 Mbit/s in indoor environments using the 60 GHz frequency band based on multicarrier modulation. WAND primary goal was to build a demonstrator in the 5 GHz band providing transmission capacity of up to 20 Mbit/s which included mobility management functions and AWACS target was to develop a demonstrator operating on

[7] Source: UMTS Forum.

the 19 GHz band (this frequency band is available in Japan for mobile broadband systems) with transmission rate of 34 Mbit/s in a TDD mode [9]. SAMBA was the only project addressing the mobile cellular broadband concept. Its main objectives were to develop and implement a prototype in the 40 GHz band to test and evaluate the main cellular functionalities, including radio handover and full duplex transmission capabilities of 34 Mbit/s [10] [11].

Standard	Family	Radio Tech	Downlink (Mbit/s)	Uplink (Mbit/s)	Notes
IEEE 802.16e	WiMAX	MIMO-SOFDMA	70	70	Quoted speeds only achievable at very short ranges, more practically 10 Mbit/s at 10 km.
UMTS W-CDMA HSDPA+HSUPA	UMTS/3GSM	CDMA/FDD	0.384 14.4	0.384 5.76	HSDPA widely deployed. Typical downlink rates today 1-2Mbit/s, ~200kbit/s uplink.
UMTS-TDD	UMTS/3GSM	CDMA/TDD	16	16	Reported speeds based on 16QAM modulation.
1xRTT	cdma2000 (2.5G)	CDMA	0.144	0.144	Obsoleted by EV-DO.
EV-DO 1x Rev. 0 EV-DO 1x Rev.A EV-DO Rev.B	cdma2000 (3G)	CDMA/FDD	2.45 3.1 4.9xN	0.15 1.8 1.8xN	N is the number of 1.25 MHz chunks of spectrum used. Not yet deployed.

Table 1.1: Main mobile technologies comparaison

The IST programme opened the door for more research activities funding new projects [12]. Examples are the BRAIN (Broadband Radio Access for IP based Networks), MIND (Mobile IP based Network Developments), PASTORAL (Platform and Software for Terminals: Operationally Re-configurable), TRUST (Transparently Re-configurable Ubiquitous Terminal), WIND-FLEX (Wireless Indoor Flexible High Bit rate Modem Architecture), OBANET (Optically Beam-formed Antennas for adaptive broadband fixed and mobile wireless access NETworks), BRAHMS (Broadband Access High data rate Multimedia Satellite), MATRICE (MC-CDMA Transmission Techniques for Integrated Broadband Cellular Systems), 4MORE (4G MC-CDMA Multiple Antenna System on Chip for Radio Enhancements) and WINNER I and II (Wireless World Initiative New Radio) [13].

The main objective of BRAIN was to provide a broadband extension to cellular systems, e.g. GPRS, EDGE and UMTS, for hot spots like airports, railway stations, campus areas, conference centres, etc., making it a true broadband multimedia IP-based radio access

technology [14]. The maximum user data rate per carrier is 20 Mbit/s and the radio interface is based on the HIPERLAN/2 standard. BRAIN access network is end-to-end IP for all real time and non-real time services. For seamless service provision in the entire coverage area, mobility functions were designed including intra and inter-system handover and the necessary QoS negotiations strategies.

Considering the new requirements of systems beyond 3G, such as the provision of seamless access to broadband services over a wide range of air interfaces and the utilisation of new business models for providing and running these services and the underlying networks, MIND project will extend the concepts of a broadband multimedia IP-based radio access technology. The research conducted by MIND included new network topologies like ad-hoc, self-organising networks, improved QoS support in IP mobile networks, enhancements of HIPERLAN/2 and investigations of spectrum requirements.

Re-configurable radio systems were addressed by the PASTORAL and TRUST projects. The first intends to provide a re-configurable, real-time platform for 3G mobile terminals based on re-configurable FPGA (Filed Programmable Gate Array) devices. The second addresses the same topic on the user perspective identifying the user requirements and needs as well as defining the system requirements, translating these requirements in technology requirements. It will investigate radio frequency architectures and circuits, baseband architectures, transceivers algorithms and other system level aspects such as spectrum sharing techniques, multimode monitoring and intelligent mode switching, radio resource allocation for software download and its security aspects.

WIND-FLEX studied a high bit-rate flexible and configurable modem architecture, which works in single-hop, ad hoc networks and can provide a wireless access to the Internet in an indoor environment where slow mobility is required. Bit rates from 64 kbit/s up to 100 Mbit/s (variable depending on the user needs and channel conditions) are considered in the band of 5 GHz, 17 GHz and 19 GHz. Flexibility and performance is attained by using a multicarrier modulation method with jointly optimised coding/decoding, multiple access method, diversity and equalisation.

OBANET project aims at studying, implementing and evaluating specific coverage area management strategies, using optical beamformers, as well as their associated technologies for performance optimisation in adaptive, fixed and mobile, broadband radio wireless access networks in the 40 GHz band.

BRAHMS addressed the satellite component and aimed to define a universal user access interface for broadband satellite multimedia services that is open to different satellite systems implementations, including GEO and LEO constellations. Two-way transmission for Direct-to-Office or Direct-to-Home multimedia services were addressed with bit rates up to 150 Mbit/s in the forward link and 20 Mbit/s in the return link. The use of IP-based satellite transmission was considered as a solution to convergence towards seamless broadband service provision.

The MATRICE project proposed innovative/cost-effective solutions for broadband component of 4G cellular systems, supporting QoS and high service rate capability in indoor and outdoor environments. The solution is based on MC-CDMA (Multi-Carrier Code Division Multiple Access) with capability of adaptation to fading channels, service requirements and channel loading conditions, utilising co-operatively space-time-coding, array processing, multi-user detection and interference cancellation techniques. The proposal concentrated on layers 1-3 and their optimisation for efficient support of IP and maximum compatibility with the 3G RAN.

In order to accommodate future services requiring high capacity, 4MORE project envisioned a broadband component with a maximum information bit rate of more than 2-20Mbit/s in a vehicular environment and possibly 50-100Mbit/s in indoor to pedestrian environments, using a 50-100MHz bandwidth. One of the most promising technologies for this broadband component is MC-CDMA which allows combining the merits of OFDM (Orthogonal Frequency-Division Multiplexing) with the ones of spread-spectrum techniques. 4MORE researched and developed an innovative architecture suitable for the advanced signal processing techniques involved in MC-CDMA. In order to validate this architecture, a cost effective, low power and integrated system solution for a 4G terminal was developed, employing multiple antennas.

WINNER I and II projects intended to look to future radio technologies for the definition of a new radio interface concept. The projects aim to develop a single ubiquitous radio access system adaptable to a comprehensive range of mobile communication scenarios from short range to wide area. The radio interface will support the challenging requirements of B3G systems. It will be scalable in terms of carrier bandwidth and carrier frequency range and it will allow the deployment in the current mobile frequency bands and potential new bands. The system will support a wide range of usage scenarios and radio environments providing a significant improvement in performance and QoS. It will optimise the usage of the radio resources through the exploitation of knowledge of the actual channel conditions, channel coding techniques optimised jointly with interactive receivers and multiple antennas technology. New networking topologies such as relaying will support cost-efficient deployments. Target data rates are 1Gbit/s for short range and 100 Mbit/s for wide range.

The research carried out by these projects has in common the fact that they intend to investigate techniques to increase the maximum transmission data rates in the radio interface (e.g. flexible and configurable modems, optical beamformers, etc.), permit the terminals access to various systems via re-configurable radio, integration of several radio access technologies for spectrum usage optimisation and promote the usage of end-to-end IP, enabling also the convergence of networks, for all real time and non-real time services, making mobile systems a true broadband multimedia IP-based radio access technology.

In terms of other international fora and bodies [15], WWRF (Wireless World Research Forum) aims to develop a common global vision for future wireless to drive research and standardisation. The IEEE runs many standards namely the IEEE 802 family addressing local, wide area networks technologies and short range communications as already mentioned in the previous section. At ITU the ITU-Radio and ITU-Telecommunications sectors have undertaken high-level vision work helping to facilitate global consensus on basic system concepts, a prerequisite to discuss and identify new spectrum for future systems.

In more regional terms [15], the FuTURE Forum of China aims at promoting exchanges and cooperation on B3G research and harmonising different views on the vision,

demands and trends of the next generation mobile communication systems. The mITF (Mobile IT Forum) of Japan was created to realize the 4G future mobile communication systems and services. Finally 3GPP continues working towards the evolution of current mobile systems being now working on the so called LTE (Long Term Evolution). Goals include improving efficiency, lowering costs, improving services, making use of new spectrum opportunities and better integration with other open standards. Download rates of 100 Mbit/s and upload rates of 50 Mbit/s for every 20 MHz of spectrum are expected to be reached. The LTE project will contribute to Release 08 of the UMTS standard. HSDPA and HSUPA technologies will be replaced by the HSOPA (High-Speed OFDM Packet Access) that makes use of OFDM and MIMO. This technology is also referred in the literature as Super 3G.

3. Future Mobile Systems Applications and Challenges

Users may care for the terminal capabilities and functionalities but certainly they are not concerned about the technology or standards used to provide the service. What is really important for the user is a total seamless transition between environments, good quality, useful services at low cost and a complete freedom to choose the network and service providers [16]. On the other hand the experts in mobile telecommunications play the complementary role since they have to design and select the most suitable technologies to fulfil and anticipate the users' needs. Whatever the role, all agree that there is a need to further evolve mobile communication systems.

UMTS and its enhancements currently available will not be able to support broadband services due to the maximum transmission rates limits that are only achievable at a very short range and under restricted mobility conditions. Capacity might become an issue since multiple users may want to run specific broadband application with acceptable quality in the same cell. A new set of mobile systems access technologies able to provide transmission capacities up to 100 Mbit/s in wide range and 1Gbit/s in short range environments to mobile users will have to emerge. This target was defined by ITU and may be considered one of the 4G systems characteristics [17]. Such a high data rate requires smart and efficient usage of spectrum and higher frequency bands for operation with all the associated technical challenges [11] [18].

Further research and technology developments will contribute to the convergence of the various access technologies leading to the seamless access paradigm and the core network evolution towards the "all IP" concept reducing the network deployment and operation costs (CAPEX - Capital Expenditure and OPEX - Operational Expenditure). Moreover, the terminals will evolve towards reconfigurability [19] and will be much more advanced multimedia devices. All these ingredients will strongly contribute to bring the 4G to the market in the few years ahead where the new paradigms will become a reality. Figure 1.5 summarises the evolution of mobile communications systems.

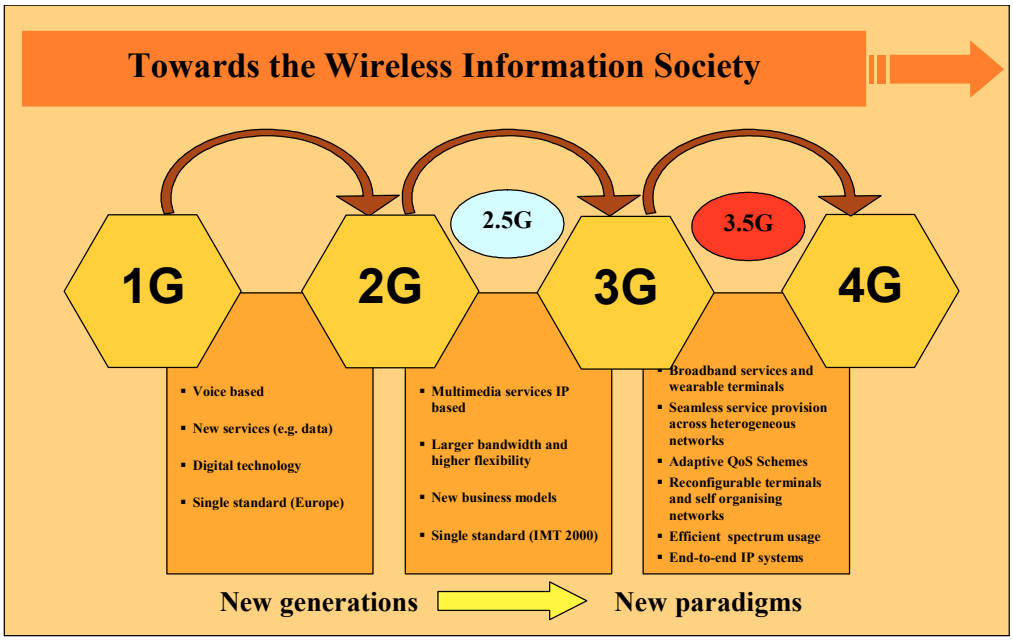

Figure 1.5: Mobile communication systems evolution

In Figure 1.6 possible broadband applications are shown being some generic and others more related with professional usage. For instance, wideband Internet access must be an example of massive utilisation given the most recent penetration figures, including the popularity of watching videos that Web 2.0[8] enables and Web 3.0 will extend. In [20] is presented a comprehensive description and classification of broadband services according to ITU-T I.211 recommendation, namely, conversational, messaging, retrieval, broadcast and cyclical services.

[8] Web 2.0 and Web 3.0 are the next generations of the Internet.

On the professional side the rescue process is, undoubtedly, an interesting candidate for using mobile broadband since it will allow communication between rescuers on the scene of an accident and co-ordinators of the rescue process and medical personnel located in hospitals. Personnel at the scene will also be provided with access to the information systems as if they were in the medical centre. Mobile equipment available at an accident location will allow remote access to the centralised information system of the rescue system and remote diagnosis by qualified doctors. The technical issue in this usage is the transfer and display of high definition images and video conferencing in order to get advice or take a major decision.

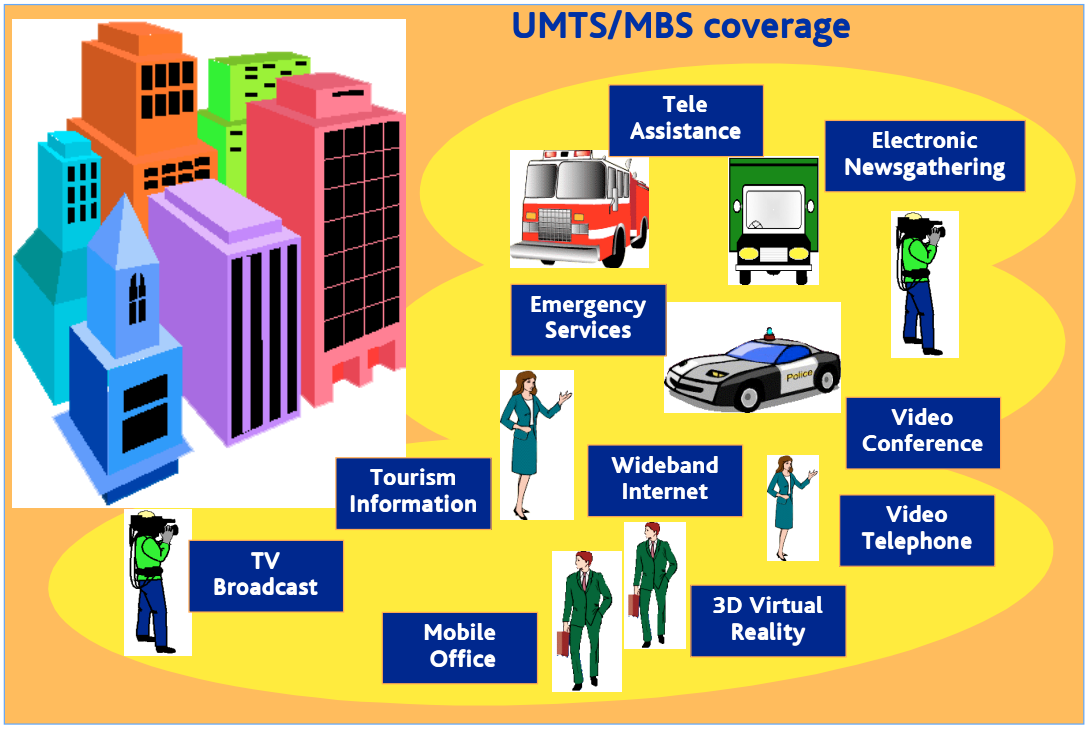

Figure 1.6: Mobile cellular broadband applications

Another example is the broadcast industry because high quality digital video signals are fundamental to most television programme making operations, and so there is a pressing need to add wireless mobility. Electronic newsgathering is also an activity that would also benefit. A public mobile broadband system would allow the team to send back pictures to the studio either directly from a wireless camera or after editing, from a news vehicle. It would be possible to have live inserts into a news programme without any advance planning, as we have today but just with voice.

Since mobile broadband systems will use millimeterwave frequency bands, the attenuation of the radio signals is higher, leading to a smaller cell size, ranging from a few to a thousand metres for the terrestrial segment. Hot spots like airports and city centres may have broadband coverage but a continuous coverage may not be provided, at least during its first deployment phase. Mobile broadband systems are seen as providing complementary capacity/coverage in indoor and outdoor environments (see Figure 1.7) for high density traffic areas. In areas where various access networks are available the concept of "always best connected" should be applied. This imposes the need for MTs to roam between different frequency bands and standards (multiband and multimode MTs).

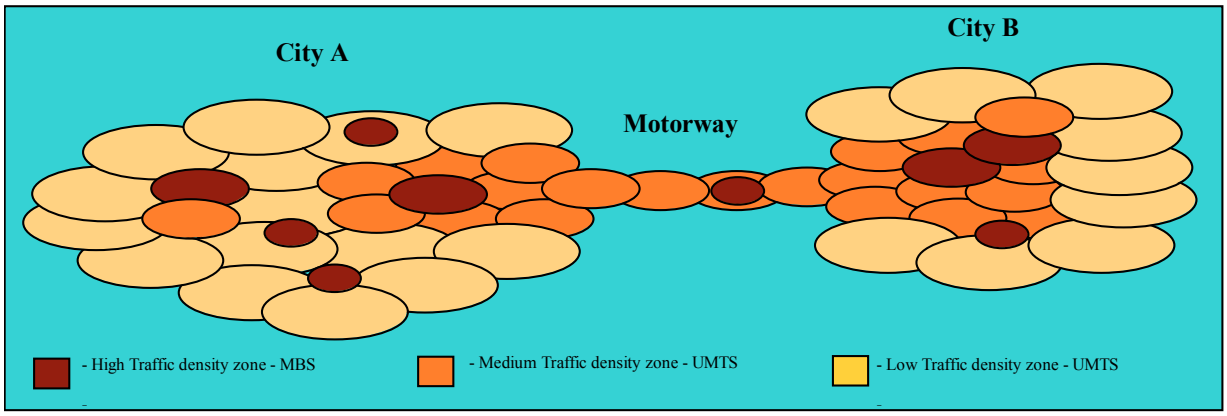

Figure 1.7: MBS and UMTS coverage scenario

Various candidate techniques are being investigated for the radio interface of future mobile broadband systems. Although the prototype developed and used in this thesis uses single carrier modulation, many researchers are considering multi-carrier (MC) modulation techniques. Examples of technique that use MC are: OFDM, OFDMA (Orthogonal Frequency Division Multiple Access) or the combination of OFDM and CDMA, such as, MC-CDMA, MC-DS-CDMA (Multi-Carrier Direct Sequence Code Division Multiple Access) or hybrid techniques like SS-MC-MA (Spread Spectrum Multi Carrier Multiple Access). The general principle behind these techniques is the splitting of the data in various parallel streams that are then transmitted in different frequency carriers. MC techniques were invented many years ago and are already in use by some commercial systems (e.g. WLANs and WiMAX) being still a hot research topic for future mobile systems.

SC-FDMA (Single carrier FDMA) modulation is still under consideration for the uplink of 3GPP LTE since it has a lower peak-to-average power ratio that greatly benefits the MT in terms of transmit power efficiency but employing equalisation in the frequency domain.

The utilisation of multiple antennas in the BS and the MT is also under research and takes advantage of the decorrelation of the radio signals received by the different antennas. This fact enables the increase of the channel capacity and the complexity of the transceivers, being more tolerable at the BS side. This is to say that the traditional channel SISO (Single Input Single Output) is becoming MISO (Multiple Input Single Output), SIMO (Single Input Multiple Output) or MIMO channel. These new type of channels can in fact be considered as a combination of several SISO channels affected by the parameters of the receiving and transmitting antennas arrays. These radio channel models are defined as vector channel models.

Antenna beamforming techniques can also be used to make spatial filtering of the radio signals.

The radio interface is a crucial part of any mobile communication system and the characterisation of the mobile radio channel is fundamental for the optimised design of new air interfaces, in particular for mobile broadband systems. This thesis intends to give a contribution to the characterisation of the radio channel in the 40 GHz frequency band using frequency domain measurement techniques as well as to test the performance of a mobile broadband system prototype namely the radio interface and radio handover performance, implemented for the first time.

The current state of the art on modelling of the radio channel is presented in the next chapter.

4. Motivation and Objectives

Research in mobile broadband systems is going on in various parts of the globe namely Europe, the USA and Japan. In Europe, a large number of project, described in section 2, gathered support from the EC during the various framework programmes. These projects

addressed different aspects of 4G systems and were the main motivation for the work presented in this thesis.

The work here presented was made possible thanks to the utilisation of a mobile broadband system prototype with innovative characteristics namely, maximum transmission data rates, frequency of operation, transmission range, achieved mobility and implemented protocols developed in the framework of the SAMBA[9] project. The author of this thesis integrated the team of collaborators from the different project partners that have actively contributed to the SAMBA project activities and had an important contribution at coordination, prototype specifications definition, planning and execution of all the field trials that took place in the Aveiro city, Portugal. The processing of the measurement results and the execution of the field trials required the involvement of several collaborators mentioned in the Acknowledgments section. The manufacturing of the prototype was performed by several partners of the project consortium.

A common characteristic of all mobile radio systems is the fact that they incorporate an air interface that interconnects the terminals and the fixed part of the mobile network. Specifically for the cellular mobile broadband systems, large spectrum bands are required to transmit the signals resulting from the usage of broadband applications while users are on the move. It is therefore mandatory and vital to make a deep characterisation of the millimeterwave radio channel, in indoor and outdoor environments. This knowledge is important for the selection of the best techniques that mitigate the mobile radio channel impairments. These aspects are the core of this thesis.

The objectives of the work presented in this thesis are to:

- Characterize the broadband mobile radio channel behaviour in the 40 GHz band and evaluate the main parameters.
- Evaluate the performance of the prototype in typical indoor and outdoor scenarios and conclude on the suitability of the selected technical options.

[9] The author's affiliation is PT INOVAÇÃO SA, the SAMBA project Coordinator.

- Evaluate different system configurations and analyse its impact on the cells coverage area.
- Evaluate the suitability of lens antennas technology for mobile broadband systems.
- Test the mobility aspects of the system and evaluate the radio handover algorithm.
- Analyse deeply the behaviour of the delay spread and coherence bandwidth of the channel.
- Analyse by simulation other typical scenarios and perform the validation of the measurements using suitable simulation models.

All these aspects were studied and results are presented in chapters 6, 7, 8 and 9.

5. Thesis Contents

This thesis is divided in ten chapters. The main purpose of the first chapter was to present an overview of mobile telecommunications evolution and the current state-of-the-art in the area. Several challenges were identified and the main projects addressing this area, co-funded by the EC were also described to frame the work developed.

Chapter 2 shows the necessary background information about radio propagation for the characterisation of narrowband and wideband channels. The various fading types, the Bello functions and the main parameters that enable the characterisation of radio channel are presented.

Chapter 3 presents a description of the aspects that should be taken into account when designing mobile broadband systems, main problems and challenges are identified and main options listed. The various types of fading are revisited and suitable mitigation techniques proposed.

The characteristics of the cellular broadband system prototype used in the experiments are described in chapter 4. This includes the system architecture, the RF modules, baseband modules, air interface, protocols and the handover algorithm.

The prototype was evaluated in typical indoor and outdoor scenarios. Chapter 5 describes the characteristics of these scenarios, which constitute important information for the

interpretation of the measurement results. The involved materials, the size and specific shape are of primary importance when dealing with the characterisation of the radio channel. The monitoring system specially designed to collect information during the realisation of the experiments is also presented as well as the calibration procedures to ensure the correct operation of the system.

Chapter 6 aggregates all the results related with the experiments performed in the outdoor scenario. A typical urban canyon type street was selected. This has enabled the test of various base station antenna heights, tilting angles, speeds of the MT, LoS and non LoS operation and penetration of the radio signals in transversal streets. Path loss modelling was also performed for this scenario. Other typical scenarios were evaluated only by simulation using a ray tracing simulation tool.

The indoor scenario results are presented in chapter 7. Similar tests were performed as for the outdoor scenario plus radio handover studies. The coverage aspects of different system configurations in terms of physical location of the base stations were evaluated. Particularly for the handover studies, the two cells coverage and transmission performance was first investigated individually and then compared with the results obtained with the handover procedure activated. The chapter also includes simulation results for other system configurations within the same indoor scenario.

Wideband radio channel characterisation results are presented in chapter 8. This chapter shows for indoor scenarios only the measurements concerning channel impulse response in different locations. Since a frequency domain method was used, the MT and the surrounding environment had to be stand still during the measurements. Comparisons with results obtained via simulation are also presented.

Chapter 9 present the measured and simulated results related with the delay spread and the coherence bandwidth parameters. The cases where the violation of Fleury's lower bond occurs are analysed and justifications presented. An analysis of the approximation formulas results usually presented in the literature is also presented.

Finally the last chapter aggregates the various conclusions of the results presented in the various chapters and shows possible future directions for new studies and work to be performed in this area.

6. Original Contributions

According to the author's knowledge this thesis presents the following original contributions:

- Characterization of the broadband mobile radio propagation channel in the 40 GHz frequency band.
- Evaluation of the transmission performance of a 34 Mbit/s radio link by using a state-of-the-art cellular broadband system prototype.
- Lens antennas radiation pattern shaping impact on the radio channel characteristics, transmission and coverage area impact.
- Evaluation of the radio handover algorithm for a 34 Mbit/s full duplex link.
- Relationship between the channel delay spread and coherence bandwidth for various propagation scenarios and verification of the Fleury lower bound principle.
- Impact of the simulation models complexity on the accuracy of the results and validation of the performed measurements in the 40 GHz band.

7. Summary and Conclusions

This chapter presents an introduction to the mobile communications area as well as its evolution through the times. After a description of the early steps, in terms of the scientific discoveries that proved the existence of the radio waves, it summarises the main characteristics of 1G, 2G and 3G systems. The 1G systems only permitted to transmit voice but currently multimedia applications are possible putting in the MT capabilities only available in personal computers in the past. Actually, MTs are more and more small computers with several integrated devices, as for instance digital cameras, various communication ports, and colour and touch screen displays. A continuous increase on the maximum data rates was possible due to the strong technology evolution supported by a heavy R&D investment in Europe and worldwide.

Since WLAN and WMAN systems play today a very important role in the field of wireless communications, these systems are also presented. The IEEE in USA has played

a very important role in this field since it has contributed to the definition of the most popular wireless systems. The main systems are described as well the latest evolutions. For what concerns WiMAX, a WMAN system that started by addressing the fixed broadband access market segment, it may play an important role since the mobility feature was added to the standard, enabling a direct competition with mobile networks, or probably just a complement to the coverage area and provided services. The market will decide.

In order to contextualise the topics and research activities going on in the world and the entities that are or have contributed to, a description of the main projects at European level are presented, focusing only on those that are more related with the specific area addressed by this thesis. Many others are available but addressing applications, user interaction issues or network aspects. A particular project named SAMBA is of primary importance since it has enabled the work here presented. This project was the only one supporting the mobile broadband cellular concept. Worldwide activities by international bodies are also summarised showing the global efforts in the evolution of mobile and wireless communications.

The main challenges that B3G and particularly broadband systems will face were presented. Possible applications were also described showing the impact that these technologies may have at professional level, mainly medical and TV applications contributing to save lives and increasing the amount and readiness of the information available to citizens. The continuous increase of the transmission rates will be necessary to improve the user experience and comfort when accessing to broadband applications or web services. The current goal is 1 Gbit/s for short range and indoor environments and 100 Mbit/s for long range and outdoor environments. Various candidate techniques are being investigated for the radio interface of future mobile broadband systems namely multi-carrier modulation techniques, e.g. OFDMA or the combination of OFDM and CDMA. However, single carrier modulation is still under consideration for the uplink of 3GPP LTE since it has a lower peak-to-average power ratio that greatly benefits the MT in terms of transmit power efficiency and employing equalisation in the frequency domain. The utilisation of multiple antennas in the BS and the MT is also under research and takes advantage of the decorrelation of the radio signals received by the different

antennas (MIMO channels). This fact enables the increase of the channel capacity, being more tolerable at the BS side due to the increase on the transceivers complexity. Antenna beamforming techniques can also be used to make spatial filtering of the radio signals. Worldwide R&D activities will continue addressing these techniques.

In this chapter are also presented the motivation, objectives of the research addressed, the thesis contents and the original contributions.

Mobile and wireless communications technologies have been adopted by the users rapidly showing its usefulness. Social impacts are already visible being hard to imagine the world without these technologies. In professional terms, a boost in productivity was also achieved, for instance in managing more efficiently the sales force or field engineering teams. This is in fact good news for businesses and companies. In the public sector the advantages are also numerous, having a direct impact in the citizens satisfaction. These facts are corroborated by an article published by ComputerWeekly.com by Stephen Pritchard on 18th of June 2007 (www.computerweekly.com). The future of mobile and wireless communications is bright!

8. References

[1] Qi Bi, G. I. Zysman and H. Menkes, "Wireless Mobile Communications at the Start of the 21st Century", IEEE Communications Magazine, pp. 110-116, January 2001.

[2] M. Zeng, A. Annamalai,Vijay K. Bhargava, "Recent Advances in Cellular Wireless Communications", IEEE Communications Magazine, Vol. 37, No. 9, pp. 128-138, Sep. 1999.

[3] Yi-Bing Lin, H. C.-H. Rao, I. Chlamtac, "General Packet Radio Service (GPRS): Architecture, Interfaces and Deployment", WILEY Wireless Communications & Mobile Computing, Vol. 1, No. 1, Jan-Mar 2001.

[4] 3GPP, http://www.3gpp.org.

[5] J. F. Huber, D. Weiler and H. Brand, "UMTS, the Mobile Multimedia Vision for IMT-2000: a Focus on Standardisation", IEEE Communications Magazine, pp. 129-136, September 2000.

[6] IEE Electronics Communications Engineering Journal, Special Issue on the Universal Mobile Telecommunications System, Vol. 13, No. 3, June 2000.

[7] L. Fernandes, "Developing a System Concept and Technologies for Mobile Broadband Communications" IEEE Personal Communications Magazine, Vol. 2, No. 1, pp. 54-59, Feb. 1995.

[8] J. Mikkonen, Ciotti Corrado, Cengiz Evci, Max Prögler, "Emerging Wireless Broadband Networks", IEEE Communications Magazine, Vol. 36, No. 2, pp. 112-117, Feb. 1998.

[9] M. Prögler, C. Evci, M. Umehira, "Air Interface Access Schemes for Broadband Mobile Systems", IEEE Communications Magazine, Vol. 37, no. 9, pp.106-115, Sept. 1999.

[10] M. Dinis, V. Lagarto, M. Prögler, J. T. Zubrzycki, "SAMBA: a Step to Bring MBS to the People", ACTS Mobile Communications Summit '97, Aalborg, Denmark, Oct. 1997 (see also http://samba.ptinovacao.pt).

[11] Manuel Dinis and José Fernandes, "Provision of Sufficient Transmission Capacity for Broadband Mobile Multimedia: a Step Towards 4G", IEEE Communications Magazine, pp. 46-54, August 2001.

[12] European Commission FP5-IST programme projects description, http://www.cordis.lu/ist/projects.htm.

[13] Marco Annoni et al. "Radio Access Networks beyond the 3rd Generation: a First Comparison of Architectures from 4 IST Projects", IST Mobile Communication Summit 2001, Barcelona, Spain 9-12 September 2001.

[14] Josef Urban et al, "BRAIN – an Architecture for a Broadband Radio Access Network of the Next Generation", WILEY Wireless Communications & Mobile Computing, Vol. 1, No. 1, Jan-Mar 2001.

[15] Rahim Tafazolli (Editor), "Technologies for the Wireless Future – Volume 2", John Wiley & Sons Ltd. 2006.

[16] T. Tjelta, M. Annoni, L. Tokarchuk, A. Nordbotten, E. Scarrone, J. Bigham, C. Adams, S. Bizzarri, M. Dinis, K. H. Craig, "Future broadband radio access systems for integrated services with flexible resource management", IEEE Communications Magazine, pp. 56-63, August 2001.

[17] L. M. Correia and R. Prasad, "An Overview of Wireless Broadband Communications", IEEE Communications Magazine, pp. 28-33, January 1997.

[18] Nobuo Nakajima and Yasushi Yamao, "Development for 4^{th} Generation Mobile Communications", WILEY Wireless Communications & Mobile Computing, Vol. 1, No. 1, Jan-Mar 2001.

[19] Enrico Buracchini, "The Software Radio Concept", IEEE Communications Magazine, pp. 138-143, September 2000.

[20] Fernando Velez, "Aspects of Cellular Planning in Mobile Broadband Systems", PhD Thesis, Chapter 2, Universidade Técnica de Lisboa – Instituto Superior Técnico, December 2000.

2nd Chapter

Narrowband and Broadband Mobile Radio Channel Characterisation and Modelling

1. Introduction

The adequate characterisation of the mobile radio channel is of primary importance since it enables the selection of the most suitable mitigation techniques to be implemented by the mobile systems radio interface.

The mobile radio channel characteristics can differ considerably from the radio channels encountered in microwave radio links or satellite systems. Due to the MT motion, LoS conditions cannot be guaranteed. Instead one must rely on the various scatters to provide coverage in shadow areas.

The presence of objects obstructing and scattering a radio wave leads to multiple waves arriving to the receiver. These waves have different amplitudes, phases and angles of

arrival and can cause either constructive or destructive interference depending on their relative phase. Moreover, due to the motion, the received signals are affected by Doppler shift, which mainly depends on the relative position and speed of the MT. These phenomena cause fast variations of the received signal envelop [1][2][3].

The full radio wave propagation properties in a given scenario are hard to describe exactly due to the high number of significant parameters and complex relationships [4]. For that reason, simplified but yet useful channel models are used based on a limited number of input parameters to predict the large-scale (path loss and shadowing) and small-scale fading. These channel models can be either physical, empirical or hybrid.

Physical models try to describe or are based on the actual propagation mechanisms, as exactly as possible, using well-known physical laws [5] [6] [7]. Accurate results need a good modelling and a very good knowledge of the propagation environment. The main disadvantage is the high demand of computational resources being many times cumbersome and not practical. Empirical models are a good compromise where the propagation characteristics are described via simplified functions based on statistics obtained through real measurements. A fairly good accuracy can be obtained if the models are applied to similar scenarios to those where the measurements were made and for the same frequency bands.

This chapter starts with a description of the free space propagation and the basic propagation mechanisms. The simplest mobile radio channel, based on the direct path and single reflection is introduced to show the effects of multipath propagation and the high frequency approximation based on the application of the geometric optics. The various types of fading caused by the path loss, shadowing, multipath propagation and the variability of the mobile radio channel are identified. The Bello functions are introduced to describe the broadband channel, which suffers from frequency selective fading and spectrum broadening due to the Doppler shift effect. The autocorrelation functions are also presented and the main parameters which are used to characterise the mobile radio channel are also derived. An extension of the scalar propagation models to vector models suitable for SIMO, MISO and MIMO type radio channels is also presented.

2. Mobile Radio Channel Propagation

The free space propagation law is well known and defined by (2.1) where P_{Rx} and P_{Tx} are the received and transmitted power, G_{Tx} and G_{Rx} are the Tx (Transmitter) and Rx (Receiver) antennas gains, d is the distance between the Tx and Rx and λ is the wavelength of the transmitted radio wave.

$$P_{Rx} = P_{Tx}\, G_{Tx}\, G_{Rx} \left(\frac{\lambda}{4\pi\, d} \right)^2 \qquad (2.1)$$

For most radio channels, where signal propagation takes place in the atmosphere and near the ground, the free space propagation model is inadequate to describe the channel and predict the system performance, since it assumes the channel free of any object that might absorb or scatter radio frequency energy and that the atmosphere behaves as a perfectly uniform and non-absorbing medium [8] [9]. In reality, mobile radio signals are affected by large-scale (path loss and shadowing) and small scale fading. Figure 2.1 illustrates and summarises the various contributions that must be taken into account when estimating a link budget for a narrowband mobile radio system. The shadowing effect is usually modelled by the log-normal distribution. The Rice and Rayleigh statistical distributions are presented latter.

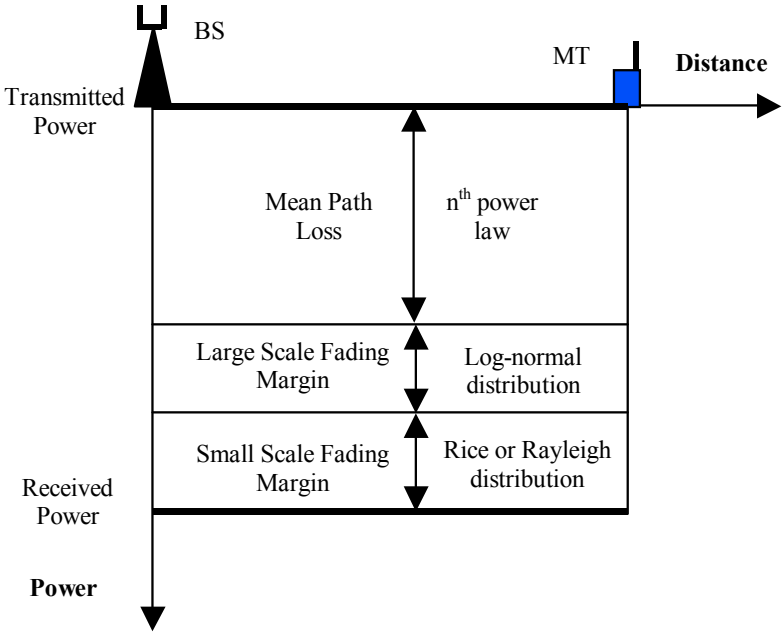

Figure 2.1: Power budget components for a mobile radio link

The application of GO (Geometric Optics) enables the derivation of physical models for the radio channel based on the ray tracing technique [10]. These models are usually applicable when the objects dimensions that compose the propagation environment are large relatively to the wavelength and the scenario is not too complex since it may lead to the need of a huge computer processing power. GO assumes an infinite frequency for the propagation signal, and hence, the dissipating energy can be considered to be radiating in infinitesimally small rays that travel in straight lines, provided that the refractive index is constant. In GO only direct reflected and refracted rays are considered and consequently abrupt transitions areas occur, corresponding to the boundaries of the regions where these rays exist. The GTD (Geometrical Theory of Diffraction) [11] and its uniform extension, the UTD (Uniform GTD) [12][13], complement the GO theory by introducing a new type of rays: the diffracted rays. The purpose of these rays is to remove the field discontinuities and to introduce proper field corrections, especially in the zero field areas predicted by the GO.

In fact, the radio waves propagate based on three mechanisms: reflection, diffraction and scattering leading to the existence of multiple paths between the receiver and the transmitter, particularly in mobile communication systems, each of them carrying a signal arriving to the receiver at a different instance of time [1]. This phenomenon is known as multipath propagation and can cause fluctuations in the amplitude, phase and angle of arrival of the received signal, leading to multipath fading. Figure 2.2 shows the basic propagation mechanisms.

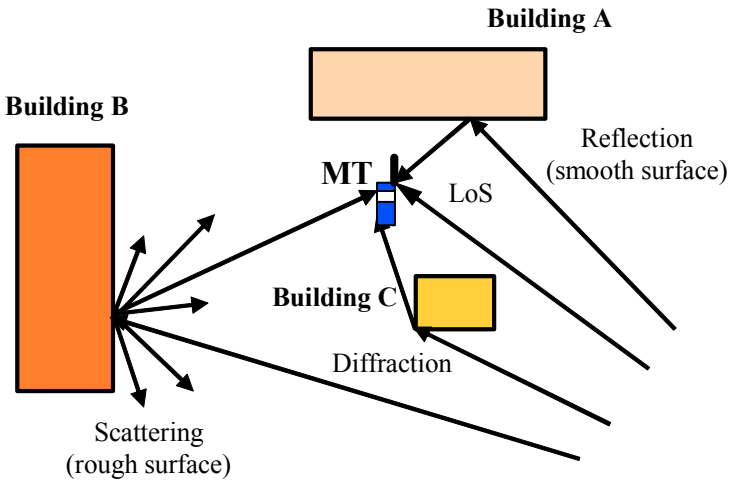

Figure 2.2: Propagation mechanisms

Reflection occurs when a radio wave hits a smooth obstacle whose dimensions are considerably larger than the wavelength of the incident wave. A reflected wave can either decrease or increase the signal level at the reception point. In cases where many reflected waves exist, the received signal level tends to be very unstable.

Diffraction happens when an obstacle whose dimensions are considerably larger than the wavelength is impinged by a radio wave in its edges where the radio wave is bended and scattered in different directions. The effect of this phenomenon in the millimetrewave frequency band for 50 and 60 GHz is reported in [14] and [15], respectively.

Scattering has similar effects as diffraction generating however radio waves in a much greater number of directions. It occurs when the radio wave impinges on either a large rough surface or any surface whose dimensions are on the order of the wavelength or less, causing the reflected energy to spread out in many directions [16].

Based on the above presented facts, the wave-front can be modelled by a ray (n) whose complex received field amplitude E_{rn} is defined by (2.2) [17].

$$E_{rn} = E_0 \, f_{tn} \, f_{rn} \, A_S(\zeta_n) \left\{ \prod_j R(\gamma_{nj}) \prod_k T(\gamma_{nk}) \prod_l A_l(s', s) \; D_l(\theta_{nl}) \right\} \frac{e^{-jkd}}{d} \tag{2.2}$$

E_o represents the reference field, f_{tn} and f_{rn} the transmitting and receiving antenna field radiation patterns in the direction of the nth ray, Rj the reflection coefficient for the j reflector, T_k the wall transmission coefficient for the k^{th} transmission and D_l the diffraction coefficient for the l^{th} diffracting edge. The diffraction coefficients are multiplied by a factor $A_l(s',s)$ which determines the correct spatial attenuation of the diffracted rays. e^{-jkd} is the propagation phase factor due to the path length d.

Since several rays arrive to the receiver due to multipath propagation, the resulting amplitude of the electric field is obtained summing coherently the contributions of all the received rays. In the Annex A, a description of the algorithm that can be used to calculate all the paths between the transmitter and receiver is presented as well as the respective addition of the electric field components [18].

The simplest mobile radio channel model comprises a LoS path and a single reflection on the conducting and flat earth surface between the transmitting and receiving antennas. Norton and Bullington have worked out this problem and based on the direct, reflected and surface wave concepts, the following formula has been derived for the electric field strength at the receiving antenna [3] [19]:

$$E_{MT} = E_{dMT}\left(1 + \rho e^{j\Delta} + (1-\rho) A e^{j\Delta} + ...\right) \qquad (2.3)$$

where E_{dMT} is the field strength at the receiving antenna due to the direct wave. Within the expression brackets, the first term represents the direct wave, the second term the reflected wave, the third term the surface wave and the remaining terms represent the induction field and secondary effects of the ground. The reflection coefficient of the ground ρ depends on the angle of incidence, the polarisation of the wave and the ground characteristics as shown in the Annex B. The symbol Δ represents the phase difference between the reflected and direct paths and A the surface attenuation factor that depends on the frequency, polarisation and the ground characteristics.

Knowing that the square of the electrical field strength envelop $|E|^2$ is proportional to the signal power and using the relation expressed by (2.3) for the received electrical field strength, the following formula can be derived for the received signal power level:

$$P_{MT} = P_{BS}\left[\frac{\lambda}{4\pi d}\right]^2 G_{BS}\, G_{MT} \left|1 + \rho e^{j\Delta} + (1-\rho) A e^{j\Delta} + ...\right|^2 \qquad (2.4)$$

$|E_{dMT}|^2$ is the maximum useful power that can be delivered to a MT matched receiver in the free space at distance d as shown by Friis in (2.1). The A factor can be neglected for distances a few wavelengths above the earth. Considering the approximations $\rho = -1$, cos (x)≈1 for small arguments and if $(h_{BS} + h_{MS})/d$ is sufficiently small, (2.4) can be approximated by (2.5) where h_{BS} and h_{MT} are the height of the BS and MT antennas, respectively. For frequencies above 100 MHz, vertical polarisation and considering an "average" type of earth surface, ρ exceeds 0.9 for angles less than 10º above the horizon. For horizontal polarisation above 100 MHz, ρ exceeds 0.5 for angles less than 5º. However, ρ figures exceeding 0.9 can only be obtained for angles in the order of a degree or less [19].

$$P_{MT} = P_{BS}\, G_{BS}\, G_{MT}\left[4\left(\frac{\lambda}{4\pi d}\right)^2 \sin^2\left(\frac{2\pi h_{BS}\, h_{MS}}{\lambda d}\right)\right] \qquad (2.5)$$

Figure 2.3 shows the path loss comparison obtained with the free space law given by equation (2.1), the two-ray propagation model given by equation (2.5) and d^{-4}, as a function of the distance, considering the following conditions: λ=0.0075 m, h_{BS}=10 m and h_{MT}=2 m. It can be observed that the power decreases with d^{-2} until the break-point (given by 4 h_{BS} h_{MT}/λ), and then for distances approximately larger than 10 600 m (when the approximation of sin x ≈ x starts being valid in (2.5)) the signal starts decreasing[1] with d^{-4}. Mobile broadband systems use small size cells due to the high attenuation in the millimeterwave bands and therefore tend to decay with slops more near two than four when operating in LoS conditions.

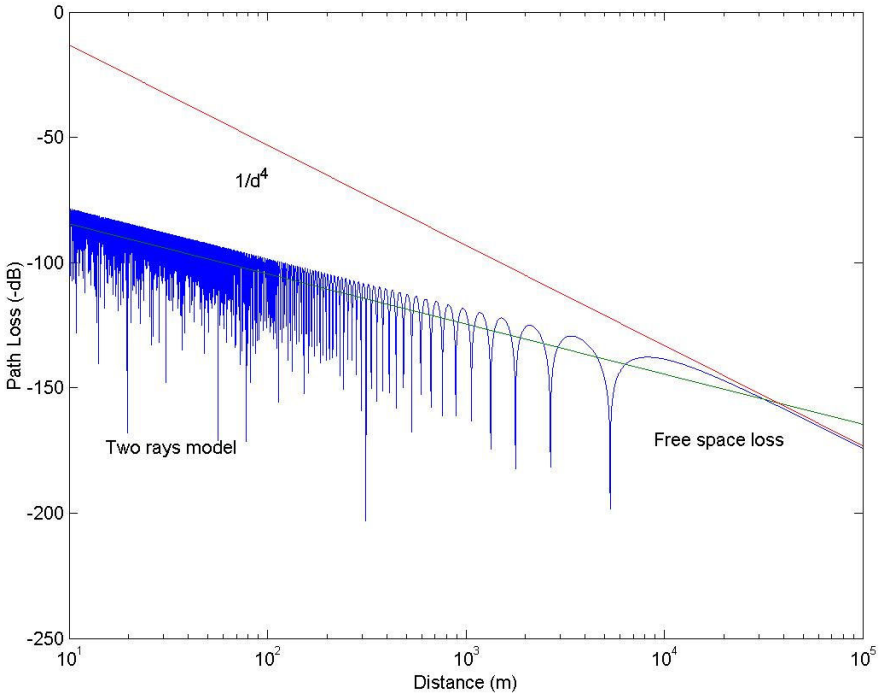

Figure 2.3: Comparison of free space and the two-ray propagation models

The accurate characterisation of the mobile radio propagation channel requires the need of more complex models taking into consideration a larger number of rays.

1 Typical values for the path loss nth power law in mobile radio channels range from 3 to 5.

The characterisation of the radio channel can also be done empirically (or statistically) [4] [5]. In the literature are available many empirical propagation models to predict path loss. In [4] a summary of these models is presented. Since they depend on the propagation environment and type of cell they are usually defined for three different types: macrocells, microcells and picocells. Moreover, the models can have different variants or parameters according to the kind of environment they are applied namely indoor, urban, suburban and open or rural areas.

Macrocells are typically used in suburban and rural areas. The range of these cells can go from a few hundred meters to several kilometres. The BS antenna is located well above the roofs or other obstacles. The MT speed is usually high reaching more than 300 km/h in high speed trains. Microcells are used in urban areas or hot spots. They range from a few tens to a few hundred meters. The BS antenna is usually located below the roof tops and the speed of the MT can reach 50 km/h. Picocells are installed in indoor environments like train stations, shopping malls, airports, etc. The speed of the MT is low typically 3 km/h (walking speed). In the millimeterwave frequency band typically only microcells and picocells can be used due to the high attenuation.

Radio waves are also affected by oxygen, water vapour and rain absorption, which is dependent on the frequency band. For instance, in the 40 GHz band the oxygen and water vapour attenuation is less than 0.1 dB/km. Rain attenuation can achieve 10 dB/km under severe rain conditions. Moreover, rain causes the depolarisation of the transmitted signal due to the medium anisotropy however for mobile communications this phenomenon is usually negligible [1] [8]. In [20] a study was performed regarding the impact of these phenomena for the 40 GHz frequency band in the Aveiro city based on rain and water vapour measurements collected for the years 1993 to 1999. Considering a distance of 250 m from the BS (typical cell size in cellular broadband systems), the impact of rain in terms of attenuation was limited to about 1.7 dB. The effects of the water vapour were find to be negligible, as well as the oxygen, contributing with a total attenuation of 0.088 dB.

3. Radio Signals Small-Scale Fading

Path loss, one of the components of large-scale fading[2], was addressed in the previous section. The other component is usually called shadowing and represents the average signal power variation about the nominal value given by the path loss model, due to motion over large areas and is a consequence of prominent terrain contours (e.g. buildings, hills, etc.) existing between the MT and the BS. The characterisation of this phenomenon gives information about how the signal strength changes about the mean value path loss [4] and is usually described by a log-normal distribution. Equation (2.6) translates these facts into a mathematical formulation where L_s (d_0) is the average reference path loss at distance d_0 (e.g. 100 m), n the path loss exponent and X_σ denotes a zero-mean Gaussian random variable which characterises the shadowing effect.

$$L(d)\big|_{dB} = L_s(d_0)\big|_{dB} + 10n\log_{10}(d/d_0) + X_\sigma\big|_{dB} \qquad (2.6)$$

This section describes the small-scale fading that is characterised by a high rate of changes in the signal amplitude and phase and is caused by multipath propagation and small changes in the MT position relatively to the BS (e.g. half-wavelength). This fading manifests itself in two ways: time spreading of the signal due to multipath (i.e. time dispersion) and time-variant behaviour of the channel due to MT or obstacles motion (i.e. frequency Doppler spreading). Therefore, on top of the attenuation suffered by the signal as a function of the distance to the BS (nth power law) and obstacles/clutter (shadowing) or the specific conditions existing in the atmosphere, the received radio signal also contains fading caused by the channel time variability and multipath propagation.

A good approximation for the complex low-pass envelop $y(t) = y_I(t) + jy_Q(t)$ of a received signal under small-scale fading is the Rice *pdf* which describes the envelop statistical behaviour when there exists or not a dominant non-fading signal component (e.g. LoS). Expression (2.7) shows the Rician *pdf* where $z(t) = |y(t)|$ is the envelop of the received signal and $I_0(.)$ the modified zero-order Bessel-function of the first kind. σ^2 represents the mean scattered signal power. The distribution of the phase is uniform in the interval [-π,π].

2 Large-scale fading can be compensated in mobile networks by using power control mechanisms.

$$p_z(x) = \begin{cases} \frac{x}{\sigma^2}\exp-\left(\frac{x^2+s^2}{2\sigma^2}\right)I_0\left(\frac{xs}{\sigma^2}\right) & for\ x \geq 0 \\ 0 & otherwise \end{cases} \quad (2.7)$$

The Rayleigh *pdf* can be obtained from the Rice *pdf* making the amplitude of the specular component s equal to zero and is applicable to situations where there is no dominant component.

$$p_z(x) = \begin{cases} \frac{x}{\sigma^2}\exp-\left(\frac{x^2}{2\sigma^2}\right) & for\ x \geq 0 \\ 0 & otherwise \end{cases} \quad (2.8)$$

The Rician K-factor is defined by (2.9) and physically represents the ratio of the power received in the specular component to the total power received via indirect scattered paths. A large K-factor implies that one path dominates over the others. A K-factor close to zero implies a more Rayleigh like distribution [1]. Minimum K-factors are found in more open areas where many scatters are visible and in non LoS where no dominant path can be distinguished.

$$K_{Rice} = \frac{s^2}{2\sigma^2} \quad (2.9)$$

The moments of the Rice distribution are given by (2.10) where Γ(.) is the gamma function and ${}_1F_1(a;b;c)$ the confluent hypergeometric function.

$$E\left[X^n\right] = \left(2\sigma^2\right)^{\frac{n}{2}}\exp-\left(\frac{s^2}{2\sigma^2}\right)\Gamma\left((2n+1)/2\right){}_1F_1\left(\frac{n+2}{2};1;\frac{s^2}{2\sigma^2}\right) \quad (2.10)$$

The squared-envelop, which is proportional to the received power, has the following non-central chi-square distribution with two degrees of freedom [3].

$$p_{z^2}(x) = \begin{cases} \frac{(K_{Rice}+1)}{s^2+2\sigma^2}\exp-\left(K_{Rice}+\frac{(K_{Rice}+1)x}{s^2+2\sigma^2}\right)I_0\left(2\sqrt{\frac{K_{Rice}(K_{Rice}+1)x}{s^2+2\sigma^2}}\right) & for\ x \geq 0 \\ 0 & otherwise \end{cases} \quad (2.11)$$

For narrowband signals where the signal bandwidth is very small compared to the carrier frequency, it suffices to derive the characteristics of the received complex band-pass signal by considering the transmission of an unmodulated carrier. For an unmodulated carrier the received complex low-pass signal is given by (2.12).

$$y(t) = \sum_{n=1}^{N} \alpha_n(t)\, e^{-j\phi_n(t)} \tag{2.12}$$

The received band-pass signal can be expressed in the quadrature form by (2.13).

$$x(t) = \mathrm{Re}\left\{ y(t)\, e^{jw_c t} \right\} = y_I(t) \cos w_c t - y_Q(t) \sin w_c t \tag{2.13}$$

The received band-pass signal PSD (Power Spectral Density) is generally given by (2.14), where $G(\theta)$ and $p(\theta)$ are the receiving antenna gain and the receiving direction *pdf*, respectively. For the case of microcells used in dense urban areas, $p(\theta)$ can be approximately given by (2.15), due to the fact that the radio waves are channelled/guided by the buildings along the street and arrive at the receiver antenna almost from a single direction. The maximum Doppler shift is represented by f_m.

$$PSD_x(f) = \frac{\frac{\left(s^2 + 2\sigma^2\right)}{2}}{\sqrt{f_m^2 - \left(f - f_c\right)^2}} \left[G(\theta)p(\theta) + G(-\theta)p(-\theta) \right] \tag{2.14}$$

$$p(\theta) = \begin{cases} \dfrac{\pi}{4|\theta_m|} \cos\left(\dfrac{\pi}{2} \dfrac{\theta}{\theta_m} \right) & |\theta| \le |\theta_m| \le \dfrac{\pi}{2} \\ 0 & \textit{elsewhere} \end{cases} \tag{2.15}$$

For what concerns the envelop z(t) and assuming isotropic scattering, the PSD is given by (2.16), where K(.) is the complete elliptical integral of the first kind [3]. The squared envelop $z^2(t)$ presents the same PSD as z(t) for the case where the environment is characterised by diffuse scattering.

$$PSD_z(f) = \frac{s^2 + 2\sigma^2}{64\pi f_m} K\left(\sqrt{1 - \left(\frac{f}{2f_m} \right)^2} \right) \quad 0 \le |f| \le 2f_m \tag{2.16}$$

4. Broadband Radio Channel Characterisation

Models usually adequate to characterise narrowband type channels[3] were presented in the previous sections[4]. The signal was usually reduced to a single carrier since it was assumed that all the frequencies in the signal were affected in the same way. The question now arises as to the adequacy of these models to describe the behaviour of broadband channels where the different frequency components of the signal are affected differently generating amplitude and phase distortion, due to the time spreading of the signal caused by the excess delay of the multipath components. Furthermore, the fast variation of the channel caused by the motion of the MT induces Doppler shift, which contributes to the degradation of the channel. The first effect causes frequency selective fading or flat fading and the second fast and slow fading as shown is Figure 2.4.

Due to the intrinsic behaviour of the broadband mobile radio channel, new parameters are required to express its characteristics. Concepts like delay, excess delay, delay spread, coherence bandwidth, coherence time, etc. become now important. In the next section are derived these parameters based on the work developed by Bello which is summarised in this section [20] [21].

Bello work constitutes a comprehensive way to model the radio channel induced fading phenomenon in broadband signals. Bello has proposed the notion of WSSUS (Wide-Sense Stationary Uncorrelated Scattering), which assumes that signals arriving with different delays are uncorrelated (Uncorrelated Scattering) and that the radio channel can be considered stationary for very short time intervals (Wide-Sense Stationary). Based in this assumption he has derived various functions that describe the radio channel.

As shown in Figure 2.5, the radio channel can be seen as a time variant linear filter whose inputs and outputs can be described in the frequency and time domains. This leads to four possible transmission functions: the input delay-spread function $h(t,\tau)$ – time-delay domain, the output Doppler-spread function $H(f,\upsilon)$ – frequency-Doppler domain, the time-variant

3 In reality the radio channel is always the same and shows the same physical properties to all radio signals. What happens is that for broadband signals it is required a more detailed characterisation of the radio channel phenomena that for narrowband signals can be ignored.

transfer function $T(f,t)$ – frequency-time domain, and the delay Doppler-spread function $S(\tau,\upsilon)$ – delay-Doppler domain.

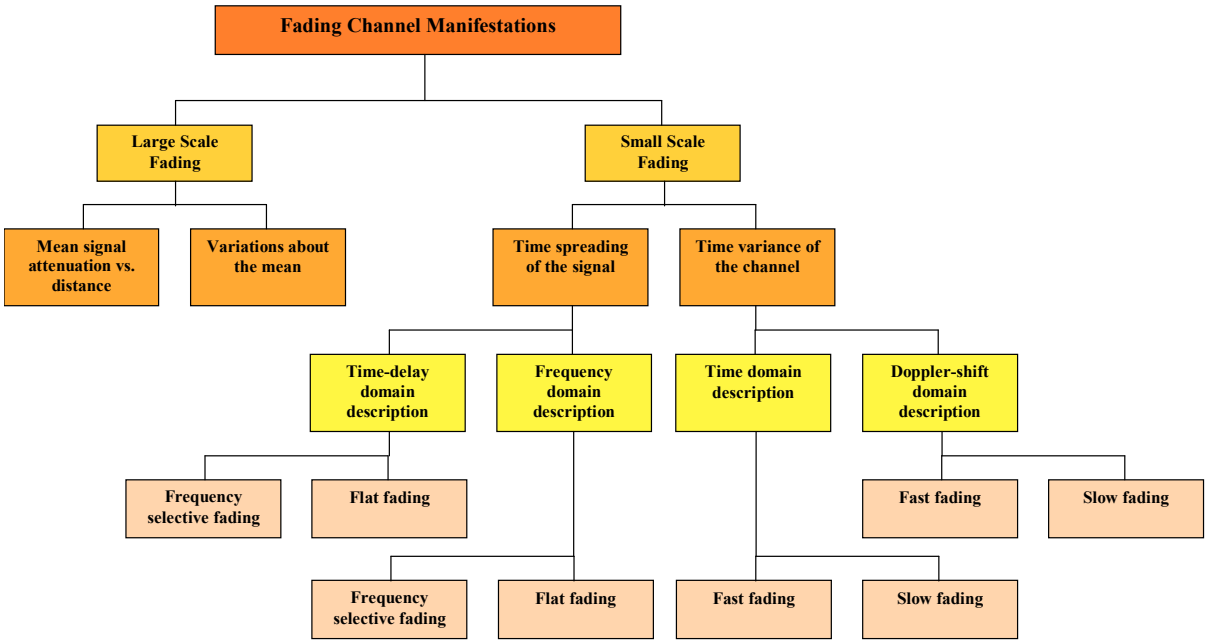

Figure 2.4: Impact of the radio channel fading

The complex low-pass impulse response $h(t,\tau)$, relates de complex low-pass input and the output time waveforms $w(t)$ and $y(t)$, respectively, via the convolution represented in (2.17) and can be represented in its discrete form by (2.18) where α_n are the amplitudes, τ_n the delays and φ_n the phases that characterise each multipath component and N the total number of multipath components generated by the surrounding environment[5]. Bello has called this function as the input delay-spread function, which can be interpreted as the channel response at time t due to a Dirac impulse applied at time $t-\tau$ and must be zero for $\tau<0$ since a physical channel cannot have an output before the input has arrived.

$$y(t) = \int w(t-\tau)\, h(t,\tau)\, d\tau = w(t) \otimes h(t,\tau) \qquad (2.17)$$

4 Narrowband models only address the envelop fluctuations and Doppler effects.

5 In reality the receiver cannot see all the rays due to the limitations caused by its time resolution, therefore usually the N rays already correspond to the coherent sum of several sub-rays that are separated by a delay less than the receiver time resolution. Only an ideal receiver with infinite bandwidth can see all the rays individually.

$$h(t,\tau)=\sum_{n=1}^{N}\alpha_n(t)\ e^{j\varphi_n(t)}\delta[\tau-\tau_n(t)] \qquad (2.18)$$

The signal amplitude will depend on the scatters properties as well as each path length, affecting the delay associated with each component. This delay is often normalised to the time of the first arriving component and then noted as excess delay.

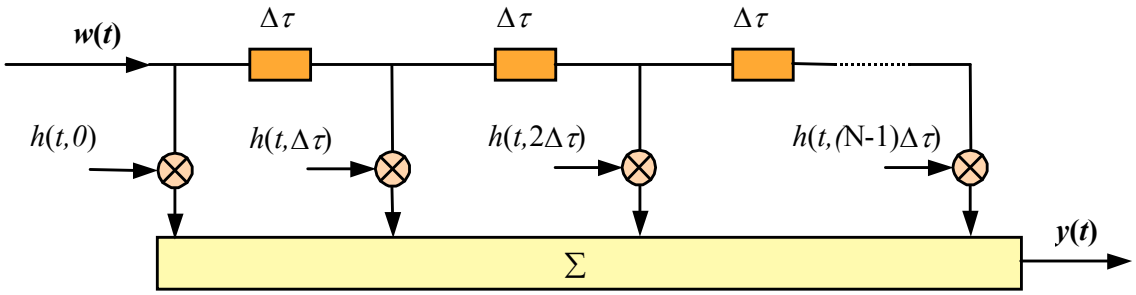

Figure 2.5: Tap delay line model of the radio channel

The radio channel can also be described in the frequency domain as a time-variant transfer function $T(f,t)$ via the Fourier transform of the impulse response. This is shown in (2.19) where the time dependency is caused by the change of the scattering environment.

$$T(f,t)=\int h(t,\tau)\,e^{-j2\pi f\tau}\,d\tau \qquad (2.19)$$

Moving the MT in relation to the BS will cause a Doppler shift given by $f_D=\frac{v}{\lambda}\cos\alpha$. Its magnitude is determined by the velocity v and the angle α between the direction in which the MT is moving and the direction of the incoming wave. Since there are many waves of different amplitude and arrival angles, the frequency shift shows statistical behaviour rather than a fixed frequency shift leading to spectrum broadening – the Doppler spectrum – defined by (2.20) as being the Fourier transform of T(f,t) with respect to time.

$$H(f,\upsilon)=\int T(f,t)\,e^{-j2\pi\upsilon t}\,dt \qquad (2.20)$$

The last Bello function is the delay Doppler-spread function and can be obtained via the Fourier transform of $h(t,\tau)$ with respect to the t variable. This function provides a measure of the scattering amplitude of the channel in terms of the time delay τ and Doppler

frequency υ. Therefore, this function explicitly describes the dispersive behaviour of the channel in terms of both time-delays and Doppler shifts.

$$S(\tau,\upsilon)=\int h(t,\tau)\,e^{-j2\pi\upsilon t}\,dt \qquad (2.21)$$

Figure 2.6 summarises all the relationships among the Bello functions.

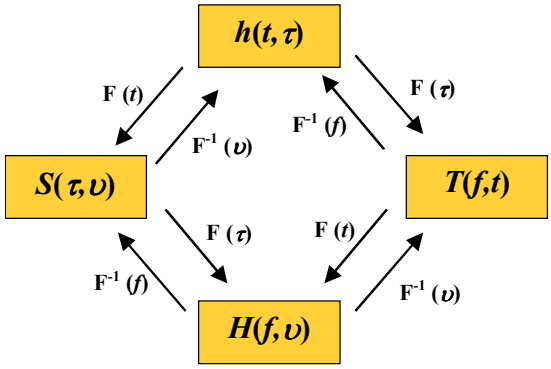

Figure 2.6: Bello functions Fourier transform relationships

In general, all the Bello transmission functions represent randomly time-variant processes (stochastic processes) and therefore a complete characterisation of the radio channel requires knowledge of all the joint *pdf* of all transmission functions. Since this is very difficult, a less accurate but more reasonable approach is to obtain statistical correlation functions for the individual transmission functions. If the underlying process is Gaussian, then a complete statistical description is provided by the means and autocorrelation functions. If we assume zero-mean Gaussian processes only the autocorrelation functions are of interest.

The four autocorrelation functions are defined by (2.22) to (2.25), where E[.] is the ensemble average and * denotes the complex conjugate.

$$E\left[h(t,\tau)\,h^{*}(\xi,\eta)\right]=R_h(t,\xi;\tau,\eta) \qquad (2.22)$$

$$E\left[T(f,t)\,T^{*}(m,\xi)\right]=R_T(f,m;t,\xi) \qquad (2.23)$$

$$E\left[H(f,\upsilon)\,H^{*}(m,\mu)\right]=R_H(f,m;\upsilon,\mu) \qquad (2.24)$$

$$E\left[S(\tau,\upsilon)\,S^{*}(\mu,\eta)\right]=R_S(\tau,\eta;\upsilon,\mu) \qquad (2.25)$$

The same autocorrelation functions but for WSSUS type channels they are defined by (2.26) to (2.29).

$$R_h(t,t+\Delta t;\tau,\eta)=\delta(\eta-\tau)\,P_h(\Delta t;\tau) \tag{2.26}$$

$$R_T(f,f+\Delta f;t,t+\Delta t)=R_T(\Delta f;\Delta t) \tag{2.27}$$

$$R_H(f,f+\Delta f;\upsilon,\mu)=\delta(\upsilon-\mu)\,P_H(\Delta f;\upsilon) \tag{2.28}$$

$$R_S(\tau,\eta;\upsilon,\mu)=\delta(\mu-\tau)\,\delta(\upsilon-\mu)\,P_S(\tau;\upsilon) \tag{2.29}$$

Where $\delta(.)$ is the Dirac impulse, $\Delta f=m-f$, $\Delta t=\xi-t$ and P_h, P_H, P_S are cross-power spectral densities, defined by the following equations:

$$P_h(\Delta t;\tau)=\int_{-\infty}^{+\infty} R_T(\Delta f;\Delta t)\,e^{j2\pi\tau\Delta f}\,d\Delta f \tag{2.30}$$

$$P_H(\Delta f;\upsilon)=\int_{-\infty}^{+\infty} R_T(\Delta f;\Delta t)\,e^{-j2\pi\upsilon\Delta t}\,d\Delta t \tag{2.31}$$

$$P_S(\tau;\upsilon)=\int_{-\infty}^{+\infty} P_H(\Delta f;\upsilon)\,e^{j2\pi\tau\Delta f}\,d\Delta f \tag{2.32}$$

Figure 2.7 show their relationship in terms of Fourier transforms.

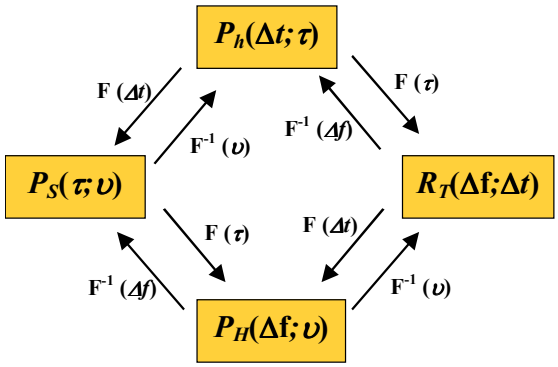

Figure 2.7: Channel autocorrelation functions Fourier transform relationships for WSSUS channels

Stationary radio channels can be characterised in a simpler manner. All formulas can be simplified if the time and Doppler shift dependencies can be removed. This is the case when we perform channel impulse response measurements in the frequency domain. For

instance equations (2.17) and (2.18) can be rewritten in the following way where ⊗ denotes the convolution:

$$y(t) = \int w(t-\tau)\, h(\tau)\, d\tau = w(t) \otimes h(\tau) \tag{2.33}$$

$$h(\tau) = \sum_{n=1}^{N} \alpha_n \; e^{j\varphi_n} \delta[\tau - \tau_n] \tag{2.34}$$

In terms of frequency domain (relationship between the input and output spectrums), equations (2.35) and (2.36) show that the input and output signal spectrums are related with *H(f)*. This is a well known result for stationary systems.

$$Y(f) = \int W(f-\upsilon)\, H(f-\upsilon,\upsilon) d\upsilon \tag{2.35}$$

$$Y(f) = W(f)\, H(f) \int d\upsilon = W(f)\, H(f) \tag{2.36}$$

It can also be shown that for stationary channels, the Bello functions reduce only to two since $h(t,\tau)$ is equal to $S(\tau,\upsilon)$ and $H(f,\upsilon)$ equal to $T(f,t)$ as shown in by equations (2.37) and (2.38).

$$H(f,\upsilon) = T(f) \int e^{-j2\pi\upsilon t} dt = T(f)\delta(\upsilon) \tag{2.37}$$

$$S(\tau,\upsilon) = h(\tau) \int e^{-j2\pi\upsilon t} dt = h(\tau)\, \delta(\upsilon) \tag{2.38}$$

5. Parameters Describing the Broadband Radio Channel

A number of important parameters can be derived from the channel complex impulse response $h(t,\tau)$. In (2.39) is shown how the impulse response relates with its cross-power spectral density when $\tau=\eta$.

$$P_h(\Delta t,\tau) = \mathrm{E}\left[h(t,\tau)\, h^*(t+\Delta t,\tau)\right] \tag{2.39}$$

If the observation time Δt tends to zero, the PSD $P_h(\tau)$ is given by (2.40), converging to the definition of the PDP (Power Delay Profile), which gives an indication of how the power is distributed as a function of the delay in the point of view of the receiving antenna

(output of the channel). The range of values over which $P_h(\tau)$ is significant is called the maximum excess delay and is denoted by Tm. The PDP can also be regarded as the scattering function $P_S(\tau;\upsilon)$ averaged over all the Doppler shifts.

$$P_h(\tau) = \mathrm{E}\left[\left|h(t,\tau)\right|^2\right] = PDP \tag{2.40}$$

The NRP (Normalised Received Power) is defined as the quotient of the received power and the transmitted power and is given by (2.41) when the transmitted signal is a Dirac impulse.

$$NRP = \int_0^\infty P_h(\tau)d\tau \tag{2.41}$$

Three other important parameters are the DS (root mean square Delay Spread), $\bar{\tau}$ (Mean Time Delay) and the SDW (Sliding Delay Window). The first two are statistical moments of $P_h(\tau)$ being the DS defined by (2.43) and the $\bar{\tau}$ defined by (2.42). The SDW is defined as the minimum time interval where x% of the PDP energy is contained as shown in (2.44), where τ_1 and τ_2 are defined by (2.45), τ_0 and τ_3 define the interval where the received power is above of a predefined threshold, possibly defined by the noise or interference level. These parameters can be computed from a single PDP or from profiles averaged over a distance of a few wavelengths.

$P_H(\Delta f;\upsilon)$ for $\Delta f=0$, $P_H(\upsilon)$, is known as the Doppler power spectral density and gives the average power at the channel output as a function of the Doppler frequency υ. The range of values over which $P_H(\upsilon)$ is significant, is called the Doppler spread and is denoted by Bd.

$$\bar{\tau} = \frac{\int_0^\infty \tau P_h(\tau)d\tau}{\int_0^\infty P_h(\tau)d\tau} \tag{2.42}$$

$$DS = \sqrt{\frac{\int_0^{\infty} (\tau - \bar{\tau})^2 P_h(\tau) d\tau}{\int_0^{\infty} P_h(\tau) d\tau}} \tag{2.43}$$

$$SDW_{x\%} = \min(\tau_2 - \tau_1) \tag{2.44}$$

$$\int_{\tau_1}^{\tau 2} P_h(\tau) d\tau = x \int_{\tau_0}^{\tau_3} P_h(\tau) d\tau = x P_{total} \tag{2.45}$$

Equations (2.42) and (2.43) can be written in its discrete version for a finite number of rays arriving to the receiver as shown in equations (2.46) and (2.47). η_p is the NRP of the received p ray.

$$\bar{\tau} = \frac{\sum_{p=1}^{N} \eta_p \tau_p}{\sum_{p=1}^{N} \eta_p} \tag{2.46}$$

$$DS = \sqrt{\frac{\sum_{p=1}^{N} \left(\tau_p - \bar{\tau}\right)^2 \eta_p}{\sum_{p=1}^{N} \eta_p}} \tag{2.47}$$

The function $R_T(\Delta f;\Delta t)$, for the case where $\Delta t=0$, $R_T(\Delta f)$ is known as spaced frequency correlation function; for the case when $\Delta f=0$, $R_T(\Delta t)$ is known as spaced time correlation function. $|R_T(\Delta f)|$ measures the frequency correlation of the channel and the channel coherence bandwidth (CB) is defined as the smallest value of Δf for which this function equals some suitable correlation coefficient (e.g. 0.5 or 0.9). Since $|R_T(\Delta f)|$ and $P_h(\tau)$ are Fourier transforms the CB has a relation with the DS and $\bar{\tau}$. Equation (2.48) expresses the relationship with the DS that is commonly available in the literature for a correlation coefficient of 0.5.

$$CB \approx \frac{1}{5DS} \tag{2.48}$$

The coherence time (Tc) of the channel depends directly on the speed of the MT and is important for evaluating the performance of coding and interleaving techniques. Since $P_H(\upsilon)$ and $R_T(\Delta t)$ are Fourier transforms pairs, there is a relation between the Doppler shift and Tc. Equation (2.49) expresses the relationship with the maximum Doppler shift f_m that is commonly referred in the literature for a correlation coefficient of 0.5.

$$Tc \approx \frac{9}{16\pi f_m} \tag{2.49}$$

Figure 2.8 summarises all the relationships. The analysis of the small-scale fading mechanisms degradation and effects can be done in four different domains leading to the definition of the following parameters: Delay Spread – DS (delay-time domain), channel coherence time - Tc (time domain), Doppler spread - Bd (Doppler shift domain) and channel coherence bandwidth - CB (frequency domain) [8] [1]. The relative comparison of these parameters with the symbol time duration (Ts) and bandwidth (BW) of the transmitted signal leads to the concept of frequency selective fading if Ts < DS or BW > CB and flat fading if Ts > DS or BW < CB, due to the multipath propagation phenomena; and a channel is said to suffer from fast fading if Ts > Tc or BW < Bd and slow fading if Ts < Tc or BW > Bd, due to the shown time variability. This justifies and confirms the channel fading classification shown in Figure 2.4. A more detail analysis of these fading phenomena effects and the respective mitigation techniques will be presented in the next chapter.

6. Channel Models for Multiple Input and Output Channels

The theory presented in the previous sections applies generically to SISO mobile radio channels. Nowadays, more and more wireless and mobile networks start incorporating space diversity techniques based on the utilisation of multiple antennas in the BS or MT to increase the channel capacity, leading to the necessity of defining channel models for MISO, SIMO and MIMO radio channels. These models are usually referred as vector models in opposite to the scalar models suitable for SISO channels [22] [23]. Typical separations between the antennas are 10λ for the BS and 0.5λ for the MT.

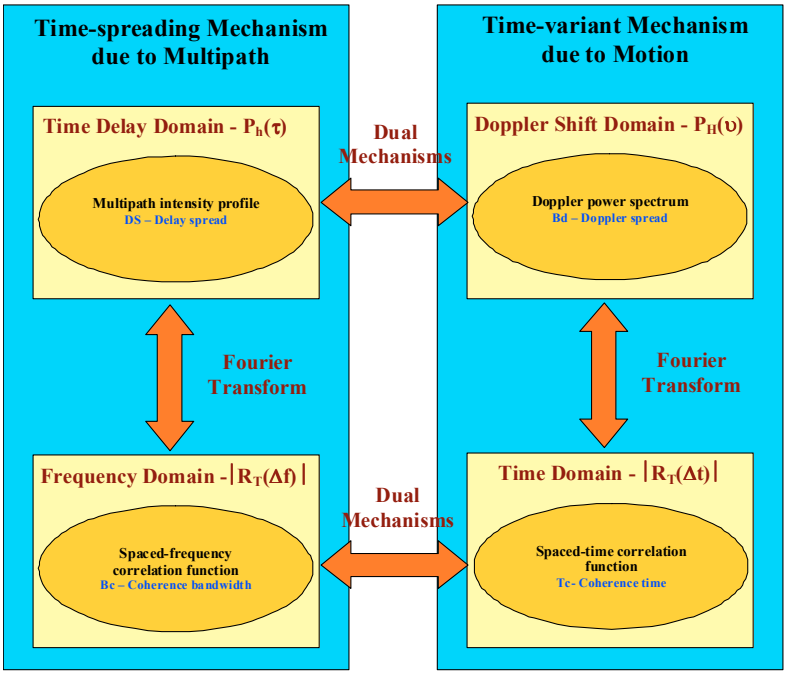

Figure 2.8: Relationship between the various domains

Figure 2.9 shows a typical representation of the MIMO channel where due to simplification reasons only some links between the n transmitters (Tx) and p receivers (Rx) are displayed. Similarly to SISO channels, equations (2.50) and (2.51) show a mathematical representation of the MIMO radio channel for a particular instant t. The input and outputs signals are now represented by vectors due to the existence of multiple transmitters and receivers. The path between each Tx and Rx antennas can be seen as a pure SISO channel characterised by its impulse response.

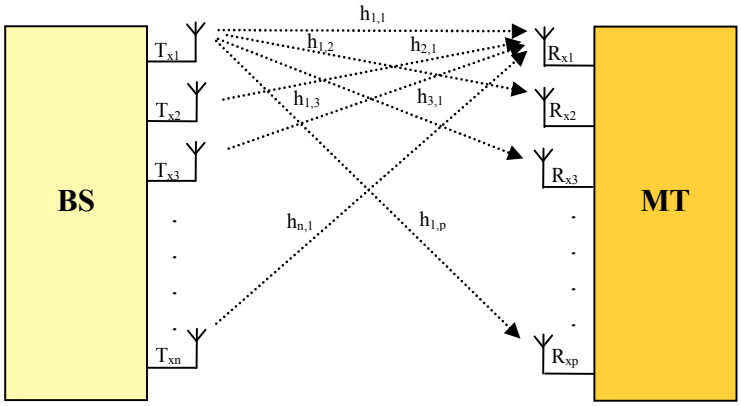

Figure 2. 9: MIMO channel representation (n antennas in BS and p antennas in the MT) showing only the paths between T_{x1} and all the R_x and all T_x and R_{x1}

$$\underline{y}(t) = \mathrm{H}(t) \bullet \underline{x}(t) + \underline{n}(t) \tag{2.50}$$

$\underline{y}(t)\, and\, \underline{n}(t) \in C^p$

$\underline{x}(t) \in C^n$

$H(t) \in C^{p \times n}$

$$\begin{bmatrix} y_1 \\ y_2 \\ . \\ y_p \end{bmatrix} = \begin{bmatrix} h_{1,1} & h_{1,2} & h_{1,3} & . & h_{1,n} \\ h_{2,1} & h_{2,2} & h_{2,3} & . & h_{2,n} \\ . & . & . & . & . \\ h_{p,1} & h_{p,2} & h_{p,3} & . & h_{p,n} \end{bmatrix} \bullet \begin{bmatrix} x_1 \\ x_2 \\ . \\ x_n \end{bmatrix} + \begin{bmatrix} n_1 \\ n_2 \\ . \\ n_p \end{bmatrix} \tag{2.51}$$

A time-varying broadband MIMO channel can be represented by equation (2.52) for L multipath components. Only H_1 contains the LoS component (direct ray).

$$\mathrm{H}(t) = \sum_{l=1}^{L} H_l \delta(t - \tau_i) \tag{2.52}$$

7. Summary and Conclusions

In this chapter the mobile radio channel main characteristics and models were presented. This channel has particular properties when compared to other radio channels namely in microwave radio links or satellite systems since LoS operation cannot be guaranteed. The full and complete radio wave propagation is hard to describe exactly due to the high number of effects and complex relations that is necessary to consider. Due to this fact, simplified models have to be adopted with a limited number of input parameters and relatively low mathematical computation complexity being however more complex than the free space propagation law.

Objects present in the scenario and the motion of the MTs have a great influence on the characteristics of the radio channel due to the arrival of multiple waves to the receiver with different amplitudes and phases causing constructive or destructive interference. This phenomenon is known as fading. On the other hand, objects scatter and diffract the radio waves energy enabling the coverage of potential shadowing areas. Moreover, radio waves are also affected by oxygen, water vapour and rain absorption, which is dependent on the specific frequency band.

The fading phenomenon can be subdivided in small-scale and large-scale fading and has a random behaviour. The last includes the shadowing and path loss. Shadowing is usually modelled by the log normal *pdf* and many models exist for the path loss being the most popular based on real propagation measurements. These models are usually available for the different type of cells and their parameters can differ according to the type of environment, namely rural or urban. For what concerns the small-scale fading, it is caused by the time dispersion of the signal due to multipath propagation and frequency Doppler spreading due to the Doppler shift and the signal envelop can be modelled by the Rice or Rayleigh *pdf* depending if the direct ray is or not present, respectively.

The GO and UTD have enabled the derivation of physical models for the radio channel based on the ray concept. Ray tracing techniques can be used to trace the various rays between the transmitter and the receiver that will be affected by the reflection, diffraction and scattering propagation mechanisms.

The simplest radio channel model includes the direct and the ground reflected rays between the transmitting and receiving antennas as derived by Norton and Bullington. In more complex scenarios this model is not good enough and therefore other models that take more rays into consideration are required.

For narrowband systems, the assumption that the entire radio signal is affected in the same way by the channel is enough, being usually considered as a single carrier. This is to say that all the signal frequency components suffer the same effects. The carrier can also be affected by Doppler shift depending on the speed and relative position of the MT. On the other hand, broadband systems signals are affected by distortion due o the time spreading of the signal caused by the excess delay of the multipath components and Doppler shift. The first effect may cause frequency selective fading and the second fast fading.

Bello has derived a set of functions that permit the characterisation of broadband channels: the input delay-spread function $h(t,\tau)$, the output Doppler-spread function $H(f,\upsilon)$, the time-variant transfer function $T(f,t)$ and the delay Doppler-spread function $S(\tau,\upsilon)$. All these functions are related by Fourier transforms. For what concerns the time-delay domain, the tap delay line model is a suitable model for broadband channels.

In general the Bello functions represent randomly time-variant processes. Due to this fact, it is more reasonable to use statistical correlation functions rather than the functions themselves, particularly when the underlying processes are Gaussian, since it enables a complete statistical description by using their means and the autocorrelation functions.

Various parameters are required for the characterisation of the broadband channels some of them related with the PDP, which gives an indication of how the power is distributed as a function of the delay, namely: NRP, Tm, $\bar{\tau}$, SDWx%, Bd, Tc, DS and CB. The NRP parameter represents the value of the power in a PDP; Tm is the maximum excess delay which measures the maximum delay observed in the PDP; $\bar{\tau}$ is the mean time delay; SDW the sliding delay window and measures the minimum time interval where x% of the PDP power is contained; Bd is the Doppler spread and is equivalent to the Tm but in the Doppler domain leading to the maximum Doppler shift; Tc is the coherence time and gives an indication of the time variation of the channel; DS is the delay spread; and CB the coherence bandwidth of the channel and shows how the different frequency components of a signal are affected. The relative comparison of these parameters with the symbol time duration Ts and bandwidth BW of the signal leads to the concept of frequency selective fading if Ts < DS or BW > CB and flat fading if Ts > DS or BW < CB; and a channel is said to suffer from fast fading if Ts > Tc or BW < Bd and slow fading if Ts < Tc or BW > Bd.

In the recent years, MIMO type channels have been considered for mobile communications. The utilisation of multiple antennas in the BS and in the MT has been studied by many researchers. Some systems already started incorporating this technology which has led to new ways of increasing the channel capacity and the transmission rates.

As final conclusion it can be stated that a good knowledge of the mobile radio channel behaviour is essential in order to select the most adequate mitigation techniques to be incorporated in the mobile systems radio interface. The various parameters have to be evaluated and analysed for the different frequency bands, type of cells, system configurations and environments enabling the derivation of broadband models used for predicting the behaviour of mobile radio systems.

8. References

[1] J. D. Parsons, "The Mobile Radio Propagation Channel", Prentech Press, London, 1992.

[2] A. Mehrotra, "Cellular Radio Performance Engineering", Artech House, 1994.

[3] Gordon L. Stüber, "Principles of Mobile Communications", Kluwer Academic Publishers, 1996.

[4] A. Neskovic, N. Neskovic and G. Paunovic, "Modern Approaches in Modelling of Mobile Radio Systems Propagation Environment", IEEE Communications Surveys, pp. 2-12, Third Quarter 2000.

[5] José Fernandes, "Modelação do Canal de Propagação Rádio Móvel de Banda Larga na Faixa das Ondas Milimétricas e seu Impacto no Desempenho de Transmissão do Sistema", PhD Thesis, University of Aveiro, 1996.

[6] Henrik Börjeson, "Radio Wave Propagation in Confined Environments – Measurements and Models", PhD Thesis, Department of Applied Electronics, Lund University, Sweden, February 2000.

[7] John D. Kraus, "Electromagnetics" McGraw-Hill, 3rd Edition, 1984.

[8] Bernard Sklar, "Rayleigh Fading Channels in Mobile Digital Communication Systems Part I: Characterization", IEEE Communications Magazine, Vol. 35, No. 9, pp. 136-146, Sep. 1997.

[9] Bernard Sklar, "Rayleigh Fading Channels in Mobile Digital Communication Systems Part II: Mitigation", IEEE Communications Magazine, Vol. 35, No. 9, pp. 148-155, Sep. 1997.

[10] C.A.Balanis, "Advanced Engineering Electromagnetics", New York: Wiley, 1989.

[11] J.B. Keller, "Geometrical Theory of Diffraction", J. Opt. Soc. Amer., Vol. 52, pp.116-130, Feb. 1962.

[12] T. Griesser and C. A. Balanis, "Reflections, Diffractions, and Surface Waves for an Interior Impedance Wedge of Arbitrary Angle", IEEE Trans. Antennas and Propagation, Vol. 37, No. 7, pp. 927-935, July 1989.

[13] R.G. Kouyoumjian and P. H. Pathak, "A Uniform GTD for an Edge in a Perfectly Conducting Surface", Proc. of the IEEE, Vol. 62, No. 11, pp. 1448-1461, Nov. 1974.

[14] G. van Dooren, "A Deterministic Approach to the Modelling of Electromagnetic Wave Propagation in Urban Environments", PhD Thesis, Eindhoven University of Technology, 1994.

[15] Luís Miguel D. B. Anunciada, "Impacto das Antenas no Canal de Propagação em Comunicações Móveis em Ondas Milimétricas", MSc Thesis, Universidade Técnica de Lisboa, Instituto Superior Técnico, Dezembro 1999.

[16] P. Beckman, A. Spizzichino, "The Scattering of Electromagnetic Waves from Rough Surfaces", Pergamon Press, New York, 1963.

[17] G.E. Athanasiadou, A.R. Nix and J. P. McGeehan, "A Microcellular Ray-Tracing Propagation Model and Evaluation of its Narrow-Band and Wide-Band Predictions", IEEE Journal on Selected Areas in Communications, Vol. 18, No. 3, pp.322-335, March 2000.

[18] P. Smulders and J. Fernandes,"Wide-Band Simulation and Measurements of mm-wave Indoor Radio Channels 5th IEEE Int. Symposium on Personal, Indoor and Mobile Radio Communications (PIMRC '94), The Hague, The Netherlands, pp. 501-504, Set. 1994.

[19] W. C. Jakes, "Microwave Mobile Communications", IEEE Press, 1974.

[20] José Emanuel Ramos Pereira Garcia, "Cobertura Celular para Sistemas de Banda Larga", MSc Thesis, University of Aveiro, 2002.

[21] P.A. Bello, "Characterization of Randomly Time- Variant Linear Channels", IEEE Transactions on Communication Systems, Vol. CS-11, no. 4, pp. 360-393, Dec. 1963.

[22] J. D. Parsons and A. M. D. Turkumani, "Characterisation of Mobile Radio Signals: Model Description", IEE Proceedings – I, Vol. 138, December 1991.

[23] R. B. Ertel, K. W. Sowerby, T. S. Rappaport and J. H. Reed, "Overview of Spatial Channels Models for Antenna Arrays Communications Systems", IEEE Personal Communications, February 1998.

3rd Chapter

Mitigation Techniques for Mobile Broadband Systems Radio Interface Design

1. Introduction

One of the main problems that system engineers face when designing a mobile system is the dimensioning of a reliable radio link that allows the user to run the desired broadband services or applications while on the move. The radio channel, being the physical medium that transports the information over the air, is without any doubt the system bottleneck [1]. Therefore, the characteristics of an air interface and physical properties of the radio channel in the various propagation environments, have a direct impact on the efficiency of the whole system.

The air interface should provide the necessary resources and functions for the transparent transfer of information with the required QoS concerning information loss and error rate as well as delay. For that, it is necessary to convert the information to be transmitted in a more

suitable form or to employ various techniques, in order to keep the number of errors at an acceptable level, while crossing the radio interface [2]. The performed conversions and employed techniques have to take into account the specific characteristics of the radio channel.

This chapter intends to give an overview of the type of fading, its impact in the transmission performance and the available mitigation techniques that can be employed to mitigate the undesirable effects. Section 2 presents the various fading types and their degradation impact on transmission. It also identifies generically the components of a generic transmission system and the various choices available to the engineers. Section 3 describes mitigation techniques to combat the various types of fading and the loss of SNR (Signal to Noise Ratio). Section 4 presents the options that are especially suitable for the design of broadband systems. Finally section 5 introduces the approach followed in the hardware prototype used to perform the experiments.

2. Fading and Degradation Categories

In Figure 3.1 a generic mobile radio system is presented and various key issues regarding transmission constrains and techniques are shown. As described in the previous chapter, the mobile radio channel suffers from changes on the received average power (as a function of the distance - path loss), shadowing, multipath propagation and time variance due to motion of the MT or any other object (e.g. trucks) in the propagation environment, leading to large-scale and small-scale fading [3] [4] [5]. The last might have a significant impact on the maximum transmission rate of the system since the large-scale fading can be mitigated using power control mechanisms and therefore its effects will not be considered in the analysis presented in this chapter. However, since mobile broadband systems use high frequency bands (e.g. 5 GHz, 17 GHz, 40 GHz and 60 GHz) they are affected by a larger free space loss and extra attenuation caused by atmosphere elements such as rain, water vapour and oxygen. Therefore, different fading margins are required when compared with systems which operate on the 900, 1800 or 2000 MHz. Obstacles show also a high opacity to the radio waves and the diffraction phenomenon has little expression being its effects considered negligible [6] [7]. In summary, mobile broadband communications, due to the

smaller symbol duration (higher data rates) and the utilisation of higher frequency bands, have therefore a higher probability of being affected by the radio channel impairments.

The analysis of small-scale fading mechanisms degradation and effects can be done in four different domains [3] [4] [8]. The relative comparison of various parameters with the symbol time duration and bandwidth of the transmitted signal leads to the concept of frequency selective fading, flat fading, fast fading and slow fading as described in the previous chapter. In order to mitigate these fading effects and to bring the performance of broadband systems as close as possible to AWGN (Additive White Gaussian Noise) channel conditions, various techniques can be used and will be described in section 3.

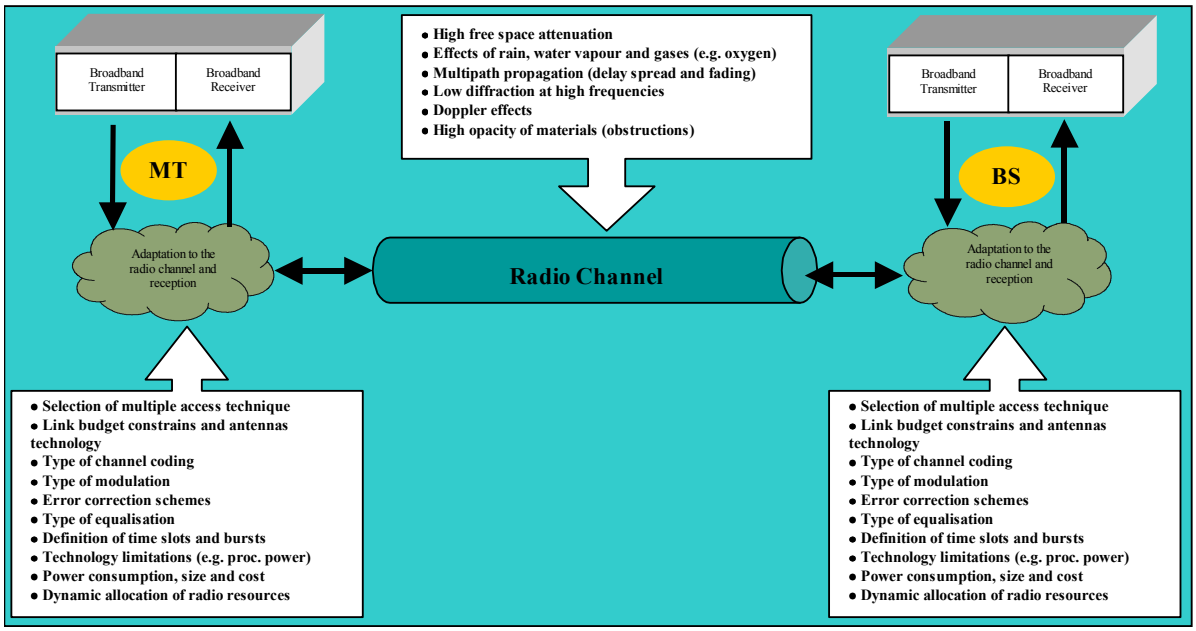

Figure 3.1: Key issues when designing broadband mobile systems

Figure 3.2 presents the various fading categories and their impact on the transmission performance of any mobile system. Frequency selective fading results from time dispersion of the transmitted signal and causes channel induced ISI (Inter Symbol Interference). On the other hand, flat fading radio channels, when seen in the time-delay domain, do not cause ISI but only degradation on the SNR. All received multipath components of a symbol arrive within the symbol time duration and therefore they are not resolvable. The performance degradation comes from the fact that the irresolvable components can add destructively, depending on the relative phase, resulting in a reduction

of the SNR. When seen in the frequency domain, flat fading implies that all the frequency components of the signal are affected in the same way.

Fast fading describes a situation when the time duration of the symbol is longer than the radio channel coherence time. Therefore the fading character will change several times during the transmission of a symbol leading to baseband pulses distortion, and resulting in a loss of SNR. In the frequency domain it manifests itself as Doppler shift. For what concerns the slow fading case, the time duration for which the channel behaves in a correlated manner is long compared to the symbol time leading to a loss in the SNR and no distortion.

Figure 3.2: Small scale fading: mechanisms, degradation categories and effects

The objective of any digital transmission systems is to lower the BER (Bit Error Rate) for a given E_b/N_0 (energy per bit over the noise spectral density). The most ideal channel is the one where only AWGN is present and therefore, for a specific modulation scheme, this is usually the best reference we can have in terms of transmission performance.

In terms of degradation, a loss of SNR is much less severe than the introduction of distortion, being the last the most difficult to deal with. In situations of high distortion (caused by frequency selective or fast fading), the BER can approach 0.5, which shows the terrible consequences of distortion for a transmission system [4].

In general if there is an increase on the E_b/N_0 the BER improves, however there are situations where an increase of the E_b/N_0 does not improve the performance. This happens when the system is in presence of an irreducible BER. In these cases mitigation techniques have to be applied to bring the system to a "non saturation" status. The performance can be further improved (after distortion mitigation) by using other techniques, for instance, diversity reception.

3. System Mitigation Techniques

As a general rule, distortion effects should be mitigated first and then combat the loss in SNR of the signal. In the following sections techniques suitable to combat frequency selective fading, fast fading and loss of SNR are presented [5] [9] [10].

3.1 Mitigation to combat frequency selective fading

Equalisation is one of the techniques that can be used to combat frequency selective fading [9] [11]. It consists basically in the gathering of the dispersed symbol energy that is causing ISI back to its original time interval. In fact, it involves the utilisation of a filter that in combination with the radio channel shows a flat response and a linear phase. Because in a mobile system the radio channel response varies with time, the equaliser filter must also be time variant, leading to the need of an adaptive equaliser. In fact an equaliser provides more than distortion mitigation since by the operation of re-timing the symbols energy back to their original time, it is recovering energy for each symbol that otherwise would be lost. In [7] and [9] various types of equalisers are presented. There are basically two classes of

equalisers: linear and non-linear equalisers. Those that operate in a non-linear manner can be subdivided in two types: DFE (Decision Feedback Equaliser) and MLSE (Maximum Likelihood Sequence Estimation). The basic idea behind a DFE equaliser is that once an information symbol has been detected, the ISI it induces in future symbols can be estimated and subtracted before the detection of subsequent symbols.

The MLSE equaliser tests all possible data sequences, and rather than decoding each symbol by itself, it chooses the data sequence that is most probable of the candidates. Because the Viterbi decoding algorithm [10] is the way in which MLSE equaliser is typically implemented it is often known as the Viterbi equaliser.

Spread-spectrum techniques Direct Sequence or Frequency Hopping [5] [12] can also be used to mitigate the effects of the frequency selective fading. Since multipath propagation is the cause of this distortion, spread spectrum systems, due to its nature, are only able to synchronise to a single multipath component if the others show a delay larger than the duration of a chip of the spreading code. This means that the energy of the other multipath components is automatically rejected and seen as interference. To compensate for this fact, and for what concerns Direct Sequence systems, a Rake receiver is needed. This receiver is equivalent to the equaliser in the time domain, it has several fingers (correlators) and each finger can synchronise with each of the multipath components. Afterwards, by estimating its relative phase and amplitude they can all be coherently combined to give a better SNR. Frequency Hopping systems can avoid the effects of multipath by changing rapidly the transmitting frequency band before the next multipath component arrives at the receiver, thus avoiding the interference.

OFDM (Orthogonal Frequency Division Multiplexing) [13] [14] can also be used in this type of channel since it is able to increase the length of the symbol duration, avoiding therefore the need for an equaliser. The signal band is partitioned into multiple sub bands, each exhibiting a lower symbol rate. The sub bands are then transmitted on multiple orthogonal carriers. The goal is to reduce the symbol rate on each carrier to be lower than the channel's coherence bandwidth.

3.2 Mitigation to combat fast fading

Fast fading can be mitigated using a robust modulation technique that is less sensitive to the signal phase variations. In conjunction, the symbol rate can also be increased by the addition of redundancy to the signal, thus contributing to the reduction of the symbol time duration, therefore less affected by the fast fading and on the other hand, the redundancy can be used to detect and correct transmission errors if an appropriate rate and coding scheme are used [10]. Interleaving can also be used to further mitigate the effects of fast fading [5]. When viewed in the frequency domain, the fast fading manifests itself as Doppler shift, whose impact can be reduced by avoiding the usage of PLLs (Phase Lock Loops) and to use additional synchronisation techniques based on the existence of a synchronisation channel (e.g. pilot channel). For the case when OFDM is used, the Doppler shift causes adjacent channel interference among the various carriers. Diversity reception is an efficient technique for combating fast fading [15].

3.3 Mitigation to combat loss in SNR

Basically, and after distortion mitigation, some form of diversity [15] or channel coding [5] [10] allowing error correction can combat the loss in the SNR caused by fading, especially flat and slow fading. These techniques will tend to approach the transmission performance to the AWGN channel.

The basic idea of diversity is to provide the receiver with various uncorrelated versions of the same signal increasing the probability of one of them being in good shape or otherwise to process and combine the various received signals and obtain a better version of it. When all received copies of the signal are in a bad status, the diversity gain does not exist therefore it is essential that the channels are uncorrelated as much as possible. There are various forms of diversity: space diversity (two antennas in the same mast or even two different BSs), time, frequency, polarisation and multipath (for instance, using a Rake receiver) [15].

Frequency Hopping spread spectrum can also be used and seen as a form of frequency diversity mechanisms although not the same information is sent in the various frequency carriers (in GSM slow Frequency Hopping is used to compensate for those cases where the

MT is not moving or only moving slowly) [10]. However, error correction coding coupled with interleaving is probably the most prevalent of the mitigation techniques used to provide improved performance in a fading environment.

4. Mobile Broadband System Options

Mobile broadband systems have symbol time duration (Ts) quite small due to the high transmission rates and signals with large bandwidths (BW). They usually suffer from frequency selective fading. In general, the fast fading effects are normally not so important since the speed of MTs is not too high given the fact that in many cases only indoor operation at walking speed is required. The exception is the cellular component where high speeds combined with the short wavelengths causes Doppler shifts that can be of concern. Although in [16] an interesting approach to overcome these problems is presented for highways it is not applicable to more generic scenarios where mobile broadband systems are expected to operate.

One of the important aspects is the selection of a suitable multiple access technique. Since the air interface is a shared medium it has to implement the mechanisms to guarantee equal MT opportunities or even to admit the existence of different user priorities when accessing to the radio resources. Moreover, the system must show flexibility to deal and accommodate the instantaneous applications and services needs for each user, without causing undesirable effects for the whole system or to specific users [17]. This obviously cannot be guaranteed when the system reaches the saturation status imposed by physical limits. In general terms, the separation of the various users can be done in the frequency, time and coding domains.

Since different options are available when designing an air interface, advantages and disadvantages have to be weighed and trade-offs performed when selecting the main parameters in order to achieve the best technical or economical solution [18]. Ideally only the user information bits should be transferred, however other information is needed e.g. for equalisation, channel coding or delimitation of the bursts/time slots necessary for the reduction of the BER and to permit the dynamic allocation of bandwidth to the MTs. Table 3.1 shows some parameters and their impact on the system design.

Due to the broadband nature, the technological state-of-the-art and the degradation categories already described, five possibilities were identified to mitigate the radio channel effects: the use of directive antennas, space diversity reception, equalisation techniques for single carrier modulation, spread spectrum and multicarrier modulation. The implementation of some of these techniques requires the need, in the MT and in the network side, of large amounts of processing power to allow operation in real time, which may be considered as a bottleneck in terms of the available technology and power consumption (of major concern on the MT side). GSM MTs need already a significant processing power to perform real time equalisation of the received signals. In the future, MTs will require much more due to the higher data rates they will support. This is more important in the case of real time services like interactive video transmission.

Options	Impact on mobile broadband communications
High frequency bands	Higher path losses limiting the cell range for the same emitted power and radiation safety limits.
Multipath propagation	Originates delay spread causing ISI and small-scale fading. Can be mitigated via diversity reception, equalisation, interleaving, channel coding, multicarrier modulation schemes, directive antennas, etc.
Shadowing	Due to the high obstacles' opacity at high frequency bands, fast power control algorithms and large dynamic ranges are necessary otherwise, LoS operation is normally required and therefore, multiple BS visibility and fast handover algorithms may reduce the impact of shadowing.
MT omnidirectional antennas	They allow a good MT movement freedom but are more exposed to negative multipath propagation and co-channel interference effects. More severe power budget requirements due to the associated low gain.
Space diversity reception	Combats small-scale fading but the RF front-end complexity and cost increases.
Power amplifier non linearity and efficiency	Selection of modulation schemes that allow non-linear power amplification. This enables the power amplifier to work close to saturation increasing its efficiency.
Modulation scheme	Directly related to the system spectrum efficiency. It may have characteristics that reduce the non-linearity effects (constant envelop).
Single carrier modulation	Requires the utilisation of an equaliser and can operate with saturated power amplifiers if an appropriate modulation scheme is used.
Multicarrier modulation	Requires the usage of large processing power for FFT calculations and needs linear power amplification.
Channel coding and interleaving	Increases the gross bit rate on the radio channel reducing however the BER. Can be adaptive as a function of the radio channel conditions to improve the system performance.
ARQ mechanism	The performance is directly related to the FEC channel coding efficiency. It increases the system end-to-end delay reducing however the BER.
MT motion	Impacts on the time variability of the radio channel (Doppler shift).

Table 3.1: Different options and its impact on mobile broadband communications

Antennas play an important role in mitigating the radio channel impairments especially at millimetrewave frequencies, where the challenge is beyond the classical gain-to-beamwidth trade-off, and therefore they can have a direct impact in the equaliser complexity if they can provide multipath discrimination. Moreover, antennas should contribute to the efficient use of the limited power levels that the power amplifiers can deliver, by distributing the energy uniformly over the cell and providing the necessary gain, facilitating the link budget design. These requirements can be summarised as follows:

- Antennas are expected to provide the best possible spatial distribution of energy, confining it to the cell limits, and avoiding over-illuminated and under-illuminated regions, reducing the power that solid state devices have to deliver (at high frequencies the power is limited), reducing the co-channel interference and avoiding possible multipath components.
- Antennas must provide high gain to favor the link budget necessary for the high data rates, but without the expense of conditioning the MT movement freedom by using very directive antennas.
- Antennas configuration must be compatible with the use of space diversity without significant mutual blocking between the various antennas.
- Antennas operation bandwidth must be enough to accommodate both frequency bands used for FDD operation.
- Antennas technology should be affordable and allow manufacturing with reasonable tolerances.

High frequency bands combined with the actual limitations of the RF technology impose severe link budgets constrains and therefore the selected antenna technology plays an important role in ameliorating these limitations. Conceptually, an adaptive multibeam antenna can cope with some of the previous requirements however the cost at millimetrewave frequencies is a strong drawback. In addition, the reduction in equaliser complexity enabled by the use of these antennas is lost due to the real-time high signal processing necessary in the antennas. Switchable beam antennas are the natural less expensive fallback solution however cost and switch loses may still be not acceptable. In

the future, adaptive multibeam antennas may be used, but the implementation of this concept at millimetrewave frequencies is still far from becoming reality due to the level of complexity. Directive, non-smart antennas, introduce limitations on the system in terms of mobility and freedom of the user and should therefore be avoided for mobile communications.

Lens type antennas that provide a fairly uniform spatial power distribution can be a more effective solution. A $\sec^2(\theta)$ radiation pattern is used to compensate the increase in path loss. This is achieved by increasing the antenna gain as the distance to the BS increases [19]. This radiation pattern can be obtained with the BS antenna alone or via a combination of the BS and MT antennas (see next chapter for more details).

Channel coding and interleaving techniques are well known and have proven to enhance the reliability of the link reducing the number of errors. Various types of codes can be applied with different capabilities to detect and correcting errors. If an ARQ (Automatic Repeat Request) technique is used [20], a certain number of time slots will be used for repetitions reducing the transmission efficiency in favour of the reliability.

The modulation should be spectrum efficient (due to the limitations on spectrum availability) and the signal envelop constant or containing low fluctuations if saturated power amplifiers are used in the transmission chain avoiding the severe effects of the non linearities, namely intermodulation products. Power amplifiers may have to work in a saturation mode to increase their efficiency that impacts directly on the power consumption and therefore reducing the autonomy of the battery.

The utilisation of spread spectrum techniques is limited by technology for large user data rates due to the high chip rates needed if reasonable processing gains have to be achieved. A hybrid multicarrier (described in the next paragraphs) spread spectrum modulation technique may however be employed to reduce the data rates per carrier and therefore lowering the requirements in terms of chip rate [21]. Power control requirements may also be of concern due to its direct impact on the system capacity.

OFDM is a special form of multicarrier modulation where the data, priori to transmission, is divided into several parallel bit streams to modulate several frequency carriers with a

much lower bit rate. OFDM is special since it uses densely spaced subcarriers with overlapping spectra and is receiving widespread interest for future wireless systems. OFDM time-domain waveforms are selected such that mutual orthogonality is ensured even though subcarrier spectra may overlap. Such waveforms can be generated using an FFT (Fast Fourier Transform) at the transmitter and receiver as demonstrated in [22] and may be considered one elegant solution for mobile communications transmitting at high symbol rate, since it can mitigate the channel time dispersion, Doppler spreading and synchronisation problems of high-performance digital radio links.

The choice between single and multicarrier modulation is basically related to the equaliser and FFT complexity, which for high transmission rates, require a high processing power. The last is also sensitive to non-linearities requiring linear power amplification, which brings down the power efficiency when compared to the operation in saturation mode (Class C amplifiers) used with single carrier modulation schemes. This has a direct impact on the battery time and the amount of heat to be dissipated, which is also of major concern in small MTs. OFDM performance can also be decreased in flat fading channels since the frequency diversity is not available. Due to the Doppler spreading, OFDM carriers loose their mutual orthogonality if rapid time variations of the channel occur. The same impact has the receiver phase jitter and frequency offsets which make subcarriers synchronisation much more difficult. These phenomena lead typically to an increase in the BER. Multicarrier modulation has been already proposed and adopted by ADSL (Asymmetric Digital Subscriber Loop), DAB (Digital Audio Broadcast), DVB (Digital Video Broadcast), HIPERLAN, WiMAX, and the 3G CDMA 2000 standards.

In this thesis only single carrier modulation was investigated and the implementation feasibility of a suitable equalisation technique. However, multicarrier modulation is an interesting research topic and in the future may become a strong candidate to be utilised for cellular mobile broadband communications, at least for the downlink direction where power constrains are not a main issue. The next section presents an example and the challenges of a high performance air interface based on single carrier modulation.

5. A Broadband Air Interface Solution Example

Considering the technology limitations and the pioneer solutions evaluated, the selected air interface for the designed prototype for cellular broadband systems evaluation [23] [24] [25], hereafter designated by Trial Platform, was selected to be FDD based. It supports a full duplex 34 Mbit/s link (user bit rate) or other sub rates including asymmetric transmission, depending on the service or application (e.g. provision of transmission of high quality digital video TV cameras signals to be injected directly in the broadcast chain for the provision of directs). A TDD approach would require much higher data rates per carrier (assuming the same bit rates) reducing therefore the symbol duration. On the other hand it would facilitate the channel estimation since the uplink and downlink would be using the same frequency carrier. In order to limit the radio channel variability and therefore simplifying the task to be performed by the equaliser, a speed limit of 50 km/h for the MTs was also assumed for this first step towards the implementation of a broadband cellular system.

Two are the minimum number of carriers required in a cell, one for uplink and one for downlink (FDD). They should however have sufficient distance from the borders and between themselves to ensure negligible levels of out-of-band radiation and adjacent channel interference. Moreover, the intended large cell overlap (to minimise the effect of LoS obstructions) precludes a significant spatial separation between the adjacent channels. The selected frequencies in the 40 GHz band were: 39.58 and 39.74 GHz (uplink) and 42.58 and 42.74 GHz (downlink) for the two cells of the system. Thus the ratio “gross bit rate-carrier spacing” is 0.4 bit/s/Hz, which provides a comfortable margin against adjacent channel interference. With this carrier choice only 32 % of each 1 GHz band will be actually used. The two-cell system is sufficient to perform first tests and studies concerning signal transmission (cell coverage area), mitigation techniques and radio handover algorithm.

The 60 GHz frequency was traditionally proposed for broadband systems and was used in a former prototype [26]. For the Trial Platform the 40 GHz band was selected due to the following benefits considering the initial deployment of cellular broadband systems:

- Lower propagation losses at 40 GHz due to the lower free space attenuation.

- Negligible oxygen absorption (≈ 0.05 dB/km and ≈15 dB/km at 60 GHz).
- Lower rain attenuation (≈ 7 dB/km and 11 dB/km at 60 GHz considering 25 mm/h).
- Higher power amplifiers output power (3 to 5 dB).
- Lower noise figure (1 to 2 dB lower).
- More linear and efficient transmitters (for the same output power).
- Lower transition and waveguide losses.
- Lower MMICs cost due to the existence of other applications/systems around the 40 GHz (larger production).

In conclusion, one could find many advantages and plausible reasons to select the 40 GHz in detriment of the 60 GHz band, at least in a perspective of a shorter term deployment. Since spectrum is managed by the regulators, the last decision belongs to these bodies that may have a different "agenda" given all the private and pubic requests and interests.

The major technical option for the Trial Platform was the one related with the multiple access technique that was decided to be TDMA. As mentioned before, this requires an adaptive equaliser, to mitigate the effects of the channel time dispersion, able to process in real time a high quantity of bit/s (64 Mbit/s for this specific case - a gross symbol rate of 32 MBd full duplex). This was one of the system components that raised more concern during the design phase. Based upon the characteristics of the radio channel, maximum expected delay spread figures and the symbol duration, we can conclude that we are in fact in presence of a broadband radio channel which exhibits frequency selective fading being for this particular case T_s = 31.25 ns, typically much lower compared to the delay spread values encountered in most expected environments for the system operation. Simulations performed for those scenarios revealed that a 250 ns equalisation depth would be enough in most cases [27]. This is therefore the maximum delay window the equaliser was designed.

The applied equalisation scheme is the Viterbi MLSE (Maximum Likelihood Sequence Estimation) algorithm with a state reduction using DFSE (Decision Feedback Sequence Estimation). The designed equaliser, able to cope with a 250 ns delay window time

dispersion (8 modulation symbols), is supposed to ensure a raw BER of at least $5 \cdot 10^{-3}$ with the help of a two-branch MRC (Maximal Ratio Combining) space diversity reception scheme [15]. Since the use of MLSE for such delay window time dispersion would require a number of states of $2^{16} = 65.536$ (16 bits time duration), which is practically impossible to implement, a state reduction algorithm was necessary, implying some performance degradation. However, in LoS environments, this degradation is relatively small justifying the utilisation of an 8-state DFSE with the help of the space diversity combining technique [27].

The MRC diversity combining technique, was first proposed by Kahn in 1954, consists in weighting the various received signals arriving to the receiver proportionally to their SNR, and then summed. The individual signals must be co-phased before combining to avoid destructive interference [15].

The structure of the air interface frame and burst is shown in Figure 3.3. In order to cope with the channel variability due to the multipath propagation and speed of the MTs, two training sequences (TS1 and TS2), each 32 modulation symbols long, are located in the middle of the first half-burst and the second half-burst. Each training sequence is required for slot/burst synchronisation purposes and for the estimation of the channel impulse response. TS1 is used to process the first half of the burst and TS2 the remaining part of it. Moreover, three 8-symbol tail sequences (TB, TM and TE) located at the beginning, the middle and the end of the burst, are used for burst delimitation.

A frame is composed of 80 slots. The burst payload corresponds to a code word of the (130, 110) Reed Solomon (RS) code, i.e. 520 modulation symbols (data plus 32 control bits plus 160 channel coding redundancy bits). The duration of the burst preamble (P) equals 1 μs (32-symbols) and was selected after taking into account both power amplifiers on/off switching time and AGC settling time parameters.

The training and tail sequences were defined by considering a worst-case time dispersion with a maximum relative delay of about 250 ns that corresponds to 8 modulation symbols. Each training sequence is required for slot/burst synchronisation purposes and, since it provides an estimate of the channel impulse response, for equalisation purposes also.

Furthermore, it is assumed the radio channel invariance during each half of the burst period when the MT speed is lower than 50 km/h.

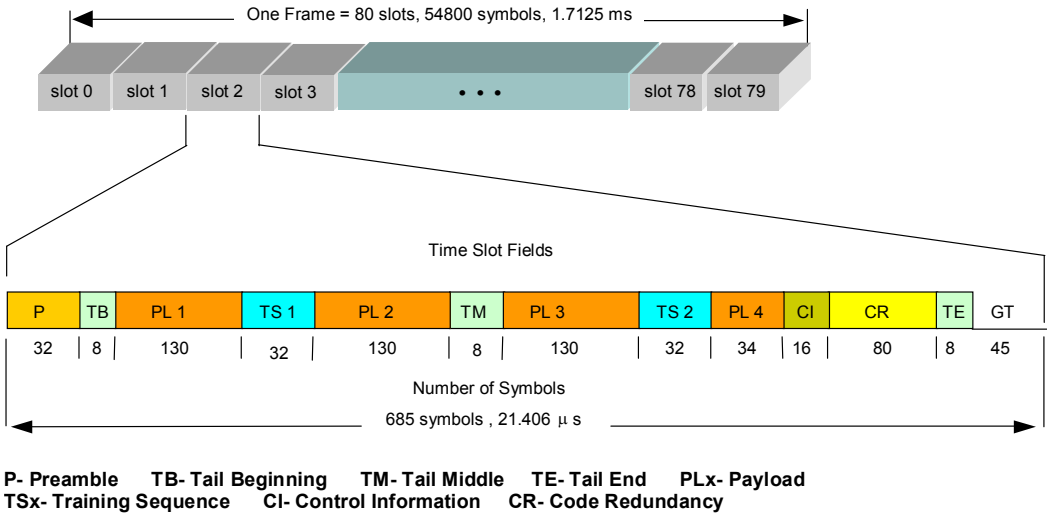

Figure 3.3: Frame and burst structure

The guard time period (GT) has duration of 1.4 μs, corresponding to 45 modulation symbols. For the predicted maximum transmission range, there is a reasonable margin against the propagation delay differences in each cell including strong time dispersion effects. Consequently, no time alignment functionality is required.

OQPSK-type modulation (Offset Quadrature Phase Shift Keying) is known to be well-suited for radio applications where saturated power amplifiers are employed since it provides a constant envelope or, at least, a low envelope fluctuation, a compact spectrum and a high detection efficiency obtained with simple low-cost receivers [5]. This is due to the fact that, in opposition to QPSK, changing the carrier phase by 180º is not allowed. Since the power amplifiers used in the Trial Platform are strongly non-linear, it is clear that an OQPSK-type scheme is an appropriate modulation choice. The OQPSK complex envelope can be expressed by:

$$s(t) = \sum_{n} c_n \, x(t - nT) \qquad (3.1)$$

Where $x(t)$ represents de modulation pulse and T the bit duration. The data sequences are $c_{2i} = \pm 1$ and $c_{2i+1} = \pm j$ and modulation symbols are concerned to pairs (c_{2i} , c_{2i+1}) therefore the symbol duration is $2T$ (31.25 ns) and the symbol rate $1/2T$ (32 MBaud). A suitable

mapping rule for deriving the sequence $\{c_n\}$ from the bit sequence $\{D_n\}$ (D_n = 0 or 1) is as follows:

$$c_n = j^n (2D_n - 1) \qquad (3.2)$$

The pulse $x(t)$ selection should take into account the non-linearities of the power amplifier. A quasi square root raised-cosine pulse shaping was selected for the Trial Platform.

The general goal of channel coding is to improve the BER at a minimum cost in bandwidth. The utilisation of structured sequences involve the addition of parity digits to the data such that the parity digits can then be employed for detecting and/or correcting specific error patterns by parity check. Two important subcategories of structures sequences can be identified: block coding and convolutional coding.

Out of the various possibilities, block codes where selected for the Trial Platform which are characterised by the (n,k) notation. The encoder transforms a block of k message symbols into a longer block of n codeword symbols. A special case of block codes is the nonbinary Reed-Solomon (RS) code that is a special subclass of the cyclic BCH (Bose-Chadhuri-Hocquenghem) codes. The selected RS code is constructed over the *Galois field* GF(2^8) [10]. It is a shortened RS (130, 110) code with an FEC (Forward Error Correction) capability of ten symbols each of 8-bit [(130-110)/2]. The full RS code is (255,235) with $n=2^8-1$ and $k=2^8-1-2t$, being t the number of correctable symbol errors. The burst payload corresponds to a code word of the (130, 110) shortened RS code, i.e. 520 modulation symbols (see next chapter).

The large number of known RS decoding algorithms can be roughly classified into time-domain and frequency-domain decoding algorithms. Frequency-domain has a higher computational complexity and therefore the time-domain Berlekamp-Massey and Euclidean algorithms were selected for implementation in the Trial Platform [27].

Table 3.2 summarises the air interface parameters. More details about the air interface together with other characteristics of the Trial Platform are described in the next chapter.

Air Interface Parameters	Type and Characteristics
Carrier frequencies	Uplink: 39.58 and 39.74 GHz Downlink: 42.58 and 42.74 GHz
Multiple access technique	TDMA
Duplexing	FDD
Modulation and symbol rate	OQPSK at 32 MBaud
Diversity	Two branch space diversity with MRC
Equalisation	DFSE – type Viterbi, 8 symbols (250 ns delay window)
Forward Error Correction (FEC)	(130,110) Reed-Solomon code, 8-bit symbols
Frame	80 time slots (1.7125 ms)
Time slot	Duration of 21.406 μs.
Bit and symbol duration	15,625 ns and 31,25 ns

Table 3.2: Air interface parameters

6. Summary and Conclusions

In this chapter were presented mitigation techniques that can be employed in the design of broadband radio interfaces as well as the specific solution used for the cellular broadband system prototype.

The various types of fading have different impacts on the radio interface. Frequency selective fading induces ISI since it is caused by multipath propagation and therefore multiple copies of the signal arrive to the receiver at different times, causing distortion. When seen in the frequency domain this fading implies that not all frequency components of the signal are affected the same way. Flat fading contributes only to the reduction of the SNR since all the multipath components arrive within the symbol time duration but can add destructively, depending on their relative phase. In opposition to frequency selective fading, all the frequency components of the signal suffer the same effects. Fast fading is caused by the fact that the channel characteristics change within the duration of a symbol. This leads to distortion and a loss in the SNR. In the frequency domain it manifests itself by Doppler shift. Finally, slow fading causes only a reduction in the SNR.

In terms of degradation, a loss of SNR is much less severe than the introduction of distortion, being the last the most difficult to mitigate. Increasing the E_b/N_0 is not sufficient to overcome the effects of distortion, and therefore other techniques are required. First distortion should be corrected and then addressed the SNR problem.

Key parameters for the radio interface are the BER, delay and loss of data. In order to minimise these three parameters, a deep knowledge of the radio channel characteristics is essential, since it allows the selection of the most suitable mitigation techniques.

Engineers when designing a broadband air interface face many challenges and options that lead to trade-offs. The air interface has to transport reliably the information from the BS to the MT and vice-versa, while the MT is on the move, in different scenarios supporting applications and services requiring high bit rates. The air interface is usually the bottleneck of the system.

Several options are available to combat the fading effects. The main target is always to bring the performance of the system as close as possible to when operating in AWGN channel conditions. Mobile broadband systems, due to the smaller symbol duration and the utilisation of higher frequency bands have therefore a higher chance of being affected by the radio channel impairments. Possible options to combat the fading effects are: type of antennas, multiple access technique, equalisation, modulation and coding.

Frequency selective fading can be mitigated with various techniques. Equalisation is one of them and consists basically in gathering the dispersed symbol energy causing ISI back to its original time interval. There are two types of equalisation: linear and non-linear, being the last sub-divided in two: DFE and MLSE. Spread spectrum techniques can also be used to combat frequency selective fading. The utilisation of a Rake receiver in Direct Sequence systems is enough since it is able to synchronise to the various multipath components avoiding the distortion. On the other hand, Frequency Hopping systems overcome this effect by changing rapidly frequency avoiding the next multipath component. OFDM can also be used since it increases the symbol time duration and therefore reduces the signal bandwidth per carrier, leading to operation within the channel coherence bandwidth.

Fast fading can be ameliorated by selecting a modulation technique robust to phase variations. The reduction of the symbol time duration, by the addition of redundancy to the signal, is also effective. Moreover, the usage of PLLs must be avoided but pilot type channels are possible and effective.

Channel coding and diversity are techniques suitable to mitigate the loss of SNR.

In fact, none of the above presented techniques is purely applicable to combat the effects described, but have multiple actions in parallel.

Mobile broadband systems are also affected by frequency selective fading and fast fading being the last less prominent since high MT speeds are not the rule due to its typical indoor and urban operation. Specifically for the prototype five options were considered to mitigate the radio channel impairments: directive lens antennas, diversity reception, equalisation, spread spectrum and multicarrier modulation.

Considering the benefits and disadvantages, a solution for the prototype broadband air interface was obtained. A 34 Mbit/s full duplex link, FDD based and allowing for asymmetric transmission was implemented. In order to minimise the channel variability, a limit of 50 km/h was added to the specifications. The 40 GHz frequency band was selected since it has several advantages over the 60 GHz band, namely lower propagation losses, negligible oxygen absorption and lower MMICs costs. The multiple access technique selected was TDMA with a symbol time duration of 31.25 ns. A single carrier modulation technique was selected due to constrains imposed in terms of linearity by the RF hardware at this frequency band. The equaliser is MLSE type and was designed to handle delay windows up to 250 ns given the propagation characteristics of the scenarios were the system expects to operate. A two-branch space diversity reception scheme was also used. The frame is composed of 80 slots and the burst payload corresponds to a code word of the (130,110) Reed-Solomon code, corresponding to 520 modulation symbols, implementing the FEC functionality. Two training sequences were used per burst to better handle the channel variability during the burst duration. The OQPSK modulation was selected due to its constant envelop and compact spectrum properties.

In summary, the mitigation techniques were presented for the various fading types, given the different degradation effects. Based on the specific characteristics of mobile broadband systems, various technical options were considered to be implemented in the prototype. Finally, the air interface employed solution was described.

7. References

[1] Olle Nilsson, "Fundamental Limits and Possibilities for Future Telecommunications", IEEE Communications Magazine, pp. 164-167, May 2001.

[2] Nobuo Nakajima and Yasushi Yamao, "Development for 4th Generation Mobile Communications", WILEY Wireless Communications & Mobile Computing, Vol. 1, No. 1, Jan-Mar 2001.

[3] Bernard Sklar, "Rayleigh Fading Channels in Mobile Digital Communication Systems Part I: Characterization"; IEEE Communications Magazine, Vol. 35, No. 9, pp. 136-146, Sep. 1997.

[4] Bernard Sklar, "Rayleigh Fading Channels in Mobile Digital Communication Systems Part II: Mitigation"; IEEE Communications Magazine, Vol. 35, No. 9, pp. 148-155, Sep. 1997.

[5] Bernard Sklar, "Digital Communications Fundamentals and Applications", Prentice Hall, 1988

[6] G. van Dooren, "A Deterministic Approach to the Modelling of Electromagnetic Wave Propagation in Urban Envirinments", PhD Thesis, Eindhoven University of Technology, 1994.

[7] José Fernandes, "Modelação do Canal de Propagação Rádio Móvel de Banda Larga na Faixa das Ondas Milimétricas e seu Impacto no Desempenho de Transmissão do Sistema", PhD Thesis, University of Aveiro, 1996.

[8] J. D. Parsons, "The Mobile Radio Propagation Channel", Prentech Press, London, 1992

[9] J. G. Proakis, "Digital Communications", New York, McGraw-Hill, 1989.

[10] Raymond Steele, "Mobile Eradio Communications", IEEE Press, 1992

[11] S. U. H. Qureshi, "Adaptive Equalisation", IEEE Proceedings, Vol. 73, No. 9, pp. 1349-1386, September 1985.

[12] Gordon L. Stüber, "Principles of Mobile Communication", Kluwer Academic Publishers, 1996.

[13] H.Sari and I.Jeanclaude, "An Analysis of Orthogonal Frequency Division Multiplexing for Mobile Radio Applications", IEEE VTC '94, pp.1635-1639, Stockholm, Sweden, June 1994.

[14] J.A.C.Bingham, "Multicarrier Modulation for Data Transmission: An Idea Whose Time Has Come", IEEE Communication Magazine, Vol. 28, No. 5, pp. 5-14, May 1990.

[15] William C. Jakes, "Microwave Mobile Communications", IEEE Press, 1974.

[16] C. D. Gavrilovich, "Broadband Communication on the Highways of Tomorrow", IEEE Communication Magazine, pp. 146-154, April 2001.

[17] T. Tjelta, M. Annoni, L. Tokarchuk, A. Nordbotten, E. Scarrone, J. Bigham, C. Adams, S. Bizzarri, K. H. Craig, M. Dinis, "Future Broadband Radio Access Systems for Integrated Services with Flexible Resource Management", IEEE Communications Magazine, August 2001.

[18] M. Dinis, V. Lagarto, M. Prögler, J.T. Zubrzycki, "SAMBA: a Step to Bring MBS to the People", ACTS Mobile Communication Summit '97, Aalborg, Denmark, Oct. 97 (Web page: http://samba.ptinovacao.pt).

[19] C. A. Fernandes, "Shaped Dielectric Lenses for Wireless Millimeter-Wave Communications", IEEE Antennas & Propagation Magazine, Vol. 41, No. 5, pp. 141-150, Oct. 99.

[20] N. Fukui, A. Shibuya and K. Murakami, "Performance of Combined ARQ with SR and GBN for Wireless Systems on a 40 GHz Band Radio Channel", IEEE Communication Magazine, pp. 122-126, September 2001.

[21] Mohamed-Slim Alouini, M. K. Simon, A. J. Goldsmith, "Performance Analysis of Single Carrier and Multicarrier DS-CDMA Systems Over Generalised Fading Channels", WILEY Wireless Communications & Mobile Computing, Vol. 1, No. 1, Jan-Mar 2001.

[22] S. B. Weinstein and P. M. Ebert, "Data Transmission by Frequency-Divisin Multiplexing Using the Discrete Fourier Transform", IEEE Transactions in Communications Technology, Vol. 19, No. 5, pp. 628-634, October 1971.

[23] Manuel Dinis and José Fernandes, "Provision of Sufficient Transmission Capacity for Broadband Mobile Multimedia: a Step Towards 4G", IEEE Communications Magazine, August 2001.

[24] M. Prögler, C. Evci, M. Umehira, "Air Interface Access Schemes for Broadband Mobile Systems", IEEE Communications Magazine, Vol. 37, no. 9, pp. 106-115, Sept. 99

[25] J. Mikkonen, Ciotti Corrado, Cengiz Evci, Max Prögler, "Emerging Wireless Broadband Networks", IEEE Communications Magazine, Vol. 36, No. 2, pp. 112-117, Feb. 98

[26] L. Fernandes, "Developing a System Concept and Technologies for Mobile Broadband Communications" IEEE Personal Communications Magazine, Vol. 2, No. 1, p. 54-59, Feb. 1995.

[27] T. Fujino, et al, "Design of Baseband Signal Processing Unit in SAMBA Trial Platform for Mobile Broadband Applications", ACTS Mobile Communications Summit '98, Rhodes, Greece, June 98.

4th Chapter

Mobile Broadband Trial Platform Architecture

1. Introduction

The Trial Platform architecture was defined based on the state-of-the-art knowledge available when the specifications were frozen to start the design and manufacturing processes. The mission was to build a mobile broadband Trial Platform where the main functionalities should be tested and evaluated. The available budget, time, technology state-off-the-art and the assumed degree of risk have limited the Trial Platform features.

Since handover was seen as a key feature, the Trial Platform is composed of two BSs (Base Stations), one BSC (Base Station Controller), a MSR (Mobility Server) and a Switch. The architecture is shown in Figure 4.1 where two MTs are also displayed [1] [2] [3] [4].

The availability of two MTs allows the possibility of testing the sharing and dynamic assignment of bandwidth in a cell. This is an important aspect due to the nature of the broadband applications that require asymmetry and variable transmission rate capabilities.

Moreover, in order to increase capacity, for each MT and for a particular instance, only the necessary bandwidth should be reserved.

The MT is composed of a standard broadband terminal connected to a MTA (Mobile Terminal Adapter) that provides the adaptation to the radio interface. The MTA is basically composed with the same modules as the BS and BSC except that only one controller is needed due to the fact that only one radio link is used at a time during the handover procedure.

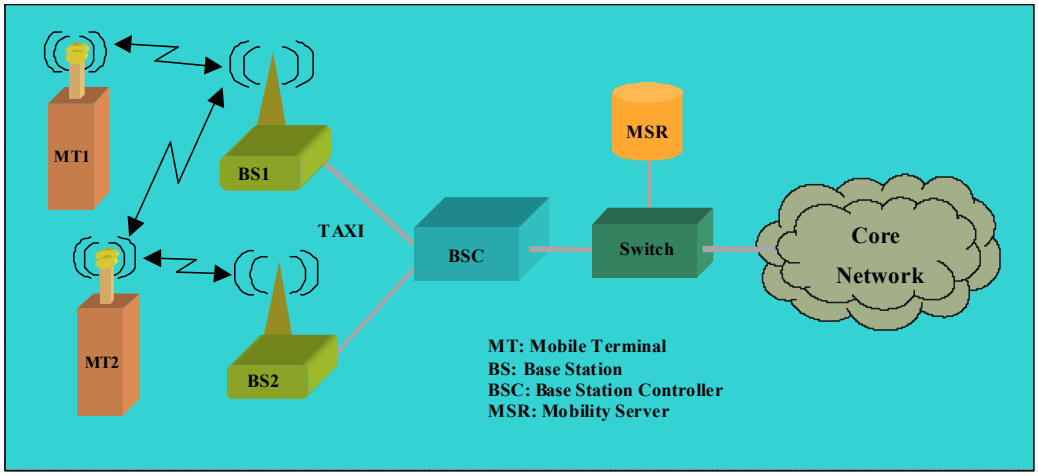

Figure 4.1: Trial Platform Arquitecture

In this chapter are described all the Trial Platform hardware and software modules main characterisitcs. It starts with a description of the cells shappe followed by the presentation of the air interface characteristics and main design options. The BS architecture (antennas, RF and baseband modules) is described followed by the BSC architecture, including the DLC (Data Link Control) protocols and mobility and resource management protocols. The chapter ends with a description of the selected radio handover algorithm.

2. Air Interface Characteristics

The air interface should provide the necessary resources and mechanisms to ensure the transparent and reliable transfer of traffic and signalling information between transceivers with the required quality of service concerning error rate and delay in the hostile mobile radio environment. Moreover it has to provide the functions to guaranty a fair policy for the access and share of the resources (MAC – Medium Access Control) and to control the link

establishment, sequence of the information and quality (LLC – Logical Link Control) e.g. error control [1] [5].

As already mentioned in the former chapter, several implementation constraints have been taken into account when the Trial Platform radio interface was designed, namely:

- Propagation constraints of the millimeterwave paired frequency band.
- Power amplification constraints in terms of limited power output and non-linearties.
- Restrictions on new ASICs (Application-Specific Integrated Circuit) and MMICs (Monolithic Microwave Integrated Circuit) production.
- Budget and time constrains.

As a consequence various simplifications had to be made in the design of the air interface, namely:

- Maximum MT speed of 50 km/h.
- Maximum time dispersion of 250 ns.
- Short range transmission (relatively small cells dimensions).
- Operation only in LoS is guaranteed.
- Usage of a single type of transmission burst.
- Implementation of radio handover only.
- No time alignment function.
- No adaptive power control.
- Spectrum efficiency concerns not taken into consideration.

Overall, two main fundamental technological options were made for proof of realisability:

- Adoption of single-carrier modulation.
- Omnidirectional MT antenna.

The first requires the utilisation of an equaliser, which is very demanding in terms of processing power affecting directly the hardware configuration and architecture, and the second is a fundamental requirement for a mobile system where no mobility restrictions should exist on the terminals. The last choice implies the utilisation of antennas with low gain having a direct impact on the link power budget.

3. Radio Cells Shape

The shape of the cells was designed to cover the most likely general type of scenarios such as streets, large squares and large indoor arenas, being however the wide cell customized and adapted for the specific needs of the Pavilhão Atlântico in Lisbon.

The selection of lens type antenna technology permits an easy design of the cell shape, a fairly uniform power flux density in the cell coverage area, fairly sharp boundaries and a reduction in the co-channel interference [5] [6]. Moreover, the signal time dispersion is maintained at acceptable levels by shaping the radiation pattern to avoid the transmission of the power to zones of no interest reducing the possible appearance of strong multipath reflections. Given these facts, it is evident that the configuration of the cells (BS location and characteristics) is of primary importance for the system performance [7] [8] [9]. Two cell types were designed to cover two different typical scenarios: a street and an arena or square. Figure 4.2 and Figure 4.3 show the dimensions of the coverage area for the wide (arena or square) and elongated (street) cells, respectively.

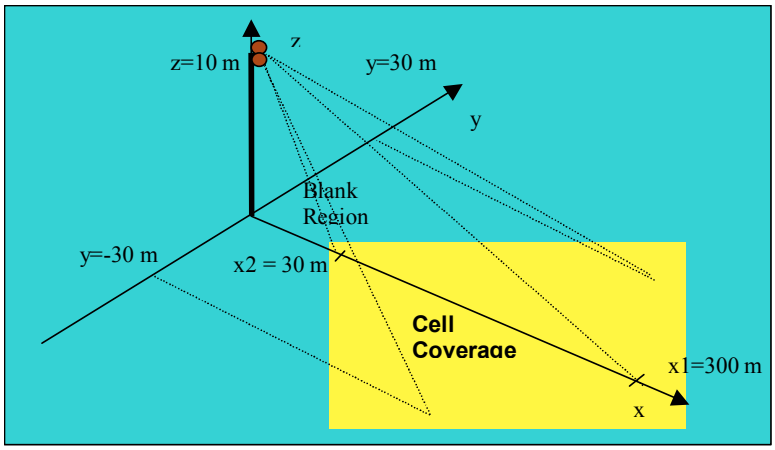

Figure 4.2: Wide Cell coverage area for z=10 m

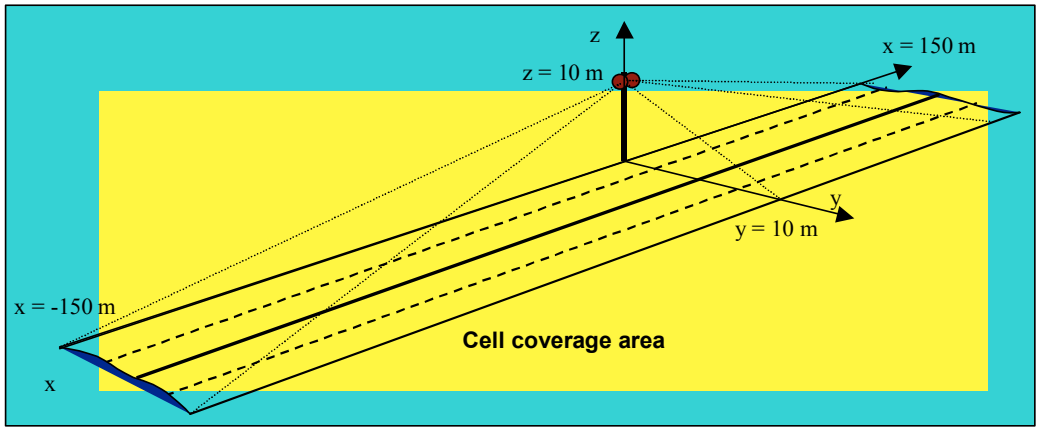

Figure 4.3: Elongated Cell coverage area for z=10 m

For the elongated cell, it was decided to use the same antenna type in the BS and MT (each with a $sec\ \theta$ radiation pattern), loosing however the movement freedom of the MT. The MT can use the hemispherical antenna though not satisfying the constant flux coverage requirement. For the wide cell case, it is the BS antenna that provides the required radiation pattern therefore the MT can use a hemispherical antenna and almost no mobility restrictions are imposed.

Adjusting the BS height and antenna tilting angle in the vertical plane, the cells dimensions can be changed allowing some degree of flexibility in controlling the coverage area and reducing the co-channel interference. For the direction pointing towards the centre of the cell (x direction), the dimensions of the wide cell can be estimated by using the following equations:

$$x_1 \cong \Delta h \tan(86.2^\circ) \quad (4.1)$$

$$x_2 \cong \Delta h \tan(71.5^\circ) \quad (4.2)$$

$$y \cong 2x_2 \tan(15^\circ) \quad (4.3)$$

where Δh is the height difference between BS and MT. For the elongated cell case the equations (4.4) and (4.5) can be used:

$$x \cong \Delta h \tan(85.2^\circ) \quad (4.4)$$

$$y \cong x/20 \quad (4.5)$$

4. Dielectric Lens Antennas

For the Trial Platform dielectric lens antennas were selected since they are inexpensive, they can be designed to produce highly shaped beams that embrace most of the already stated characteristics, they can be easily moulded and manufactured with high tolerances and have sufficient bandwidth for FDD operation (up to 10% of the carrier frequency) [5] [6] [10]. The lenses design problem lies in the determination of the lens surface that transforms the known feed pattern into the desired output radiation pattern. Geometrical optics theory can be used for this design when the dimensions are much larger than the wavelength. A more accurate design is obtained using the physical optics theory that takes into account the diffraction phenomenon.

Since two types of cell were designed for the Trial Platform suitable for the most likely scenarios to be covered in outdoor and indoor environments: wide and elongated cells, three different types of antennas were manufactured to meet the requirements – two for the BS and one for the MT. Figure 4.4 to Figure 4.6 show the antennas radiation patterns.

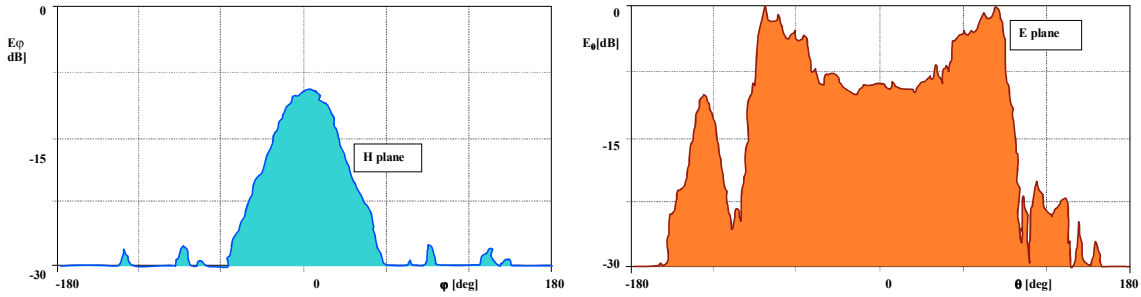

Figure 4.4: Elongated cell antenna radiation patterns – horizontal and vertical planes

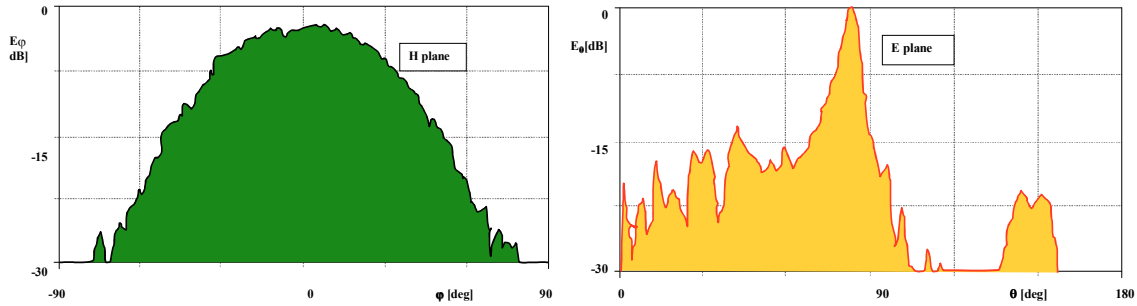

Figure 4.5: BS Wide cell antenna radiation patterns – horizontal and vertical planes

The implementation of space diversity reception requires the design of two receiving antennas separated in space having therefore impact in terms of mutual blocking that should be minimised. Therefore the radiation patterns, the mechanical fixing and relative position of the lens must be taken into account. Figure 4.7 shows all the antennas where it can be seen the two lenses being one for transmission and reception and the other just for reception. The antennas are separated by 14 λ to guarantee a low correlation level of the received signals.

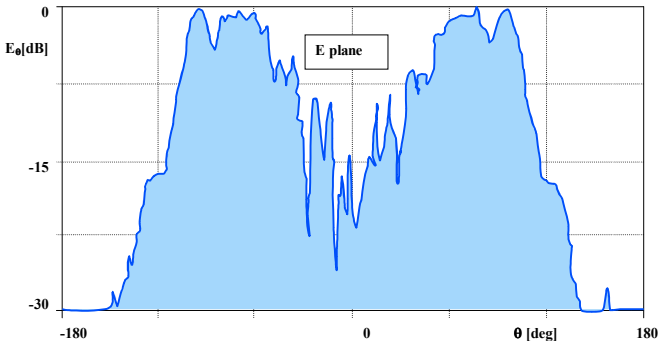

Figure 4.6: MT antenna radiation pattern – vertical plane

The choice of the dielectric material for the antennas was based on electric and mechanical characteristics. Two conflicting arguments involve the electrical characteristics:

- The permittivity of the dielectric should be as high as possible to favour the high refraction angles that are required for energy flux cases enabling the reduction of the lens depth.
- The wave impedance mismatch at the radiating lens surface decreases with the decreasing of the permittivity values.

Permittivity values on the range 2.0 to 2.5 have shown to be a good compromise. Another important aspect for dielectric selection is the dissipation loss. Due to the fact that lens dimensions are large compared with the wavelength, extremely low-loss materials are required. The selected materials used for the lens fabrication are homogenous, isotropic, impermeable to moisture and machinable, being Polystyrene ($\varepsilon r = 2.43$ & $\tan \delta < 0.001$) and Polyethylene ($\varepsilon r = 2.35$ & $\tan \delta < 0.0005$), respectively for the elongated and wide cell antennas. Table 4.1 summarises the antennas main characteristics [10] [11].

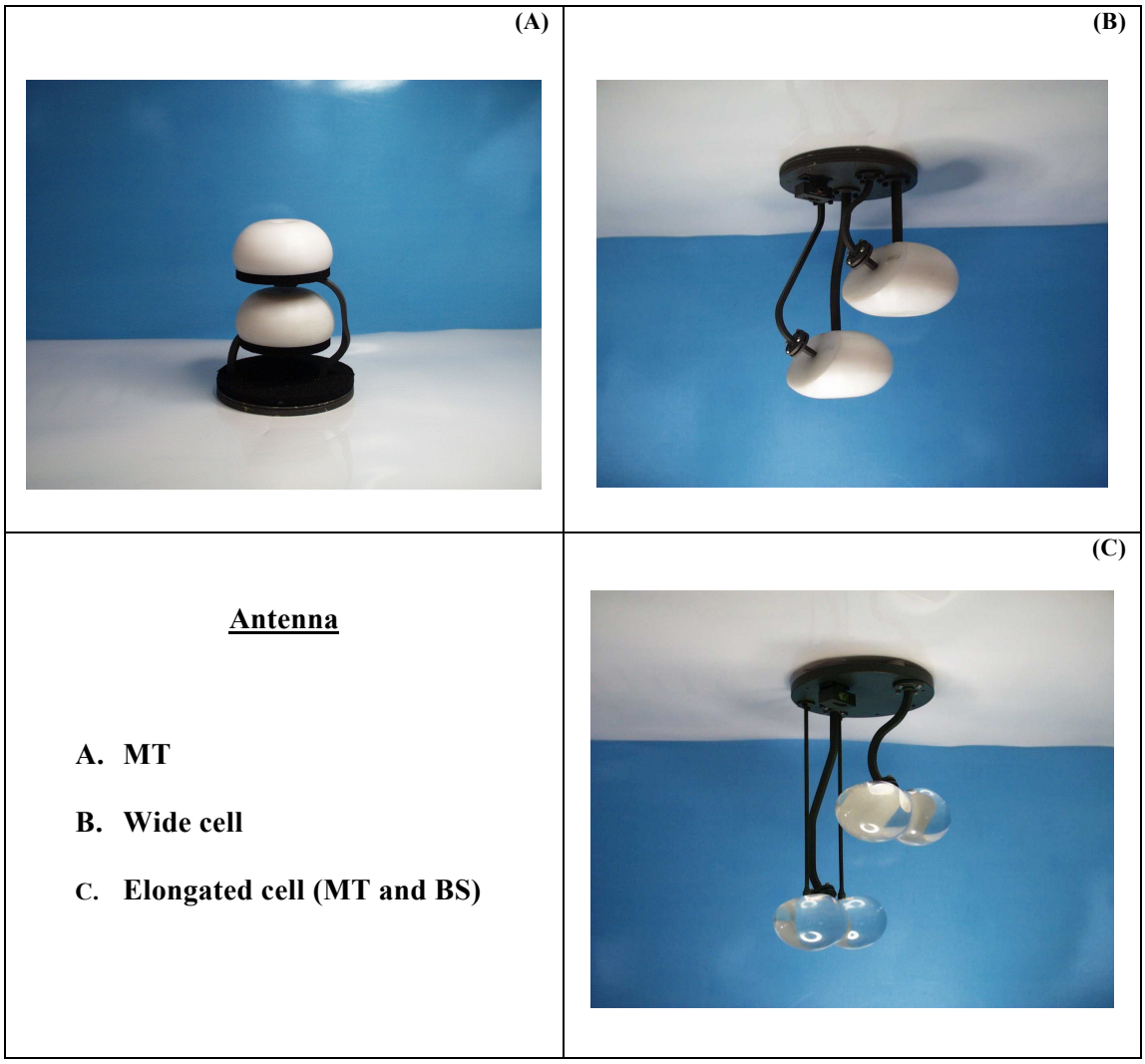

Figure 4.7: BS and MT lens antennas

Parameter	Value
Frequency	40 GHz band
Gain	19 dBi (wide cell) 11 dBi (elongated cell) 4 dBi (MT)
Lens material	Polystyrene ε_r = 2.43; Losses = 0.43 dB (elongated cell) Polyethylene ε_r = 2.35; Losses = 0.2 dB (wide cell and MT)
Polarisation	Vertical
Radiation pattern	Secant squared (wide cell) Secant (elongated cell) Hemispherical (MT)
Return loss	Higher than 15 dB
Diversity reception	Antenna separation of 14λ

Table 4.1: Antenna characteristics

5. RF and IF Modules

Figure 4.8 shows the Trial Platform three main modules: RF (Radio Frequency) front-end, which includes the High IF (Intermediate Frequency) and Low IF sub-modules, the BBPU (Baseband Processing Unit) and the CU (Control Unit). In the following sections a detailed description of these modules is presented.

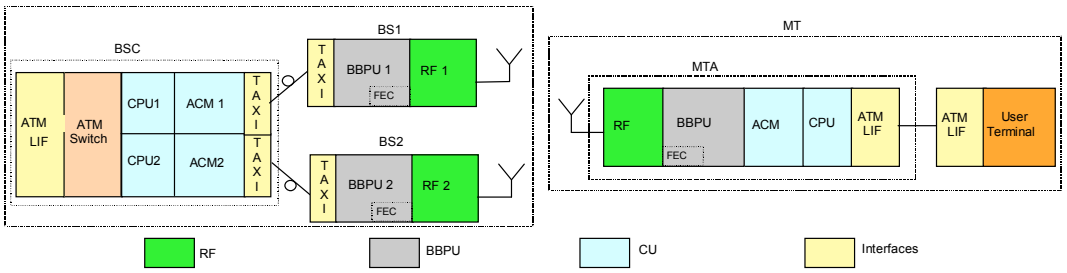

Figure 4.8: Trial Platform main modules

The RF/IF modules were designed to support full duplex operation and its main task is to convert the I-Q baseband signal received from the BBPU into modulated carrier frequency bursts in the 40 GHz band to be transmitted over the air and to perform the reverse operations in the receiving direction, therefore they deliver I-Q baseband signals to the BBPU [12]. Space diversity is used and therefore two independent reception branches are needed. Since the same antenna is used for transmission and reception a diplexer is also required. The RF/IF functionalities were split into three different modules [13]:

- The RF module (RF section).
- The High IF module (High IF).
- The Low IF module (Low IF).

In the transmitting direction, NRZ I-Q baseband signals delivered by the BBPU are passed to the Low IF module, which converts them to the Low IF frequency (1600 MHz). This module uses an internal IF frequency at the output of the modulator of 320 MHz. The Low IF frequency is up-converted to the High IF frequency by the High IF module and then upconverted to the transmitting frequency by the RF front-end. The RF module operates in the paired frequency bands 39.5-40.5 GHz (uplink) and 42.5-43.5 GHz (downlink) with an uplink-downlink frequency separation of 3 GHz. For the particular implementation of the

Trial Platform, only two BSs were specified each with one pair of carriers, thus the frequency carriers 39.58 and 39.74 GHz for the uplink and 42.58 and 42.74 GHz for the downlink were used (see Figure 4.9, Figure 4.10 and Figure 4.13).

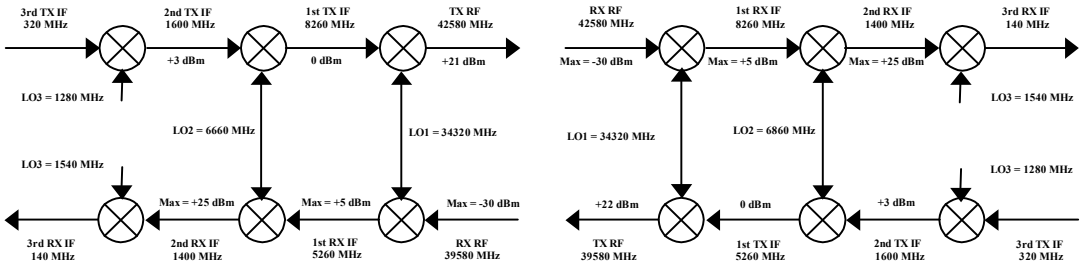

Figure 4.9: Frequency plan 1

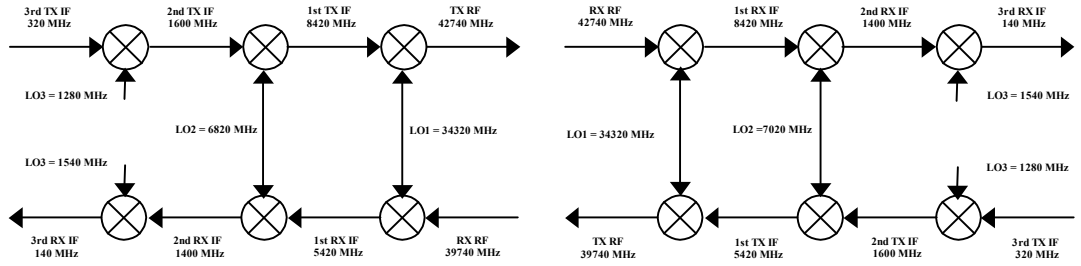

Figure 4.10: Frequency plan 2

In the receiving direction, after the diplexer filter, the two diversity branches received signals are amplified using a low-noise amplifier based on HEMT (High Electron Mobility Transistors) technology and a simple low-loss microstrip filter suppresses the image noise of the low noise amplifier. Then, a mixer down-converts the signal to the High IF frequency, being different for the BS and MT, since the uplink and downlink directions use different frequency bands. The frequency range was selected so that the image rejection and LO (Local Oscillator) filtering causes no problem, even with low-quality millimetrewave microstrip filters. Due to the fact that the first millimetrewave LO (34.32 GHz) is fixed and is used for the transmitter and receiver (the reference frequency for all LOs is an oven controlled 10 MHz crystal oscillator), the High IF frequency is different in accordance with the selected transmitting or receiving carrier frequency.

The LO source for the second down-conversion is the synthesiser used for channel selection, which is also used for up conversion. The Low IF operates at a fixed frequency being 1400 MHz for the receiving direction. The last IF frequency is 140 MHz, internal to

the Low IF module, appearing before the demodulator. The dynamic compression takes place at this frequency using an AGC controlled linear amplifier. Finally, the OQPSK quadrature demodulator provides the analogue in-phase and quadrature outputs to the BBPU.

The Tx and Rx Low IF frequencies have to be different, in order to guarantee that the image frequency of the up-converted transmitter frequency is not exactly the same as the receiving frequency. This approach was selected, as it does not seem practical to reduce that spurious frequency below the sensitivity level of the receiver, which is necessary to prevent degradations. Figure 4.11 shows photographs of the RF modules.

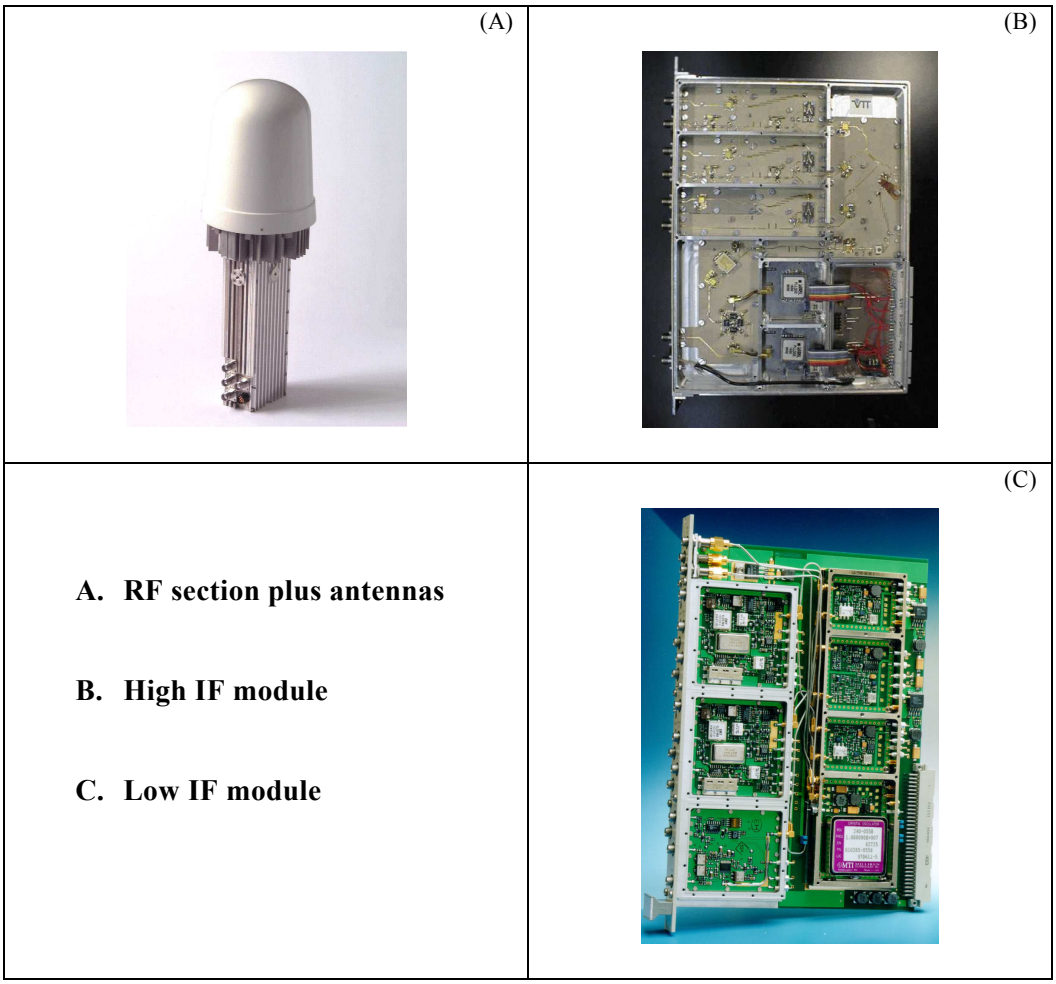

Figure 4.11: RF/IF Modules photographs

6. Baseband Processing Unit

The primary function of the BBPU is the digital processing of the baseband signals, both for reception and transmission and is located between the MWT (MillimetreWave Transceiver) unit and the CU as shown in Figure 4.12 [14] [15]. Its main requirements were the support of MT speeds up to 50 km/h and a maximum cell size of approximately 300 m (distance from the BS). Figure 4.14 shows the BBPU components in more detail.

At the reception side, the BBPU receives the two space diversity branches I and Q signals and converts them to a digital format (sampled at 64 MHz and 8-bit quantisation). The BBPU synchronises its slot timing to the received signals by UWD (Unique Word Detection) in the "TS Detection" module and is maintained via a flywheel mechanism based on the synchronisation information of the previous burst. This allows the detection of the beginning and end of each burst. The UWD is within the training sequence (see Figure 4.17) of the burst. The same module is also responsible for the evaluation of the CIR (Channel Impulse Response) to be used for the equalisation process only. The access to this information for the radio channel study was not possible due to technical constrains and confidentiality aspects.

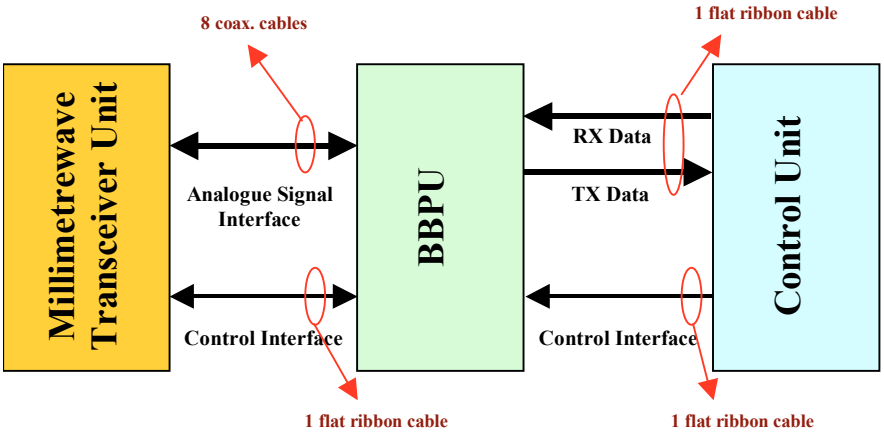

Figure 4.12: Interfaces to CU and MWT

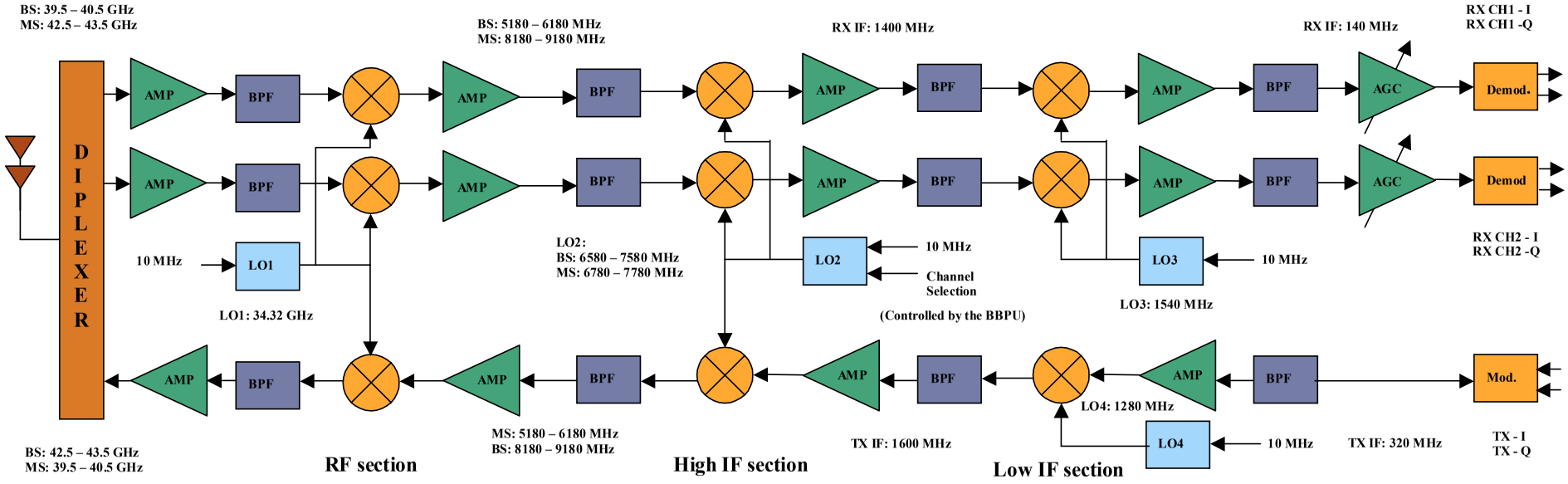

Figure 4.13: RF-to-Baseband and Baseband-to-RF converters

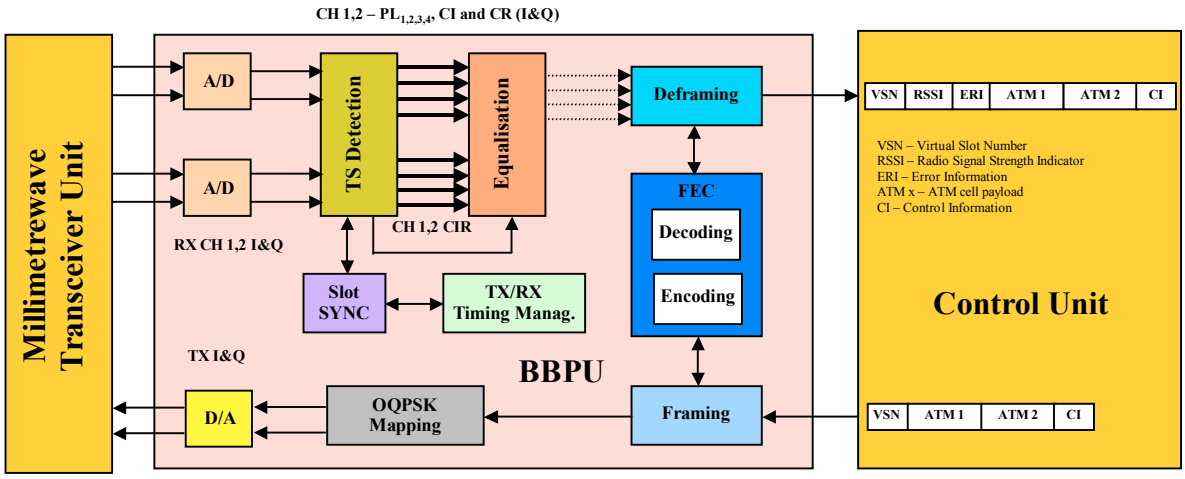

Figure 4.14: Baseband modules block diagram

The BS slot synchronisation is based on the state machine shown in Figure 4.15 and must be maintained for each MT. The MT must operate the state machine only for one of the 80 slots that constitute the frame.

The four states are defined as follows:

- **Out-of-Sync** – The out of synchronisation state occurs when the MT is powered on. The whole received burst is then searched for the training sequence.

- **Sync-Protection B** – The synchronisation protection B state occurs when the unique word is detected and the burst is declared valid. This state is maintained until a certain number of training sequences non-detections occurred, then the Out-of-Sync state is re-entered. If the detections are successful and the bursts are valid, the state In-Sync is entered.

- **In-Sync –** The in synchronisation state is the state when in normal operation where the burst are detected and declared valid. However if a training sequence failed to be detected, the Sync-Protection F state is entered.

- **Sync-Protection F –** The synchronisation protection F state occurs when the training sequence is not detected, but synchronisation is considered kept and the burst is declared valid. When the training sequence is detected the In-Sync state is

re-entered. However this state cannot be kept for more than a certain number of bursts. After that the Out-of-Sync state is entered.

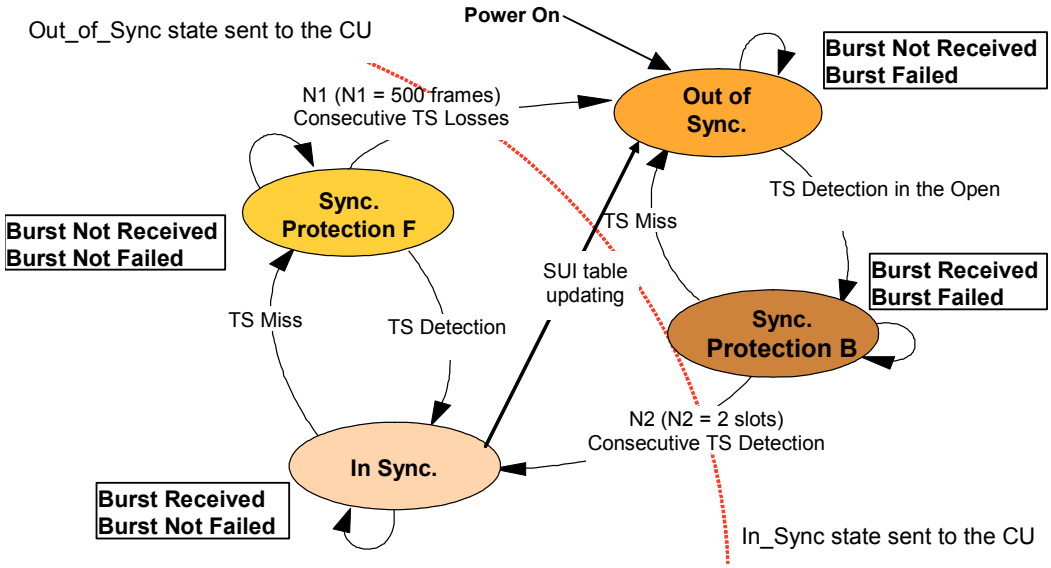

Figure 4.15: Slot Synchronisation state machine

The equalisation module combines the two 64 Mbit/s channels to produce a reliable received signal, and performs the adaptive equalisation to mitigate the effects of the multipath dispersion of the time-varying channel, based on the two training sequences existing on the burst. The equalizer 8-state DFSE Viterbi-type also performs diversity combining and is able to cope with high time dispersion (250 ns – 8 modulation symbols) ensuring a raw BER of $5x10^{-3}$ at redundancy check (see Figure 4.16), the payload is extracted (comprising descrambling and deframing) and is then passed to the FEC codec, which detects and corrects the transmission errors based on the contents of the CR field. The used code is the shortened Reed-Solomon (130,110) over the GF(2^8) (Galois Field) is capable of correcting up to 10 symbol errors per burst, each symbol consisting of 8 bits. The two decoding algorithms are time-domain based (Berlekamp-Massey and Euclidean algorithms). The decoded payload is finally delivered to the CU in the BSC for further processing.

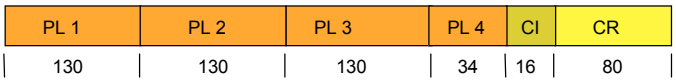

Figure 4.16: Output of the equalizer data

For transmission, the CU delivers the payload (data and control information) to the BBPU. The data is encoded by the FEC codec, and afterwards the "Framing" module builds the burst. This procedure consists in extracting from the MAC-PDU (Packet Data Unit) the data and the control information, add the CR produced by the FEC, scramble the obtained result, perform segmentation and finally add in between the payloads fields the training sequences and the tailing bits. Subsequently, digital modulation is performed (OQPSK mapping). The two analogue non-return-to-zero I and Q baseband signals are then passed to the first IF stage of the RF module.

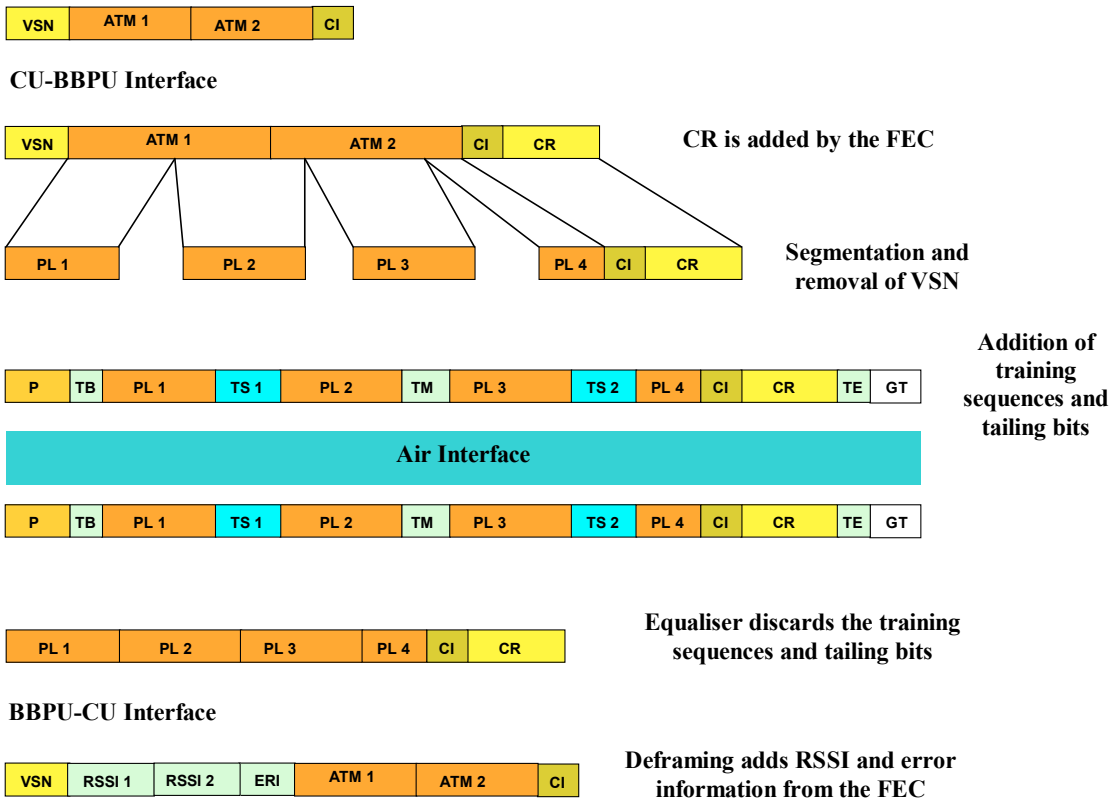

Figure 4.17: Framing and Deframing process

Timing management is a very important task for synchronisation and is relevant to various modules in the BBPU. It indicates the frame timing and slot timing in both transmit and receive directions based in two frame counters with accuracy of one modulation symbol and one frame range (80 slots). Frame timing and slot timing on the uplink are synchronised to the downlink with a time shift to compensate for processing and propagation delays. Therefore in the MT the transmit counter is synchronised to the start of

the received frame and the receive counter is synchronised to the training sequence detection timing. In the BS, the receive counter is synchronised to the start of the transmit slot and the transmit counter to the local clock. Furthermore, in the MT in order to absorb the jitter in the received frame timing the start of the received frame timing is averaged. The CU performs the frame synchronisation because the BBPU does not know the real slot number running on the air interface. A VSN (Virtual Slot Number) is used that is reset to zero when the first valid burst is detected on the MT and then incremented for each received burst. The MT transmits the VSN to the CU that is different for all MTs. On the other direction, the CU indicates to the BBPU which slot should be used for the transmission of the burst. The slot structure in the uplink must be determined with an offset relatively to slot zero on the downlink taking into account all delays that are caused by the CU, BBPU and MWT. This inter-slot offset is in the range of slots and is a parameter located in the CU. An intra-slot offset (needed only on the MT) is also specified to be able to shift the transmitted slot in the range of a slot and compensates for BBPU processing delay.

The interface between the BBPU and CU is asynchronous relatively to the processing of the CU since FIFO buffers are implemented in the CU to store the MAC-PDUs in receive and transmit directions. As shown in Figure 4.17, MAC-PDUs in transmit (888 bits) and receive (912 bits) directions are different. In the receiving direction, the fields RSSI 1 (Received Signal Strength Indication), RSSI 2 and ERI (ERror Information) contain the two channels signal strength indication and error information (number of corrected errors in each MAC-PDU) after combination, respectively. The CI filed includes information for the MAC and LLC protocols.

The RSSI signals are generated by the Low IF module and delivered to the BBPU for digitisation. The excursion of the signal is from 0.1 V to 1 V, corresponding to the input power (received by the antenna) from –90 dBm to –40 dBm (50 dB dynamic range) and are converted by the BBPU to 8-bit words (256 levels) corresponding the 0 V to 00000000 and the 1 V to 11111111 (RSSI voltage = 0.018 P_{RX} + 1.72 and level = Int (RSSI x 255). Since the minimum RSSI voltage is 0.1 V, the minimum level is 25. Moreover due to the quantification process an uncertainty of approximately 0.2 dB exists. The bandwidth of the RSSI signal is 1 MHz (1 μs time resolution) and in order to enable measurements at time

slot level (duration of 21.406 µs) the RSSI signal converges in less than 3 µs, which is about the middle of the first payload field (PL1) in the burst. Therefore RSSI measurements can be done for whatever time slot in the frame although only once per frame.

When the MT is switched on in an area covered by the BS, first it has to determine which cell should be used for a connection attempt. Therefore, the MT starts RSSI measurements on the first frequency, switches frequencies and collects RSSI values for the second frequency. A dynamic average algorithm compiles the RSSI values into measurement reports. Based on these reports the MT selects the new radio cell and starts after slot synchronisation the frame synchronisation procedure as shown in Figure 4.18. The association is timer controlled and restarted if synchronisation has not been achieved before the timer has expired.

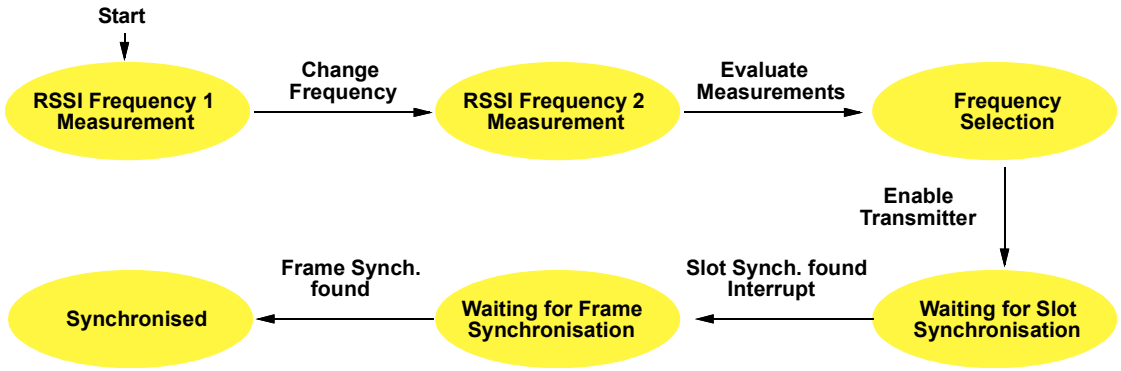

Figure 4.18: Initial Synchronisation

Some additional functions are performed by the BBPU like radio channel quality management using RSSI signals, control of the RF front-end for scanning other BSs carriers and to perform radio handover. Figure 4.19 shows the BBPU housing.

7. Control Unit

The BSC is composed of two CUs and an internal Switch for handover between the two cells as can be seen in Figure 4.8 and Figure 4.20. The CU processes the DLC protocols for the MAC and LLC functions [16][17]. Besides DLC processing, the CU also performs functions for mobility support and resource management as well as monitoring and configuration of the Trial Platform (see Figure 4.21).

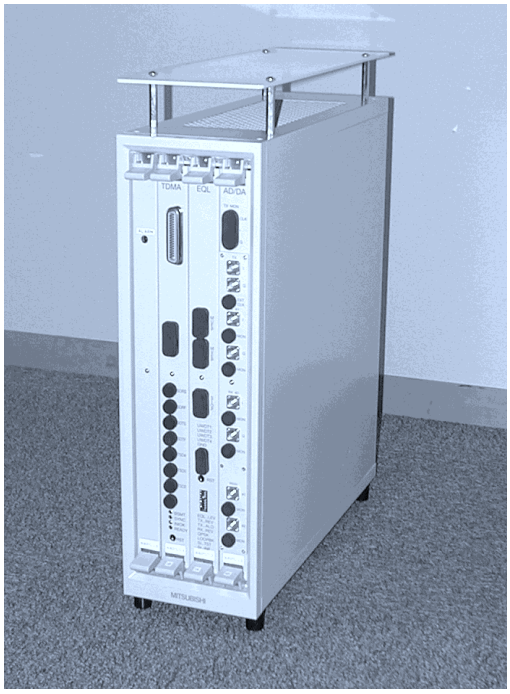

Figure 4.19: BBPU Housing (H - 437mm, W – 140 mm and D – 400 mm)

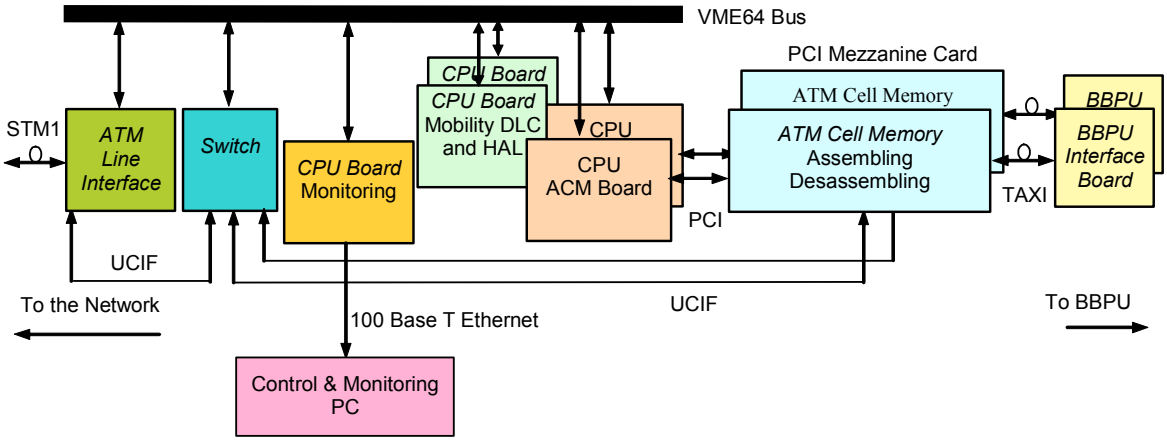

Figure 4.20: BSC architecture

The basic functionality is provided by the RTOS (Real Time Operating System) called pSOS+(m), a scaleable multitasking multiprocessor kernel. pSOS+(m) acts as the supervisory software that performs services on demand, manages resources and co-ordinates multiple asynchronous activities. The DLC software resides on top of the RTOS and the HAL (Hardware Abstraction Layer). It uses services provided by both software components to address the CU hardware. Mobility and Resource Management supporting software is on top of the DLC and uses services of the DLC software. Monitoring is located

at the side of the stack for direct access to all layers. The HAL has been designed to enable the DLC to access the physical layer enabling commands for:

- Sending or receiving data via the fixed access.
- Sending or receiving information via the air interface (data and control information).
- Radio handover.
- Hardware control of CU, BBPU and Switch.

The main goal of the CU design was to decouple the data flow of different transceivers at the BSC and to unburden the VME (Versa Module Eurocard) backplane from data traffic. The CU module exists on the BSC and MTA and is based on a VME bus backplane connecting one ATM LIF (Line Interface), one or more CPU and ACM (ATM Cell Memory) boards and one ATM switch (only BS). The BIF (BBPU Interface) boards are required for interconnection to the BBPU. One ACM-CPU board combination is able to control and manage the traffic of one radio cell. This includes DLC processing, monitoring and configuration of the Trial Platform.

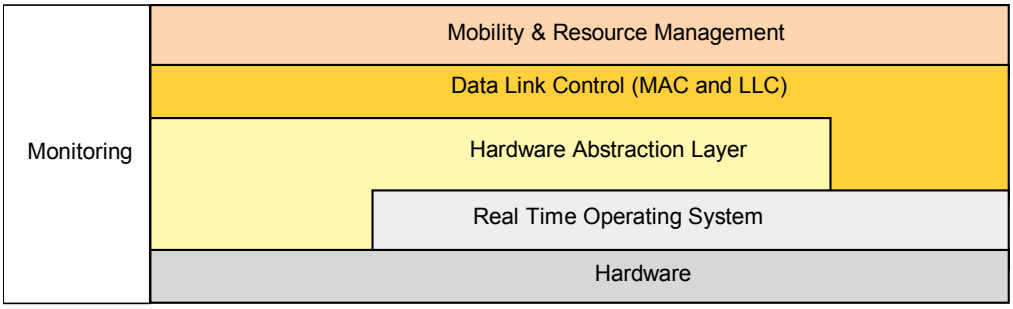

Figure 4.21: CU Software architecture

Incoming data traffic from the network arrives at the ATM LIF (Line Interface) card and is transported to an internal switch (4x4) via the UCIF (User Console Interface). The switch routes data to the ACM board and unburdens the CPU-ACM board combination of additional routing. Again the UCIF is used for transportation. Incoming data from the air interface also arrive via BIF at the ACM board. The CPU board connected via PCI provides control information flow on the ACM board. Additionally, the CPU board via ACM board and BIF board also performs communication with the BBPU for control purposes.

The CU is implemented in two versions, one as part of the BSC and the other part of the MT as shown in Figure 4.21 and Figure 4.22, respectively. The CU of the MTA is also VME bus based and in contrast to the BSC, no switch is required because the MTA operate with a single BBPU and RF front-end. It acts as a wireless terminal adapter and provides an STM1 ATM LIF to the user terminal. The LIF is directly connected to the ACM board. PDUs (Protocol Data Unit) arriving from the air interface also arrive at the BIF board and are directly sent via optical connection to the ACM board. The LIF is directly connected to the ACM board via a UCIF. PDUs arriving from the air interface also arrive at the BIF board and are directly sent via optical connection to the ACM board. Again one CPU board controls the information flow on the ACM board via PCI connection and also supports BBPU control. In contrast to the BSC, no ATM switch is required, because MTAs operate with a single BBPU and RF front-end.

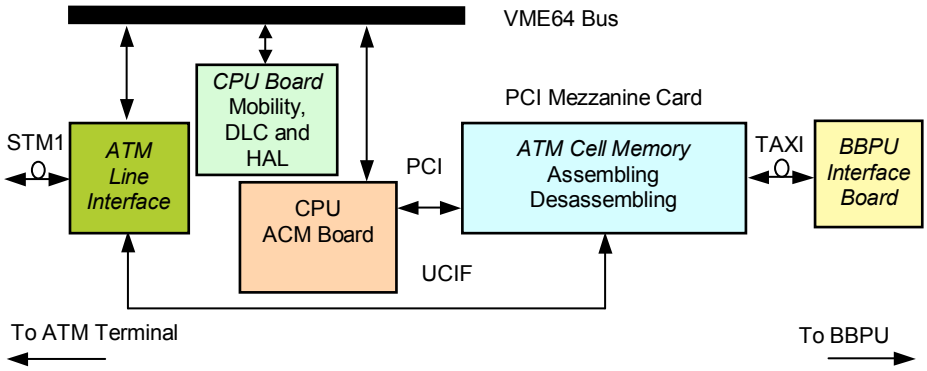

Figure 4.22: MT CU architecture

7.1 Data link control protocols

The DLC layer must provide the same functionality and QoS to the ATM layer as fixed networks do or it must be at least acceptable for ATM connections. It also has to improve the physical layer so that the required quality is achieved. The LLC has to perform all the functions of the ATM layer which are related to a specified VC (Virtual Channel) and which have to be adapted to the specific conditions of the air interface. The MAC is responsible for multiplexing the data of all virtual channels on the radio resources. The MAC layer and the LLC layer share the data scheduling [18].

7.1.1 MAC layer

The MAC layer is required to co-ordinate the competition of terminals for the shared radio channel. The approach followed for the design of the protocol has taken into account the fact that the performance of ATM networks is highly dependent on the cells multiplexing algorithm used in the network nodes. In the Trial Platform, the BSC controls the MAC protocol centrally and co-ordinates the access to the radio channel according to the order of data previously defined by the scheduler. The scheduler decides, based on the service categories (e.g. CBR and VBR), which wireless terminal is permitted to transmit or has to receive data or the selection of the VC that is allowed to transmit or receive after the selection of the MT.

The MAC protocol is reservation-based and period oriented since it is able to dynamically allocate time slots. Each period consists of four phases. The downlink signalling phase marks the beginning of the period and consists of the broadcast to all MTs of information indicating what the time slots are that a specific MT is allowed to transmit or receive its data in. The transmission of announcement messages permits the MTs to leave the physical channel for short time intervals (e.g. to scan other channels or to switch to power saving mode) without loosing synchronisation or missing any messages. During the downlink data phase data is transmitted to the MTs in the downlink direction. Each time slot transports data and additional protocol information in the CI field (see Figure 4.14). The uplink data phase does exactly the opposite and therefore data and signalling is transmitted in the uplink direction from the MTs to the BS. Finally, there is the uplink signalling phase where random access to the MTs is provided which gives the terminals opportunity to indicate their need for capacity in the uplink direction for data transmission. In the Trial Platform a slotted Aloha algorithm is used since the random access is not optimised for throughput but for short delays.

The capacity requests are transmitted over the uplink to provide information about the occupancy state of the MTs send buffers for the data scheduler in the BS. Since transmission is not continuous the following states are possible for the MTs:

- **IDLE** – corresponds to an empty send buffer and therefore no capacity request needs to be transmitted.

- **REQUEST** – state after an ATM cell arrives to the send buffer. The terminal tries to transmit its capacity request message in the random access channel.
- **RESERVATION** – After a successful transmission the terminal enters into this state and will be served by the scheduler according to the urgency of the data. With the transmission of an ATM cell in a reserved slot, the scheduler is informed about the newest capacity demand by means of a piggyback mechanism.

When no more capacity is required, no capacity requests are transmitted and the BS recognises that the MT has returned to the IDLE state. A special case is defined when the terminal is in state RESERVATION and an urgent ATM cell (high priority service category) is received. In this case the terminal can force the REQUEST state to demand more bandwidth via the random access channel.

7.1.2 LLC layer

The LLC layer contains the functions for connection establishment, connection control and methods for error recovery to improve the transmission reliability of the link. For the last an ASR-ARQ (Adaptive Selective Repeat – ARQ) mechanism can be used [19]. ATM cells are retransmitted as long as a specific maximum delay is not exceeded. When the due date is exceeded the ATM cell will be discarded. Discarding old cells contributes to avoiding and resolving congestion events, since the delay of the following cells can be shortened and the probability of exceeding further due dates is reduced.

The functions within the LLC layer are based on the processing of single ATM cells and additional protocol control information (sequence number, ARQ Identifier and a Poll bit). The sequence number is used to detect if any cells are missing. The VPI (Virtual Path Identifier) and VCI (Virtual Circuit Identifier) are mapped to an ARQ Identifier that is used as a short address and reduces the signalling overheads (5 bit length). After the transmission over the radio link the original content of the VPI/VCI fields is restored. The Poll bit is used to indicate that the sender expects the transmission of an acknowledgement because the ARQ window is filled up with transmitted cells that have not yet been acknowledged.

7.2 Mobility and resource management signalling

Since ATM is used on both sides of the radio interface, the Trial Platform operates as a local access system to the public ATM network so that all mobility functions and radio link support are kept inside the Trial Platform. From the point of view of the two ends, it behaves like a fixed access, hiding the wireless component, which should be completely transparent allowing the connection of pure ATM terminals to the MTA. The ATM mobility server entity is the heart of the Trial Platform that controls and is physically connected to an ATM switch, which also provides the interconnection to the fixed core network. Together they work like an Enhanced Switch that supports and integrates the signalling protocols needed to manage MTs as well as to establish and release switched virtual circuits. Specific mobility and resource management protocols have been developed for the Trial Platform [20] [21] [22].

Standard ATM protocols are used when possible and new ones were developed specifically to support functionalities not available in ATM, such as mobility. The existence of a wireless interface implies the need to manage radio resources among the various users. As far as standard ATM is concerned the UNI 3.1 protocol is used and this is supported at both the mobile and network sides. For CC (Call Control), e.g. call establishment and release, the standard ATM UNI 3.1 signalling protocol was used. This enables the utilisation of fixed standard ATM terminals.

The signalling protocols of the Trial Platform control plane can be separated in the ATM control plane and radio control plane. The first serves all protocols specified for standard ATM terminals, e.g. UNIsig (UNI signalling) for call control. The UNIsig uses the service of the SAAL (Signalling ATM Adaptation Layer) for reliable message transmission and the air interface is completely transparent. However, for reliable transmission in the radio interface, specific MAC and LLC are used.

A specific protocol for mobility and resource management (MRP) was developed for the radio control plane and it is located in the MTA, BSC and MSR. The adaptation of this protocol to the ATM layer is provided by the AAL 5 (ATM Adaptation Layer type 5). The protocols stack is shown in Figure 4.23.

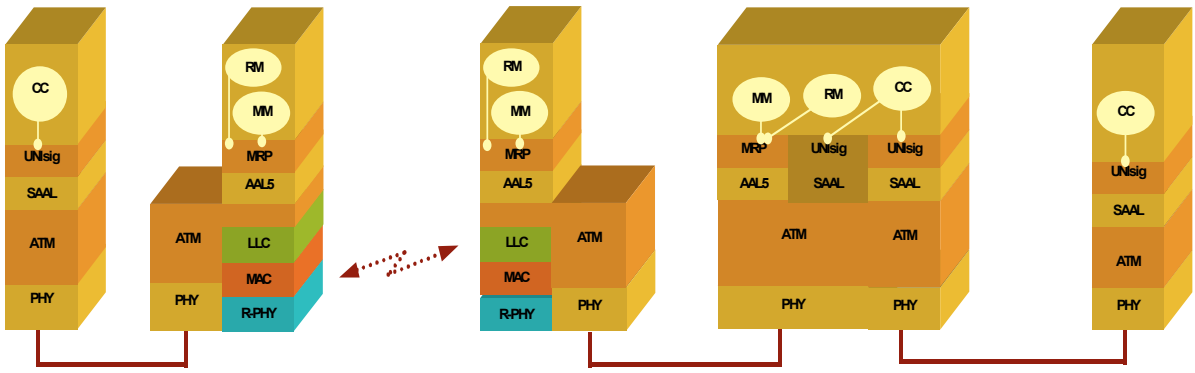

Figure 4.23: Trial Platform protocol stack

The use of different protocols also implies the need for different signalling channels, therefore a different dedicated virtual channel connection has to be maintained. Since the MTA and BSC have to be transparent to UNI signalling, a dedicated virtual channel connection is maintained between the ATM terminal and the MSR. As far as the MRP signalling is concerned, two types of virtual channel are maintained: one connection between the MTA and BSC for each MT and one connection between the BSC and MSR. Finally, for the ILMI (Interim Local Management Interface) protocol signalling, a dedicated virtual channel connection is maintained between the ATM terminal and MSR this being transparent to the MTA and BSC as in the case of UNI signalling.

7.2.1 Resource management

The Resource Management (RM) protocol has to serve two types of resources: the radio resources and the ATM virtual channel connections. Radio resources are not permanently allocated to the MTs leading to the need of resources management schemes. Network procedures for requesting radio resources and establishing radio connections are mandatory. Moreover, radio handover is a responsibility that also lies in the RM domain.

The procedure for allocating radio resources is triggered by the MSR. It transmits the requested connection parameters allowing the BSC to decide whether the request can be granted or not and consequently radio admission control is performed at the BSC. If the radio resources cannot be allocated it sends back a negative acknowledgement to the MSR aborting the setup procedure.

As far as the ATM virtual channel connections are concerned, the MSR has control providing the ATM resources management and their allocation by instructing the ATM switch. It is responsible for the establishment, maintaining and release of the connections. More specifically, for the UNIsig VPI/VCI = 0/5 and for ILMI VPI/VCI = 0/16 are used. This implies the use of switched virtual channels to support this standard ATM signalling.

7.2.2 Mobility management

ATM was not designed to support mobility and therefore enhancements to the existing protocols had to be identified and developed. MTs requesting access to the network have first to be registered and located. Moreover, the network has to keep track of the terminals roaming within the service area. A database maintains an updated list of active MTs and their location in the network in order to forward the mobile terminated call requests. Protocols to support Registration and Location Management were implemented. These functions are part of the MM (Mobility Management).

Due to the fact that a standard ATM terminal plus a terminal adapter (MTA) compose the MT, two addresses have to be stored. The MTA is identified by its unique mobile identification, which is communicated to the network during the Registration and stored. The ATM terminal is identified by its ATM address, which is communicated to the network during the address registration procedure of the ILMI protocol, i.e. the same procedure that is used in a fixed access. The MSR provides the logical linkage between these two addresses. The following states are possible for the MTA: not known, known but not registered and registered. For the ATM terminal only the first two states are possible.

A two stage approach is used for the location management. When the MT changes from one cell to another that is under the control of the same BSC, only the information available in the BSC needs to be updated. When the BSC changes, the MSR needs to be informed and the database information changed. This allows a reduction in the amount of location management signalling, although in the Trial Platform only one BSC is available.

7.2.3 Radio handover

A radio handover is executed when the MT changes between two cells connected to the same BSC or between two carriers of the same cell and usually the main objective is to

obtain a better radio link. The handover process can be divided in three phases (see Figure 4.24):

1. Measurements of the link quality on the current cell and neighbouring cells.

2. Handover decision and initiation based on the measurements.

3. Handover execution, which implies the switching of the link to the new cell and the cancelling of the previous link.

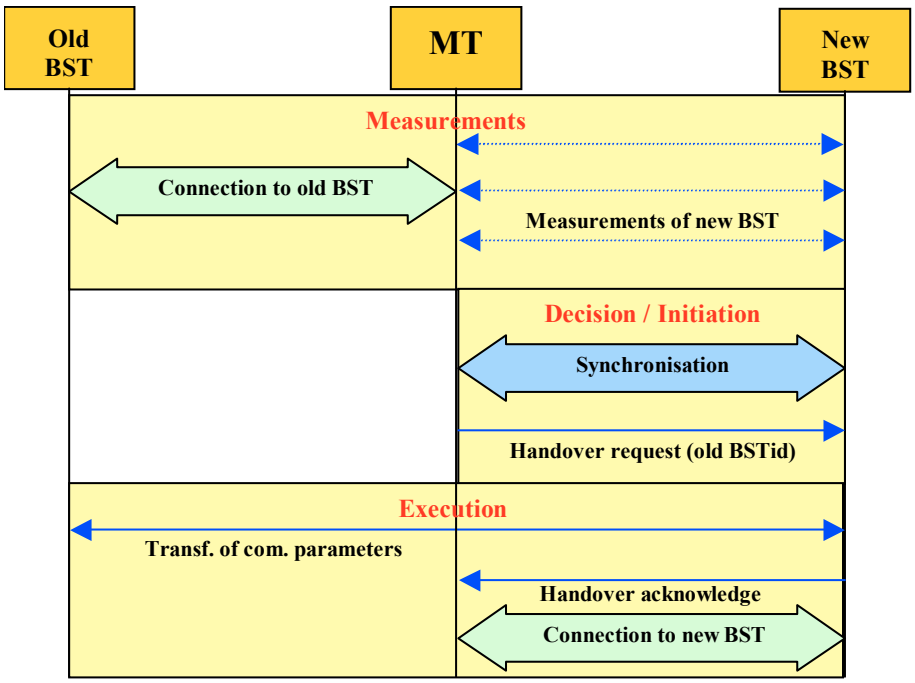

Figure 4.24: Forward handover phases

For a MT controlled radio handover it is necessary for the MT to know about the reception quality of neighbouring base stations. Therefore, the MT performs a neighbourhood scan, i.e. the MT switches its receiver periodically to the alternative frequency and collects some measurements. The functionality is fully supported by the BBPU. The CU only programs the neighbourhood scan registers with the VSN that determines the start of the scan process and with the duration in slots. These values mainly depend on the processing delays and are the result of some experiments. In the current implementation the scan process is triggered every 1000th frame (approx. every two seconds) at VSN 30 for 20 slots. During these 20 slots the RSSI values inside the uplink MAC PDU represent the link quality of the

alternative base station. The BBPU sets the MSB (Most Significant Bit) of the RSSI values to indicate their origin from the neighbouring cell. These values are compiled to neighbourhood measurements reports that serve together with the measurement reports of the actual radio cell as input for the handover algorithm. BER information is not considered as an input. The MT attempts to handover to the other radio cell if:

- RSSI_NH ≥ (RSSI_ACT + THRES) or
- RSSI_ACT ≤ LOW_THRES or
- SLOTSYNCLOST

Parameter	Description
RSSI_NH	Measurement report of the neighbouring radio cell.
RSSI_ACT	Measurement report of the actual radio cell.
THRES	Threshold to avoid the ping-pong problem.
LOW_THRES	If the link quality drops below this value the MT attempts to handover to another cell.
SLOTSYNCLOST	If slot synchronisation is lost by the BBPU the only possibility is the handover to a neighbouring cell.
HO_PROHIBIT	Time that has to pass before another handover is permitted. (700 frames, approx. 1.4 s)

Table 4.2: Parameters of handover algorithm

After a successful handover the next handover can only be initiated after a timer set to HO_PROHIBIT has expired, to avoid “ping-pong” handovers and to provide a minimum of processing time to empty the transmission queues. Table 4.2 explains the parameters and gives some values, which highly depend on the environment the system is deployed in. The presented values were used in an indoor scenario.

The short switching times and the immediate start of the neighbourhood scanning process are only possible because the RF unit is equipped with two oscillators. Thus, the RF unit only switches between the oscillators and no time is needed for reprogramming and restarting the oscillator.

8. Summary and Conclusions

This chapter presented the mobile broadband system prototype, also called Trial Platform, which was used in the field trial campaign to gather the measurements results processed

and analysed in chapters six, seven, eight and nine. The Trial Platform hardware and software components were described in detail.

The Trial Platform architecture was defined based on the state-of-the-art technology available when the specifications were frozen and the main objective was to design a cellular broadband system where the main functionalities would be tested and evaluated. Handover was envisaged as a key feature and therefore the Trial Platform is composed by two BSs, one BSC, a Mobility Server, and two MTs. The two MTs are crucial to test the sharing of the radio resources given the specific needs of each of the applications. When analysed in more detailed, the Trial Platform is composed of antennas, RF, IF and Baseband and CU modules and DLC, mobility and resource management protocols. In terms of architecture, there is not much difference between the MT and the BS side, except for the case of the BSC that has to duplicate functions since it has to deal with two cells and process the handover function.

The radio cells shape is very dependent on the antennas characteristics, namely the antennas radiation pattern. The dielectric lens antennas are inexpensive, they can easily moulded and manufactured with high tolerances and have sufficient band for FDD operation. In this particular case, lens type antennas were used given the facility in designing the cell shape with sharp boundaries and its adaptation to a specific scenario providing a uniform power flux density in the coverage area. Controlling the power distribution has a positive impact on the channel time dispersion since it avoids the transmission of the power to undesirable zones what also contributes to the elimination of possible strong multipath components. Two cell types were designed: the wide and elongated cells. The first is more appropriate to cover arenas, squares or indoor scenarios. The last is suitable for streets and outdoor environments. By adjusting the BS characteristic such as the height and antenna tilting angles, the cell shape can be modified or adjusted, which is a powerful tool to control the co-channel interference, for example. The control of the multipath propagation also easies the design of the air interface that was already described in the previous chapter. Since diversity reception was used, the two receiving antennas were separated by 14λ to guarantee a low level of correlation between the received signals. In terms of the dielectric material characteristics, the permittivity should be as high as possible to favour high diffraction angles reducing the lens depth. On the

other side, the wave impedance mismatch increases with the permittivity. Therefore a trade-off is required in terms of the electrical properties. Typical materials are Polystyrene ($\varepsilon_r = 2.43$) and Polyethylene ($\varepsilon_r = 2.35$).

The RF and IF modules were designed to support full duplex operation and its main function is to convert the I-Q baseband signals received from the BBPU into modulated carrier frequency bursts in the 40 GHz band and the reversing operation in the receiving direction. Due to the diversity reception, one antenna is simultaneously used for transmission and reception and therefore a diplexer is required. Three modules implement these functionalities: RF, High IF and Low IF modules. Two intermediate frequencies are used for the up and down conversions. Since two cells were planned, two uplink (39.58 and 39.74 GHz) and two downlink carriers (42.58 and 42.74 GHz) were defined for FDD operation.

The BBPU main function is the digital processing of the baseband signals and is located between the IF and CU modules. This module was specified to handle speeds up to 50 km/h and cells size up to 300 m. At the reception side the two diversity branches I-Q signals are converted to digital format. The synchronisation is performed by UWD that is included within the training sequences of the burst and then maintained by a flywheel mechanism. Four synchronisation states are possible: Out-of-Sync, Sync-Protection B, In-Sync and Sync-Protection F. The BBPU is also able to calculate the CIR but is used for equalisation purposes only. Adaptive DFE type equalisation is performed based on two training sequences available in the burst and is fundamental to mitigate the effects of the radio channel. For time dispersions up to 250 ns a raw BER of $5x10^{-3}$ is guaranteed. The FEC is also implemented in the BBPU which detects and corrects errors based on the content of the CR burst field. Reed-Solomon coding is used and able to correct up to 10 symbol errors per burst. The recovered data is then delivered to the CU for further processing as well as the error correction information. RSSI signals are generated in the Low IF module and are digitised by the BBPU, which are then further transmitted to the CU. In the transmission direction, the CU delivers the payload to the BBPU, the data is encoded by the FEC codec and the burst built. Subsequently OQPSK modulation is performed and the I-Q signals passed to the IF modules.

The BSC is composed of two CUs and an internal switch for handover purposes. The CU processes the DLC protocols for MAC and LLC as well as functions for mobility and resources management, monitoring and configuration purposes. The CU is powered by a scalable multitasking multiprocessor kernel.

The MAC layer is required to co-ordinate the competition of terminals for the shared radio channel. The design of this protocol has taken into account the characteristics of the underlying technology. The BSC controls centrally this protocol and coordinates the access to the radio channel according to the order previously defined by the scheduler. On the other hand, the scheduler decides which MT is permitted to transmit or receive data based on the service categories. The MAC protocol is reservation-based and period oriented since it is able to dynamically allocate time slots. Each period consist of four phases: the downlink signalling phase marks the beginning of the period and consists of the broadcast to all MTs of information indicating what the time slots are that a specific MT is allowed to transmit or receive data. The transmission of announcement messages permits the MTs to leave the physical channel for short time intervals (e.g. to scan other channels or to switch to power saving mode) without loosing synchronisation or missing any messages. During the downlink data phase, data is transmitted to the MTs in the downlink direction. Each time slot transports data and additional protocol information in the CI field. The uplink data phase does exactly the opposite and therefore data and signalling is transmitted in the uplink direction from the MTs to the BS. Finally, there is the uplink signalling phase where random access to the MTs is provided which gives the terminals opportunity to indicate their need for capacity in the uplink direction for data transmission. A slotted Aloha algorithm is used since the random access is not optimised for throughput but for short delays. When no more capacity is required, no capacity requests are transmitted and the BSC recognises that the MT is in the IDLE state.

The LLC protocol handles the functions for connection establishment, connection control and methods for error recovery. For the last an ASR-ARQ mechanism is used. Data is transmitted as long as a maximum delay is not exceeded otherwise a data discard is performed to avoid congestion problems.

The fact that radio resources are not permanently allocated to MTs leads to the need of resource management protocols. The procedure for allocating radio resources is triggered by the MSR. It transmits the requested connection parameters allowing the BSC to decide whether the request can be granted. If the radio resources are not free, the BSC sends back to the MSR a negative acknowledge message aborting the setup procedure.

MTs requesting access to the network have first to be registered and located. Furthermore, the network has to keep track of the terminals roaming within the service area. For mobility management purposes, a database maintains an updated list of active MTs and their location in the network in order to forward the mobile terminated call requests. Registration and location management protocols were developed and implemented in the Trial Platform. A two stage approach is used for the location management. When the MT changes from one cell to another that is under the control of the same BSC, only the information available in the BSC needs to be updated. When there is a change in the BSC, the MSR needs to be informed and the database information changed. This allows for a reduction in signalling. Although the Trial Platform has only one BSC, the mobility management protocol has been designed to support larger networks and not specifically the prototype developed.

Radio handover is a key feature of the Trial Platform and is generically executed when a MT changes between two cells while in a call. The handover procedure has three phases: 1) Measurements of the link quality on current and neighbouring cells; 2) Handover decision and initiation; and 3) Handover execution. The last phase implies the effective switching of the link to the new cell and the cancelling of the link in the previous cell. During the first phase the MT performs a neighbouring scan procedure in order to assess the quality of all the carriers available and collects measurements. These measurements are important during the second phase where an algorithm is run to select the next cell. The decision is based on the RSSI levels or synchronisation information rather than BER. After a successful handover, a new handover cannot be initiated after a timer has expired contributing to avoid the “ping-pong” effect.

In conclusion, a broadband cellular radio prototype comprising two BSs was described which was crucial for the realisation of this thesis since all the measurements results

presented in the next chapters were gathered with this equipment. Not all aspects were studied and evaluated being the work here presented more related with the radio interface, including radio handover performance aspects.

9. References

[1] M. Dinis, V. Lagarto, M. Prögler, J.T. Zubrzycki, "SAMBA: a Step to Bring MBS to the People", ACTS Mobile Communication Summit '97, Aalborg, Denmark, October 1997.

[2] Manuel Dinis and José Fernandes, "Provision of Sufficient Transmission Capacity for Broadband Mobile Multimedia: a Step Towards 4G", IEEE Communications Magazine, August 2001.

[3] Manuel Dinis et al, "Integration of the Trial Platform – Version 1", CEC Deliverable Number: A0204/PTIN/SRM/DS/P/6v2/b1, 30/03/99, Submitted to the European Commission in the framework of the SAMBA project.

[4] E. Macedo, Manuel Dinis et al, "Integration of the Trial Platform – Version 2", CEC Deliverable Number: A0204/PTIN/SRM/DS/P/6v2/b1, 30/01/2000, Submitted to the European Commission in the framework of the SAMBA project.

[5] M. Prögler, C. Evci, M. Umehira, "Air Interface Access Schemes for Broadband Mobile Systems", IEEE Communications Magazine, Vol. 37, no. 9, pp. 106-115, Sept. 99

[6] C. A. Fernandes, "Shaped Dielectric Lenses for Wireless Millimeter-Wave Communications", IEEE Antennas & Propagation Magazine, Vol. 41, No. 5, pp. 141-150, Oct. 99.

[7] J. Fernandes, A. Marques, J. Garcia, "Cellular Coverage for MBS Using the Millimetre-Wave Band", ACTS Mobile Communications Summit '99, Sorrento, Italy, June 99.

[8] J. Fernandes and J. Garcia, "Multiple Coverage for MBS Environments", PIMRC'2000, London, UK, September 2000.

[9] J. Fernandes, C. Fernandes, "Impact of Shaped Lens Antennas on MBS Systems", PIMRC 98 – 9th International Symposium on Personal, Indoor and Mobile Radio Communications, Boston, USA, Sept. 98.

[10] Luís Miguel D. B. Anunciada, "Impacto das Antenas no Canal de Propagação em Comunicações Móveis em Ondas Milimétricas", MSc Thesis, Universidade Técnica de Lisboa, Instituto Superior Técnico, Dezembro 1999.

[11] C. A. Fernandes, "Description and Test Report on Antennas", CEC Deliverable Number A0204/IST/DEC/DS/R/010/b1, 30/01/99, Submitted to the European Commission in the framework of the SAMBA project.

[12] A. Plattner, B. Byzery, C. Fernandes, T. Karttaavi, "A Compact, Portable 40 GHz Transceiver for the Mobile Broadband System", ACTS Mobile Communications Summit '98, Rhodes, Greece, June 98.

[13] A. Plattner, "Description and Test of Millimetrewave Transceiver", CEC Deliverable Number A0204/Dasa/VS/DS/P/009/b1, 30/07/98, Submitted to the European Commission in the framework of the SAMBA project.

[14] T. Fujino, et al, "Design of Baseband Signal Processing Unit in SAMBA Trial Platform for Mobile Broadband Applications", ACTS Mobile Communications Summit '98, Rhodes, Greece, June 98.

[15] T. Fujino et al, "Baseband Signal Processing Technologies for 64 Mbit/s Radio Transmission for Mobile Broadband Systems", ACTS Mobile Communications Summit '97, Aalborg, Denmark, Oct. 97.

[16] Günter Seidel, "Report on Control Unit", CEC Deliverable Number A0204/FV/Bosch/DS/I/008/b1, 30/11/98, Submitted to the European Commission in the framework of the SAMBA project.

[17] Günter Seidel, "Control Unit Enhancement", CEC Deliverable Number A0204/FV/Bosch/DS/I/008A/b1, 10/11/99, Submitted to the European Commission in the framework of the SAMBA project.

[18] U. Vornefeld, A. Krämling, N. Esseling, "Implementation of WATM-DLC protocols for a 34 Mbit/s FDD Air Interface", ACTS Mobile Communications Summit '98, Rhodes, Greece, June 98.

[19] N. Fukui, A. Shibuya and K. Murakami, "Performance of Combined ARQ with SR and GBN for Wireless Systems on a 40 GHz Band Radio Channel", IEEE Communication Magazine, pp. 122-126, September 2001.

[20] A. Kadelka, "Specification of the Mobility Management Functions", CEC Deliverable Number A0204/UA/Comnets/DS/P/007/b1, 30/11/97, Submitted to the European Commission in the framework of the SAMBA project.

[21] A. Kadelka and J. Zidbeck, "Description of the Mobility Server", CEC Deliverable Number A0204/UA/Comnets/DS/P/007A/b1, 30/03/98, Submitted to the European Commission in the framework of the SAMBA project.

[22] J. Zidbeck, "Report on Assembly and Test of the Mobility Server", CEC Deliverable Number A0204/VTT/IT/DS/P/013/b1, 30/01/99, Submitted to the European Commission in the framework of the SAMBA project.

5th Chapter

Equipment Set-up, Parameters and Scenarios

1. Introduction

The experimental evaluation of a mobile broadband system prototype is a huge task since it requires a lot of logistics and manpower. Typical scenarios should be selected in order to anticipate the behaviour of the future system and to confirm if the selected technical options were adequate or should be modified according to the obtained results from the field trials [1].

A public mobile broadband cellular system must operate in various environments namely indoor and outdoor. For both types, there are certainly a huge number of examples that could be identified if we consider the different materials that buildings are made and their respective shape and size. The same applies for the outdoor scenarios where we can have different terrain morphologies, different streets or roads, roundabouts, motorways, and the respective placement of the obstacles including buildings. All these facts

influence definitively the performance of the system, which ideally should be able to work in all of them at least with the expected minimum performance.

Several scenarios were planned to perform the field trials but unfortunately it was not possible to perform measurements in all of them. Therefore only one outdoor and two indoor scenarios were selected as the most representative. Several types of measurements were performed, considering different conditions for the system, e.g. height of the BS antenna, tilting angles, speed of the MT, etc.

As presented in chapter 4, the Trial Platform implements many functionalities and protocols [2] [3]. In this thesis only the aspects related with the physical layer are analysed being left out other very important aspects such as: dynamic channel assignment mechanisms; MAC protocol performance; evaluation of the LLC protocols namely the implemented ARQ protocol [4]; connection set-up and release performance with different type of traffic sources; test of the network functions such as those related with the mobility management; and evaluation of the system suitability for the specified applications, namely the electronic newsgathering and the medical rescue applications.

This chapter starts with a description of the hardware necessary for setting up the trials scenarios and the necessary logistics for each environment. This includes the description of the BS towers, the system configuration in the field and the impact of tilting angles. A description of the C&M (Controlling and Monitoring) system and how the Trial Platform is calibrated to ensure correct and reliable operation are presented. The most fundamental parameters and type of graphics generated are identified. Finally a description of the selected scenarios in terms of physical dimensions and type of materials and the identification of the paths where the MT was moved are presented, as well as specific aspects related with the CIR measurements.

2. Trial Platform Configurations

Three different Trial Platform configurations were used being one composed by a single cell, another by two cells to allow the evaluation of the radio handover algorithm and a third one for the CIR measurements using only the Trial Platform MH (Millimetrewave Heads) and respective antennas (both wide and elongated). A specific C&M system was

developed in parallel with the Trial Platform to help in its evaluation during the field trials [1]. This system is described in the next section.

Figure 5.1 depicts the system configuration including the Trial Platform hardware main components already presented in chapter 4 that allows the evaluation of single cell coverage aspects, the impact of the MT speed and the BS different configurations.

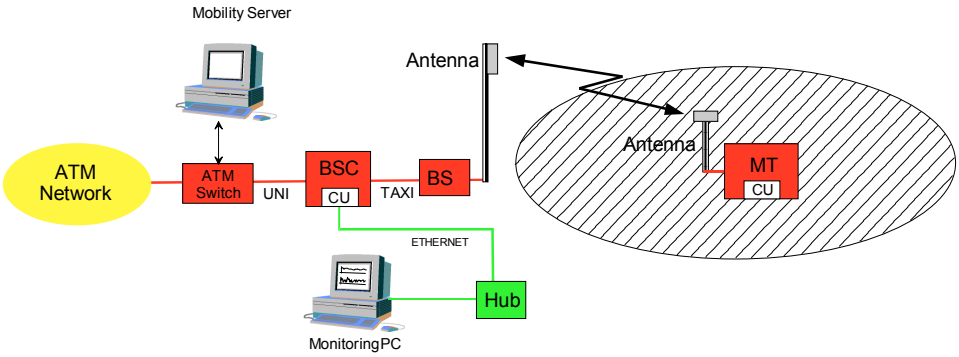

Figure 5.1: Single BS configuration

Figure 5.2 show the configuration used to evaluate the radio handover algorithm where two cells are connected to the same BSC. The MT was moved between the two cells in different directions to analyse the behaviour of the handover algorithm.

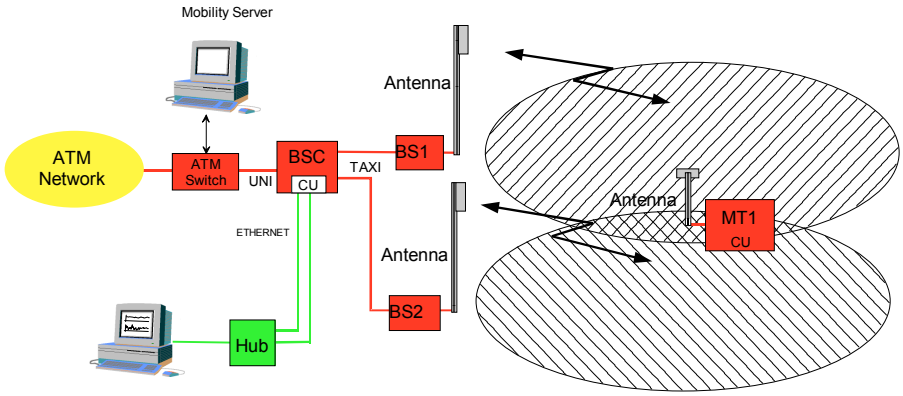

Figure 5.2: Two BSs configuration

As can be seen in the two figures above, the same C&M system was used for both situations to acquire the necessary data for the characterisation of the system behaviour.

For the CIR measurements, only the RF modules and the antennas were necessary in conjunction with two mixers to up and down convert the RF signal. A NA (Network

Analyser)[1], two frequency synthesisers and a 10 MHz Rubidium reference generator were necessary. Figure 5.3 shows how these elements were interconnected to perform the CIR measurements, including a 20 dB amplifier to compensate for the signal losses in the 50 m cable to permit greater distances between the BS and the MT.

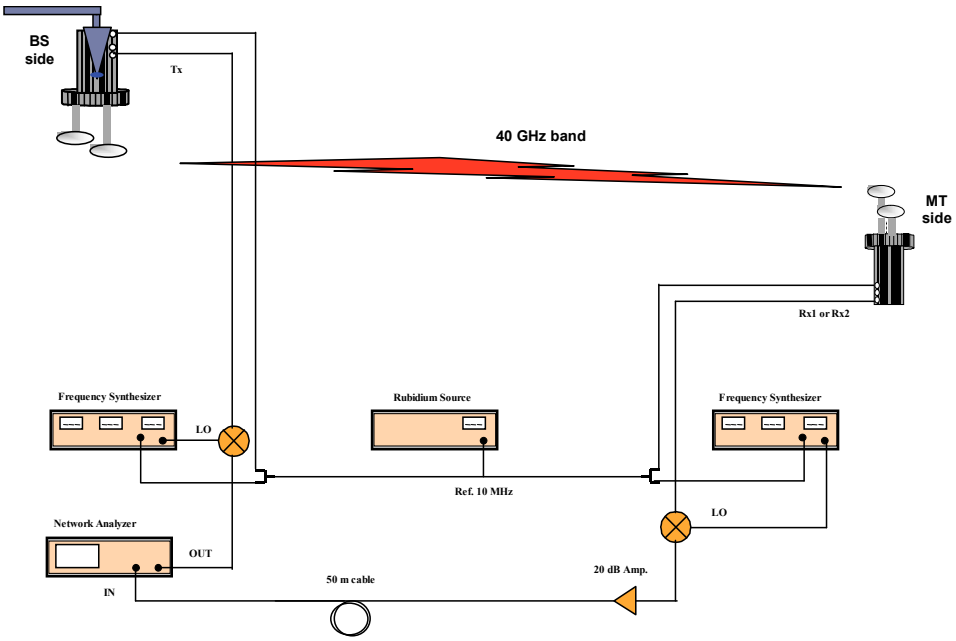

Figure 5.3: System configuration for CIR measurements

In order to minimise the losses in the 50 m cable the signal was generated by the NA approximately at 1.6 GHz and distributed at this frequency (the cable losses are about 17 dB at 1.6 GHz). Since the RF heads input and output frequency is 8.26 GHz, two synchronized frequency synthesizers were used as LO for the mixers generating both a 6.66 GHz carrier.

To obtain the amplitude and the phase of the frequency response it is necessary to use a unique reference signal. For that purpose, a Rubidium source was used to generate the 10 MHz reference signal injected in all modules in the system to guarantee the phase coherency. This reference signal was also distributed to the receiver side using a 50 m cable.

1 from HP (HP8753D.06.14).

The S_{21} parameter was acquired by the NA in amplitude and phase in a 400 MHz bandwidth centred in 1600 MHz. This corresponds to the frequency band of 42.380 - 42.780 GHz in the radio interface for the system downlink direction. At the input and output of the MHs, the IF signal was centred at 8.260 GHz. The frequency conversions were made using a 6.660 GHz external LO signal. For the uplink measurements, the same equipment set-up was used however different LO frequencies were selected since the uplink frequency band is different (39.380 - 39.780 GHz).

The NA resolution bandwidth was set to 10 Hz to reduce the noise level to about –110 dBm. By averaging the received signal, the noise floor was further reduced. The NA was set to acquire 801 samples (N) equally spaced in the 400 MHz band (B). The measuring bandwidth is inversely proportional to the time resolution being for this case 1/B=2.5 ns. This is the minimum time separation between two signal replicas that the system is able to detect. The maximum measurable delay, which guarantees that all the signal replicas with sufficient energy are collected by the system, is given by equation (5.1). In our case, the maximum delay is τ_{max} = 2 μs which is more than enough given the selected indoor scenarios dimensions.

$$\tau_{\max} = \frac{N-1}{B} \qquad (5.1)$$

3. C&M System Description

In order to allow the performance evaluation of the Trial Platform a C&M system was developed, as depicted in Figure 5.4. It enables the real time recording of a set of parameters in realistic environments for later processing and the following functions [1]:

- Monitoring of the proper operation of the Trial Platform.
- On-line screen presentation of signals and Trial Platform status.
- Off-line screen presentation of stored signals and Trial Platform status.
- Recording of selected signals and system status.

The C&M system includes a telemetry system that sends to the BS side the signals over the air in the 170 MHz band using DTMF (Dual Tone Multiple Frequency) coding for the path

mark. A Peiseler wheel generates these signals concerning the MT travelled distance that are received by a PC, which synchronises this information with the information gathered by the BSC. The resolution of the path mark pulses can be chosen between 0.1 m, 1 m and 10 m. For demonstration and debugging purposes, real time or off-line display of the measured data can also be provided. The interconnection between the C&M system and the Trial Platform is shown in Figure 5.9.

Figure 5.5 shows an example window where RSSI information for both receiving channels plus BER information are displayed, together with the path mark representing the distance travelled by the MT relatively to the BS.

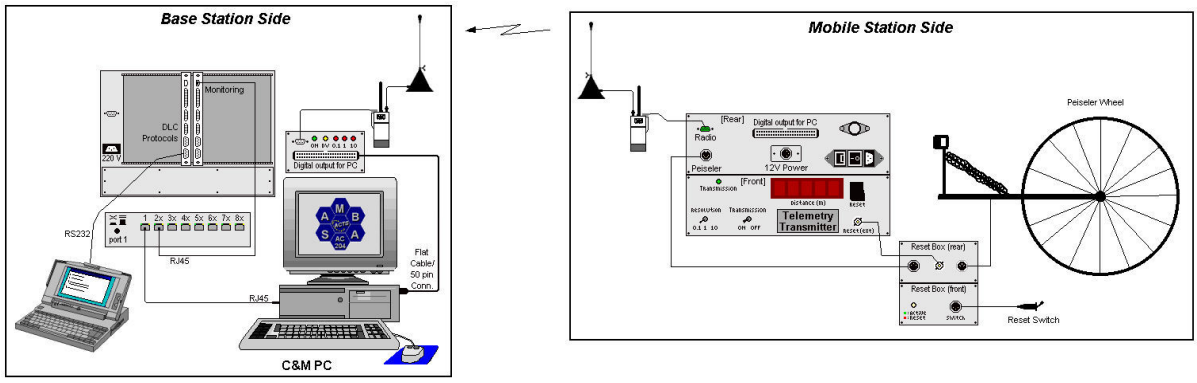

Figure 5.4: Control & Monitoring system

Several parameters are measured simultaneously and gathered through the C&M system (see Table 5.1). The recorded signals are derived from the transported information over the air interface collected by the BSC for each BS radio link. They are obtained within one frame to form one 13 Bytes sample per BS and frame. RSSI information is derived from one slot per frame. From n consecutive frames a series of n samples are collected by the CU and sent as one packet per BS to the C&M system via a Fast Ethernet LAN (Local Area Network).

Table 5.2 shows the characteristics of the RSSI signal. The RSSI digital values (256 levels) calculated by the BBPU are sent to the CU and then to the C&M system. The C&M system calculates back the RSSI voltages and then, via the obtained calibration curve for all BSs and MT, relates the RSSI voltage to the antenna received power level in the range of –90 dBm to –40 dBm (50 dB dynamic range).

Parameters	Description	Comments
RSSI 1	Radio Signal Strength Indicator of Channel 1	The sampling period for the power level is 1.7125 ms (one slot per frame) which corresponds to a sampling rate of 583.9 Hz The distance resolution depends on the velocity of the MT (e.g. for 10 km/h = 4.8 mm/sample; for 50 km/h = 23.8 mm/sample) Acquisition system data transfer rate = 583.9 x 13 Bytes = 59.3 kbit/s
RSSI 2	Radio Signal Strength Indicator of Channel 2	
TransAct	Indicates the number of slots with valid data in a frame	
BitErrors	Number of bit errors in a frame before FEC	
ByteErrors	Number of byte errors in a frame before FEC	
Frequency channel	Radio carrier being used	
Distance information	Distance travelled by the MT	

Table 5.1: Parameters recorded for evaluation

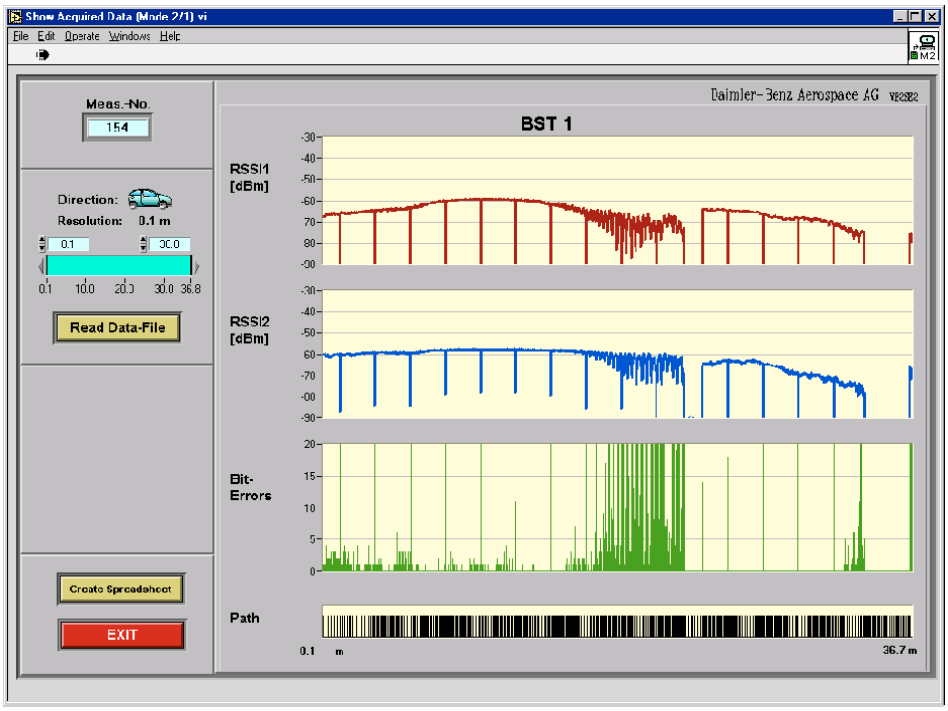

Figure 5.5: Acquisition data application window

Parameter	Range
RSSI range in terms of power	-90 to -40 dBm
RSSI output voltage	0.1 to 1 V into a 50 Ω load
Imbalance between the two diversity branches	< 1.5 dB
RSSI settling time	3 µs
Bandwidth of RSSI branch	1 MHz

Table 5.2: RSSI signal characteristics

4. Measurements Set-up and Logistics

For the field trials other equipments, hardware and software were acquired and developed to help the implementation of different Trial Platform configurations. In this section these equipments are presented [5].

Two specially built metal masts were designed and manufactured according to the requirements allowing the antennas of the BSs to be installed at different heights up to 12 m (see Figure 5.6). A shorter version of the mast is also available, which can be used for indoor environments. Moreover, since the variation of the antenna tilting was one of the requirements, and to facilitate its adjustment from the floor, a special electromechanical device was developed to control remotely the antenna front-end rotations in the vertical plane permitting the up and downward tilting.

During the field trials campaign the MT has moved along several pre-defined paths. For outdoor field trials, the MT was installed in a van and for indoor in a trolley. The van option was selected due to the speeds to be achieved (at least 50 km/h) and also to cope with the relatively long travelled distances (about 350 m). For the installation of the MT in the van new equipment and special adaptations were needed, namely:

- External connection point for the Peiseler wheel (Figure 5.7 - a).
- Support for antenna front-end in the rooftop (Figure 5.7 - b).
- Power supply for the MT plugged into the van generator (Figure 5.7 - c on the left).
- Internal rack attachment point (Figure 5.7 - c on the right).

Figure 5.8 shows the trolley used for the indoor trials and how it was moved manually along the specified paths at walking speeds. The MT was safely fixed on the metal structure of the trolley and two persons were required to push and drive it along the paths marked on the floor. The radio transmitter and the Peiseler wheel of the telemetry system were attached on the rear. During the movement of the trolley the persons involved always tried to minimise the interference with the radio link, avoiding as much as possible the LoS obstruction.

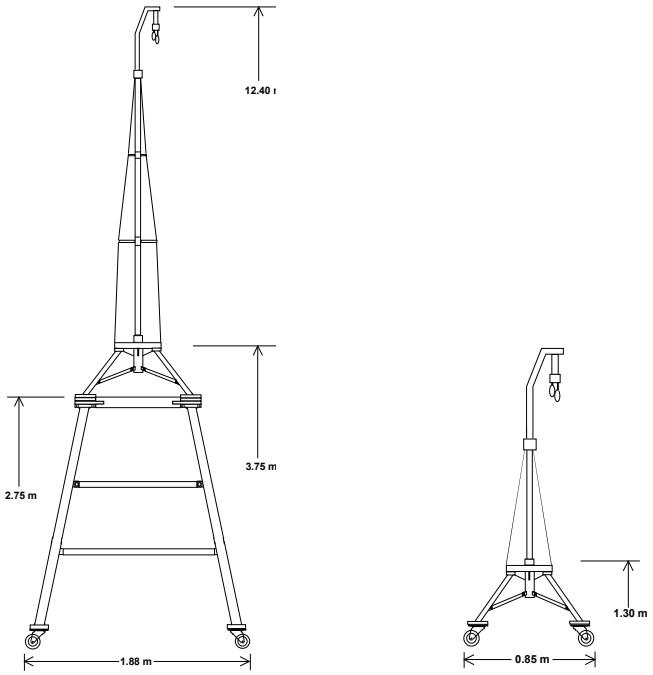

Figure 5.6: Outdoor and indoor metal masts

(a) **(b** **(c)**

Figure 5.7: Details of the MT van: a) Peiseler wheel; b) Antenna and front-end; c) MT inside the van

Figure 5.8: MT on a trolley during the trials in the sports pavilion

Figure 5.9 shows the whole configuration of the Trial Platform using both BSs. The interconnection with the C&M system is shown together with the petrol power generator necessary, while operating in the outdoor environment, since there was no access to the public electricity.

5. Trial Platform Calibration

In order to guarantee the correctness of the measured data for the performed measurements, a calibration procedure was defined for both BSs and MT for what concerns the RF branches of each receiver chain. The calibration has basically three main objectives [6]:

- Ensure that the whole RF system comprising all RF boards and components are running properly (i.e. MH, High IF, Low IF and RF cables). All these modules were described in the previous chapter.
- Ensure that both Rx channels are power balanced. A compensation is required attenuating the stronger signal if a hardware mismatch exists (a difference between Rx1 and Rx2 power levels). This is important for the correct functioning of the MRC technique in the equalizer.
- Calculation of the calibration curves, i.e. derive the correspondence between the Rx power levels versus RSSI figures for each Rx channel (two per receiver chain). The RSSI signals are a measure of the received power that in this particular case are referenced to the receiver antenna input.

For CIR measurements, the calibration was performed to eliminate all the effects introduced by the cables, mixers, amplifiers, and RF modules, excluding the antennas, measuring only the antennas and radio interface effects.

5.1.1 Calibration of the RF modules

Considering first the calibration of the RF modules, a table of correspondence between the front-end antennas received power and the RSSI voltage is created in order to generate the calibration curves for the C&M system. It is based on these curves that the C&M system is able to convert RSSI voltages in RF power levels. The main characteristics of the RSSI signals were described in section 3.

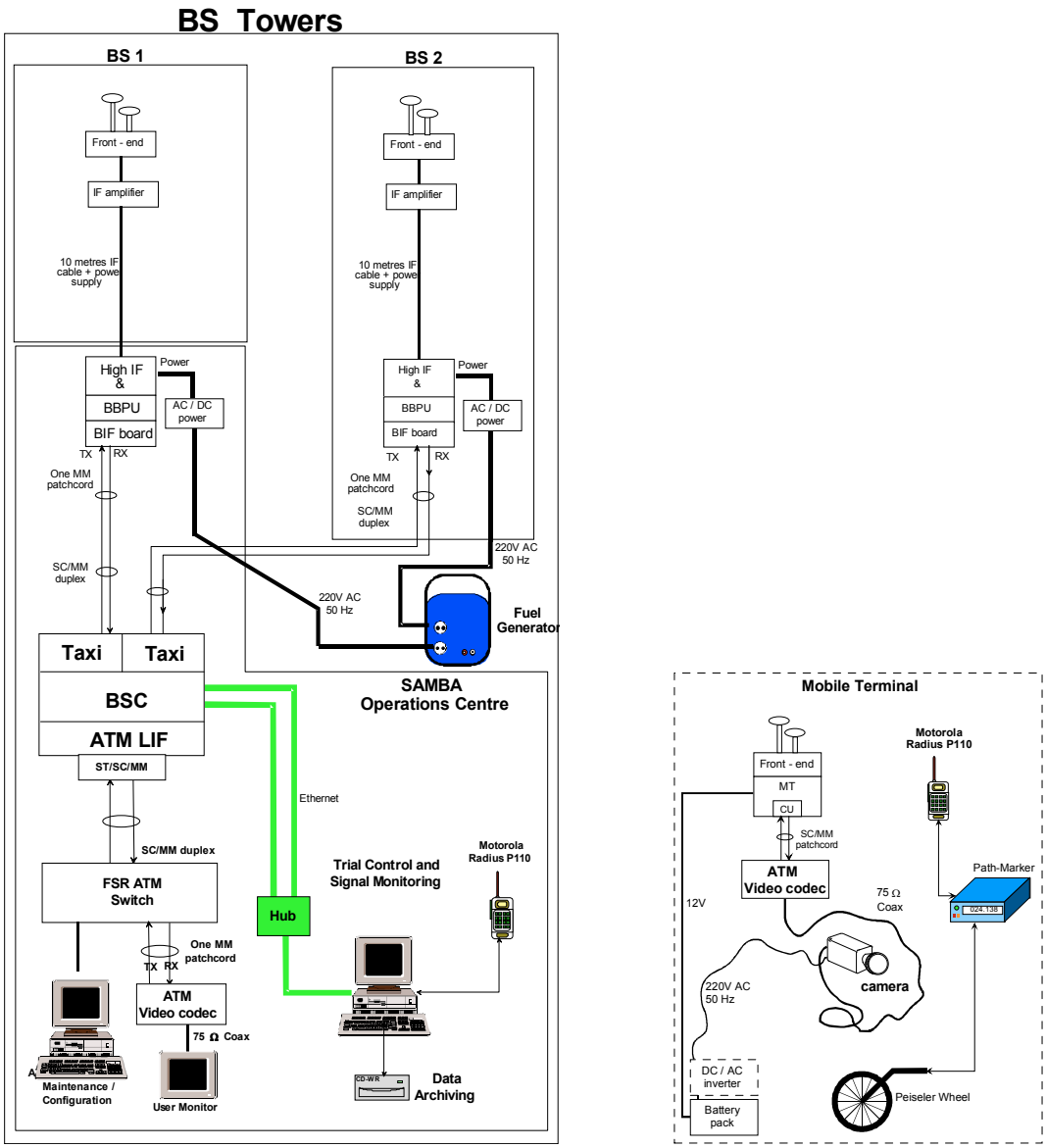

Figure 5.9: Trial Platform and interconnection to the C&M system

Since the antennas and the MHs were characterised in specific measurements procedures, their gains are well known and consequently the RF-front-end can be bypassed during the calibration procedure by injecting directly the signal in the RF cables that interconnect to the High IF module. As indicated in Figure 5.10, the received power $P_{B,}$, can be obtained by the sum of the received power at the antennas and the MHs gain (in dB), $P_B=P_A+G_{MH}$ (dBm).

The RSSI calibration procedure requires the utilisation of some laboratory equipment namely a spectrum analyser or a power meter, a CW (Continuous Wave) frequency synthesiser and a multimeter.

The following steps are necessary to execute the BSs calibration procedure (see Figure 5.11):

1. For each BS (with the BBPU powered on) a CW signal is fed into the RF coaxial cables, including the cable amplifier for cable loss compensation, in the right frequency plan (see previous chapter).

2. The RSSI voltage figures in the BBPU RSSI output connectors are registered with the help of the multimeter and the correspondence to the injected power by the CW generator is made. The procedure is done for both receiving channels (Rx1 and Rx2) separately.

3. The operation specified in step 2 is performed until enough points (RF power versus RSSI values) are obtained to characterise the behaviour of the BS, i.e., CW power sweeping over the dynamic range of the system for both Rx channels.

4. After performing this task for both Rx channels, a check regarding possible channel unbalance or hardware problems is performed. The RSSI curves versus received power for both channels (Rx1 and Rx2) should match. If not, it is necessary to attenuate the strongest Rx channel.

5. After achieving a good balance for both channels, Rx1 and Rx2, the calibration tables are generated and inserted in the C&M system.

The same procedure is applicable for the MT calibration. Figure 5.12 shows the necessary set-up.

Figure 5.13 and Figure 5.14 show the calibration curves for the MT and one of the BSs. It can be concluded that there is a good match between both channels and that the BS curve saturates at approximately –50 dBm. For what concerns the MT, the match between the two channels is a bit worse but the saturation point is approximately at –45 dBm. These curves are used by the C&M system to convert power levels to RSSI values.

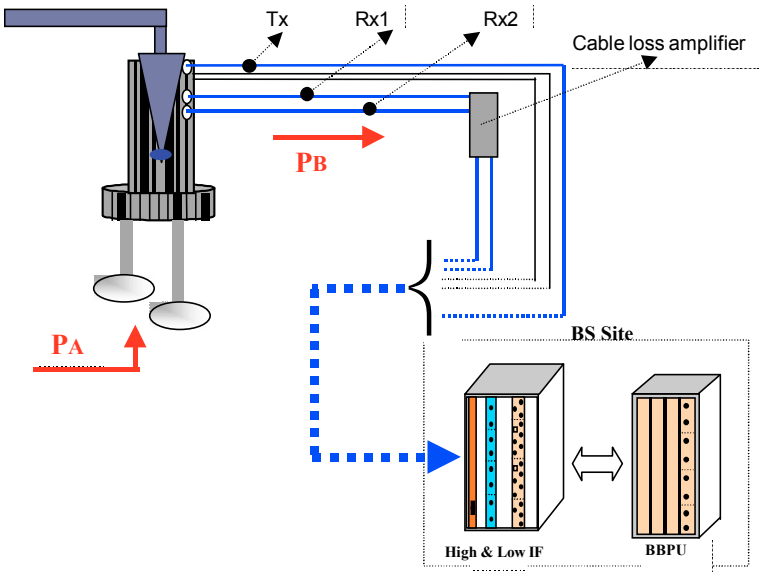

Figure 5.10 - RF connection at the BS

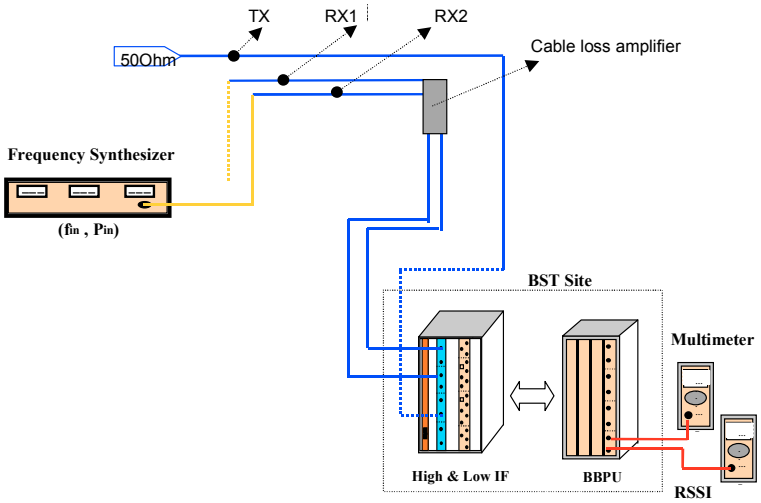

Figure 5.11: RSSI calibration set-up for the BS

5.1.2 CIR measurement system calibration

Figure 5.15 shows the configuration used for calibration concerning the CIR measurements. The same general procedure was used as for the measurement of any other device under test when using a NA.

A waveguide with a 50 dB attenuator was used to interconnect the two MHs in replacement of the air interface. The waveguide was also characterised individually to enable the subtraction of the effects not related with the air interface. The same set of cables was used to perform this procedure ensuring the same conditions during the real CIR measurements.

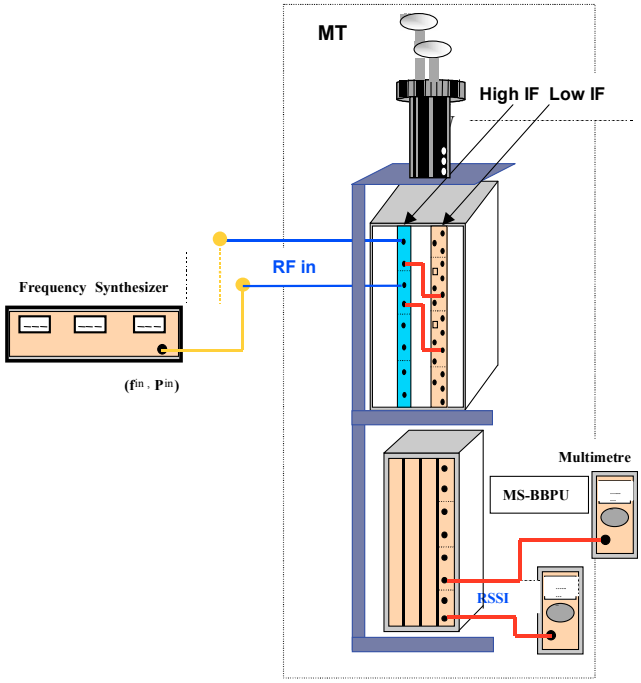

Figure 5.12: RSSI calibration set-up for the MT

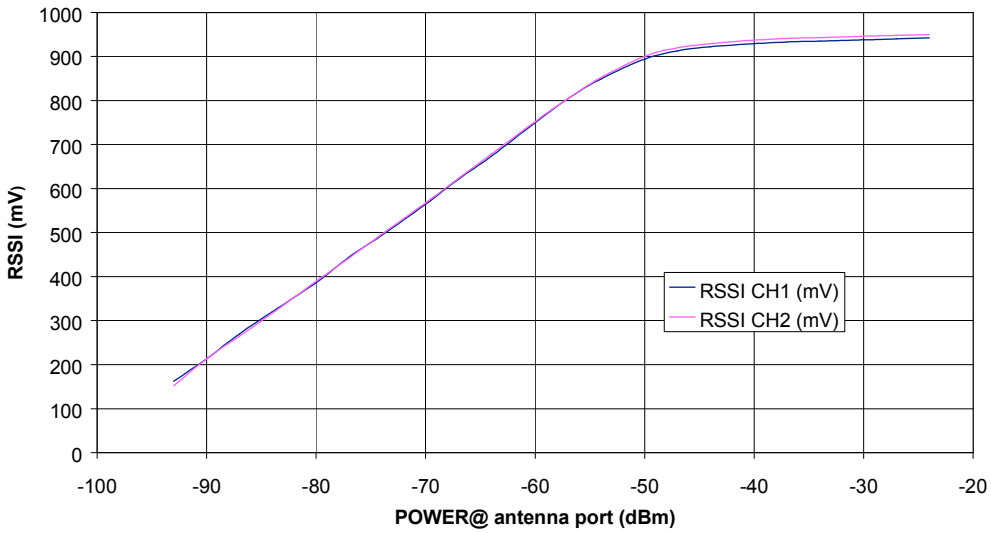

Figure 5.13: RSSI calibration curves for one of the BSs

The main idea of this calibration is to enable the removal of all the effects not introduced by the air interface and antennas when performing the CIR measurements. The system transfer function $H(k)$ is defined by equation (5.2) where $C_{antenna\&radio\_channel}(k)$ represents the transfer function of the radio channel. $H_{MHx}(k)$ is the transfer function of each MH and $H_{Other\_components}(K)$ the remaining system components as for example cables, connectors, etc.

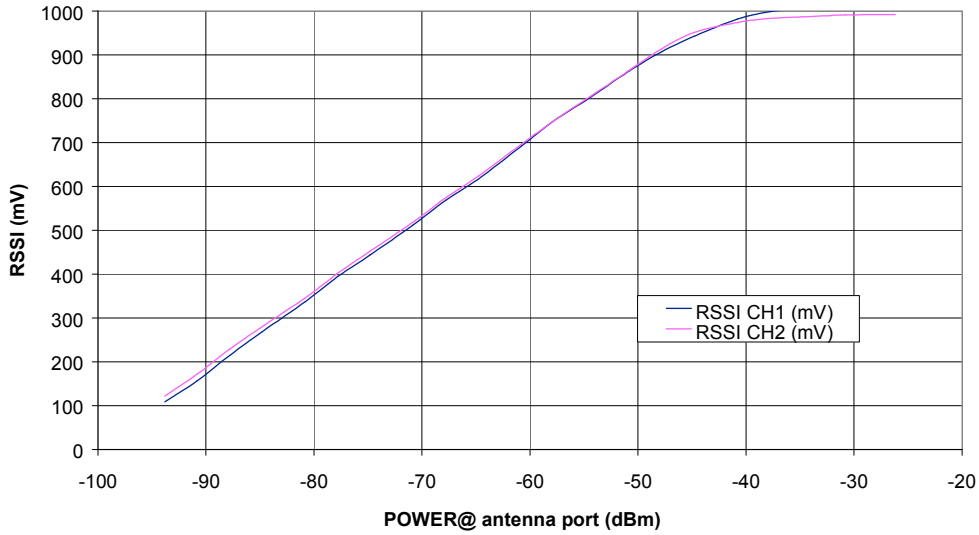

Figure 5.14: RSSI calibration curve for the MT

$$H(k) = H_{MH1}(k) \times C_{antenna\&radio\_channel}(k) \times H_{MH2}(k) \times H_{Other\_components}(k) \quad (5.2)$$

Equation (5.3) represents the transfer function of the system $H_w(k)$ when the air interface is replaced by the waveguide. $C_w(k)$ is the transfer function of the waveguide itself.

$$H_w(k) = H_{MH1}(k) \times C_w(k) \times H_{MH2}(k) \times H_{Other\_components}(k) \quad (5.3)$$

Dividing equation (5.2) by (5.3) we can obtain the result shown in equation (5.4) which enables the calculation of the air interface transfer function $C_{antenna\&radio\_channel}(k)$ based on the knowledge of the waveguide and the whole system transfer function when the radio interface is replaced by the waveguide and the whole system transfer function $H(k)$ measured by the NA.

An approximation to the impulse response $h_{antenna\&radio\_channel}(n)$ can be obtained using the IDFT (Inverse Discrete Fourier transform) after truncating the transfer function $C_{antenna\&radio\_channel}(k)$ with the most appropriate window $w(k)$, as indicated in (5.5).

$$C_{antenna\&radio\_channel}(k) = H(k) \times \frac{C_w(k)}{H_w(k)} \quad (5.4)$$

$$h_{antenna\&radio\_channel}(n) = IDFT\left[C_{antenna\&radio\_channel}(k) \times w(k)\right] \quad (5.5)$$

The CIRs were estimated by multiplying first the radio channel transfer function $C_{antenna\&radio\_channel}(k)$ both by a rectangular and a three terms Blackman-Harris windows. The use of a Blackman-Harris window reduces the time resolution when compared to a

rectangular window, although improving the capacity of detecting smaller impulses, due to the lower secondary lobes (see chapter 8 for a more detailed description of the windows properties).

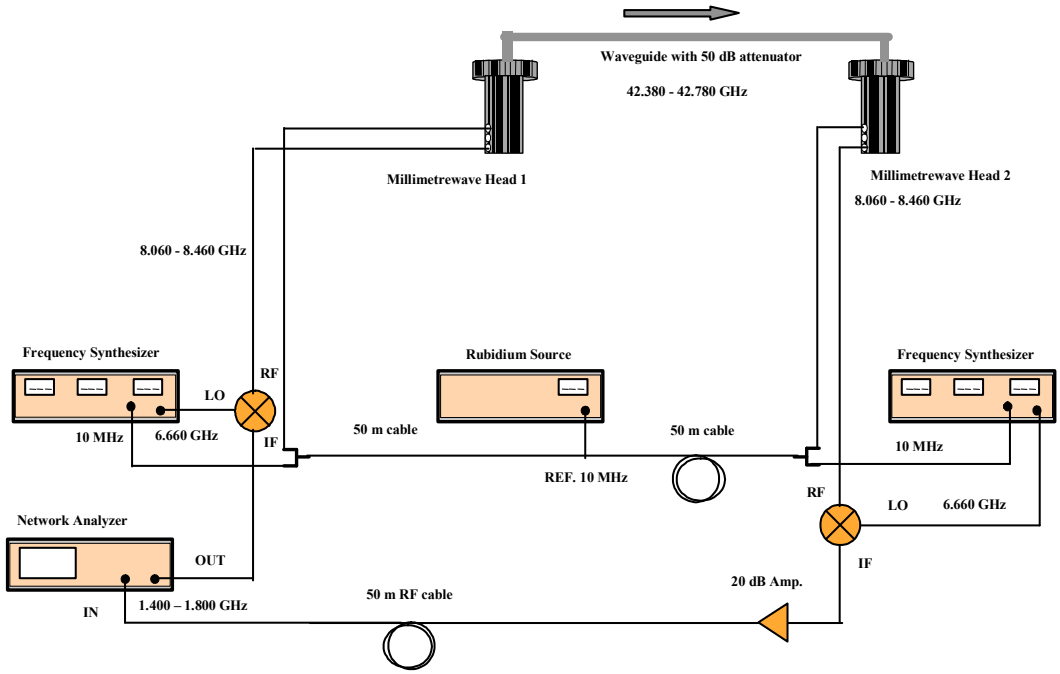

Figure 5.15: Calibration for CIR measurements (indicated values are for downlink)

With the rectangular window and for the considered bandwidth, the resulting CIR has a time resolution of 2.5 ns. In our analysis, the CIR time resolution of 2.5 ns and the used 801 samples were considered sufficient since most of the multipath components could be determined.

6. Parameters Calculation and Graphics

The acquired information by the C&M system was saved in ASCII files. In order to register the measurement conditions, a specific document was generated for each measurement named "Propagation Measurement Sheet" where the specific conditions were registered. An example can be seen in Figure 5.16.

Next are described several parameters that were used to analyse the system behaviour in the following chapters.

```
                          PROPAGATION MEASUREMENT SHEET
                          =============================


 Identification:
 ---------------
 Measure #: 47
 Date: 22-04-1999
 Time: 15:02
 Start position [m]: 0
 Resolution [m]: 1
 End position [m]: 237
 Measurement personnel: Manuel Dinis
 Measured by Partner: IT/PT/CET
 Place: Nova (street)

 Transmitter: - BASE STATION
 ------------
 Power [dBm]: 21,2
 Downlink Frequency [GHz]: 42,74
 Antenna:
 Type: Wide Cell
 Height [m]: 7
 Gain [dBi]: 19,5
 Orientation Horiz. [degrees]: 0
 Orientation Vert. [degrees]: 0

 Receiver: - MOBILE STATION
 ---------
 Antenna:
 Type: Wide Cell
 Height [m]: 2,5
 Gain [dBi]: 2
 Orientation Vert. [degrees]: 20

 Scenario:
---------
 Environment Classification: Outdoor
 Weather Conditions: Cloudy, weak wind
 Speed MT [Km/h]: 10
 Measurement Distance [m]: 237
 Comments:
 NOVA street, Tilt BST at 0 degrees.
 Tilt MS at 20 degrees towards the front of the Van.
 Starting position near the power generator (22m from the BS).
 Physical Link lost at 237m by timeout.

 Surface Layout and Sketch: See 'Planning for the Aveiro Trials' document.
```

Figure 5.16: Propagation measurement sheet example

6.1 Wide cell tilting angles and impact

Although two types of antennas have been designed for the BS, only the wide cell antenna was used extensively in almost all measurements (indoor and outdoor). The elongated cell was used only to perform CIR measurements in the sports pavilion to compare the two antennas radiation pattern impact on the radio channel. This section presents a more detailed analysis of the wide cell configuration and results obtained by simulation for the NRP in the pavilion surface and the impact of the titling on the BS and MT as a function of the distance to the BS.

The wide cell was designed to guarantee an almost constant flux power density up to a distance of approximately 150 meters from the BS being therefore optimised to cover indoor arenas and large squares. For what concerns the radiation pattern, this corresponds to an angle of 86.6^{o} where the gain reaches the maximum value (see Figure 5.18). The coverage area is however a function of the antenna height.

For a distance between 150 m and 300 m the antenna gain is approximately constant, therefore, the signal is affected mainly by the free space loss. Moreover, due to the fact that the cell starts at 30 m (there is a blank coverage zone near the BS) and ends at 300 m, the corresponding angle in the vertical plane varies from 82^{o} to 88.3^{o} (see Figure 5.17). For distances beyond 330 m (hence already beyond the accepted cell limits), the gain starts decreasing contributing to enhance the signal attenuation. Figure 5.18 shows a zoom of the BS and MT antennas radiation patterns in the angles of interest.

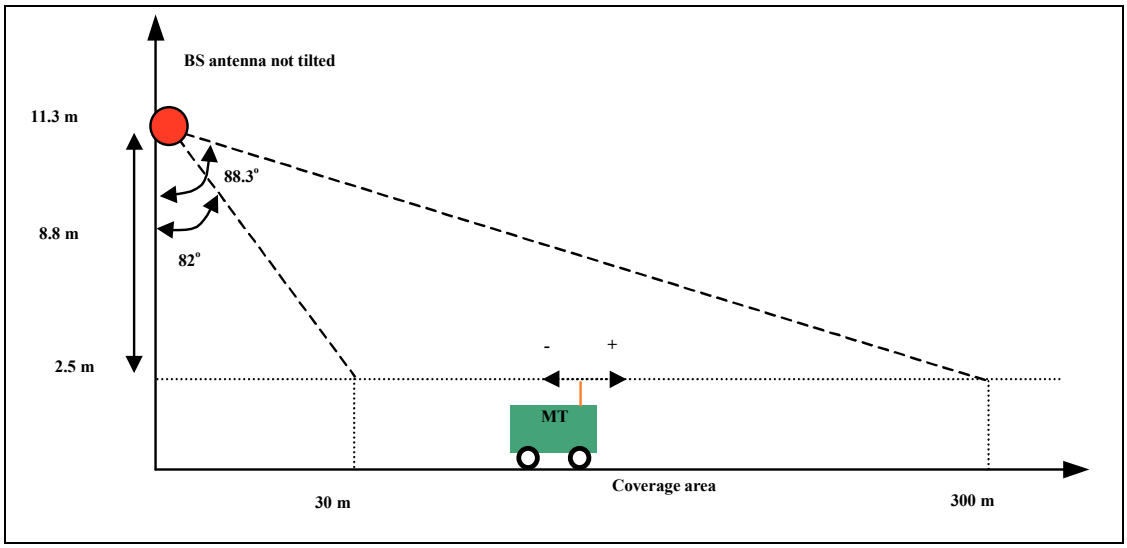

Figure 5.17: Wide cell coverage area geometry

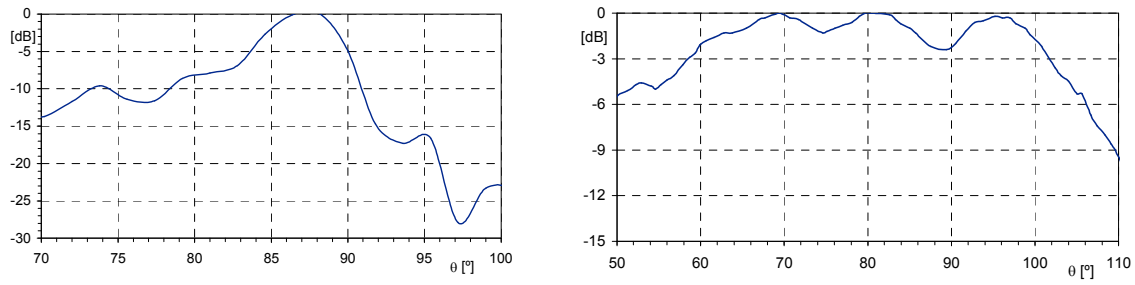

Figure 5.18: Zoomed BS (left) and MT (right) vertical plan antenna radiation patterns

Figure 5.19 shows the NRP level, obtained by simulation, in an open area scenario with the BS antenna located at 12 m height and using the MRC technique for space diversity reception [5] [6] [7]. It can be seen that the power level decreases as the distance to the BS increases and that there are areas with no coverage (in black) laterally to the BS due to the specific antenna radiation pattern. Moreover, the fading depth increases as the distance to the BS increases. The coverage is in accordance with what was predicted in Figure 5.17, showing that the used antenna radiation pattern model that was obtained by direct measurement is appropriate to model the wide cell antenna.

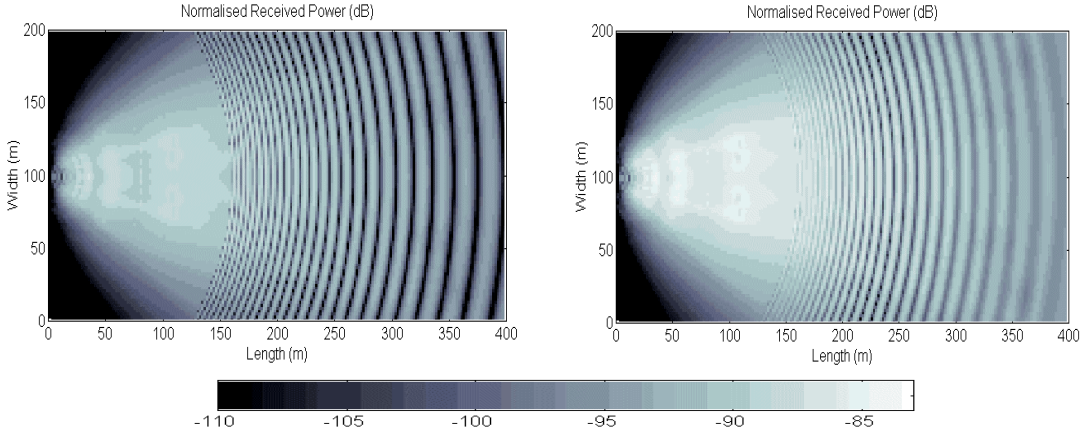

Figure 5.19: NRP distribution in an open space: Single antenna (left); Two antennas and MRC (right)

The impact of the BS antenna tilting angle is shown in Figure 5.20 (rotation in the vertical plane). Increasing the antenna tilting angle (rotation towards the floor direction) reduces the cell size. This technique can be used to reduce the co-channel interference in a cellular system. In the same figure on the right side are also presented simulation results for the received power levels when the height of the BS antenna changes influencing also the cell dimensions.

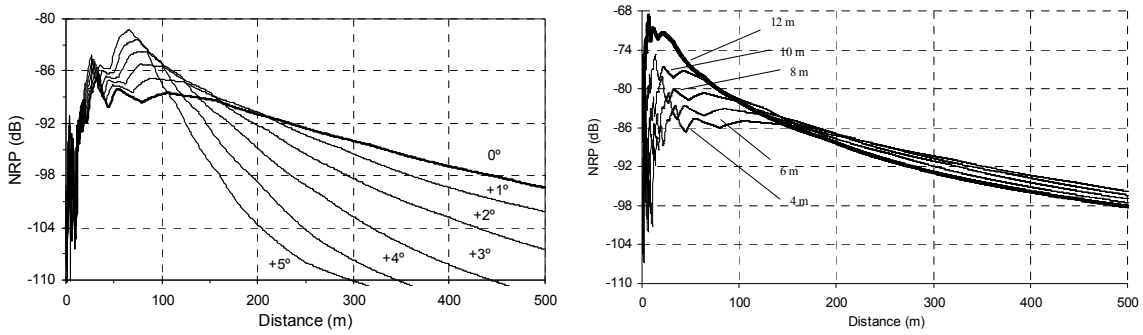

Figure 5.20: Effect of BS tilting angles between 0° and +5° (left) and antenna height (right)

MT antenna tilting angles effects are displayed in Figure 5.21. Negative angle values (towards the BS) have negligible impact on the NRP. Positive angles (towards opposite the BS) the cell size decreases. This different behaviour is justifiable due to the radiation pattern of the MT antenna (see Figure 5.18 on the right). For tilting angles outside the range -25 to +20 degrees the degradation is considerable. This radiation pattern allows for a considerable freedom on the MT mobility.

These simulation results intend to give an idea of how the system should behave and will be confirmed by real measurements presented in the next chapters.

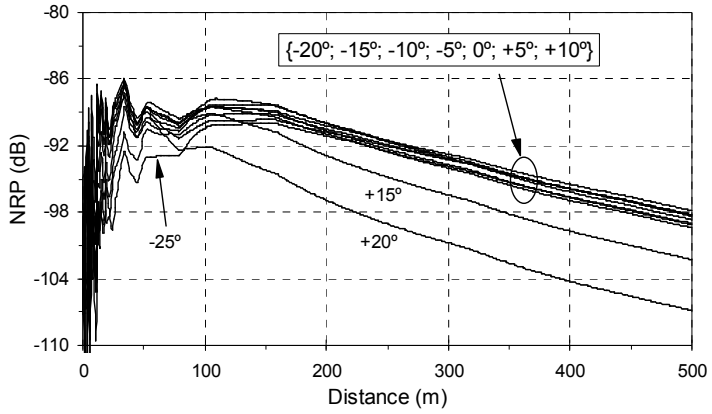

Figure 5.21: Effect of MT tilting angles between -25° and +20°

6.2 System noise floor

In the absence of interference all systems are limited by thermal noise, which is intrinsic to the physics of materials. Equation (5.6) gives the theoretical minimum power level received at the receiver input for a specific BER (E_b/N_o).

$$P_r = \left.\frac{E_b}{N_0}\right|_{dB} + 10\log R_b + KT\big|_{dB} + F\big|_{dB} \quad (dBW) \tag{5.6}$$

where E_b/N_o is the ratio of bit energy to the noise spectral density, R_b the bit rate (64 Mbit/s, the gross bit rate), K the Boltzman's constant (-228.6 dBW/Hz/K), T the temperature (293 K) and F the receiver noise figure (6 dB), therefore, using the figures specific to the Trial Platform, we obtain the following result (5.7):

$$P_r = \left.\frac{E_b}{N_0}\right|_{dB} - 90 \quad (\text{dBm}) \tag{5.7}$$

The noise level is obtained for E_b/N_0 = 0 dB, i.e. P_r= –90 dBm. The measured level for the system noise floor is about –92 dBm which matches well with the theoretical prediction.

6.3 Calculation of the NRP

The NRP was defined in chapter 2 as the ratio between the received and transmitted power. If *x(t)* is an impulse signal transmitted at a rate $1/T_s$ the transmitted power P_t is defined by (5.8), where *k* is a constant. The received signal is the convolution of *x(t)* with the CIR and its power defined by equation (5.9).

$$P_t = \frac{k}{T_s}\int_{-\infty}^{+\infty}\left|x(t)\right|^2 dt \tag{5.8}$$

$$P_r = \frac{k}{T_s}\int_{-\infty}^{+\infty}\left|\sum_{i=0}^{N-1}\alpha_i e^{j\phi_i} x(t-\tau_i)\right|^2 dt \tag{5.9}$$

Depending if we are in presence of a narrowband or wideband/broadband radio channel, equation (5.9) can be simplified in two different ways. For a narrowband channel ($\tau_{max} << T_s$), the approximation shown in equation (5.10) is valid, where $\bar{\tau}$ represents the received signal replicas average delay and therefore the NRP can be calculated using (5.11).

$$P_r = \frac{k}{T_s}\int_{-\infty}^{+\infty}\left|\sum_{i=0}^{N-1}\alpha_i e^{j\phi_i}\right|^2 \left|x(t-\bar{\tau})\right|^2 dt = P_t\left|\sum_{i=0}^{N-1}\alpha_i e^{j\phi_i}\right|^2 \tag{5.10}$$

$$NRP = \left|\sum_{i=0}^{N-1}\alpha_i e^{j\phi_i}\right|^2 \tag{5.11}$$

Equation (5.11) shows that, for a narrowband radio channel, the PDP can be considered as having a single component that is calculated summing as vectors all the multipath components. This is the same to say that the receiver does not have enough time resolution to separate multipath components and sees just a single signal.

For a wideband/broadband radio channel (τ_{max}>>T_s), the received impulses $x(t-\tau_i)$ arrive to the receiver with different delays. Assuming their phases ϕ_i uniformly distributed in the interval $[-\pi, \pi]$, the approximation shown in equation (5.12) is valid being the NRP given by equation (5.13).

$$P_r = \frac{k}{T_s}\int_{-\infty}^{+\infty}\sum_{i=0}^{N-1}\alpha_i{}^2\left|x(t-\tau_i)\right|^2 dt = \sum_{i=0}^{N-1}\alpha_i{}^2\,\frac{k}{T_s}\int_{-\infty}^{+\infty}\left|x(t-\tau_i)\right|^2 dt = P_t\sum_{i=0}^{N-1}\alpha_i{}^2 \qquad (5.12)$$

$$NRP = \sum_{i=0}^{N-1}\alpha_i{}^2 \qquad (5.13)$$

Analysing this result it can be concluded that the NRP is now exclusively dependant on the power of each multipath component since the phase is not taken into account in the calculations. For this case, the time resolution is considered to be infinite, the receiver receives all the signal multipath components separately and therefore interference is not experienced among them. For the work presented in this thesis, this approach was used to calculate the NRP parameter.

6.4 Calculation of MRC and BER parameters

The MRC signal was not available for collection at any of the outputs due to the fact that this procedure is done inside the equaliser chip, and therefore a best case was considered for the MRC calculation based on the two received signals. The phase information was not available and an in-phase situation was assumed leading to the direct sum of the two signals. Averaging over several frames was also performed.

The BER was calculated based on the parameters BitErrors and TransAct (see Table 5.1 and chapter 4), as indicated in equation (5.14), and can be displayed per frame or averaged over various frames (e.g. 100 frames). When averaged over less than 10 frames, the BER values were truncated to a minimum of 10^{-4}; less than 100, to a minimum of 10^{-5}; and less than 1000 to a minimum of 10^{-6}, due to statistical reasons.

$$BER = \frac{BitErrors}{(PL + CI + CR)\times TransAct} \qquad (5.14)$$

6.5 Calculation of AFD and LCR parameters

To provide enough graphical resolution the AFD (Average Fade Duration) parameter was calculated for 100 different thresholds equally spaced between the minimum and maximum values of the signal (Ch. 1, 2 or MRC). For each threshold the various fade durations were calculated corresponding to the time the signal is below the threshold and then the average is calculated for each threshold. The following steps are executed:

- Search for the point where the signal crosses the threshold.
- Search the point where the signal crosses again the threshold in the opposite direction.
- Calculate the elapsed time and store its value.
- Repeat the above procedure for all the available points.
- Calculate the average of all the time intervals.
- Change threshold and repeat for all thresholds.

For the LCR (Level Crossing Rate) the procedure was similar and the number of times the signal crosses the threshold in the positive (or negative) directions was calculated and the result divided by the total time of the analysed interval.

6.6 Type of graphics generated

The following types of graphics were generated:

- Received power versus travelled distance (Ch. 1, Ch. 2 and MRC).
- BER and MRC versus travelled distance.
- CDF curves of BER.
- CDF curves of the received power (Ch. 1, Ch. 2 and MRC).
- BER versus the received power (MRC).
- Number of bit errors versus distance.

- Number of byte errors versus distance.
- Number of bit errors over number of byte errors versus distance.
- Correlation coefficient between the Ch. 1 and Ch. 2 and Rice factor (K_{Rice}).
- CDF of the received power (Ch. 1, Ch. 2 and MRC) versus the estimated Rice distribution parameters for intervals with constant average power.
- AFD versus the threshold.
- LCR versus the threshold.
- CIR.
- NRP.
- Delay spread.
- Average mean delay.
- SDW90%.
- Coherence bandwidth.

Specifically for the CIR graphs, the time (delay) axis was limited to 600 ns and the magnitude axis to –50 dB. These assumptions were made based on the analysis of all the measurements, previously obtained simulations results and the dynamic range of the system.

7. Measurement Scenarios Description

In this section typical indoor and outdoor scenarios selected for experimental evaluation of the mobile broadband system prototype are described in terms of its mains physical characteristics [6] [8]. One outdoor and two indoor scenarios were selected. Scenarios considered just for simulation purposes will not be described here, but when the simulation results are presented.

7.1 Outdoor scenario

The outdoor scenario is a typical urban residential area containing two parallel streets, car parks and buildings. The buildings on one side have a height of five floors and, on the other, from four to eight floors being separated by a distance of 36 m across the streets. Their exterior surface is made of concrete with some windows per floor as displayed in Figure 5.22. On the left side and in between the two streets there is a row of small trees[2]. The pavement is made of asphalt, the walking areas and sidewalks are of concrete and there are large areas of grass with a few small trees. There are two parking areas, one made of asphalt and the other of granite. Moreover, perpendicular streets were also available enabling the testing of the signal penetration in shadow areas [9].

As the outdoor measurements were performed with the MT antenna on the top of a van, the antenna height is fixed to 2.5 m. In this scenario, the BS antenna was located at a maximum of 11.3 m near the central part of the main street as shown in Figure 5.22, denoted by BS, and pointing towards the end of the street, i.e., parallel to the buildings that exist on both sides. The most relevant distances are also indicated in the figure and the main paths used by the MT when moving along the various streets.

Figure 5.22 indicates also the paths selected to move the MT. The main path (central) was the path most used for the performed experiments, namely different antenna heights, antenna tilting angles, etc. Path number two, parallel to the former, was also used to investigate the robustness of the radio link when operating in non-LoS, caused by the trees. Path three was used to study the behaviour of the radio link when the MT travelled in transversal streets moving into the trees and buildings shadowing (corner effect). This study is important for what concerns the handover algorithm design and co-channel interference related aspects.

7.2 Indoor scenarios

As a representative example of an indoor scenario, a sports pavilion was selected (See Figure 5.23). The pavilion's floor is synthetic, the walls are made of concrete and bricks,

2 Plane-trees.

and large glass windows of about 2 m height cover the region 2 m above the floor level. The ceiling is supported by a metallic structure and there are a few rows of public seats made of concrete on one of the sides of the pavilion. The dimensions of the pavilion are about 45 m by 35 m as shown in Figure 5.24.

Two different cell layout configurations, depicted in Figure 5.24, were used to cover the sports pavilion. For an easy reference they will be designated by configuration A and B. The experimental procedure was quite similar for both configurations, however configuration B allows the study of handover and in configuration A, a single BS covers the entire pavilion floor surface. For configuration A, the BS antenna was set at a height of 6.5 m, rotated –40º in the horizontal plane in order to point along the pavilion's diagonal and no rotation was used in the vertical plane.

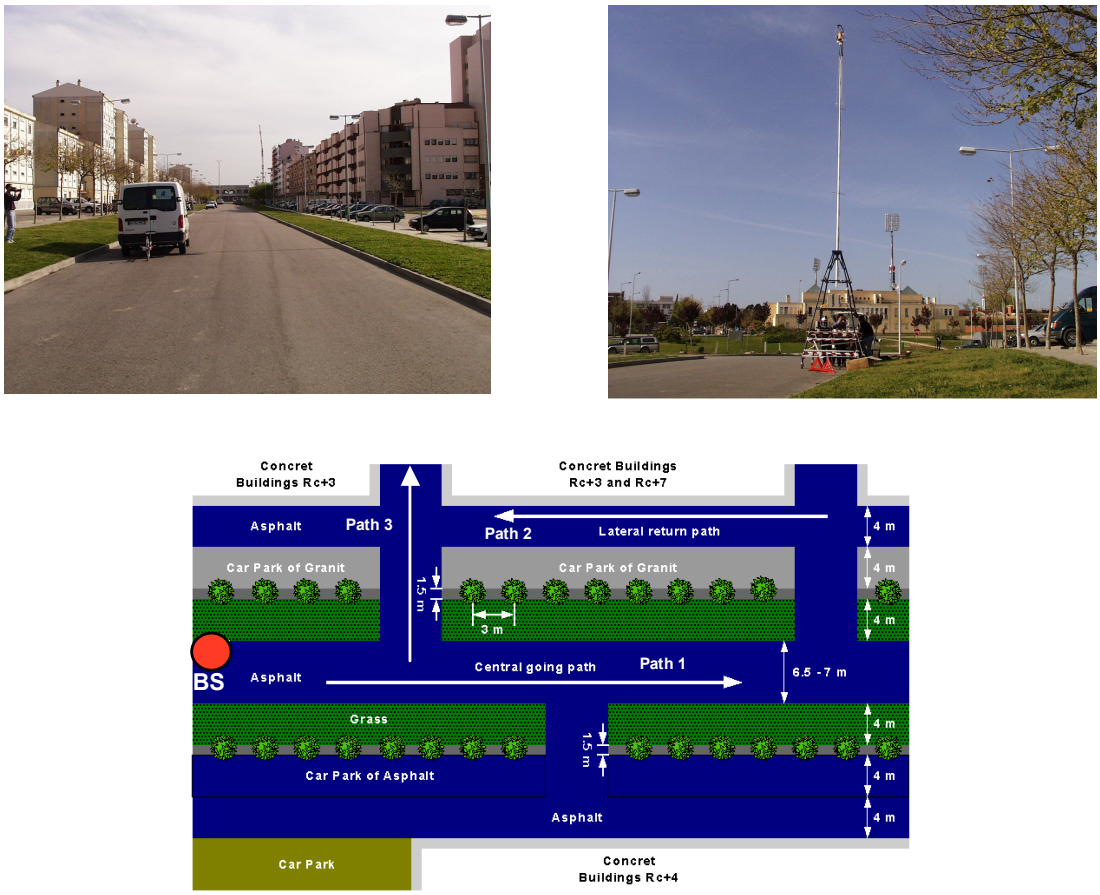

Figure 5.22: Outdoor scenario

In configuration B, the BSs antennas height was 5.85 m in order to avoid possible LoS obstruction by some advertising placards near the ceiling. The antenna of BS1 is rotated

10.5º downwards and the antenna of BS2 is rotated 12.5º downwards and 180º in the horizontal plane. The rotation angles used in each BS were determined in order to have BS1 covering half of the scenario and BS2 the other half, with a sufficient overlapping zone. The difference of 2º between both rotation angles was introduced in order to compensate the higher front-end gain of BS2.

The MT was mounted on a trolley with its antenna height set fixed to 1.5 m and moved along the several paths at a velocity of approximately 3.6 km/h (walking speed). The paths included longitudinal, transversal and diagonal (the longitudinal paths were separated by 1 meter).

Handover studies were performed using configuration B. Two different movement directions were considered for the MT: moving from BS1 to BS2, designated by Fw (Forward) direction; and in the opposite direction, from BS2 to BS1, by Bw (Backward).

The CIR measurements were performed in the frequency domain (see chapter 8 for other techniques), inside the sports pavilion and a room in IT (Instituto de Telecomunicações, Aveiro) and is referred as the IT Room, having different characteristics in terms of construction materials and size. During the measurements and for each frequency-sweeping, the entire scenario was static since Doppler effects cannot be measured with this technique.

Specific spatial locations were selected to perform the CIR measurements and various measurements were taken around the same location to obtain an average frequency response. The selected set of points (seven), here designated by positions[3], for each location were separated approximately by one wavelength (7.83 mm) to ensure spatial de-correlation and reduce the probability of repeating the same unfavourable measurement condition, leading to a better characterisation of the CIR for each location [10]. The spatial distribution of the positions for each location is shown in Figure 5.25.

In the pavilion, various locations were selected to perform the CIR measurements (a total of eleven) and various measurements were made in the uplink and downlink directions,

3 The words location and position are here used with a different meaning. By position is meant a few millimetres MT antenna deviation for the same MT location.

for the two diversity reception channels, with the wide and elongated antennas and with and without LoS as shown in Table 5.3. A total of 700 measurements were performed.

Moreover, the frequency response measurements were averaged to reduce the noise (five measurements per position). The BS location was selected as indicated in Figure 5.26 (This BS configuration is also designated by Configuration C in chapter 7 and 8). The height of the BS was set to 5.85 m and placed 1.4 m away from the field limit marks in the direction of the wall. The height of the MT antenna was 1.2 m for the wide cell and 1.25 for the elongated cell, in this case "facing" towards the benches of concrete.

Figure 5.23: Indoor scenario: sports pavilion

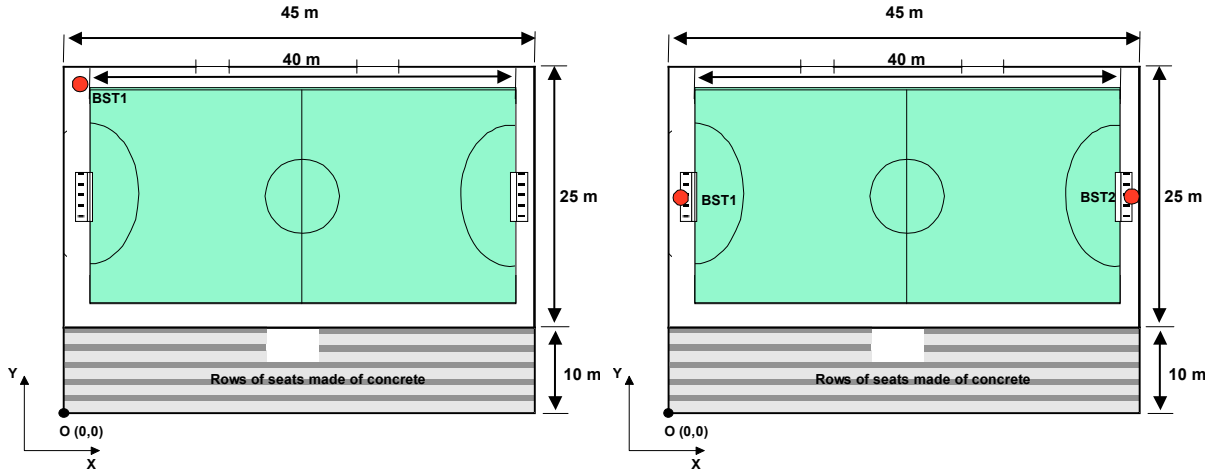

Figure 5.24: Indoor scenario: cells' configuration A (left) and B (right)

Figure 5.23 shows a detailed view of the sports pavilion where are visible the windows, concrete columns, benches in concrete and the complex ceiling metallic structure. The MT locations were chosen in order to characterise the propagation channel in all the extent of

the pavilions surface (different regions of the cell coverage area). The MT locations distribution were such that locations 1, 2, 3, 7, and 11 are within the cell planned coverage area, locations 4, 8, 6 and 10 are at its boundary and locations 5 and 9 are clearly outside the cell.

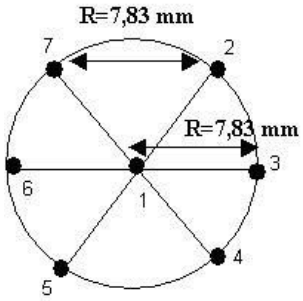

Figure 5.25: Seven measurement positions for each location

The CIR for each MT location was calculated as the IDFT of the seven frequency responses averaged in the frequency domain. Moreover, in order to ensure time invariance for each frequency response measurement and to remove random effects in the acquired signal, five acquisitions were performed for the same MT position. Subsequently, an average of these measured signals was performed.

Location	Experiments	Total acquisitions
1	LoS only (downlink and RX2)	35
2	LoS only (downlink and RX2)	35
3	LoS only (downlink and RX2)	35
4	LoS only (downlink and RX2)	35
5	LoS only (downlink and RX2)	35
6	LoS only (downlink and RX2)	35
7	With and without LoS (downlink and RX2)	70
8	With and without LoS(downlink and RX2)	70
9	With and without LoS (downlink and RX2)	70
	With and without LoS (downlink and RX1)	70
	With the elongated cell antenna (downlink and RX2)	35
	With and without LoS (uplink and RX1)	70
10	LoS only (downlink and RX2)	35
11	With and without LoS (downlink and RX2)	70
	Total measurement acquisitions	700

Table 5.3: Locations and type of experiment performed

Figure 5.27 shows the IT room and the BS and MT location selected for the measurements. A total of 64 locations have been selected covering evenly all the floor area. The BS height

was 2 m and located at (1 m, 3.3 m). The physical spacing between locations is 0.8 m starting at (1.5 m, 0.5 m). The MT antenna height was set to 1.2 m. Since the measurements in this room were done after the analysis of the preliminary data from the pavilion, it was concluded that the 7 positions did not add very much to the CIR, therefore it was decided just to make the 5 measurements for each location giving a total of 5x64=320 measurements. The same number was made for non LoS conditions giving a grand total of 640 measurements.

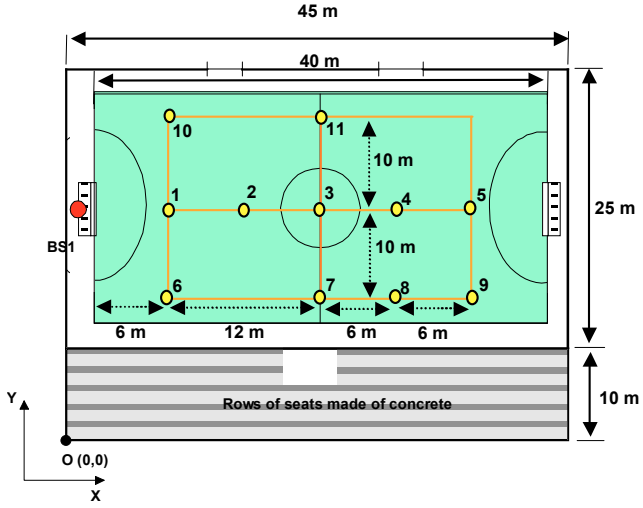

Figure 5.26: Configuration used during CIR measurements

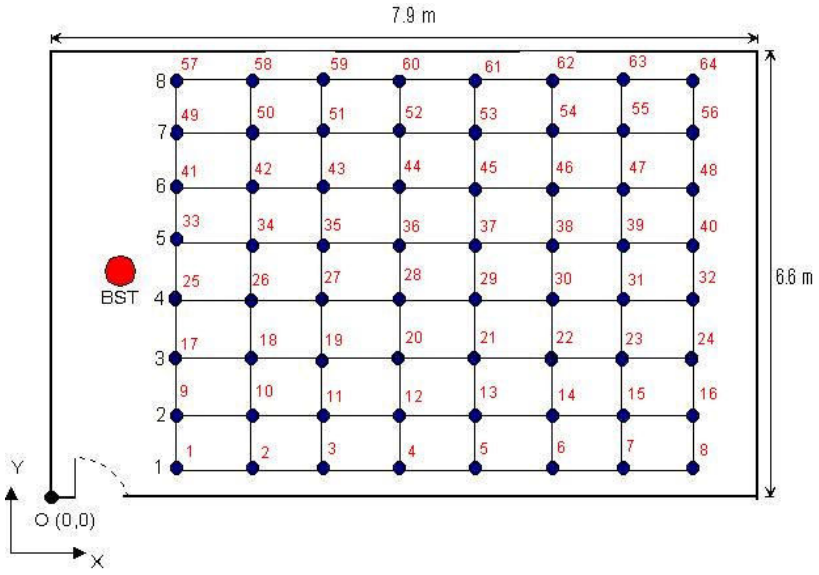

Figure 5.27: View of selected locations inside the IT Room

8. Summary and Conclusions

A description of the hardware necessary for setting up the trials scenarios, the necessary logistics, the C&M system and how the Trial Platform was calibrated to ensure correct and reliable operation was presented in this chapter. The most fundamental parameters and type of graphics generated for the analysis of the measurements data were identified. A description of the selected scenarios in terms of physical dimensions, type of materials, objects and the identification of the paths where the MT was moved, was presented as well as specific aspects related with the CIR measurements.

The Trial Platform was operated in different configurations: one BS, two BS and a reduced and specific configuration used exclusively for CIR measurements. The single cell configuration was selected to test coverage aspects of different scenarios and system configurations. The two cells configuration was required to evaluate the radio handover performance as well as coverage aspects. For CIR measurements, only the antennas and the MHs were used plus a set of laboratory equipment, namely frequency synthesisers, a Rubidium reference generator and a NA. The NA was set to acquire 801 samples in a 400 MHz bandwidth and therefore a time resolution of 2 ns and a maximum excess delay of 2 μs was possible to measure, which is enough given the specific scenarios where the measurements took place.

Given the amount of experimental work planned and the amount of data expected to be collected, a specific C&M system was developed for that purpose. This system allows also to monitor the proper operation of the Trial Platform and the on-line screen presentation of the data and status. The C&M system includes a telemetry system that sends to the BSC distance information collected using a Peiseler wheel. This information is then synchronised with the information gathered by the BSC and stored. Various parameters can be measured simultaneously and they are calculated for each frame. Examples are: RSSI, number of bit errors, carrier being used, etc.

The logistics for the measurements was quite complex and involved a lot of manpower. Two specially designed BS towers were used to install the antennas at different heights, being one for outdoor and the other for indoor operation. The antenna tilting angle was remotely setup and adjusted via a specific step motor system also developed on purpose. In

the outdoor scenario, the MT was installed in a van to allow for speeds up to 50 km/h and to cope for the relatively long travelled distances. For the indoor scenarios, a trolley was used.

In order to guarantee the correct operation of the Trial Platform, calibration procedures were executed. This was the case of the RF and IF modules where, beyond its correct operation, the two receiver chains had to be adjusted in order to guarantee the power balance between the two channels for correct MRC technique operation in the MT and BS sides. Calibration curves were measured and used in the C&M system to derive the correspondence between RSSI and received antenna input power levels. For what concerns the CIR measurements, the removal of all system components not being parte of the radio channel, but necessary to perform the measurements, was fundamental. To measure the impact of other system components the air interface was replaced by a fully characterised waveguide.

Various parameters were adjusted, others calculated and graphics generated for a more convenient analysis of the results. The tilting angles play an important role in mobile communications since they are important to control the channel time dispersion and co-channel interference. The height of the BS antennas was also adjusted to control the cell size. The system noise floor was calculated in order to evaluate the minimum power the system was able to operate and noted to be approximately -90 dBm. The NRP calculation was based on the broadband channel approach and therefore the NRP corresponds to the sum of all rays power present in the CIR. For the MRC signal calculation, since the MRC is performed inside a chip and the signal phase information was not available, a perfect in-phase situation was assumed. BER calculations were based on the parameters collected from the BBPU, namely the BitErrors parameter, available at the output of the FEC codec. AFD and LCR parameters were also calculated from the measured data.

The measurements were performed in three different scenarios: one outdoor and two indoor. The outdoor scenario is a typical urban residential area containing streets, car parks and buildings. The buildings exist on both sides of the road, separated by a distance of 36 m, with heights ranging from four to eight floors. The streets' pavement is made of asphalt and the walking areas made of concrete. A total of three streets were evaluated being one of

them perpendicular enabling to test the signal penetration is shadowing areas. Zones with small trees and grass were also available between the streets. The car parks are made of asphalt and granite.

The indoor scenarios comprise a sports pavilion and a room at the Instituto de Telecomunicações located in the university of Aveiro campus. The pavilion's floor is synthetic, the walls made of concrete and bricks and large glass windows of about two meters height. The ceiling is supported by a metallic structure and there are a few rows of public seats made of concrete on one side of the pavilion. The dimensions of the pavilion are 45 m by 35 m. Handover studies were performed in this scenario and coverage of the pavilion was achieved by two different BS configurations, one of them with two BSs. Each BS covers approximately half of the pavilion guaranteeing however an overlapping zone. CIRs were also performed inside the pavilion and for that purpose a set of specific locations were selected. Since a frequency domain technique was used, the scenario had to be static during the CIR measurements since Doppler effects cannot be measured. To ensure spatial decorrelation seven measurements were performed for each location, being separated by approximately one wavelength (7.83 mm). Moreover, to further reduce the noise floor, for each position five measurements were performed and averaged. In the pavilion various measurement were made in the uplink and downlink directions, for the two diversity reception channels, with the wide and elongated antennas and with and without LoS. A total of 700 measurements were performed.

The room at the institute was used for CIR measurements only. A total of 64 locations have been selected for measurements being 0.8 m the physical spacing between locations. Since the measurements in this room were done after the analysis of the preliminary data from the pavilion, it was concluded that the 7 positions measurements approach did not improve significantly the CIR precision, therefore it was decided to make only the 5 measurements for each location. LoS and non LoS conditions were tested and a total of 640 measurements performed.

In conclusion, a huge amount of measurement data was gathered during the measurements campaign. Coverage, transmission, handover and CIR aspects have been analysed for different scenarios, indoor and outdoor. The logistics was complex and special measures

had to be taken in order to minimise the impact and reduce security risks, due to wind conditions, for example. A quite comprehensive analysis of the mobile broadband system prototype was carried out and the results are presented in the next chapters.

9. References

[1] M. Dinis and V. Lagarto, "Definition of the Trial Platform Infrastructure and Applications", CEC Deliverable Number – A204/PT/CET/DS/P/005/b1, September 1997. Submitted to EC in the framework of the ACTS/SAMBA project.

[2] Manuel Dinis et al, "Integration of the Trial Platform – Version 1", CEC Deliverable Number: A0204/PTIN/SRM/DS/P/6v2/b1, 30/03/99, Submitted to the European Commission in the framework of the SAMBA project.

[3] E. Macedo, Manuel Dinis et al, "Integration of the Trial Platform – Version 2", CEC Deliverable Number: A0204/PTIN/SRM/DS/P/6v2/b1, 30/01/2000, Submitted to the European Commission in the framework of the SAMBA project.

[4] N. Fukui, A. Shibuya and K. Murakami, "Performance of Combined ARQ with SR and GBN for Wireless Systems on a 40 GHz Band Radio Channel", IEEE Communication Magazine, pp. 122-126, September 2001.

[5] José Fernandes, Manuel Dinis, Max Prögler, Wolfgang Herzig, John Zubrzyck, "The SAMBA Trial Platform: Initial Results", ACTS Mobile Communication Summit '98, 8th – 11th June, Rhodes, Greece, 1998.

[6] M. Dinis and P. Jesus, "Evaluation Report of the Trials", CEC Deliverable Number – A0204/PTIN/SRM/DS/P/015/b1, October 2000. Submitted to EC in the framework of the ACTS/SAMBA project.

[7] J. Fernandes, A. Marques, J. Garcia, "Cellular Coverage for MBS Using the Millimetre-Wave Band", ACTS Mobile Communications Summit '99, Sorrento, Italy, June 99.

[8] Manuel Dinis, José Fernades, Max Prögler, Wolfgang Herzig, "The SAMBA Trial Platform in the Field", ACTS Mobile Communications Summit '99, 8th – 11th of June 1999, Sorrento, Italy.

[9] M. Dinis, J. Fernandes, "Effect of the System Layout and Transversal 40 GHz Signal Penetration in Perpendicular Streets Experimental Results Using an MBS Platform", IST Mobile Communications Summit 2000, Galway, Ireland, Oct. 2000.

[10] Jean-François Frigon, B. Daneshrad, J. Putnam, E. Berg, R. Kim, T. Sun and H. Samueli, "Field Trial Results for High-Speed Wireless Indoor Data Communications", IEEE Journal on Selected Areas in Communications, Vol. 18, No. 3, March 2000.

6th Chapter

Cell Coverage, Transmission Analysis and Path Loss Modelling for the Outdoor Scenario

1. Introduction

This chapter deals with cell coverage and transmission performance over the air interface analysis plus path loss modelling for the outdoor scenario. The measurements were performed in the scenario described in chapter 5 – a main street, a street parallel to the main street and a perpendicular street – all three streets located in a residential area in the Aveiro city. In order to not interfere with traffic and pedestrians as well as for security and weather (rain and wind) reasons it was not possible to leave all equipment installed in place for the day after to continue the trials. Long periods of time were necessary for setting up the system every day.

The objective of the filed trials was to evaluate the cell coverage characteristics provided with the lens type antennas (shaped radiation pattern) and the transmission performance on the air interface (BER), including the impact of different system configurations and MT speeds, in order to validate the technical options made for the Trial Platform in terms of equalisation, FEC and diversity reception techniques. Based on the measurements, path loss modelling was performed for different system conditions. These are key issues for all radio transmission systems, and to the author's knowledge, they have never been done for this frequency band and for these specific conditions and system characteristics.

The main street exhibits characteristics of a canyon type street. The BS with the wide cell type antenna was installed in the beginning of the street. The MT is shown in Figure 6.1 and was driven along several paths while data was acquired by the C&M system. Distance information was gathered using a Peiseler wheel. Several conditions where changed during the field trials, namely: BS antenna height, BS antenna tilting angle, MT antenna tilting angle and the MT speed.

Figure 6.1: MT installed in a van equipped with Peiseler wheel and antenna in the rooftop

As pointed out in chapter 5, the C&M system is able to gather various parameters. Particularly relevant for this chapter are: RSSI for the two receiving channels, BitErrors

and the MT distance to the BS. Based on these parameters others were calculated, namely: MRC signal, received power, BER CDFs, Rice distribution parameters, AFD, LCR and path loss slop.

Simulations were also performed based on the ray-tracing technique. Parameters such as the NRP and SDW 90% were evaluated. The first parameter includes the gain of transmitting and receiving antennas, and it was of major importance for the link budget and definition of the cell boundaries. The SDW containing 90% of the channel impulse response energy is used as a measure of the channel time dispersion. Simulations were compared with the measurements to validate the results.

This chapter starts with a description of the results concerning the cell coverage evaluation and transmission performance. Various antennas heights, antenna tilting angles, different velocities and studies of coverage in other parallel and transversal streets, are presented. Path loss modelling results are presented afterwards and the chapter ends with a section on simulation results for other typical mobile cellular broadband scenarios that could not be measured yet, namely a roundabout and a city square.

2. Cell Coverage and Transmission Performance

Based on the gathered information during the measurement campaign made possible by using the trial platform described in chapter 4, the following sub-sections present an analyses of main results obtained for the main, parallel and transversal streets [1] [2]. The study focuses on the main street itself since it is the most important environment due to the most likely necessity to rely on LoS conditions for the millimetrewave band. The transmitted frequency was 39.74 GHz (uplink direction only) with a transmitting power of 21.2 dBm.

Although many measurements were performed in this outdoor scenario (several runs) only are presented results for the central path in the main street (path #1), one parallel street path (path #2) and one path in the transversal street (path #3) [2] [3] [4] [5] [6] [7] [8].

2.1 Main street path measurement results

Figure 6.2, on the left, depicts the received power in both channels (Ch.1 and Ch.2) and the combination of the signals from both channels, using the MRC technique, as a function of the distance between the BS and MT measured along the street at constant speed of 10 km/h and a BS height of 11.2 m.

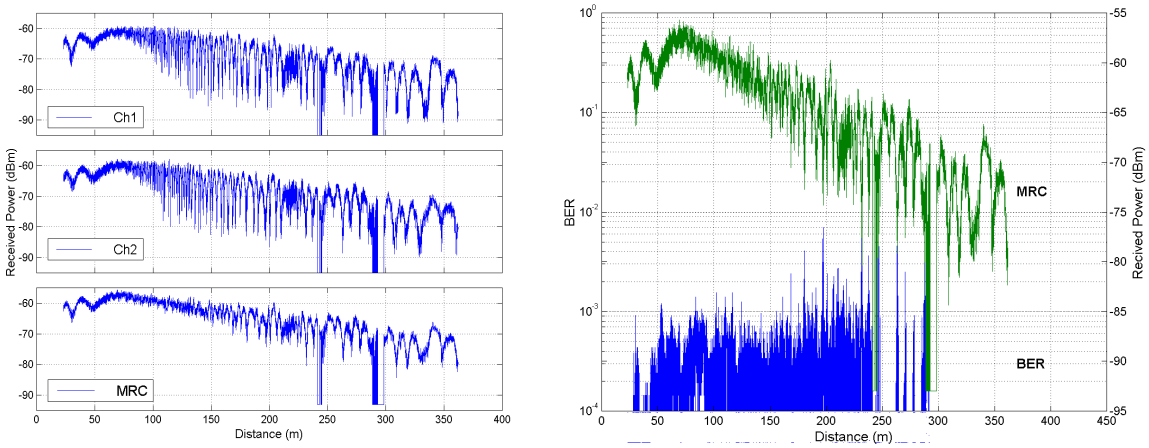

Figure 6.2: Received power sampled per frame (left) and MRC and BER (right) versus the distance

As shown in chapter 5, the cell has a blank zone nearby the BS up to a distance of 30 m. From this point and up to the 50 m, the signal suffers variations caused by the BS and MT antennas radiation pattern fluctuations. The average received power level dynamic range on the first 150 m is rather low due to the shaped radiation pattern of the BS antenna and the small-scale fading depth increases significantly for distances above 100 m as the MT moves away from the BS with a visible improvement when diversity is employed.

Analysing the signal level variations along the path it can be verified that during the first part (up to approximately 100 m) the variations are fast and of small amplitude in contrast with the second part where they are slower and deeper. This behaviour can be explained by the fact that in the first part the LoS component dominates, imposing the average level of the signal. For the second part, the two rays model is a good approximation, since in this case there is a clear dominant effect of the direct and ground reflected rays although other multipath components are superimposed creating the signal fluctuations. This confirms the simulation results presented in chapter 5 regarding the wide cell coverage.

The MRC power level is depicted in Figure 6.2, on the right, together with the BER per frame as a function of distance. The BER is calculated based on the information provided by the FEC chip. This means that the BER figures are the raw BER, at the output of the equaliser. All the error information was computed at least averaging over one frame.

Based on theoretical calculations, the system noise floor is about –90 dBm (see chapter 5) which implies a signal to noise ratio of about 12 dB for distances up to 350 m away from the BS. This value complies with the two deep fades that occur near 250 m and 300 m, which were due to the presence of obstacles (the road traffic was not stopped during the measurements campaign) in the street during the measurements. The BER slightly increases for distances above 180 m until 240 m. Just after the first deep shadow fading the BER recovers quite well because the power level is significantly high. After the second deep fade, the system could not recover anymore due to the fact that the system had a manual reset (signal power levels were still recorded after the baseband subsystem stops running). This figure also shows that the BER rises with the increase of the small-scale fading depth and also with the decrease of the average power level. However, even when the average power level is high enough (distances below 100 m), the BER sometimes is slightly above $1E10^{-3}$.

Figure 6.3 depicts the bit error over the byte error (left) and the BER as a function of the received power level after MRC (right). Figure 6.4 presents the behaviour of the equaliser in an AWGN channel (left) and a two rays multipath channel (BER versus Eb/No). The word experiment shown in the figure does not have the same meaning as the used previously due to the fact that not a real radio channel was used, but a piece of hardware that emulated a radio channel with only two rays and a certain delay between them [9] [10]. As can be seen, the results comply quite well with the predicted behaviour of the equaliser (Eb/No of less than 10 dB is enough to guarantee a BER of $5E10^{-3}$). Another important conclusion that can be drawn is that in general there are up to 3 bit errors per each erroneous byte.

The cumulative distributions of the received power levels and BER per frame, 10 frames and 100 frames are shown in Figure 6.5, respectively on the left and right. The diversity reception improvement is well stated on the power level after MRC. Moreover, it is also

evident that the individual channels are well balanced which confirms the success of the platform calibration procedure described in chapter 5. It can also be observed that in 90% of the cases the BER is lower than $4E10^{-4}$ therefore below the specification target ($5E10^{-3}$). Maintaining the BER below this figure ensures that the FEC mechanism is able to correct the errors. To lower further the BER, ARQ schemes were evaluated experimentally and by simulation and the results are displayed in [11].

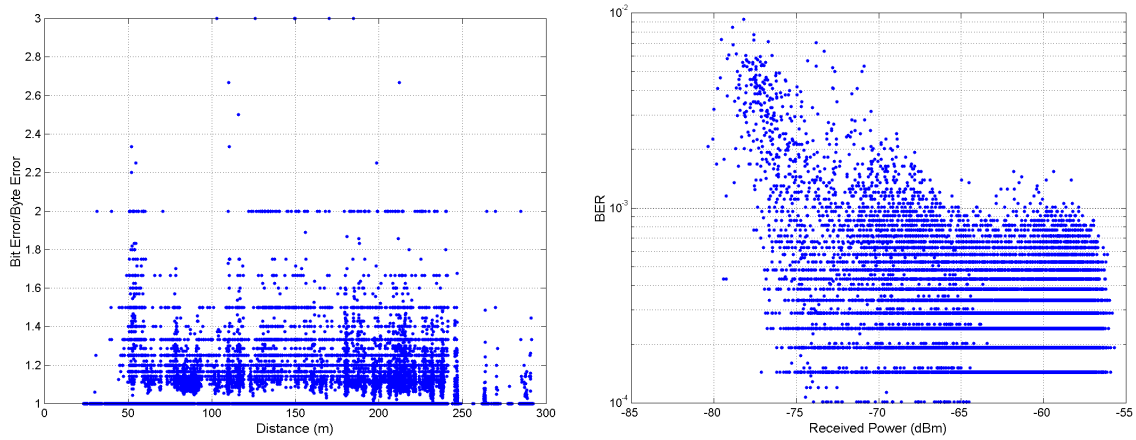

Figure 6.3: Bit over byte errors versus distance (left) and BER versus MRC power level per frame (right)

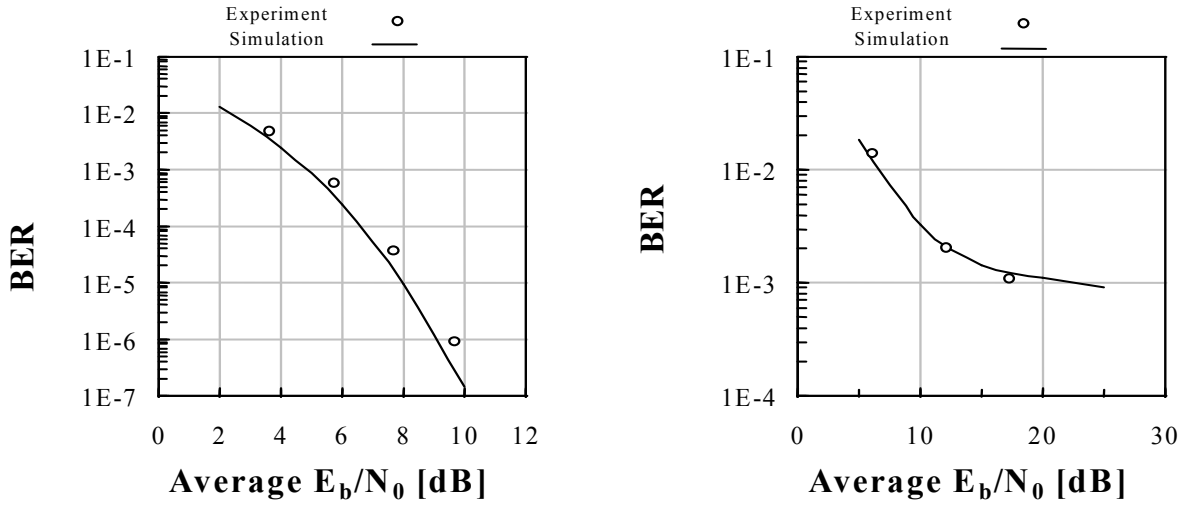

Figure 6.4: Equaliser performance: AWGN (left); Multipath channel (right)

2.2 Simulation results and models validation

Simulations were performed for various paths in the main street [12]. Figure 6.6 shows the results for both receiving channels and MRC, for two different BS antenna heights being 11.2 m and 7 m, left and right, respectively, for one of the paths.

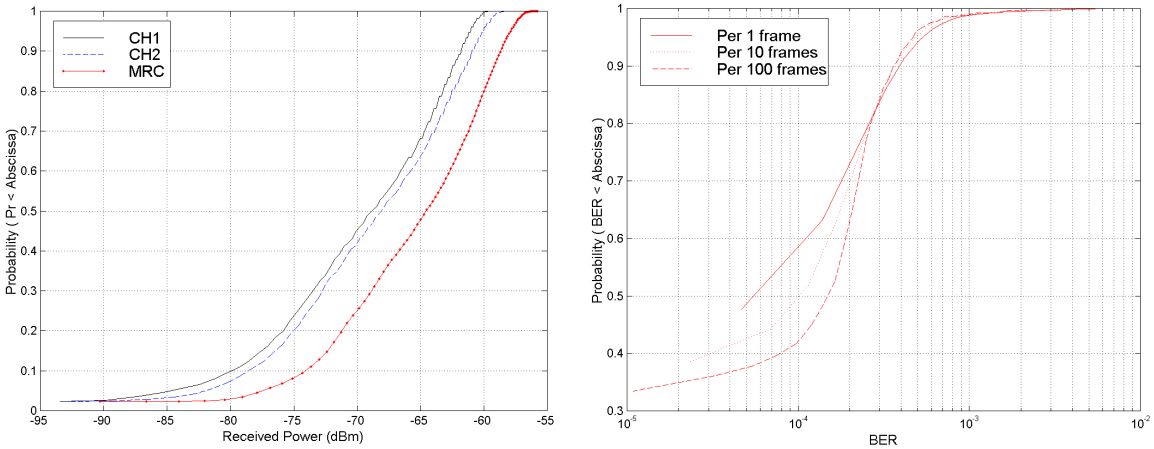

Figure 6.5: Received power CDF of both channels and after MRC (left) and BER CDF (right)

Observing Figure 6.6 it can be conclude that a good similarity exists between the measurements and the simulation results leading to the conclusion that the scenario models are suitable to predict the power levels. Comparing generally the results, one may see that there is a reduction of the cell length when the BS antenna height is lowered. Indirectly, and based on the known antenna radiation pattern, it may be said also that there is a reduction on the cell width. This reduction on the cell width has a direct impact on the fading depth, due to the confinement of the multipath components by the lateral buildings. Therefore the fading depth observed is lower for the lower antenna height. The measured results allow confirming that, when using shaped lens antennas, adjusting the BS antenna height can control the cell dimensions and the energy at its boundaries [14]. Moreover, the simulated power distribution has more fading than the measured one. The main reason for this fact is the difficulty to accurately characterise the electromagnetic properties of the materials within the scenario and the fact that only the reflections in specular directions are considered in the simulator. Nevertheless a quite accurate estimation of the mean received power distribution was achieved. In [12] simulation results for the parallel street are presented confirming the good match between simulations and measurements.

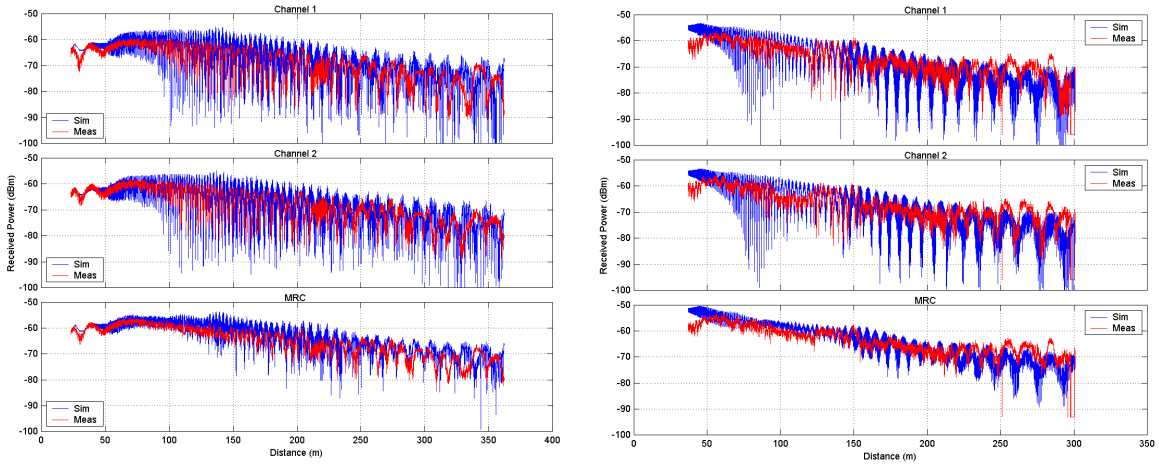

Figure 6.6: Measured and simulated received power for BS heights of: 11.2 m (left); 7 m (right)

Figure 6.7 shows simulation results for the NRP and SDW 90% parameters based on a simplified model of the scenario, which includes only the major objects (trees and parked cars were excluded), to minimise the computational complexity and therefore the simulation time. The BS antenna height was 11.2 m (the maximum height of the BS tower). With this antenna height, there is always a strong LoS component and the trees only introduce attenuation for the reflected rays on the lateral building walls, justifying the option taken relatively to the scenario definition in the simulator (trees have shown to have little impact in the average power distribution). In the top part, the dark pixels correspond to the deep fading areas. In the bottom part, light pixels to areas where the time dispersion is higher, but stills below the maximum supported by the system (250 ns).

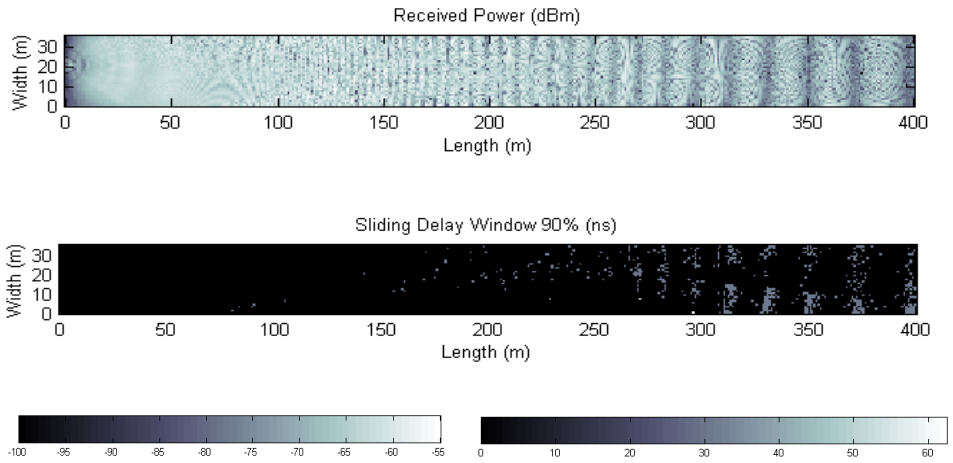

Figure 6.7: Simulation results for the main street: NRP (top); SDW 90% (bottom)

2.3 Data fitting to the Rice distribution

For LoS conditions, the measured data can be fitted to a Rice distribution to obtain the Rician curve parameters. Short path intervals with average power level approximately constant can be selected for the fitting. In order to accelerate the fitting convergence process, a first estimation of the Rice parameters r_{si} and σ_i was obtained as indicated in equation (6.1).

$$\begin{cases} r_{si} = r_{\max} \\ \sigma_i = \left\{ \sigma : \min \ of \left[\bar{r} - E[r] \right] \right\} \end{cases} \tag{6.1}$$

The maximum value of r in the interval under study is denoted by r_{max} and $\bar{r}$ is the arithmetic mean. $E[r]$ represents the first moment of r being for the Rice distribution given by (6.2) where $P_{avg} = \frac{1}{2} E\left[r^2\right] = \frac{r_s^2}{2} + \sigma^2$ represents the average power of the received signal.

$$E[r] = \sigma \sqrt{\frac{\pi}{2}} \, e^{-\left[\frac{1}{2}\left(\frac{P_{Avg}}{\sigma^2}-1\right)\right]} \left[\frac{P_{Avg}}{\sigma^2} I_0\left[\frac{1}{2}\left(\frac{P_{Avg}}{\sigma^2}-1\right)\right] + \left(\frac{P_{Avg}}{\sigma^2}-1\right) I_1\left[\frac{1}{2}\left(\frac{P_{Avg}}{\sigma^2}-1\right)\right] \right] \tag{6.2}$$

The estimation of the Rice parameters can be done using the Nelder-Mead method implemented via FMINS[1] in the MatLab software tool. This function returns a vector X that is a local minimum of F(X) near the starting vector X_0. This method is a numerical commonly used nonlinear optimization algorithm for minimising an objective function in a many-dimensional space when the objective function varies smoothly.

For the results presented in this section, two short path intervals were selected from the previously described path (path #1) to illustrate the diversity performance in two distinct situations: low small-scale fading depth (44.6 – 55.4 m) and high small-scale fading depth (117.4 – 124.6 m). The paths had to be sufficiently small to ensure that the signal average is approximately constant.

Figure 6.8 shows the CDF of the received power levels. The symbols represent the experimental data and the continuous line the theoretical fitting using the Rice distribution, being the parameters of each curve represented in Table 6.1. It can be verified that the

1 The function *FMINSEARCH could also be used.*

diversity gain is much greater in the second than in the first interval, although the correlation coefficients of the two received signals are relatively low and similar (0.50 and –0.68 respectively). Considering the 10% probability reference level, the diversity gain is about 3.5 dB and 9 dB respectively. In the first case the diversity gain is modest because the small-scale fading depth is very small and therefore the diversity gain is close to the non-fading situation, i.e. approximately 3 dB.

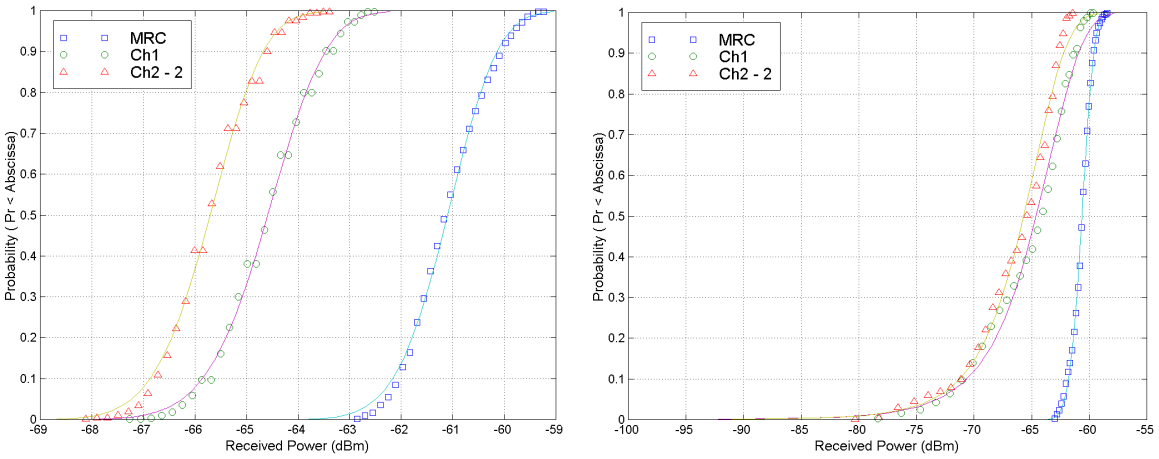

Figure 6.8: Received power CDF in two intervals along the path: 44.6-53.4 m (left) and 117.4-124.6 m (right). The curve corresponding to Ch.2 is shifted –2 dB

Regarding the fitting of the data of both paths and the MRC signal, to the Rice distribution parameters, a very good match was obtained between the theoretical Rice distribution and the corresponding measured data, leading to an almost complete overlap of the curves. For Ch.1 (similar to Ch.2) the Rice factor is 16.4 dB and 3.5 dB for the first and second intervals while the Rice factors corresponding to the MRC is 17.8 dB and 17.2 dB (see Table 6.1). The K-factor is much lower for the second interval both for Ch.1 and Ch. 2, showing the existence of more multipath components. The variance also shows a larger figure for the second interval confirming the deeper fades. After MRC the two paths show a similar behaviour enhancing the gain when using diversity.

Path Interval (m)	Ch 1			Ch 2			MRC		
	P_{Avg} (dBm)	K (dB)	σ	P_{Avg} (dBm)	K (dB)	σ	P_{Avg} (dBm)	K (dB)	σ
44.6 – 55.4	-64.54	16.4	2.0E-6	-63.53	17.1	2.0E-6	-61.04	17.8	2.5E-6
117.4 – 124.6	-64.56	3.5	7.9E-6	-63.65	4.3	8.2E-6	-60.60	17.2	2.9E-6

Table 6.1: Parameters of the Ricean curves

AFD and LCR were also calculated for these short path intervals, and Figure 6.9 and Figure 6.10 depict these parameters plotted as a function of the received power level.

Analysing the graphs shown in Figure 6.9 it can be concluded that typically the AFD ranges from 2 ms to 100 ms for both paths and the three signals, being more spread on the second path for Ch. 1 and Ch. 2 due to the larger small-scale fading depth, although both MRC signals have the same excursion reinforcing the fact that there is a strong diversity gain.

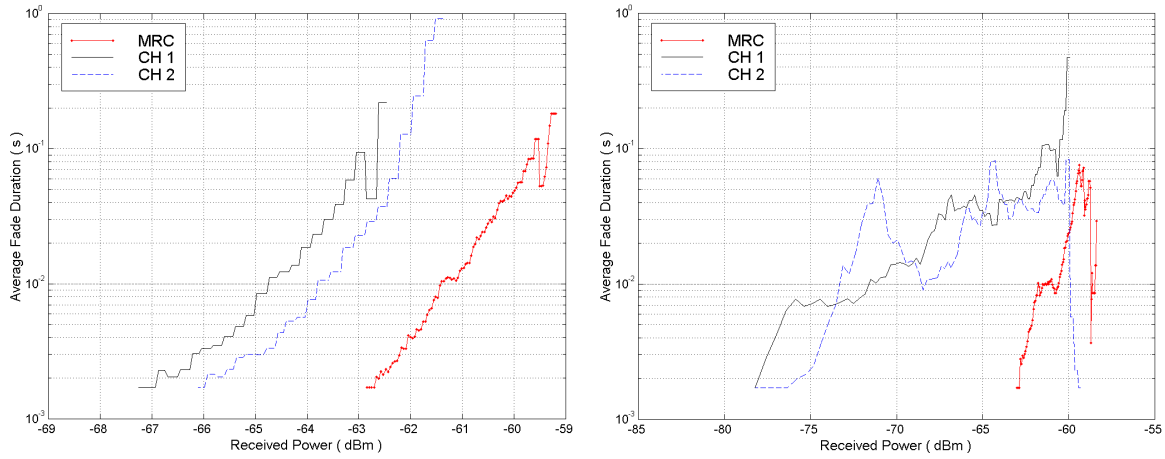

Figure 6.9: AFD as a function of the received power (threshold) for the intervals: 44.6-53.4 m (left) and 117.4-124.6 m (right)

The small-scale fading for the first interval can be again confirmed observing Figure 6.10 since it shows a maximum value for the LCR of about 50 crossings per second for Ch. 1 and Ch. 2 when compared to the second path where the maximum value is about 15 crossings per second. However, the LCR is approximately the same in both analysed intervals, for what concerns the MRC signal, reaching a maximum figure of approximately 45 crossings per second.

Figure 6.11 represents a zoom of the received power levels for the two short path intervals 44.6-53.4 m (left) and 117.4-124.6 m (right), where a high correlation between Ch.1 and Ch.2 and a quite low fading depth can be observed (left) and lower correlation with significantly higher fading depth for 117.4-124.6 m interval (right).

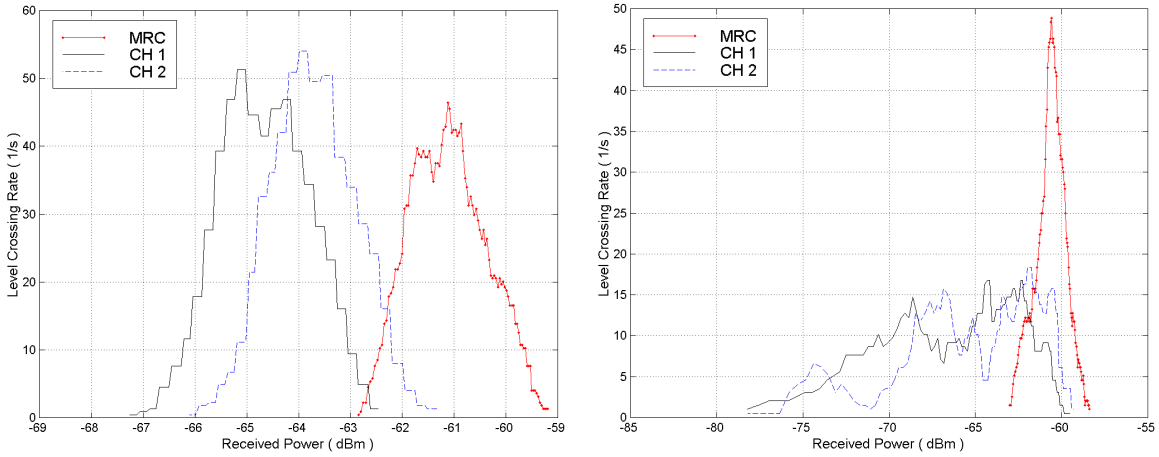

Figure 6.10: LCR as a function of the received power (threshold) for the intervals: 44.6-53.4 m (left) and 117.4-124.6 m (right)

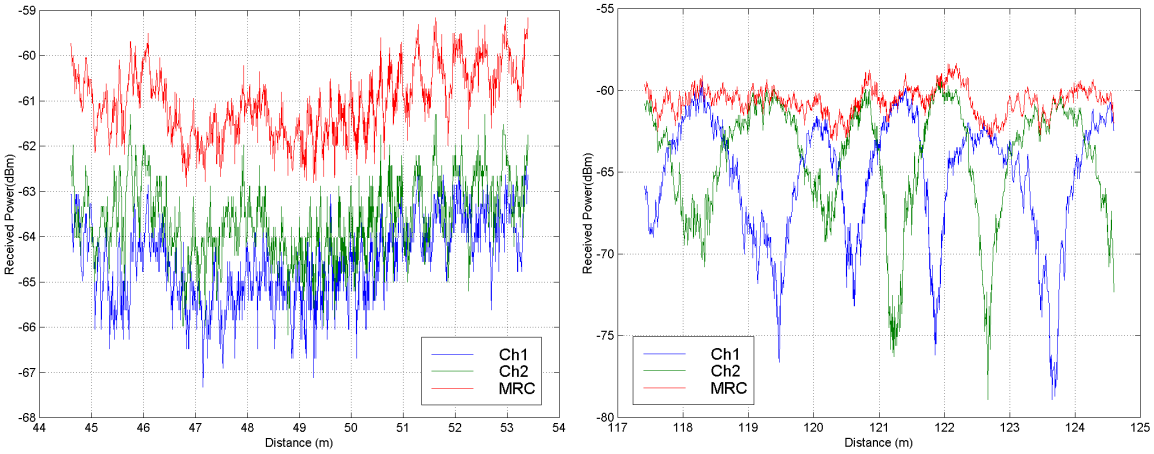

Figure 6.11: Received power levels in the intervals 44.6-53.4 m (left) and 117.4-124.6 m (right)

2.4 Effect of the BS antenna tilting

The impact of the BS shaped lens antenna downwards tilting was assessed based on measurements collected along the central path. It was considered a height of 7 m for the BS antenna, a MT speed of approximately 10 km/h and tilting angles from 2 and 6 degrees. Figure 6.12 shows the BS antenna on the mast (left) and MT antenna on the van (right).

Figure 6.13 shows that when the BS antenna tilting angle increases, the power level decreases faster with the distance and the BER increases correspondingly due to the SNR reduction. For a BS antenna tilting of 0º, the MT starts at 32 m away from the BS, which corresponds to a LoS component incidence angle of 82º in the vertical plane. The radiation

pattern of the BS antenna exhibits a gradual gain increase (see chapter 5) from 82º to 86.5º and as the MT is at 2.5 m height and the BS at 7 m, the 86.5º corresponds to a distance of 74 m between the BS and the MT. This explains why the average received power level without BS antenna tilting increases up to 74 m. For higher distances, the power decreases slowly due to the shaped radiation pattern of the BS antenna. For a distance of 300 m, which corresponds to an angle of 89º, the attenuation due to the radiation pattern is only about 3 dB relatively to the maximum value.

For a BS antenna tilting angle of 6º, the MT started the path at 23 m from the BS, which corresponds to a direct ray angle of 79º with the vertical. Once the BS antenna is tilted 6º, the corresponding antenna gain must be read in the radiation pattern for an 85º angle. The maximum antenna gain corresponds, in this case, to a distance of 27 m (86.5º). This is confirmed by the experimental curve shown in Figure 6.13. Moreover, from 88º to 93º the antenna radiation pattern has an abrupt decrease (about 18 dB). Again, this can be confirmed by the experimental curve, were an abrupt decrease on the average power level from 32 m (88º) to 86 m (93º) can be observed. From 86 m to 300 m (95º) the curve has a softer decrease because the gain is constant. The analysis of the LCR and AFD values for some short paths intervals with identical average power levels did not show any significant variations with the BS antenna tilting.

Figure 6.12: BS antenna on the mast (left) and MT antenna on the van (right)

2.5 Effect of the MT antenna tilting

Several measurements were performed also for different MT antenna tilting angles, in the range of -20 to +20 degrees, keeping the BS antenna aligned horizontally in order to evaluate the user movement freedom in the vertical plane. These measurements were also performed with a BS antenna height of 7 m and the same speed for the MT. In this study, positive tilting angles mean that the MT antenna is tilted downwards relatively to the horizontal plane looking to the front direction of the van (see Figure 6.12 right), and negative angles mean an upward rotation.

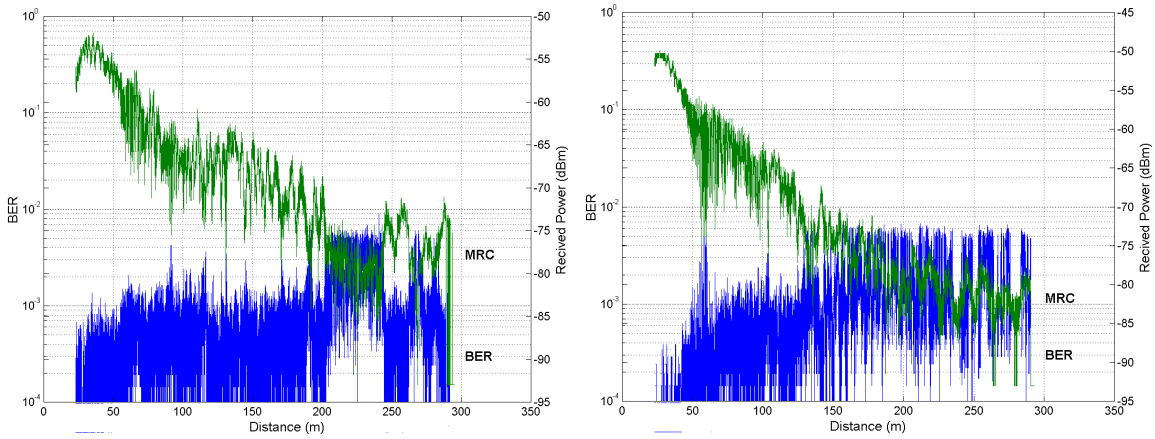

Figure 6.13: MRC received power and BER as a function of distance: BS tilted 2º (left) and BS tilted 6º (right)

Comparing the results obtained without any tilting with the ones obtained with –20º (Figure 6.14), the average power level is slightly higher. This fact can be explained by the characteristics of the radiation pattern of the MT antenna (see chapter 5), showing a higher gain for 70º (90º-20º) than for 90º. For the +20º tilting angle, the results show that the average power level decreases along the entire path.

Since the MT starting points are 32 m for 0º and 23 m for –20º and +20º and the final distance about 300 m, the direct ray path changes from 82º to 89º; from 59º to 69º and from 89º to 109º, respectively for 0º, –20º and +20º tilting angles. Analysing these angles range, it can be conclude that the first and the second range are identical with a maximal attenuation of about 2 dB, although the first decreases while the second increases. The range that corresponds to the +20º tilting angle decreases more abruptly with a maximal

attenuation of about 8 dB at the end of the path. This justifies the relative behaviour of the experimental curves shown in Figure 6.14 being that for the +20º tilting case the small-scale fading depth is smaller. This is because when the antenna is tilted in the positive direction the ray reflected on the ground is more attenuated.

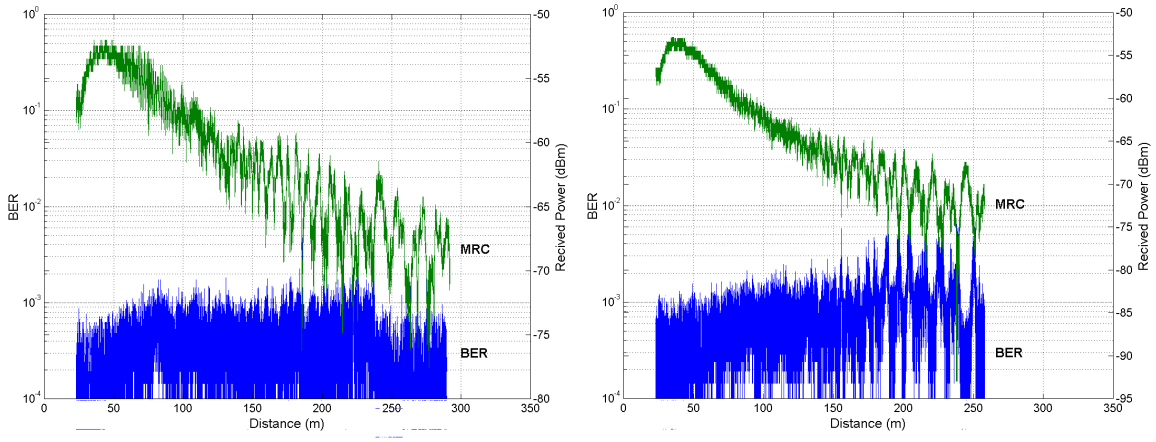

Figure 6.14: MRC power and BER versus distance: MT tilted –20º (left) and MT tilted +20º (right)

Considering the LCR and AFD parameters a comparison was made for some identical short path intervals. Comparing the results obtained for the 0º and –20º cases, no significant variations could be detected. On the other hand, comparing the results of these curves with the ones of the +20º curve, it was observed that in general the LCR is higher, the AFD is lower and the amplitude range is quite small. These results are consistent with the lower fading depth observed for the +20º case. These results are due to the strong attenuation of the ground reflected ray and hence a signal behaviour dominated by the other multipath components leading to faster variations and lower amplitude range.

The results presented in this section allow to conclude that no significant impact was detected on the MT mobility freedom for the studied MT rotation angles. Comparing the experimental and simulated results (see Figure 6.15), they match quite well although the slightly slower decrease of the received power values regarding the simulation results.

Figure 6.16 compares and shows the impact of the rotations in the MT and BS. The BS antenna is much more sensitive to the rotations than the MT antenna, as expected and desirable. The power decay rate obtained via simulation is lower than via measurements but the relative behaviour is similar.

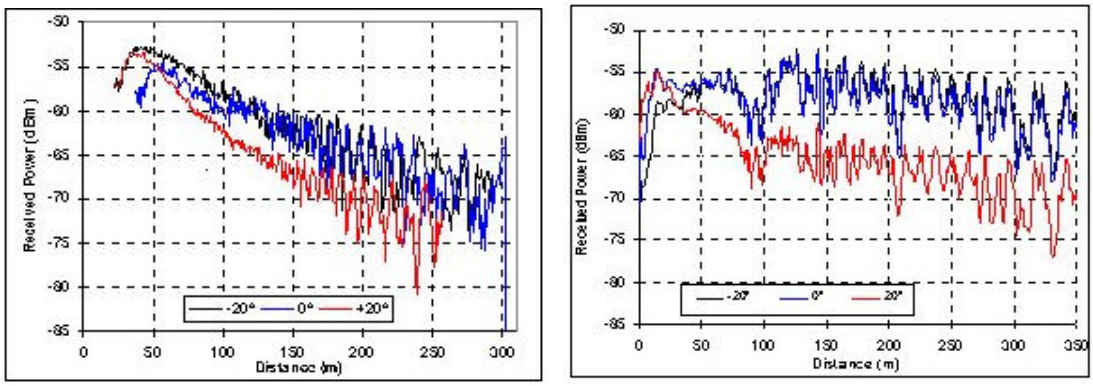

Figure 6.15: Comparison of the MRC received power versus distance for a BS antenna height of 7 m and -20º, 0º and 20º tilting on the MT: measured results (left) and simulation results (right)

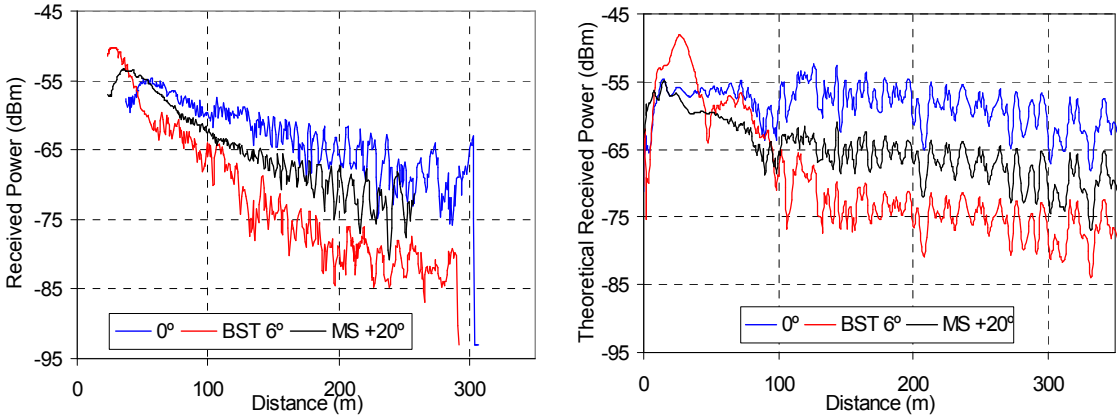

Figure 6.16: Comparison of MRC received power versus distance for a BS antenna height 7 m and no tilting, 6º tilting on the BS and 20º tilting on MT: measured results (left) and simulation results (right) averaged over 100 frames

2.6 Effect of the MT speed

In order to evaluate the effects of the MT motion on the radio channel, two different speeds were considered for the MT being 16 km/h and 42 km/h, approximately. The results show that for these speeds, there are no significant differences relatively to the average power level and BER. This indicates that the equaliser used in the Trial Platform can still cope with this type of channel. Relatively to the AFD and LCR, Figure 6.17 and Figure 6.18 show these results for the short path interval 95 – 115 m. It can be realised that for a given power threshold, the AFD decreases and the LCR increases when the speed increases, as expected since the MT is now moving faster, which results in a lower time interval between signal dips.

Figure 6.19 shows the received power level and the BER versus distance for a speed of 60 km/h. The main noticed difference is the faster signal variations, especially between 100 and 300 m. These faster signal variations are due to the Doppler shift and lead to the increase of the LCR and the decrease of the AFD for the same power levels considered at lower speed. The BER shows an increase (the number of very low values has diminished) however the equaliser can still cope with the faster signal variations, which allows concluding that the system is robust when used at speeds up to 60 km/h (maximum speed the system was tested, however the specification was 50 km/h).

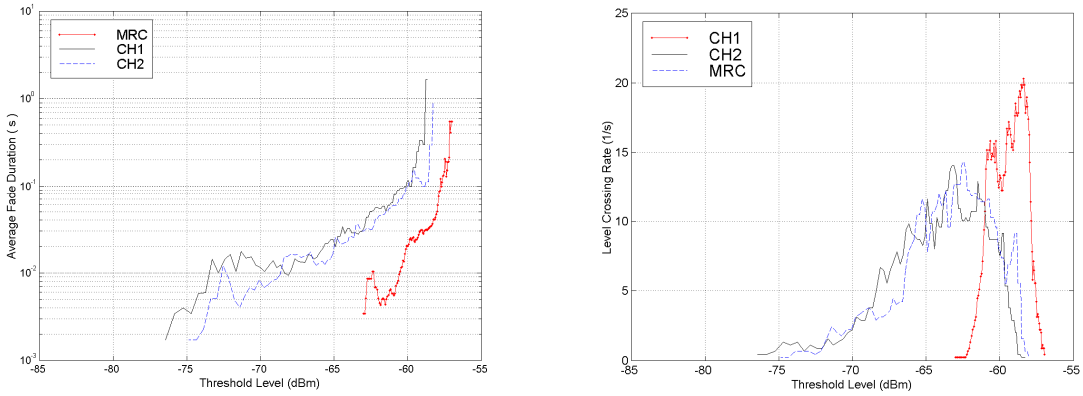

Figure 6.17: AFD (left) and LCR (right) as a function of received power along the path interval: 95 – 115 m for MT speed of 16 km/h.

2.7 Parallel street path

This path is parallel to the main street where the BS is installed and is partially obstructed by trees (see chapter 5). Observing Figure 6.20 it can be seen that the average power level is slightly lower when compared with the main central path displayed on Figure 6.2. The trees that exist between the BS and MT attenuate the LoS causing a decrease on the average power level. Therefore, the BER is slightly higher. Although the system was designed to operate on LoS, there is still sufficient margin for operation with the attenuation of trees.

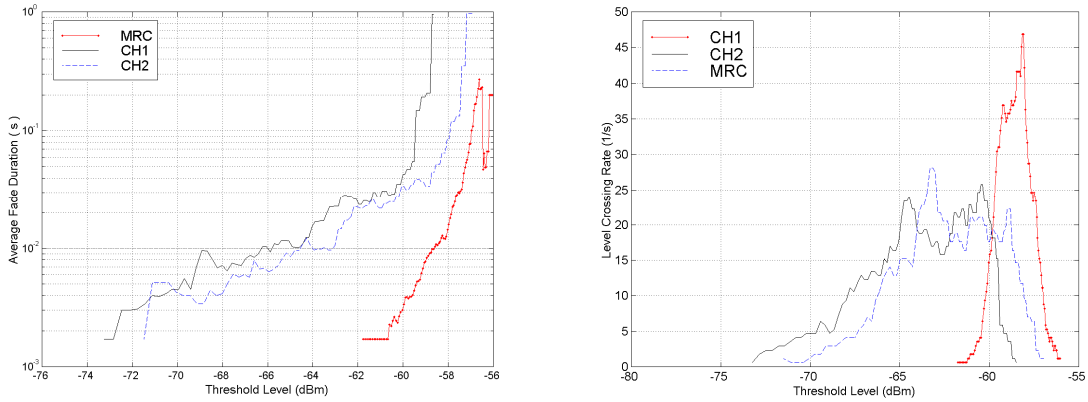

Figure 6.18: AFD (left) and LCR (right) as a function of received power along the path interval: 95 – 115 m for MT speed of 42 km/h.

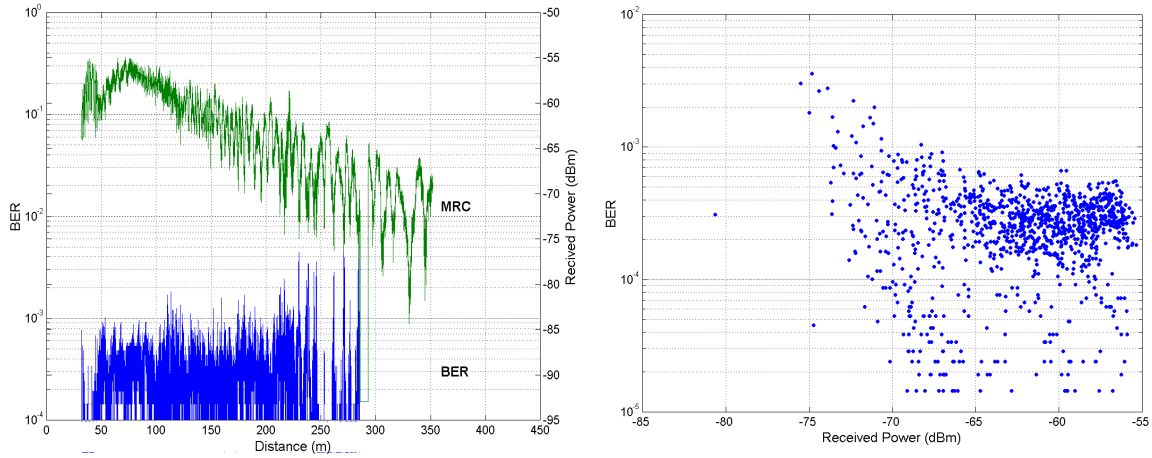

Figure 6.19: MRC received power and BER as a function of distance (for 60 km/h)

AFD and LCR parameters were also analysed for this configuration. However, the results indicate that they remain approximately constant along the entire path displayed in Figure 6.20. This happens because the signal shows an almost uniform behaviour around the average along the path in opposite to the central path where a clear increase of the fades was observed. The absolute value of the correlation coefficient is always below 0.5 along the entire path between the two receiving channels. This was expected because the multipath components are stronger due to the LoS obstruction. Moreover the small-scale fading depth is considerably high and therefore the diversity gain is good.

2.8 Signal penetration in transversal streets

The analysis of the signal penetration is very important in terms of co-channel interference and handover purposes. The measurements were done with a BS antenna height of 7 m and MT speed of approximately 10 km/h. The studied transversal street is located at about 87 m away from the BS on the left side (see chapter 5). In Figure 6.21 the 0 m distance corresponds to the beginning of the transversal path #3 that is about 19 m away from the buildings. Moreover, at the beginning of the path the average power level is –60 dBm, which is in accordance with what was measured for the longitudinal path (crossing point).

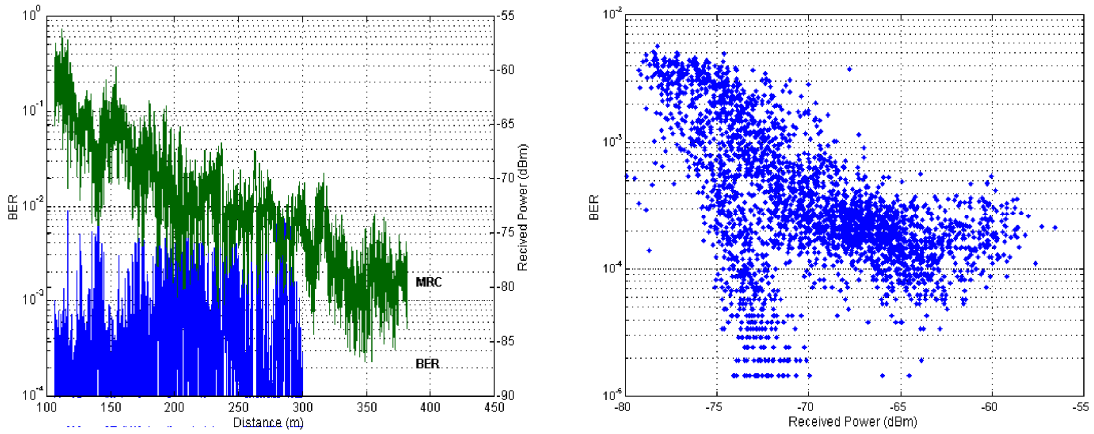

Figure 6.20: MRC received power and BER as a function of the distance

As indicated by Figure 6.21, the received signal maintains the average level during the first 6 m to 7 m since the distance to the BS is kept almost constant. For a better interpretation, the signal was averaged over 10 frames. Beyond this point the signal is strongly attenuated (approximately 15 dB), which is caused by the presence of trees with large foliage. Then, from 15 m to 19 m the signal recovers approximately 8 dB due to the existence of trees with less and smaller foliage. After the 19 m there is as strong decrease on the average power level (approximately 12 dB in the first 5 m), because the system started operating under LoS obstruction due to the buildings, as expected, the BER increases strongly. This example shows a penetration of approximately 5 m after the signal starts being obstructed by the buildings, which gives an idea about how fast should the handover algorithms be and that co-channel interference is probably not difficult to control. Other transversal paths, further away from the BS, have been analysed and similar conclusions reached.

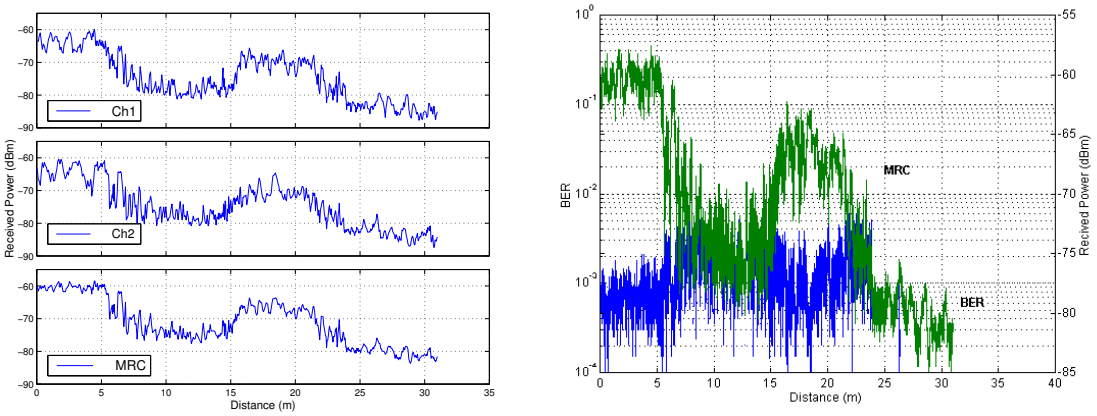

Figure 6.21: Received power averaged over 10 frames (left), MRC and BER versus distance for path #3

3. Path Loss Modelling

Path loss modelling is fundamental to understand how the average power changes as we move away or approach the BS and is a good starting point to predict the coverage of a mobile system since appropriate fading margins can be added to the path loss to cover the impact of other slow or fast signal variations (shadowing and small-scale fading).

Path loss fitting consists in finding the most suitable n for equation (6.3). If logarithms are applied to both sides of the equation, (6.4) is obtained which is easily recognisable as a straight-line equation of the type $y = b - nx$.

$$P_{RX} = P_0 \times d^{-n} \tag{6.3}$$

$$10 \log P_{RX} = 10 \log P_0 - n \times 10 \log d \tag{6.4}$$

A linear regression analysis can therefore be applied to find the b, n and r parameters being b and n defined by (6.5) and (6.6), respectively. The r parameter, defined by (6.7), shows the correlation coefficient of the data with the straight line. The total number of samples is k.

$$b = \frac{\sum Y - n \sum X}{k} \tag{6.5}$$

$$n = \frac{k \sum XY - \sum X \sum Y}{k \sum X^2 - \left(\sum X\right)^2} \tag{6.6}$$

$$r = \frac{k\sum XY - \sum X \sum Y}{\sqrt{\left\{k\sum X^2 - \left(\sum X\right)^2\right\}\left\{k\sum Y^2 - \left(\sum Y\right)^2\right\}}} \tag{6.7}$$

The main objective of the work presented in this section is to calculate the value of n in equation (6.3) that better fits the measured signal. For the free space the value of n is 2, but for mobile radio environments it can be much higher due to the multipath propagation effects, therefore depends on the propagation scenario characteristics. Moreover, when lens type antennas are used the value of n can also be less than 2 due to the specific characteristics of the radiation pattern.

In a first step the measured data were compared with the results given by the two rays model (see chapter 2) and a reasonable match was observed. This confirms that in this specific scenario (canyon street type) and since LoS exists, the two stronger rays arriving to the receiver are the direct and the reflected in the ground. An observed fact was that the power level of the measured signals was always higher and therefore a new model was experimented.

Nearby the BS and beyond the blank zone up to the point where the lens antenna radiation pattern shaping has effect, the received power should be reasonably constant, by principle. Observing the radiation pattern displayed in chapter 5 for the BS, it can be concluded that this happens for an angle up to 86º, where the effect of the lens stop. This clearly indicates that at least two different zones with different slops exist for the path under study. This fact is a direct consequence of the antenna radiation pattern that is not predicted by the two rays model. The antenna shaping should lead to a constant received power up to d_0 but in practice this was not achieved since the slop is not null due to multipath. In fact, to be more precise, a three-slop model should be used since nearby the BS and after the blank zone the power level increases rapidly, however the intention of the performed study was not to characterise this zone of the path.

To show the influence of what was said in the former paragraphs, a first attempt to fit the whole path was made and the result displayed in Figure 6.22, on the left, for a BS antenna tilting angle of 0º and height of 11.2 m. The slop *n* obtained was 2.52. The fitting is generically not so good and therefore a reference distance d_0 from the BS was selected as

breaking point. This approach is illustrated in Figure 6.23 (two slop model). A good estimation for d_0 can be obtained via equation (6.8).

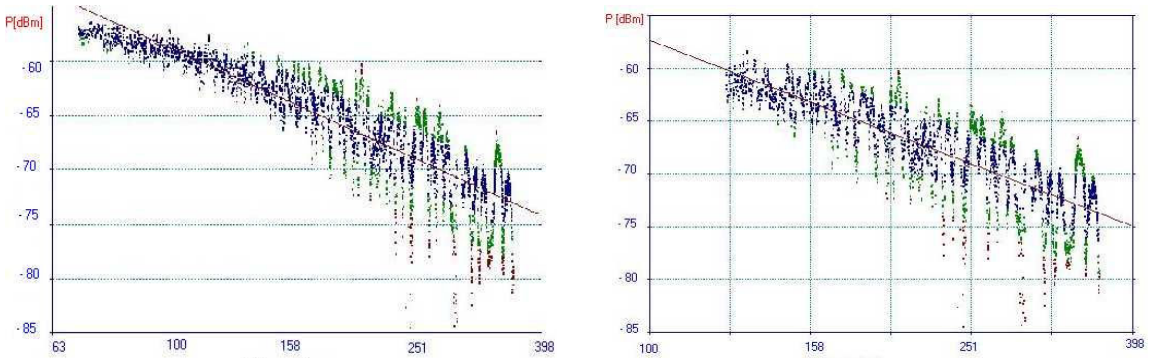

Figure 6.22: MRC received power and path loss fitting versus distance in meters (left) and the same considering d_0=125 m (right)

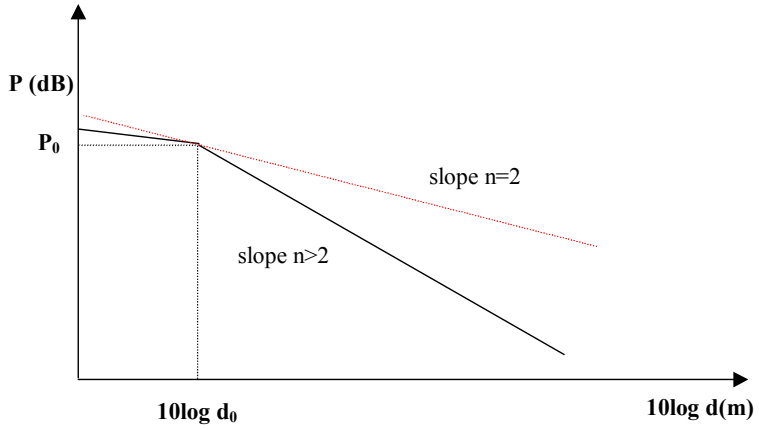

Figure 6.23: Typical path loss variation with distance to the BS in a mobile environment

Analysing the BS antenna radiation patterns, we can conclude that theta[2] in equation (6.8) is 4º (90º-86º). The height of the MT antenna was kept constant and equal to 2.5 m. Resolving (6.8) we obtain a $d_0 \approx 125$ m for h_{BS}=11.2 m and h_{MT}=2.5 m. After d_0 the signal is expected to decrease with a slop *n* higher than 2 due to the multipath propagation caused by the buildings and trees existing in both sides of the street and the effect of the antenna gain reduction.

$$d_0 = (h_{BS} - h_{MS}) \times \frac{1}{\tan(\theta + |tilting|)} \qquad (6.8)$$

2 Theta is the complementary angle where the BS antenna radiation pattern shows its maximum, considering a tilting equal to zero degrees.

In Figure 6.22 on the left, the missing part of the path (before the 65 m) was cut due to the blank zone caused by the antenna radiation pattern. The different colours in the figure represent the separation between the measured data and the straight line of slope 2.52 (2.5 dB per colour change). The MT speed for this specific case was 10 km/h.

A much better fitting could be obtained by using the two-slope model. Figure 6.22 on the right, shows the results after applying the fitting for the new conditions with a slop *n* of 2.89. The correlation coefficient was now much better and the effects of multipath propagation more highlighted, as expected, due to the slop increase from 2.52 to 2.89. Table 6.2 shows the average slop obtained for various paths considering the same system conditions.

BS tilting angle (degrees)	BS and MT antenna heights (m)		Average slope (n)	Cutting point d_0 (m)
0º	11.2	2.5	2.92	125

Table 6.2: Average values of slope n for BS antenna tilting angles equal to 0º

In the next subsections the same study is performed for different system configurations namely, different BS and MT antenna tilting angles. All results displayed in the figures assume a two-slope model for a better fitting, which was confirmed by the better correlation coefficient.

3.1 BS antenna tilting effect on path loss

Studies have been performed with tilting angles of 2º and 6º in the BS but with a different antenna height (from the one used for 0º) due to dangerous wind conditions and for this reason the height was set to 7 m. Figure 6.24 on the left shows the fitting results for a tilting angle of 2º. The slope obtained was n = 2.41 for a d_0 of 43 m. On the right, are presented the fitting results for a tilting angle of 6º in the BS antenna. The slope obtained was n = 2.74 for a d_0 of 25 m.

Observing the previous graphs it can be concluded that the slope increases when the tilting angle of the BS antenna increases, which obviously confirms the fact that the signal power drops faster when the tilting angle increases reducing therefore the size of the cell and the power radiated to the surrounding obstacles.

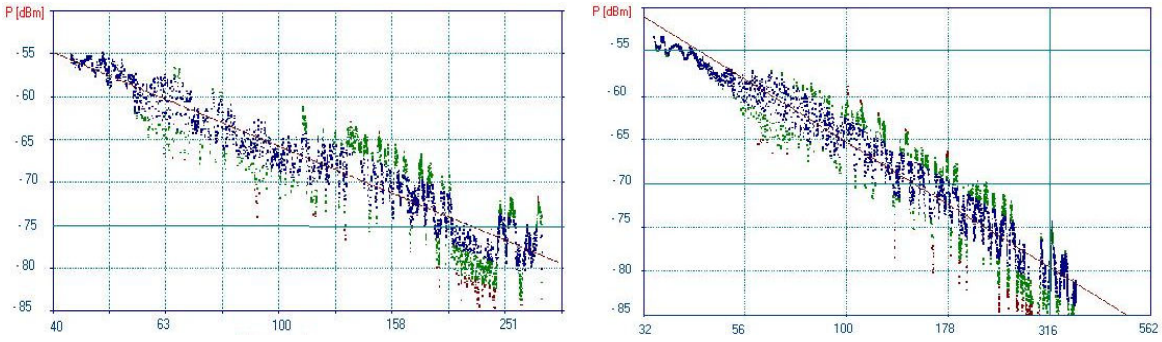

Figure 6.24: MRC received power and path loss fitting for d_0=43 m and tilting angle of 2º (left) and MRC received power and path loss fitting for d_0=25 m and tilting angle of 6º (right) versus distance in meters

The results presented in Table 6.3 are the average of all processed data in the specified conditions for different BS antenna tilting angles.

BS tilting angle (degrees)	BS and MT antenna heights (m)		Average slope (n)	Cutting point d_0 (m)
2º	7	2.5	2.37	43
6º	7	2.5	2.68	25

Table 6.3: Average values of slope n for different BS antenna tilting angles

It is interesting to note that the slop is higher for a BS antenna height of 11.2 meters even with a 0º antenna tilting angle. This fact can be explained due to the existence of a higher number of multipath components since more power is sent towards the street lateral obstacles (trees, buildings, etc.).

3.2 MT antenna tilting effect on path loss

Studies have been performed with tilting angles of +20º and -20º in the MT antenna. The positive direction is towards the front of the MT van (direction of motion). The BS height was set to 7 m, the speed of the MT to 10 km/h and the BS antenna tilting angle of 2º. Figure 6.25 on the left, shows the fitting results for a tilting angle of +20º in the MT antenna. The slope obtained was n = 2.66 for a d_0 of 65 m. On the right, it is shown the fitting results for a tilting angle of -20º in the MT antenna. The slope obtained was n = 2.39 for a d_0 of 65 m, which is almost the same as for the 2º BS antenna tilting case, therefore confirming that a tilting angle of –20º in the MT does not impact significantly on the system behaviour.

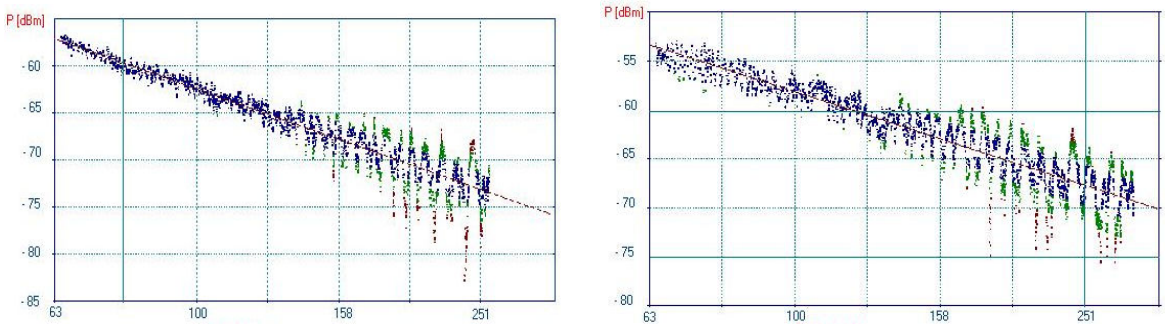

Figure 6.25: MRC received power and path loss fitting for d_0=65 m and MT tilting angle of +20º (left) and d_0=65 m and MT tilting angle of -20º (right) versus distance in meters

Table 6.4 shows average results for the two MT antenna tilting angles. It is obvious that positive tilting angles imply a higher slope due to the specific MT antenna radiation pattern (see chapter 5).

The MT antenna tilting angle does not affect the cutting point d_0 having however an impact on the received power level for large positive tilting angles.

MT tilting angle (degrees)	BS and MT antenna heights (m)		Average slope (n)	Cutting point d_0 (m)
-20º	7	2.5	2.39	65
20º	7	2.5	2.66	65

Table 6.4: Average values of slope n for different MT antenna tilting angles

Observing Figure 6.15 it can be verified that the fading depth for the tilting angle of +20º e lower. This fact can be explained based on the radiation pattern of the antennas that collects less energy from the reflected ray on the ground (lower gain). It is also interesting to note that tilting 20º the MT antenna was equivalent, in terms of slop, to tilt the BS antenna 6º.

4. Other Outdoor Scenarios

In this thesis and due to the fact that only one outdoor scenario was characterised via an extensive measurements campaign, experimental results are only presented for this scenario. A ray tracing simulation tool was used to make a preliminary evaluation of other outdoor scenarios where the system is also expected to operate.

Given the good matching between the measured and simulated results for the canyon type street, this fact gives a good confidence on the simulator and therefore we assumed

that the ray tracing simulator has been validated and is now applicable for other scenarios. Previous validations in relatively small rooms and only indoor environments were already reported in [15].

Based on the previous assumptions, simulation results are presented for more two typical outdoor scenarios, namely: a square and a roundabout. All the considered scenarios are from the Aveiro city. The analysis was based on the NRP and SDW parameters.

4.1 Urban square

This square is located in the Aveiro city historical centre being therefore a touristic area per excellence. It is surrounded by small buildings with a maximum height of three floors. As shown in Figure 6.26, several objects exists in the square made of different materials, namely wood, glass, marble and ceramics in the roofs. The pavement is made of calcareous as well as the pavement of several small streets that leave the square. Since this is a pedestrian zone many people concentrate in the square mainly during the summer evenings.

Due to the relative dimensions of the square and the Wide Cell antenna coverage area, large time dispersions were observed. To reduce this problem and still guaranteeing a sufficient coverage of the surrounding streets, the power that is reflected on the buildings walls, opposite to the BS, had to be reduced. One way of doing so is by rotating the BS antenna and keeping the height at sufficient levels to guarantee the required coverage area.

In order to determine the best configuration for the BS, simulations were performed with the antenna at 8 m height and using different rotation angles for the antenna. In general, the obtained NRP simulation results for all rotation angles are quite uniform and the penetration of the signal in the surrounding streets is good enough to guarantee the necessary overlap between neighbouring cells. The time dispersion is however in some cases too high to be handled by the system equaliser (assuming the current characteristics of the Trial Platform) but in general is lower than 40 ns. Figure 6.27 shows the simulation results for the NRP and SDW considering the BS at (5, 33, 8) m and rotated 6° down in the elevation plane and 45° in the azimuth. This configuration guarantees good coverage and time dispersion being the best of all configurations simulated. As can be observed, the most

critical situations in terms of time dispersion occurs in locations opposite to the BS and near the iron/marble objects.

4.2 Urban roundabout

The selected roundabout is located in Aveiro city centre, being one of the areas with more traffic in the city. The floor is made of granite as well as all the streets that converge to the roundabout. In its middle there is a garden. In the surrounding area there exists buildings from one two five floors. Due to the dimensions of the scenario and the height of the buildings care should be taken in order to minimise the signals time dispersion. Moreover, the need to guarantee enough signal penetration in the streets that converge to the roundabout, advice for a careful selection of the BS location, height and rotation angle of the antenna.

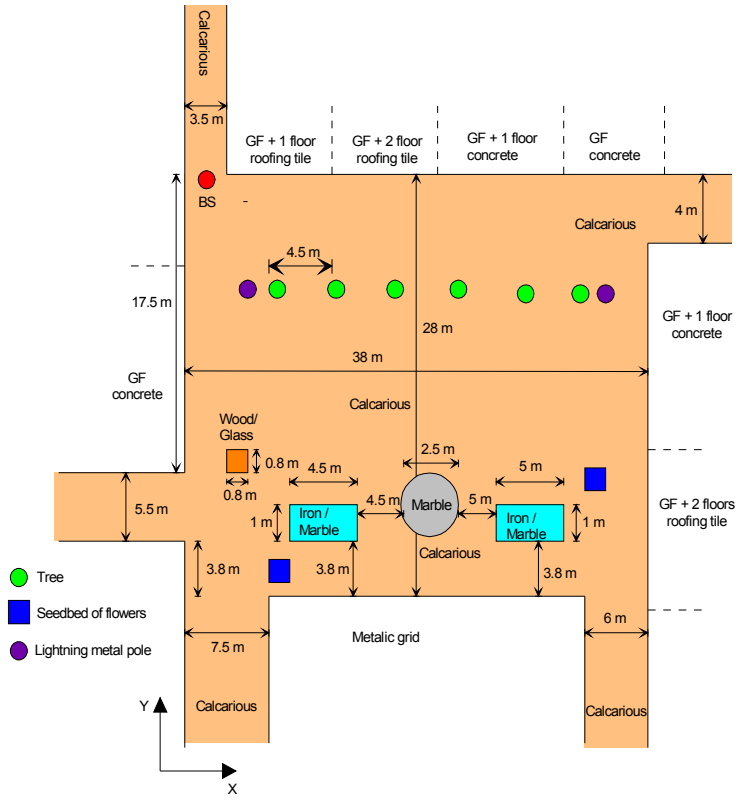

Figure 6.26: Square in Aveiro city

The selected location for the BS is shown in Figure 6.28. This location guarantees enough penetration of the signal in surrounding streets as can be seen in Figure 6.29. The NRP distribution is quite uniform in the entire scenario and the time dispersion is also kept

bellow the system limits in the cell coverage area. Observing the bottom part of Figure 6.29, there are indeed areas were the time dispersion is much higher than the equaliser can handle, reaching sometimes 700 ns (in the figure the values are truncated to 250 ns). This area can however be served by the cell that would cover the street. A reduction of the BS height would lead to a reduction on the time dispersion reducing however the penetration of the signal in the streets.

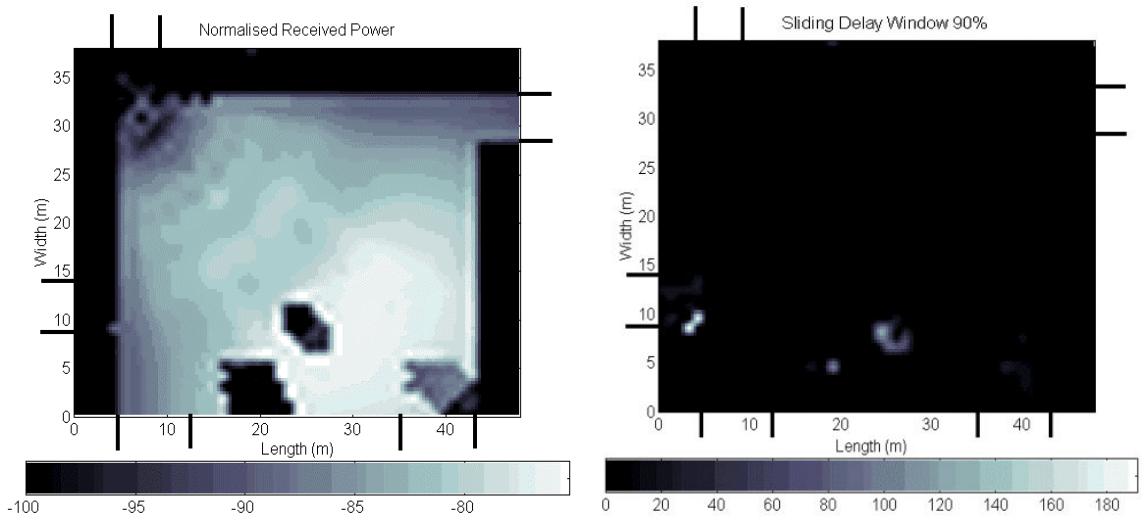

Figure 6.27: Simulation results with the BS located at (5, 33, 8) m and rotated 6°down in the elevation plane and 45° in the azimuth: NRP (left) and SDW90% (right)

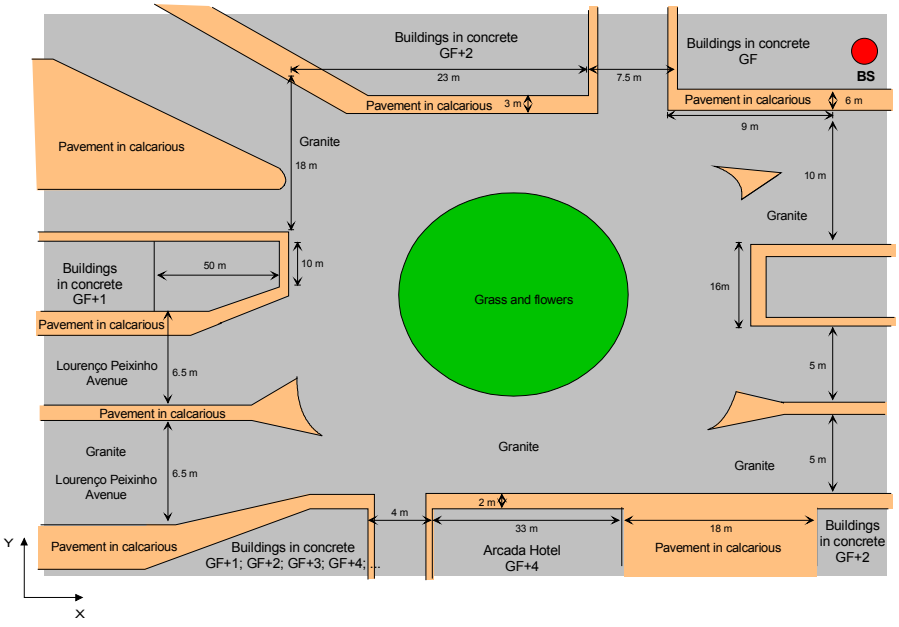

Figure 6.28: Roundabout in Aveiro city

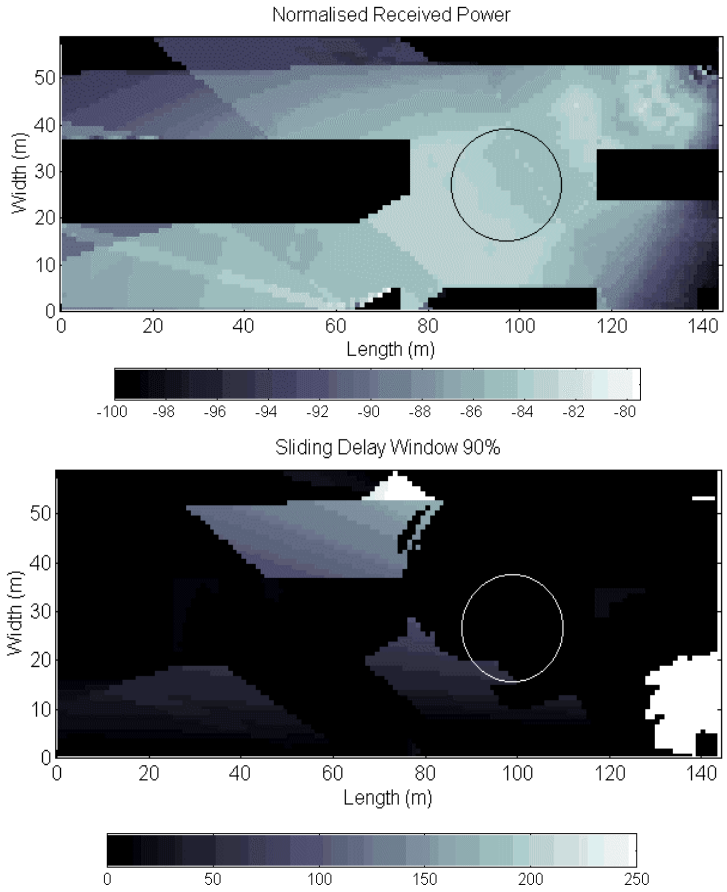

Figure 6.29: Simulation results with the BS located at (143, 54, 8) m and rotated -148º in the azimuth plane: NRP (top) and SDW 90% (bottom)

In [12] [13] other antenna configurations were studied, including the utilisation of multiple BSs for better coverage of the same area (using the same or a different frequency carriers) to assess the impact of macro-diversity.

5. Summary and Conclusions

This chapter presented cell coverage and transmission performance aspects plus path loss modelling for one outdoor scenario located in a residential area in Aveiro comprising a main street, a street parallel to the main street and a perpendicular street. The objective of the experiments was to evaluate the cell coverage characteristics provided with the lens type antennas and the transmission performance on the air interface in terms of experienced BER, including the impact of different system configurations and MT speeds, in order to validate the technical options made for the Trial Platform in terms of equalisation, FEC and diversity reception techniques. The MT was driven along several paths while data was

acquired by the C&M system. Particularly relevant for the results presented in this chapter were the RSSI for the two receiving channels, BitErrors and the MT distance to the BS. Based on these parameters others were calculated, namely: MRC signal, received power, BER CDFs, Rice distribution parameters, AFD, LCR and path loss slop. Several conditions were changed during the field trials, namely: BS antenna height, BS antenna tilting angle, MT antenna tilting angle and the MT speed. Simulations were also performed based on the ray-tracing technique for other scenarios namely a roundabout and a city square. Parameters such as the NRP and SDW 90% were evaluated. The first parameter includes the gain of transmitting and receiving antennas, and it was of major importance for the link budget evaluation and definition of the cell boundaries. The SDW containing 90% of the channel impulse response energy is used as a measure of the channel time dispersion.

For what concerns the main street, the average received power level variation range on the first 150 m from the BS, is rather low due to the impact of the shaped radiation pattern of the BS lens antenna. Moreover, as expected and demonstrated in chapter 5, the small-scale fading depth increases as the distance to the BS increases. There is however a visible improvement with the diversity reception contributing to the reduction of the fading depths.

The BER increases with the distance to the BS and the depth of the small-scale fading. In 90% of the cases it is below $4E10^{-4}$ which is under the maximum specified target $5E10^{-3}$ for the FEC codec showing the good performance of the equalizer. The typical maximum detected number of bit errors per byte was three. ARQ mechanisms have also proved to be required since the BER exceeds the specified limit for the FEC to be able to cope with.

Since the system was operated in LoS conditions, the measured data was fitted to the Rice model using the MatLab software tool. For that purpose, two small path intervals with average power level approximately constant were selected one with a higher small-scale fading depth than the other (different distances to the BS). In both situations a good match to the Rician curves was obtained showing that the model was adequate. The path interval closer to the BS had shown a much stronger Rician factor which indicates a much higher contribution of the LoS component to the signal power. The AFD was calculated for the same paths, ranging from 2 ms to 100 ms typically. On the other hand, the LCR is much higher for the path closer to the BS for what concerns the two receiving channels, reaching

50 crossings per second. The MRC signal presents a much more similar behaviour reaching a maximum of 45 crossings per second showing the impact of the diversity reception in reducing the small-scale fading depth.

Simulation results have shown a good agreement with the measurements which indicates that the used scenario models were good enough to predict the power levels. By changing the BS antenna height (from 11.2 m to 7 m) the cell width and length also changes. The small-scale fading depth is lower for the 7 m height case since the multipath components are less due to the fact that the power is more confined and reaches a fewer number of objects. The time dispersion was observed to be higher as the distance to the BS increases, but still under the limit handled by the equaliser (250 ns).

BS tilting angles (zero to six degrees in the vertical plane) effects were analysed and confirmed in terms of impact since an increase in the tilting angle reduced the cell size. No significant impact was noticed in the ADF and LCR parameters. This confirms the importance of this technique to reduce the co-channel interference and the possible elimination of strong reflections contributing to the excess delay. MT antenna tilting was performed in the range of -20 to +20 degrees (in the vertical plane), given the expected high mobility freedom for a mobile device. Positive tilting angles have a more pronounced effect given the specific characteristics of the MT antenna radiation pattern and the respective stronger impact on the direct ray, leading to an average power level decrease along the entire path. For negative tilting angles the effects were generically negligible or even an increase in the power level was experienced. For what concerns the AFD and LCR, and for positive tilting angles, it was observed that in general the LCR is higher and the AFD is lower. This confirms the lower contribution of the LoS component. Simulation results have corroborated the measurement results for what concerns the impact of the tilting angles in the received power levels.

In order to evaluate the impact of the MT motion in the radio channel, various different speeds were analysed. In terms of average power level no significant differences were noticed. The BER figures did not suffer a significant change showing that the equaliser can still cope with the channel variations. Relatively to the AFD and LCR parameters the first

decreased and the last increased. The mobile broadband system prototype proved to be able to operate at velocities up to 60 km/h, although the specification was 50 km/h.

The signal propagation in other streets in the same scenario was also analysed. Particularly in the perpendicular street since it is especially important for handover. In the last case, the signal experiences a strong attenuation when the LoS obstruction by the buildings occurred. A signal penetration of 5 meters in the shadow was measured. This figure gives an indication of how fast the handover procedure should be. The BER figures also presented a strong increase when penetrating in the shadow.

Based on the data gathered during the measurements, path loss modelling was performed. Linear regression analysis was used to find the slop of the best fit straight line. In a first step a comparison with the two rays propagation model was performed and a reasonable match was obtained. This confirmed the fact that the stronger rays are the direct and ground reflected rays. However, and due to the effects caused by the constant power flux provided by the BS lens antennas, a two slop model was adopted with better results. The break-point was defined as the distance from the BS where the constant power flux principle could not apply anymore. This break-point has nothing to do with the break-point of the two rays model and a formula for its calculation was derived. An average figure of 2.92 was found for the slop which is less than the experienced figures in mobile radio systems macrocell currently in operation. From the two rays model, and given the fact that the distances from the BS are clearly below the break-point, as demonstrated in chapter 2, a slop closer to two would be expected. This shows that the two rays model is too simple and more rays should be considered. The slop has also shown to be lower for lower BS heights due to the less reflected rays generated in the less visible obstacles. In terms of MT antennas tilting angles, only positive angles have resulted in an increase of the slop.

Measurements could not be done in all planned scenarios for various reasons. A simulation tool was used to evaluate other two scenarios where mobile broadband systems are expected to operate: an urban square and an urban roundabout. In the square and due to its dimensions and surrounding buildings time dispersion was more difficult to control when guaranteeing enough coverage in the surrounding streets. A final optimised configuration was reached being the height of the BS antenna 8 m, the tilting angle of 6 degrees and the

azimuth angle of 45 degrees. With this configuration the time dispersion was kept within the equaliser limits being higher near the marble and iron objects, opposite to the BS. The same process was followed for the roundabout scenario case. The best configuration was reached for a BS height of 8 m and an azimuth angle of -148 degrees. This configuration could not eliminate completely the zones with time dispersion higher than 250 ns but could reduce it to a smaller area that could be served by a neighbouring cell.

6. References

[1] M. Dinis and V. Lagarto, "Definition of the Trial Platform Infrastructure and Applications", CEC Deliverable Number – A204/PT/CET/DS/P/005/b1, September 1997. Submitted to EC in the framework of the ACTS/SAMBA project

[2] Manuel Dinis and José Fernandes, "Provision of Sufficient Transmission Capacity for Broadband Mobile Multimedia: a Step Towards 4G", IEEE Communications Magazine, pp. 46-54, August 2001

[3] Susana Mota, Adão Silva, Manuel Dinis and José Fernandes, "Radio Transmission and Experimental Channel Characterisation Using an MBS Platform Operating in the 40 GHz Band", Wireless Personal Communications Journal, Issue 21:3, June 2002.

[4] M. Dinis and P. Jesus, "Evaluation Report of the Trials", CEC Deliverable Number – A0204/PTIN/SRM/DS/P/015/b1, October 2000. Submitted to EC in the framework of the ACTS/SAMBA project

[5] M. Dinis, J. Fernandes, "Effect of the System Layout and Transversal 40 GHz Signal Penetration in Perpendicular Streets Experimental Results Using an MBS Platform", IST Mobile Communications Summit 2000, Galway, Ireland, Oct. 2000

[6] M. Dinis, V. Lagarto, M. Prögler, J.T. Zubrzycki, "SAMBA: a Step to Bring MBS to the People", ACTS Mobile Communication Summit '97, Aalborg, Denmark, October 1997

[7] José Fernandes, Manuel Dinis, Max Prögler, Wolfgang Herzig, John Zubrzyck, "The SAMBA Trial Platform: Initial Results", ACTS Mobile Communication Summit '98, 8th – 11th June, Rhodes, Greece, 1998

[8] Manuel Dinis, José Fernades, Max Prögler, Wolfgang Herzig, "The SAMBA Trial Platform in the Field", ACTS Mobile Communications Summit '99, 8th – 11th of June 1999, Sorrento, Italy

[9] T. Fujino, et al, "Design of Baseband Signal Processing Unit in SAMBA Trial Platform for Mobile Broadband Applications", ACTS Mobile Communications Summit '98, Rhodes, Greece, June 98.

[10] E. David, "Report on Baseband Processing Unit", CEC Deliverable Number – A0204/ITEN/TCL/DS/P/011/b1, November 1998. Submitted to EC in the framework of the ACTS/SAMBA project

[11] N. Fukui, A. Shibuya and K. Murakami, "Performance of Combined ARQ with SR and GBN for Wireless Systems on a 40 GHz Band Radio Channel", IEEE Communication Magazine, pp. 122-126, September 2001

[12] José Emanuel Ramos Pereira Garcia, "Cobertura Celular para Sistemas de Banda Larga", MSc Thesis, University of Aveiro, 2002

[13] J. Fernandes and J. Garcia, "Multiple Coverage for MBS Environments", PIMRC'2000, London, UK, September 2000

[14] J. Fernandes, C. Fernandes, "Impact of Shaped Lens Antennas on MBS Systems", PIMRC 98 – 9th International Symposium on Personal, Indoor and Mobile Radio Communications, Boston, USA, Sept. 98

[15] José Fernandes, "Modelação do Canal de Propagação Rádio Móvel de Banda Larga na Faixa das Ondas Milimétricas e seu Impacto no Desempenho de Transmissão do Sistema", PhD Thesis, University of Aveiro, 1996.

7th Chapter

Cell Coverage, Radio Transmission and Handover Analysis for an Indoor Scenario

1. Introduction

This chapter deals with cell coverage validation and analysis of the transmission performance plus radio handover evaluation for the indoor scenario described in chapter 5 – a sports pavilion – based on the same type of parameters already used for the outdoor scenario. Moreover, radio handover was also tested and evaluated. These are key issues for mobile radio system and to the author's knowledge they have never been performed before for this frequency band and for these specific conditions and system characteristics.

For the experiments presented in this chapter, the BSs with the wide cell antenna were installed in different configurations and the MT was installed in a trolley, as shown in Figure 7.1, and driven along several paths while data was acquired by the C&M system

already described in chapter 5 [1] [2]. The first measurements were performed with the BS in a corner of the pavilion to cover the whole area with a single cell pointing along the pavilion's diagonal (configuration A). The second configuration was used to evaluate the coverage with multiple cells and the handover algorithm. For that purpose two BSs were placed one each side of the pavilion (in the smaller side of the rectangle) each covering approximately half of it (configuration B). A third configuration (configuration C) was used to perform the CIR measurements with the BS installed in one of the sides of the pavilion, having the antenna pointing exactly to the centre of the field. The CIR experiment results will be described in the next chapter. Moreover, simulations were performed based on the ray-tracing technique for configurations A, B, C and D, the last corresponding to two BSs placed in the two corners opposite to the benches (seats of concrete). Parameters such as the NRP and SDW90% were evaluated.

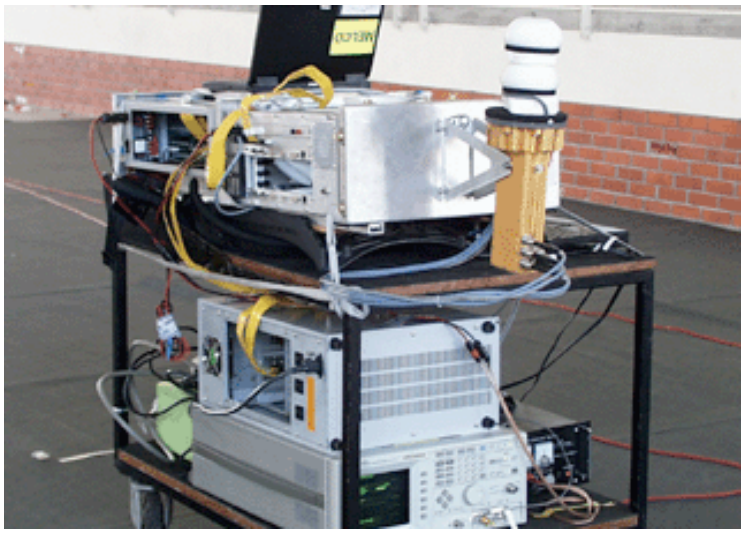

Figure 7.1: MT trolley for the indoor field trials

From the large amount of data collected during the experiments (paths separated by 1 m were selected), a choice of representative paths, for each system configuration, was made. Figure 7.2 on the left shows the selected paths for configuration A. The first C_A path is exactly in the centre of the pavilion field and the lateral paths (L_A and R_A) approximately 10 m from the centre. Path T_A is situated at approximately 41 m from the BS. On the right are shown the selected paths for configuration B. Path C_B is central to the sports field and the lateral paths (path R_B and L_B) are separated by 4 m from path C_B.

This chapter starts with the presentation of the results concerning the wide cell coverage and transmission evaluation in configuration A for the four selected paths. Section 3 presents the results relative to configuration B. The section starts with a description of the coverage and transmission characteristics of each cell and then the handover measurements for the three paths. The section ends with an analysis of the handover algorithm performance, transmission and coverage with two BSs. To conclude the chapter, section 4 presents simulation results for system configurations not yet submitted to experimental evaluation.

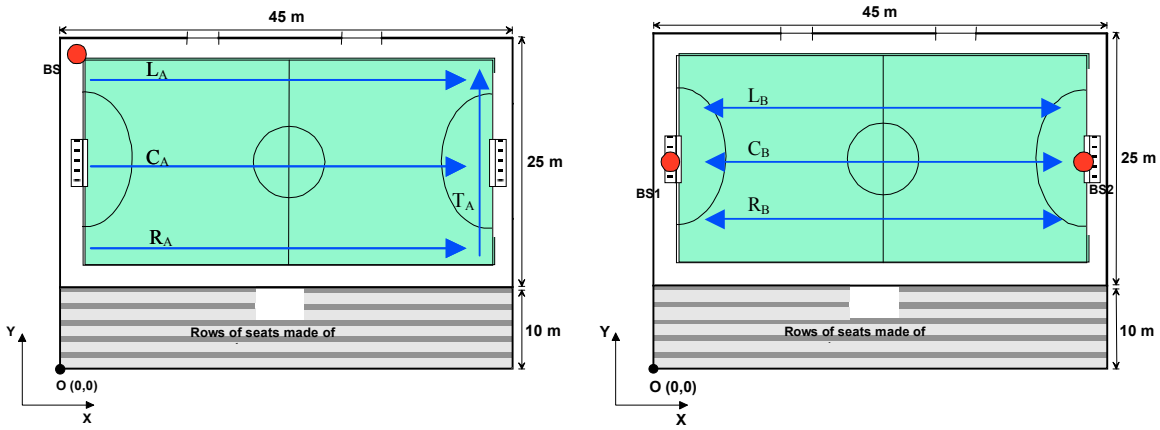

Figure 7.2: Paths analysed in this chapter: configuration A (left); configuration B (right)

2. Sports Pavilion – Configuration A

The BS was installed in the corner with coordinates (X=1.9;Y=33.3) m (see Figure 7.2 on the left). The height of the BS antenna was 6.5 m and the transmitted frequency 39,74 GHz (uplink direction only) with a transmitting power of 21.2 dBm. The BS was rotated –40º in the azimuth plane in order to radiate towards the pavilion's diagonal. The MT average speed was 3.6 km/h and the antenna height 1.5 m.

In the following subsections only the paths shown in Figure 7.2, on the left, will be considered namely, R_A (Right), C_A (Central) and L_A (Left). A transversal path is also presented (path T_A) [3] [4] [5] [6] [7]. The A subscript indicates the system configuration.

2.1 Coverage and transmission analysis of path R_A

Analysing Figure 7.3 on the left, we can verify that the average power level is high for this path. However, in the initial and final parts of the path the average power level is slightly lower than in the central zone, which is the zone where the BS antenna has a higher gain. The small-scale fading depth is also more pronounced in the end of the path than in the beginning due to the higher distance to the BS and the existence of important multipath components. Beyond 15 m the average signal power level is almost constant being a clear effect of the BS antenna shaped radiation pattern. Again diversity was successfully used to mitigate the small-scale fading depth as can be seen by observing the MRC signal in Figure 7.3. The small-scale fading has a direct impact on the BER showing however higher values in the beginning of the path. This fact can be explained due to the lower average received power level.

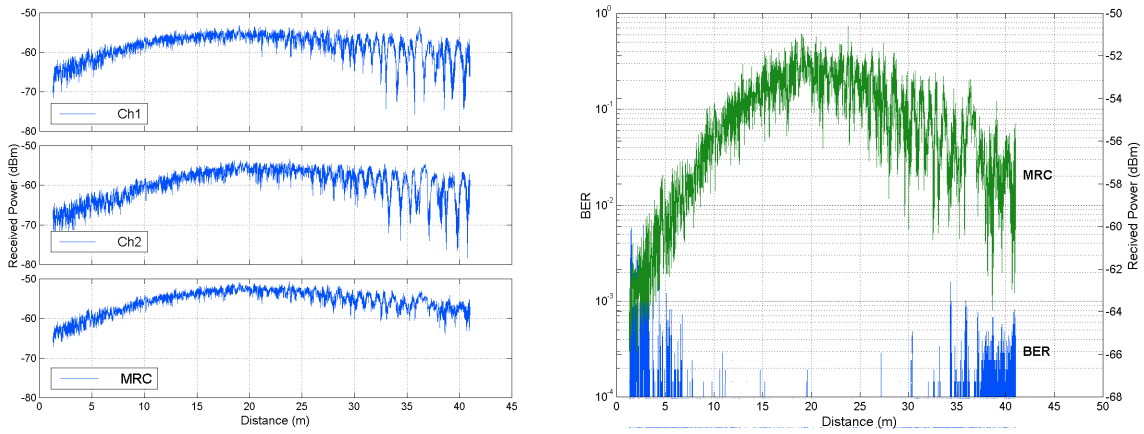

Figure 7.3: Received power sampled per frame (left) and MRC and BER (right) versus distance: path R_A

Figure 7.4 shows on the left the bit over byte errors versus distance and on the right, the BER versus MRC received power level. Maximum two bit errors occur per byte error and the errors happen all along the path being however in much higher density in the extremities of the path. The BER figures confirm that the behaviour of the equaliser is as expected since only in very few situations the BER exceeds $5E10^{-3}$. In these cases, an ARQ scheme must be used [8]. The minimum received MRC power level is approximately –67 dBm.

In terms of statistical results, the CDFs of the received power and the BER, allow to conclude that for 90% of the cases the received power after MRC combining is higher than –62 dBm and the BER lower than 1.5E10^{-4} (see Figure 7.5).

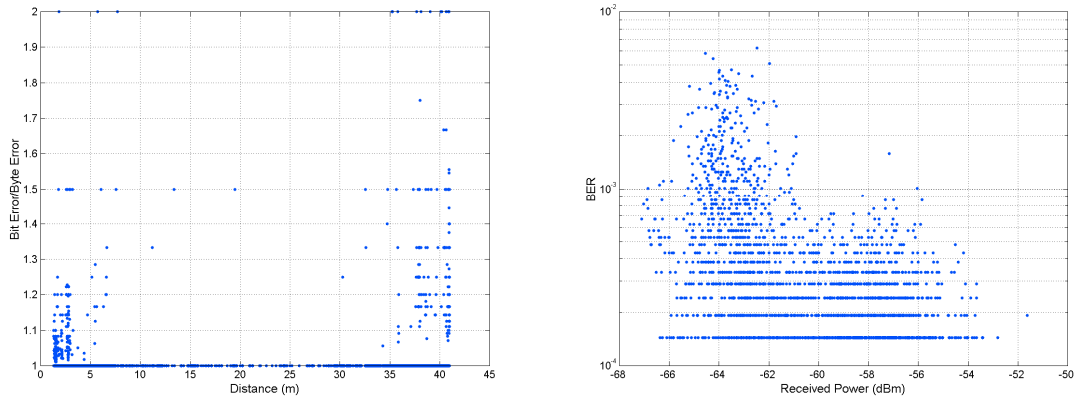

Figure 7.4: Bit over byte errors versus distance (left) and BER versus MRC received power level (right)

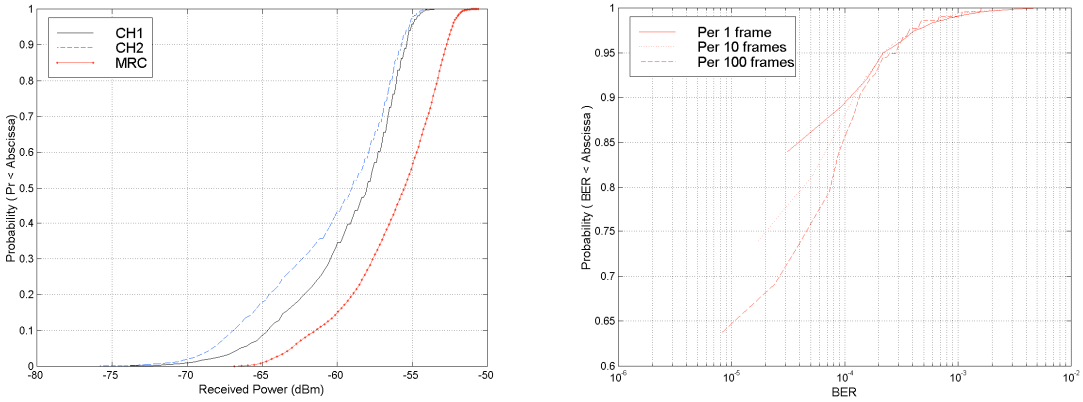

Figure 7.5: Received power CDF of both channels and after MRC (left) and BER CDFs (right)

Making a global analysis of the results presented in this section it is possible to verify that the behaviour of the system in an indoor environment is quite similar to the one observed on the outdoor scenario. However, the average power level is higher (smaller distances and more multipath components) and the fading depth is lower leading to lower diversity gains. Both factors combined result in lower BER levels.

Two short path intervals were selected from the previously described path to illustrate the diversity performance in two distinct situations: low small-scale fading depth (4.5 – 6.1 m) and high small-scale fading depth (37.7 – 40.5 m). The paths had to be sufficiently small to

ensure that the signal average is approximately constant as explained in the previous chapter.

Figure 7.6, shows the cumulative distribution functions (CDF) of the received power levels. The symbols represent the experimental data and the continuous line the theoretical fitting using the Rice distribution, being the parameters of each curve represented in Table 7.1. It can be verified that the diversity gain is greater in the second than in the first interval being for a 10% probability reference level about 7.5 dB. In the first case the diversity gain is modest because the small-scale fading depth is very small and therefore the diversity gain is close to the non-fading situation, i.e. approximately 3 dB.

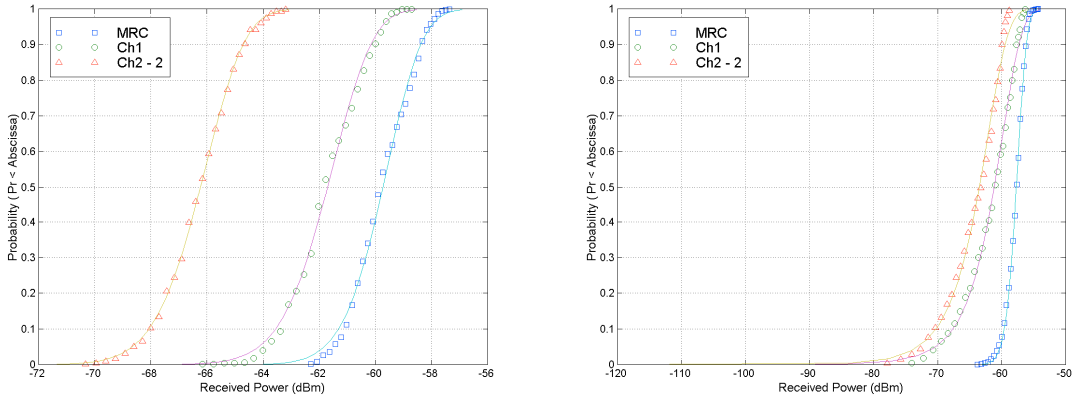

Figure 7.6: Received power CDF in two intervals along the path (measured and theoretical): 4.5 – 6.1 m (left) and 37.7 – 40.5 m (right)

Path interval (m)	Ch 1			Ch 2			MRC		
	P_{Avg} (dBm)	K (dB)	σ	P_{Avg} (dBm)	K (dB)	σ	P_{Avg} (dBm)	K (dB)	σ
4.5 – 6.1	-61.61	13.3	3.9E-6	-64.14	13.4	2.9E-6	-59.66	14.6	4.3E-6
37.7 – 40.5	-61.04	2.8	1.3E-5	-61.37	2.1	1.3E-5	-57.69	13.2	6.3E-6

Table 7.1: Parameters of the Ricean curves for paths 4.5 – 6.1 m and 37.7 – 40.5 m

Regarding the fitting of the data of both paths and the MRC signal, to the Rice distribution parameters, a very good match was obtained between the theoretical Rice distribution and the corresponding measured data, leading to an almost complete overlap of the curves. For Ch.1 (similar to Ch.2) the Rice factors are 13.3 dB and 2.8 dB for the first and second intervals while the Rice factors corresponding to the MRC signal are 14.6 dB and 13.2 dB (see Table 7.1). The K-factor is much lower for the second interval both for Ch.1 and Ch. 2, showing the existence of more multipath components. The variance also shows a larger

figure for the second interval confirming the deeper fades. The two paths MRC signals show a similar behaviour demonstrating the diversity gain.

Figure 7.7 and Figure 7.8 show the AFD and the LCR calculated for the same short path intervals (Ch.1, Ch.2 and MRC). Analysing the graphs shown in Figure 7.7 it can be concluded that the AFD of the MRC signal ranges from 2 to 400 ms, being more spread on the second path for Ch. 1 and Ch. 2 due to the larger small-scale fading depth, although both MRC signals have the same excursion reinforcing the fact that there is a strong diversity gain.

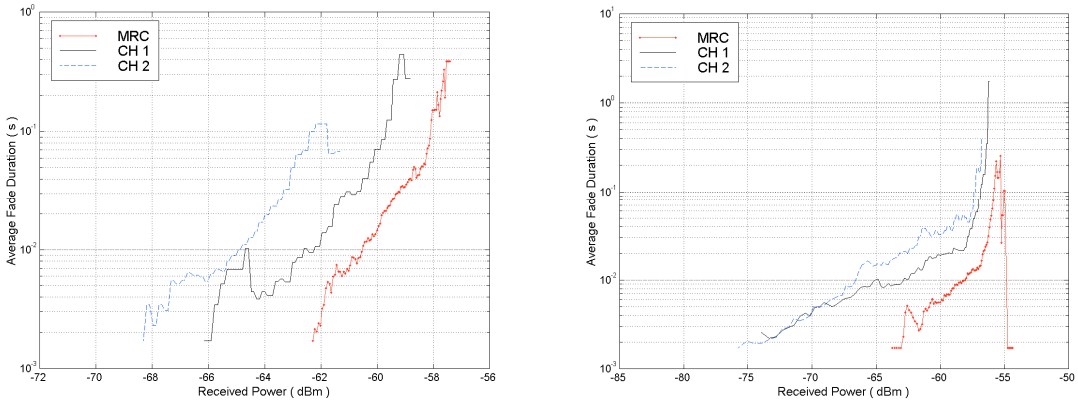

Figure 7.7: AFD as a function of the received power (threshold) for the intervals: 4.5 – 6.1 m (left) and 37.7 – 40.5 m (right)

The small-scale fading for the first interval can be again confirmed observing Figure 7.8 since it shows a maximum value for the LCR of about 35 crossings per second for Ch. 1 and Ch. 2 when compared to the second path where the maximum value is about 27 crossings per second. However, the LCR of the MRC signal is much higher for the second interval reaching a maximum figure of approximately 50 crossings per second.

2.2 Coverage and transmission analysis of path C_A

The results presented in this subsection for path C_A confirm the good system performance in this indoor environment as observed for the outdoor environment. The similar analysis was performed for this particular path however not fully presented here, due to the similarity of some results.

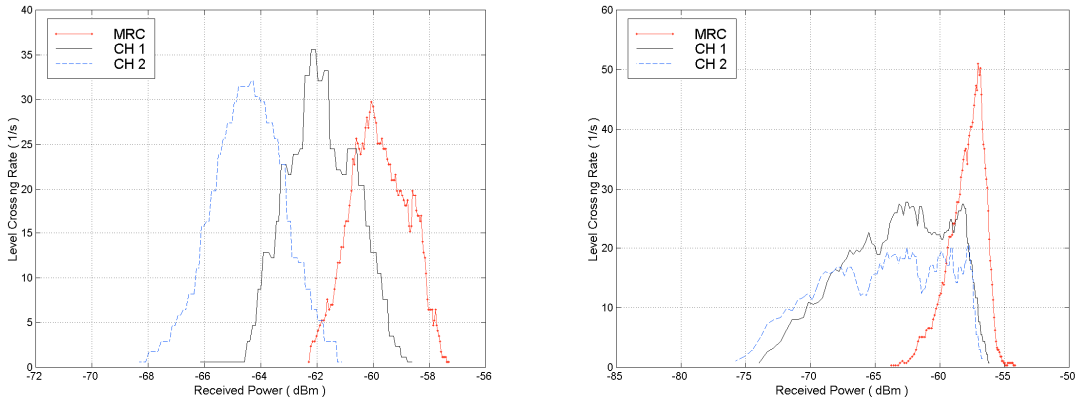

Figure 7.8: LCR as a function of the received power (threshold) for the path intervals: 4.5 – 6.1 m (left) and 37.7 – 40.5 m (right)

The major difference regarding the results presented in the previous sub-section (2.1) is that the average received power level is higher leading to lower BER values, as shown in Figure 7.9. This is due to the fact that, for all positions in this path, the distance to the BS is smaller than for path R_A. Moreover, path R_A is located at the edge of the cell (see Figure 7.2) and, due to the horizontal plane radiation pattern of the BS antenna the power levels are lower. For positions near the end of path C_A there is a fast reduction of the received power levels and hence, at the edge of the path there is a significant increase of the BER. Concerning the statistical behaviour of the fading, no significant differences were observed relatively to the results obtained for path R_A.

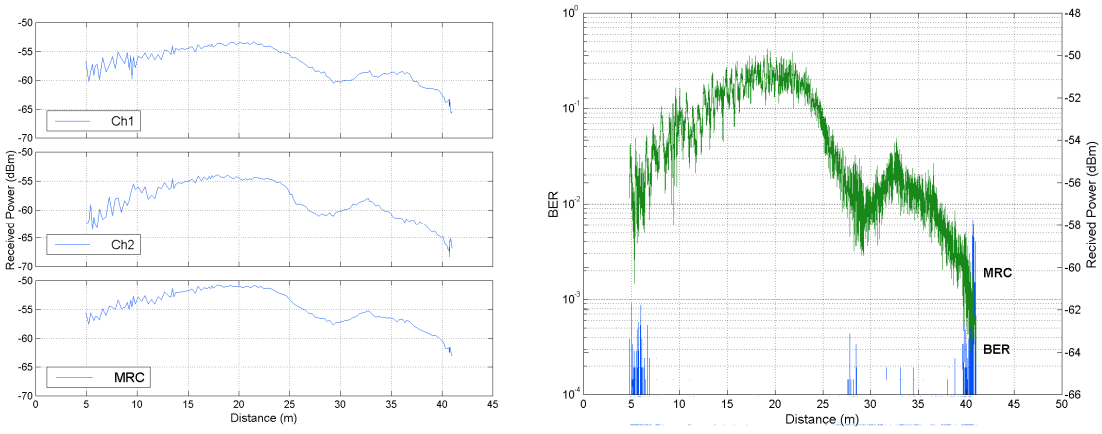

Figure 7.9: Received power averaged over 100 frames (left) and MRC received power and BER (right) versus distance: path C_A

Figure 7.10 shows the BER versus the received power. The BER figures confirm the good performance behaviour of the equaliser in indoor environments. The minimum received MRC power level is approximately –63.5 dBm.

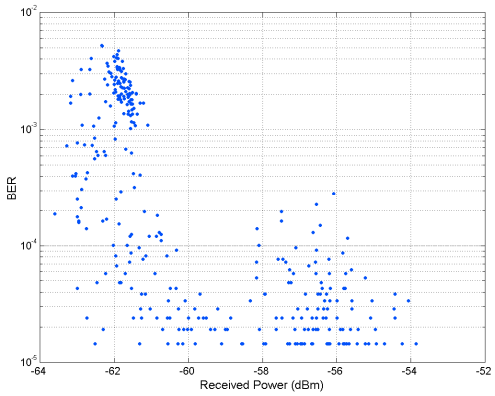

Figure 7.10: BER versus the MRC received power

2.3 Coverage and transmission analysis of path L_A

Comparing the results obtained for this path with those ones presented in sub-section 2.1 (path R_A), one may conclude that they are quite similar, due to the fact that both paths are located at the edges of the cell. This fact leads to lower received power levels and higher BER relatively to the ones obtained for path C_A. Although the similarity between the results obtained for this path and the ones obtained for path R_A, the average received power level at the beginning of path L_A is lower (see Figure 7.11) due to the wide cell BS antenna blank zone. Also from Figure 7.11, it is possible to observe that as soon as the MT leaves the wide cell's blank zone, there is a sharp increase of the received power levels and a reduction of the BER. Except for the blank zone, the results are quite similar to the ones presented for path R_A that is also true for the fading statistics.

Figure 7.12 shows the BER versus the received power. The BER figures confirm the behaviour of the equaliser. The minimum received MRC power level is approximately –69.5 dBm. Path L_A shows the lowest power levels due to the blank zone.

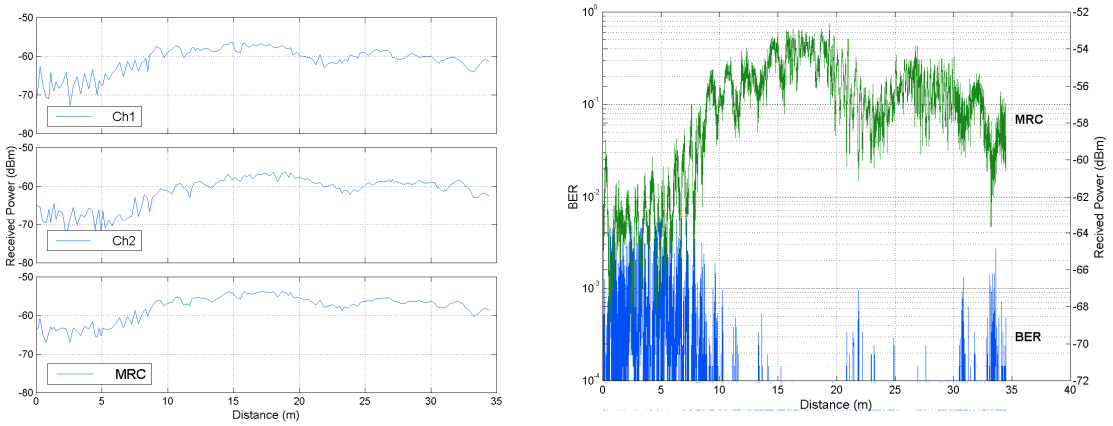

Figure 7.11: Received power averaged over 100 frames (left) and MRC received power and BER (right) versus distance: path L_A

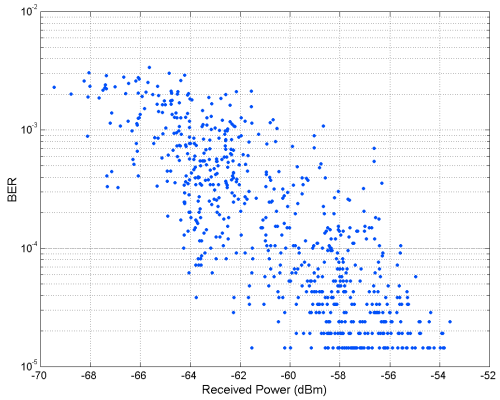

Figure 7.12: BER versus the MRC received power

2.4 Coverage and transmission analysis of path T_A

Figure 7.13 shows the results for the selected transversal path. The average power level is in general high and almost constant since the distance to the BS does not change much. The small-scale fading depth is high for the whole path becoming more pronounced when the MT reaches the path end, approaching the border of the cell. The behaviour in this path could already be anticipated in Figure 7.3 for a distance of 40 m since this transversal path is perpendicular to the longitudinal ones. Diversity was successfully used to mitigate the small-scale fading depth as can be seen by observing the MRC signal. The BER, in Figure 7.13 on the right, shows high values for the whole path due to the bad conditions of the signal, specially the higher channel time dispersion. As can be observed the BER values

follow the power level fluctuations. This path crosses one of the worst areas in terms of power levels, fading and signal time dispersion in the pavilion.

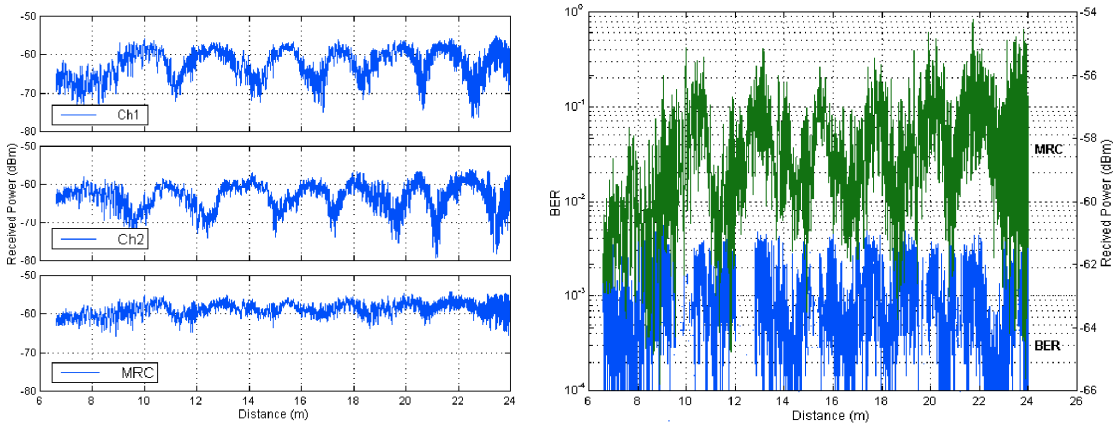

Figure 7.13: Transversal path received power (left) and BER (right) as a function of distance: path T_A

2.5 Simulation results and models validation for the indoor scenario

In order to validate the results simulations were performed for configuration A. Figure 7.14 shows the results for both receiving channels and MRC for one of the measured paths. It can be conclude that a good similarity exists between the measurements and the ray tracing simulation results leading to the conclusion that the indoor scenario model is suitable to predict the power level. This confirms the results already presented in [9] for smaller scenarios at 60 GHz.

A key issue concerning simulation is the accurate modelling of the simulation scenario. The pavilion shape, dimensions and the materials electromagnetic properties have to be taken into account. In this specific case, the pavilion's floor is synthetic, the walls are made of concrete and from the floor up to 2 m bricks cover the wall (see chapter 5). The pavilion has large windows 1 m and 2 m height, the ceiling is supported by a complex metallic structure and in one of the laterals benches exist for the public to watch the events. All these details have been taken into consideration for the simulation model, however, a still simplified model[1] had to be used to lower the computing processing requirements, and therefore not all object details have been included.

1 The simulation model is described in chapter 8.

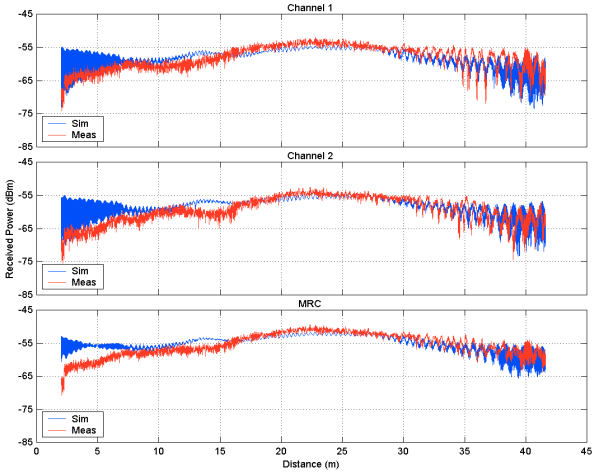

Figure 7.14: Simulation and measured results for BS located at (1, 34, 6.5) m and rotated 9° in the elevation plane and -40° in the azimuth plane for one of the transversal path along the pavilion

The same pavilion simulation model was used to evaluate the NRP and the SDW90% distribution along the whole pavilion for configuration A. The size of the pavilion, although quite large for buildings of this kind, is relatively small for the designed wide cell antenna coverage area, resulting in an excessive power sent towards the walls and consequently to an increase of the received signal time dispersion. Therefore, tilting angles in the elevation plane had to be used. After trying several configurations for the system and the respective assessment of the NRP and SDW90% distribution achieved with the wide cell antenna, it could be concluded that it was possible to find a configuration that would guarantee enough uniformity in terms of power distribution but the time dispersion would not be within the equaliser limit, especially near the benches. To reduce the time dispersion a tilting angle of 9º was used. As illustrated in Figure 7.15, the power level peak is almost centred in the pavilion decreasing as we move away from the centre. Near the wall there are zones where the deep fades exist, mainly nearby the blank zone where the BS is located. The benches are not very well covered mainly the ones situated at a higher altitude. In terms of time dispersion, the highest figures are situated in the benches area increasing as we move away from the pavilions' diagonal. Opposite to the BS there is an area, starting at d= 32 m, where a higher time dispersion exists. In general it can be concluded that for lower power levels a higher time dispersion is experienced.

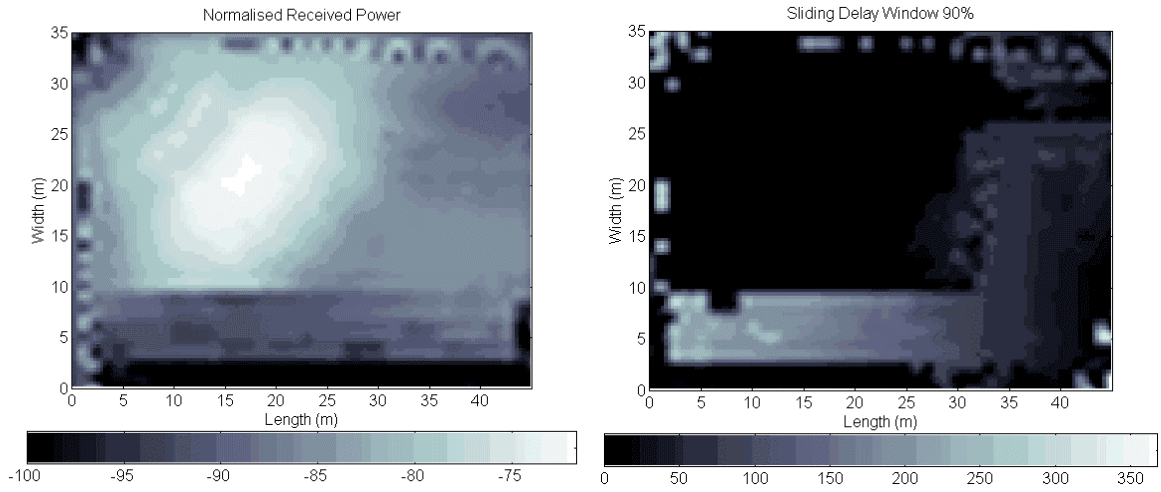

Figure 7.15: Simulation results with the BS located at (1, 34, 6.5) m and rotated 9° in the elevation plane and -40° in the azimuth plane: NRP (dB) (left) and SDW90% (ns) (right)

3. Sports Pavilion – Configuration B

As for configuration A, several paths were selected for the evaluation of the system performance, namely, longitudinal, transversal and diagonal. More than 300 paths were measured in the 39.74 GHz frequency band (uplink direction only). The BS1 and BS2 were installed in the middle of the field with coordinates (X=1.9;Y=23) m and (X=43.1;Y=23) m, respectively (see Figure 7.2 on the right).

The study started with an evaluation of the coverage provided by each cell individually (BS1 and BS2). An initial height of 2.5 m was selected for the BSs to have a clear idea about the coverage (very small cell) and various tilting angles were tested. The final configuration was selected with the BS antenna height of 5.85 m. BS1 antenna had a tilting angle of 10.5º and BS2 12.5º in the elevation plane and 180º in the azimuth plane. Although the simulation results indicated a titling angle of 7º (these results are presented in subsection 3.4), the former figures were selected based on the experiments made for each cell individually. Moreover, to compensate for the BS2 higher gain a higher tilting angle was used. The MT average speed was 3.6 km/h, the antenna height 1.5 m and the longitudinal paths were separated by 1 m.

The handover measurements were taken in two different directions: from BS1 to BS2[2] – direction D12; and from BS2 to BS1 – direction D21. In the following subsections only the non-consecutive paths represented in Figure 7.2 on the right will be considered and analysed [3] [4] [5] [6] [7] [10].

The following subsections present first the behaviour of the system for each BS individually in terms of coverage and transmission aspects, followed by the whole pavilion analysis and radio handover performance.

3.1 BS1 cell coverage and transmission characterisation

In this study, only BS1 was considered. Analysing the data collected during the measurement campaign, one may see from the received power distributions of paths C_B, L_B and R_B (Figure 7.16), that the cell length is about 22.5 m. Nevertheless the radio link only breaks down at about 27 m to 28 m. With this configuration one BS covers half the scenario and the other BS covers the other part. At positions further away from 22.5 m deep fading problems occur until the link breaks down. We can see that the maximum received power is obtained for positions around 17 m. This fact can be explained considering the BS and MT antennas radiation pattern. For a distance of 17 m and attending that the BS height is 5.85 m and the MT antenna height 1.5 m, the incident angle is therefore 75.6º. Due to the fact that the BS antenna is tilted 10.5º downwards, the incident angle becomes 75.6º plus 10.5º that leads to 86.1º. This incident angle is very near the angle of maximum in the radiation pattern of the BS antenna (see chapter 5) [11].

Observing in more detail Figure 7.16 (top left) it can be seen that in the beginning of the path there exists a higher BER due to the blank zone since these are results for the central path. All the rest of the path, within the cell boundaries, shows quite low BER figures and this applies to the other paths as well, increasing only for distances between 25 m and 27 m. This behaviour is caused by the sharp reduction of the power levels, the appearance of deep fading problems and the increase of the channel time dispersion, imposed by the radiation pattern of the BS antenna and its rotation angle. At the end of path R_B deeper fades are experienced when compared to the other two paths.

2 In some figures BS1 and BS2 are referenced as BST1 and BST2, respectively.

Figure 7.17 on the left represents the bit over byte error and, on the right, the BER versus the received power after MRC. It can be concluded that there are up to 2 bit errors per each byte error. Moreover, there are only high BER values for the lower power levels obtained for distances where deep fading problems occur. The obtained BER levels are within the expected limits for the equaliser.

One important aspect to notice is that due to the neighbouring scan process, needed for handover, there is a periodic short interruption of the link and the consequent increase of the BER, as shown by the spikes in Figure 7.16. However, synchronisation is maintained and due to the sharp nature of the interruptions there is no degradation of the link quality (the errors are not statistically important). For these measurements, the handover feature had to be activated since two cells cover the pavilion.

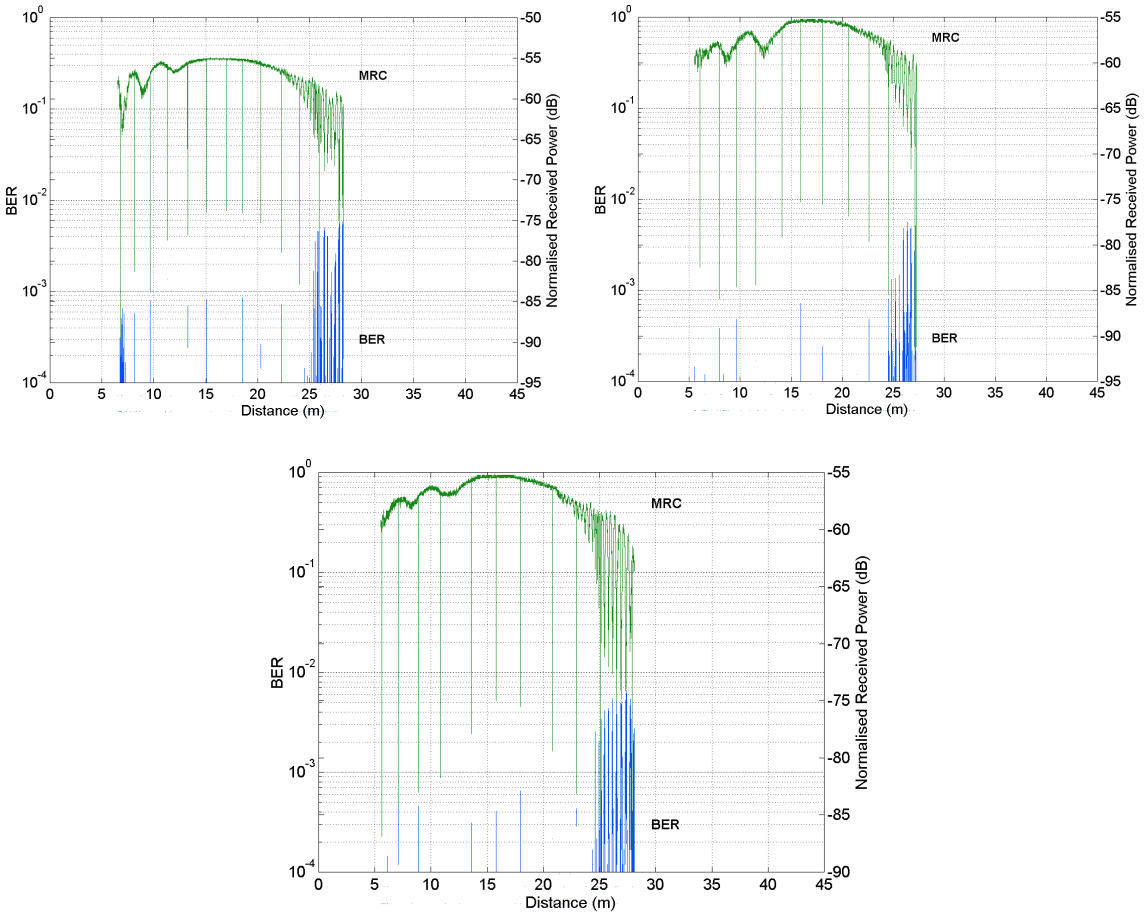

Figure 7.16: MRC received power and BER as a function of distance for path C_B (top left), path L_B (top right) and path R_B (bottom) and for BS1

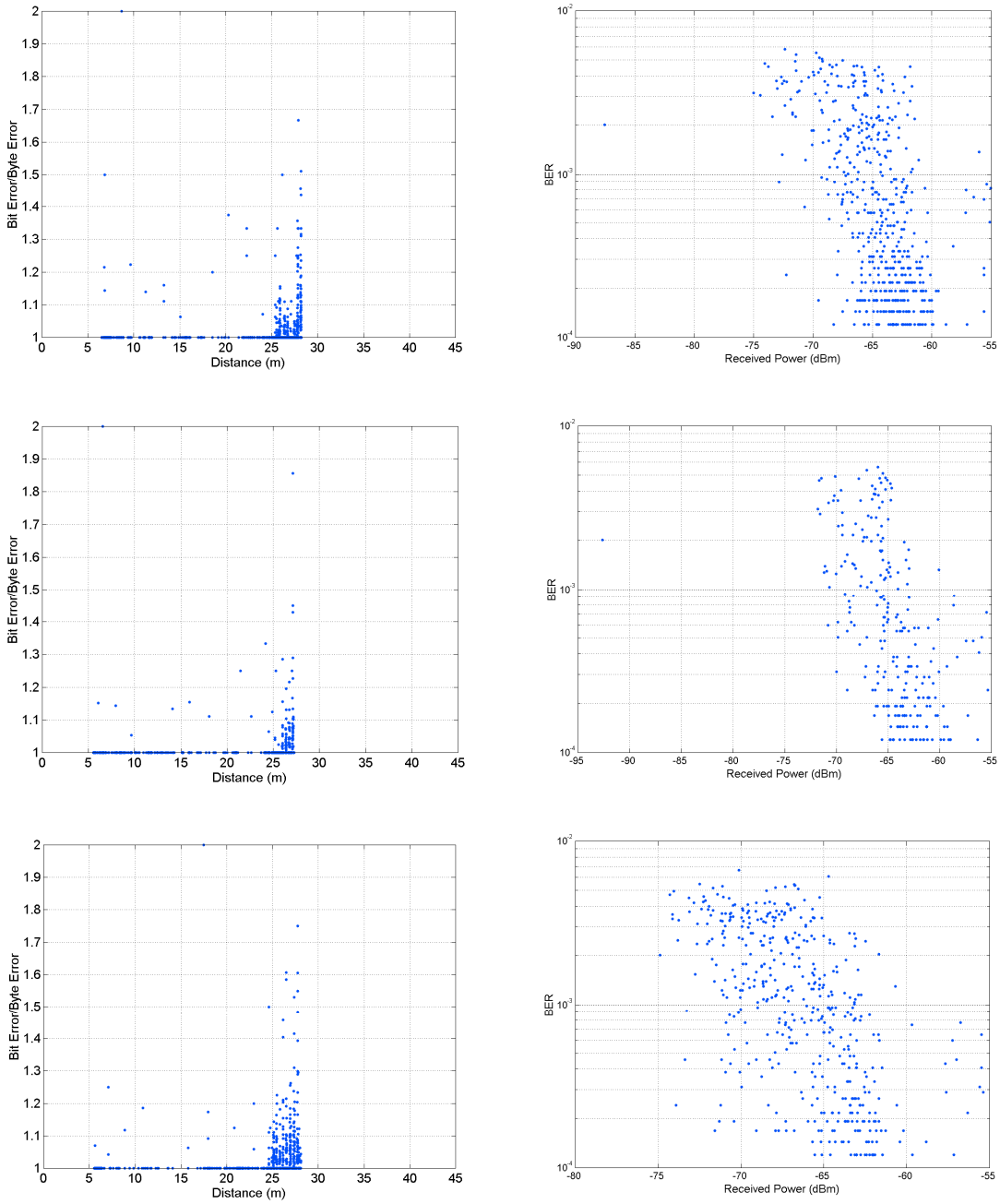

Figure 7.17: Bit over byte errors versus distance (left) and BER versus MRC received power level (right) for path C_B (top), path L_B (centre) and path R_B (bottom) for BS1

A convenient statistical analysis of both the received power and the BER can be made by observing their cumulative distribution functions shown in Figure 7.18. The main conclusion which can be drawn is that for 90% of the cases the received power levels obtained using MRC combining are above –61 dB and the BER values are bellow $7E10^{-5}$ for path C_B, $1E10^{-5}$ for path L_B and $1E10^{-4}$ for path R_B. Although the differences between the BER cumulative distribution functions, these levels are in agreement with the expected

behaviour of the equaliser and can be further improved using FEC allowing the required quality of service. From all paths, path R_B is the one that shows higher BER figures, most likely due to the presence of the benches in concrete. This effect can also be noticed in the deeper fades experienced.

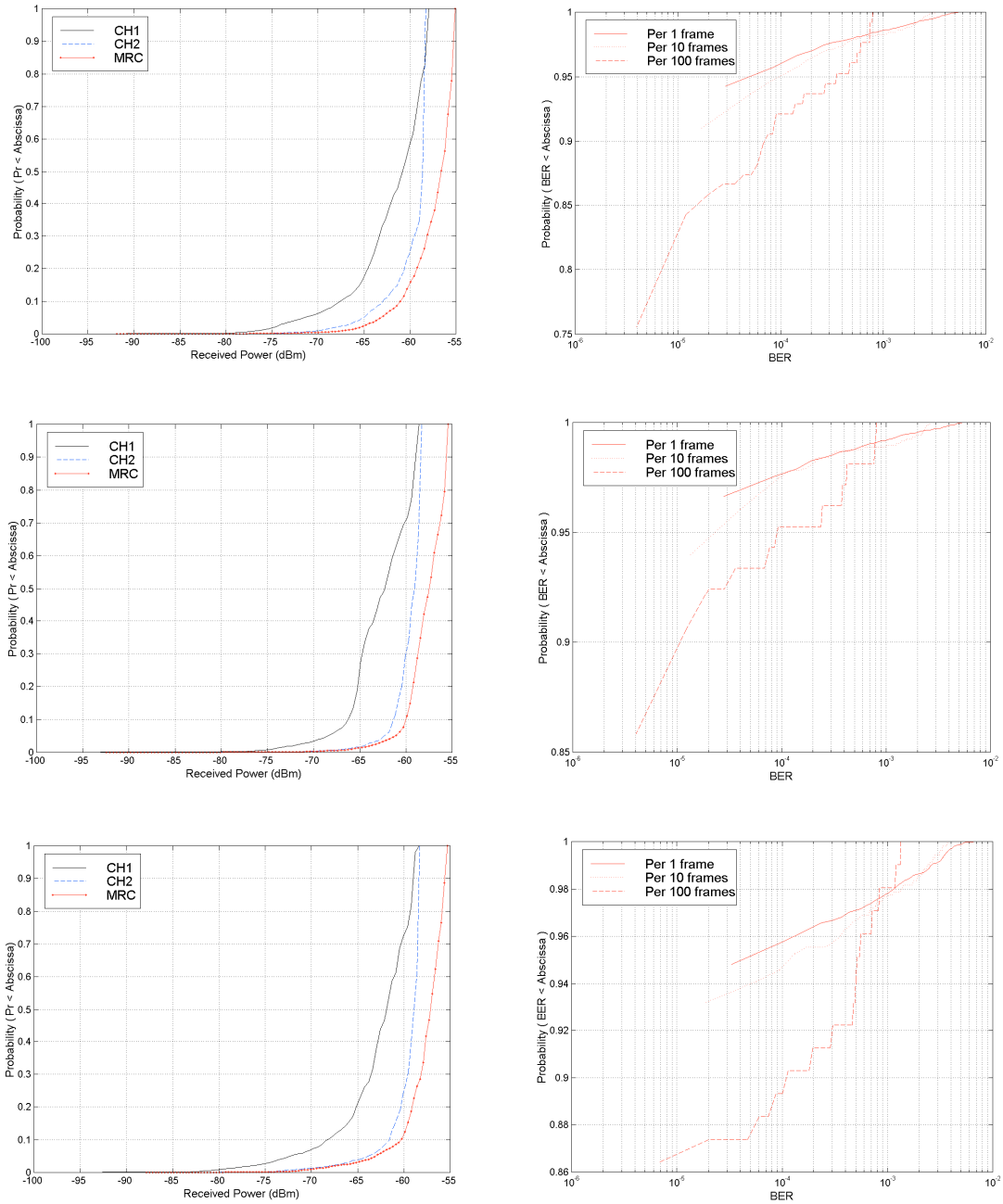

Figure 7.18: Received power CDF of both channels and after MRC (left) and BER CDFs (right) for path C_B (top), path L_B (centre) and path R_B (bottom) for BS1

3.2 BS2 cell coverage and transmission characterisation

The study carried out in this section is very similar to the one performed in section 3.1, the difference is this time only BS2 is considered. The MT movement direction is now from BS2 to BS1 and therefore the reference for the distance is BS2. Measurements where performed in the entire pavilion surface but results will be shown only for paths C_B, L_B and R_B.

From the received power distributions presented in Figure 7.19 it can be seen that the cell length is about 22.5 m, which is the same value, obtained considering only BS1. Also from the power distributions it can be observed that the link breaks down at a distance of 27 m to 28 m and that deep fading appears at distances from 22.5 m to the position where the link breaks down. Another important thing to notice is the link breakdown for path L_B at 24 m due to lack of power, but it recovers at 26.5 m because there is a sufficient increase of the power levels. At a distance of 29.5 m the link breaks down definitively.

One important difference between the received power distributions of both BSs is that for BS2 the maximum received power is obtained for a distance of 15 m instead of 17 m obtained for BS1. This difference can be explained considering the radiation pattern of the BS antenna and its tilting angle. For a distance of 15 m and attending that the BS height is 5.85 m and the MT antenna height is 1.5 m, the incident angle is therefore 73.8º. Due to the fact that the BS antenna is tilted 12.5º downwards, the incident angle becomes now 86.3º. This incident angle is very near 86.5º, which corresponds to the angle of maximum in the radiation pattern of the BS antenna [11].

Analysing now the BER by observing Figure 7.20 (left and right), one may conclude that as for the case of BS1 the BER values are quite low within the cell boundaries increasing only for distances between 25 m and 28 m. This behaviour is caused by the sharp reduction of the power levels, the appearance of fading problems and the increase of the channel time dispersion, imposed by the radiation pattern of the BS antenna and its rotation angle. It can be also seen that the number of bit errors per each byte error can be up to 2, and for paths L_B and R_B it does not exceeds 1.8.

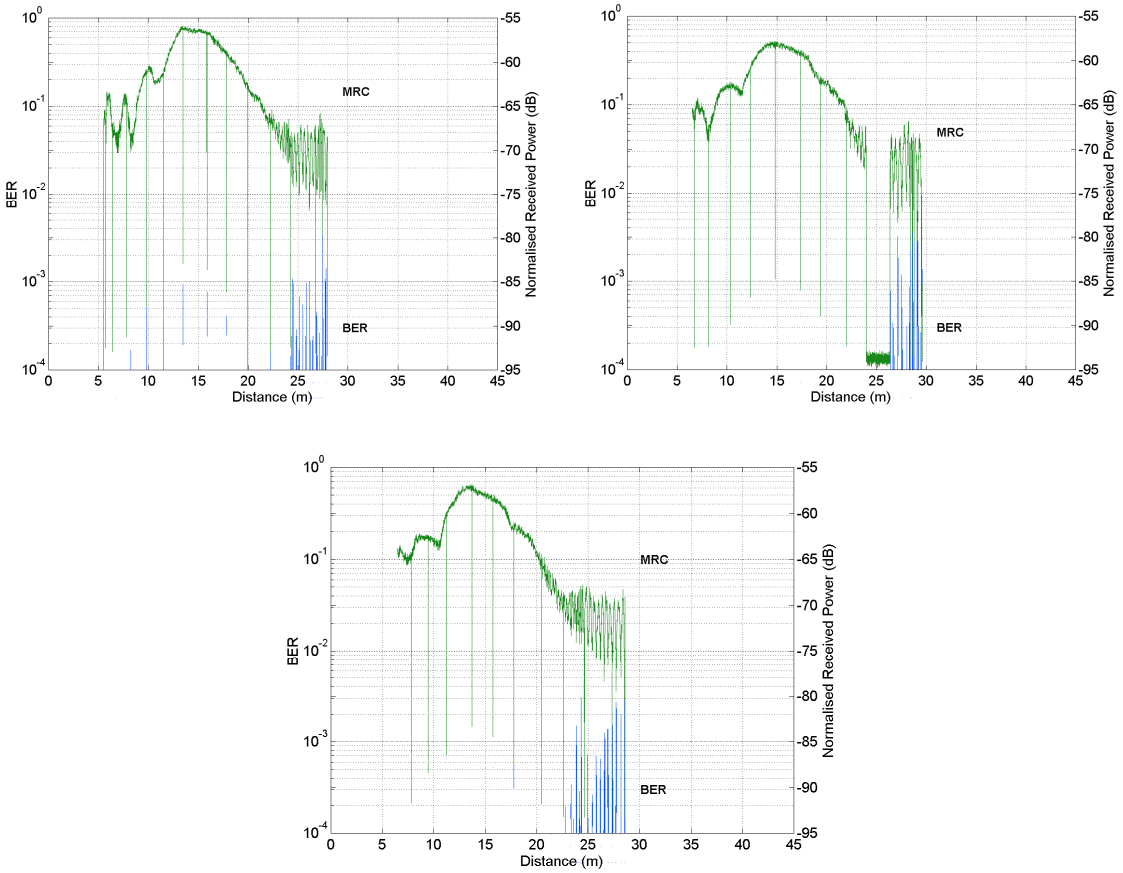

Figure 7.19: MRC received power and BER as a function of distance for path C_B (top left), path L_B (top right) and path R_B (bottom) and for BS2

Figure 7.21 depicts the cumulative distribution functions for both the received power and the BER, allowing to conclude that for 90% of the cases the received power levels obtained using MRC are above –70 dB for paths C_B and R_B and –77 dB for path L_B. These values are lower than the ones obtained for BS1, due to the fact that the tilting angle of BS2's antenna is greater, leading to a decrease on the received power levels within the cell. Considering the BER, in 90% of the cases it is bellow $1E10^{-5}$, which is in agreement with the expected behaviour of the equaliser.

3.3 Handover and two BSs coverage and transmission analysis

In the previous two sections, the coverage of each BS was assessed individually. This section intends to assess the simultaneous coverage of both BSs and evaluate the behaviour of the handover algorithm described in chapter 4. For this purpose, the same paths are considered in order to be able to compare the single and multiple BS coverage approach.

Since the handover algorithm comprises hysteresis and the fading is different for the two cells in its border (overlapping area), the direction of motion of the MT is important and therefore two directions were considered: from BS1 to BS2 – direction D12; and from BS2 to BS1 – direction D21. Except in Figure 7.25, Figure 7.29 and Figure 7.33 the distance reference used for the graphs referring to BS2 is the BS2 location.

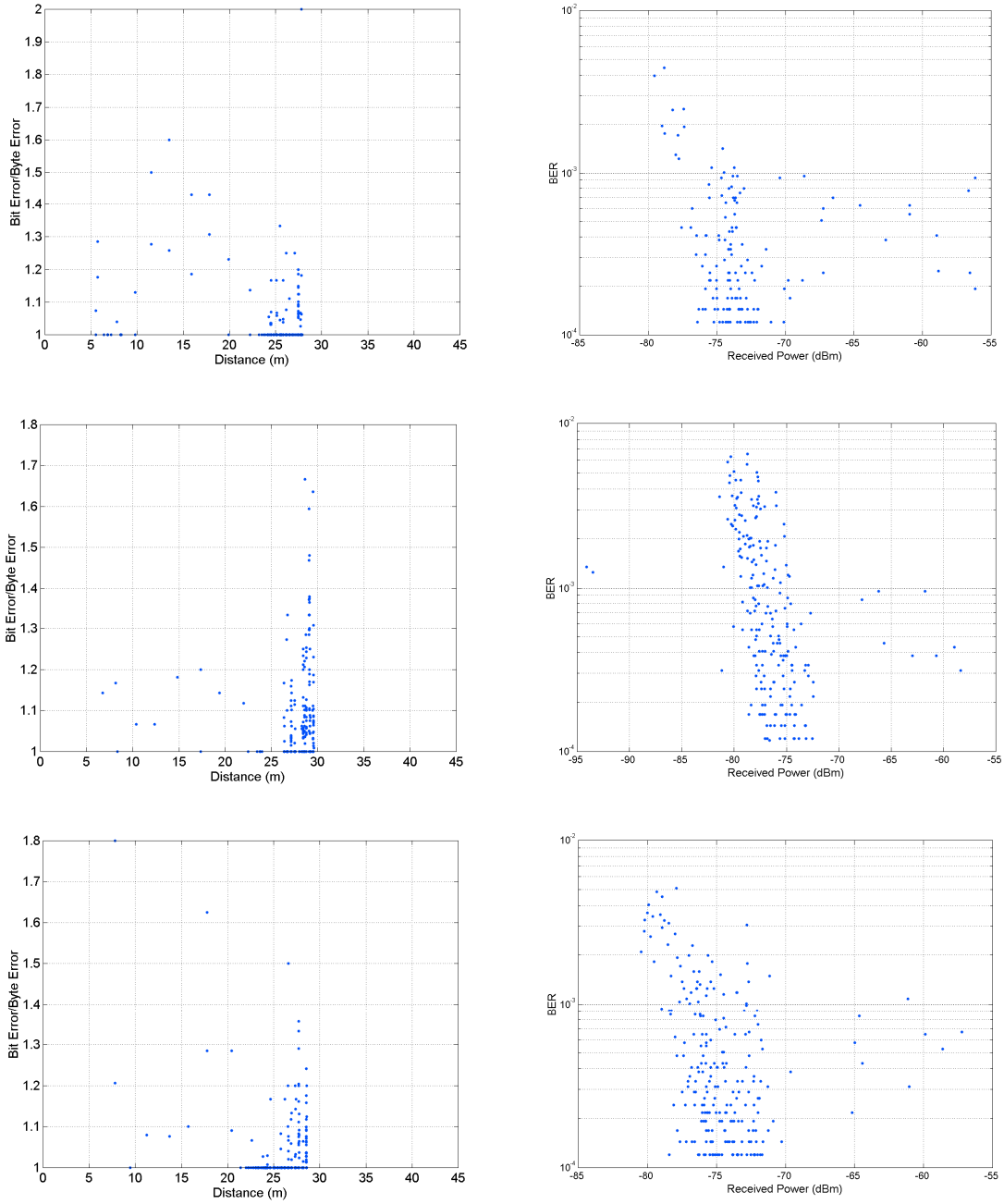

Figure 7.20: Bit over byte errors versus distance (left) and BER versus MRC received power level (right) for path C_B (top), path L_B (centre) and path R_B (bottom) for BS2

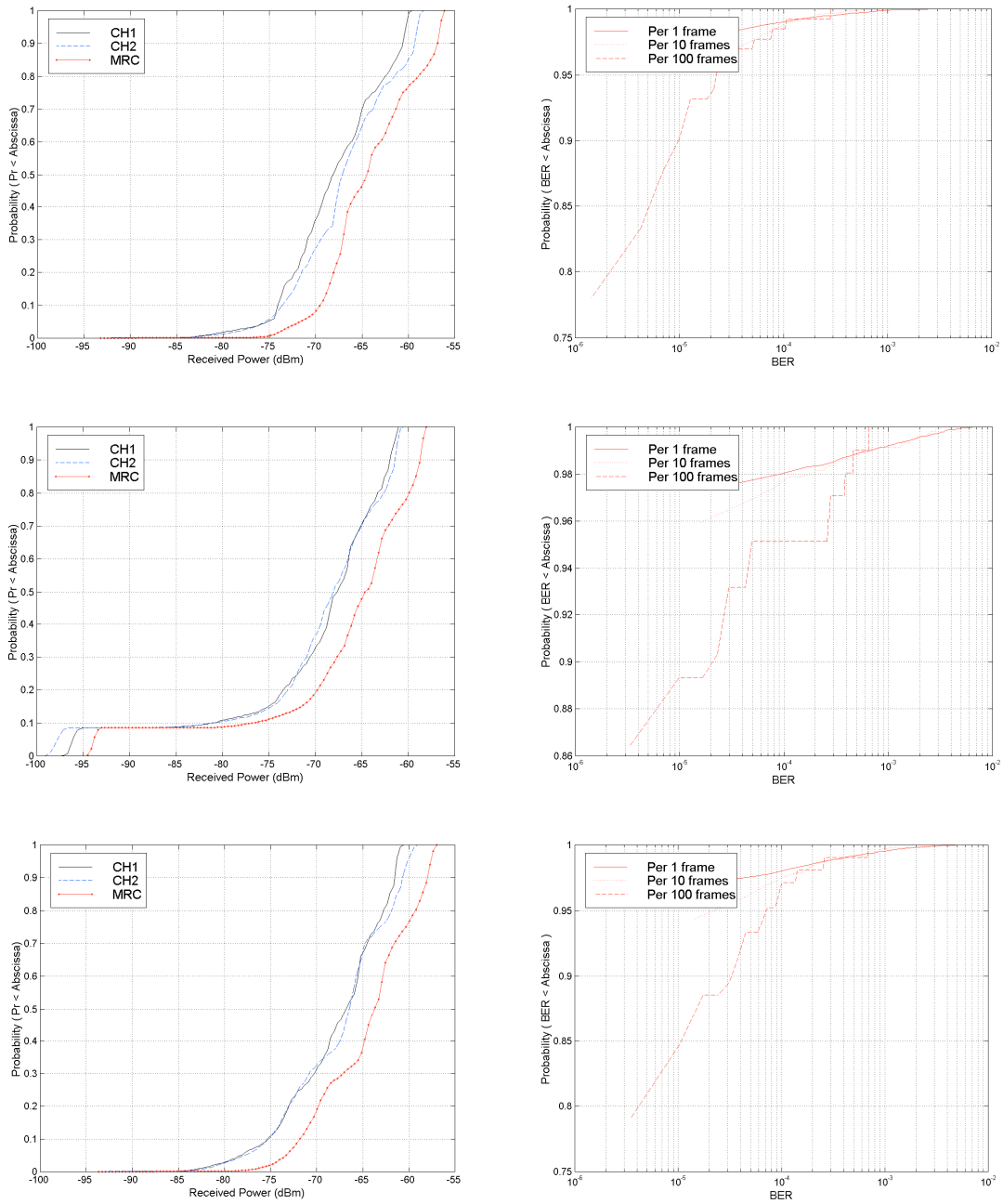

Figure 7.21: Received power CDF of both channels and after MRC (left) and BER CDFs (right) for path C_B (top), path L_B (centre) and path R_B (bottom) for BS2

3.3.1 Handover, transmission and coverage analyses for path C_B

The received power distributions obtained for both movement directions are depicted in Figure 7.22 and it can be seen that they are a concatenation of the two individual cells. The maximum received power levels are obtained for two different positions, one at a distance of 17 m from BS1 and the other at 15 m from BS2. This result is in agreement with the

results obtained in sections 3.1 and 3.2, confirming that the cells are asymmetric – the cell of BS1 is longer.

The handover occurs at approximately 27 m from BS1 and from 22 m from BS2. The antenna configuration used in both BSs was such that each BS would cover half of the scenario, ensuring a sufficient overlapping zone so that the handover could be performed successfully. The middle distance between the two BSs is 21.4 m and therefore it is intended that the covered region of each BS should extend from 0 m to at least that distance. As the rotation angle of BS2's antenna is larger than the one of BS1, the power within its cell decreases faster and when the MT moves towards BS1 handover occurs at a distance of 22 m from BS2. For the opposite movement direction, handover occurs only at a distance of 28 m from BS1, because the power within its cell has a smother decay. The rotation angles chosen for both BSs antennas intended to ensure a sufficient overlapping zone, and from sections 3.1 and 3.2 it is possible to conclude that it is around 10 m.

Another important aspect to notice from Figure 7.22 is that the handover algorithm has a good performance in presence of deep fadings, as the MT stays within the cell of BS1 although being in a severe fading region. This feature avoids the effect of multiple and successive handovers ("ping-pong" effect) which introduces an unnecessary system overhead.

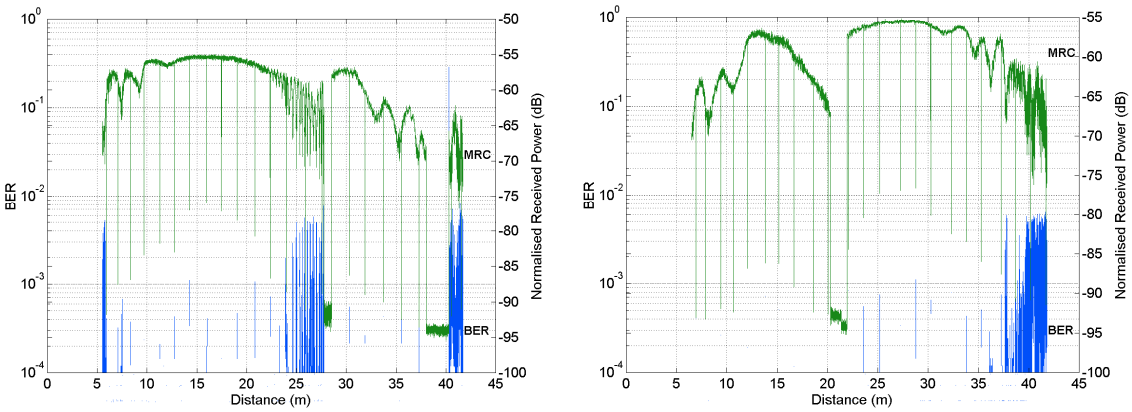

Figure 7.22: MRC received power and BER as a function of distance for path C_B for movement direction D12 (left) and movement direction D21 (right)

Close to BS2 the link breaks down due to the lack of power but the system is able to recover, nevertheless about 2 m after the link falls definitely and the system is unable to

recover once again. This fact is a consequence of BS2's antenna rotation angle which leads to the decrease of the power levels and the reduction of its uniformity in regions near the BS.

Regarding the BER, there is not a considerable difference between the results obtained in this section and the ones obtained in sections 3.1 and 3.2 for the same path. Figure 7.23 shows the distribution of the BER and MRC power levels as a function of distance, being the BER levels very low within each cell and only increasing in regions at the cell's limits and near the BSs, due to the reduction of the received power. For each byte error there are at most 2.5 bit errors for movement direction D12 and 1.5 for movement direction D21, which complies quite well with the results of sections 3.1 and 3.2. From Figure 7.23 one may conclude once again that the BER levels are very similar to the ones obtained for each BS operating separately and hence, are within the expected behaviour of the equaliser.

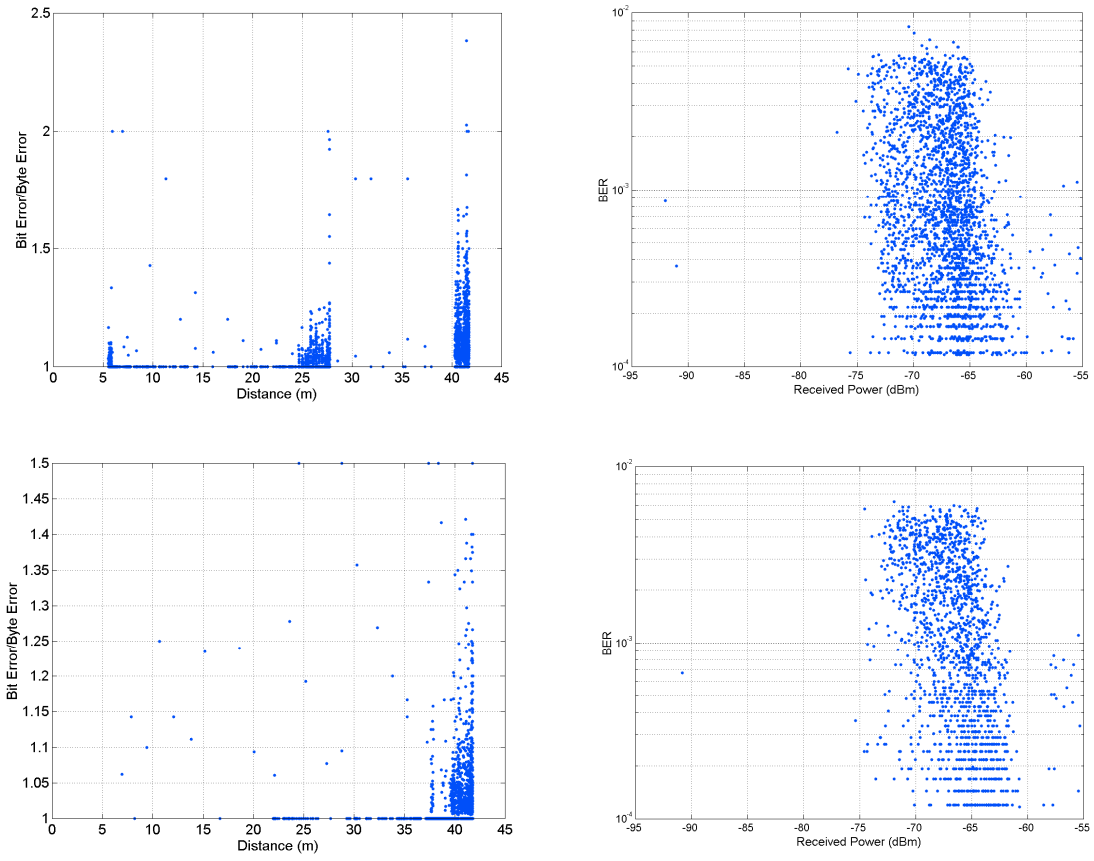

Figure 7.23: Bit over byte errors versus distance (left) and BER versus MRC received power level (right) for path C_B for movement direction D12 (top) and movement direction D21 (bottom)

The statistical behaviour of both the received power and the BER is shown in Figure 7.24, allowing to conclude that for 90% of the cases the received power levels obtained using MRC are above –70 dB. Comparing this result with the ones of sections 3.1 and 3.2 it is possible to conclude that there is not any increase on the received power distribution uniformity. For the BER, in 90% of the cases its value is below $5E10^{-4}$ for movement direction D12 and $6E10^{-5}$ for direction D21. The difference between the results obtained for the two movement directions, is caused by the fact that there is a deep fading region in the received power distribution when the MT moves in direction D12 and is leaving BS1, which does not exist in direction D21. Therefore the BER increases in that region degrading its statistical behaviour.

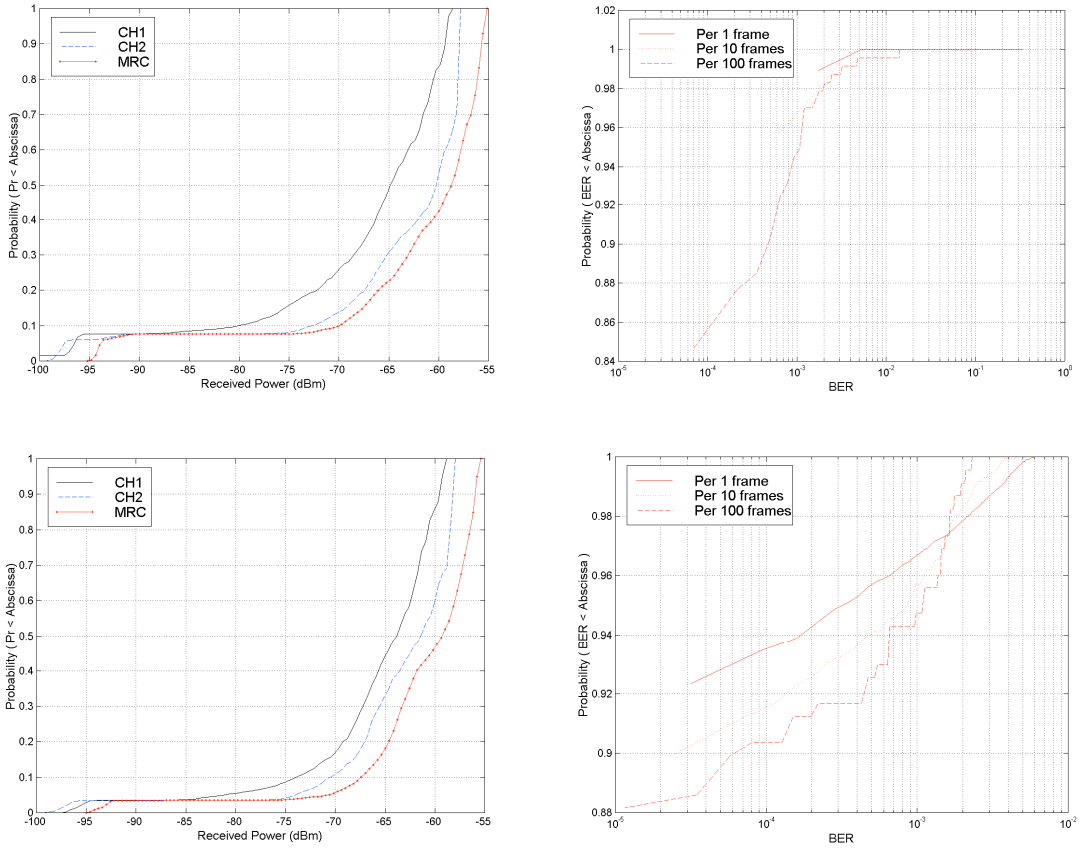

Figure 7.24: Received power CDF of both channels and after MRC (left) and BER CDFs (right) for path C_B for movement direction D12 (top) and movement direction D21 (bottom)

Attending to the number of samples collected during the measurements performed in this path and to the sampling rate used in the control and monitoring software, it is possible to determine the average velocity of the MT and the handover elapsed time. The handover

elapsed time corresponds to the time interval between the instant when the decision of performing a handover is taken and the instant when it is performed successfully. In the figures of the received power distribution, it corresponds to the time interval between the instant when the power falls bellow –90 dB and the instant when it rises again to a level imposed by the carrier frequency to which the MT has switched. The average velocity of the MT in this path was 3.22 km/h for movement direction D12 and 3.24 km/h for direction D21, which leads to a handover time of 0.62 s and 1.01 s respectively. It is important to notice in Figure 7.22, although in a deep fading region, the MT performs the handover successfully requiring a handover time lower than the one required for the opposite movement direction. This fact is due to the high power levels of the carrier frequency of BS2, which makes easier the synchronisation process between the MT and that BS.

Figure 7.25 shows the MRC received power for each cell in the top part of the figure for path C_B and the coverage achieved with two BSs measured in both directions, D12 in the middle and D21 in the bottom. In this figure all the distances are referenced to BS1 for better comparison.

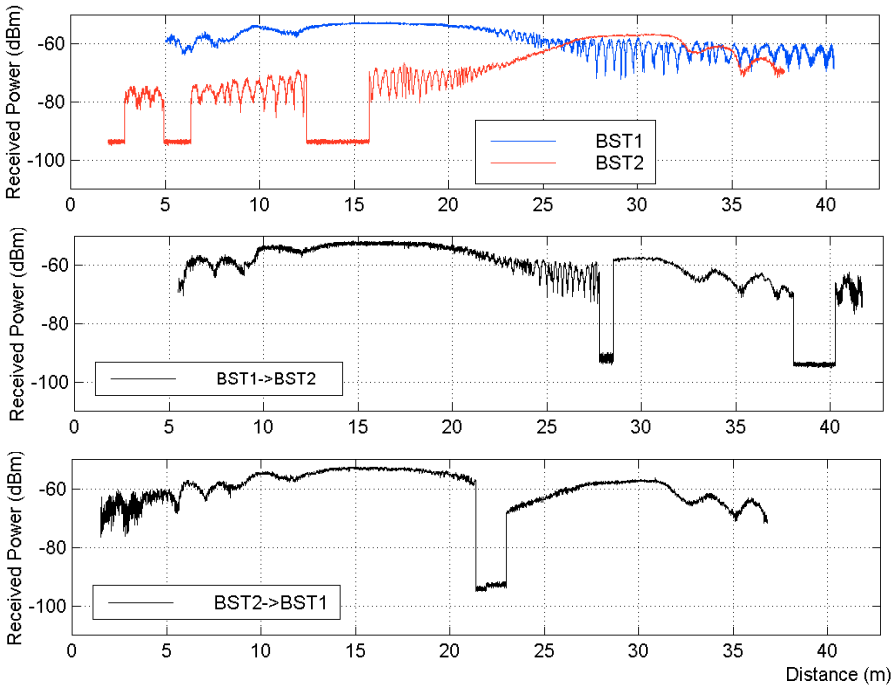

Figure 7.25: Individual and both cells MRC received power for path C_B considering movement directions D12 and D21

3.3.2 Handover, transmission and coverage analyses for path L_B

Analysing now path L_B based on the received power distributions shown in Figure 7.26, it can be seen that handover occurs at a distance of 28 m from BS1 for movement direction D12 and at 22 m from BS2 for movement direction D21. These results are in agreement with the results obtained in section 3.3. The maximum values positions are also at a distance of 17 m from BS1 and 15 m from BS2, as expected from the results obtained in sections 3.1, 3.2 and 3.3.1. Therefore one important conclusion, which can be drawn, is that the power distribution for both paths C_B and path L_B is quite similar when handover is used.

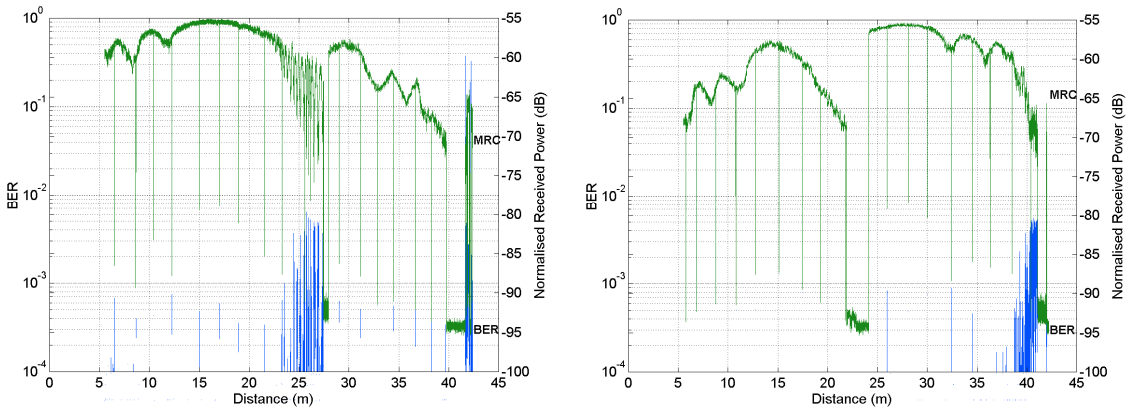

Figure 7.26: MRC received power and BER as a function of distance for path L_B for movement direction D12 (left) and movement direction D21 (right)

Also in this path it is possible to observe a deep fading region for movement direction D12 and the respective good performance of the handover algorithm, not allowing multiple and successive handovers to occur when the MT is within that region.

For this path another handover occurs when the MT moves in direction D12 at 2 m from BS2. This fact can be explained by the radiation pattern of the BS antenna and its rotation angle which lead to a reduction of the power in that region and thus to a handover to the BS1cell. It is important to notice that although in a region of bad conditions regarding the power levels, the link does not breakdown. The same effect occurs for the opposite movement direction, but handover only takes place when the MT is very close to BS1.

Figure 7.26 and Figure 7.27 allow the BER behaviour analyses regarding the MT distance to the BS and the received power levels. Once again it is possible to conclude that there is a

certain similarity with the results of sections 3.1 and 3.2 for path L_B. The differences are only due to the handovers that happen at the end of the paths, for both movement directions. Therefore the MT changes to a different carrier frequency and the link does not fall down, but the received power levels and the fading that is present increases the BER. Although this fact the results comply quite well with the ones obtained for sections 3.1, 3.2 and 3.3.1 and the average number of bit errors per byte does not exceed 2.3 for movement direction D12 and 2 for direction D21.

A statistical analysis can be made for both the received power levels and the BER by observing Figure 7.28 and it can be concluded that for 85% of the cases the received power levels obtained using MRC are above –70 dB. Comparing this result with the ones of sections 3.1 and 3.2 it is possible to conclude that there is a reduction of the received power distribution uniformity, due to the behaviour of the system at the end of the path. For this region, due to the fading and the low power levels, handover takes a longer time and there are several positions with very low power values, which degrade the CDF of the received power. Regarding the BER, in 90% of the cases its value is bellow $9.5E10^{-4}$ for movement direction D12 and $1E10^{-5}$ for direction D21. As for section 3.3.1 the difference between the results obtained for the two movement directions, is caused by the deep fading region in the received power distribution obtained for movement direction D12.

Concerning the MT's average velocity during the measurements performed in path L_B, the results obtained were 2.99 km/h for movement direction D12 and 4.04 km/h for direction D21. For movement direction D12, the handover elapsed time obtained for the first handover was 0.37 s and for the second 2.11 s. The first handover elapsed time is smaller than the second one, due to the fact that in that region, the power levels of the carrier frequency for which the MT switches are higher than the power levels of the region where the second handover occurs. Higher power levels favour the process of resynchronisation to a different frequency in the MT and hence led to a lower handover execution time. For movement direction D21 the handover execution time was 1.90 s.

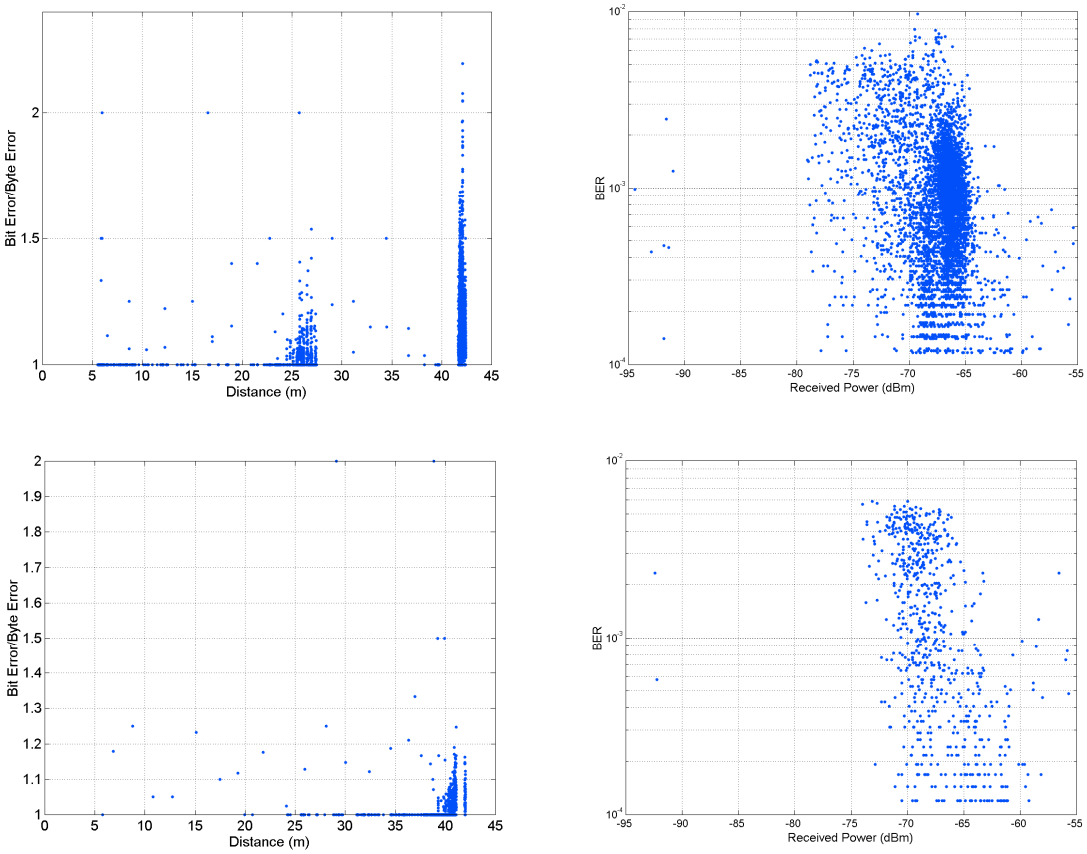

Figure 7.27: Bit over byte errors versus distance (left) and BER versus MRC received power level (right) for path L_B for movement direction D12 (top) and movement direction D21 (bottom)

Figure 7.29 shows in the top part of the figure the MRC received power for each cell for path L_B and the coverage achieved with two BSs measured in both directions, D12 in the middle and D21 in the bottom.

3.3.3 Handover, transmission and coverage analyses for path R_B

Observing Figure 7.30, representing the received power distributions obtained for path R_B in both movement directions, the first conclusion which can be drawn is that the power distribution is quite similar to the ones of sections 3.3.1 and 3.3.2. For movement direction D12 handover takes place at a distance of 28 m from BS1 and for direction D21 it occurs at 24 m from BS2. The maximum received power levels are also around 17 m from BS1 and 15 m from BS2. For movement direction D12, there is a second handover near BS2 (1 m from it) as happened for paths C_B and L_B. Also in Figure 7.30 it is possible to observe deep fading regions for movement directions D12 and D21, and once again the good

performance of the handover algorithm, not allowing to occur multiple and successive handovers in those regions.

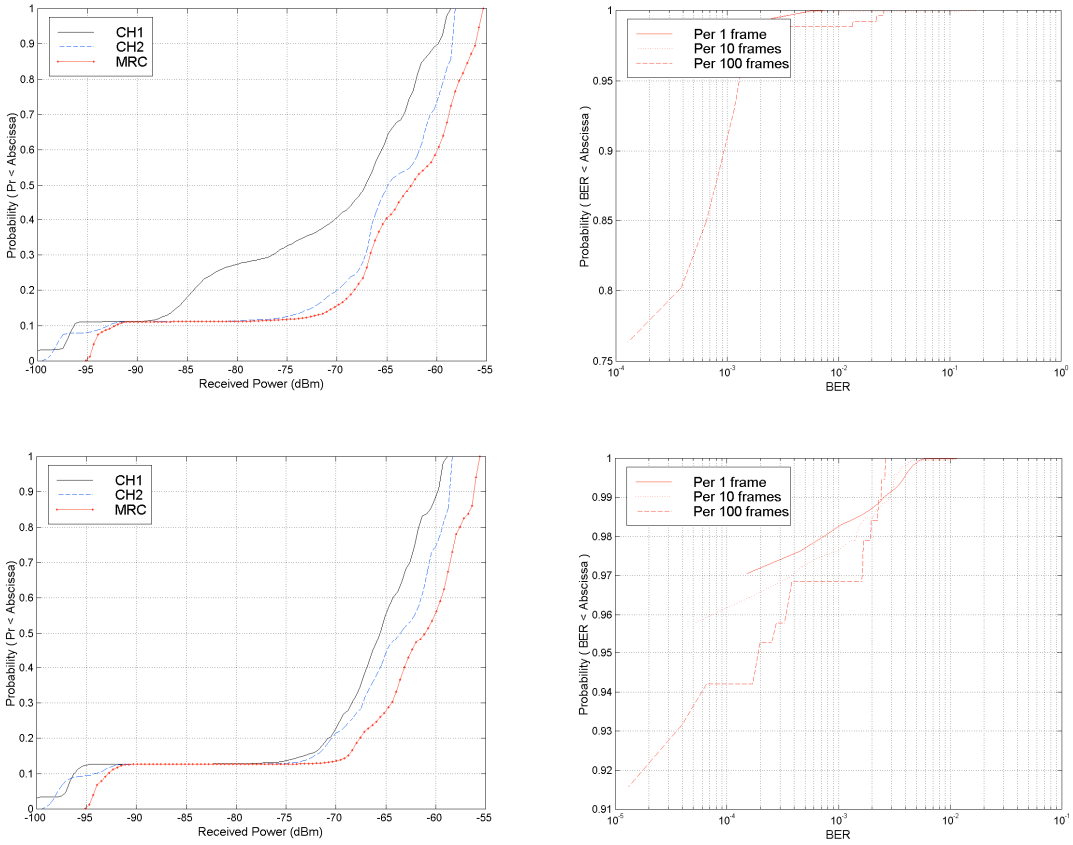

Figure 7.28: Received power CDF of both channels and after MRC (left) and BER CDFs (right) for path L_B for movement direction D12 (top) and movement direction D21 (bottom)

The results presented in Figure 7.30 and Figure 7.31 are once again very similar to the ones of section 3.3.2 and on average, for each byte error there are up to 2 bit errors for movement direction D12 and 2.2 for direction D21. Regarding the statistical behaviour of both the received power levels and the BER shown in Figure 7.32, one can concluded that for 85% of the cases the received power levels obtained using MRC are above –72 dB and the BER is bellow $4E10^{-4}$ for movement direction D12 and $9E10^{-4}$ for direction D21. It is important to notice the similarity between these two values, because although the increase of the BER due to the fading region (22 m to 27 m) in the received power distribution of movement direction D12, there is also an increase of the BER for direction D21, due to the low power levels near BS1. Therefore the statistical behaviour is similar for both movement directions as shown by the BER CDF.

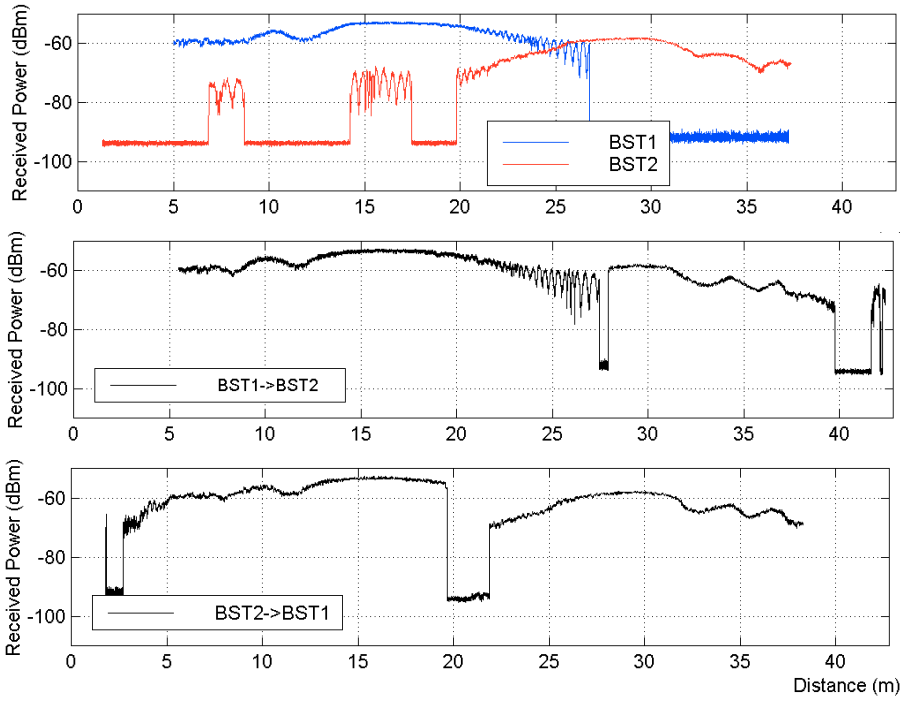

Figure 7.29: Individual and both cells MRC received power for path L_B considering movement directions D12 and D21

In this path the MT's average velocity during the measurements was 4.34 km/h for movement direction D12 and 4.11 km/h for direction D21. For movement direction D12, the handover execution time of the first handover was 1.63 s and of the second one 2.07 s. As for path L_B, the handover execution time of the first handover is smaller than the handover execution time of the second one, due to the higher power levels obtained in the region of the first handover, which favour the resynchronisation process in the MT. Regarding movement direction D21 the handover execution time obtained was 0.93 s.

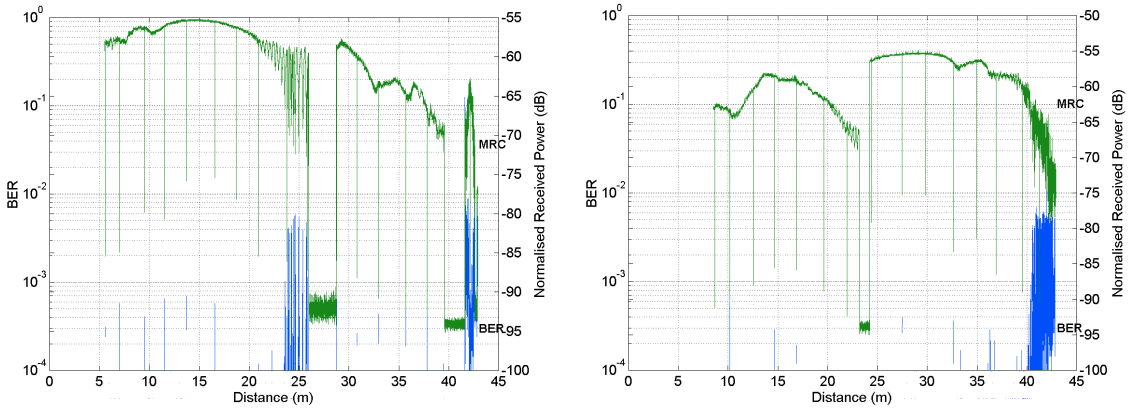

Figure 7.30: MRC received power and BER as a function of distance for path R_B for movement direction D12 (left) and movement direction D21 (right)

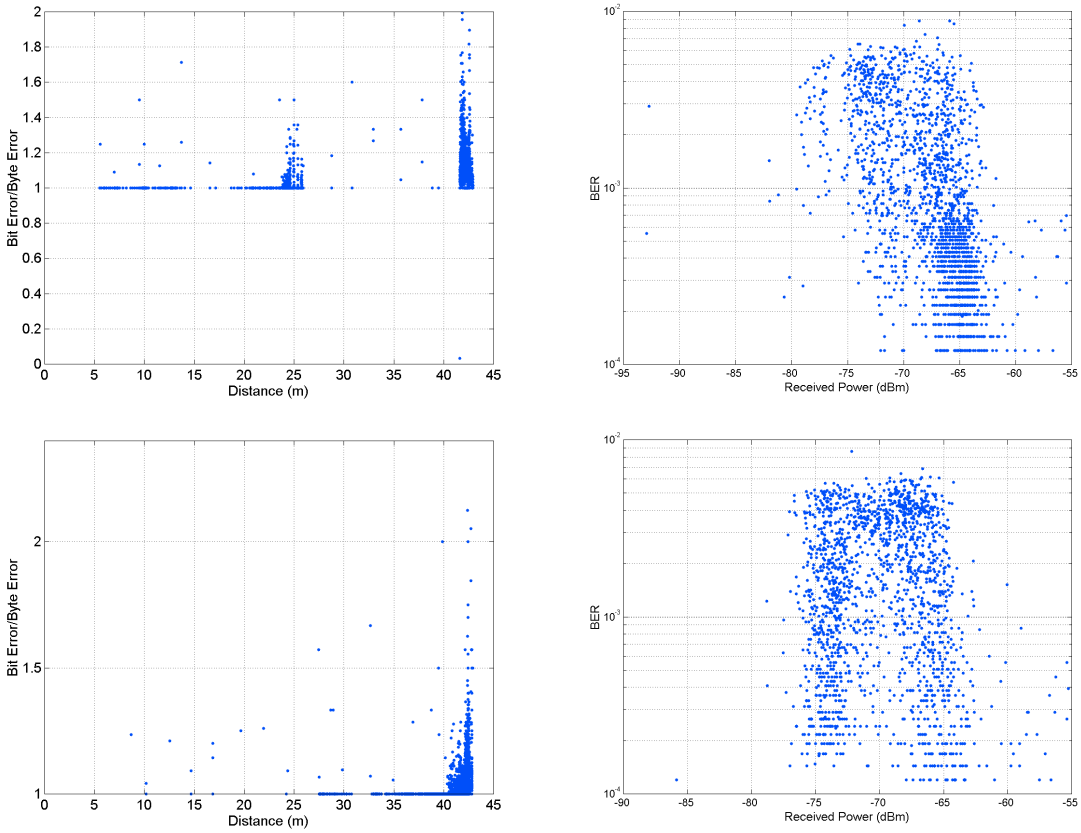

Figure 7.31: Bit over byte errors versus distance (left) and BER versus MRC received power level (right) for path R_B for movement direction D12 (top) and movement direction D21 (bottom)

Figure 7.33 shows the MRC received power for each cell in the top part of the figure for path R_B and the coverage achieved with two BSs measured in both directions, D12 in the middle and D21 in the bottom.

3.4 Whole pavilion coverage, transmission and handover analyses

3.4.1 Configuration A and B coverage and transmission analysis

Configuration B has also been evaluated by simulation. Tilting has proved to be required in this configuration to reduce the power reflected by the pavilion walls. The simulation results are displayed in Figure 7.34 for a tilting angle of 7º.

Figure 7.35, on the left, show a 2D graphical representation of BS1 coverage measurements (MRC received power) and Figure 7.35, on the right, a 3D representation of the same data.

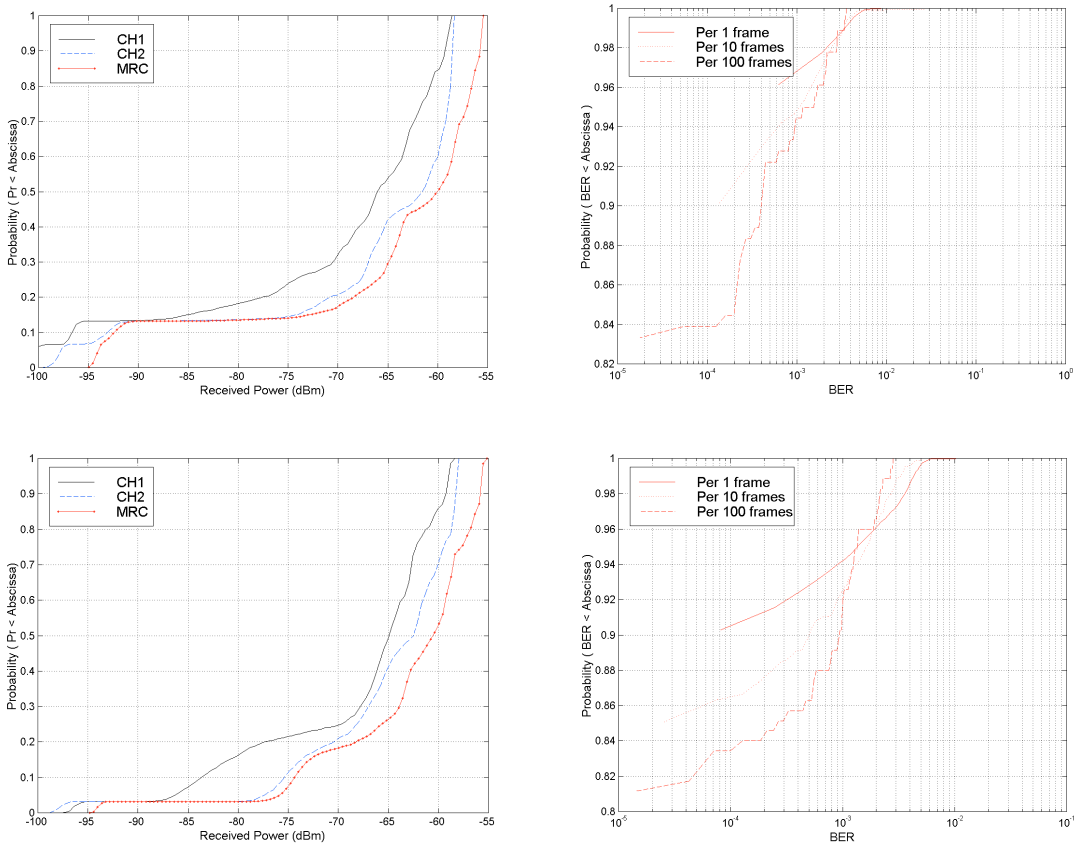

Figure 7.32: Received power CDF of both channels and after MRC (left) and BER CDFs (right) for path R_B for movement direction D12 (top) and movement direction D21 (bottom)

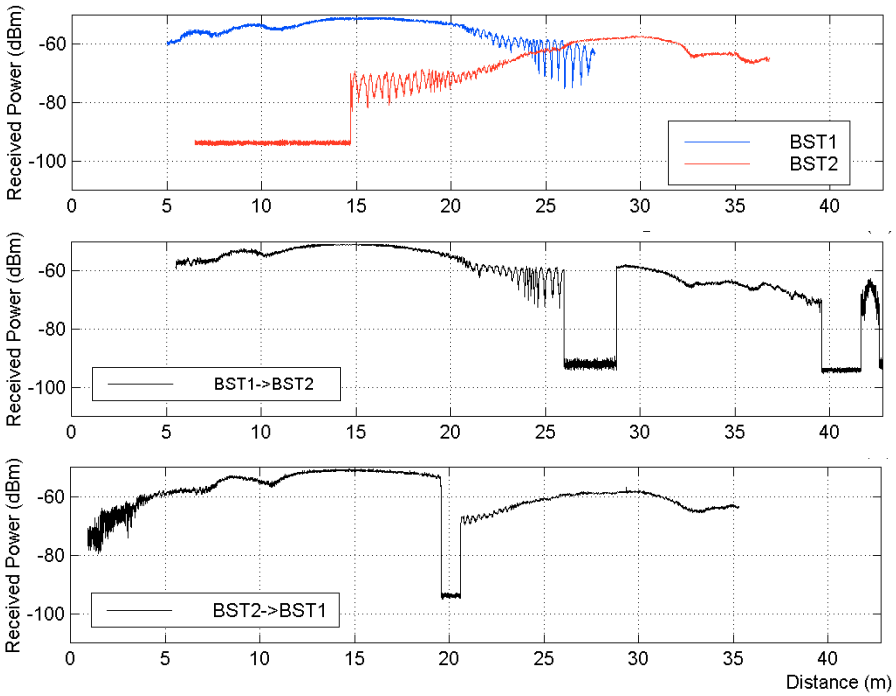

Figure 7.33: Individual and both cells MRC received power for path R_B considering movement directions D12 and D21

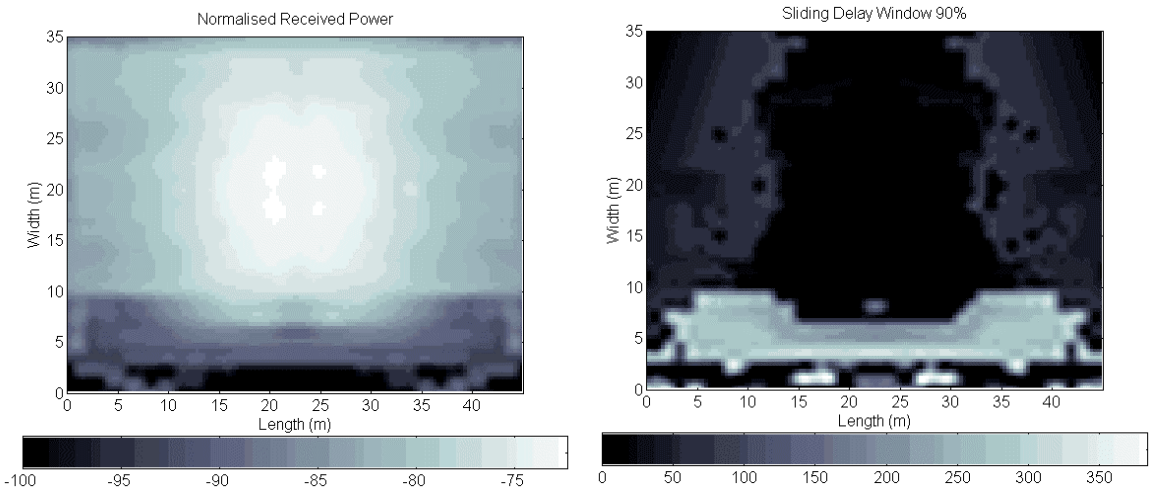

Figure 7.34: Simulation results for BSs at (0.5, 20, 6.5) m and (44.5, 20, 6.5) m and both rotated 7° in the elevation plane and 0° and 180º in the azimuth plane, respectively: NRP (left) and SDW90% (right)

The coverage area of BS1 is delimited approximately by the line which crosses at d=25 m. As we move away form the central path the received power reduces due to the shape of the antenna radiation pattern. Comparing Figure 7.34 and Figure 7.35 it can be seen the influence of the considered different tilting angle 7º and 10.5º, respectively. The cell size is smaller in the second case. The fading can also be observed mainly after reaching the cell border.

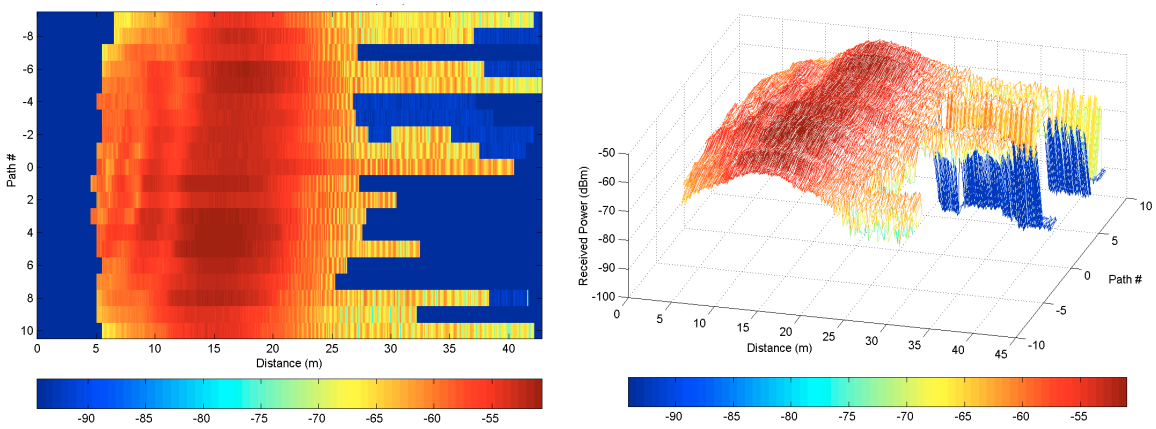

Figure 7.35: BS1 coverage (MRC received power): 2D (left) and 3D (right)

Analysing now the coverage area of BS2 it may be concluded that it is restricted to the line which crosses at d=23 m. As we move away form the central path the received power reduces as well due to the shape of the antenna radiation pattern. Comparing Figure 7.34 and Figure 7.36 it can be seen the influence of the considered tilting angle of 12.5º. The

cell size is smaller than the cell created by BS1. It is also clear that both cells differ being therefore asymmetric in terms of coverage area and that the overlapping area was not selected optimally. This can be confirmed since the middle of the pavilion is at d=21.5 m. The compensation for the BS2 higher gain was not successful and as a consequence a distorted coverage was achieved.

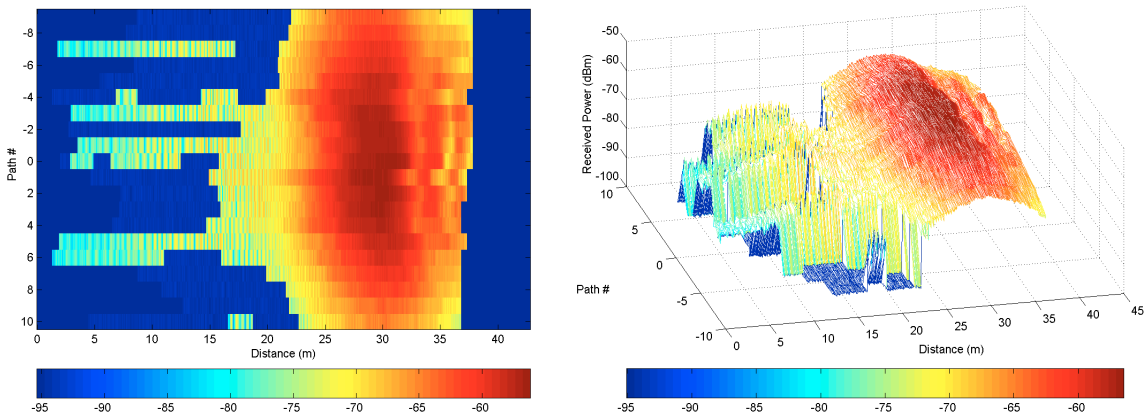

Figure 7.36: BS2 coverage (MRC received power): 2D (left) and 3D (right)

Figure 7.37 shows the coverage obtained with both BSs when the MT is driven in direction D12. The handover happens in the region delimited by d=25 m and d=30 m, which is in accordance with the fact that the BS1 cell ends approximately at d=25 m. It is also evident that the handover execution time is higher when we move away from the central path. This fact may be explained based on the destination cell power fading levels since the antennas radiation pattern optimises the coverage for the central area of the pavilion. The region where handover happens seems also to be moving right when we move away from the central path. This is a consequence of the cell egg shape and therefore near the borders of the pavilion the power levels are lower.

Figure 7.38 shows the coverage obtained with both BSs when the MT is driven in direction D21. The handover happens generically between d=23 m and d=17 m. The distance to the BS is less in this case since the cell has smaller dimensions.

The “best server” analysis is shown in Figure 7.39. This graph was obtained by simulation, selecting for each pixel the best BS coverage which is different from the handover algorithm. Hysteresis is not considered here and therefore the parameter THRESH is 0 dB, corresponding to an ideal situation but in practice the “ping-pong” effect precludes this

implementation. It is also evident how the BS1 coverage dominates showing that the selected technique to reduce the impact of BS2 having a higher gain, was not the best strategy!

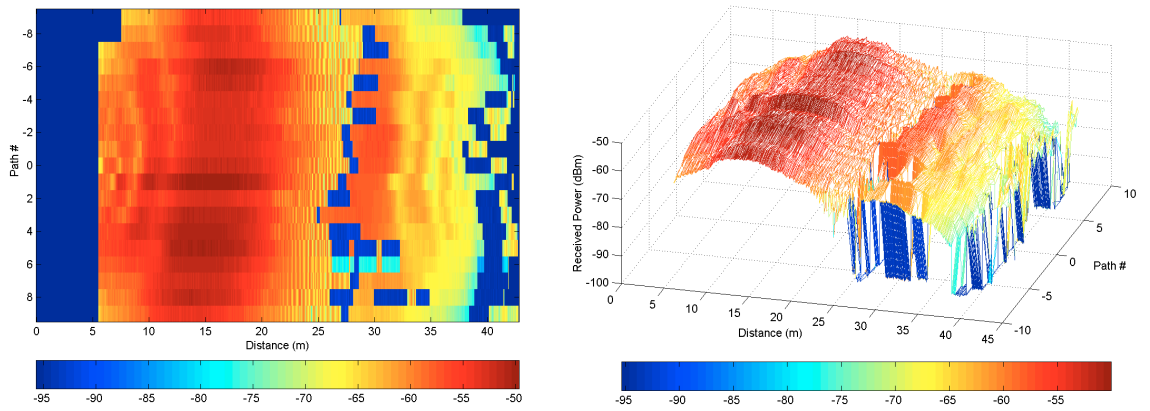

Figure 7.37: Coverage for handover direction D12 (MRC received power): 2D (left) and 3D (right)

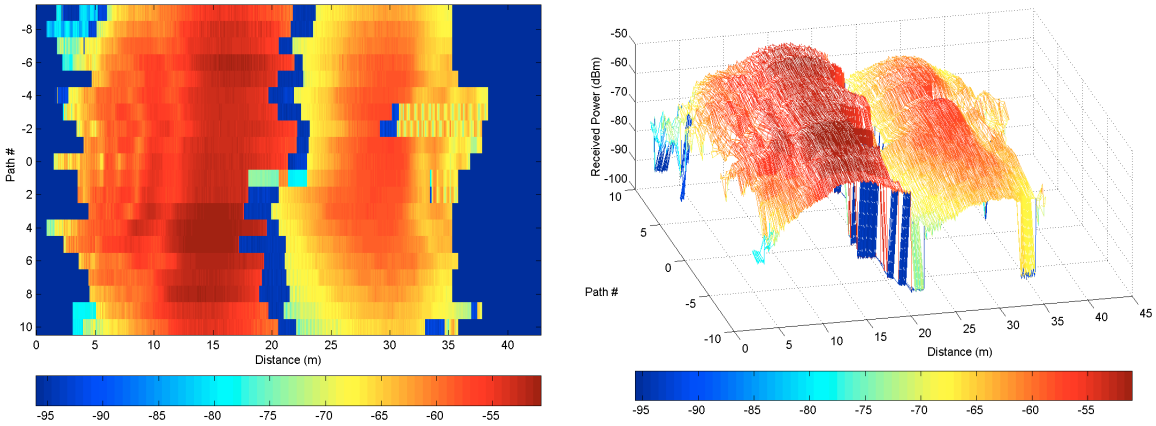

Figure 7.38: Coverage for handover direction D21 (MRC received power): 2D (left) and 3D (right)

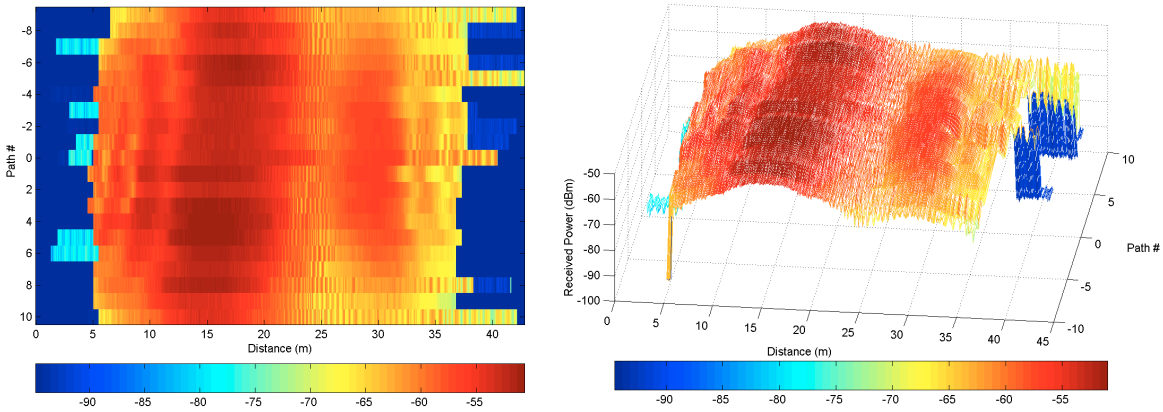

Figure 7.39: Coverage for "best server" (MRC received power): 2D (left) and 3D (right)

Having completely defined the coverage achieved with two BSs (configuration B) it is important to perform a comparison with the situation where only one BS was used to cover the whole area (configuration A). Figure 7.40 shows the coverage area for configuration A. The antenna is clearly pointing towards the centre of the pavilion achieving a good coverage. As we move away from the centre, moving to the left and the right, the power level decreases. It is also evident the impact of the stronger multipath components nearby the BS since some fading exists (colour change between yellow and light blue). Comparing this approach with the two BSs case, we can conclude that a better coverage can be achieved with two BSs since the power levels are higher.

In section 2.5 simulation results were presented for this configuration. It is evident that the tilting angle in both configurations is not the same since the "power peak" does not occur in the same area.

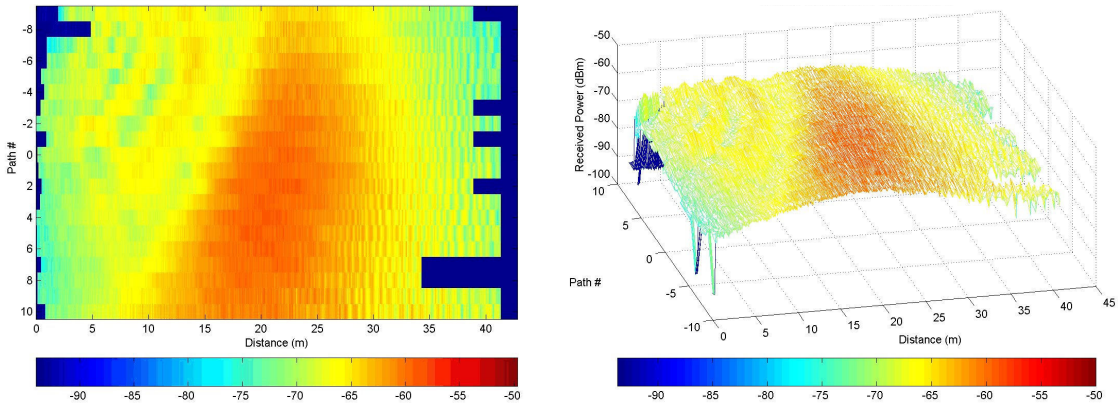

Figure 7.40: Coverage for BS in configuration A (MRC received power): 2D (left) and 3D (right)

Figure 7.41, Figure 7.42 and Figure 7.43 show a comparison in terms of BER results for configuration A and B considering both directions of MT motion. Observing Figure 7.41 it can be concluded that the BER for configuration B and direction D12 has two zones of concern. The first in the middle of the pavilion in the overlapping zone with higher intensity on the left side and a second zone in the extremity of the pavilion, nearby BS2. It is also visible that nearby BS1 there is also, in little areas, a higher BER. Therefore, there is a high correlation between the BER figures and the received power. The fading has also a negative impact on the BER figures. All the remaining areas of the pavilion show a good behaviour in terms of BER. Considering now the results for the opposite direction shown in Figure 7.42, it can be concluded that the central part of the pavilion, in opposite to the

previous case, shows a good BER behaviour. The zone of concern nearby BS2 is now smaller showing therefore also an improvement. The zones where a high BER exists is in the majority of the times caused by the connection to BS1 in the beginning of the path when starting from BS2 (direction D21). The zone presenting more degradation is the area nearby BS1 that visibly shows worse performance than in the previous direction.

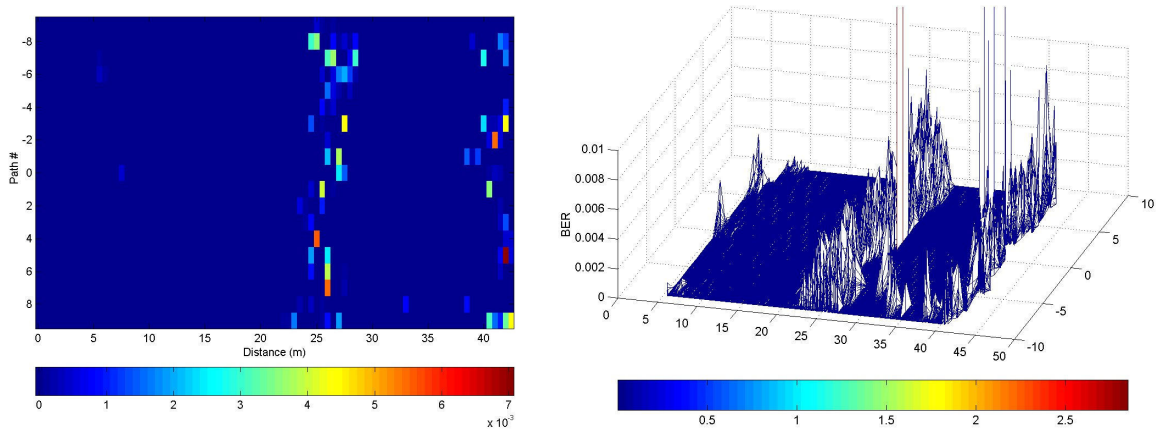

Figure 7.41: BER for BSs in configuration B and handover in direction D12: 2D (left) and 3D (right)

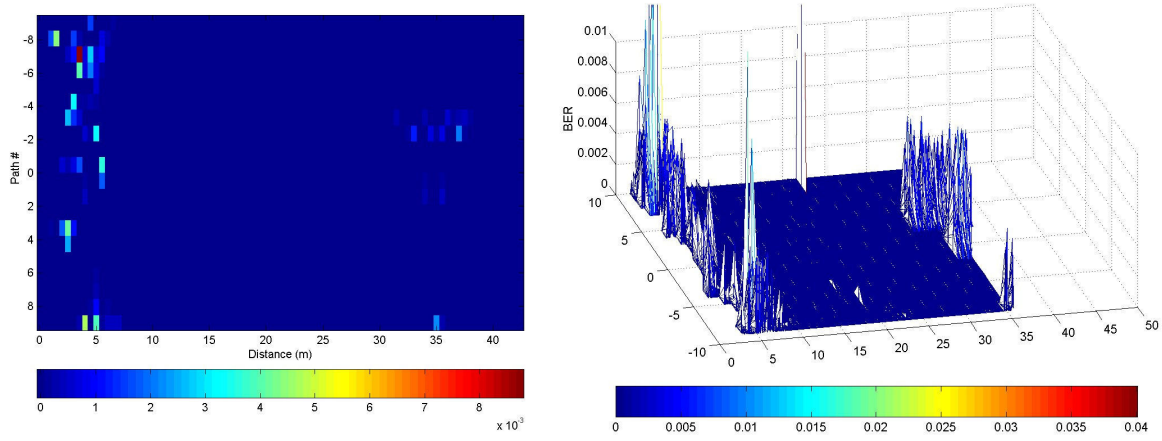

Figure 7.42: BER for BSs in configuration B and handover in direction D21: 2D (left) and 3D (right)

Observing Figure 7.43 it may be concluded that the BER behaviour is generically different showing “small peaks” in the whole pavilion surface. However, the most critical zones are nearby the BS and in the other extremity of the pavilion being more pronounced on the left side of the pavilion, which coincides with the region where the power lever is also lower. For this configuration the BS antenna does not have tilting which also causes the power to be distributed to the walls increasing the time dispersion of the signal. As a final conclusion it can be said that configuration B shows better performance in terms of BER

and received power, however the cells should be better dimensioned to show a symmetrical shape and sharing equally the pavilion coverage[3].

3.4.2 Handover analysis

In this section are presented some statistics regarding handovers. The pavilion was divided in two zones: central coverage area (better coverage) and lateral coverage area (worst coverage). For the cases where in the same path two handovers occurred, the second handover is also characterised.

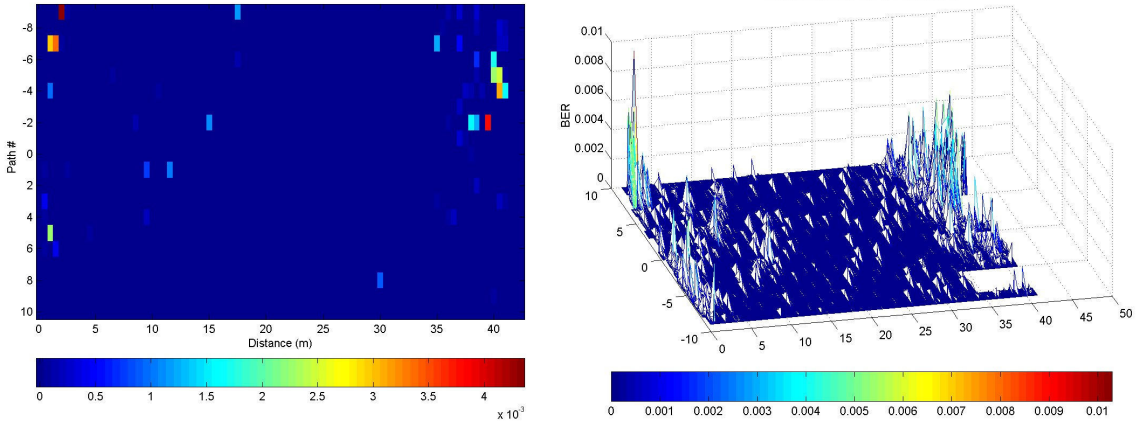

Figure 7.43: BER for BS in configuration A: 2D (left) and 3D (right)

Direction D12: 1st handover

For the best coverage area, in average the handover takes place at a distance of 26.8 m and stops at 27.9 m. The duration is about 807 ms and in 95% of the times, the handover durations is between 465 ms and 1148 ms.

For the worst coverage area, the handover starts in average at 27.6 m and stops at 30.1 m. The handover average duration is 1493 ms, being 95% of the time between 595 ms and 2392 ms, which indicates a quite large variation.

These results confirm that when we move away from the pavilion centre the handover happens latter and its duration is also longer. This is a direct consequence of the cell shape. In the laterals of the pavilion, the power level of BS2 is lower for the same distances and

3 The antennas were not designed specifically for the Aristides Hall sports pavilion, but for Pavilhão Atlântico in Parque das Nações in Lisbon, a pavilion with much larger dimensions.

therefore the handover happens later. Regarding the handover duration, it is directly related with the power of the destination cell. In general, if the power is higher the handover last less time.

Direction D12: 2nd handover

For the best coverage area, in average the handover takes place at a distance of 38.9 m and stops at 40.6 m. The duration is about 1579 ms and in 95% of the times, the handover durations are between 1111 ms and 2047 ms.

For the worst coverage area, the handover starts in average at 39.6 m and stops at 41.3 m. The handover average duration is 1533 ms, being 95% of the time between 1183 ms and 1882 ms.

It can be concluded that there is not much difference between the two coverage regions and this is because the second handover happens already nearby BS2 and in any case the signal is bad. In terms of duration and when compared with the 1st handover, it is longer. The power offered by the destination BS is always lower making the handover process more difficult.

Direction D21: 1st handover

For this direction and in the zone of better coverage the handover happens between 21.8 m and 20.1 m, with average duration of 1447 ms being 95% of the time between 1141 ms and 1752 ms. When compared with the previous direction, there is however a higher uniformity in the handover starting and finishing point.

In the worst zone the handover starts at 22.0 m and typically ends at 20.1 m, lasting for 1504 ms being 95% of the time between 1241 ms and 1766 ms.

Direction D21: 2nd handover

In this direction, much less 2nd handovers have occurred. The average duration was 662 ms for the central area and 1045 ms for the worst coverage area.

Seamless handovers

Although in this section it was presented handover duration figures relatively high leading to a non-seamless handover for non-real-time applications such as voice, there were situations were the handover has occurred almost instantaneously. An example is shown in Figure 7.44, for the central path with a different system configuration and for direction D12. A video transmission was performed to evaluate the impact of the handover and the interruption was almost unnoticeable.

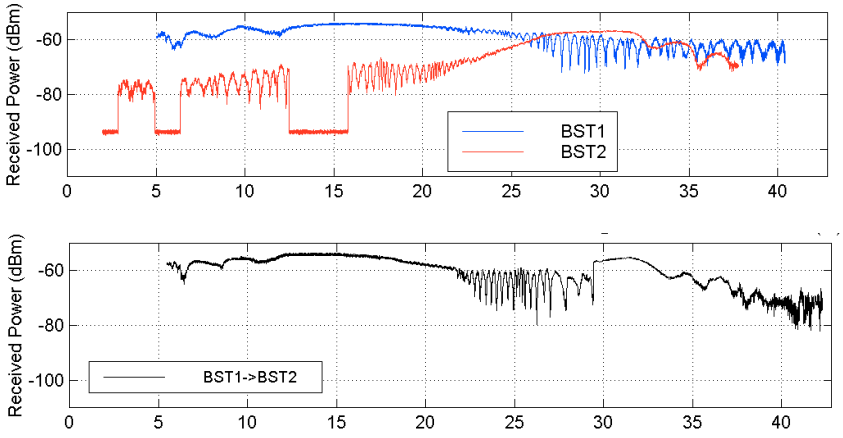

Figure 7.44: Cell coverage and seamless handover in direction D12 for the pavilion central path

4. Analysis by Simulation of Other System Configurations

Other system configurations were only evaluated by simulation, namely: a single BS placed in one of the small sides that covers all the sports pavilion (configuration C, also used for CIR measurements) and two BSs placed each one in the corners of the pavilion in its larger side (configuration D). In [7] [12] other configurations are analysed including the utilization of multiple BSs with the same frequency carrier to create artificially macro diversity.

As reported in section 2.5, in configuration A even when the BS antenna is tilted to 9º the time dispersion is still too large to be handled by the equaliser. To overcome the time dispersion problem, a system configuration with two BSs in each of the corners on the same side of the pavilion was tried. These results are shown in Figure 7.45 were both BSs antenna tilting angles are 9º in the elevation plane. For this configuration, the time

dispersion was kept under the equaliser limit of 250 ns (180 ns for this specific case). Moreover, as expected, the power distribution is much more uniform.

The second system configuration evaluated corresponds to the utilisation of a single BS to cover the whole pavilion, as in configuration A, but now placed in a similar location than Configuration B and is designated by configuration D. This scenario was used to test how would be the pavilion coverage with a single BS placed in a different location than in configuration A.

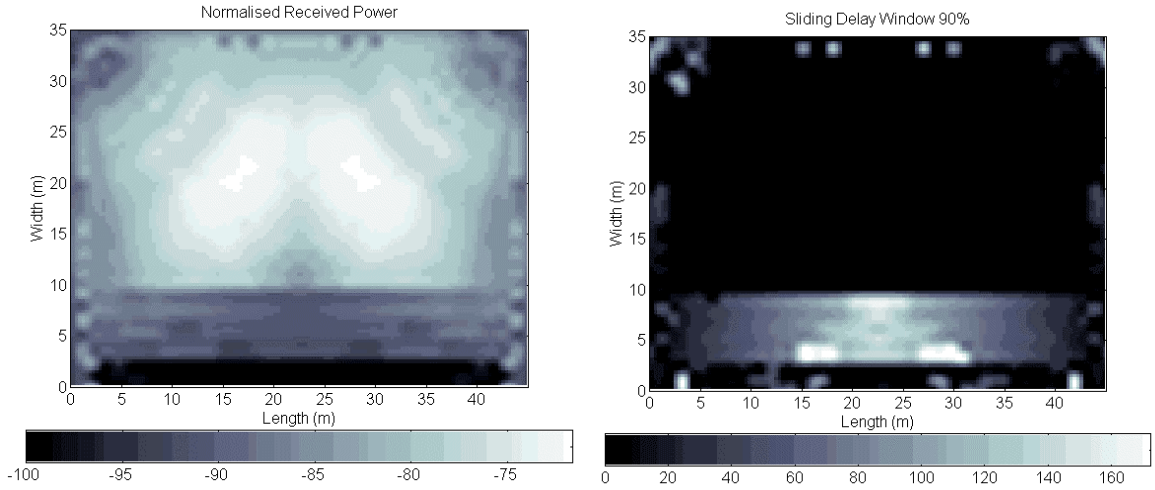

Figure 7.45: Simulation results for BSs at (1, 34, 6.5) m and (44, 34, 6.5) m and both rotated 9° in the elevation plane and 40° and 140º in the azimuth plane, respectively: NRP (left) and SDW90% (right)

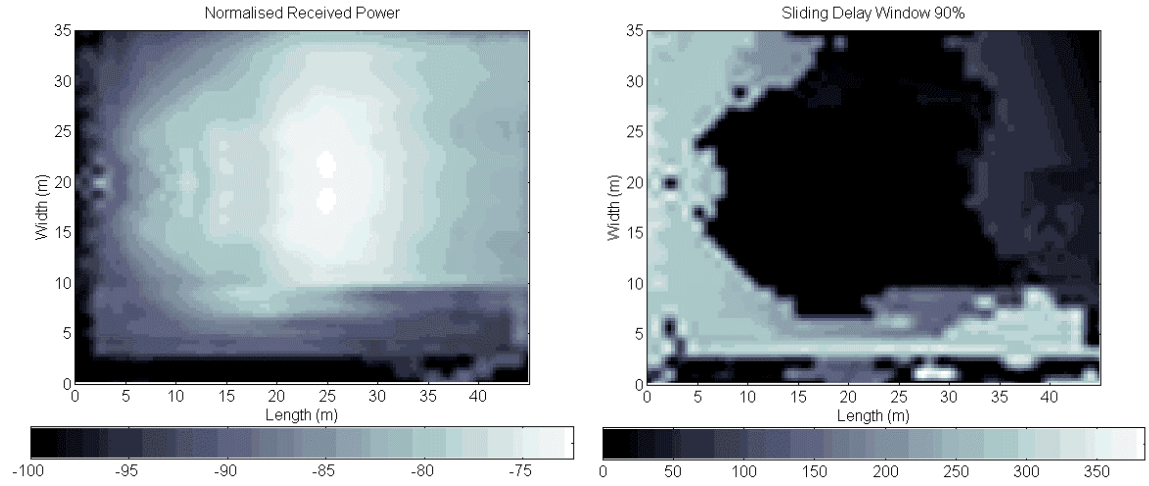

Figure 7.46: Simulation results with the BS located at (0.5, 20, 6.5) m and rotated 7° in the elevation plane: NRP (left) and SDW90% (right)

Based on the results we can conclude that multiple BS coverage is better than single since time dispersion is much lower. Locating the BSs in the pavilion corners and rotating the antennas by 9º, a good coverage exists, although worsening near the benches but guarantying time dispersion values within the limits of the equaliser. The reduction of the BS height, *per si*, did not show good results since the coverage becomes less uniform and the time dispersion remains quite high.

5. Summary and Conclusions

In this chapter were presented measurement results performed in a sports pavilion. The objective of the experiments was to evaluate key issues for mobile radio systems such as radio handover, cell coverage characteristics provided with the lens type antennas and the transmission performance including the impact of different system configurations. The BSs with the wide cell antenna were installed in different locations and the MT in a trolley and driven along several paths in the pavilion while data was acquired by the C&M system. The first measurements were performed with the BS in a corner of the pavilion to cover the whole area with a single cell pointing along the pavilion's diagonal (configuration A). The second configuration was used to evaluate the coverage with multiple cells and the handover algorithm. For that, two BSs were placed on each side of the pavilion (in the smaller side of the rectangle) each covering approximately half of it (configuration B). From the large amount of data collected during the experiments, a selection of representative paths for each system configuration was made and a detailed analysis presented. Moreover, simulations were performed based on the ray-tracing technique for these and other configurations and the parameters NRP and SDW90% evaluated.

Analysing the results of the lateral path R_A in configuration A it could be verified that the average power level is high, showing lower figures in the beginning and at the end of the path. Beyond 15 meters, the average power level decreases slowly. These facts can be explained by the BS antenna shaped radiation pattern. The small-scale fading depth is more pronounced in the end of the path than in the beginning due to the increase of the distance to the BS and the impact of important multipath components. Analysing the MRC signal it can be concluded that diversity reception was successfully used to mitigate the small-scale fading depth. Due to the lower small-scale fading depth than in the outdoor scenario

analysed in the previous chapter the diversity gain is not so high. The average power levels and the small-scale fading depth have shown a clear impact on the BER figures with worst performance in the beginning and at the end of the path. A maximum of two bit errors per byte was observed. The BER figures confirmed that the equaliser behaved as expected since they only exceeded the $5E10^{-3}$ in very few cases. In 90% of the cases the BER was lower than $1.5E10^{-4}$. The ARQ mechanism is also important for this scenario but much less than in the outdoor scenario. Two short path intervals, one at the beginning and another at the end of the path, were selected for fitting with the Rice distribution and a good match achieved. The Rice factor has shown higher value for the short path near the beginning of the path due to the stronger direct ray component. In terms of AFD and for the MRC signal, it ranges from 2 ms to 400 ms being slightly lower for the short path further away from the BS. In terms of LCR, the short path near the BS shows a higher figure for the two receiving channels since the small-scale fading depth is much less pronounced, reaching 35 crossings per second. However, and due to the diversity reception feature, the MRC signal for the path further away from the BS showed a higher LCR figure reaching 50 crossings per second.

The central path showed a good performance and comparing with the lateral path on the right of the pavilion, the average power level is higher and the BER figures lower. This can be explained due to the smaller distances to the BS and a more important contribution of the BS antenna shaped radiation pattern characteristic. The only exception is the end of the path where the power reduced significantly and hence an increase of the BER was observed due to the reach of the cell edge. For what concerns the third path analysed in configuration A, on the left hand side of the pavilion, the results compare very well with the path on the right side. Due to the fact that the beginning of the path is situated on the cell blank zone, the power level is lower than in the other paths and the BER higher. For all paths the behaviour of the equaliser was according to the specifications.

The transversal path showed an almost constant average power level since the distance to the BS does not change much. The small-scale fading depth is high for the whole path becoming more pronounced when the MT reaches the path end, approaching the boarder of the cell. Diversity was successfully used to mitigate the small-scale fading depth as can be seen by observing the MRC signal. The BER showed high values for the whole path due to

the bad conditions of the signal, specially caused by the high channel time dispersion. This path crosses one of the worst areas in terms of power levels, fading and signal time dispersion in the pavilion.

Simulation results were performed for the same scenario. A good match was achieved between the measured and simulated results showing that the simulation model, although not including all the objects in the scenario, is good enough to predict the power levels. Based on the analyses of the NRP and SWD90% parameters, various system configurations were tried in order to find one with better performance in terms of power distribution and time dispersion. Simulation tools have revealed to be very important to design the best system configuration for a specific scenario feeding also the requirements for the lens antennas design, leading to more uniformity in the power distribution, reducing the time dispersion and lowering the requirements in terms of equalisation needs.

In configuration B two BS were used to cover the pavilion and test handover. In a first step the cell coverage and transmission performance was studied individually for each BS. As for configuration A, only results for specific paths were presented. The length of BS1 cell is about 22.5 m and the average power level presented fluctuations in the beginning of the paths and deep fades towards the end (about half of the pavilion). The BER showed higher figures also in these zones of the paths. Up to two bit errors per byte were observed and for 90% of the cases the BER is below $1E10^{-4}$. The length of the BS2 cell is also 22.5 m. Comparing BS1 and BS2 cells it may be noticed that the peak of the power does not happen at the same distance from the BSs, being for BS1 17 m and 15 m for BS2 due to the different antennas tilting angles. In terms of BER a better performance was observed reaching $1E10^{-5}$ in 90% of the cases.

For the handover studies two different directions were defined due to the hysteresis and different characteristics of the cells. Observing the power levels provided by each cell, it can be seen that the cells are not symmetric. An overlap zone of approximately 10 m between the two cells was measured. The handover algorithm has shown a good performance in avoiding the “ping-pong” phenomenon since it could “resist” to the small-scale fading even if a better carrier was available. For what refers to the handover elapsed time, 0.62 s and 1.01s were observed for path C_B direction D12 and D21, respectively. By

analysing other paths (L_B and R_B) it can be concluded that the handover does not occur at the same distance form the BSs but depends on the specific characteristics of the link, as the algorithm indicates. In general the behaviour is similar to path C_B. Sometimes when the MT reached the end of the cell (nearby the BS tower) a 2nd handover occurred to the other BS. This is caused by the fact that nearby the towers there is a blank zone being the power from the other BS higher, leading to a handover. In terms of handover elapsed time figures of 0.37 s, 0.93 s, 1.63 s, 1.9 s, 2.07 s and 2.11 s were measured. In absolute terms and given the requirements of real time services, these figures are not good enough and improvements are required. Longer handover elapsed times were experienced for lower power levels because in these circumstances the synchronisation process to a different frequency carrier is unfavoured. The BER figures in handover situations were kept below the equaliser specification, showing its good operation.

Analysing now all the paths measured in the pavilion it can be concluded that the cell generated by BS1 is larger than the cell generated by BS2. This is due to the higher tilting angle used in BS2 antenna. The overlapping zone was also not selected optimally for all paths due to the distortion introduced in the coverage area by BS2. The attempting to compensate for the higher gain has revealed not recommended in terms of coverage. It was observed that the handover elapsed time increased as we move away from the central path. Comparing the performance in terms of coverage when considering configuration A and B, it can be concluded that a better coverage and BER is achieved using configuration B, being however more costly. For the best coverage area and direction D12, in average the handover took place at a distance of 26.8 m and stops at 27.9 m. The duration is about 0.807 s and in 95% of the times, the handover durations between 0.465 s and 1.148 s. For the worst coverage areas, the handover starts in average at 27.6 m and stops at 30.1 m. The handover average duration is 1.493 s, being 95% of the time between 0.595 s and 2.392 s, which indicates a quite large variation. For direction D21 and in the zone of better coverage the handover happens between 21.8 m and 20.1 m, with average duration of 1.447 s being 95% of the time between 1.141 s and 1.752 s. When compared with the previous direction, there is however a higher uniformity in the handover starting and finishing point. In the worst zone the handover starts at 22.0 m and typically ends at 20.1 m, lasting for 1.504 s being 95% of the time between 1.241 s and 1.766 s. Although handover duration figures

relatively high were found when compared with currently operated mobile systems, there were situations where the handover has occurred almost instantaneously. A video transmission was performed to evaluate the impact of the handover and the interruption was almost unnoticeable.

Two other configurations were evaluated by simulation recurring to the NRP and SDW90% parameters. With two BSs in the pavilion corners, the time dispersion is lower than in configuration A being kept below the equaliser limits and the power distribution much more uniform. The configuration with a single BS place in the centre of the pavilion presented time dispersions not compatible with the equaliser limit. In conclusion, multiple BS coverage has proved to be more adequate given the specifications of the mobile broadband system prototype, leading in general to more friendly conditions.

6. References

[1] Manuel Dinis and V. Lagarto, "Definition of the Trial Platform Infrastructure and Applications", CEC Deliverable Number – A204/PT/CET/DS/P/005/b1, September 1997. Submitted to EC in the framework of the ACTS/SAMBA project

[2] Manuel Dinis, V. Lagarto, M. Prögler, J.T. Zubrzycki, "SAMBA: a Step to Bring MBS to the People", ACTS Mobile Communication Summit '97, Aalborg, Denmark, October 1997

[3] Manuel Dinis, José Fernades, Max Prögler, Wolfgang Herzig, "The SAMBA Trial Platform in the Field", ACTS Mobile Communications Summit '99, 8th – 11th of June 1999, Sorrento, Italy

[4] Manuel Dinis and José Fernandes, "Provision of Sufficient Transmission Capacity for Broadband Mobile Multimedia: a Step Towards 4G", IEEE Communications Magazine, pp. 46-54, August 2001

[5] Susana Mota, Adão Silva, Manuel Dinis and José Fernandes, "Radio Transmission and Experimental Channel Characterisation Using an MBS Platform Operating in the 40 GHz Band", Wireless Personal Communications Journal, Issue 21:3, June 2002.

[6] Manuel Dinis and P. Jesus, "Evaluation Report of the Trials", CEC Deliverable Number – A0204/PTIN/SRM/DS/P/015/b1, October 2000. Submitted to EC in the framework of the ACTS/SAMBA project

[7] José Emanuel Ramos Pereira Garcia, "Cobertura Celular para Sistemas de Banda Larga", MSc Thesis, University of Aveiro, 2002

[8] N. Fukui, A. Shibuya and K. Murakami, "Performance of Combined ARQ with SR and GBN for Wireless Systems on a 40 GHz Band Radio Channel", IEEE Communication Magazine, pp. 122-126, September 2001

[9] José Fernandes, "Modelação do Canal de Propagação Rádio Móvel de Banda Larga na Faixa das Ondas Milimétricas e seu Impacto no Desempenho de Transmissão do Sistema", PhD Thesis, University of Aveiro, 1996.

[10] Filipe Matos and Nuno Oliveira, "Análise e Processamento de Medidas Experimentais Obtidas com uma Plataforma de Comunicações de Banda Larga MBS (Mobile Broadband System)", Final year project report, University of Aveiro, September 2001

[11] J. Fernandes and C. Fernandes, "Impact of Shaped Lens Antennas on MBS Systems", PIMRC 98 – 9th International Symposium on Personal, Indoor and Mobile Radio Communications, Boston, USA, Sept. 98

[12] J. Fernandes and J. Garcia, "Multiple Coverage for MBS Environments", PIMRC'2000, London, UK, September 2000

8th Chapter

Indoor Frequency Domain Channel Impulse Response Measurements and Analysis

1. Introduction

As already mentioned in previous chapters the accurate characterisation of the mobile radio channel is extremely important, since the knowledge of its properties enables the definition of robust techniques to mitigate the radio channel impairments. This is even more important for broadband channels where, for instance, the different frequency components of the signal are affected differently generating distortion [1].

In the literature many propagation and radio channel measurements studies in different scenarios and conditions can be found [2] [3] [4] [5] [6] [7] [8] [9] [10] [11] [12] [13] [14] [15] [16] [17]. However specifically in the 40 GHz frequency band and for mobile cellular

broadband systems, up to the author knowledge, measurements have not been performed before.

The radio channel can be seen as a time variant linear filter whose inputs and outputs can be described in the frequency, Doppler, delay and time domains. This leads to four possible transmission functions: the input delay-spread function $h(t,\tau)$ – time-delay domains, the output Doppler-spread function $H(f,\upsilon)$ – frequency-Doppler domains, the time-variant transfer function $T(f,t)$ – frequency-time domains, and the delay Doppler-spread function $S(\tau,\upsilon)$ – delay-Doppler domains, which are related via the Fourier transform (see chapter 2 for more details). The knowledge of any of these transmission functions is sufficient to characterise the radio channel [18]. The results here presented are based on measurements of the time-variant transfer function, for specific time instants, therefore considered static in the time domain and only dependent on the frequency domain - $T(f)$. The input delay-spread function $h(\tau)$ was obtained via mathematical processing.

This chapter starts with an introduction as background information to channel sounding techniques and signal processing, including the DFT (Discrete Fourier Transform) and type of windowing used and its impact in the dynamic range and time resolution. Section 2 focuses on analysis of the CIR gathered in the sports pavilion and the IT Room for several positions and locations and results are presented for different situations: with and without LoS, uplink and downlink directions, impact of the antenna type and diversity receiving channels (some are only available for the pavilion). PDPs (Power Delay Profile) were calculated for all positions/locations and compared with ray tracing simulation results, considering different degrees of complexity for the scenario model and different reflection order for the rays (between 4 and 6). From the PDPs, various parameters were calculated: NRP, DS and $\bar{\tau}$. These results are presented in Section 3.

1.1 Radio channel measurements techniques

The selection of a technique that enables measuring any of the referred transmission functions depends on the complexity and the exact parameters that we want to obtain. The measurements can be performed in the time, delay, frequency or Doppler domains. Three techniques are usually employed [19] [17]:

- **Periodic pulse technique** – This is the simplest technique, at least conceptually. It consists in the transmission of a sufficiently narrow pulse (time domain) and to observe the received signal. The received signal is the convolution of the channel impulse response with the transmitted pulse. Critical are the repetition period and the duration of the pulse. The first must be sufficiently fast to register the time variation of the channel, but, on the other hand, should allow sufficient time between pulses to register the necessary echoes (with reasonable amplitude) arriving via multipath propagation without overlap. The maximum propagation delay is therefore set by the pulses repetition period. The pulse duration is directly related with the time and spatial resolution of the measurements since it determines the minimum time interval between two echoes that it is possible to receive individually. This technique allows also Doppler shift measurement if a coherent modulation technique is employed. The major limitation of this technique is the high peak power required to obtain a good signal to noise ratio in the receiver side.

- **Pulse compression technique** – If we apply white noise to the input of a linear system and if we correlate the output with a delayed replica of the input signal of τ seconds, the result is proportional to the system impulse response, for τ seconds. This technique can therefore be used to measure the radio channel impulse response, if white noise can be generated and transmitted across the radio channel. Usually binary pseudo noise sequences are used to emulate white noise. The sliding correlator technique is based in this principle and uses a pseudo noise sequence in the receiver with a different frequency (different duration of the pulses) to enable the expansion of the testing pulses.

- **Frequency sweeping technique** – This method consists in transmitting several carriers to a receiver, to cover the whole bandwidth of the system, which registers their amplitude and phase. It is therefore a frequency domain technique enabling the measurement of the channel transfer function. The low pass channel impulse response can then be obtained via the IDFT (Inverse Discrete Fourier Transform). The time resolution depends on the measurements bandwidth and the type of window used to truncate the frequency domain response. The disadvantage is the

fact that it does not allow the measurement of the Doppler shift since during the measurements the receiver and the environment must be static [20].

The frequency sweeping technique was selected to perform the measurements presented in this chapter since it enabled to use part of the hardware already developed for the Trial Platform [21] [22]. The Trial Platform was not specifically designed to perform this type of measurements and therefore a different configuration had to be used. The MHs in conjunction with some other laboratory equipment were used to complete the experimental set-up.

1.2 Fourier transforms and windowing

The discrete transfer function of a system can be obtained via the DFT from its discrete impulse response. On the other hand, the IDFT allows the calculation of the impulse response knowing the transfer function. Considering that computers cannot handle infinite sequences and that abrupt time transitions generates high frequency components some techniques have to be used to bypass these two problems. For the first, a finite approximation is required and therefore a truncation to the ideal response *h(n)* outside the interval $0 \le n \le N\text{-}1$ is required. This is shown in equation (8.1) where $h_T(n)$ is *h(n)* truncated to N samples. This operation is equivalent to the multiplication of the ideal impulse response *h(n)* by a rectangular (Dirichlet) window *w(n)* as defined by (8.2) [23] [1]. The Fourier transform $H_T(k)$ is therefore given by equation (8.3).

$$h_T(n) = \begin{cases} h(n), & n = 0,1,...,N-1 \\ 0, & \text{Others} \end{cases} \tag{8.1}$$

$$w(n) = \begin{cases} 1, & n = 0,1,...,N-1 \\ 0, & \text{Others} \end{cases} \tag{8.2}$$

$$H_T(k) = \sum_{n=0}^{N-1} h(n)w(n)e^{-j2\pi nk/N} = \sum_{n=0}^{N-1} h_T(n)e^{-j2\pi nk/N} \tag{8.3}$$

The multiplication of *h(n)* by *w(n)* can be seen in the frequency domain as a convolution of *W(k)* with *H(k),* where *W(k)* is the DFT of *w(n)*. This convolution is what originates the Gibbs phenomenon [24]. This phenomenon can also be seen as the impact of performing abrupt truncations and the consequent introduction of frequency components not existing the in original signal. The number of samples N, when too low, may also cause the aliasing

phenomenon [25]. Hereafter, $H_T(w)$ and $h_T(n)$ will be designated by the transfer function (or frequency response) and CIR of the system, respectively. The T subscript will be removed from now on as illustrated in equations (8.4) and (8.5). Thus, these equations are approximations of the system transfer function and CIR since they are dependent on the type of window used to perform the truncation, being directly applicable to finite and casual sequences.

$$H(k) = \sum_{n=0}^{N-1} h(n) e^{-j2\pi kn/N} \qquad 0 \le k \le N-1 \tag{8.4}$$

$$h(n) = \frac{1}{N} \sum_{k=0}^{N-1} H(k) e^{j2\pi kn/N} \qquad 0 \le n \le N-1 \tag{8.5}$$

The calculations of the DFT and IDTF can be done using the FFT (Fast Fourier Transform) algorithm [24] [25]. Since the DFT is by definition obtained by sampling one period of the Fourier Transform with N samples, therefore $H(k)$ is also a periodic function. Moreover, after the sampling process, $h(n)$ becomes also periodic with N samples.

The minimisation of the Gibbs phenomenon is achieved using special truncation windows. The selection of the type of window to be used depends on the necessary trade-off between the window main lobe width and amplitude of its secondary lobe. Thus, a better time resolution implies higher amplitude of secondary lobes and therefore a lower dynamic range.

Windows of the type $\cos^{\alpha}(x)$ have good characteristics and within this family, windows with the coefficients shown in (8.6), offer even better results [23]. According to (8.6), we can obtain windows of whatever number of terms m, however to obtain windows with a main lobe not too narrow, M should be restricted to a small integer value, being 3 or 4 reasonable figures.

$$w(n) = \sum_{m=0}^{M} (-1)^m a_m \cos\left[\frac{2\pi}{N} mn\right], \quad n = 0,1,\ldots,N-1 \tag{8.6}$$

Blackman has studied windows with $M = 3$ [23]. Re-writing (8.6) for $M = 3$ leads to (8.7).

$$w(n) = a_0 - a_1 \cos\left(\frac{2\pi}{N} n\right) + a_2 \cos\left(\frac{2\pi}{N} 2n\right) \quad n = 0,1,\ldots,N-1 \tag{8.7}$$

Blackman-Harris windows are based on Blackman windows optimised by Frederic Harris for harmonic analysis [23]. He has derived windows with 3 and 4 terms with secondary lobes amplitude of –67 dB and –92 dB, respectively. Table 8.1 shows some Blackman-Harris window coefficients for 3 and 4 terms.

The time resolution, after application of the truncation window, is given by the product of the number of window terms and the resolution obtained before window truncation (1/B), being B de system bandwidth [23]. Table 8.2 shows the time resolutions and the secondary lobs amplitude that can be obtained for the Blackman-Harris and rectangular windows.

Coefficients	3 terms (-67 dB)	4 terms (-92 dB)
a_0	0.42323	0.35875
a_1	0.49755	0.48829
a_2	0.07922	0.14128
a_3	---	0.01168

Table 8.1: 3 and 4 terms Blackman-Harris windows coefficients

A Blackman-Harris window with 3 terms and the rectangular window were selected for the work presented in this chapter. This selection was based on the fact that the rectangular window has the best time resolution, but the worst effect in terms of the dynamic range, and the Blackman-Harris 3 terms window shows a reasonable compromise between the secondary lobes amplitude and the degradation of the time resolution. Both windows were used in all CIR calculations.

Window type	Secondary lobes (dB)	Time resolution (s)
Rectangular	-13	(1/B)
Blackman-Harris 3 terms	-67	3x(1/B)
Blackman-Harris 4 terms	-92	4x(1/B)

Table 8.2: Secondary lobes and time resolution degradation after windowing

2. CIR Measurements Analysis

The next sections show the most relevant results for each experiment type made in the pavilion and in the IT Room [26] [27]. In the sports pavilion the configuration C described

in chapter 5 was used for the measurements. In the same chapter is also described the configuration used for the IT Room.

2.1 Sports pavilion measurements

2.1.1 Analysis of position measurements for a given location

As described in chapter 5, 35 measurements were performed for each location and therefore the global system transfer function was obtained by first averaging five transfer functions collected for the same position (to eliminate random components) and subsequently by averaging the seven positions transfer functions (7x5). The same procedure could also be performed in the time domain after calculating all the CIRs.

In this section is analysed the impact of having performed measurements in several positions for the same location with a spatial separation of a distance slightly greater than the wavelength. Although the distance is quite small (7.83 mm) there are in fact differences in the frequency response and consequently in the impulse response, as predicted by the theory.

Two positions from two different locations, one belonging to an area that is part of the cell and another outside the cell coverage area are here displayed and analysed in more detail. Table 8.3 shows the PDP parameters for locations 2 and 7, using the 3 terms Blackman-Harris window. For location 2 the four parameters are very similar for the seven positions. The only position that deviates more is position 3. For all the others the deviation is small. For location 7 the parameters have a larger variation.

Figure 8.1 shows the frequency response phase and magnitude for positions 3 and 7 from location 2 therefore belonging to the cell coverage area. Figure 8.2 shows the CIRs for the same positions and location in dB and linear units. Making a visual inspection to the frequency responses for the two positions of location 2, they have a similar behaviour in the entire band, clearly showing selective fading. The CIRs reflect also the similarities of the frequency response showing a similar shape. For position 3 the width of the “direct ray” is larger.

Figure 8.3 shows the frequency response phase and magnitude for positions 3 and 6 from location 7 therefore not belonging to the cell coverage area and Figure 8.4 shows the CIRs for the same positions and location in dB and linear units. The differences are much more evident, justifying also a major discrepancy in the PDP parameters. The same is evident for the CIRs since the location outside the cell has a less strong direct ray, leading to a lower NRP and a larger DS, as expected.

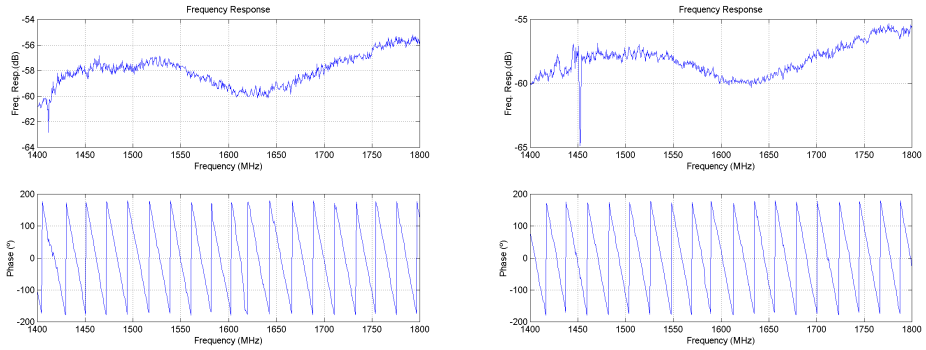

Figure 8.1: Frequency response for location 2: position 3 (left) and 7 (right)

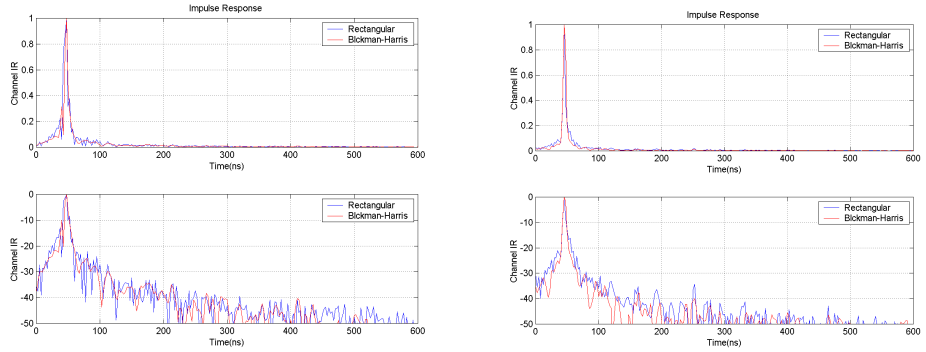

Figure 8.2: CIR for location 2: position 3 (left) and 7 (right)

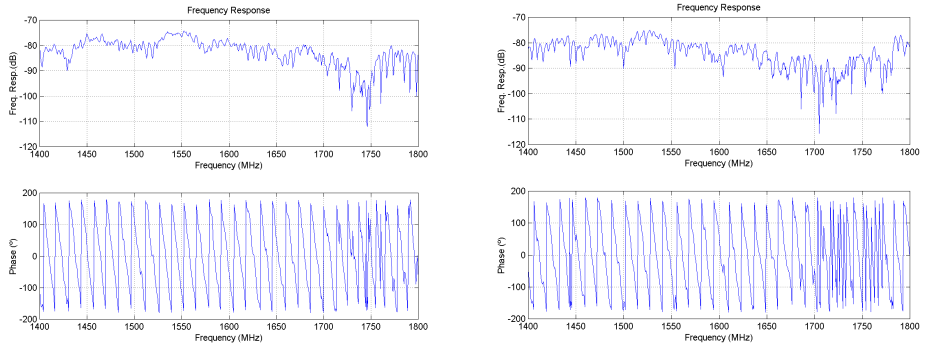

Figure 8.3: Frequency response for location 7: position 3 (left) and 6 (right)

There is also a difference between the CIR obtained using a rectangular window and the Blackman-Harris window, as expected, due to the different characteristics of the windows (see Figure 8.5). This difference is also reflected in the respective PDP parameters.

In summary, there is in fact a difference for all positions but for positions inside the cell they are less significant. Moreover, in statistical terms, it was verified that the differences were not so substantial, reason why this technique was not used for the measurements in the IT Room, facilitating the measurements procedures. The windows impact also exists and is unavoidable. For this reason all the CIRs were calculated with two different windows and the results analysed for both cases, although sometimes only the results for a particular window are shown.

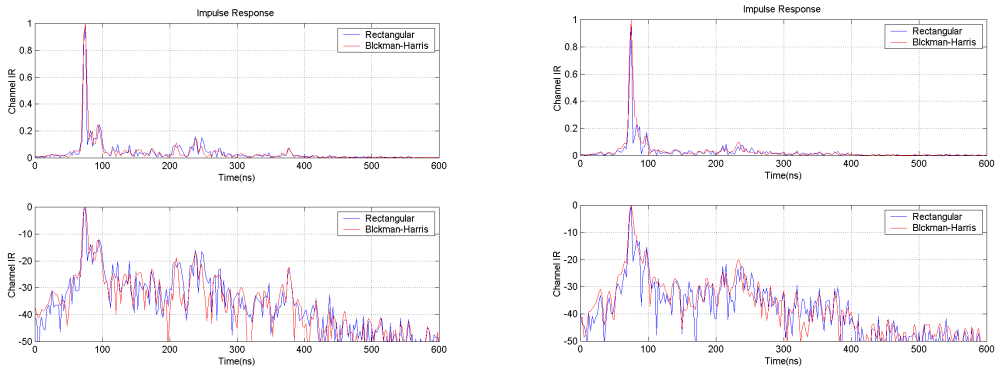

Figure 8.4: CIR for location 7: position 3 (left) and 6 (right)

Positions	NRP (dB)		DS (ns)		$\bar{\tau}$ (ns)	
	Loc 2	Loc 7	Loc 2	Loc 7	Loc 2	Loc 7
1	-64.27	-87.29	10.93	48.38	49.51	93.38
2	-64.29	-85.00	11.11	43.46	49.35	90.75
3	-65.75	-89.17	17.81	56.29	53.10	99.04
4	-64.41	-87.87	10.75	53.03	49.32	96.27
5	-64.32	-88.18	10.81	52.23	49.42	96.45
6	-64.31	-85.93	11.70	37.26	49.80	87.90
7	-64.42	-87.38	10.69	46.61	49.26	93.48

Table 8.3: PDP parameters using the Blackman-Harris for location 2 and location 7

2.1.2 Analysis of LoS operation

In this section are analysed the 11 locations that were measured inside the sports pavilion in LoS conditions. Here and beyond, all the results presented are based on the spatial averaging of all positions in the same location.

Figure 8.6 shows the CIR for location 2 and 7 and Figure 8.7 for location 3 and 9 after spatial averaging. There is a clear correlation between the locations and the shape of the CIR. For locations outside the cell main coverage area, the direct ray relative strength is lower when compared with the reflected rays. Moreover, there are many more reflected rays with relevant power, leading to an increase of the DS.

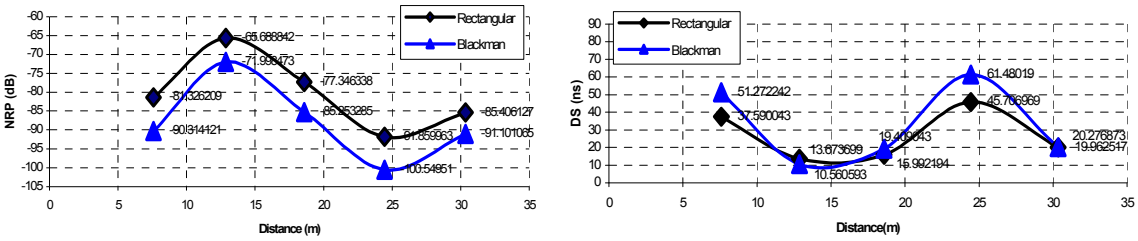

Figure 8.5: Central path NRP (left) and DS (right) obtained with two different windows

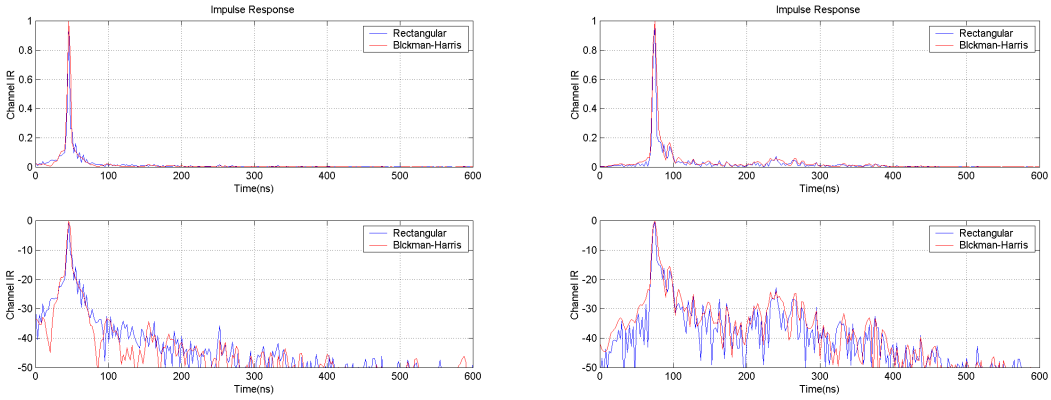

Figure 8.6: CIR for location 2 (left) and 7 (right) with the seven positions averaged

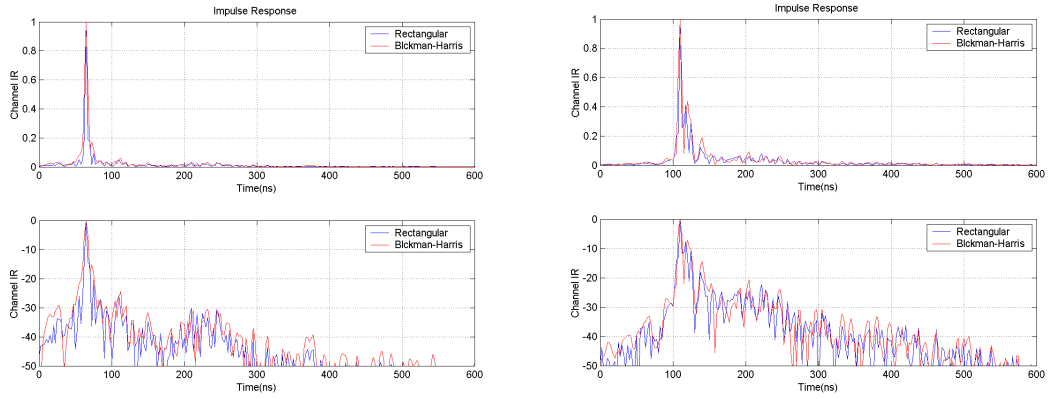

Figure 8.7: CIR for location 3 (left) and 9 (right) with the seven positions averaged

Table 8.4 presents the NRP, DS and $\bar{\tau}$ parameters obtained from the PDP using both a rectangular and a Blackman-Harris window in LoS conditions. It can be easily verified that the PDP parameters have different values if a rectangular or a Blackman-Harris window is used. Concerning the NRP, one may conclude that the values obtained with a Blackman-Harris window are always lower than the ones obtained with a rectangular window. This fact is due to an attenuation penalty in the PSD of the signal resulting from the multiplication of the original frequency response by the Blackman-Harris window. As can be seen from the table, the differences between the NRP values obtained with the two windows vary from 4 to 9 dB and are in range of the difference between the energies of both windows. There are also differences in the time dispersion parameters but these differences do not follow any special rule or common behaviour. This is due to the different windows time resolution and the different amplitudes of the multipath components caused by the attenuation of the PSD of the signal after multiplying by the Blackman-Harris window.

2.1.3 Impact of link obstruction by a metal plane (Non LoS)

Table 8.5 shows the parameters but for non LoS for the locations where this type of measurements were performed. Analysing LoS and non LoS propagation it is quite clear from the table that there is a significant decrease of the NRP values and an increase of the channel time dispersion in non LoS conditions.

Locations	NRP (dB)		DS (ns)		$\bar{\tau}$ (ns)	
	BH	Rect	BH	Rect	BH	Rect
1	-90.31	-81.33	51.54	38.18	43.95	37.76
2	-70.00	-65.69	11.72	15.40	49.40	49.73
3	-85.25	-77.35	20.07	16.95	70.82	69.72
4	-100.55	-91.86	61.56	45.84	119.97	102.51
5	-91.10	-85.41	20.68	20.46	112.49	112.41
6	-93. 60	-85.63	49.43	39.34	58.41	53.63
7	-91.93	-86.44	35.22	35.40	86.72	86.01
8	-91.65	-84.93	35.47	32.78	105.13	103.97
9	-94.43	-88.18	27.93	28.32	122.55	121.63
10	-91.79	-86.71	39.36	43.04	55.70	57.89
11	-91.66	-87.69	31.25	37.25	85.26	87.89

Table 8.4: LoS seven positions average PDP parameters for the Blackman-Harris window and the rectangular window

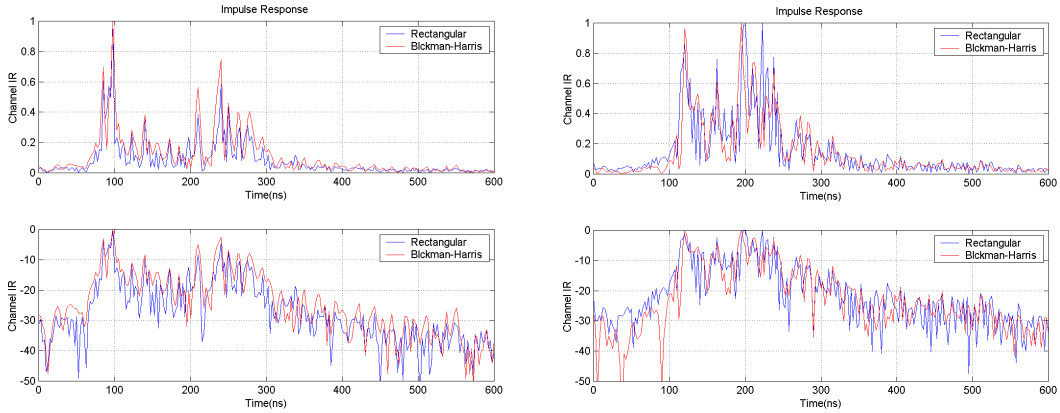

Figure 8.8: Non LoS CIR calculations for location: 7 (left) and 9 (right)

2.1.4 Comparison of uplink and downlink directions

All the results presented so far were obtained for the downlink direction and therefore measured in the MT side. The results presented in this section are relative to the uplink direction, for LoS and non LoS, for location 9, measured at the BS side.

Locations	NRP (dB)		DS (ns)		$\bar{\tau}$ (ns)	
	BH	Rect	BH	Rect	BH	Rect
7 non LoS	-99.90	-93.67	97.67	97.67	97.67	80.35
8 non LoS	-103.73	-96.27	75.11	75.11	75.11	59.99
9 non LoS	-107.91	-101.09	83.78	83.78	83.78	87.46
11 non LoS	-97.67	-94.15	17.67	17.67	17.67	23.68

Table 8.5: PDP parameters for locations in non LoS

Analysing the results obtained for the downlink direction and comparing them with the CIRs obtained for the uplink (Figure 8.9), there is a clear difference. This is justifiable by the fact that the wavelength is different (another frequency band) and therefore the rays in the CIR can in fact be different, due to the phase component that is used to sum all the rays that fit in the same time bin. Moreover, the fact that it is a different frequency band also affects the attenuation aspect. This shows clearly that using the channel quality information in one direction for the other may not be effective since we are in presence of a different radio channel. This is a fact to be taken into account when dealing with FDD systems.

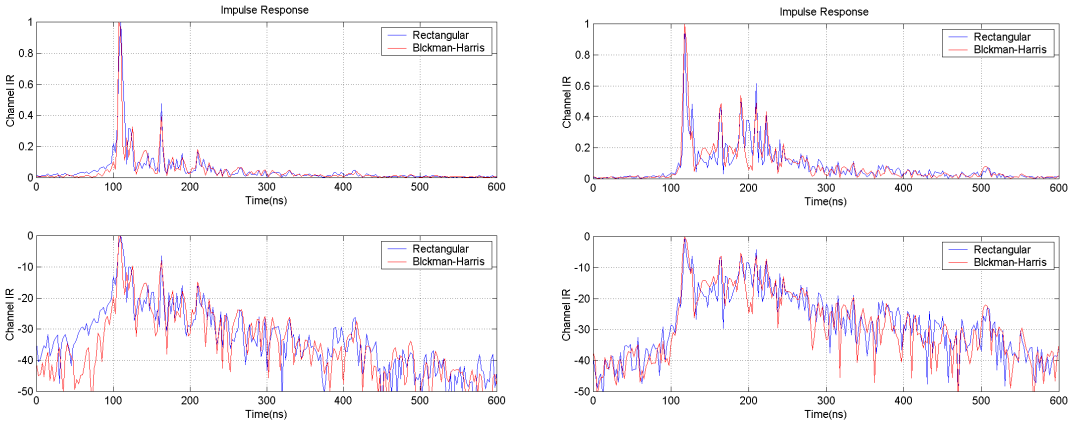

Figure 8.9: Uplink direction CIR for location 9: LoS (left) and non-LoS (right)

2.1.5 Impact of antennas type in the MT

All the measurements were made with the Wide cell antenna in the MT. To test the impact of a different antenna in the MT, the CIR was measured with the Elongated antenna also in position 9 (Figure 8.10). Comparing with

Figure 8.7, it can be concluded that the direct ray is much more attenuated and that there are other multipath components that reach the MT with approximately the same power. This is justified due to the fact that this antenna is much more directive than the wide cell antenna.

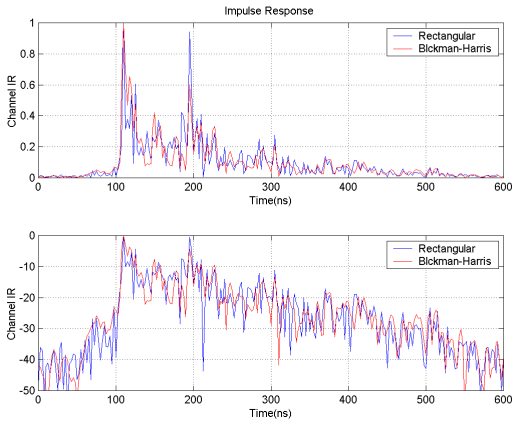

Figure 8.10: CIR obtained with the Elongated cell in the MT

2.1.6 Comparison of RX1 and RX2 reception

The hardware system has the diversity reception feature being therefore equipped with two receiving channels. All the measurements were done for channel 2 (RX2). In this section the two receiving channels are analysed and compared for LoS and non LoS.

Figure 8.11 shows the CIR for the RX1 channel in LoS and non LoS for position 9. Comparing with the RX2 CIRs, it can be concluded that the LoS case, although similar, it still shows reflected rays with more relative power. For non LoS situation, the differences are much more evident. This leads to the conclusion that the antenna separation used for the diversity reception is in fact enough to generate a radio channel with different characteristics.

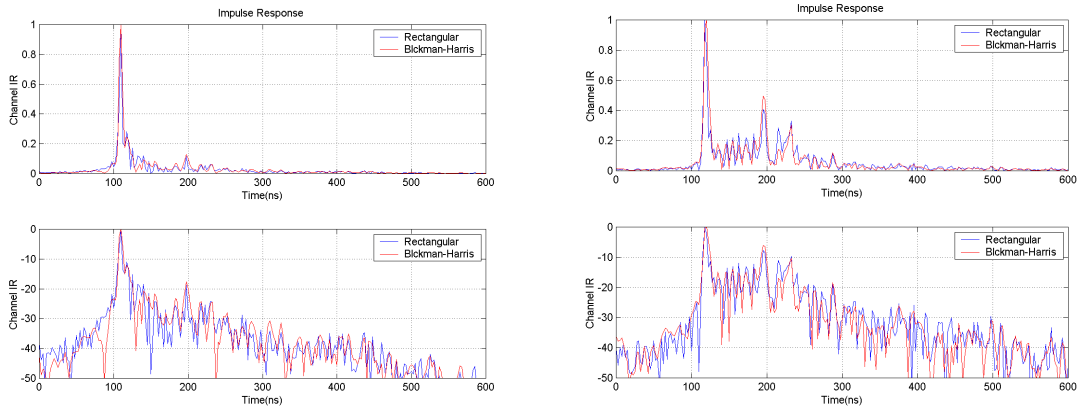

Figure 8.11: RX1 channel CIR: LoS (left) and non LoS (right)

2.2 IT Room measurements

The next sections show the most relevant results for the experiments made in the IT Room. All results presented in this section are based only in 5 measurements for each location and not 35 as in the case of the pavilion. This fact has enabled the collection of much more measurements in different locations (64 locations) in the room in a shorter time.

Out of the 64 locations four were selected for a deeper analysis, namely: 13, 27, 31 and 53. Location 13 and 53 are in the border of the cell in the lateral. Location 27 is inside the cell coverage area (good power level) and 31 also in the border but at farther distance and

different direction (more aligned with the BS). Los and non LoS conditions are analysed for these locations.

2.2.1 LoS analysis

Based on the CIR measured for 64 locations for both LoS and non LoS propagation conditions, power and time dispersion parameters distributions could be obtained in a 5.6 m × 5.6 m surface corresponding to the grid sketched in chapter 5 (8 rows by 8 columns matrix). Moreover, the CB was also obtained for 0.5 and 0.9 coherence levels.

In order to have an overall view, the experimental results were processed in MatLab resulting in the graphs displayed in Figure 8.12 where the NRP, DS and CB parameters are shown for LoS. The NRP shows its maximum towards the end of the room and the minimum nearby the BS. The DS distribution shows its larger values in the cell's boundaries where the NRP is also the lowest. Although results were also obtained for the $\bar{\tau}$, they are not shown in the figure because this parameter has a similar behaviour as the DS and therefore the conclusions derived for the DS are generally applicable to it.

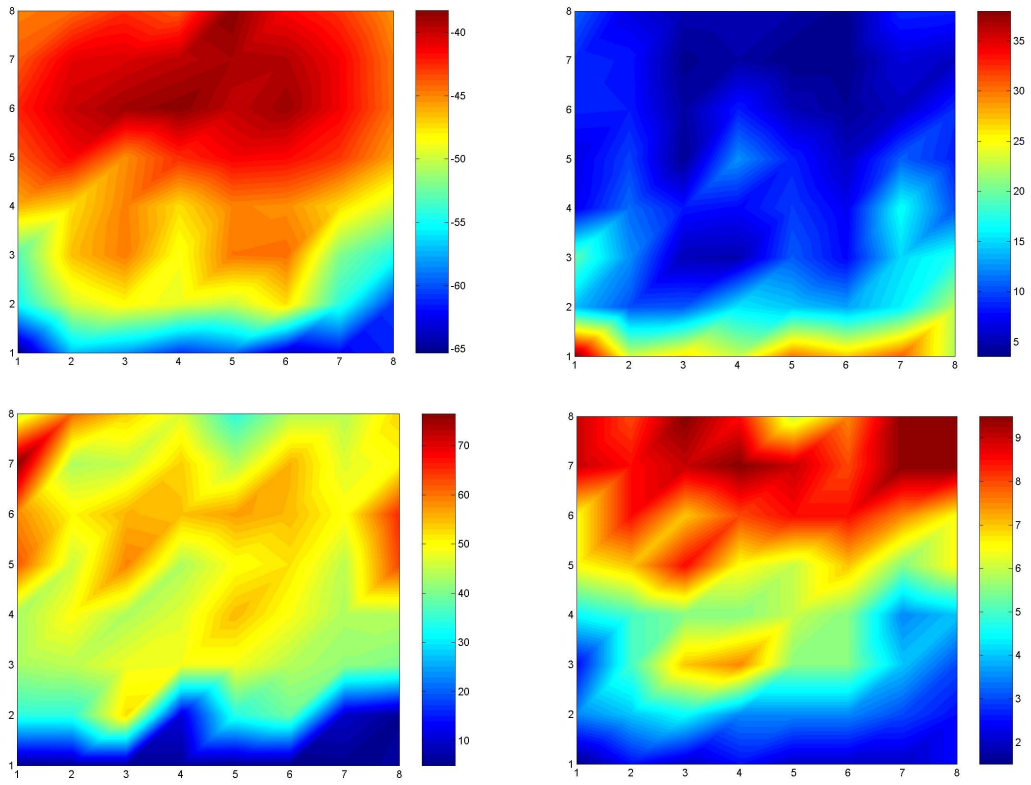

Figure 8.12: LoS NRP (dB) (top left) and DS (ns) (top right) and CB 0.5 (MHz) (bottom left) and CB 0.9 (MHz) (bottom right)

The CB has also its minimum nearby the BS. The larger values occur where good power conditions exist, although there is not a complete match between power and CB levels, indicating that there is not a direct relationship between both parameters. There is however a better match for the coherence level of 0.9 with the NRP.

In Figure 8.13 are shown de CIRs for four specific locations inside the room. Out of the four, location 31 is the one with highest power. Observing its impulse response, it is clear the dominance of the direct ray. Reflected rays have a power level below 20 dB relatively to the direct ray. Locations 13 and 53 show a similar CIR because they are more or less in a symmetrical position in the room and relatively to the BS. Since they are in the border of the cell, reflected rays are more visible. Finally location 27, closer to the BS, shows some reflected rays but with a lower relative power.

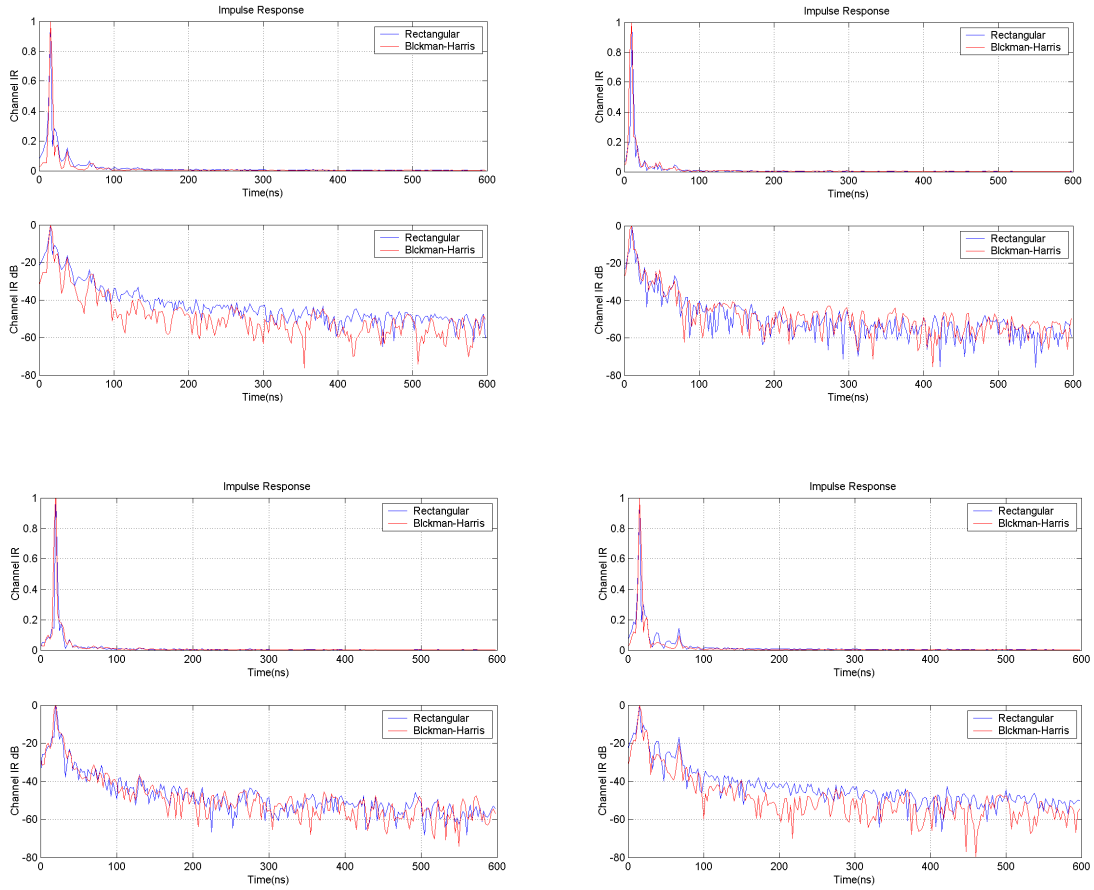

Figure 8.13: LoS CIR for locations: 13 (top left), 27 (top right), 31 (bottom right) and 53 (bottom left)

Table 8.6 shows the PDP parameters for the four locations. Clearly the location with highest NRP and lowest time dispersion is location 31, as expected and the CIR indicated. Parameters for locations 13 and 53 are very similar. Location 27 has the lowest NRP level and time dispersion parameters equivalent to locations 13 and 53. The parameters confirm what was observed by direct inspection of the CIR graphics.

Locations	NRP (dB)		DS (ns)		$\bar{\tau}$ (ns)	
	BH	Rect	BH	Rect	BH	Rect
13	-50.44	-41.47	5.73	9.73	4.02	7.14
27	-57.60	-48.67	4.60	4.99	2.37	3.55
31	-48.07	-39.78	4.22	4.60	2.34	1.08
53	-51.42	-42.86	6.14	10.81	4.09	5.30

Table 8.6: LoS PDP parameters for the Blackman-Harris and the rectangular windows for locations 13, 27, 31 and 53

2.2.2 Non LoS analysis

The distributions of the NRP, DS and CB values measured for a non LoS propagation condition are depicted in Figure 8.14. The obstruction of the LoS was obtained by inserting a metal plane in between the BS and the receiver (MT). The parameters show now a much more uneven distribution inside the room and the antenna radiation pattern is no more identifiable by direct inspection of the graphics. The minimum power level does not occur nearby the BS since the direct ray is reflected by the metal plane and sent back in the direction of the BS. This fact has also impact on the DS and CB parameters.

Comparing Figure 8.13 and Figure 8.15 it is now visible an increase in the number and amplitude of the reflected rays as expected. As presented in Table 8.7, The NRP is lower and the time dispersion parameters have increased considerably due to the impact of the reflected rays in the CIR. The lowest power is received in location 31 and the highest in location 13. Location 31 shows also the highest figure for the DS which is justifiable due to the fact that is the location more apart from the BS (longer travelling distances for the reflected rays).

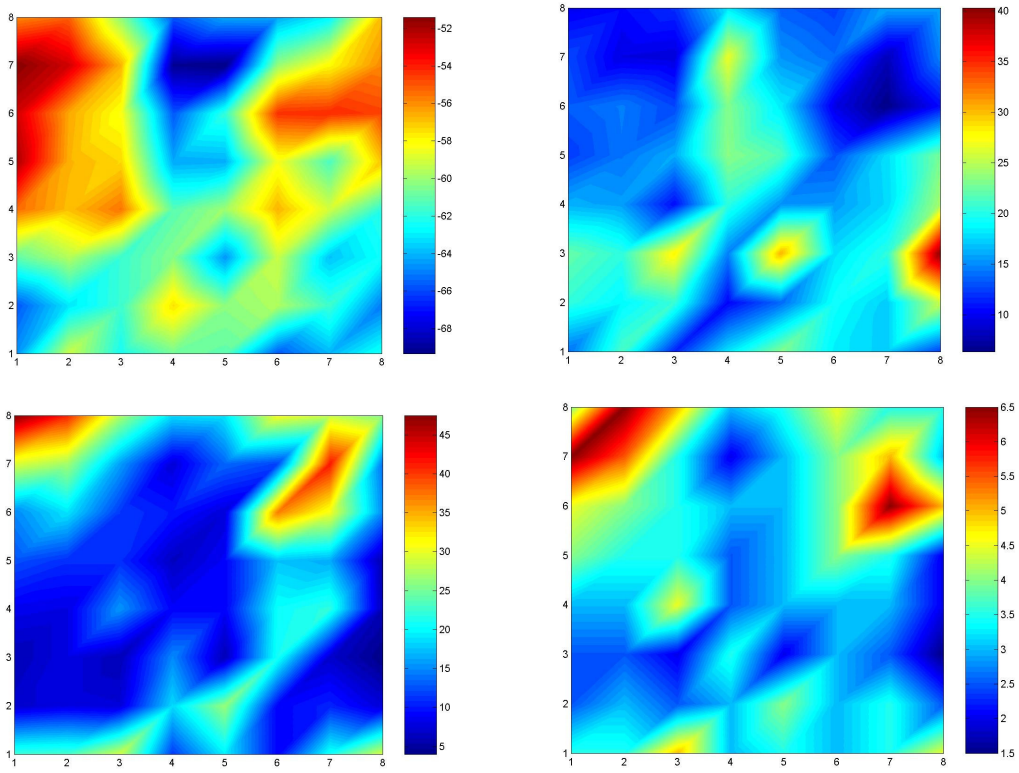

Figure 8.14: Non LoS NRP (dB) (top left) and DS (ns) (top right) and CB 0.5 (MHz) (bottom left) and CB 0.9 (MHz) (bottom right)

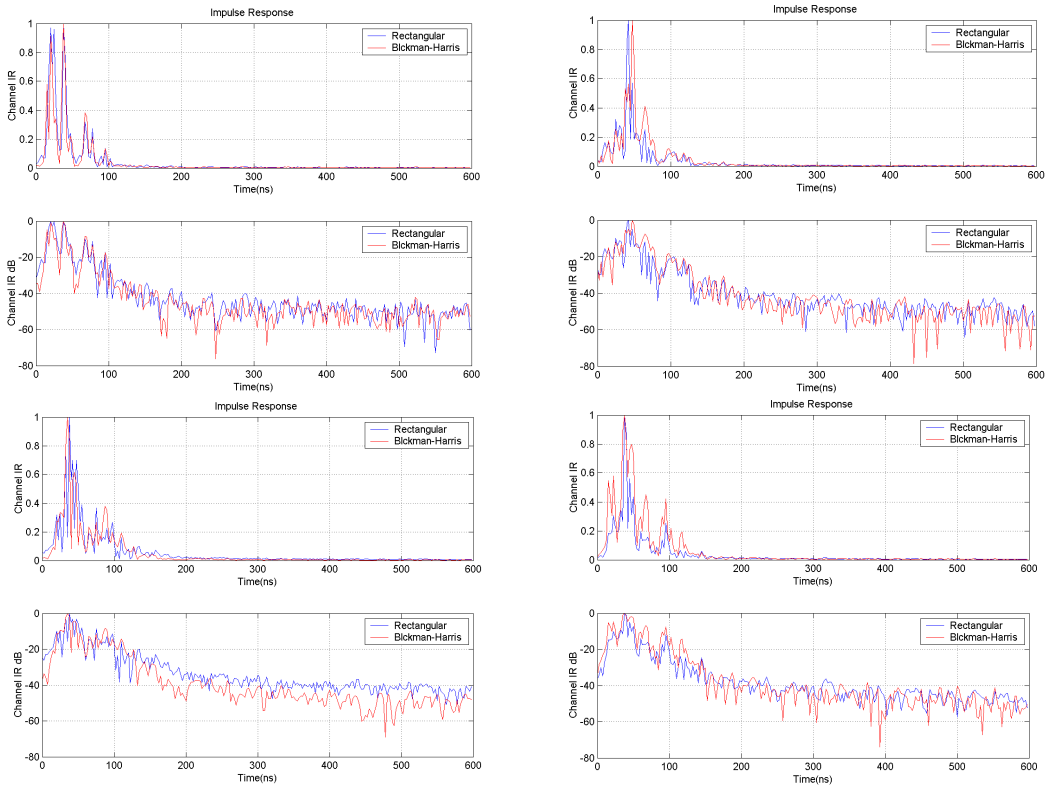

Figure 8.15: Non LoS CIR for locations: 13 (top left), 27 (top right), 31 (bottom right) and 53 (bottom left)

Locations	NRP (dB)		DS (ns)		$\bar{\tau}$ (ns)	
	BH	Rect	BH	Rect	BH	Rect
13	-65.68	-56.66	16.17	14.23	18.45	15.98
27	-70.25	-60.34	15.17	14.67	24.76	18.71
31	-76.43	-69.12	22.35	26.69	26.45	30.39
53	-73.05	-61.40	21.10	17.79	30.37	20.44

Table 8.7: Non LoS PDP parameters for the Blackman-Harris and the rectangular windows for locations 13, 27, 31 and 53

3. CIR Simulations versus Measurements

3.1 Sports pavilion

3.1.1 Scenario modelling

Several simulation models were used in this study, due to the complexity of the pavilion in terms of metal and concrete structures, but results will be presented only for four of them[1]. As can be seen in chapter 5 the scenario is very complex, due to computational constraints, the models complexity levels become critical and some compromises have to be done. These models differ in its complexity level, which rises from moderate to high because, although low complexity models proved in previous chapters to be suitable for coverage studies (NRP), they are very poor for more in-depth CIR studies, like comparing the simulated and measured PDPs.

Nevertheless, the analysis of the PDP performed in this section for different locations, corresponding to different coverage regions, allows an in-depth evaluation of the simulation model and to clearly identify its main advantages and limitations in coverage studies. Moreover, the comparison of measured data and simulation results obtained with several models with different complexity levels, allows an evaluation of their suitability to represent such a complex scenario.

Four models have been used to characterise the indoor sports pavilion. Models 1, 2 and 4 neglect the concrete columns in the walls considering them plain surfaces, but consider the metallic structure of the ceiling, modelled in three slightly different ways. Model 1, shown in Figure 8.16, considers the ceiling structure as being two metallic planes, one

1 A rectangular window was used for this study.

horizontal, 0.45 m width and the other vertical with 1 m high. Model 2 considers only the horizontal planes and Model 4 reduces the vertical planes height to 0.5 m. Model 3 considers the metallic structure as in Model 2 but includes the concrete columns as depicted in Figure 8.17, where the metallic planes modelling the ceiling structure can be easily identified.

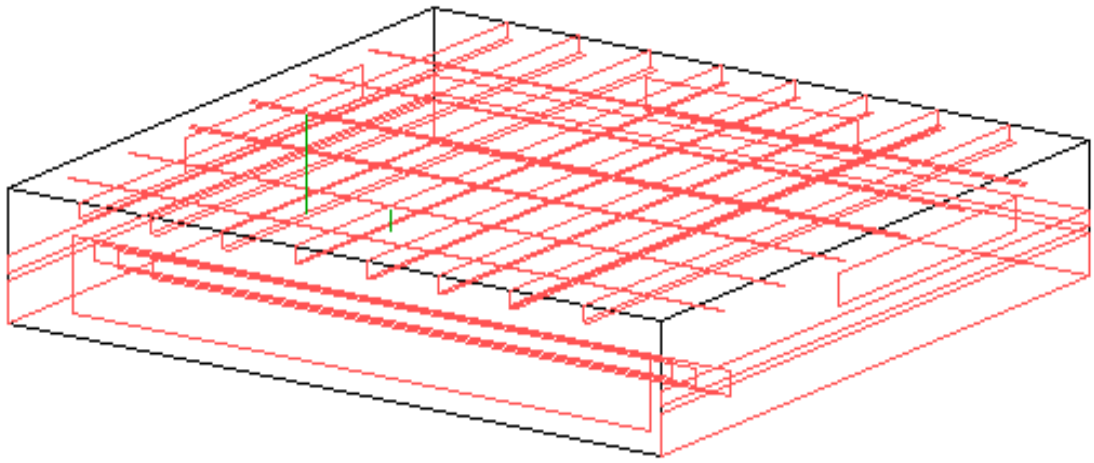

Figure 8.16: Objects considered from the pavilion in Model 1

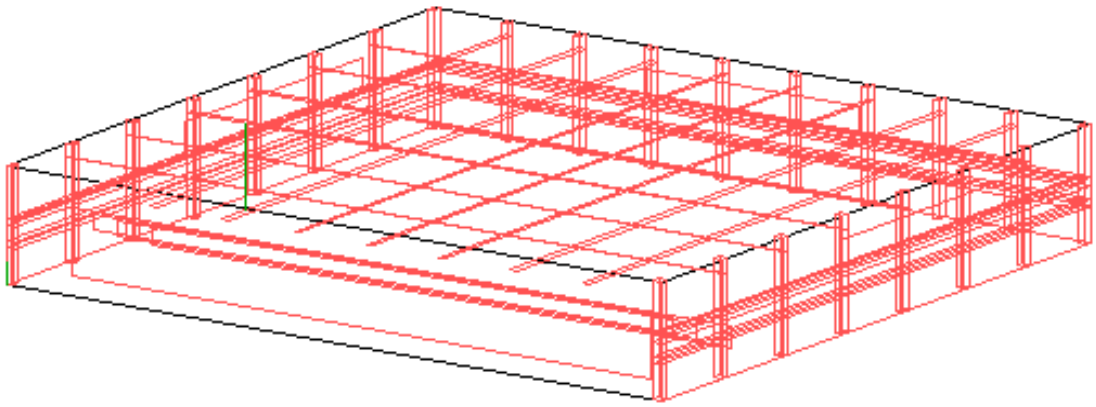

Figure 8.17: Objects considered from the pavilion in Model 3

3.1.2 Parameters analysis and comparison

Analysing now more in detail the results presented in Table 8.4 and considering the central path (other locations have also been analysed but not included here), the only longitudinal path that is complete in terms of number of measurements (locations 1 to 5), we may verify that location 1 corresponds to a region in the BS antenna blank zone, leading to a low NRP value and high DS and $\bar{\tau}$. In location 2, as expected from previous results, the NRP is

maximum and the time dispersion the lowest. The LoS component power decreases gradually for locations 3, 4, and 5, leading to a reduction of the NRP value and an increase of the time dispersion parameters. It is important to notice that, despite location 5 is the one farther away from the BS, the NRP value is higher than the one of location 4. Although there is a reduction of the direct ray power level, the other multipath components have power levels in the order of the LoS component and the combination of all those components leads to an increase of the NRP value.

Locations 6 to 9 belong to the lateral path where the radiation pattern of the BS antenna reduces the power of the LoS component and, therefore, the NRP values of all the locations are around –85 dB. This reduction of the NRP for lateral locations, in respect to locations in the central path, can be easily verified comparing the NRP values obtained for locations 7, 3 and 11. Locations 6 to 9 are at the cell boundaries, justifying the low NRP and the high channel time dispersion values. It is important to notice that the PDP parameters for this lateral path are very similar for all the locations but the NRP of location 9 is the lowest due to the reduction of the LoS component power with the distance to the BS. Another aspect to be noticed is the increase of the DS of location 6 in respect to the remainder locations of the path, which is due to the fact that the MT is in the BS antenna's blank zone. As can be seen, the results for locations 10 and 11 are very similar to the ones obtained for the opposite lateral path.

The analyses of the PDP parameters, NRP, DS and $\bar{\tau}$, revealed that the time dispersion parameters are the most dependant on the simulation model and that the NRP has insignificant variations from low and moderate complexity models to high complexity ones. This fact can be verified comparing results obtained for Models 1 and 3, depicted in Figure 8.18. Although Model 3 is considerably more complex than Model 1, by including the concrete columns of the walls, the corresponding NRP distributions are quite similar and the differences are insignificant. Regarding the DS and $\bar{\tau}$ distributions one may verify that they are considerably different, especially for locations of the MT further away from the BS. For those locations, the multipath components become more preponderant in the PDP and the differences between the simulation models reveal themselves both in the PDP and in the time dispersion parameters.

Figure 8.18 allows also analysing the quality of both models in PDP parameters predictions using a raytracing simulator. The first conclusion that can be drawn is that the parameters predictions are quite good for the locations within the cell main coverage area (the first 3 locations), but can be quite poor for locations in the cell's limits[2]. For locations within the cell, the dominance of the LoS component reduces the impact of bad raytracing predictions of multipath components, caused by limitations in the simulation model. Therefore, for locations where the LoS component is strongly dominant (first 2 locations) quite good predictions of the PDP parameters can be obtained even with low to moderate complexity models. Nevertheless, for locations where this dominance is not so strong or even non-existent (last 3 locations) the predictions of the PDP parameters can be quite poor. The most critical location is the last one where none of the models could lead to good or reasonable estimations of the PDP parameters. This last location is in the cell limit and the power of the LoS component and other multipath components become very near being necessary to increase the simulation model complexity in order to achieve better quality estimations.

Comparing the two simulation models it is quite clear that Model 3 leads to better power and channel time dispersion estimations. From the results obtained for Model 1 one may conclude that the metallic structure of the ceiling is being worst case modelled and consequently the channel time dispersion parameters obtained for locations where the LoS component is less dominant, are considerably higher than the measured ones. This fact leads to the study of scenario models where the multipath components originated by the ceiling structure have a less impact in the PDP. Models 2 and 4 are examples of possible models to overcome this problem.

Observing the channel time dispersion parameters represented in Figure 8.20 and comparing them with the ones depicted in Figure 8.18, it can be easily concluded that the quality of the estimations is better when Model 2 and Model 4 are used instead of Model 1. Thus, the estimations for all the MT locations are closer to the measured DS and $\bar{\tau}$ values, but still the predictions for locations 3 and 5 are quite poor. Nevertheless, for

2 The BS antenna was not dimensioned for the sports pavilion, but for Pavilhão Atlântico where demonstrations took place. This means that the radiation pattern could be different and adapted to the particular characteristics of this

location 3 the estimations are significantly better using Model 2 and Model 4 than using Model 1. Another important conclusion which can be drawn is that the results obtained for Model 3 are similar to the ones obtained for models 2 and 4 although its complexity is considerably higher.

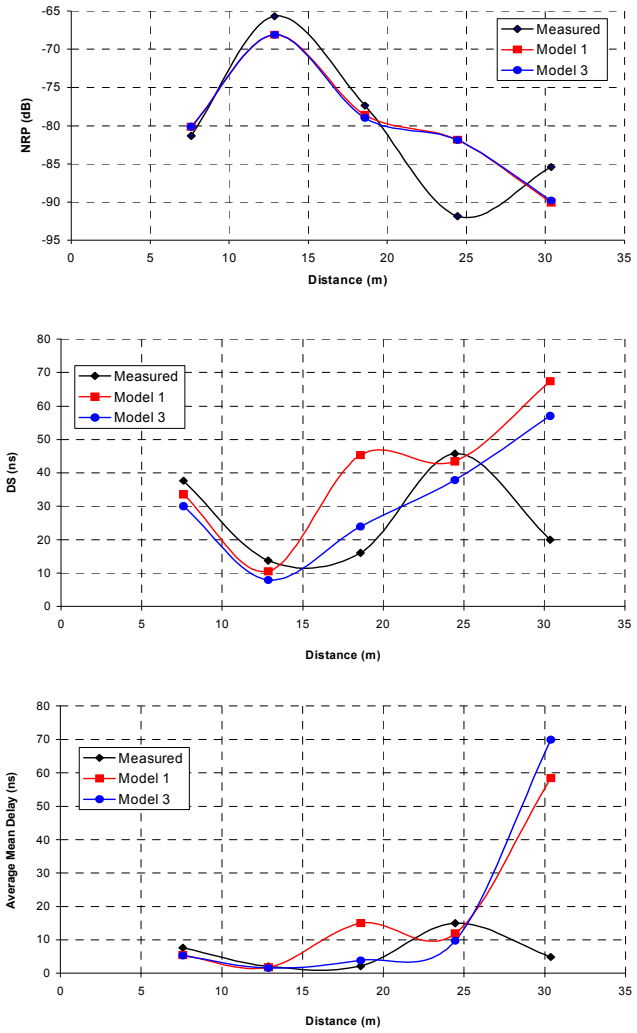

Figure 8.18: PDP parameters obtained via measurements and simulated for models 1 and 3 for the central path: NRP (top); DS (centre); and $\bar{\tau}$ (bottom)

In all the simulations, the reflection order used in the simulator was 6 but for Model 3, due to its complexity, the simulation order had to be reduced to 5. For this model the computational resources did not allowed to use a reflection order of 6, which certainly would lead to better results because the simulation model is closer to the real scenario. A

indoor scenario and therefore better coverage characteristics could be achieved.

better evaluation of the simulation models can be done by analysing directly the PDPs obtained using each of them.

3.1.3 PDPs analyses and comparison

As examples of the PDPs obtained from the CIR measurement campaign and its estimations, Figure 8.21 and Figure 8.22 present measured and simulated results for locations inside and in the border of the cell. Locations 3 and 4 were selected since they were identified, together with location 5, as the most critical from the analyses of the PDP parameters. From the analyses of the PDP parameters and from the performed PDP studies it was concluded that none of the models used were capable of achieving reasonable PDP estimations for location 5. For this location, as the power of the LoS component and other multipath components are identical, the limitations of the models are revealed. Thus, to obtain reasonable estimations, it is necessary to use higher complexity models and a reflection order of 6. It is important to notice that even with Model 3 and a simulation order of 5 the quality of the predictions is very poor.

The main objective of any propagation model is to obtain good estimations for all locations within the cell coverage area. The performance of this model is better for the main cell coverage area and deviates more for locations where coverage is guaranteed mainly via multipath components. This is shown in Figure 8.19 where clearly there are two main areas: one that is the “heart” of the cell with good coverage and predictions and another where coverage exists but with a lower power level. Redesigning the antenna radiation pattern it would be possible to extend the “heart” of the cell coverage area to the whole pavilion. The locations near the walls have a power value close to the sensitivity of the normal receivers.

From Figure 8.21, one may conclude that in Model 1 the ceiling structure is modelled as a worst case approach, leading to multipath components estimated with a power greater than the measured. These components have time delays between 100 ns and 200 ns and will reflect themselves in an increase of the channel time dispersion as verified in section 3.1.2. Models 2, 3 and 4 lead to better estimations for time delays between 100 ns to 200 ns and therefore to a better overall quality of the PDP and parameters prediction. Another conclusion which can be drawn is that Model 3, even using a simulation order of 5,

allows the estimation of the most significant multipath components. Increasing the simulation order to 6 would increase the quality of the PDP estimation, but as the LoS component is still dominant in location 3 the quality of the PDP parameters is quite good for the considered reflection order.

Observing now Figure 8.22, one can conclude that Model 1 does not lead to an estimation of multipath components with powers greater than the measured ones, as observed in Figure 8.21. This fact is due to the greater distance between the BS and the MT, which reduces the significance of the multipath components caused by reflections in the ceiling structure. Still due to the greater distance between the BS and the MT, the high order multipath components have lower power levels, assuming a lower significance in the PDP obtained by simulation using Model 3 resembles the ones obtained using the other models. Although being a location outside the cell, the PDP predictions obtained with all the models are quite good, since the LoS component still dominates the PDP. This fact reflects itself in the good quality of the DS and $\bar{\tau}$ estimations, observed in section 3.1.2. These results allow concluding that the difference between the NRP values obtained by simulation and the measured ones is due to the fact that the estimated absolute power of the LoS component is greater than the measured one.

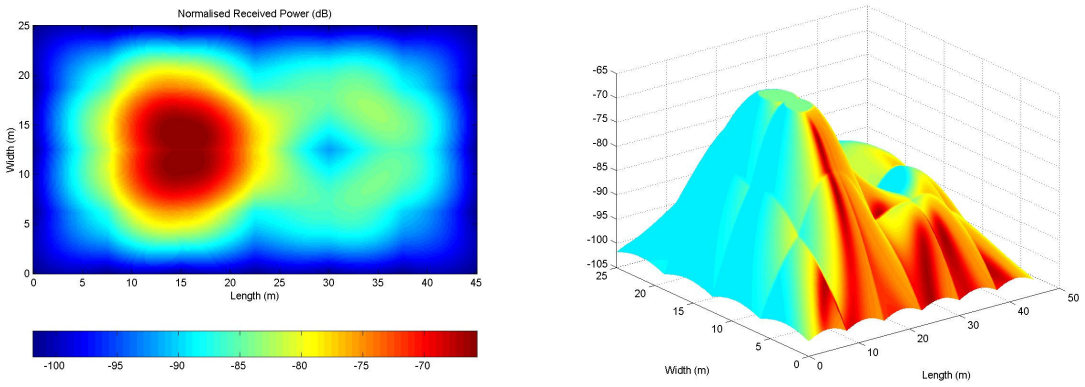

Figure 8.19: NRP distribution obtained via measurements: 2D (left) and 3D (right)[3]

3 The pavilion has been considered symmetrical in terms of power levels distribution for what concerns the locations not measured. Only the central path corresponds uniquely to real measurements.

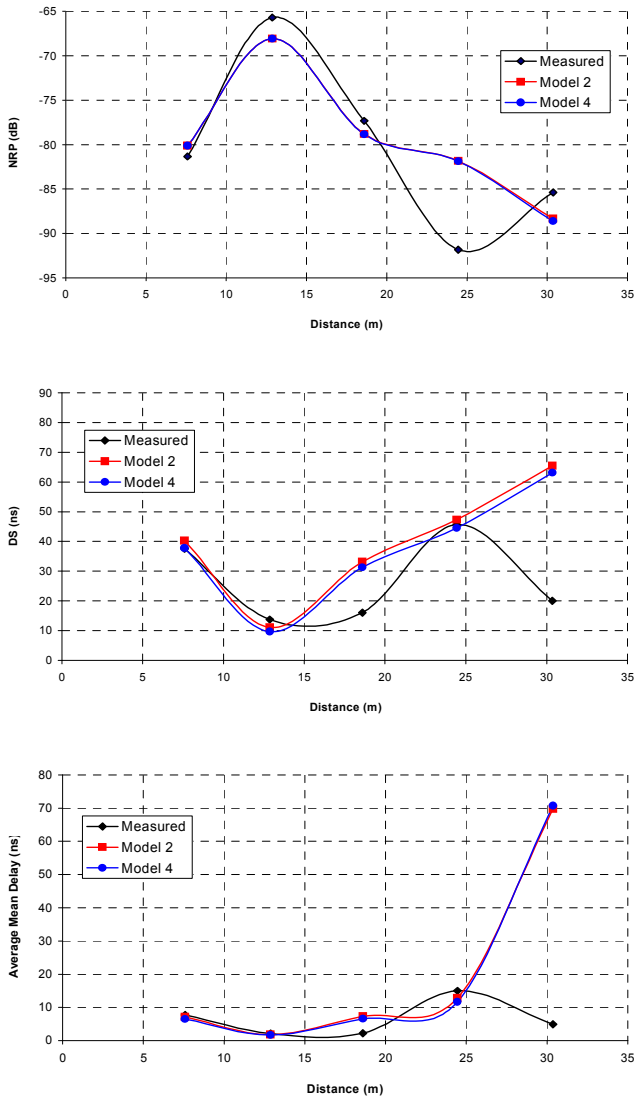

Figure 8.20: PDP parameters obtained via measurements and simulated for models 2 and 4: NRP (top); DS (centre); and $\overline{\tau}$ (bottom)

In order to quantitatively evaluate each of the simulation models and summarise the main results and conclusions, Table 8.8 represents the MSE (Mean Square Error) of the multipath components amplitude estimations for all the locations. It can be verified that the MSE obtained for location 3 using Model 1 is larger than for the remaining models, due to the worst case modelling of the ceiling structure. For location 5, all PDP estimations obtained for each one of the models are very poor as can be conclude from the large MSE values obtained. Another important fact to notice is the good PDP predictions obtained with Model 3, despite the reflection order being only 5. Furthermore, for location 3 the MSE is significantly lower than the ones obtained using

the other models, due to a greater significance of the multipath components originated from the walls.

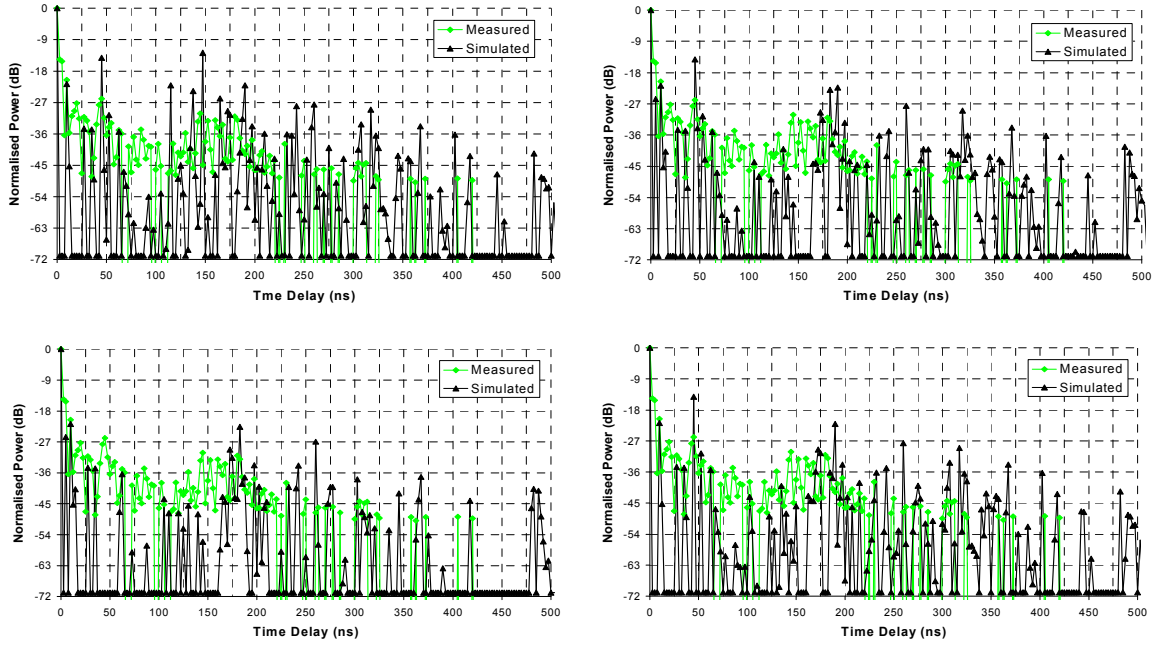

Figure 8.21: PDP of location 3, measured and simulated using: Model 1 (top left); Model 2 (top right); Model 3 (bottom left) and Model 4 (bottom right)

Combining these results with the ones from section 3.1.2, one may conclude that Model 1 is the worst of the four models and that any of the remaining three is appropriate for propagation and coverage studies within the pavilion, for locations within and in the cell limits. This fact is due to the predictions of the PDP parameters, which are normally the quantities of interest in coverage studies, obtained with Model 1 being quite different from the measured ones, even for locations within the cell. For locations clearly beyond the cell's limits, like location 5, it can be necessary to increase the complexity level of the simulation model, even further than the complexity used in Model 3.

Location	Model 1	Model 2	Model 3	Model 4
1	6.729E-04	6.838E-04	6.701E-04	6.768E-04
2	8.535E-04	8.397E-04	8.365E-04	8.345E-04
3	7.627E-04	4.280E-04	3.235E-04	4.935E-04
4	1.124E-03	1.147E-03	1.128E-03	1.129E-03
5	6.287E-03	9.804E-03	9.322E-03	9.253E-03

Table 8.8: MSE for all locations

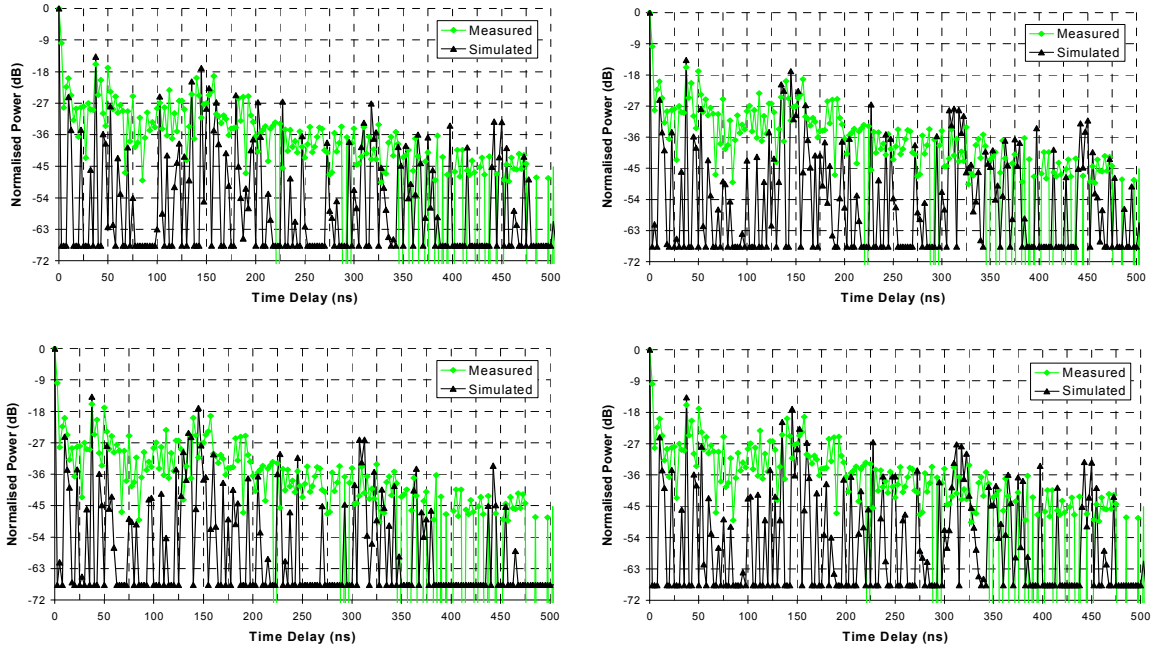

Figure 8.22: PDP of location 4, measured and simulated using: Model 1 (top left); Model 2 (top right); Model 3 (bottom left) and Model 4 (bottom right)

3.2 IT Room

3.2.1 Scenario modelling

Since the room was completely empty, the model used to simulate the IT Room was very simple being just a "box". All the walls are made of the same material and the dimensions are 7.9mx6.6mx3m. This was in fact the main reason that motivated the selection of this particular room in the IT building. In chapter 5 are indicated the paths and locations that will be analysed in the next sections.

3.2.2 Parameters analysis and comparison

In Figure 8.23 are presented the NRP results for the 64 locations measured inside the IT Room. It can be observed that the region where the minimum power is received is nearby the BS and the maximum power towards the end of the room, near the wall on the right. This power distribution is justifiable given the BS antenna radiation pattern (wide cell antenna). There is however a fact not expected: the coverage "minimum" that occurs at (1.5 m, 3 m). Since only one position was measured for each location, this can be one of

the locations where a local minimum was captured by the measurements, which could be avoided if the same pavilion measurements procedures would be used for the IT Room.

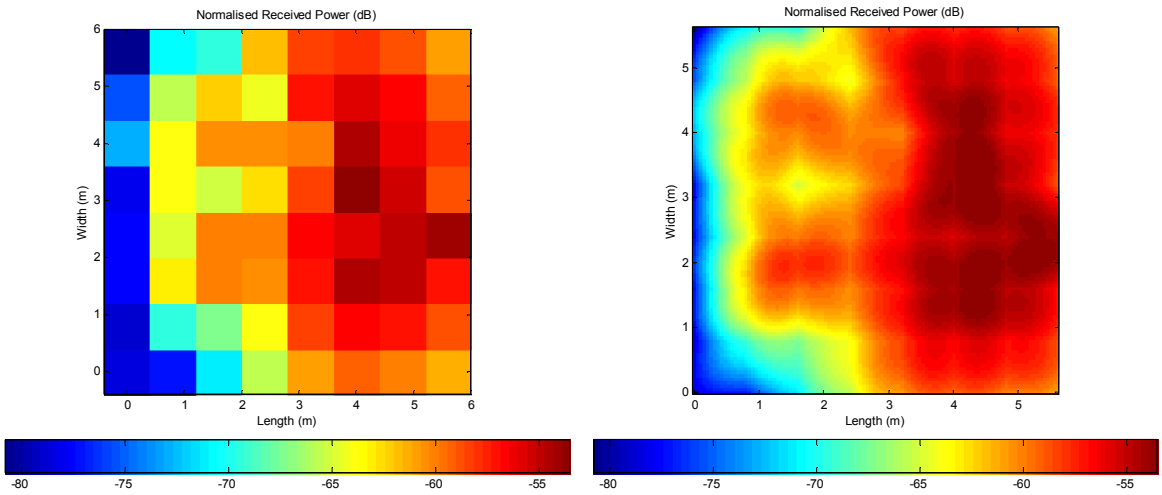

Figure 8.23: NRP distribution: non interpolated (left); interpolated (right)

The same 64 locations were simulated and the NRP and DS parameters obtained. The NRP distribution is shown in Figure 8.24. Comparing the result with the measurements displayed in Figure 8.23, there is a more uniform distribution of the power inside the room. The maximum of the power has moved away from the wall on the right. The areas with lower power are also nearby the BS, being however with a slightly different power distribution and with figures of approximately of -69 dBm. Measurements have shown a minimum power of approximately -80 dBm.

In Figure 8.25 and Figure 8.26 the NRP and DS for paths 1 and 8 are represented (longitudinal lateral paths). For both paths the simulations show a better match towards the end of the room (further away from the BS). Near the BS the mismatch is about 12 to 13 dB, for what concerns the NRP (for path 8 approximately 10 dB).

The DS simulation results have also a better match with measurements for locations further away from the BS, however showing a better match. For path 1, only near the BS the deviation is considerable.

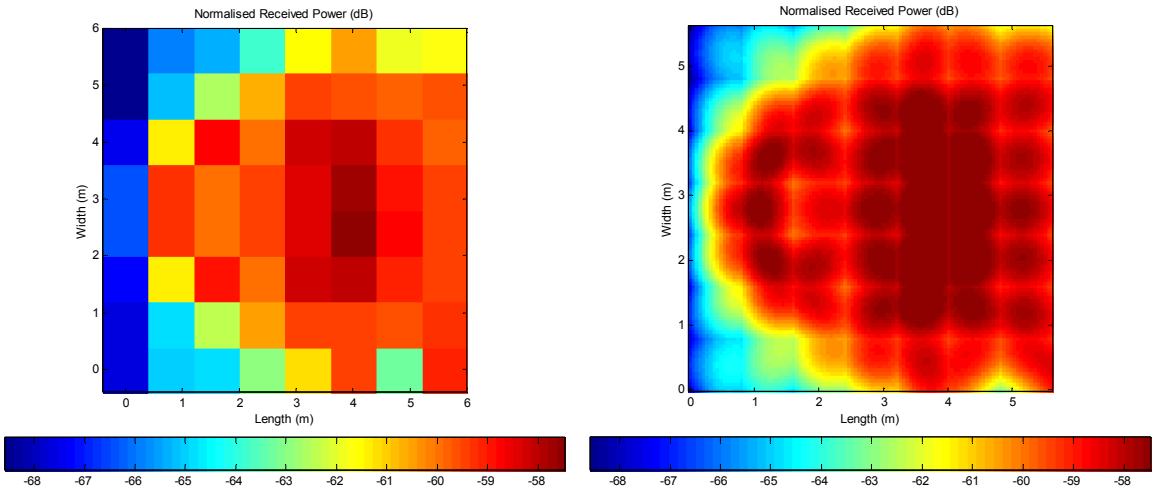

Figure 8.24: NRP distribution: non interpolated (left); interpolated (right)

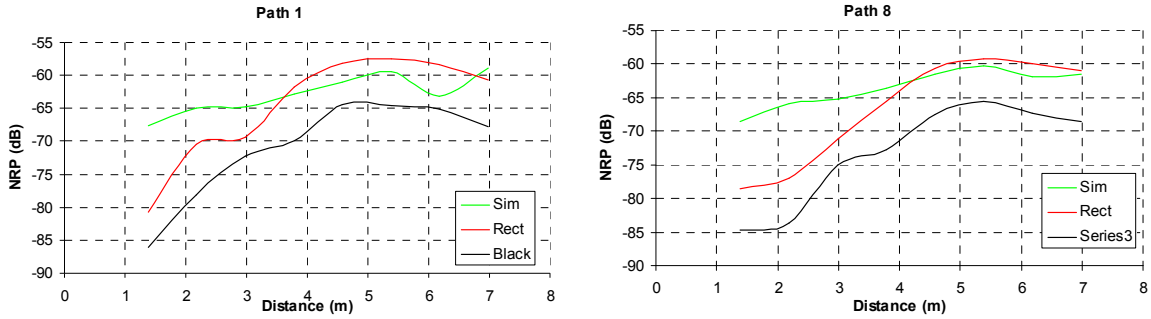

Figure 8.25: NRP distribution: path 1 (left) and path 8 (right)

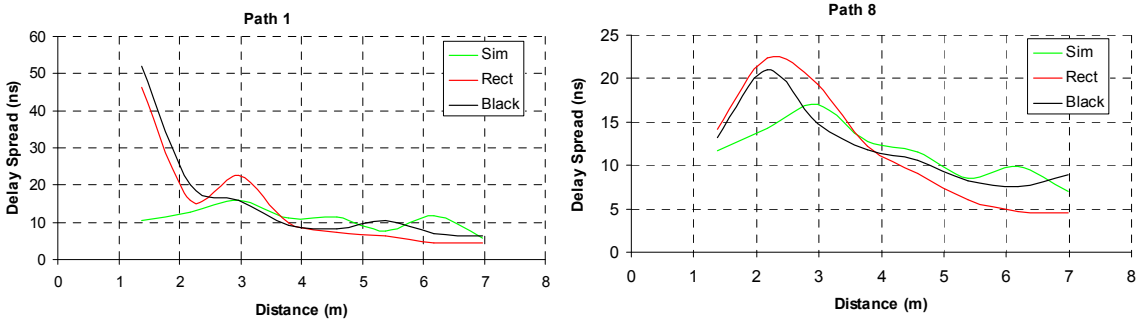

Figure 8.26: DS distribution: path 1 (left) and path 8 (right)

In Figure 8.27 and Figure 8.28 the NRP and DS for paths 4 and 5 are represented (central paths). Relatively to the NRP, a similar problem arises, since a good match is only obtained for locations further away form the BS. Clearly the measurements show a much lower NRP close to the BS than the simulation model. In terms of DS, the match is good enough.

Observing the previous presented results, we could conclude that either the simulation model used is not good (although very simple) or the measurements were not made under the same conditions assumed for the simulations. In order to check the first possibility, several simulations were done changing the time resolution (check for the NRP approximation calculation – phases are ignored), the ε_r of the walls and tanδ, with no big change in the obtained results. The conclusion was that the model was suitable for the room.

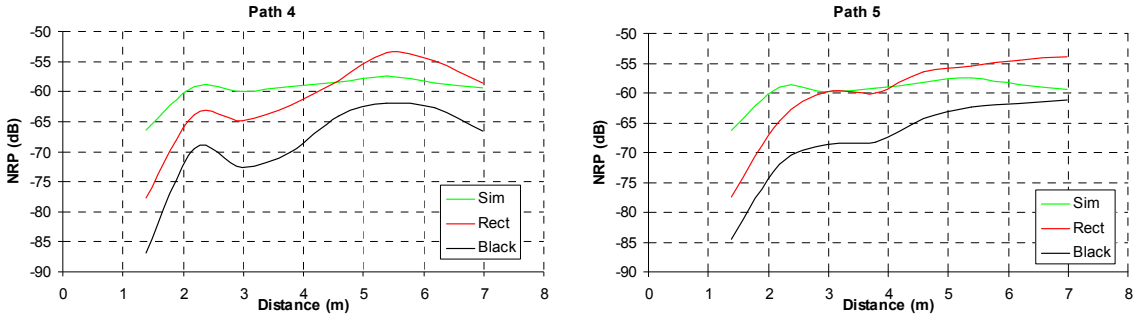

Figure 8.27: NRP distribution: path 4 (left) and path 5 (right)

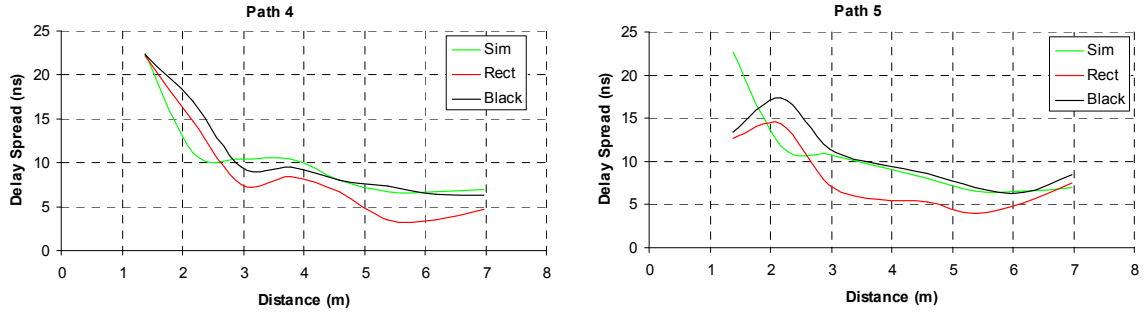

Figure 8.28: DS distribution: path 4 (left) and path 5 (right)

We started investigating other measurement conditions related with the antenna gain (different link budget), possible rotation of the antenna in the vertical plane, leading to a different power distribution and too high noise floor level. The first two hypotheses are very likely since it was difficult to measure the rotation angle of the antenna and to have a very accurate link budget.

To eliminate the last option, all the PDP components lower that -40 dB were eliminated. This fact did not also produce enough impact to justify the mismatch.

Several pares of antenna rotation and gain were trialled. Here only the one with best match is presented. The simulation results for the new antenna and gain configuration are shown in Figure 8.29. These results were obtained for a gain of + 2dB and a rotation of 4 degrees in the vertical plane.

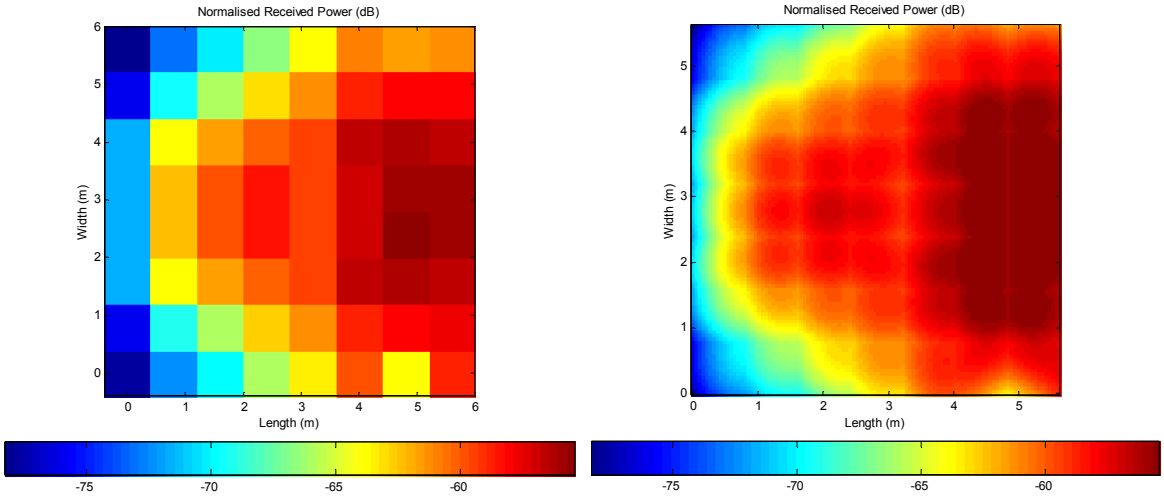

Figure 8.29: New NRP distribution with a gain of + 2dB and a rotation of 4 degrees in the vertical plane: non interpolated (left) and interpolated (right)

In Figure 8.30 are presented the results for the NRP for path 1 and 8. A much better mach was now achieved being the main factor the rotation of the antenna of 4 degrees. The DS distribution still shows a reasonable match with measurements, as can be seen in Figure 8.31.

For what concerns paths 4 and 5, the performance is very similar if not slightly better when comparing with the former scenario for both parameters (Figure 8.32 and Figure 8.33). These results show that in fact it is possible for this simpler scenario to obtain a good match between the measurement and simulation results. The difficulties related with the measurement of the antenna rotation angle and possible extra gain/attenuations have led to the discrepancy between the simulated and measured results. The results obtained with the rectangular window for all paths are closer to the ones obtained by simulation.

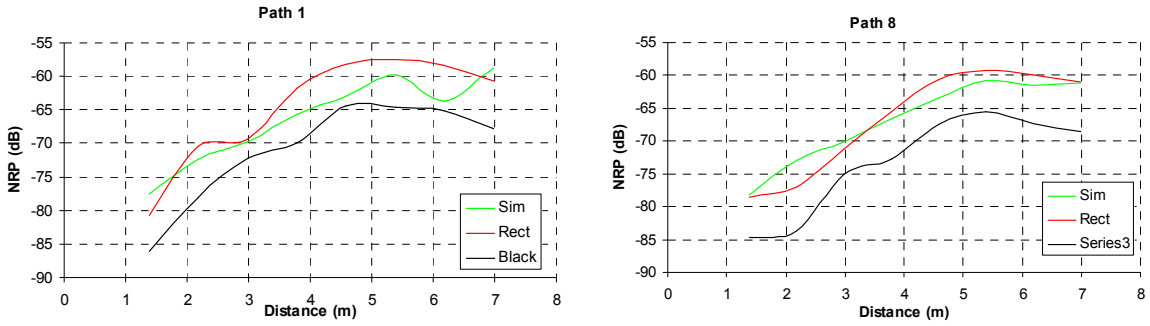

Figure 8.30: NRP distribution: path 1 (left) and path 8 (right)

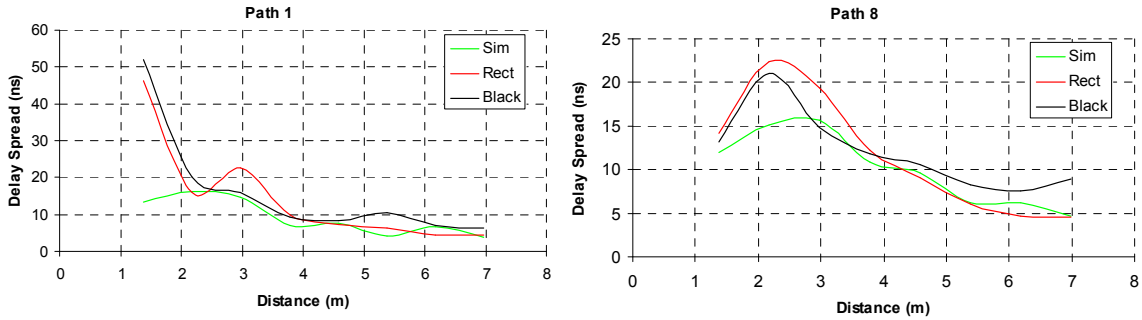

Figure 8.31: DS distribution: path 1 (left) and path 8 (right)

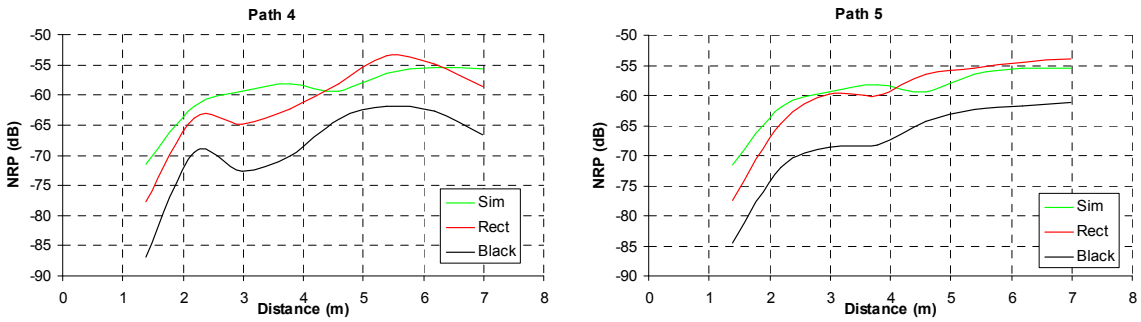

Figure 8.32: NRP distribution: path 4 (left) and path 5 (right)

3.2.3 PDPs analyses and comparison

Six PDPs of six different locations are here presented and analysed. The simulation results were obtained in the favourable conditions reported in the previous section. A rotation of 4 degrees and a +2dB gain was selected. A limit of -50 dB for the noise level for what concerns the multipath components was considered, being these components reset to -150 dB (the simulator noise level). This explains why the next figures do not show any ray with amplitude less that -50 dB. For the calculation of the parameters this limit was also used.

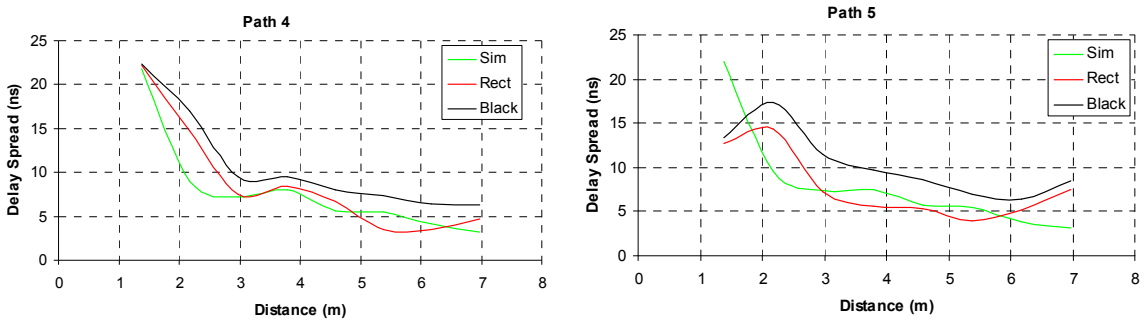

Figure 8.33: DS distribution: path 4 (left) and path 5 (right)

The analysis of Figure 8.34, Figure 8.35 and Figure 8.36 reveals that there is a good match between the measured PDPs and the simulated ones, at least for the first 100 ns, justifying the results presented in the previous section. Even for locations nearby the BS, the rays predicted match very well with the measurement results. For position 10 it is visible that some simulated reflected rays have larger amplitude leading to a higher NRP. The same is visible for location 57 for reflected rays very close to the direct ray. These facts contribute for the shown higher power levels predicted by simulation for regions close to the BS. The other locations show a good match between simulations and measurements, as expected given the results presented earlier.

The set of locations here presented was selected to give a good representation of all regions inside the room (in the cell main coverage area and also near the border). The PDPs were zoomed showing rays only up to 200 ns and the simulated and measured PDPs were aligned in time being the zero the instant when the direct ray was received. This alignment allows for a better analysis of the PDP rays.

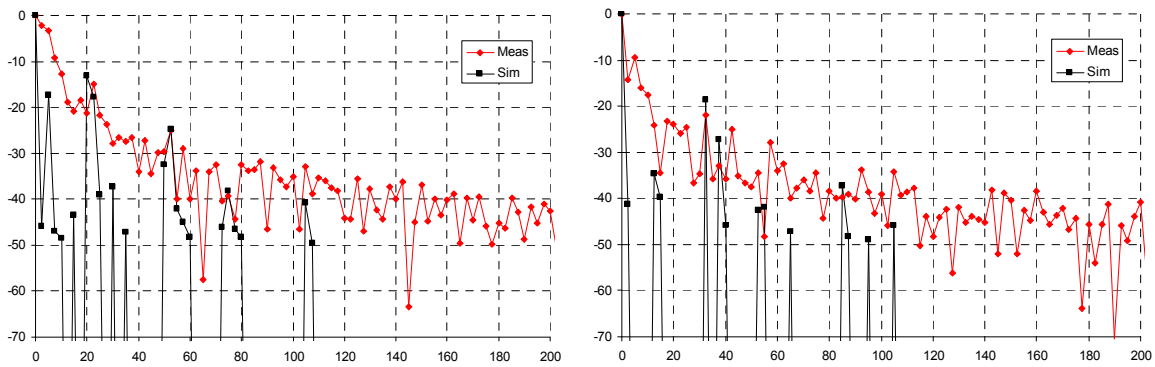

Figure 8.34: PDPs of locations 14 (left) and 28 (right)

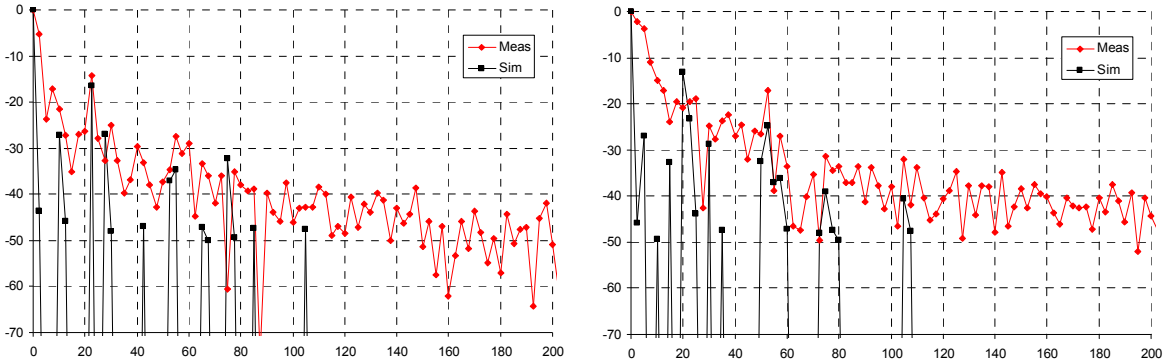

Figure 8.35: PDPs of locations 32 (left) and 54 (right)

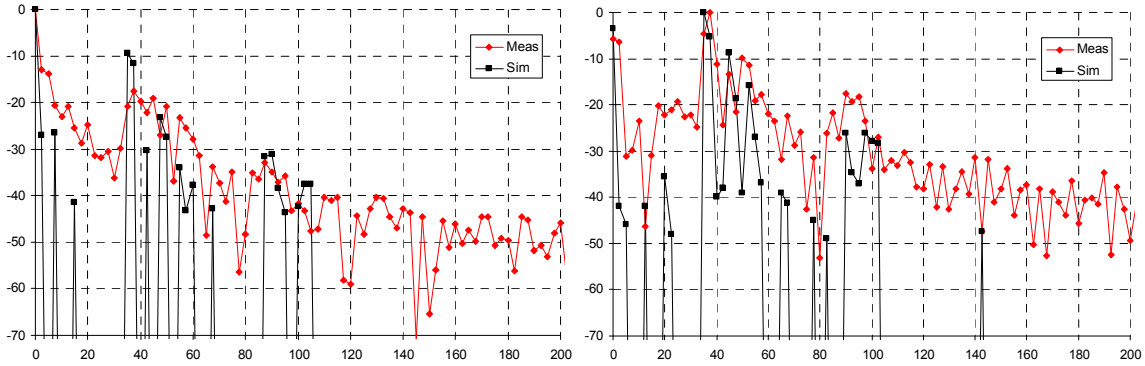

Figure 8.36: PDPs of locations 10 (left) and 57 (right)

4. Summary and conclusions

The radio channel can be seen as a time variant linear filter whose inputs and outputs can be described in the frequency, frequency Doppler shift, time delay and time domains. In this chapter the analysis of the broadband radio channel at 40 GHz was performed based on measurements of the time-variant transfer function $T(f,t)$ – frequency-time domains. Given that a frequency domain technique was used to sound the radio channel, the scenario had to be static during the measurements and therefore the transfer function depends only on the frequency - $T(f)$. The input delay-spread function $h(\tau)$ was obtained via mathematical processing. The chapter started with an introduction to channel sounding techniques, signal processing, type of windows used and its impact in the dynamic range and time resolution. The analysis of the CIRs gathered in the sports pavilion and the IT Room for several positions and locations were presented considering different situations: with and without LoS, uplink and downlink directions, impact of the antenna type and diversity receiving

channels. All CIRs were obtained using a rectangular and a Blackman Harris window since they have different time resolutions and dynamic ranges. Measured PDPs for various positions/locations were obtained and compared with ray tracing technique simulation results, considering different degrees of complexity for the simulation model and reflection orders for the rays. Various parameters were calculated: NRP, DS and $\bar{\tau}$.

In the sports pavilion all the measurements in each location were repeated 35 times and averaged (time and space average) in order to reduce the chances of measuring a very particular situation (deep fade for instance) and reduce the noise levels leading to a total of 700 measurements. The different positions for each location were separated approximately by a wavelength. In fact it was observed a difference for all positions in terms of transfer function and CIR but for positions inside the cell they are less significant since the signal spatial changes are smoother. Moreover, in statistical terms the differences are not so significant and this is why this technique was not used for the measurements in the IT Room easing the measurements procedure for each location although the number of locations analysed per unit of area was increased. The impact of the windows in the calculation of the CIR is unavoidable since it is intrinsic to the methodology and this is the reason why all the CIRs were calculated using two different widows and the results analysed for both cases. The NRP was always larger for the rectangular window.

Several situations were measured in the sports pavilion and analysed based on the PDP parameters calculated for different cell regions namely within, at the borders and outside the cell coverage area. Regarding the LoS and non LoS operation modes, the CIRs clearly reflect the fact that the direct ray is attenuated leading to a higher relative power of the reflected rays. The delay parameters also reflected this fact by showing higher figures. The uplink and the downlink directions were measured and compared. They are in fact different confirming that the status of the radio channel in one direction cannot be inferred by what is going on in the other, for systems operating in the FDD mode. This implies the use of different techniques in TDD systems. The impact of the antenna radiation patterns was also evaluated and for that purpose, two different antennas were used. Since the two antennas differ quite substantially in terms of the radiation patterns, the CIRs also reflected this fact. The diversity reception feature was analysed by measuring channels RX1 and RX2 and a

different behaviour was observed but more pronounced for the non LoS case. All the results obtained are in line with what the theory predicts also indicating that the measurement system was working properly and the assumptions made were valid. Due to the fact that this study was performed for the 40 GHz millimetrewave frequency band, this type of measurements is more critical due to the smaller wavelength and the stronger requirements in terms of phase reference information which involved the utilisation of long cables for the measurements.

In the IT Room the CIR measurement were performed only for LoS and non LoS conditions for the entire room floor surface. A total of 64 locations were measured and a total of 640 measurements performed. In LoS the dominance of the direct ray is clear leading to small figures for what concerns the time dispersion parameters. The power distribution in the room is in line with the antenna radiation pattern of the wide cell antenna. For non LoS, the parameters have shown a much odd distribution. The reflected rays have a more prominent role in the CIR, leading to an increase of the time dispersion parameters. The NRP is much lower than in LoS due to the absence of the direct ray. Given the shorter dimensions of the room, lower time dispersion figures were observed when comparing with the sports pavilion.

Simulation results were performed in order to validate the used sports pavilion simulation models and measurements performed. The main idea was to evaluate the impact of excluding some objects in the validity of the simulation results. The simplification of the model allows for a shorter simulation time which is crucial when performing simulation studies. Several simulation models were used but in the thesis only the results for four of them were presented. These models present a different degree of complexity as a direct consequence of the number of objects they took into consideration. By analysing the PDP parameters, it could be concluded that time dispersion parameters are much more dependent on the simulation model that the NRP, which has shown only small variations. In general the simulation results have shown a good agreement with the measurements in locations inside the cell coverage area where the spatial variability of the radio channel is much less due to the strong contribution of the direct ray to the PDP. This fact reduces the importance of possible deficiencies or inaccuracies in the prediction of reflected rays by the simulation model since they have a much lower weight and contribution to the results.

Outside the cell main coverage area more deep fades and lower power levels are experienced which confirms a much more important role of the reflected rays. In terms of the analysed simulation models, Model 3 is the one that in general presented best results in terms of power and time dispersion parameters although a reflection order of 5 had to be used, due to the lack of computational resources to handle the necessary calculations.

The direct inspection and analysis of the PDPs allows inferring that the different simulation models also impacted on the number, delay and amplitude of the received rays, being clearly more close to the measurements for locations that fit inside the cell main coverage area. The design of lens antennas for the specific characteristics of the sports pavilion would result in a much better distribution of the power and a more even coverage. Considering the prediction of the PDP parameters, one may conclude that Model 1 is the worst of the four models and that any of the remaining three is appropriate for propagation and coverage studies within the pavilion, for locations within and in the cell limit. Simulation results obtained with Model 1 are quite different from the measured ones, even for locations within the cell. For locations clearly beyond the cell's limit, it is necessary to increase the complexity level of the simulation model or the order of reflection or both, even further than the complexity used in Model 3.

In an attempt to remove the dependency on the simulation models complexity the IT Room with very few objects was selected for analysis by simulation as well. The simulation model is quite simple being a parallelepiped. It can be observed that the region where the minimum power is received is nearby the BS and the maximum power towards the end of the room. Simulation results for all locations indicated a slightly different power distribution in the room being the peak of the power closer to the BS, keeping however the general shape imposed by the wide cell antenna radiation pattern. In general the minimum power levels obtained by simulation are higher than via the measurements indicating a worst match between the measurements and simulations in areas closer to the BS. The same general behaviour was observed for the DS figures. In order to explain these discrepancies, various simulations were performed considering different electrical properties of the room walls and other system configuration parameters, namely the antenna rotation angle and gain. By maintaining the electrical parameters and increasing the antenna gain in 2 dB and introducing an antenna rotation in the vertical plane of 4

degrees it was possible to obtain a good match between the measurement and the simulation results for NRP and DS parameters.

A set of locations in the room were selected for a more in-depth PDPs analysis which has revealed a good match between the measured and the PDPs obtained by simulation, especially for the first 100 ns. Even for locations nearby the BS, the rays predicted match very well with the measurement results confirming the conclusions presented above.

The main conclusion drawn is that these simulation models allowed quite good estimates for both the PDP parameters and the PDP itself, for locations inside and at the cells limits. For locations clearly outside the cell it might be necessary to increase the complexity level of the simulation model. Although the very high frequency band used, the analysis in the frequency domain proved to work well with the inherent disadvantage that no motion is allowed while performing the measurements precluding the analysis of the Doppler effects. The calculated parameters are according to the expected and suitable explanations were presented for the observed behaviour in the selected measurement scenarios and system configurations.

5. References

[1] Theodore S. Rappaport, "Wireless Communications Principles and Practice", Prentice-Hall, 1996.

[2] Homayoun Hashemi and David Tholl, "Statistical Modelling and Simulation of the RMS Delay Spread of Indoor Radio Propagation Channels" IEEE Transactions on Vehicular Technology, vol. 43, No. 1, February 1994.

[3] Jean-François Frigon, B. Daneshrad, J. Putnam, E. Berg, R. Kim, T. Sun and H. Samueli, "Field Trial Results for High-Speed Wireless Indoor Data Communications", IEEE Journal on Selected Areas in Communications, Vol. 18, No. 3, March 2000.

[4] Theodore S. Rappaport, "Characterisation of UHF Multipath Radio Channels in Factory Buildings", IEEE Transactions on Antennas and Propagation, Vol. 37, No. 8, August 1989.

[5] Henrik Börjeson, "Radio Wave Propagation in Confined Environments – Measurements and Models", PhD Thesis, Department of Applied Electronics, Lund University, Sweden, February 2000.

[6] Luís Miguel D. B. Anunciada, "Impacto das Antenas no Canal de Propagação em Comunicações Móveis em Ondas Milimétricas", MSc Thesis, Universidade Técnica de Lisboa, Instituto Superior Técnico, December 1999.

[7] H. J. Thomas, R. S. Cole and G.L. Siqueira, "An Experimental Study of the Propagation of 55 GHz Millimeter Waves in an Urban Mobile Radio Environment", IEEE Transactions on Vehicular Technology, Vol. 43, No. 1 February 1994.

[8] Hao Xu, Theodore S. Rappaport, R. J. Boyle and J. H. Schaffner, "Measurements and Models for 38-GHz Point-to-Multipoint Radiowave Propagation", IEEE Journal on Selected Areas in Communications, Vol. 18, No. 3, March 2000.

[9] Larry J. Greenstein, Vinko Erceg, Yu Shuan Yeh and Martin V. Clark, "A New Path-gain/Delay-Spread Propagation Model for Digital Cellular Channels", IEEE Transactions on Vehicular Technology, Vol. 46, Nº 2, May 1997.

[10] C. Evci, "Final Report of AWACS project", CEC Deliverable Number AWACS/CIT/PM1/DS/P/015/b1, 15/09/1998, Submitted to the European Commission in the framework of the AWACS project.

[11] G. Morrison, M Fattouche 'Super-Resolution Modeling of the Indoor Radio Propagation Channel' IEEE Transactions on Vehicular Technology, vol. 47 No. 2 May 98.

[12] M. Lienard, P. Degauque, 'Propagtion in Wide Tunnels at 2 GHz: A Statistical Analysis' IEEE Transactions on Vehicular Technology, vol. 47 No. 4Nov. 98.

[13] A. Molisch, 'Statistical Properties of RMS Delay-Spread of Mobile Radio Channels with Independent Rayleigh-Fading Paths' - Correspondence, IEEE Transactions on Vehicular Technology, vol. 45 No. 1 Feb. 96.

[14] A. Hammoudeh, M. Sánchez, E. Grindrod, 'Experimental Analysis for Propagation at 62 GHz in suburban Mobile Radio Microcells', IEEE Transactions on Vehicular Technology, vol. 48 No. 2 Mar 99.

[15] G. Kalivas, M. Tanany S. Mahmoud, 'Millimetre-Wave Channel Measurements with Space Diversity for Indoor Wireless Communications', IEEE Transactions on Vehicular Technology, vol. 44 No. 3 Aug 95.

[16] M. J Gans, 'A Power-Spectral Theory of Propagation in the Mobile-Radio Environment', IEEE, Trans. on Vehic. Technology, vol. vt-21, No. 1 Feb 1972.

[17] José Fernandes, "Modelação do Canal de Propagação Rádio Móvel de Banda Larga na Faixa das Ondas Milimétricas e seu Impacto no Desempenho de Transmissão do Sistema", PhD Thesis, University of Aveiro, 1996.

[18] P. A. Bello, 'Characterization of Randomly Time-Variant Linear Channels', IEEE Trans. On Communications Systems, vol. CS-11, no 12 Dec. 1963.

[19] D. Tholl, M. Fattouche, R.J.C. Bultitude, P. Melançon and H. Zaghloul, "A Comparison of Two Radio Propagation Channel Impulse Response Determination Techniques" IEEE Transactions on Antennas and Propagation, vol. 41 No 4, April 1993.

[20] Steven J. Howard and Kaveh Pahlavan, "Measurement and Analysis of the Indoor Radio Channel in the Frequency Domain", IEEE Transactions on Instrumentation and Measurement, vol. 39 No 5, October 1990.

[21] M. Dinis, J. Fernandes, M. Prögler and W. Herzig, "The SAMBA Trial Platform in the Field", ACTS Mobile Communications Summit '99, Sorrento, Italy, pp. 1013-1018, June 1999.

[22] José Garcia, Manuel Dinis and José Fernandes, "Performance Evaluation of a Cellular Millimetrewave Mobile Broadband System Demonstrator", CONFTELE 2001, Figueira da Foz, 23 - 24 April 2001.

[23] Frederic Harris, "On the Use of Windows for Harmonic Analysis with Discrete Fourier Transform", Proceedings of the IEEE, vol. 66 No. 1, Jan 1978.

[24] Leland B. Jackson, "Digital Filters and Signal Processing", Third Edition, KAP.

[25] Roman Kuc, "Introduction to Digital Signal Processing", McGRAW-HILL International Editions, 1988.

[26] Manuel Dinis, José Garcia, Valdemar Monteiro and Nelson Oliveira, "Millimetre-wave Channel Impulse Response Experimental Evaluation and Relation Between Delay Spread and Channel Coherence Bandwidth", PIMRC' 2002, September, Lisbon, Portugal.

[27] Manuel Dinis, José Garcia, Valdemar Monteiro and Nelson Oliveira, "Millimetre-wave Channel Impulse Response Measurements and Comparison with Raytracing Simulation Results", PIMRC' 2002, September, Lisbon, Portugal.

9th Chapter

Channel Coherence Bandwidth, Delay Spread and Fleury Lower Bond Analysis

1. Introduction

The study presented in this chapter was first motivated by the fact that in the literature, when addressing the relationship between DS and CB, usually is described an approximation dependent on the considered correlation factor [1]. These relationships are described by equations (9.1) and (9.2) for correlation coefficients of 0.5 and 0.9, respectively.

$$CB_{0.5} \approx \frac{1}{5DS} \tag{9.1}$$

$$CB_{0.9} \approx \frac{1}{50DS} \tag{9.2}$$

It is commonly accepted that there is not a direct and unique relationship between these two parameters being generically the CB inversely proportional to the DS independently of the envisaged correlation level as shown by equation (9.3). Furthermore, CB figures obtained from the frequency response measurements performed in the two indoor scenarios, indicated that usually the obtained CB figures were in general much larger that those predicted by the former presented equations.

$$CB \alpha \frac{1}{DS} \tag{9.3}$$

Several questions came to our minds such as what would be the validity of the presented expressions? How much error is present in the approximation? Are they applicable to all frequency bands and scenarios? These questions have motivated a deep literature survey [2] [3] [4] [5] [6] [7] [8] [9] [10] [11] [12] [13].

As reported in chapter 2, although not addressed in this thesis, due to the duality between the channel time-spreading and time-variant mechanisms, a similar relationship exists between f_m and T_c as expressed by equation (9.4).

$$T_c \alpha \frac{1}{f_m} \tag{9.4}$$

This chapter starts with a description of the Fleury mathematical formulation for the relationship between the DS and CB. Based on the CIR measurements performed for the two indoor scenarios, the DS and CB were evaluated and its relationship analysed following a similar methodology as described in [4]. A comparison of the obtained figures and the results collected directly using equations (9.1) and (9.2) are presented. Moreover, to further clarify the relationship between the DS and CB and the confirmation of the Fleury lower bond applicability in multiple conditions and scenarios, simulation results were performed for three indoor scenarios using different antenna types, measurement bandwidths, correlation coefficients and LoS and non LoS conditions.

2. Fleury Lower Bond

In [4] and [5] it was demonstrated mathematically that for WSSUS channels the relationship between the DS and the CB is an uncertainty relation of the same kind as the

Heisenberg's uncertainty principle. The uncertainty relation between DS and CB is translated by the inequality shown in equation (9.5) where $D_c[R(\Delta f)]$ is the CB at coherence level c of the frequency correlation function R(Δf)[1], and $\sigma[S(y)]$ the DS of the delay scattering function S(y) also denoted in chapter 2 by $P_h(\tau)$.

$$D_c[R(\Delta f)] \geq \frac{\arccos(c)}{2\pi} \frac{1}{\sigma[S(y)]} \tag{9.5}$$

In fact, what Fleury states is that the channel CB is lower bounded by a function dependent on the DS and c. This fact is shown in Figure 9.1 extracted directly from [4] where measurements in the 900 MHz frequency band obtained in an indoor environment are plotted. The solid straight line (due to the logarithm scale) shows the referred lower bond. Only very few measurements are below the Fleury lower bond line and Fleury suggests that it happens probably due to measurement errors or lack or precision.

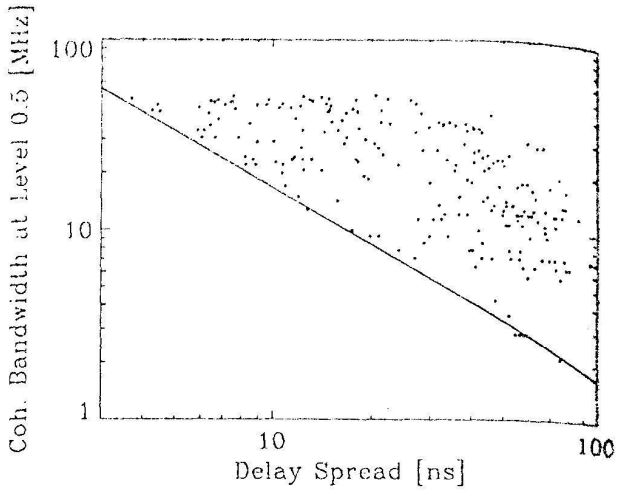

Figure 9.1: CB at c=0.5 versus DS for an indoor environment and the Fleury lower bond

Expression 9.5 was derived based on the following assumptions [4] [5]. Let G(x) denote a continuous complex process which satisfies the following three conditions:

1 Also denoted by $R_T(\Delta f)$ in chapter 2 to show its linkage with the time-variant transfer function T(f,t).

1. G(x) is a WSS with zero mean.

2. $E[|G(x)|^2] < \infty$ for any x being a real number.

3. G(x) is continuous in the mean-square-sense.

If G(x) represents the time-variant transfer function T(f,t) for an arbitrary time t_0, its autocovariance function is by definition:

$$R(\Delta f) = \mathrm{E}\left[G(f)^* G(f+\Delta f)\right] \tag{9.6}$$

with E[.] denoting the mathematical expectation. The coherence interval at a specified level c ε [0,1] of G(f) is defined to be the minimum value of the lag Δf such that the correlation between the random variables G(f) and G(f+Δf) drops below c. $D_c[R(\Delta f)]$ is in fact defined as half the width of the main lobe of |R(Δf)| at level c. This corresponds exactly to the channel CB.

By the Bochner-Khinchin theorem there exists a uniquely determined finite measure S(y), which is the spectral measure of R(Δf) and by extension of G(f), such that:

$$R(\Delta f) = \int_R e^{j2\pi\Delta f y} S(dy) \tag{9.7}$$

The mean spectral shift and the spectral spread of R(Δf) and by extension of G(f) are defined to be the centre of gravity and the square root of the second central moment of S(y), respectively, i.e.:

$$\mu[S(y)] = \frac{1}{P}\int_R y\, S(dy) \tag{9.8}$$

$$\sigma[S(y)] = \left[\frac{1}{P}\int_R (y-\mu[S(y)])^2 S(dy)\right]^{1/2} \tag{9.9}$$

with P=R(0).

Moreover inequality (9.5) holds with equality if and only if two real numbers y_1 and y_2 exist such that:

$$S(y) = \frac{P}{2}\left[\delta(y-y_1) + \delta(y-y_2)\right] \tag{9.10}$$

in which case $\sigma[S(y)]=|y_2-y_1|/2$. In expression (9.10) $\delta(y-y_0)$ corresponds to a Dirac impulse at y_0.

In [4] it is demonstrated that a better lower bond for the frequency correlation function R(Δf) when compared to others early derived, is given by (9.11):

$$\left|\frac{1}{P}R(\Delta f)\right| \geq Cos\left(2\pi\sigma[S(y)]\Delta f\right) \tag{9.11}$$

being Cos(x) defined as follows:

$$Cos(x)=\begin{cases}\cos(x);\ x\in[-\pi,+\pi] \\ -1 \qquad \text{elsewhere}\end{cases} \tag{9.12}$$

After manipulation of expression (9.11) and considering the fact that $\sigma[S(y)]$ is always positive, equation (9.5) can be obtained since $\left|\frac{1}{P}R(\Delta f)\right|$ equals to c.

For c = 0.5 the expression (9.5) becomes:

$$D_{0.5}[R(\Delta f)]\geq\frac{\arccos(0.5)}{2\pi}\frac{1}{\sigma[S(y)]}\Leftrightarrow D_{0.5}[R(\Delta f)]\geq\frac{1.047}{2\pi}\frac{1}{\sigma[S(y)]} \tag{9.13}$$

and for c = 0.9 becomes:

$$D_{0.9}[R(\Delta f)]\geq\frac{\arccos(0.9)}{2\pi}\frac{1}{\sigma[S(y)]}\Leftrightarrow D_{0.9}[R(\Delta f)]\geq\frac{0.451}{2\pi}\frac{1}{\sigma[S(y)]} \tag{9.14}$$

Comparing expressions (9.1) and (9.13) it can be concluded that expression (9.1) is a good approximation to the Fleury lower bond. On the other hand, comparing expressions (9.2) and (9.14) the same cannot be stated since 2π/0.451 = 13.931 which differs considerably from 50. Therefore a better approximation is expected for c=0.5 than for c=0.9. There is however a conceptual difference between the presented expressions. The first are just approximations and the second ones express a lower bound, being by definition all correct.

To the authors' knowledge no measurements were done in the millimeterwave frequency band to verify the relationship between the DS and the CB or if the same assumptions hold in the typical scenarios where mobile broadband system will be operated. This has motivated the work presented in the next sections where measurement and simulation

results are presented and analysed for the CB, DS and the theoretical Fleury lower bond considering different conditions.

3. Measurements Performed

The measurements presented in this section were performed in the sports pavilion and the IT Room already presented in the previous chapters [14]. The same locations are here analysed but in a different perspective and goal. In both scenarios the same system hardware configuration was used.

This section starts with an analysis of the discrepancies associated with the different equations presented in the previous sections when compared with the figures obtain via the measurements for both scenarios.

3.1 Sports pavilion

Figure 9.2 shows the frequency correlation function positive axis obtained via measurements and expression (9.11) for locations 7 and 11 in LoS conditions. It can be observed that in fact the expression derived by Fleury is a lower bond and almost coincides for higher coherence levels (c larger than 0.9). This result is in line with the conclusions presented in [4].

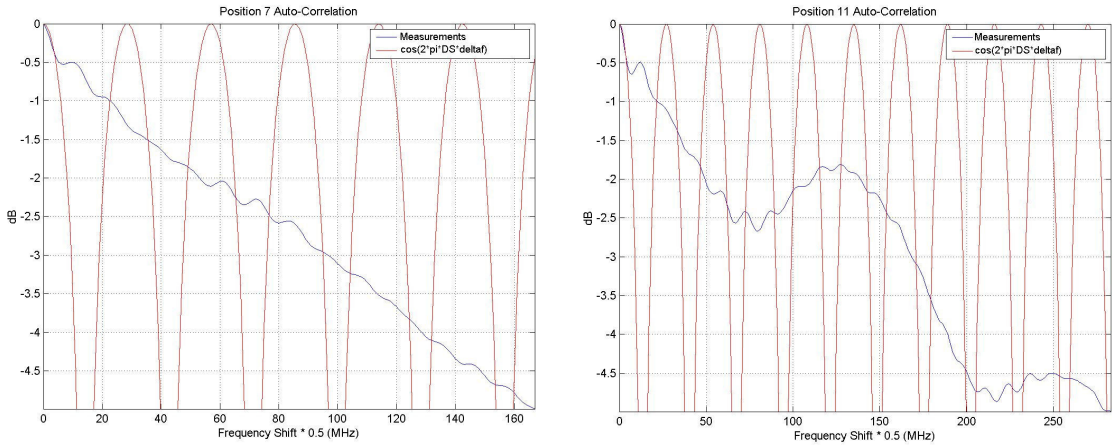

Figure 9.2: CB analysis for measurements and theoretical lower bond for location 7 and 11

Table 9.1 presents all the calculations of the CB for all locations measured in the sports pavilion (LoS and non LoS) and the respective difference in terms of percentage. The same

results are also presented graphically in Figure 9.3 and Figure 9.4. For what concerns c=0.5 and LoS the Fleury lower bond and the approximation equation (9.1) are quite different from the measurement results.

Location	DS (ns)	$CB_{0.5}$ Meas. (MHz)	$CB_{0.5}$ by (9.13) (MHz)	Δ (%)	$CB_{0.5}$ by (9.1) (MHz)	Δ (%)	$CB_{0.9}$ Meas. (MHz)	$CB_{0.9}$ by (9.14) (MHz)	Δ (%)	$CB_{0.9}$ by (9.2) (MHz)	Δ (%)
1	25.68	58.5	6.49	89	7.79	87	5.5	2.80	49	0.78	86
2	6.77	78	24.62	68	29.54	62	12.5	10.60	15	2.95	76
3	13.00	64.5	12.82	80	15.38	76	6.5	5.52	15	1.54	76
4	21.78	39.5	7.65	81	9.18	77	3.5	3.30	6	0.92	74
5	20.02	73.5	8.33	89	9.99	86	3.5	3.59	2	1.00	71
6	24.43	74	6.82	91	8.19	89	6	2.94	51	0.82	86
7	44.44	37.5	3.75	90	4.50	88	1.5	1.62	8	0.45	70
8	31.66	54	5.26	90	6.32	88	2	2.27	13	0.63	68
9	37.93	17	4.39	74	5.27	69	1.5	1.89	26	0.53	65
10	40.01	80	4.17	95	5.00	94	1.5	1.79	20	0.50	67
11	32.47	76.5	5.13	93	6.16	92	2	2.21	11	0.62	69
7 no LoS	77.89	2	2.14	7	2.57	28	1	0.92	8	0.26	74
8 no LoS	70.38	2	2.37	18	2.84	42	1	1.02	2	0.28	72
9 no LoS	65.08	2.5	2.56	2	3.07	23	1	1.10	10	0.31	69
11 no LoS	63.70	2.5	2.62	5	3.14	26	1	1.13	13	0.31	69

Table 9.1: CB at level 0.5 and 0.9 obtained by measurements, Fleury lower bond and the approximation formula for the sports pavilion

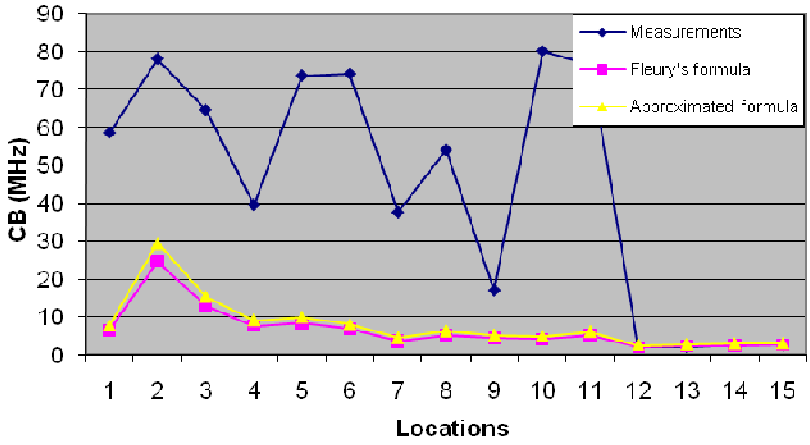

Figure 9.3: CB at 0.5 coherence level calculations differences for all locations

In opposite, for non LoS, the results almost coincide. This good approximation is explained by the fact that for non LoS conditions the CB is smaller due to the absence of the direct ray and therefore the multipath components become more important. The good match between expression (9.1) and the Fleury lower bond is very visible in the figure.

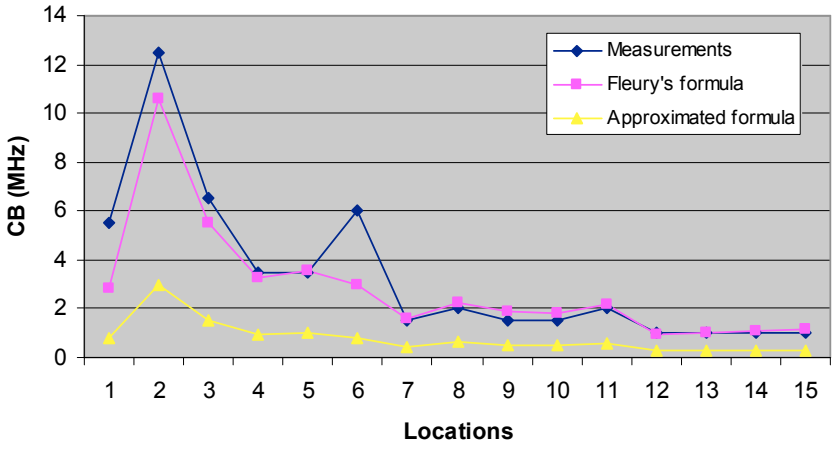

Figure 9.4: CB at 0.9 coherence level calculations differences for all locations

Analysing now the c=0.9 case the measured figures are very close to the Fleury lower bond. As shown in Figure 9.2, when c increases the measured figures are closer to the Fleury lower bond. This is even more evident in the situation where LoS does not exist. For what concerns the approximation equation, the results are always below the Fleury lower bond which indicates that it is very conservative. Some of the measurements are also slightly below the Fleury lower bond and this fact will be analysed in more depth in the next subsections where are presented graphically measurement results in the same format as presented in [4] where the Fleury lower bond is represented by a straight line due to the logarithmic scale.

3.1.1 LoS locations

In an attempt to understand how the measurements behave for the same location, firstly are analysed the 70 measurements (7x5x2) made for locations 1 and 2 (inside and at the border of the cell main coverage area) for LoS. Figure 9.5 shows the measurement results for location 1. All measurements respect the Fleury lower bond. The CB shows a much larger variation than the DS. This shows that even a small space distance variation has influence on the radio channel characteristics due to the small wavelength at millimeterwave frequency bands. For c=0.9 (Figure 9.6) the CB variation is much smaller and the values moved towards the Fleury lower bond line, as expected. A few measurements are below the Fleury lower bond.

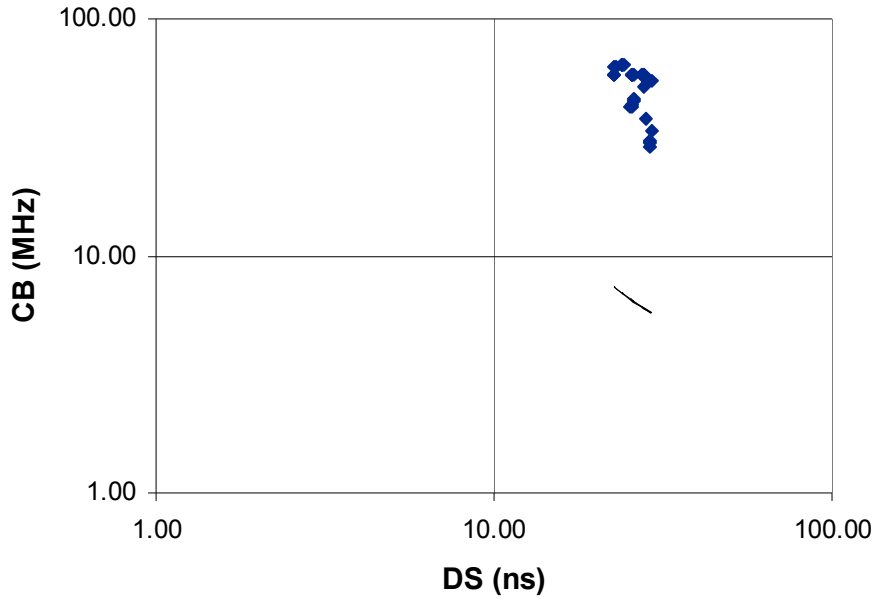

Figure 9.5: CB versus DS at c=0.5, location 1 and LoS

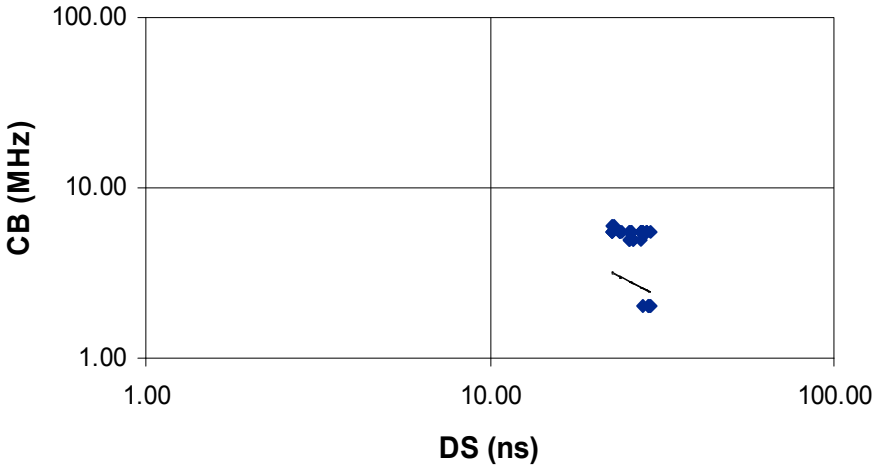

Figure 9.6: CB versus DS at c=0.9, location 1 and LoS

Analysing now the location well inside the cell coverage area (Figure 9.7), it can be seen that the DS is much smaller and all measurements are well above the Fleury lower bond for c=0.5. This location also shows higher figures for the CB and lower for the DS, which shows a "good channel" pattern. For c=0.9 (Figure 9.8), only one measurement does not respect the Fleury lower bond, being all very close to the straight line. Even well inside the cell, there is one measurement that is below the Fleury lower bond.

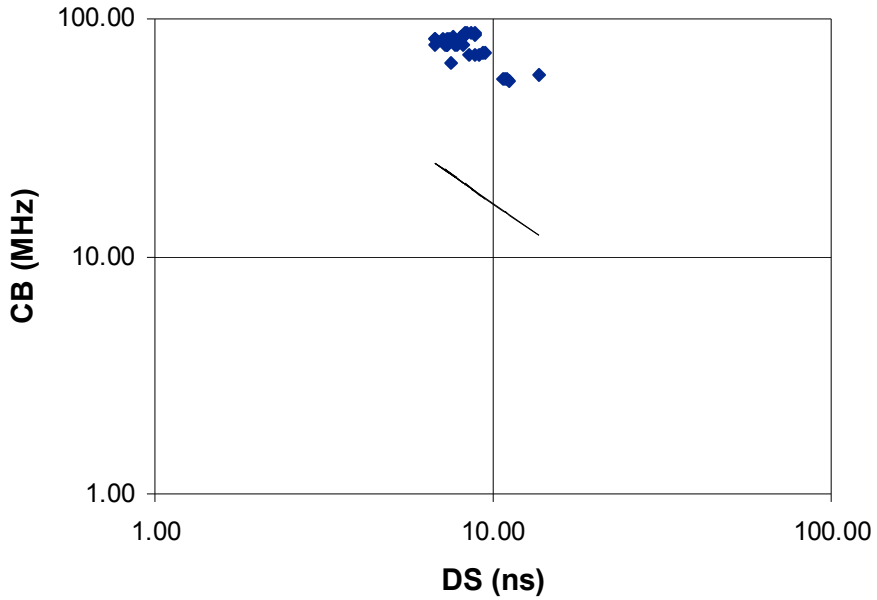

Figure 9.7: CB versus DS at c=0.5, location 2 and LoS

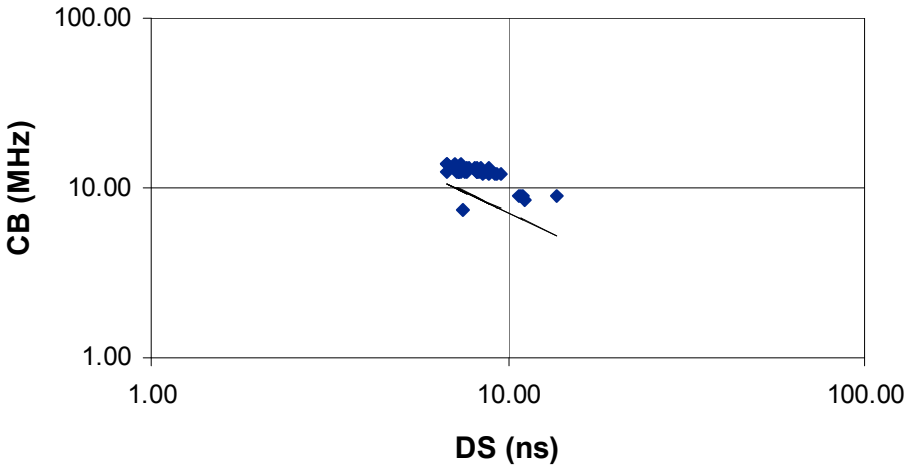

Figure 9.8: CB versus DS at c=0.9, location 2 and LoS

Figure 9.9 shows the measurements after being averaged (space and time) for all locations and c=0.5. The Fleury lower bond is respected and it can also be observed that the DS and the CB figures have a considerably large span in the pavilion. For c=0.9 (Figure 9.10), the situation is quite different. The measurements are very near to the Fleury lower bond as expected but some of them are even below. The fact is that the locations that are below do not differ considerably from the Fleury lower bond and happen mainly for low CB values. The notion of inverse proportionality between CB and DS is very clear in Figure 9.10, but not that clear in the previous case.

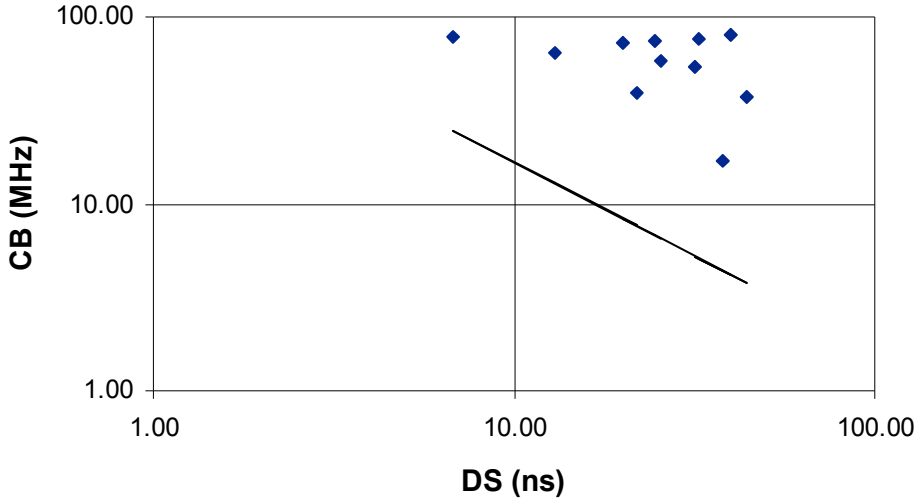

Figure 9.9: CB versus DS at c=0.5, all locations and LoS

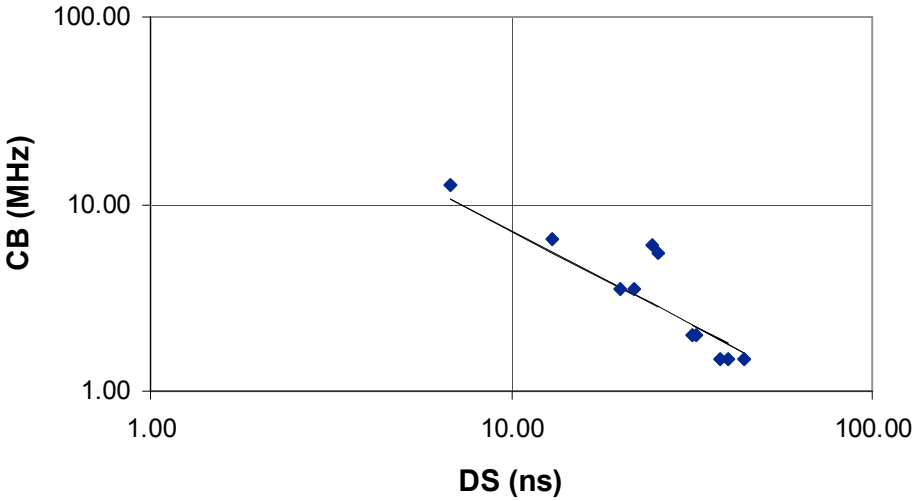

Figure 9.10: CB versus DS at c=0.9, all locations and LoS

3.1.2 Non LoS locations

In the pavilion only four locations where measured in non LoS conditions during the measurements campaign. Observing Figure 9.11 and Figure 9.12 where the available measurement results are displayed, it can be concluded that the CB values are quite low and the DS figures large, leading to a situation where all the measurements reside very close to the Fleury lower bond, being some of them even below.

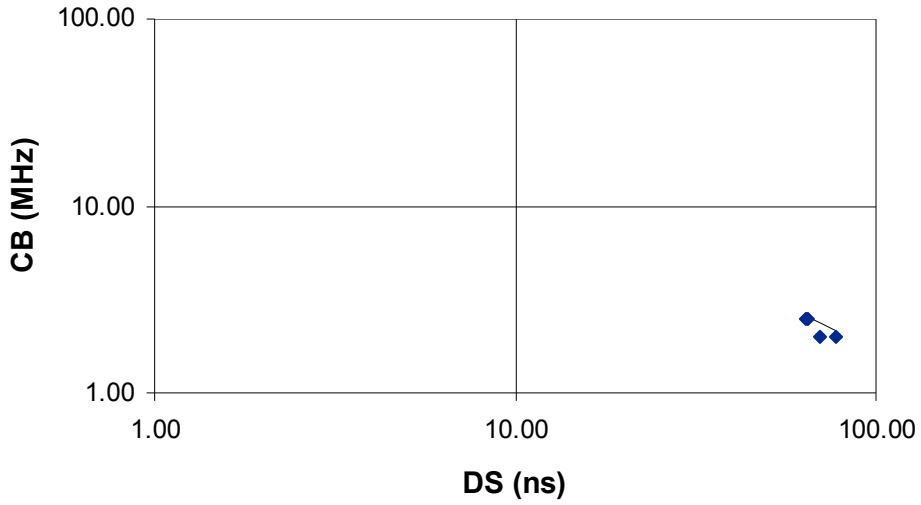

Figure 9.11: CB versus DS at c=0.5, all locations and non LoS

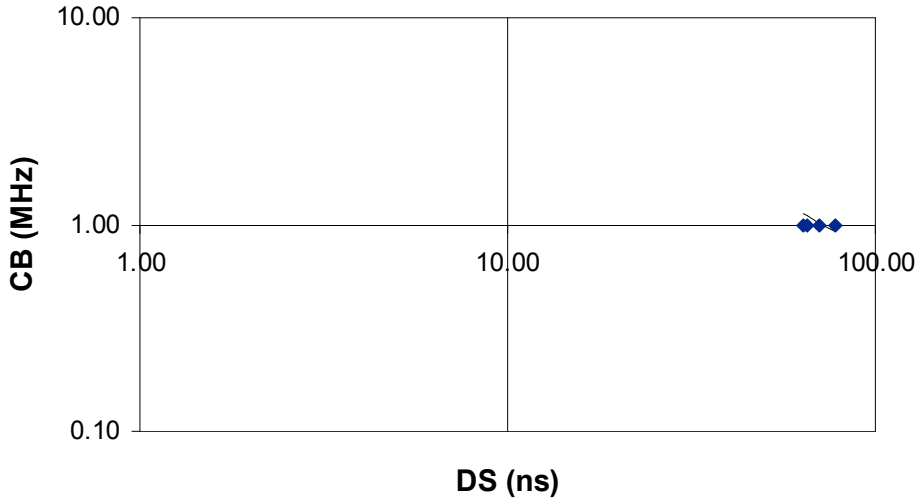

Figure 9.12: CB versus DS at c=0.9, all locations and non LoS

3.2 IT Room

In this section the same study will be presented for this particular scenario. The number of measurement locations was 64 distributed in a regular grid (8 by 8). In this scenario only five measurements were performed for each location instead of the 35 in the case of the pavilion.

Figure 9.13 shows the behaviour of the measurements in LoS and the figures obtained based on the two early presented equations for c=0.5. First of all we can see a kind of periodic behaviour along the rows in the room. The measurements are clearly above the

Fleury lower bond and as already noticed before a good match exists between the Fleury lower bond and the approximation formula. For low values of the CB the approximation is very good.

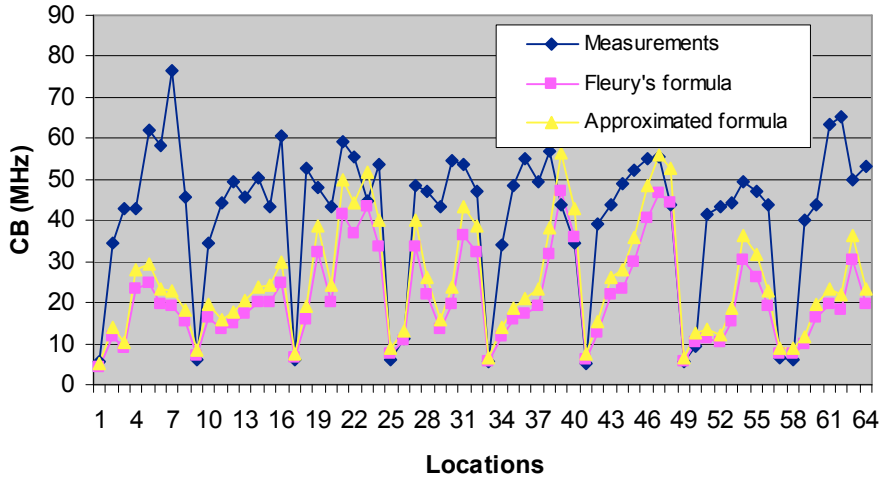

Figure 9.13: CB at 0.5 coherence level calculations differences for all locations in LoS

Figure 9.14 shows the same results but for c=0.9. Although some rows are quite near the Fleury lower bond, the generality of the measurements do not respect the Fleury lower bond. For what concerns the approximation formula it stills shows to be very conservative since the results are always below the Fleury lower bond. As lower the CB figures are the better is the match between the three alternatives used to calculate the CB.

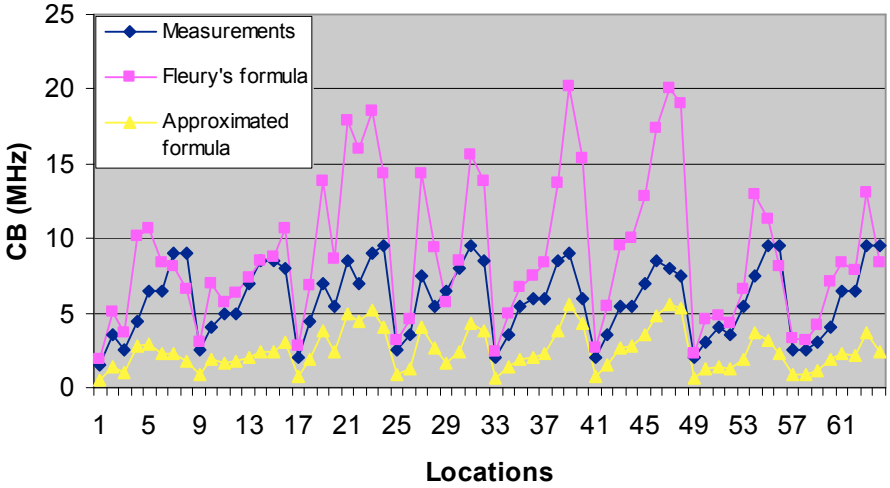

Figure 9.14: CB at 0.9 coherence level calculations differences for all locations in LoS

For non LoS the behaviour is similar than for LoS. Also in this case the Fleury lower bond is not respected for the generality of the measurements for c=0.9. This is shown in Figure 9.15 and Figure 9.16.

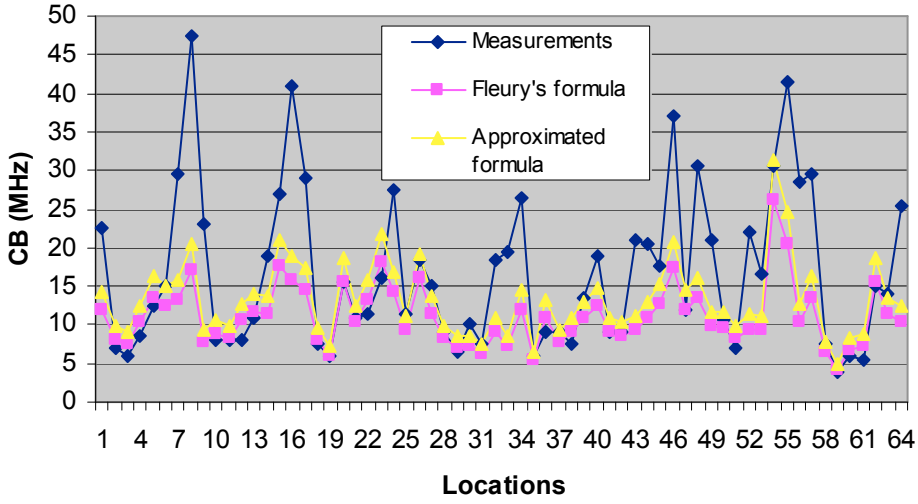

Figure 9.15: CB at 0.5 coherence level calculations differences for all locations in non LoS

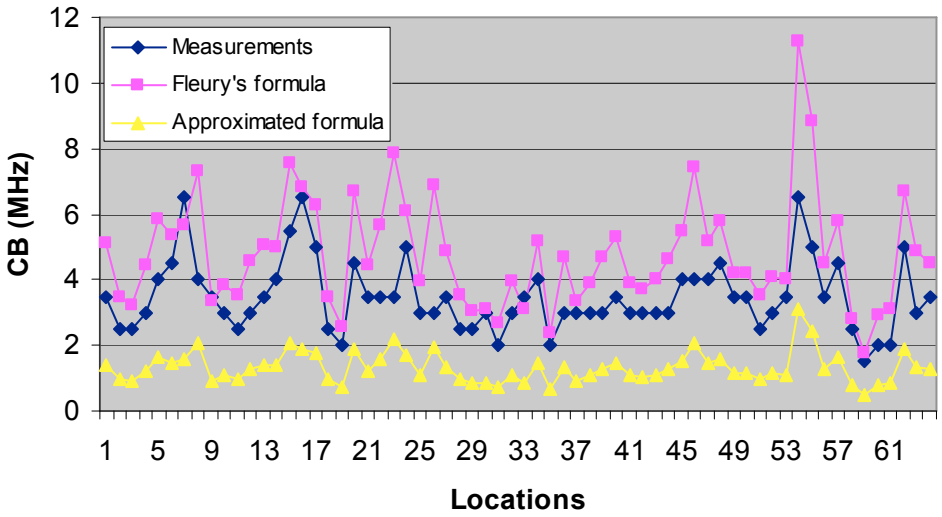

Figure 9.16: CB at 0.9 coherence level calculations differences for all locations in non LoS

3.2.1 LoS locations

Analysing Figure 9.17 and Figure 9.18 it can be observed that for c=0.9 the Fleury lower bond is not respected in general. For the case of c=0.5, only a few measurements do not respect the lower bond. The inverse proportionality nature of the DS and CB is more evident on the first case.

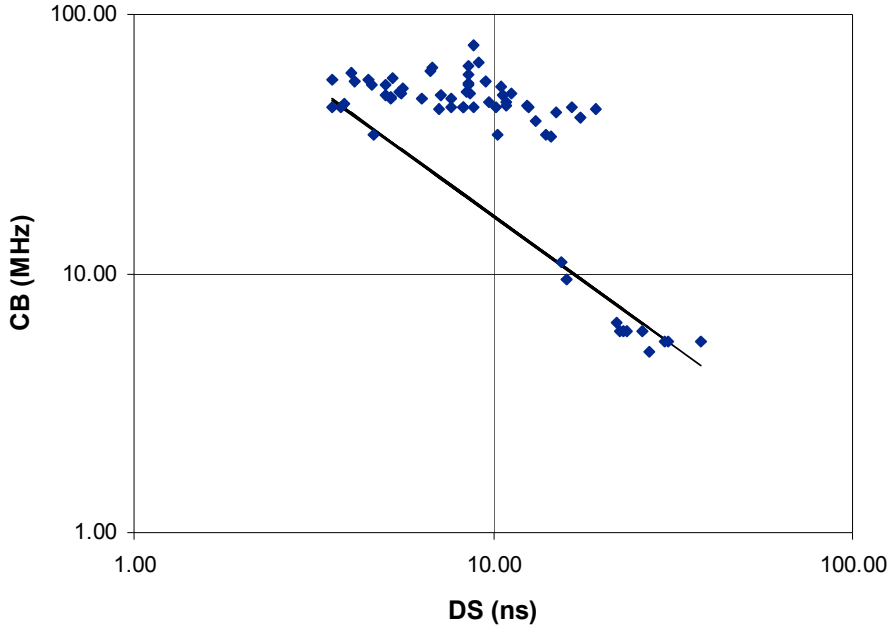

Figure 9.17: CB versus DS at c=0.5, all locations and LoS

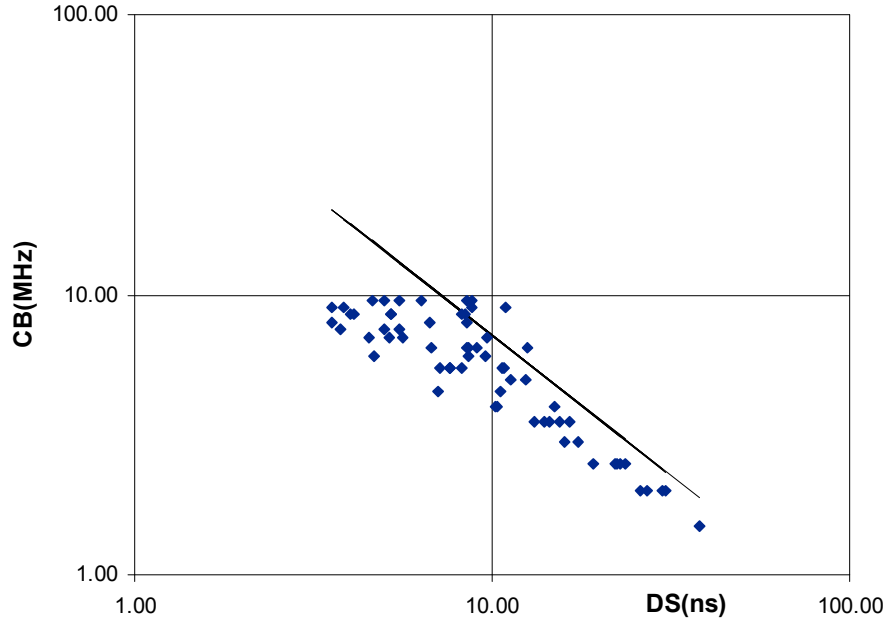

Figure 9.18: CB versus DS at c=0.9, all locations and LoS

3.2.2 Non LoS locations

The results for the non LoS situation are presented in Figure 9.19 and Figure 9.20. For this particular case, the situation is even more acute since the majority of the measurements are

very close to the Fleury lower bond straight line. In both cases (c=0.5 and c=0.9) the inverse proportionality relationship between DS an CB is clear.

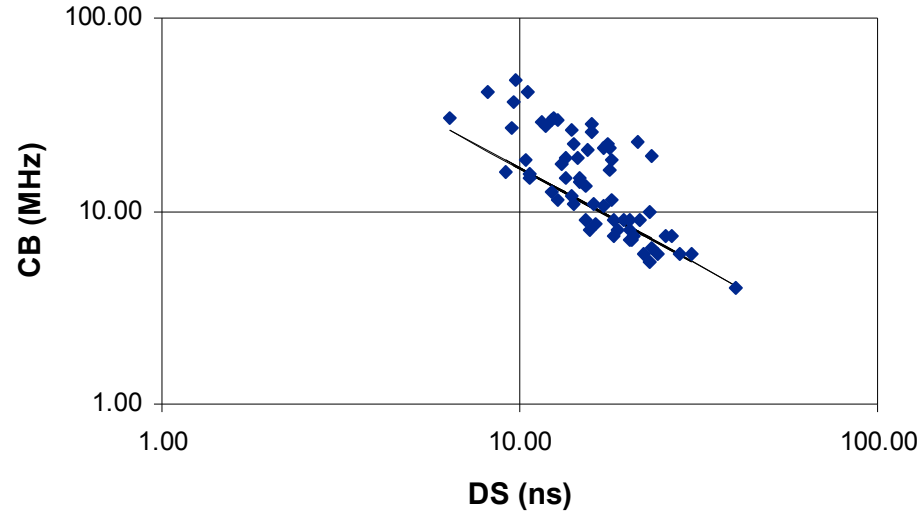

Figure 9.19: CB versus DS at c=0.5, all locations and non LoS

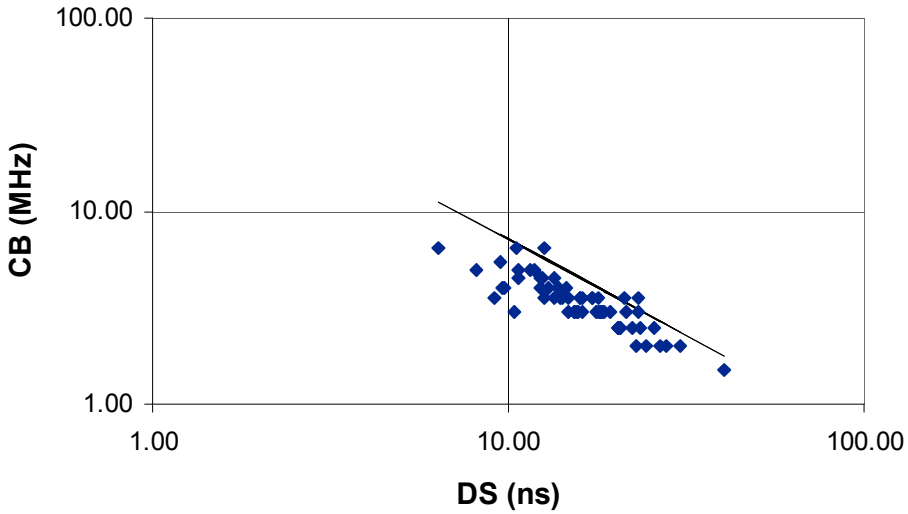

Figure 9.20: CB versus DS at c=0.9, all locations and non LoS

4. Analysis by Simulation

As stated previously, the measurements revealed several locations were the Fleury lower bond was not respected, mainly in non LoS and for a correlation coefficient of 0.9. The explanation for that fact could be several but one – errors and lack of precision – could

always be associated with experimental work. This was actually the hypotheses raised by Fleury for the points not respecting the lower bond in Figure 9.1. In order to eliminate or cross check this possibility, simulations were performed based on a ray tracing simulation tool in three different scenarios. Different measurement bandwidths, 400 MHz and 1 GHz were also used in order to trace problems related with the system time resolution and therefore lack of precision [14].

4.1 Simulation scenarios

The simulation scenarios were initially the same as those selected for measurements: the IT Room and the sports pavilion. In order to extend the validity of the simulation results an intermediate size room was defined having 10m by 30m totally empty and uniform. This is to say that this room is totally uniform in terms of materials and a pure "box" in terms of shape – a parallelepiped (no windows, no furniture and a single material for the walls, ceiling and floor).

To increase the number of cases, beyond different scenarios, also different antennas were used: isotropic and the wide cell antennas and different bandwidths: 400 MHz and 1GHz. All simulations were performed for LoS and non LoS and for correlation figures of c=0.5 and c=0.9. A total of 48 different situations were considered and 10 000 locations distributed in a regular grid were simulated for each of the scenarios, leading to a total of 30 000 locations analysed. The idea behind this number of locations was to increase the space resolution to a much better level than the one used for measurements.

4.2 Sports pavilion

Here are presented the pavilion simulation results for the different configuration considered. The simulation model for the pavilion was described in chapter 8. The size of the pavilion is 46.35m x 36.15m x 8m. For the walls an ε_r=6.14 was selected.

4.2.1 Isotropic antenna

This subsection presents the results obtained with an isotropic antenna in the BS and in the mobile terminal. The reason to include this configuration was to test the results against a different distribution of the power.

4.2.1.1 400 MHz

In Figure 9.21 are displayed the results obtained for LoS and non LoS considering as well two values for the correlation coefficient: 0.5 and 0.9. The duration of the PDP time bin is 2.5 ns corresponding to the system time resolution. The Fleury lower bond is just not respected for non LoS and c=0.9. A few locations failed but not significantly. The fact that in the figure the graph shows some points aligned in horizontal lines is related with the frequency resolution that is 0.5 MHz. The failures could be explained by lack of precision in the frequency dimension. Since in this case a bandwidth of 400 MHz was used the maximum coherence bandwidth is limited to 200 MHz as indicated by the graphs. The inverse proportionality rule is not very clear in the graphs.

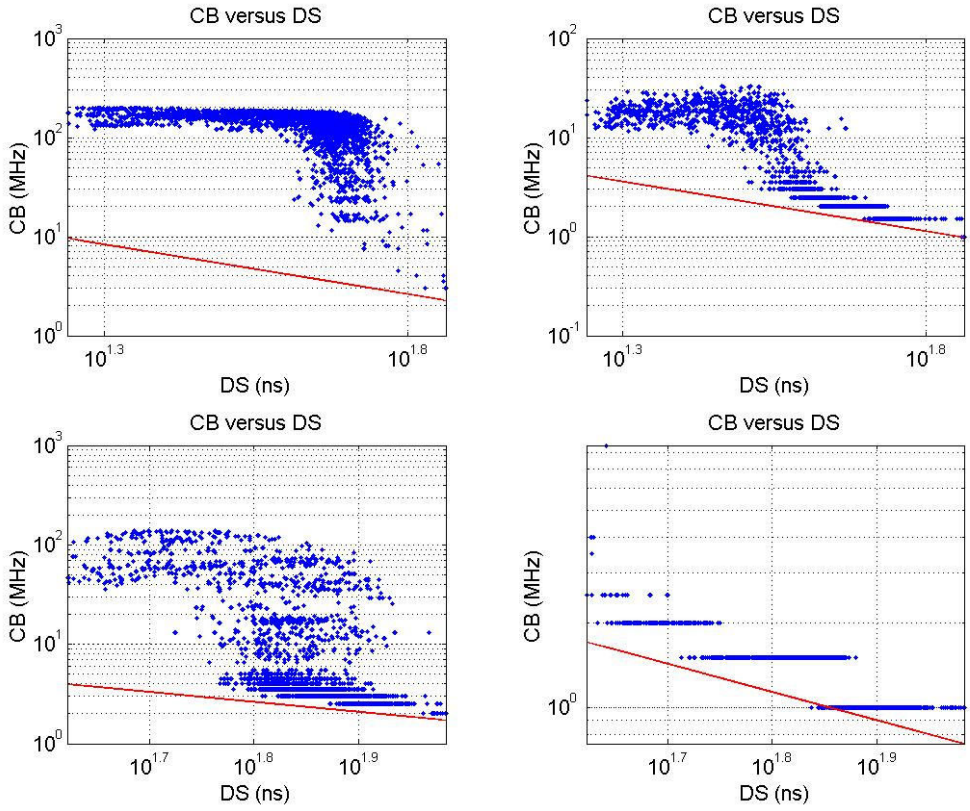

Figure 9.21: CB versus DS: c=0.5 and LoS (top left), c=0.9 and LoS (top right), c=0.5 non LoS (bottom left) and c=0.9 non LoS (bottom right)

Figure 9.22 shows the NRP figures for LoS and non LoS. The non LoS was obtained just by removing the direct ray from the PDP. The power generally deceases as we move away form the BS due to the antenna radiation pattern. The figure does not shows pure circles do to the different scales used in the horizontal and vertical axis.

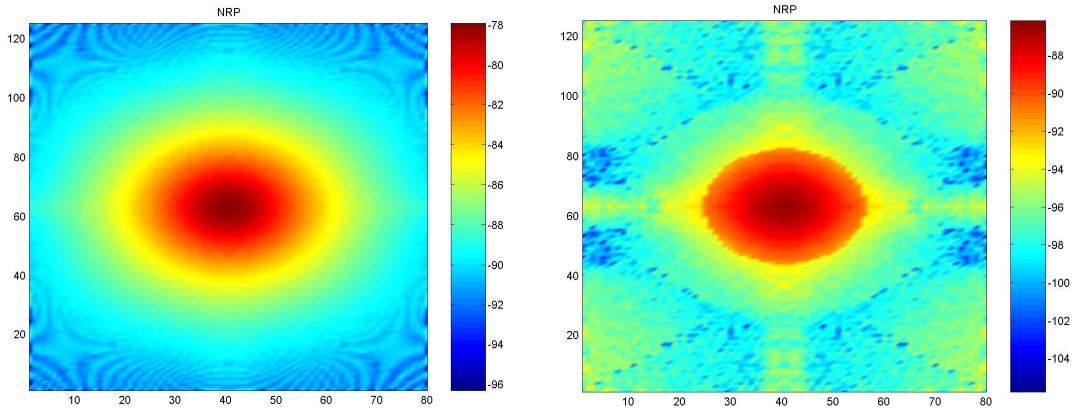

Figure 9.22: NRP: LoS (left) and non LoS (right)

Figure 9.23 shows how the CB changes across the pavilion. The CB figures are higher near the BS, decreasing as we move away from it in a radial direction. As expected the situation that shows the lowest figures for the coherence bandwidth is the non LoS at c=0.9.

As observed in Figure 9.24, the DS has an opposite behaviour since it increases as we move away from the BS, showing generally an inverse proportionality relationship with the CB. It is also visible that there is not a fixed relation between DS and CB.

4.2.1.2 1000 MHz

This subsection shows the results for the same scenario but now with a higher time resolution (larger bandwidth). In practice this reduces the frequency step to 0.25 MHz and the maximum possible CB is now 500 MHz.

In opposite to the measurements that were obtained in the frequency domain and then using IFFT converted to the time domain, the simulations were done in the time domain and then converted to the frequency domain. The results were obtained by redoing the simulations with the new time resolution and not by reutilizing the simulation results obtained for 400

MHz. This means that the values of NRP and DS are not exactly the same since they were calculated using different PDPs.

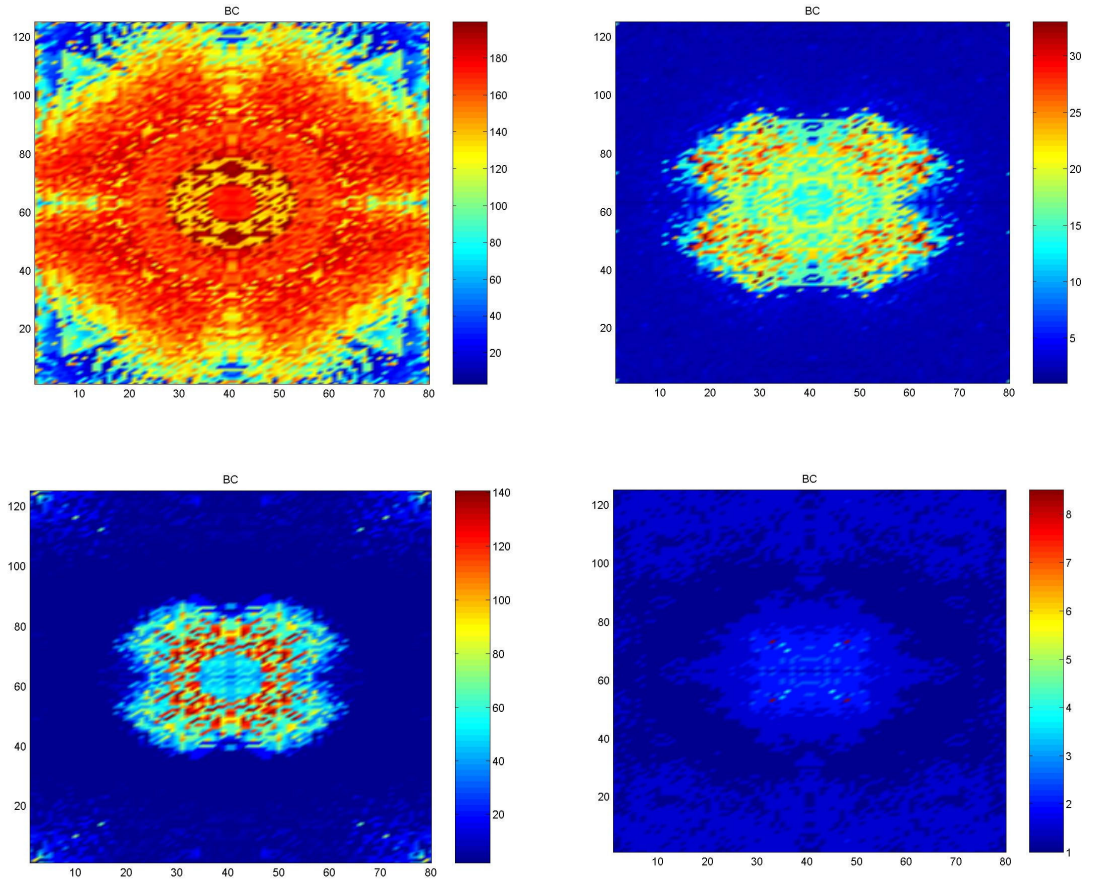

Figure 9.23: CB: C=0.5 and LoS (top left), c=0.9 and LoS (top right), c=0.5 non LoS (bottom left) and c=0.9 non LoS (bottom right)

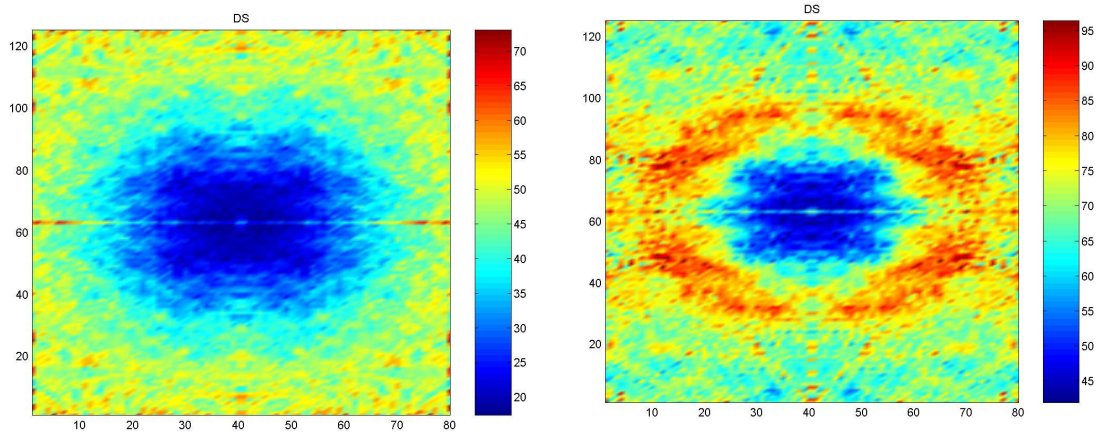

Figure 9.24: DS: LoS (left) and non LoS (right)

Analysing the results presented in Figure 9.25, and comparing with the ones obtained for 400 MHz, we can see that now the maximum CB is larger than 200 MHz (graph on the top left). However, there are still some locations where the Fleury lower bond is violated (graph on the bottom right), although the step for the CB is now 0.25 MHz. Therefore the situation did not change with the increment of the time resolution.

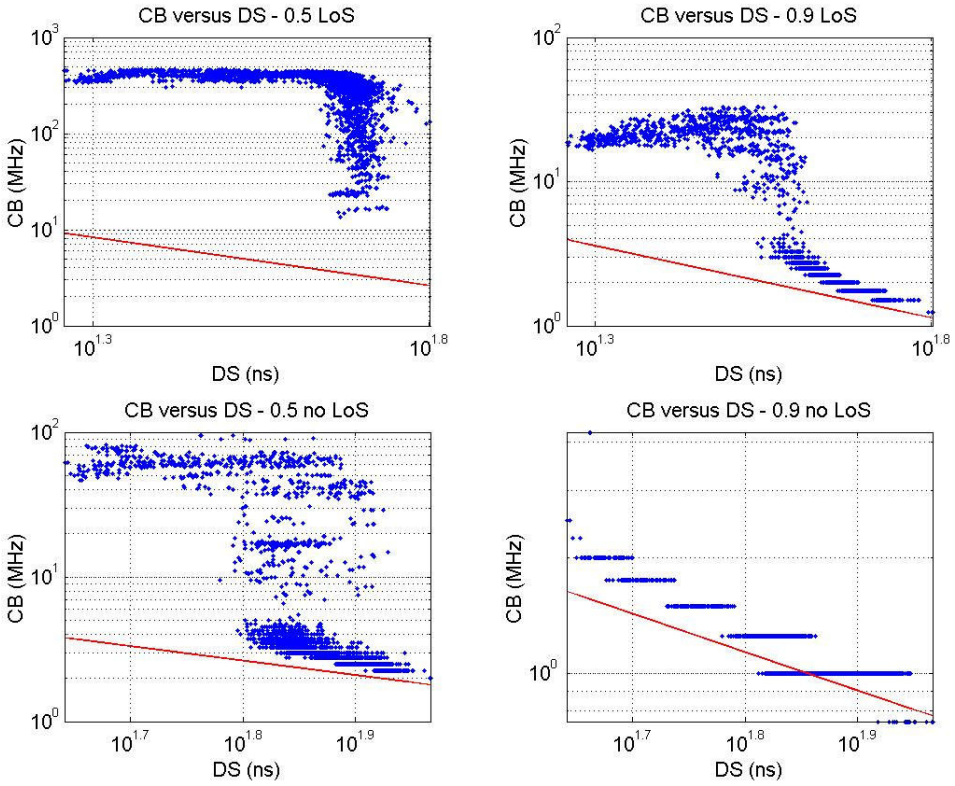

Figure 9.25: CB versus DS: c=0.5 and LoS (top left), c=0.9 and LoS (top right), c=0.5 non LoS (bottom left) and c=0.9 non LoS (bottom right)

In Figure 9.26 is presented how the CB behaves inside the pavilion. In terms of the general shape of the graphs and comparing to the 400 MHz results, we can conclude that it is basically the same. The main difference is the fact that the CB is larger reaching in some cases more than 450 MHz. Concerning the NRP and the DS displayed in Figure 9.27 and Figure 9.28, they show in general the same behaviour when compared to the 400 MHz case. There are however larger values of DS and lower values of NRP for the 400 MHz case.

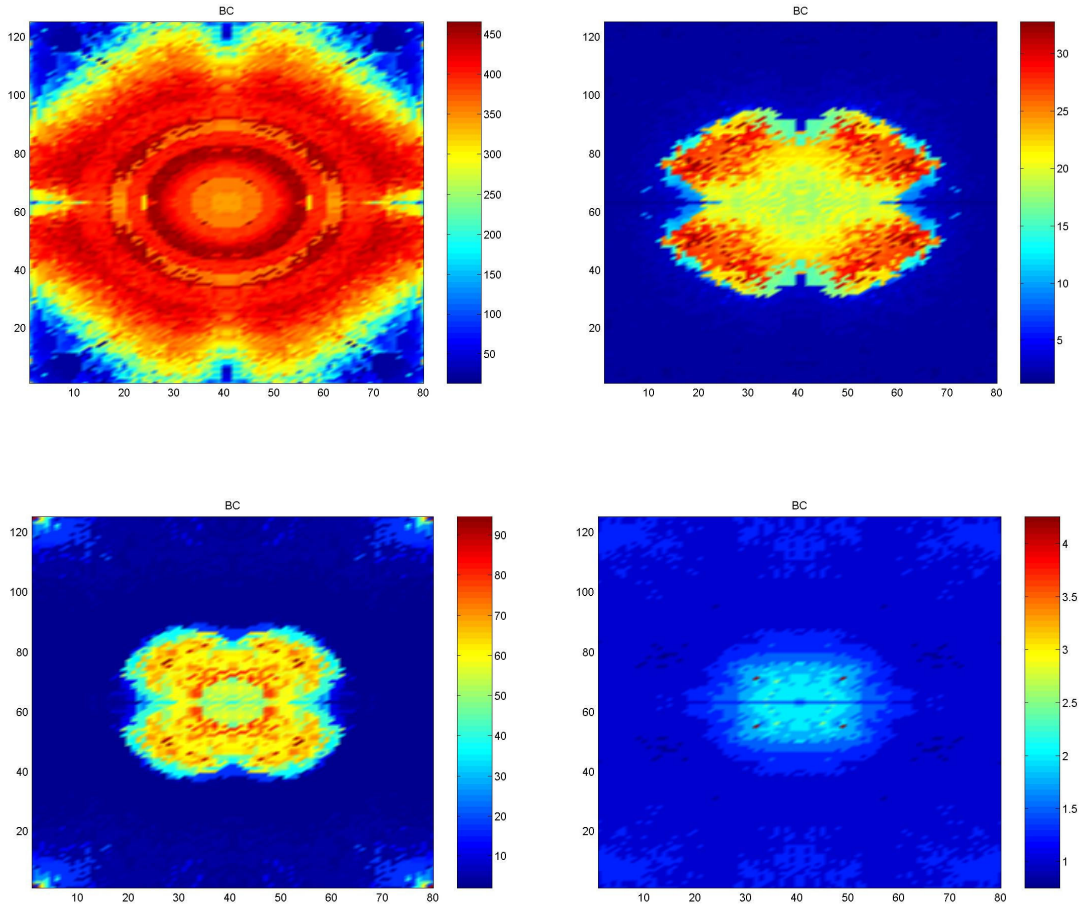

Figure 9.26: CB: c=0.5 and LoS (top left),c= 0.9 and LoS (top right), c=0.5 non LoS (bottom left) and c=0.9 non LoS (bottom right)

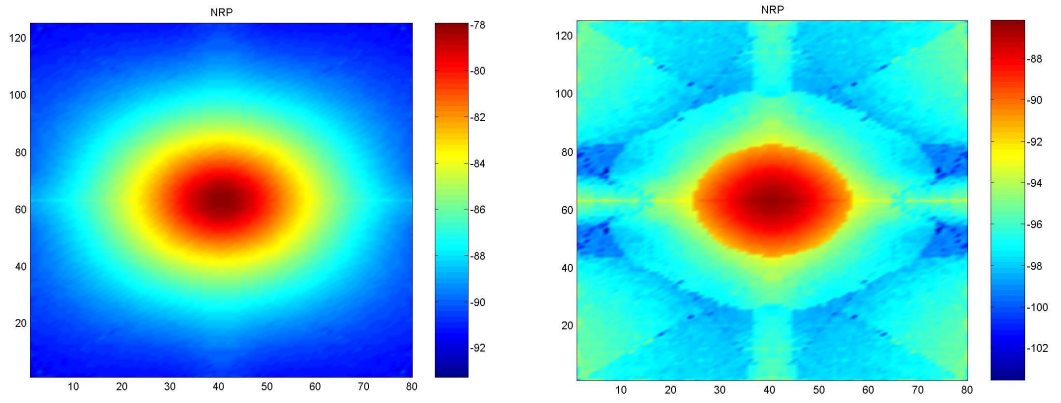

Figure 9.27: NRP: LoS (left) and non LoS (right)

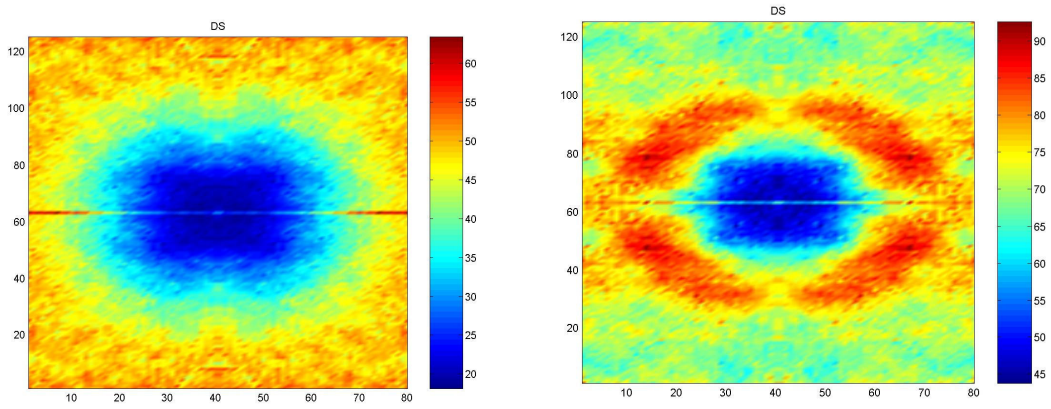

Figure 9.28: DS: LoS (left) and non LoS (right)

4.2.2 Wide Cell antenna

The same type of antenna used in the measurements was also used for the simulations. The results are presented in this subsection.

4.2.2.1 400 MHz

In Figure 9.29 are presented the results for this new antenna configuration with a 400 MHz bandwidth. All locations respect the Fleury lower bond being some of them very close to it. Comparing with the measurement results it can be concluded that the simulation results are in line with the measurements since the locations that did not respect the lower bond were not that far from it and the reason could be caused by the errors and the effects of the windowing when processing the data leading to lack of precision.

The NRP and DS distributions can be seen in Figure 9.30 and Figure 9.31, respectively. These results show clearly the impact and shape of the Wide Cell antenna radiation pattern. For LoS conditions the largest figures of the DS are situated in the left and right side of the BS, being the area where less power is delivered by the antenna.

Figure 9.32 shows how the CB changes along the pavilion for the Wide Cell antenna configuration. The areas with better CB correspond to areas where the coverage is good and the DS is low. The CB is generically quite low except for the case in LoS and c=0.5.

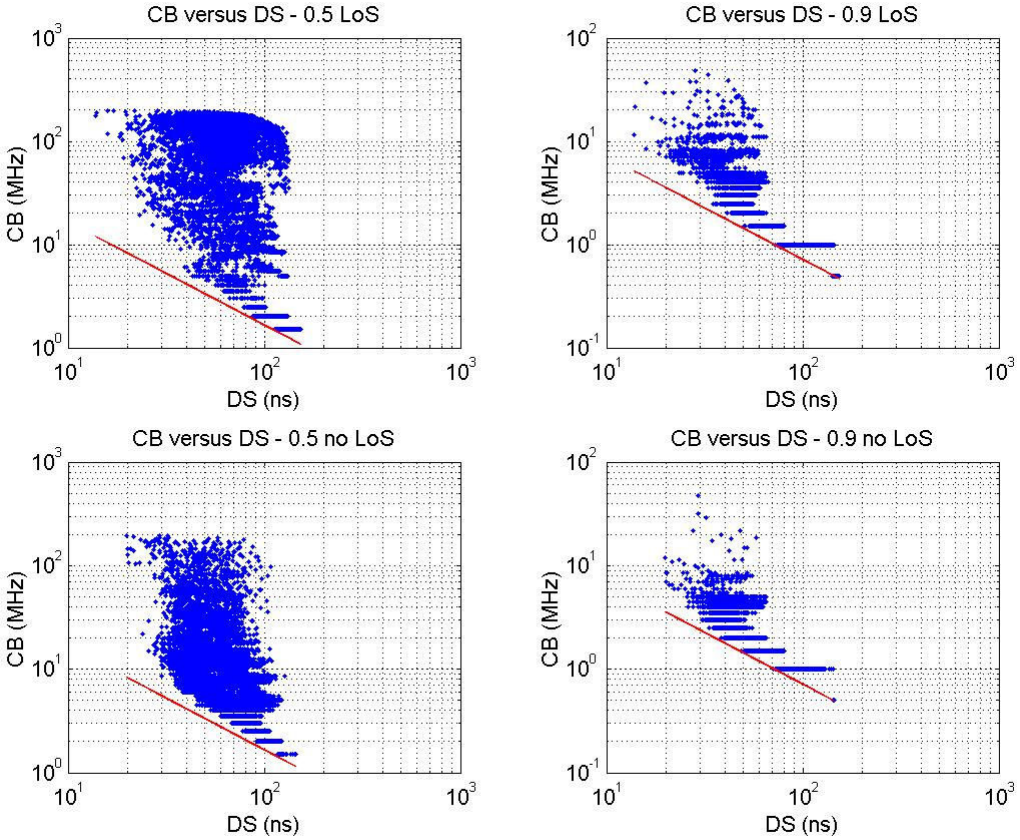

Figure 9.29: CB versus DS: c=0.5 and LoS (top left), c=0.9 and LoS (top right), c=0.5 non LoS (bottom left) and c=0.9 non LoS (bottom right)

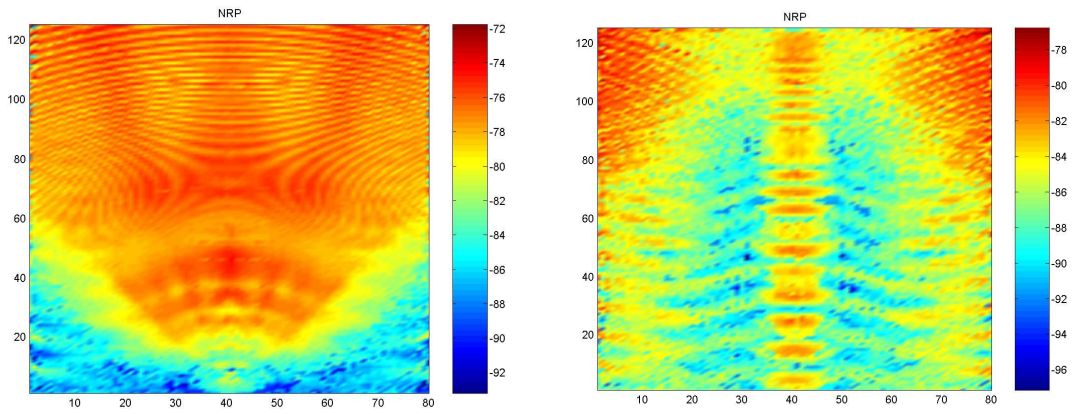

Figure 9.30: NRP: LoS (left) and non LoS (right)

4.2.2.2 1000 MHz

In Figure 9.33 are displayed the results for 1000 MHz. The Fleury lower bond is also respected for all locations again in line with the measurement results. The NRP

distribution has a very similar shape but with a more uniform distribution of the power. The same applies to the DS.

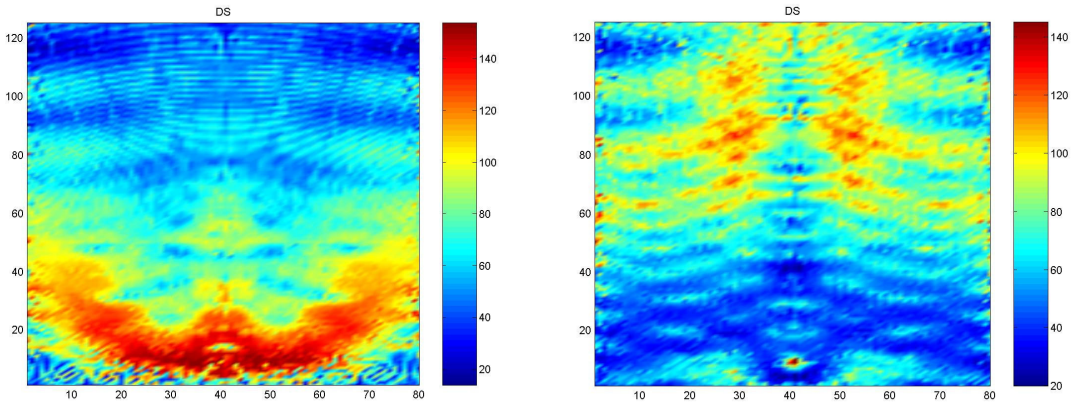

Figure 9.31: DS: LoS (left) and non LoS (right)

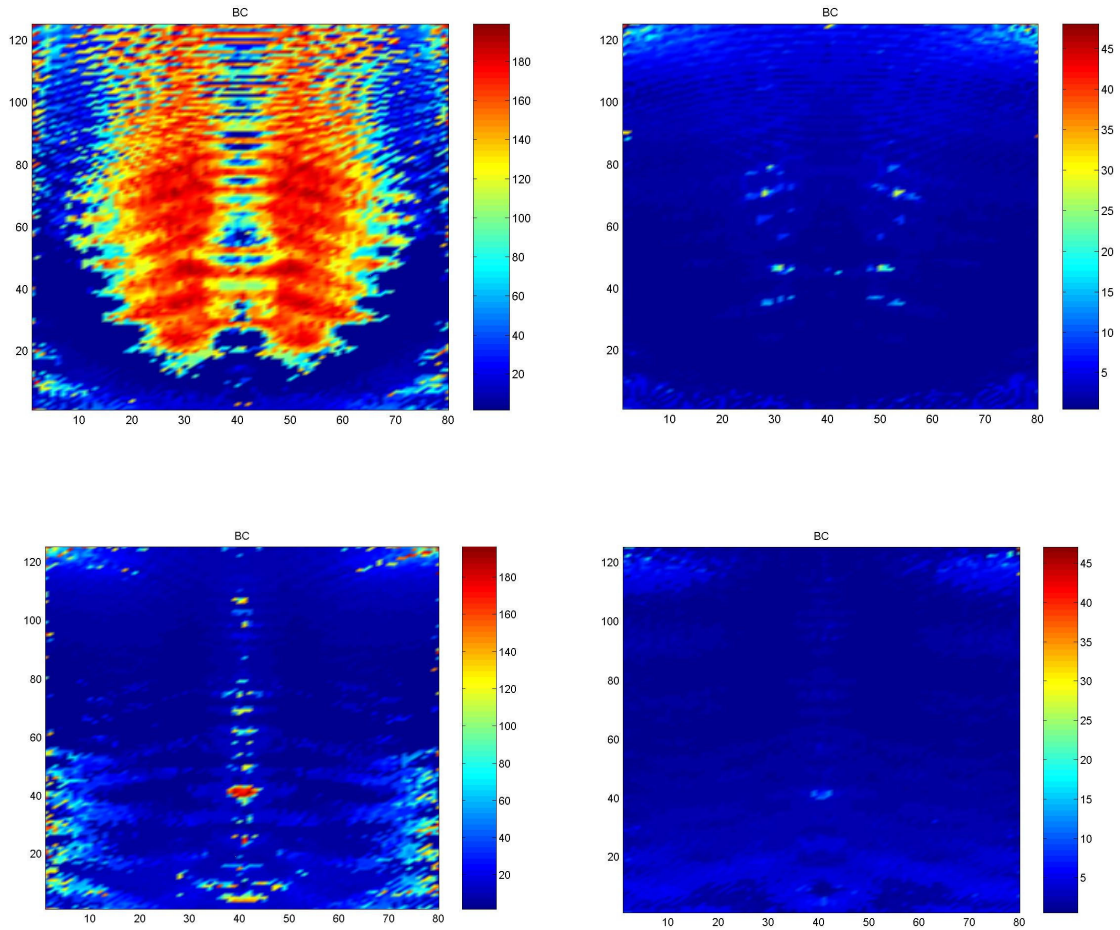

Figure 9.32: CB: c=0.5 and LoS (top left), c=0.9 and LoS (top right), c=0.5 non LoS (bottom left) and c=0.9 non LoS (bottom right)

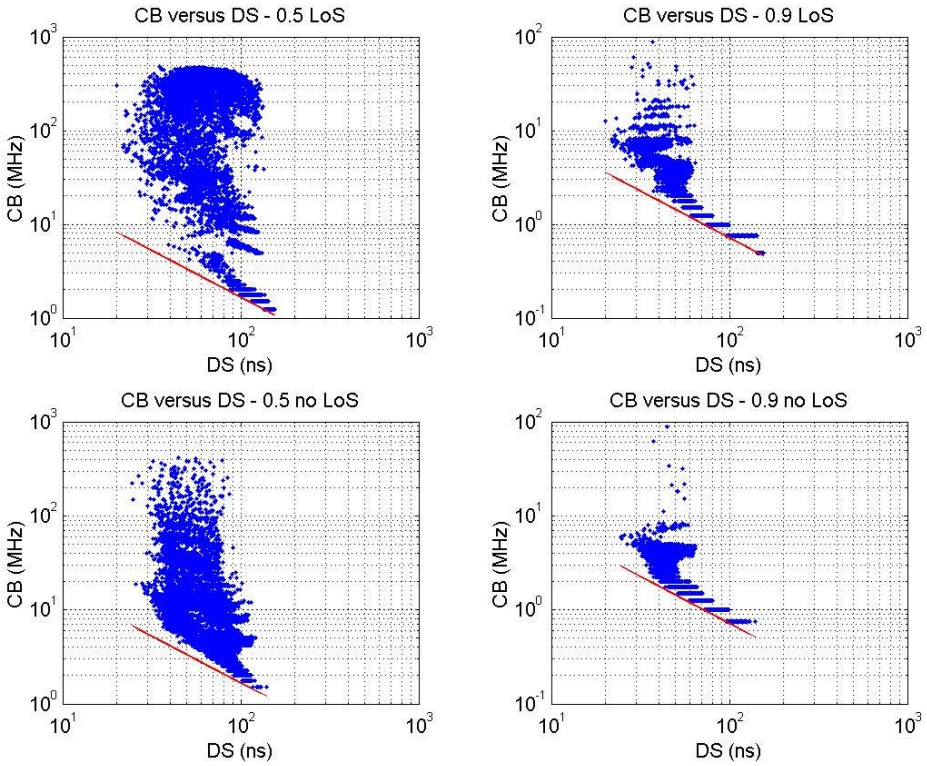

Figure 9.33: CB versus DS: c=0.5 and LoS (top left), c=0.9 and LoS (top right), c=0.5 non LoS (bottom left) and c=0.9 non LoS (bottom right)

4.3 IT Room

The IT Room is also a scenario where measurements were performed. Again, two antenna types were considered although for the measurements only the Wide Cell antenna was used. The size of the room is 8m x 6.6m x 3m. For the walls an $\varepsilon_r = 10$ was selected.

4.3.1 Isotropic antenna

Figure 9.34 shows the results for the isotropic antenna and 400 MHz. The number of locations that violated the Fleury lower bond is considerable. The violations exist for about 16% of the locations even for the LoS and c=0.9 case. For the non LoS case we have experienced that 28% of locations violate the Fleury lower bond.

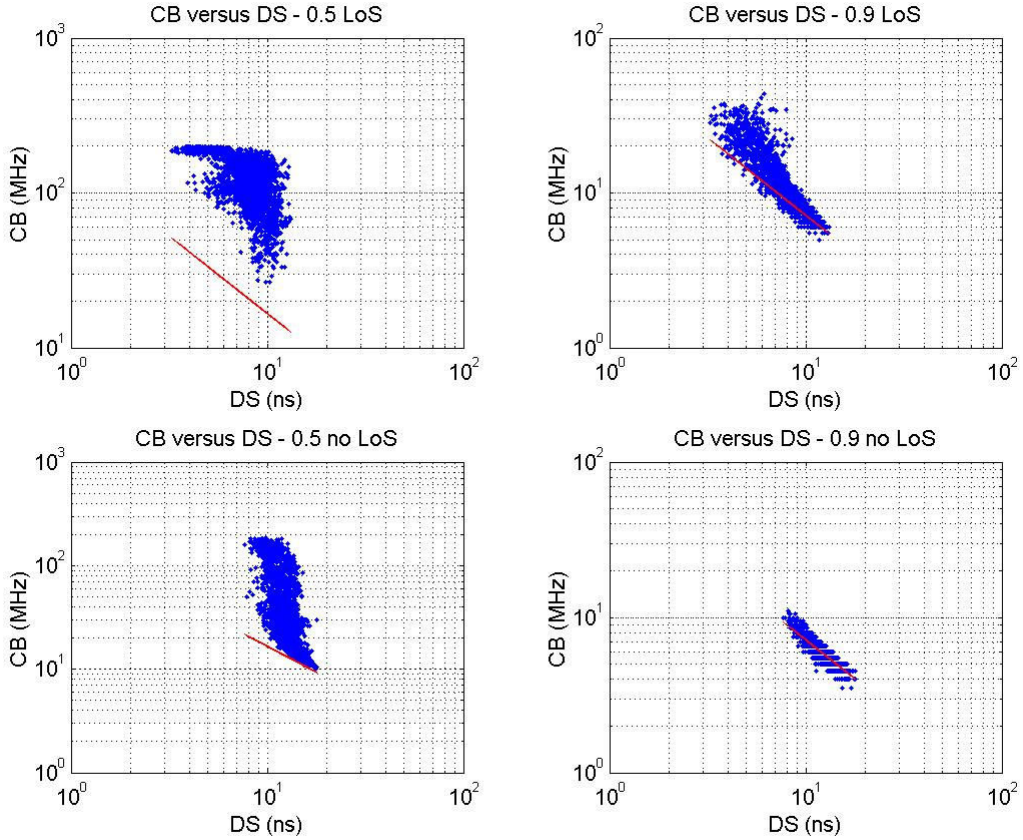

Figure 9.34: CB versus DS: c=0.5 and LoS (top left), c=0.9 and LoS (top right), c=0.5 non LoS (bottom left) and c=0.9 non LoS (bottom right)

Figure 9.35 shows the results for 1000 MHz. Clearly fewer locations violate the Fleury lower bond, namely 0.5% for LoS and 8% for non LoS (for c=0.9). This fact could indicate that a larger bandwidth (a better time resolution) could eliminate completely the correlation between the rays in the time bins (infinite time resolution) leading to a pure uncorrelated scattering situation, or at least just dependent on the scenario and not on the radio signals receiving system characteristics or limitations in terms of bandwidth. An infinite bandwidth system is not possible to realise and the bandwidth is usually very limited, therefore it is not possible to eliminate completely the correlation between the different rays since the receiver cannot see them separately.

4.3.2 Wide Cell antenna

Measurements with this antenna configuration were also performed in the IT Room. Figure 9.36 shows the results obtained by simulation with a bandwidth of 400 MHz. For

this antenna configuration there are also violations of the Fleury lower bond for the same situations of the isotropic antenna case, namely 7% for LoS and 18% for non Los. This confirms the results obtained via measurements indicating that the Fleury lower bond does not apply, likely due to the fact that the assumptions of a WSSUS channel does not hold for such a small room due to the scattering correlation.

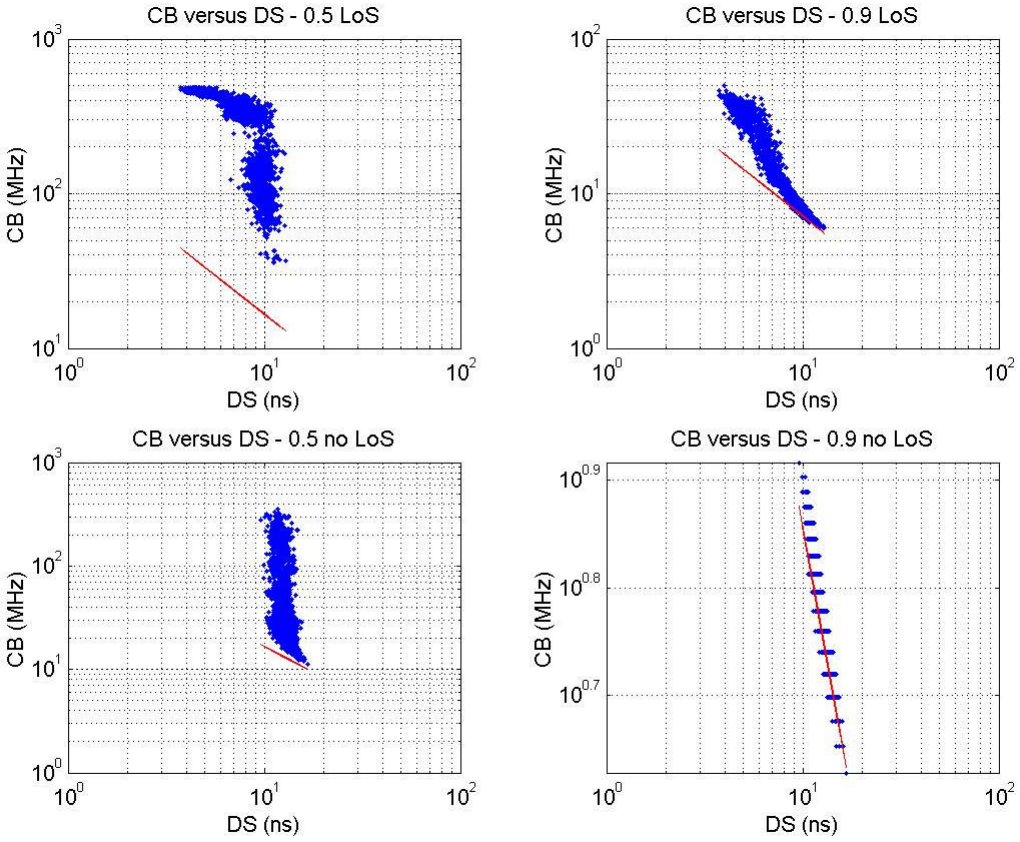

Figure 9.35: CB versus DS: c=0.5 and LoS (top left), c=0.9 and LoS (top right), c=0.5 non LoS (bottom left) and c=0.9 non LoS (bottom right)

In Figure 9.37 are presented the simulation results for 1000 MHz. The number of locations that violate the Fleury lower bond is clearly less, confirming the relation with the considered bandwidth (time resolution). Only 1% for LoS and 2% for non LoS do violate the lower bond.

Figure 9.38 presents the NRP, CB and DS for the two antenna scenarios considered for the bandwidth of 1000 MHz. It is clear that the highest levels of CB happen for the best levels of power and the lowest levels of DS. The results are in line to what should be expected.

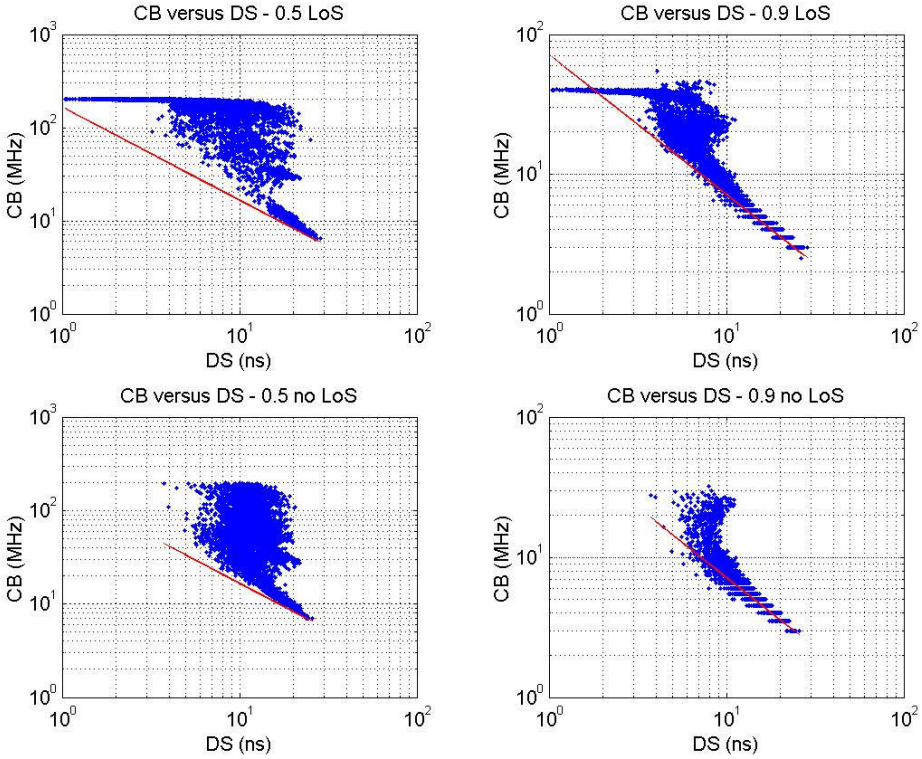

Figure 9.36: CB versus DS 400 MHz: c=0.5 and LoS (top left), c=0.9 and LoS (top right), c=0.5 non LoS (bottom left) and c=0.9 non LoS (bottom right)

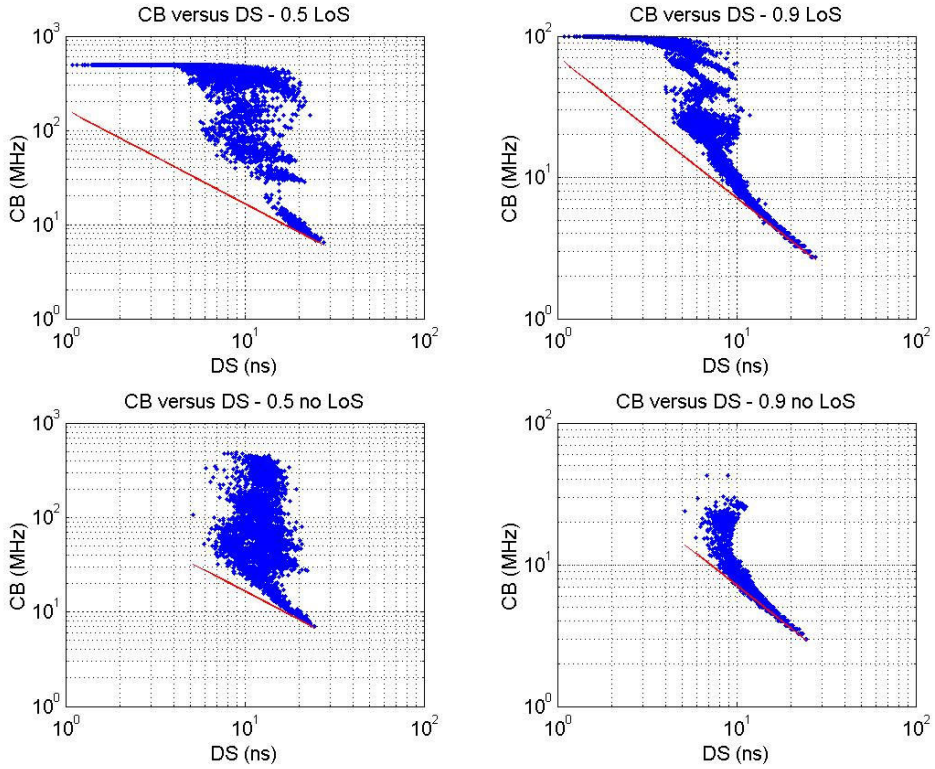

Figure 9.37: CB versus DS 1000 MHz: c=0.5 and LoS (top left), c=0.9 and LoS (top right), c=0.5 non LoS (bottom left) and c=0.9 non LoS (bottom right)

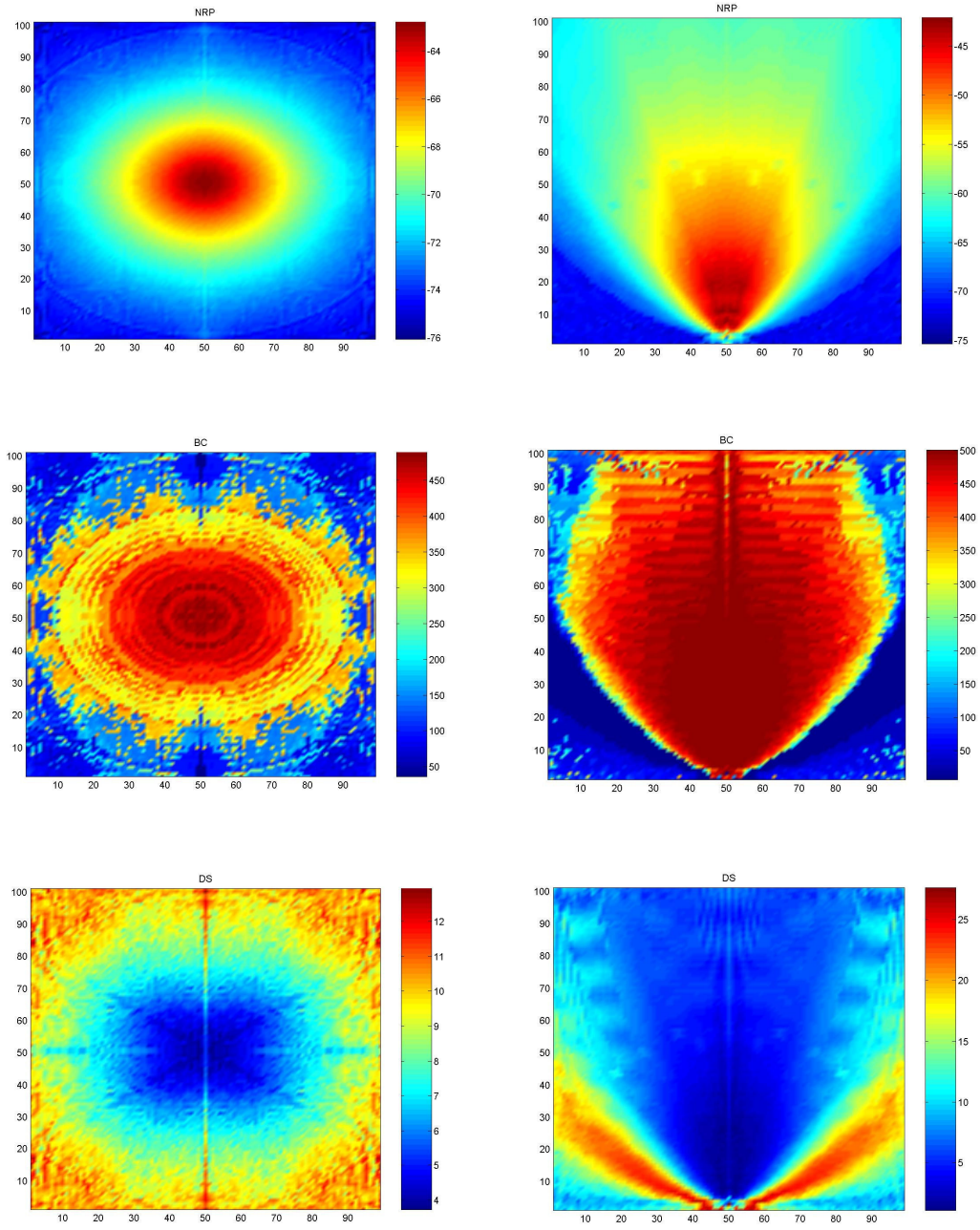

Figure 9.38: NRP, CB and DS in LoS, 1000 MHz: isotropic antenna (left) and wide cell antenna (right)

4.4 Room 10 m by 30 m

In order to check the dependency on the size of the room and the possibility of the loss of uncorrelation due to size, an intermediate scenario was simulated. No real measurements are available for this imaginary room. The dimensions of the room are 10 m wide by 30 m

length. The same height of the IT Room was considered (3m). For the walls an $\varepsilon_r = 10$ was selected. As previously, the same type of antennas were used.

4.4.1 Isotropic antenna

Figure 9.39 shows the results for the 400 MHz case. Very few locations violate the Fleury lower bond showing that for this room size the assumption of uncorrelated scattering is still valid. The channel is still WSSUS since no changes to the scenario or motion of the receiver are allowed during the simulations being therefore stationary.

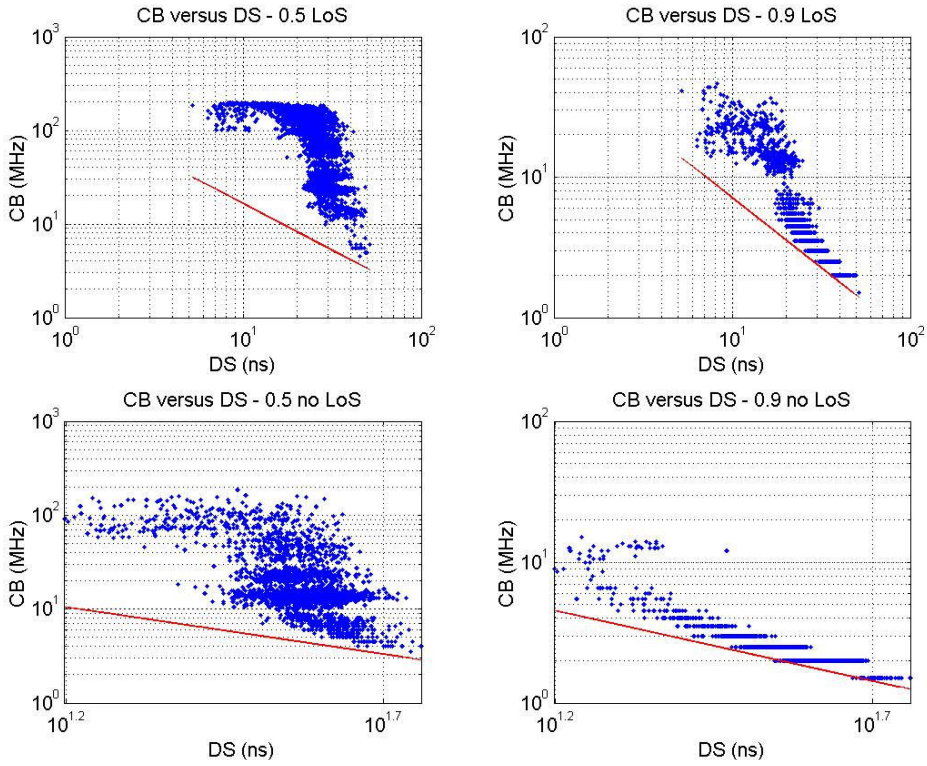

Figure 9.39: CB versus DS for 400 MHz: c=0.5 and LoS (top left), c=0.9 and LoS (top right), c=0.5 non LoS (bottom left) and c=0.9 non LoS (bottom right)

Observing Figure 9.40 where the results for 1000 MHz are displayed it is clear that there are no locations that violate the Fleury lower bond, showing that for a better time resolution the correlation is decreased. Nevertheless, the degree of violation experienced for 400 MHz is not very much. What is clear is that this room behaves much better than the small room and that correlation is not experienced in a large degree. The only difference between this room simulation model and the small room in the IT building is the size

(length and width). Even the electromagnetic properties of the walls were considered the same with ε_r=10.

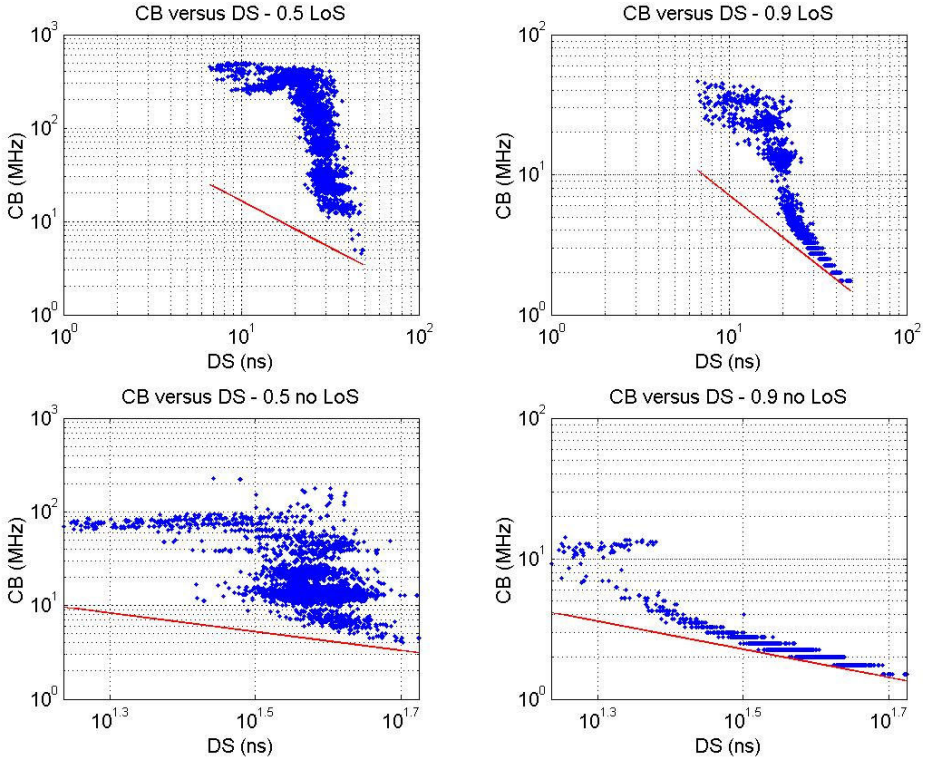

Figure 9.40: CB versus DS for 1000 MHz: c=0.5 and LoS (top left), c=0.9 and LoS (top right), c=0.5 non LoS (bottom left) and c=0.9 non LoS (bottom right)

4.4.2 Wide Cell antenna

Figure 9.41 and Figure 9.42 show the results for the Wide Cell antenna. All the locations respect the Fleury lower bond for this antenna configuration again showing that the channel can be considered WSSUS.

In Figure 9.43 is shown how the NRP, CB and DS changes across the room for the two antennas type for the 1000 MHz case. First it should be highlighted that the room is not a square but a rectangle. Therefore, the shape of the NRP for the isotropic antenna type is not an ellipse but a circumference. This is to say that the vertical dimension is shrunk leading to the ellipse effect. Regarding the power, the Wide Cell antenna provides a much better and uniform coverage of the room. For what concerns the CB, locations near the BS and with higher power levels tend to show a larger coherence bandwidth. DS figures are larger in areas where the power level is lower and the CB is usually also low.

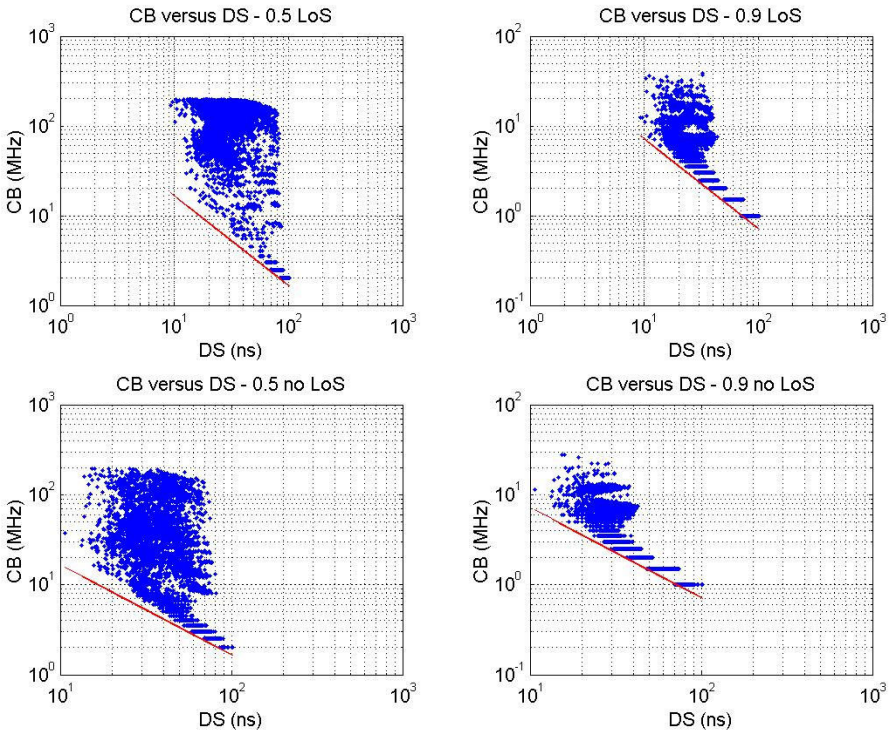

Figure 9.41: CB versus DS for 400 MHz: c=0.5 and LoS (top left), c=0.9 and LoS (top right), c=0.5 non LoS (bottom left) and c=0.9 non LoS (bottom right)

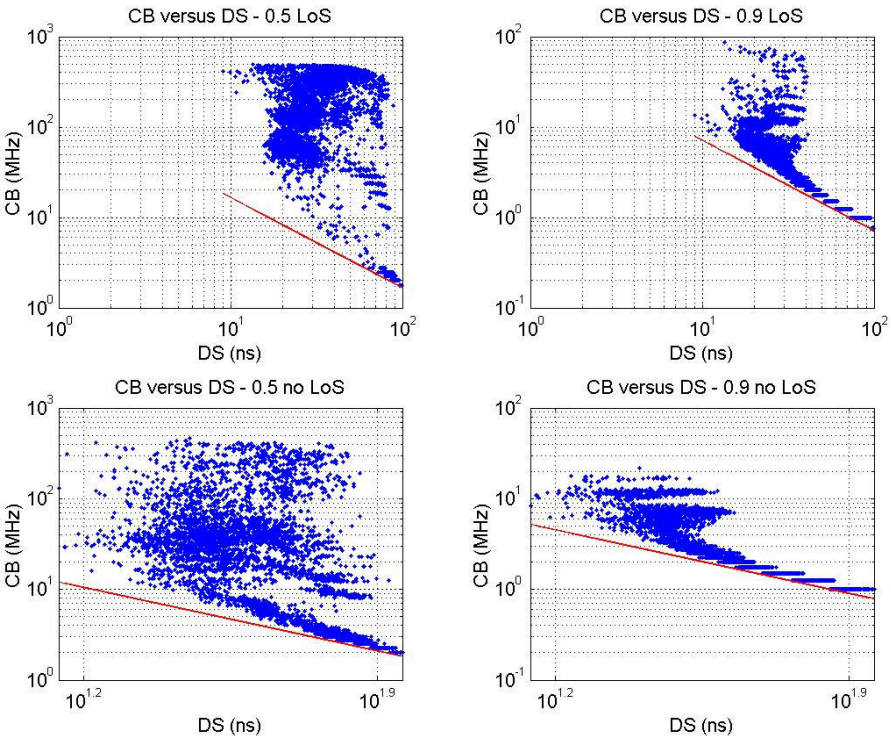

Figure 9.42: CB versus DS for 1000 MHz: c=0.5 and LoS (top left), c=0.9 and LoS (top right), c=0.5 non LoS (bottom left) and c=0.9 non LoS (bottom right)

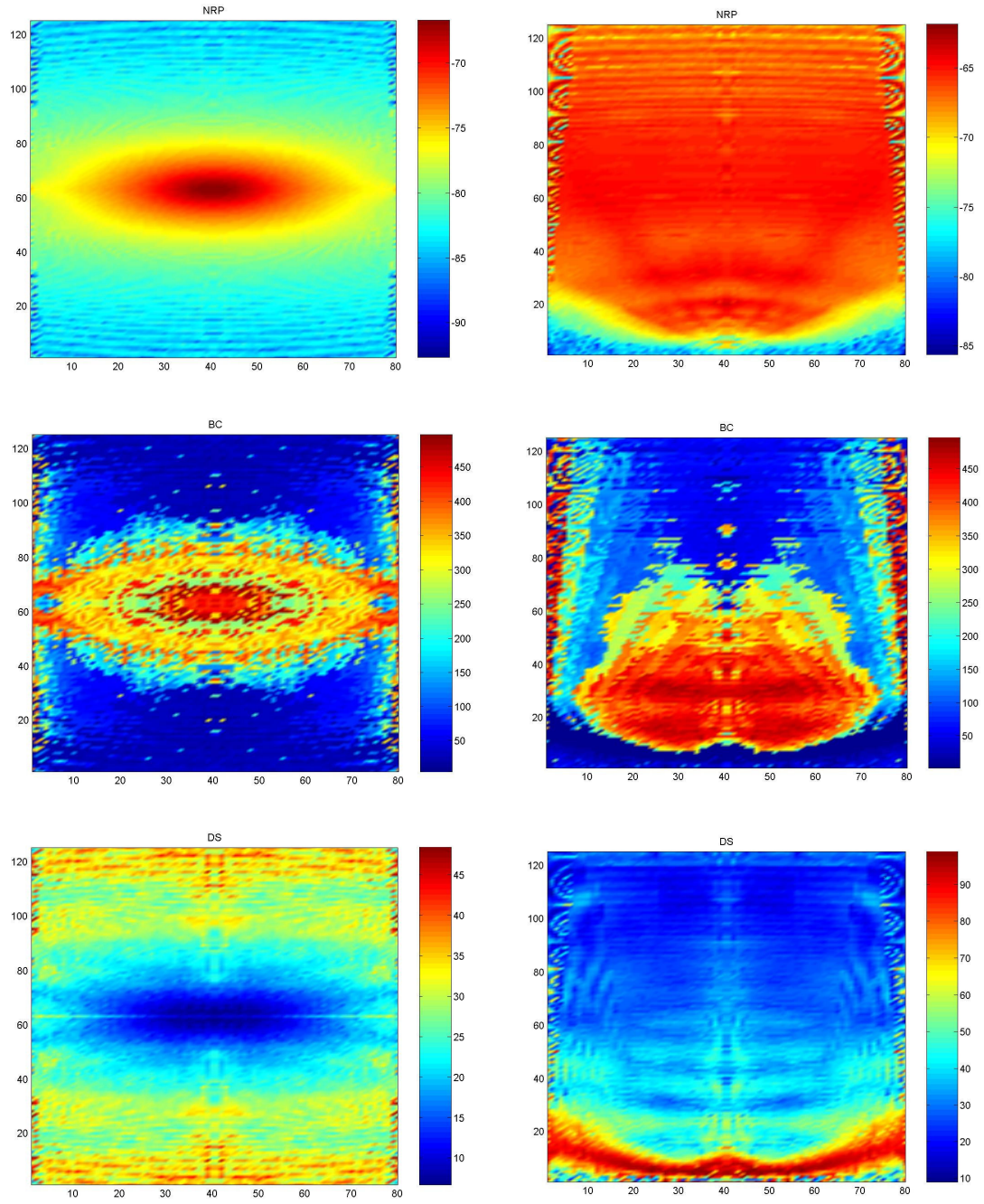

Figure 9.43: NRP, CB and DS in LoS, 1000 MHz: isotropic antenna (left) and wide cell antenna (right)

5. Summary and conclusions

This chapter presented the Fleury mathematical relationship between the DS and CB. Based on the CIR measurements performed for the two indoor scenarios the DS and CB were evaluated and its relationship analysed. A comparison of the obtained figures for all locations and the results collected directly using the approximation formulas presented in

literature was performed, showing the poor approximations results obtained in some cases. In order to further clarify the relationship between the DS and CB and the confirmation of the Fleury lower bond applicability in multiple conditions and scenarios, simulation results were performed using different antenna types, correlation coefficients, measurement bandwidths and LoS and non LoS conditions and the results analysed.

Concerning the sports pavilion, it can be concluded that for both LoS and non LoS cases the Fleury lower bond is generally respected by all measurements and those that do not respect, the fact could be explained by measurement errors or other effects due to the processing of the data, since the discrepancy is very little in relation to the Fleury lower bond. Moreover, as the correlation coefficient c approaches to one, the measurements and the Fleury lower bound tend to converge and this was observed and confirmed for all analysed scenarios.

In the IT Room many measurements did not respect the Fleury lower bond for c=0.9. This fact, in opposite to the sports pavilion, is maybe more difficult to explain based on errors related with the experimental procedures. Another possible explanation is the fact that the Fleury conditions used for the derivation of the mathematical formulation do not hold true in this scenario, namely the uncorrelated scattering assumption. Being the room small the different rays tend to have similar behaviours (particularly true for empty rooms as was this case). The same phenomenon is accentuated by the fact that the time resolution of the measurement system is limited and may not be enough for this particular scenario generating correlation for what concerns adjacent rays. To clarify these hypotheses simulation results were performed.

All the simulation results obtained for the pavilion for the two antenna configurations are in line with the expected and also in line with the measurement results for what concerns specifically the Wide Cell antenna configuration. For the isotropic antenna, there are locations that fail in terms of the Fleury lower bond, being however quite close to it. Errors introduced during the processing of the results could justify this result. Not much difference is observed between the 400 MHz and 1000 MHz cases, except for the maximum CB that is limited to 200 MHz in the first case. It is always for c=0.9 and non LoS that the worst results are obtained what is inline with the expected. Moreover, it is

always for the lowest figures of the CB that the violations of the Fleury lower bond occur and in this particular case, for CB figures near 1 MHz. In conclusion, it can be stated that simulation and measurements results match well and that the discrepancies between what would be expected and the results obtained may be justified by errors introduced by the approximations and its propagation, namely the windowing process, which cannot be bypassed when calculating the IFFT.

The IT Room simulation results indicated that several locations violate the Fleury lower bond for the 400 MHz bandwidth. Increasing the bandwidth to 1 GHz, a reduction of the number of locations was observed being namely 0.5% for LoS and 8% for non LoS both for c=0.9. This fact could indicate that a larger bandwidth (a better time resolution) could eliminate completely the correlation between the rays in the time bins leading to a pure uncorrelated scattering situation, or at least just dependent on the scenario and not on the radio signals receiving system limitations in terms of bandwidth. An infinite bandwidth system (infinite time resolution) is not possible to realise and the bandwidth is usually very limited, therefore it is not possible to eliminate completely the correlation between the different rays since the receiver cannot see then separately.

In the room 10mx30m, very few locations violate the Fleury lower bond showing that for this room size the assumption of uncorrelated scattering is still valid. The channel is still WSSUS since no changes to the scenario or motion of the receiver are allowed during the simulations being therefore stationary. For the 1000 MHz bandwidth there are no locations that violate the Fleury lower bond, confirming that for a better time resolution the correlation is decreased.

As general conclusion it can be stated that increasing the system bandwidth or time resolution the correlation among the different rays diminishes and therefore the number of violations of the Fleury lower bond reduce as well. Moreover, for larger and more complex scenarios, the correlation is less having as a direct impact a decrease also on the number of locations that violate the Fleury lower bond. The Fleury mathematical formulation holds valid for the analysed scenarios and different cases except when the WSSUS condition is violated. The approximation formulas presented in the literature are very conservative for c=0.5 except for non LoS situations. In this case the approximation and the Fleury lower

bond almost coincide. The approximation for c=0.9 always presents results lower than the Fleury lower bound being even more conservative and the measured results are always very close to the Fleury lower bond. As higher the c is the more the results approach to the Fleury lower bond.

6. References

[1] Theodore S. Rappaport, "Wireless Communications Principles and Practice", Prentice-Hall, 1996

[2] Homayoun Hashemi and David Tholl, "Statistical Modeling and Simulation of the RMS Delay Spread of Indoor Radio Propagation Channels" IEEE Transactions on Vehicular Technology, vol. 43, No. 1, February 1994.

[3] Larry J. Greenstein, Vinko Erceg, Yu Shuan Yeh and Martin V. Clark, "A New Path-gain/Delay-Spread Propagation Model for Digital Cellular Channels", IEEE Transactions on Vehicular Technology, Vol. 46, Nº 2, May 1997

[4] Bernard Henri Fleury, "An Uncertainty Relation for WSS Processes and It's Application to WSSUS Systems", IEEE Transactions on Communications, Vol. 44, Nº 12, December 1996

[5] Bernard Henri Fleury, "New Bounds for the Variation of Mean-Square-Continuous Wide- Sense-Stationary Processes", IEEE Transactions on Information Theory, Vol. 41, Nº 3, May 1995

[6] Donald C. Cox and Robert P. Leck, "Correlation Bandwidth and Delay Spread Multipath Propagation Statistics for 910 MHz Urban Mobile Radio Channels", IEEE Transactions on Communications, Vol. 23, nº11, November 1975

[7] A. Molisch, "Statistical Properties of RMS Delay-Spread of Mobile Radio Channels with Independent Rayleigh-Fading Paths", Correspondence, IEEE Transactions on Vehicular Technology, vol. 45 No. 1 Feb. 96

[8] S. Ichitsubo, A. Akeyama, S Sakagami, "Correlation Bandwidth Characteristics for Paths Between Base Station and Building Roofs", IEEE Transactions on Vehicular Technology, vol. 48 No. 1, Jan. 99

[9] A. Hammoudeh, M. Sánchez, E. Grindrod, "Experimental Analysis for Propagation at 62 GHz in suburban Mobile Radio Microcells", IEEE Transactions on Vehicular Technology, vol. 48 No. 2 Mar 99

[10] M. J. Gans, "A Power-Spectral Theory of Propagation in the Mobile-Radio Environment", IEEE, Trans. on Vehic. Technology, vol. vt-21, No. 1 Feb 1972

[11] P. A. Bello, "Characterization of Randomly Time-Variant Linear Channels", IEEE Trans. On Communications Systems, vol. CS-11, no 12 Dec. 1963

[12] Theodore S. Rappaport, "Characterisation of UHF Multipath Radio Channels in Factory Buildings", IEEE Transactions on Antennas and Propagation, Vol. 37, No. 8, August 1989.

[13] Henrik Börjeson, "Radio Wave Propagation in Confined Environments – Measurements and Models", PhD Thesis, Department of Applied Electronics, Lund University, Sweden, February 2000.

[14] Manuel Dinis, José Garcia, Valdemar Monteiro and Nelson Oliveira, "Millimetre-wave Channel Impulse Response Experimental Evaluation and Relation Between Delay Spread and Channel Coherence Bandwidth", PIMRC' 2002, September, Lisbon, Portugal.

10th Chapter

Final Conclusions and Future Work

1. Introduction

Mobile and wireless communications technologies are a significant milestone in the human society evolution. The social impacts are already visible being difficult to imagine the world without these technologies. The way people socialise and work has changed considerably during the last decades. Mobile phones are not seen just as communication machines but as status tools and wonderful gadgets.

Technologically the evolution of the mobile and wireless systems was tremendous. The first generation mobile phones were bulky, heavy, with very little battery autonomy, just permit the voice service and very expensive. Nowadays 3.5G devices are not just phones but small computers with multiple functionalities integrated in the same box. They are multimedia devices Internet capable with colour and touch screen displays, long battery

autonomy and with very small dimensions. Several device are integrated in the same package namely phone, videophone, camera, MP3 player, agenda and calendar, calculator, clock, word processor, calculus sheet, email and messaging, etc. transforming the communicator devices in the modern Swiss knifes.

This chapter presents the final conclusions and gives some hints one possible future work in this area in the context of B3G or 4G systems. The increase on the maximum transmission rate trend, possible due to the strong technology evolution supported by a heavy R&D investment, will continue to satisfy the demand of ubiquitous new services and applications becoming higher than 1 Gbit/s. The current network architectures and business models will be challenged and new solutions proposed. Telecommunication operators are facing the challenge of moving to a quadruple play paradigm and will continue fighting to survive in a very competitive market with users more and more empowered and looking for personalisation and uniqueness. Enhancements to the human-machine interface are required and possible voice commands based on voice recognition mechanisms will free the hands of users making more natural the interaction with this type of machines. In particular this evolution step may have a similar impact comparable to when man started using machines to replace the manual work as was the case during the industrial revolution. These and other topics will make the happiness of researchers in the coming years.

2. Final Conclusions

The utilisation of a cellular mobile broadband system prototype developed in the framework of the SAMBA project was a fundamental tool for the realisation of the work presented in this thesis. However not all aspects were studied and evaluated being the thesis work more related with the radio interface including radio handover performance aspects. The 40 GHz frequency band was selected instead of the 60 GHz since it has several advantages, namely lower propagation losses, negligible oxygen absorption and lower MMICs costs.

The Trial Platform architecture was defined based on the state-of-the-art technology and the main objective was to design a cellular broadband system where the main functionalities would be tested and evaluated. Handover was envisaged as a key feature and

therefore the Trial Platform is composed by two BSs, one BSC, a Mobility Server and two MTs. When analysed in more detailed, the Trial Platform is composed of antennas, RF, IF and Baseband and CU modules and DLC, mobility and resource management protocols.

Various parameters are required for the characterisation of the broadband channels some of them related with the PDP, which gives an indication of how the power is distributed as a function of the delay, namely: NRP, Tm, $\bar{\tau}$, SDWx%, Bd, Tc, DS and CB. The relative comparison of the last four parameters with the symbol time duration Ts and bandwidth BW of the signal leads to the concept of frequency selective fading if Ts < DS or BW > CB and flat fading if Ts > DS or BW < CB; and a channel is said to suffer from fast fading if Ts > Tc or BW < Bd and slow fading if Ts < Tc or BW > Bd.

The various types of fading have different impacts on the radio interface. Frequency selective fading induces ISI since it is caused by multipath propagation and therefore multiple copies of the signal arrive to the receiver at different times, causing distortion. When seen in the frequency domain, this fading implies that not all frequency components of the signal are affected the same way. Flat fading contributes only to the reduction of the SNR since all the multipath components arrive within the symbol time duration but can add destructively, depending on their relative phase. In opposition to frequency selective fading, all the frequency components of the signal suffer the same effects. Fast fading is caused by the fact that the channel characteristics change within the duration of a symbol. This leads to distortion and a loss in the SNR. In the frequency domain it manifests itself by Doppler shift. Finally, slow fading causes only a reduction in the SNR.

In terms of degradation, a loss of SNR is much less severe than the introduction of distortion, being the last the most difficult to mitigate. Increasing the E_b/N_0 is not sufficient to overcome the effects of distortion, and therefore other techniques are required. First distortion should be corrected and then addressed the SNR problem. Key parameters for the radio interface are the BER, delay and loss of data. In order to minimise these three parameters, a deep knowledge of the characteristics of the radio channel are essential, since it allows for the selection of the most suitable mitigation techniques.

Engineers when designing a broadband air interface deal with many challenges and options that lead to trade-offs. The air interface has to transport reliably the information from the

BS to the MT and vice-versa, while the MT is on the move, in different scenarios supporting applications and services requiring high bit rates. The air interface is usually the bottleneck of the system. Possible options are: type of antennas, multiple access technique, equalisation, modulation, coding, etc.

Mobile broadband systems are also affected by frequency selective fading and fast fading being the last less prominent since high MT speeds are not the rule due to its typical indoor and urban operation. Specifically for the Trial Platform five options were considered to mitigate the radio channel impairments: directive lens antennas, diversity reception, equalisation, spread spectrum and multicarrier modulation.

The radio cells shape is very dependent on the antennas characteristics namely the antennas radiation pattern. Dielectric lens antenna technology was used since they are inexpensive, can be easily manufactured with high tolerances, have sufficient band for FDD operation and present a high flexibility in the design of the cell shape with sharp boundaries enabling a customisation to each specific scenario. Moreover, the main advantage is the provisioning of a uniform power flux density in the coverage area with obvious advantages in terms of the radio channel. Two cell types were designed: the wide and elongated cells. The first is more appropriate to cover squares, wider areas or indoor scenarios and the last specifically designed for streets.

An air interface supporting a 34 Mbit/s full duplex link, FDD based and allowing for asymmetric transmission was implemented. In order to minimise the channel variability, a limit of 50 km/h was added to the specifications. The multiple access technique selected was TDMA with a symbol time duration of 31.25 ns. A single carrier modulation technique was selected due to constrains imposed in terms of linearity by the RF hardware at this frequency band. The equaliser is MLSE type and was designed to handle delay windows up to 250 ns given the propagation characteristics of the scenarios were the system expected to operate. The frame is composed by 80 slots and the burst payload corresponds to a code word of the (130,110) Reed-Solomon code, corresponding to 520 modulation symbols, implementing the FEC functionality and able to correct up to 10 symbol errors per burst. Two training sequences were used per burst to better handle the channel variability during the burst duration. The OQPSK modulation was selected due to its constant envelop and

compact spectrum properties. Since diversity reception was used the separation between the two antennas was set to 14λ.

The MAC layer is required to co-ordinate the competition of terminals for the shared radio channel. The scheduler decides which MT is permitted to transmit or receive data based on the service categories. The MAC protocol is reservation-based and period oriented since it is able to dynamically allocate time slots. A random access is provided to the MTs which gives the terminals opportunity to indicate their need for capacity in the uplink direction for data transmission. A slotted Aloha algorithm was used since the random access was not optimised for throughput but for short delays.

The LLC protocol handles the functions for connection establishment, connection control and methods for error recovery. For the last an ASR-ARQ mechanism is used. Data is transmitted as long as a maximum delay is not exceeded otherwise a data discard is performed to avoid congestion problems.

MTs requesting access to the network have first to be registered and located. Furthermore, the network has to keep track of the terminals roaming within the service area. For mobility management purposes, a database maintains an updated list of active MTs and their location in the network in order to forward the mobile terminated call requests.

Radio handover is a key feature of the Trial Platform and is generically executed when a MT changes between two cells while in a call. The handover procedure has three phases: measurements of the link quality on current and neighbouring cells; handover decision and initiation; and handover execution. The last phase implies the effective switching of the link to the new cell and the cancelling of the link in the previous cell.

The Trial Platform was operated in different configurations: one BS, two BS and a reduced and specific configuration used exclusively for CIR measurements. The single cell configuration was selected to test coverage aspects of different scenarios and system configurations. The two cells configuration was required to evaluate the radio handover performance as well as coverage aspects. For CIR measurements, only the antennas and the MHs were used plus a set of laboratory equipment, namely frequency synthesisers, a Rubidium reference generator and a network analyser.

Given the amount of experimental work planned and the amount of data expected to be collected, a specific C&M system was developed for that purpose. This system allowed also monitoring the proper operation of the Trial Platform and the on-line screen presentation of the data and status. The C&M system includes a telemetry system that sends to the BSC distance information collected using a Peiseler wheel.

The logistics for the measurements was quite complex and involved a lot of manpower. Two specially designed BS towers were used to install the antennas at different heights, being one for outdoor and the other for indoor operation. The antenna tilting angle was remotely setup and adjusted via a specific step motor system also developed on purpose. In the outdoor scenario, the MT was installed in a van to allow for speeds up to 50 km/h and to cope for the relatively long travelled distances. For the indoor scenarios, a trolley was used.

In order to guarantee the correct operation of the Trial Platform, calibration procedures were executed. Calibration curves were measured and used in the C&M system to derive the correspondence between RSSI and received antenna input power levels. For what concerns the CIR measurements, the removal of all system components not being parte of the radio channel, but necessary to perform the measurements, was fundamental.

The measurements were performed in three different scenarios: one outdoor and two indoor. The outdoor scenario is a typical urban residential area containing streets, car parks and buildings. The buildings exist on both sides of the road, separated by a distance of 36 m, with heights ranging from four to eight floors. The streets' pavement is made of asphalt and the walking areas made of concrete. A total of three streets were evaluated being one of them perpendicular enabling to test the signal penetration is shadowing areas. Zones with small trees and grass were also available between the streets. The car parks were made of asphalt and granite.

The indoor scenarios comprised a sports pavilion and a room at the Instituto de Telecomunicações located in the University of Aveiro campus. The pavilion's floor was synthetic, the walls made of concrete and bricks and large glass windows of about two meters height. The ceiling was supported by a metallic structure and there were a few rows of public seats made of concrete on one side of the pavilion. The dimensions of the

pavilion are 45 m by 35 m. Handover studies were performed in this scenario and coverage of the pavilion was achieved by two different BS configurations, being one of them with two BSs covering each approximately half of the pavilion guaranteeing however an overlapping zone. CIRs were also performed inside the pavilion and for that purpose, a set of specific locations were selected. Since a frequency domain technique was used, the scenario had to be static during the CIR measurements since Doppler effects cannot be measured. In the pavilion various measurement types were made in the uplink and downlink directions, for the two diversity reception channels, with the wide and elongated antennas and with and without LoS. A total of 700 measurements were performed.

The room at the institute was used for CIR measurements only. A total of 64 locations have been selected for measurements being 0.8 m the physical spacing between locations. LoS and non LoS conditions were tested and a total of 640 measurements performed.

A huge amount of measurement data was gathered during the measurements campaign. Coverage, transmission, handover and CIR aspects have been analysed for different scenarios, indoor and outdoor. A quite comprehensive analysis of the mobile broadband system prototype was carried out. Cell coverage and transmission performance aspects plus path loss modelling for the outdoor scenario comprising a main street, a street parallel to the main street and a perpendicular street were analysed. The objective of the experiments was to evaluate the cell coverage characteristics provided with the lens type antennas and the transmission performance on the air interface in terms of experienced BER, including the impact of different system configurations and MT speeds, in order to validate the technical options made for the Trial Platform in terms of equalisation, FEC and diversity reception techniques. The MT was driven along several paths while data was acquired by the C&M system. Particularly relevant for the results presented in this chapter were the RSSI for the two receiving channels, BitErrors and the MT distance to the BS. Based on these parameters others were calculated, namely: MRC signal, received power, BER CDFs, Rice distribution parameters, AFD, LCR and path loss slop. Several conditions were changed during the field trials, namely: BS antenna height, BS antenna tilting angle, MT antenna tilting angle and the MT speed. Simulations were also performed based on the ray-tracing technique for other scenarios namely a roundabout and a city square. Parameters such as the NRP and SDW90% were evaluated. The first parameter includes the gain of

transmitting and receiving antennas, and it is of major importance for the link budget evaluation and definition of the cell boundaries. The SDW containing 90% of the channel impulse response energy is used as a measure of the channel time dispersion.

For what concerns the main street, the average received power level variation range, on the first 150 m from the BS, is rather low due to the impact of the shaped radiation pattern of the BS lens antenna. Moreover the small-scale fading depth increases as the distance to the BS increases. There is however a visible improvement with the diversity reception contributing to the reduction of the fading depths.

The BER increases with the distance to the BS and the depth of the small-scale fading. In 90% of the cases it is below $4E10^{-4}$ which is under the maximum specified target $5E10^{-3}$ for the FEC codec showing the good performance of the equalizer. The typical maximum detected number of bit errors per byte was three. ARQ mechanisms have also proved to be required since the BER exceeds the specified limit for the FEC to be able to cope with.

Since the system was operated in LoS conditions, the measured data was fitted to the Rice model using the MatLab software tool. A good match to the Rician curves was obtained showing that this model is adequate. The path interval closer to the BS has shown a much stronger Rician factor which indicates a much higher contribution of the LoS component to the signal power. The AFD was calculated for the same paths ranging from 2 ms to 100 ms typically. On the other hand, the LCR is much higher for the path closer to the BS for what concerns the two receiving channels, reaching 50 crossings per second. The MRC signal shows a much more similar behaviour reaching a maximum of 45 crossings per second showing the impact of the diversity reception in reducing the small-scale fading depth.

Simulation results have shown a good agreement with the measurements which indicates that the used scenario models are good enough to predict the power levels. By changing the BS antenna height (from 11.2 m to 7 m) the cell width and length also changes. The small-scale fading depth is lower for the 7 m height case since the multipath components are less due to the fact that the power is more confined and reaches a fewer number of objects. The time dispersion was observed to be higher as the distance to the BS increases, but still under the limit handled by the equaliser (250 ns).

BS tilting angles (0 to 6 degrees in the vertical plane) effects were analysed and confirmed in terms of impact since an increase in the tilting angle reduced the cell size. No significant impact was noticed in the AFD and LCR parameters. This confirms the importance of this technique to reduce the co-channel interference and the possible elimination of strong reflections contributing to the excess delay. MT antenna tilting was performed in the range of -20 to +20 degrees (in the vertical plane), given the expected high mobility freedom for a mobile device. Positive tilting angles have a more pronounced effect given the specific characteristics of the MT antenna radiation pattern and the respective stronger impact on the direct ray, leading to an average power level decrease along the entire path. For negative tilting angles the effects are generically negligible or even an increase in the power level was experienced. For what concerns the AFD and LCR, and for positive tilting angles, it was observed that in general the LCR is higher and the AFD is lower. This confirms the lower contribution of the LoS component. Simulation results have corroborated the measurement results for what concerns the impact of the tilting angles in the received power levels.

In order to evaluate the impact of the MT motion in the radio channel, various different speeds were analysed. In terms of average power level no significant differences were noticed. The BER figures did not suffer a significant change what shows that the equaliser can still cope with the channel variations. Relatively to the AFD and LCR parameters the first decreased and the last increased. The mobile broadband system prototype proved to be able to operate at velocities up to 60 km/h, although the specification was 50 km/h.

The signal propagation in other streets in the same scenario was also analysed. Particularly in the perpendicular street since it is especially important for handover. In the last case, the signal experiences a strong attenuation when the LoS obstruction by the buildings occurred. A signal penetration of 5 meters in the shadow was measured. This figure gives and indication of how fast the handover procedure should be. The BER figures also presented a strong increase when penetrating in the shadow.

Based on the data gathered during the measurements, path loss modelling was performed. Linear regression analysis was used to find the slop of the best fit straight line. In a first step a comparison with the two rays propagation model was performed and a reasonable

match was obtained. This confirmed the fact that the stronger rays are the direct and ground reflected rays. However, and due to the effects caused by the constant power flux provided by the BS lens antennas, a two slop model was adopted with better results. The break-point was defined as the distance from the BS where the constant power flux principle could not apply anymore. This break-point has nothing to do with the break-point of the two rays model and a formula for its calculation was derived. An average figure of 2.92 was found for the slop. From the two rays model, and given the fact that the distances from the BS are clearly below the break-point, as demonstrated in chapter 2, a slop closer to two would be expected. This shows that the two rays model is too simple. The slop has also shown to be lower for lower BS heights due to the less reflected rays generated in the less visible obstacles. In terms of MT antennas tilting angles, only positive angles have resulted in an increase of the slop.

Measurements could not be done is all planned scenarios for various reasons. A simulation tool was used to evaluate other two outdoor scenarios where mobile broadband systems are expected to operate: an urban square and an urban roundabout. In the square and due to its dimensions and surrounding buildings time dispersion was more difficult to control still guaranteeing enough coverage in the surrounding streets. A final optimised configuration was reached being the height of the BS antenna 8 m, the tilting angle 6 degrees and the azimuth angle 45 degrees. With this configuration the time dispersion was kept within the equaliser limits being higher near the marble and iron objects, opposite to the BS. The same process was followed for the roundabout scenario case. The best configuration was reached for a BS height of 8 m and an azimuth angle of -148 degrees. This configuration could not eliminate completely the zones with time dispersion higher than 250 ns but could reduce it to a smaller area that can be served by a neighbouring cell.

The objective of the sports pavilion experiments was to evaluate radio handover, cell coverage characteristics and the transmission performance on the air interface, including the impact of different system configurations in an indoor scenario. The BSs with the Wide Cell antenna were installed in different locations and the MT in a trolley and driven along several paths in the pavilion while data was acquired by the C&M system. The first measurements were performed with the BS in a corner of the pavilion to cover the whole area with a single cell pointing along the pavilion's diagonal (configuration A). A second

configuration was used to evaluate the coverage with multiple cells and the handover algorithm. For that two BSs were placed on each side of the pavilion (in the smaller side of the rectangle) each covering approximately half of it (configuration B). From the large amount of data collected during the experiments, since the paths were separated by 1 m, a selection of representative paths for each system configuration, was made and only for these a detailed analysis presented. Moreover, simulations were performed based on the ray-tracing technique for these and other configurations and the parameters such as the NRP and SDW 90% evaluated.

Analysing the results of the lateral path R_A in configuration A it could be verified that the average power level is high, showing lower figures in the beginning and at the end of the path. Beyond 15 meters the average power level decreases slowly. These facts can be explained by the BS antenna shaped radiation pattern. The small-scale fading depth is more pronounced in the end of the path than in the beginning due to the increase of the distance to the BS and the impact of important multipath components. Analysing the MRC signal it can be concluded that diversity reception was successfully used to mitigate the small-scale fading depth. Due to the lower small-scale fading depth than in the outdoor scenario analysed in the previous chapter the diversity gain is not so high. The average power levels and the small-scale fading depth have shown a clear impact on the BER figures having therefore worst performance in the beginning and at the end of the path. A maximum of two bit errors per byte was observed. The BER figures confirmed that the equaliser behaved as expected since the BER figures only exceeded the $5E10^{-3}$ in very few cases. In 90% of the cases the BER was lower than $1.5E10^{-4}$. The ARQ mechanism is also important for this scenario but much less than in the outdoor scenario. Two short path intervals, one at the beginning and another at the end of the path, were selected for fitting with the Rice distribution and a good match achieved. The Rice factor has shown higher value for the short path near the beginning of the path due to the stronger direct ray component. In terms of AFD and for the MRC signal, it ranges from 2 ms to 400 ms being slightly lower for the short path further away from the BS. In terms of LCR, the short path near the BS shows a higher figure for the two receiving channels since the small-scale fading depth is much less pronounced, reaching 35 crossings per second. However, and due to the diversity reception

feature, the MRC signal for the path further away from the BS showed a higher LCR figure reaching 50 crossings per second.

The central path showed a good performance and comparing to the lateral path on the right of the pavilion, the average power level is higher and the BER figures lower. This can be explained due to the smaller distances to the BS and a more important contribution of the BS antenna shaped radiation pattern characteristics. The only exception is the end of the path where the power reduced significantly and hence an increase of the BER was observed due to the reach of the cell edge. For what concerns the third path analysed in configuration A, on the left hand side of the pavilion, the results compare very well with the path on the right side. Due to the fact that the beginning of the path is situated on the cell blank zone, the power level is lower than in the other paths and the BER higher. For all paths the behaviour of the equaliser was according to the specifications.

The transversal path showed an almost constant average power level since the distance to the BS does not change much. The small-scale fading depth is high for the whole path becoming more pronounced when the MT reaches the path end, approaching the boarder of the cell. Diversity was successfully used to mitigate the small-scale fading depth as can be seen by observing the MRC signal. The BER showed high values for the whole path due to the bad conditions of the signal, specially caused by the high channel time dispersion. This path crosses one of the worst areas in terms of power levels, fading and signal time dispersion in the pavilion.

Simulation results were performed for the same scenario. A good match was achieved between the measured and simulated results showing that the simulation model, although not including all the objects in the scenario, is good enough to predict the power levels. Based on the analyses of the NRP and SWD90% parameters, various system configurations were tried in order to find one with better performance in terms of power distribution and time dispersion. Simulation tools have revealed to be very important to design the best system configuration for a specific scenario feeding also the requirements for the lens antennas design, leading to more uniformity in the power distribution and reducing the time dispersion lowering the requirements in terms of equalisation needs.

In configuration B two BS were used to cover the pavilion and test handover. In a first step the cell coverage and transmission performance was studied individually for each BS. As for configuration A, only results for specific paths were here presented. The length of BS1 cell is about 22.5 m and the average power level presented fluctuations in the beginning of the paths and deep fades towards the end (about half of the pavilion). The BER showed higher figures also in these zones of the paths. Up to two bit errors per byte were observed and for 90% of the cases the BER is below $1E10^{-4}$. The length of the BS2 cell is also 22.5 m. Comparing BS1 and BS2 cells it may be noticed that the peak of the power does not happen at the same distance from the BSs, being for BS1 17 m and 15 m for BS2 due to the different antennas tilting angles. In terms of BER a better performance was observed reaching $1E10^{-5}$ in 90% of the cases.

For the handover studies two different directions were defined due to the hysteresis and different characteristics of the cells. Observing the power levels provided by each cell, it can be seen that the cells are not symmetric. An overlap zone of approximately 10 m between the two cells was measured. The handover algorithm has shown a good performance in avoiding the "ping-pong" phenomenon since it could "resist" to the small-scale fading even if a better carrier was available. For what refers to the handover execution time, 0.62 s and 1.01s were observed for path C_B direction D12 and D21, respectively. By analysing other paths (L_B and R_B) it can be concluded that the handover does not occur at the same distance form the BSs but depends on the specific characteristics of the link, as the algorithm indicates. In general the behaviour is similar to path C_B. Interesting enough and when the MT reached the end of the cell (nearby the BS tower), some times a second handover occurred to the other BS. This is caused by the fact that nearby the towers there is a blank zone being the power from the other BS higher, leading to a handover. In terms of handover execution time the following figures 0.37 s, 0.93 s, 1.63 s, 1.9 s, 2.07 s and 2.11 s were measured. In absolute terms and given the requirements of real time services, these figures are not good enough and improvements are required. Longer handover execution times were experienced for lower power levels being justifiable due to the fact that the synchronisation process to a different frequency carrier is unfavoured in these circumstances. The BER figures in handover situations were kept below the equaliser specification showing its good operation.

Analysing now all the paths measured in the pavilion it can be concluded that the cell generated by BS1 is larger than the cell generated by BS2. This is due to the higher tilting angle used in BS2 antenna. The overlapping zone was also not selected optimally for all paths due to the distortion introduced in the coverage area by BS2. The attempting to compensate for the higher gain has revealed not recommended in terms of coverage. It was observed that the handover execution time increased as we move away from the central path. Comparing the performance in terms of coverage when considering configuration A and B, it can be concluded that a better coverage and BER is achieved using configuration B, being however more costly. For the best coverage area and direction D12, in average the handover took place at a distance of 26.8 m and stops at 27.9 m. The duration is about 0.807 s and in 95% of the times, the handover durations between 0.465 s and 1.148 s. For the worst coverage areas, the handover starts in average at 27.6 m and stops at 30.1 m. The handover average duration is 1.493 s, being 95% of the time between 0.595 s and 2.392 s, which indicates a quite large variation. For direction D21 and in the zone of better coverage the handover happens between 21.8 m and 20.1 m, with average duration of 1.447 s being 95% of the time between 1.141 s and 1.752 s. When compared with the previous direction, there is however a higher uniformity in the handover starting and finishing point. In the worst zone the handover starts at 22.0 m and typically ends at 20.1 m, lasting for 1.504 s being 95% of the time between 1.241 s and 1.766 s. Although handover duration figures relatively high were found when compared with currently operated mobile systems, there were situations where the handover has occurred almost instantaneously. A video transmission was performed to evaluate the impact of the handover and the interruption was almost unnoticeable.

Two other configurations were evaluated by simulation based to the NRP and SDW90% parameters. With two BSs in the pavilion corners, the time dispersion is lower than in configuration A being kept below the equaliser limits and the power distribution much more uniform. The configuration with a single BS place in the centre of the pavilion presented time dispersions not compatible with the equaliser limit. In conclusion, multiple BS coverage has proved to be more adequate given the specifications of the mobile broadband system prototype, leading in general to more friendly conditions.

The analysis of the broadband radio channel at 40 GHz was performed based on measurements of the time-variant transfer function $T(f,t)$ – frequency-time domains. Given that a frequency domain technique was used to sound the radio channel, the scenario had to be static during the measurements and therefore the transfer function depends only on the frequency - $T(f)$. The input delay-spread function $h(\tau)$ was obtained via mathematical processing. The chapter started with an introduction to channel sounding techniques, signal processing, type of windows used and its impact in the dynamic range and time resolution. The analysis of the CIRs gathered in the sports pavilion and the IT Room for several positions and locations were presented considering different situations, namely: with and without LoS, uplink and downlink directions, impact of the antenna type and diversity receiving channels. All CIRs were obtained using a Rectangular and a Blackman Harris window since they have different time resolutions and dynamic ranges. Various parameters were calculated: NRP, DS and $\bar{\tau}$. Measured PDPs for all positions/locations were compared with ray tracing technique simulation results, considering different degrees of complexity for the simulation model and reflection orders for the rays.

In the sports pavilion all the measurements in each location were repeated 35 times and averaged (time and space average) in order to reduce the chances of measuring a very particular situation (deep fade for instance) and reduce the noise levels leading to a total of 700 measurements. The different positions for each location were separated approximately by a wavelength. In fact it was observed a difference for all positions in terms of transfer function and CIR but for positions inside the cell they are less significant since the signal spatial changes are smoother. Moreover, in statistical terms the differences are not so significant and this is why this technique was not used for the measurements in the IT Room easing the measurements procedure for each location but the number of locations analysed per unit of area was increased. The impact of the windows in the calculation of the CIR is unavoidable since it is intrinsic to the methodology and this is the reason why all the CIRs were calculated using two different widows and the results analysed for both cases. The NRP parameter was always larger for the rectangular window.

Several situations were measured in the sports pavilion and analysed based on the CIR parameters calculated for different cell regions namely within, at the borders and outside

the cell coverage area. Regarding the LoS and non LoS operation modes, the CIRs clearly reflect the fact that the direct ray is attenuated leading to a higher relative power of the reflected rays. The delay parameters also reflected this fact by showing higher figures. The uplink and the downlink directions were measured and compared. They are in fact different confirming that the status of the radio channel in one direction cannot be inferred by what is going on in the other, for systems operating in the FDD mode. The impact of the antenna radiation patterns was also evaluated and for that purpose, two different antennas were used. Since the two antennas differ quite substantially in terms of the radiation patterns, the CIRs also reflected this fact. The diversity reception feature was analysed by measuring channels RX1 and RX2 and a different behaviour was observed but more pronounced for the non LoS case. All the results obtained are in line with what the theory predicts also indicating that the measurement system was working properly and the assumptions made were valid. Due to the fact that this study was performed for the 40 GHz millimetrewave frequency band, this type of measurements is more critical due to the smaller wavelength and the stronger requirements in terms of phase reference information.

In the IT Room the CIR measurement were performed only for LoS and non LoS conditions for the entire room floor surface. A total of 64 locations were measured and 640 measurements performed. In LoS the dominance of the direct ray is clear leading to small figures for what concerns the time dispersion parameters. The power distribution in the room is in line with the antenna radiation pattern of the wide cell antenna. For non LoS, the parameters have shown a much odd distribution. The reflected rays have a more prominent role in the CIR, leading to an increase of the time dispersion parameters. The NRP is much lower than in LoS due to the absence of the direct ray. Given the shorter dimensions of the room, lower time dispersion figures were observed when comparing with the sports pavilion.

Simulation results were performed in order to validate the used sports pavilion simulation models and measurements performed. The main idea was to evaluate the impact of excluding some objects in the validity of the simulation results. The simplification of the model allows for a shorter simulation time which is crucial when performing simulation studies. Several simulation models were used but in the thesis only the results for four of them were presented. These models present a different degree of complexity as a direct

consequence of the number of objects they took into consideration. By analysing the CIR parameters, it could be concluded that time dispersion parameters are much more dependent on the simulation model than the NRP, which has shown only small variations. In general the simulation results have shown a good agreement with the measurements in locations inside the cell coverage area where the spatial variability of the radio channel is much less due to the strong contribution of the direct ray to the PDP. This fact reduces the importance of possible deficiencies or inaccuracies in the prediction of reflected rays by the simulation model since they have a much lower weight and contribution to the results. Outside the cell main coverage area more deep fades and lower power levels are experienced which confirms a much more important role of the reflected rays. In terms of the analysed simulation models, Model 3 is the one that in general presented best results in terms of power and time dispersion parameters although a reflection order of 5 had to be used, due to the lack of computational resources to handle the necessary calculations.

The direct inspection and analysis of the PDPs allows inferring that the different simulation models also impacted on the number, delay and amplitude of the received rays, being clearly more close to the measurements for locations that fit inside the cell main coverage area. The design of lens antennas for the specific characteristics of the sports pavilion would result in a much better distribution of the power and a more even coverage. Considering the prediction of the PDP and the CIR parameters, one may conclude that Model 1 is the worst of the four models and that any of the remaining three is appropriate for propagation and coverage studies within the pavilion, for locations within and in the cell limit. Simulation results obtained with Model 1 are quite different from the measured ones, even for locations within the cell. For locations clearly beyond the cell's limit, it is necessary to increase the complexity level of the simulation model.

In an attempt to remove the dependency on the simulation models complexity the IT Room with very few objects was selected for analysis by simulation as well. The simulation model is quite simple being a parallelepiped. It can be observed that the region where the minimum power is received is nearby the BS and the maximum power towards the end of the room. Simulation results for all locations indicated a slightly different power distribution in the room being the peak of the power more close to the BS, keeping however the general shape imposed by the wide cell antenna radiation pattern. In general

the minimum power levels obtained by simulation are higher than via the measurements indicating a worst match between the measurements and simulations in areas closer to the BS. The same general behaviour was observed for the DS figures. In order to explain these discrepancies, various simulations were performed considering different electrical properties of the room walls and other system configuration parameters, namely the antenna rotation angle and gain. By maintaining the electrical parameters and increasing the antenna gain in 2 dB and introducing an antenna rotation in the vertical plane of 4 degrees it was possible to obtain a good match between the measurement and the simulation results for power and DS parameters.

A set of locations in the room were selected for a more in-depth PDPs analysis which has revealed a good match between the measured and the PDPs obtained by simulation, especially for the first 100 ns. Even for locations nearby the BS, the rays predicted match very well with the measurement results confirming the conclusions presented in the previous paragraph.

The main conclusion drawn is that these simulation models allowed obtaining good estimates for both the CIR parameters and the PDP, for locations inside and at the cells limits. For locations clearly outside the cell it might be necessary to increase the complexity level of the simulation model. Although the very high frequency band, the analysis in the frequency domain proved to work well with the inherent disadvantage that no motion is allowed while performing the measurements precluding the analysis of the Doppler effects. The calculated parameters are according to the expected and suitable explanations were presented for the observed behaviour in the selected measurement scenarios and system configurations.

Based on the CIR measurements performed for the two indoor scenarios the DS and CB were evaluated and its relationship analysed. A comparison of the obtained figures for all locations and the results collected directly using the approximation formulas presented in literature was performed showing the bad approximations results obtained in some cases. In order to further clarify the relationship between the DS and CB and the confirmation of the Fleury lower bond applicability in multiple conditions and scenarios, simulation results

were performed using different antenna types, correlation coefficients, measurement bandwidths and LoS and non LoS conditions and the results analysed.

Concerning the sports pavilion, it can be concluded that for both LoS and non LoS cases the Fleury lower bond is generally respected by all measurements and those that do not respect, the fact could be explained by measurement errors or other effects due to the processing of the data, since the discrepancy is very little in relation to the Fleury lower bond. Moreover, as c approaches to one, the measurements and the Fleury lower bound tend to converge and this was observed and confirmed for all analysed scenarios.

In the IT Room many measurements did not respect the Fleury lower bond for c=0.9. This fact, in opposite to the sports pavilion, is more difficult to explain based on errors related with the experimental procedures. Another possible explanation is the fact that the Fleury conditions used for the derivation of the mathematical formulation do not hold true in this scenario, namely the uncorrelated scattering assumption. Being the room small the different rays tend to have similar behaviours (particularly true for empty rooms as was this case). The same phenomenon is accentuated by the fact that the time resolution of the measurement system is limited and may not be enough for this particular scenario generating correlation for what concerns adjacent rays. To clarify these hypotheses simulation results were performed.

All the simulation results obtained for the pavilion for the two antenna configurations are in line with the expected and also inline with the measurement results for what concerns specifically the Wide Cell antenna configuration. For the isotropic antenna, there are locations that fail in terms of the Fleury lower bond, being however quite close to it. Errors introduced during the processing of the results could justify this result. Not much difference is observed between the 400 MHz and 1000 MHz cases, except for the maximum CB that is limited to 200 MHz in the first case. It is always for c=0.9 and non LoS that the worst results are obtained what is inline with the expected. Moreover, it is always for the lowest figures of the CB that the violations of the Fleury lower bond occur and in this particular case, for CB figures near 1 MHz. In conclusion, it can be stated that simulation and measurements results match well and that the discrepancies between what would be expected and the results obtained may be justified by errors introduced by the

approximations and its propagation, namely the windowing process, which cannot be bypassed when calculating the IFFT.

The IT Room simulation results indicated that several locations violate the Fleury lower bond for the 400 MHz bandwidth. Increasing the bandwidth to 1 GHz, a reduction of the number of locations was observed being namely 0.5% for LoS and 8% for non LoS both for c=0.9. This fact could indicate that a larger bandwidth (a better time resolution) could eliminate completely the correlation between the rays in the time bins leading to a pure uncorrelated scattering situation, or at least just dependent on the scenario and not on the radio signals receiving system limitations in terms of bandwidth. An infinite bandwidth system (infinite time resolution) is not possible to realise and the bandwidth is usually very limited, therefore it is not possible to eliminate completely the correlation between the different rays since the receiver cannot see then separately.

In the room 10 m x 30 m, very few locations violate the Fleury lower bond showing that for this room size the assumption of uncorrelated scattering is still valid. The channel is still WSSUS since no changes to the scenario or motion of the receiver are allowed during the simulations being therefore stationary. For the 1 GHz bandwidth there are no locations that violate the Fleury lower bond, confirming that for a better time resolution the correlation is decreased.

Increasing the system bandwidth or time resolution the correlation among the different rays diminish and therefore the number of violations of the Fleury lower bond reduce as well. Moreover, for larger and more complex scenarios, the correlation is less having as a direct impact a decrease also on the number of locations that violate the Fleury lower bond. The Fleury mathematical formulation holds valid for the analysed scenarios and different cases except when the WSSUS condition is violated. The approximation formulas presented in the literature are very conservative for c=0.5 except for non LoS situations. In this case the approximation and the Fleury lower bond almost coincide. The approximation for c=0.9 always presents results lower than the Fleury lower bound being even more conservative and the measured results are always very close to the Fleury lower bond. As higher the c is the more the results approach to the Fleury lower bond.

3. Future Work

Broadband mobile communications research activities are continuing worldwide driven by the mobile communications importance increasing and penetration rates, in many countries well above 100%. Governments and other transnational institutions continue supporting the R&D in this area by co-funding projects leveraging the industry and giving incentives to the important cooperation between industry and universities. Future work in this section is addressed in two perspectives: one based on the current work and further improvement of the existing prototype as well as using it in different scenarios; and by identifying other areas of interest that justify by themselves the development of a new prototype.

As already mentioned the prototype air interface design was a trade-off between what was desirable and possible with the available limitations. The following possibilities for improvements were already identified:

- Provision of higher bit rates by using liner high-level modulation schemes, more powerful equalization and diversity schemes and more sophisticated adaptive antennas.
- Provision of several bursts formats chosen according to transmission needs and environment characteristics.
- Utilization of time alignment techniques for the reduction of guard times.
- Provision of more efficient error control using adaptive coding schemes.
- Provision of time division duplex or multicarrier transmission.
- Improvement of the spectrum efficiency by using power control.
- Provision of more efficient and dynamic resources assignment.
- Utilization of different ARQ parameters/protocols depending on the service type.
- Utilization of priority schemes according to the type of multimedia service allowing for a more efficient usage of the available resources.

- Realization of measurements in other scenarios that currently were just addressed by simulation.
- Test radio handover algorithm enhancements in order to correct the current limitations namely for what concerns the handover execution time.

Opening the future horizon, the main challenges of B3G/4G systems encompass a range of new applications serving professionals as well as individuals in their private lives and adapted to the particular needs and likes of each user. The increasing popularity of watching videos that Web 2.0 enables and that Web 3.0 will extend over the Internet is a clear indication that the continuous increase of the transmission rates will be necessary to improve the user experience and comfort when accessing to broadband applications or the Internet. The current goal is 1 Gbit/s for short range and indoor environments and 100 Mbit/s for long range and outdoor environments. Antenna beamforming techniques can also be used to make spatial filtering of the radio signals.

Networks will continue being based in the IP protocol due to the explosion of the Internet but post IP protocols are staring being investigated. No doubt that IP is seen as a possible candidate technology for the 4G mobile systems where the convergence concept is a key issue. IP was responsible for many changes in the telecommunication sector, although not designed since the beginning for that purpose. Particularly for the air interface, the utilization of IP protocol is not efficient. End-to-end IP networks for real time and non-real time services in public and private, licensed and non-licensed networks is a topic that is being addressed by researchers . For seamless service provision in the entire coverage area, mobility functions are being proposed including intra and inter-system handover and the necessary QoS negotiation strategies. Further research and technology developments will contribute to the convergence of the various access technologies leading to the seamless access paradigm and the core network evolution towards the “all IP” concept reducing the network deployment and operation costs (CAPEX and OPEX). For what concerns the terminals, they will evolve towards reconfigurability and will be much more advanced multimedia devices.

Since mobile broadband systems will use millimetrewave frequency bands, the attenuation of the radio signals is higher, leading to a smaller cell size, ranging from a

few to a thousand metres for the terrestrial segment. Hot spots like airports and city centres may have broadband coverage but a continuous coverage may not be provided, at least during its first deployment phase. Mobile broadband systems are seen as providing complementary capacity/coverage in indoor and outdoor environments for high density traffic areas. In areas where various access networks are available the concept of "always best connected" should be applied. This imposes the need for MTs to roam between different frequency bands and standards (multiband and multimode MTs).

Various candidate techniques are being investigated for the radio interface of future mobile broadband systems namely multi-carrier modulation techniques. Examples are: OFDM, OFDMA or the combination of OFDM and CDMA, such as, MC-CDMA, MC-DS-CDMA or hybrid techniques like SS-MC-MA. Single carrier modulation (SC-FDMA) is still under consideration for the uplink of 3GPP LTE since it has a lower peak-to-average power ratio.

The utilisation of multiple antennas in the BS and the MT is also under research and takes advantage of the decorrelation of the radio signals received by the different antennas. This fact enables the increase of the channel capacity and the complexity of the transceivers, being more tolerable at the BS side. This is to say that the traditional channel Single Input Single Output (SISO) is becoming MISO (Multiple Input Single Output), SIMO (Single Input Multiple Output) or MIMO channel. These new type of channels can in fact be considered as a combination of several SISO channels affected by the parameters of the receiving and transmitting antennas arrays. These radio channel models are defined as vector channel models.

The increasing separation between service and network providers is leading to the creation of new business models applicable for instance to mobile virtual operators. An effective management of such a complex scenario (a Network Provider may work with several Service Providers and users may have the freedom to select the Service Provider on the spot) is a challenge to network management technologies.

Innovative air interface capable of providing scalable and flexible connectivity among all devices and self-organising networks that enable the routing of the information in a dynamic way may play a crucial role in the future. The pervasive device interconnection

tendency appeals for the need of large network addresses space. All IP networks are gaining more and more momentum incorporating access, core and mobility management capabilities. A single IP core network may be shared by various telecommunication technologies ranging from fixed, mobile, LANs and even broadcasting paving the way for the true and full networks convergence. Terrestrial and satellite access segments for telecom and broadcasting services will have to be provided. This will lead to the seamless service provision across heterogeneous networks based on reconfigurable and probably wearable terminals.

Worldwide R&D activities will continue addressing these techniques what will result in new standards and new generations of mobile communication systems.

Annex A

Ray Tracing Algorithm and Scenarios Modelling

1. Introduction

Ray tracing is a technique based on the GO and is an approximate method for estimating a high frequency electromagnetic field. GO assumes an infinite frequency for the propagation signal, i.e. $\lambda \rightarrow 0$, and therefore the energy can be considered to be radiating in infinitesimal tubes, designated by rays representing the wave front. Each ray is normal to the surface wave front, lies in the direction of propagation and travels in straight lines, provided that the refractive index of the medium is constant. GO considers only direct, reflected and refracted rays, and consequently abrupt transition areas occur, corresponding to the boundaries where these rays exist. The GTD and its uniform extension (UTD), compliment the GO theory by introducing a new type of rays – the diffracted rays. The purpose of these rays is to remove the field discontinuities and to introduce proper field corrections, especially in areas where the GO fails. The Fermat principle and the principle of local field are two concepts extensively used in the ray models. The first states that a ray follows the shortest path from a source to a field point, while the second states that the high

frequency boundary processes, such as reflection, refraction and diffraction, depend only on the electrical and geometrical properties of the scatter in the immediate neighbourhood of the point of interaction.

In a propagation scenario various rays arrive to the receiver due to multipath propagation. These rays can arrive either directly, when LoS exists, or via multiple reflections on the obstacles. We say that a ray is of order *m* when it suffers *m* reflections before arriving to the receiver. The vector sum of all rays arriving to the receiver is the channel impulse response when the transmitter sends a Dirac impulse. This fact enables us therefore to calculate the impulse response of a radio channel as defined by (A.1), whatever the environment is if it can be modelled adequately.

$$h(t,\tau) = \sum_{n=1}^{N} \alpha_n(t)\,\delta\left[\tau - \tau_n(t)\right] e^{j\varphi_n(t)} \qquad \text{(A.1)}$$

The steps required to calculate the channel impulse response of a given propagation scenario are:

1. Calculate all the rays arriving to the receiver (LoS and reflected) up to the m-order. The order to be considered depends on the scenario but basically a ray should be considered if its energy when arriving to the receiver is still significant.

2. Calculate for each ray the αn,τn, and φn parameters. αn is calculated based on the Friis formula being affected by the reflection coefficient of each surface which the ray interacts with (as shown in Annex B); the relative phase φn is also affected by the reflection coefficient; τn is calculated based on the difference of travelling times between the ray under consideration and the shortest path (travelled distance divided by the speed of light).

3. If the receiver and transmitter do not use omnidirectional antennas, the ray must be weighted by the antennas radiation pattern according to the direction it leaves the transmitter and arrives to the receiver. The antennas polarization must also be taken into account.

4. To obtain the channel impulse response, the received rays in the same time bin are added as vectors (this defines the time resolution).

5. Finally, based on the channel impulse response, other important parameters can be calculated to characterise the system (for instance the DS, SDW, NRP, etc.).

Of concern should also be the algorithm used to generate the rays. Basically two techniques exist: the image*s* or the ray launching methods. The first consists in calculating successively the virtual position of the transmitter (or receiver) relatively to a specific plane, obtaining then the point of reflection by the intersection of the straight line that contains this image and the other receiver (or transmitter). For rays of order *n* it is necessary to calculate *n* images of the transmitter (or receiver). The second technique starts with the transmitter and launching rays to all directions with a certain angular resolution. The rays suffer successive reflections and the process is stopped when the energy associated with the ray is below a specific threshold. Therefore, only a certain number of rays arrive to the receiver. There are techniques to improve the angular resolution however, the images method performs better for a scenario up to 10 faces and for rays up to the 4th order [3]. Since most scenarios can be modelled up to this complexity level, this method was selected for implementation and is described in more detail in the next sections.

A scenario is typically described using a 3D coordinates system ($\hat{\mathbf{e}}_x,\hat{\mathbf{e}}_y,\hat{\mathbf{e}}_z$). Each object is defined by a finite set of planes and each plane by a point of application X and two vectors, **u** and **v**. The electromagnetic characteristics and surface roughness (σ_h) of the surface are also associated to each plane.

2. Algorithm description: Images method

This ray-tracing algorithm finds possible paths between the transmitter (Tx) and receiver (Rx) defined by rays using the Snell's law of reflection. In Figure A.1 is displayed an example with rays up to the 3rd order.

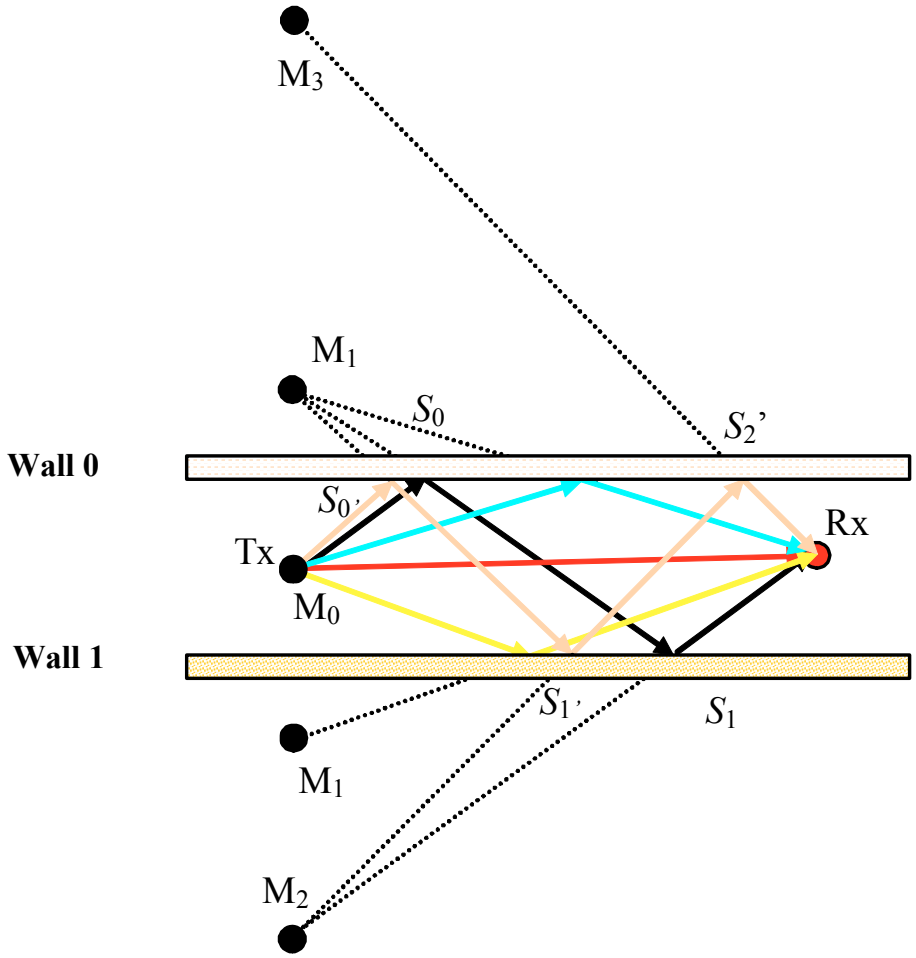

Figure A.1: Ray-tracing of mth order rays (m=0, 1,2 and 3) between Tx and Rx without obstacles

If the total number of reflections is know in advance, it is possible to find all the rays from Tx to Rx for a specific scenario configuration (location of Rx and Tx and the surrounding obstacles), by using the following algorithm:

Tracing of rays

```
M0 = Tx;
i = 0;
j = 0;
while i < "desired number of reflections" do
  begin
    Mi+1 = Wallj.Mirror(Mi);
    i = i + 1;
    j = (j + 1) mod 2;
  end
```

Check for ray validity

```
P0 = Rx;
P1 = Mi;
do
  if Wallj.InterSection(P0, P1, Si) then
    begin
      i = i - 1;
      j = (j + 1) mod 2;
      P0 = Si;
      P1 = Mi;
    end
  else "Intersection point not on wall. Not a valid ray";
until i = 0;
```

The function Wallj.Mirror(M_i) mirrors the vector position with respect to Wall j, where *j* is the number of the wall under consideration. The function Wallj.InterSection(P_1, P_2, S) returns TRUE if there is an intersection point S between Wall j and the straight line between P_1 and P_2. The algorithm has been presented for two faces but can easily be extended for more complex scenarios. Furthermore, in the case of the existence of obstacles it is also necessary to check if the ray is obstructed and therefore does not reaches the Rx. Moreover, the obstacles can change the direction of the rays and still arrive to the Rx.

In the next paragraphs the equations needed to implement the above algorithm are derived. Two functions are used intensively: first the calculation of the image of some point in space with respect to the illuminated face of the object, and second the calculation of the intersection point between some line section and a face of an object.

Each wall can be described as a plane V

$$V\text{: } (\mathbf{n},\mathrm{X}), \text{ where } \quad n = \frac{u \times v}{|u \times v|} \tag{A.2}$$

(A.2) is known as the normal equation of a plane. **u** and **v** denote the direction vectors of the plane and **X** denotes the application point with respect to the origin O. The normalized external product is called the normal vector **n**. Using **n**, the mirror point M_{i+1} of the original point M_i with respect to plane V can be written as shown in (A.4).

$$d = n.(M_i - X) \tag{A.3}$$

$$M_{i+1} = M_i - 2d.n \tag{A.4}$$

Let us consider a line section that begins at P_1 and ends at P_2 (generic points as shown in Figure A.2). If that line section intersects the plane V, P_1 has to be on one side and P_2 on the other, hence

$$[n.(P_1 - X)][n.(P_2 - X)] < 0 \tag{A.5}$$

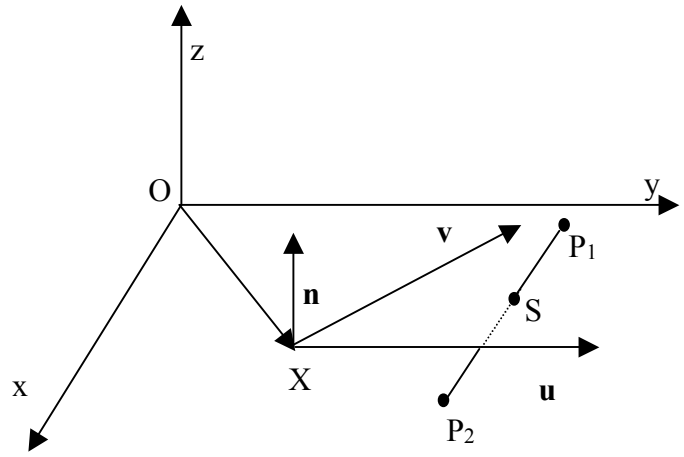

Figure A.2: Intersection of the V plane at point S

If the above property holds then the intersection point S can be calculated according to (A.6) for an infinite plane V.

$$S = P_1 - (P_1 - P_2)\frac{n.(P_1 - X)}{n.(P_1 - P_2)} \tag{A.6}$$

Since the objects in a scenario and walls are finite, let V be bounded by the length of the spanvectors **u** and **v** and (**u**.**v**)=0, then the following inequalities have to hold.

$$0 < (\frac{u}{|u|}.(S - X)) < |u| \quad \text{and} \quad 0 < (\frac{v}{|v|}.(S - X)) < |v| \tag{A.7}$$

3. Calculation of the Fields Vectors

In order to calculate the polarization changes at the reflection points and the resulting electric field components at the receiving antenna we define a reference plane Vr: ($\mathbf{n_r}$,O). At an arbitrary point along a ray path the electric field originating from the transmitting antenna has polarization components with amplitudes E_θ and E_ϕ in the direction of the vector $\mathbf{e_\theta}$ and $\mathbf{e_\phi}$ respectively; $\mathbf{e_\theta}$ lies in the reference plane while $\mathbf{e_\phi}$ is perpendicular to $\mathbf{e_\theta}$ and $\mathbf{r_i}$ which points in the propagation direction. The direction vectors $\mathbf{e_\theta}$ and $\mathbf{e_\phi}$ can be described with respect to the reference plane as

$$e_\phi = \frac{n_r \times r_i}{|n_r \times r_i|} \quad \text{and} \quad e_\theta = \frac{e_\phi \times r_i}{|e_\phi \times r_i|} \tag{A.8}$$

For convenience the xy-plane (floor) is chosen as reference plane. This implies that $\mathbf{n_r} = \mathbf{e_z}$.

Let us consider the situation of a reflection against some face of an object or room. For that we have to determine the components perpendicular and parallel to the plane of incidence (see Figure A.3) of the electrical field, to apply the Fresnel reflection coefficients and obtain the reflected field.

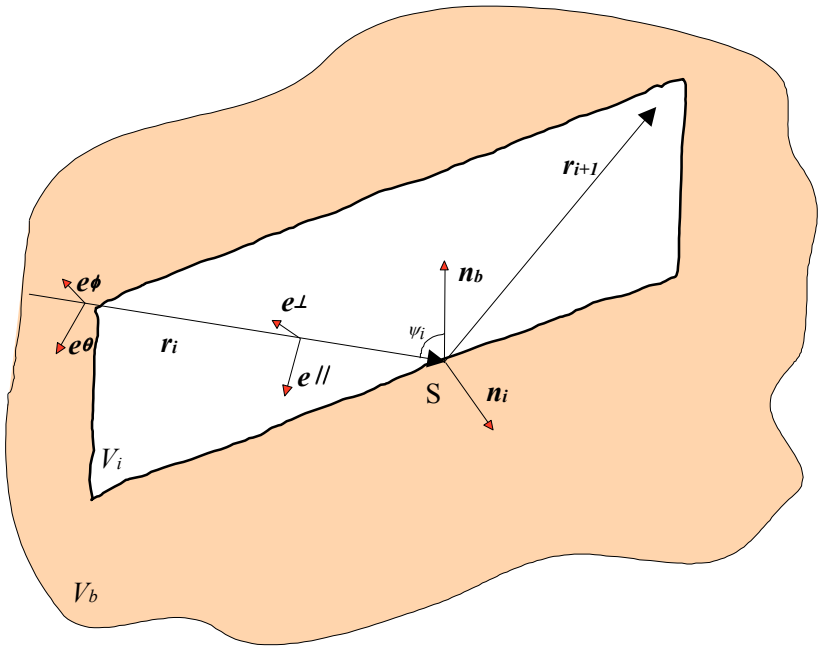

Figure A.3: Plane of incidence Vi and reflecting plane Vb

The perpendicular vector $\mathbf{e}\perp$ can be found based on the fact that the incidence plane Vi: ($\mathbf{n_i}$, S_i) is perpendicular to the reflecting plane Vb: ($\mathbf{n_b}$, X_b), with X_b being the position point of Vb, and that the ray lies in the incidence plane. The parallel vector $e_\parallel$ is perpendicular to the ray direction $\mathbf{r_i}$ and vector $\mathbf{e}\perp$, hence

$$e_\perp = \frac{n_b \times r_i}{|n_b \times r_i|} \quad \text{and} \quad e_\parallel = \frac{e_\perp \times r_i}{|e_\perp \times r_i|} \tag{A.9}$$

The angle between the two coordinate systems ξ can be obtained by $\cos \xi = (\mathbf{e_\theta}.\mathbf{e}_\parallel)$. The rotation from $<\mathbf{e_\theta},\mathbf{e_\phi}>$ **to** $<\mathbf{e}_\parallel,\mathbf{e}_\perp>$ thus yields

$$\begin{pmatrix} E_\parallel \\ E_\perp \end{pmatrix} = \begin{bmatrix} \cos\xi & \sin\xi \\ -\sin\xi & \cos\xi \end{bmatrix} \cdot \begin{pmatrix} E_\theta \\ E_\phi \end{pmatrix} \tag{A.10}$$

The angle of incidence of ray $\mathbf{r_i}$ into the plane Vb: ($\mathbf{n_b}$, S), is equal to arccosine of the internal product of the normal vector $\mathbf{n_b}$ with $\mathbf{r_i}$. Using this property we can write the Fresnel reflection coefficients as

$$\rho_{\perp} = \frac{\left|(n_b.r_i)\right| - \sqrt{\varepsilon_r(1-\tan\delta) - 1 + (n_b.r_i)^2}}{\left|(n_b.r_i)\right| + \sqrt{\varepsilon_r(1-\tan\delta) - 1 + (n_b.r_i)^2}} \tag{A.11}$$

$$\rho_{\parallel} = \frac{-\varepsilon_r(1-\tan\delta)\left|(n_b.r_i)\right| + \sqrt{\varepsilon_r(1-\tan\delta) - 1 + (n_b.r_i)^2}}{\varepsilon_r(1-\tan\delta)\left|(n_b.r_i)\right| + \sqrt{\varepsilon_r(1-\tan\delta) - 1 + (n_b.r_i)^2}} \tag{A.12}$$

Multiplying each of the field components by their reflection coefficients results in

$$\begin{pmatrix} E_{r\parallel} \\ E_{r\perp} \end{pmatrix} = \begin{bmatrix} \rho_{\parallel} & 0 \\ 0 & \rho_{\perp} \end{bmatrix} . \begin{pmatrix} E_{i\parallel} \\ E_{i\perp} \end{pmatrix} \tag{A.13}$$

$$\begin{pmatrix} E_{r\phi} \\ E_{r\theta} \end{pmatrix} = \begin{bmatrix} (e_{\theta}.e_{\parallel r}) & -(e_{\theta}.e_{\perp r}) \\ (e_{\theta}.e_{\perp r}) & (e_{\theta}.e_{\parallel r}) \end{bmatrix} . \begin{pmatrix} E_{r\parallel} \\ E_{r\perp} \end{pmatrix} \tag{A.14}$$

Using the above equations repeatedly for all reflections suffered by a ray, the total attenuation and polarisation can be calculated.

4. Received Power and Excess Delays

Let us assume, that N rays (1,…,n,…,N) appear at the receiving antenna and that the field vector of n^{th} received ray is:

$$E_{Rxn} = E_{\theta_{Rxn}}\, e_{\theta} + E_{\phi_{Rxn}}\, e_{\phi} \tag{A.15}$$

being therefore

$$E_{Rxn} = \begin{bmatrix} E_{\theta Txn} \\ E_{\phi Txn} e^{j\delta} \end{bmatrix} \frac{e^{j\beta r_n}}{r_n} \prod_{i=0}^{m-1} [R_i] \tag{A.16}$$

where $E_{\theta Txn}$ and $E_{\phi Txn}$ denote the amplitude of the n^{th} transmitted wave in the θ and ϕ directions, whereas r_n denotes the path length of n^{th} ray. R(ε,ψ) accounts for reflection effects which depends respectively on the material dielectric characteristics and angle of incidence. Furthermore, $\beta=2\pi/\lambda$ is the wavenumber whereas δ denotes the phase difference between the θ and ϕ components. If E_{θ} or E_{ϕ} is null, or $\delta=k\pi$ k=0, ±1, ±2, ±3, …., the wave is linearly polarized. The circular polarisation occurs when $E_{\theta}=E_{\phi}$ and $\delta=\pm(\pi/2)$. *m* is the total number of reflections suffered by the ray *n*.

At the receiving antenna the E-field must be weighted with the gain function of the antenna. As in general several rays hit the receiving antenna arriving from different directions and with different propagation delays, all the rays have to be added as vectors.

(A.17) shows the polarisation efficiency, which is given by the hermitian inner product (after the French mathematician Charles Hermite) of the vector antenna effective length and the incident wave [4] [5].

$$\Gamma = l_e . E_{Rx} \tag{A.17}$$

with l_e defined as $\{l_{e\theta}, l_{e\phi}, \delta\}$. This enables to define the antenna polarisation in a very easy way. If we write the vectors in matrices form we obtain (A.18). The minus sign results from the difference in the pointing vector direction of the Rx antenna and the arriving ray.

$$l_e . E_{Rx} = \begin{bmatrix} l_{e\theta} \\ -l_{e\phi} e^{j\delta} \end{bmatrix}^{T^*} \cdot \begin{bmatrix} E_{\theta Rx} \\ E_{\phi Rx} e^{j\delta_r} \end{bmatrix} = l_{e\theta} E_{\theta Rx} - l_{e\phi} E_{\phi Rx} e^{j(\delta_r - \delta)} \tag{A.18}$$

If we denote the amplitude, phase and excess delay of the nth received ray as α_n, φ_n and τ_n respectively, then we may write

$$\alpha_n = \frac{\lambda}{4\pi} \left| l_e . E_{\theta Rx n} \right| \tag{A.19}$$

$$\varphi_n = \arg\left\{ l_e . E_{\theta Rx n} \right\} \tag{A.20}$$

$$\tau_n = \frac{(r_n - r_0)}{c} \tag{A.21}$$

These parameters enable the calculation of the radio channel impulse response.

5. Scenarios Modelling

The simulator is based on a ray tracing algorithm and allows the determination of all possible rays between the BS and the MT, based on the Snell's reflection law and GTD. The algorithm consists in the calculation of the direct ray (LoS), all the reflected, transmitted and diffracted rays until a certain order m, being m an integer depending on the environment under study. It allows the determination of the attenuation α_n, the propagation delay τ_n and the phase shift φ_n of each ray as defined by equations presented in the previous sections.

In order to enable the simulator to perform all the necessary calculations and to determine the impulse response of a particular propagation environment, it is necessary to define some input parameters such as: the scenario and objects, the BS and MT positions, the transmitter and receiver antennas radiation patterns, and its polarisation. The calculations are performed considering the propagation mechanisms (reflection, transmission and diffraction) experienced by each ray-path. Simulations can be performed for any reflection order and any number of objects given enough computer processing power and memory are available. Moreover, three-dimensional rotation of the transmitting and receiving antenna radiation patterns are possible to evaluate antenna-tilting effects.

The input parameters are defined in specific files containing the positions of the MT and BS (*.POS), the transmitter antenna radiation pattern and rotation (antenna.tx), the receiver antenna radiation pattern and rotation (antenna.rx), the scenario configuration (*.CFG) and the simulation mode, wanted results and simulation options (*.OPT).

In the simulator a particular indoor or outdoor scenario is defined by a set of faces having one or two visible sides (nvf), corresponding to a compartment and a set of objects within it. The faces can contain *subfaces* and each object can contain all the configuration components of the scenario: faces, *subfaces*, cylinders and *tfaces* (faces that contribute only in the transmission mode with a certain attenuation). A face is defined as a finite plain requiring an origin point of the plain and two director vectors. The lengths of these vectors define the dimensions of the face. For instance, if P = (0,0,0) is the origin and U = (10,0,0) and V = (0,5,0) are the span vectors, then the face is a rectangle with dimensions 10 m x 5 m in the position (0,0,0). When defining a face as having only one visible side, this side is the one pointed by the U and V external product vector. Each face has also to be characterised electromagnetically according to the properties of the material that constitutes the face, being indicated by the Electrical Permittivity (εr), the Loss Tangent (tan δ), the Roughness (rg) and Thickness (d). When defining the configuration file of the room (*.CFG) it is necessary to indicate all these characteristics for all the defined faces. The face last parameter in the configuration line is the number of *subfaces* (nsf) that it contains. A *subface* is defined as a plane, omitting only the number of visible sides and the number of *subfaces*. The *tfaces* are defined in the same manner as the faces and can also contain *subfaces*.

The definition of cylinders is slightly different, consisting only in a point (x,y,z) representing the centre of the cylinder's base, the radius, an axis vector of any direction and three characteristics of its material: εr, tan δ and rg. The length of the axis vector represents the cylinder's length and the simulator calculates its thickness. Cylinders, as the *tfaces*, only contribute for attenuation due to transmission. Figure A.4 represents an example of a scenario definition – ROOM.CFG and Figure A.5 shows the graphical representation of the room and defined objects.

```
#Number of room faces
6
#Definition of scenario planes                                  εr  tan δ  rg  d        nvf  nsf
0  0  0                0  0  3.7          11.3  0  0          6.14  0.049  0  0       1    0  #Wall 1
11.3  0  0             0  0  3.7          0  7.8  0           6.14  0.049  0  0       1    0  #Wall 2
11.3  7.8  0           0  0  3.7          -11.3  0  0        6.14  0.049  0  0       1    1  #Wall 3
11.3  7.8  1.1         0  0  1.6          -11.3  0  0        6.13  0.033  0  0            #Window
0  7.8  0              0  0  3.7          0  -7.8  0         6.14  0.049  0  0       1    1  #Wall 4
0  2  0                0  0.8  0          0  0  2.1          1.50  0.068  0  0            #Door
0  0  0                11.3  0  0        0  7.8  0          3.08  0.014  0  0       1    0  #Floor
0  0  3.7              0  7.8  0          11.3  0  0        6.14  0.049  0  0       1    0  #Ceiling
#Number of objects
3
#Objects to be defined in the following order: first – faces and subfaces, second – cylinders and third - tfaces.
2  0  0    #Number of faces, Number of cylinders and Number of tfaces – two faces object
9.3  1.5  0.5          0.7  0  0          0  5.5  0          3     0.017  0  0     1    0
10  1.5  0.5          0  0  0.4          0  5.5  0          3     0.017  0  0     1    0

0  1  0  #Number of faces, Number of cylinders and Number of tfaces - cylinder
3  3  0                0  0  2          0.5                  1.5   0.068  0

0  0  2  #Number of faces, Number of cylinders and Number of tfaces – two faces object
5  1  0.5              5  0  0          0  0.7  0           3     0.017  0  0     1    0
5  1  0.5              0  0  0.4          5  0  0          3     0.017  0  0     1    0
```

Figure A.4: Example of a scenario definition file (*.CFG)

For the ray tracing simulation results presented along the thesis, the εr and tan δ figures considered for the different materials, existing in the considered scenarios, are displayed in

Table A.1. These figures were obtained in laboratory experiments and collected from the literature and in some cases have been slightly modified to be more adapted to the specific characteristics of the materials existing in the considered scenarios (average values have been considered).

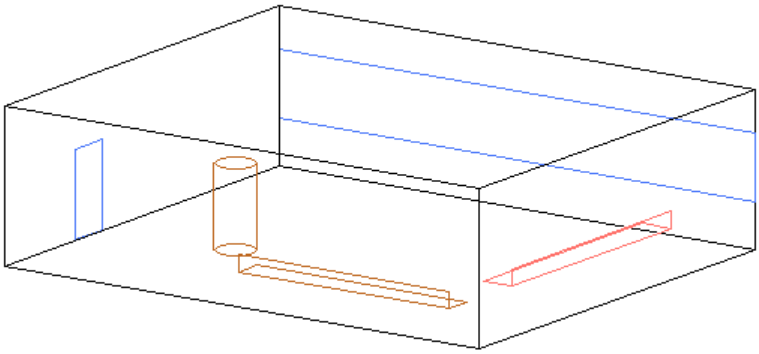

Figure A.5: Graphical representation of the scenario

Material	ε_r	$tan\delta$
Concrete	6.14	0.0491
Granite	6.72	0.0661
Calcareous	8	0.03
Marble	11.56	0.0067
Asphalt	10	0.02775
Glass	6	0.05
Thick glass	5.29	0.0480
Metal	0	0
Roof	8.58	0.0230
Bricks	8.58	0.0230
Plastic	3.08	0.0135
Synthetic fibre	2.81	0.0164
Wood	1.64	0.0547
Trees	1.57	0.000175
Grass	3	0.015

Table A.1: Electromagnetic properties of several materials used for the simulations

6. References

[1] José Fernandes, "Modelação do Canal de Propagação Rádio Móvel de Banda Larga na Faixa das Ondas Milimétricas e seu Impacto no Desempenho de Transmissão do Sistema", PhD Thesis, University of Aveiro, 1996.

[2] P. F. M. Smulders and José Fernandes, "Wide-band Simulations and Measurements of MM-Wave Indoor Radio Channels", 5th International Symposium on Personal, Indoor and Mobile Radio Communications (PIMRC '94), The Hague, The Netherlands, Sep. 1994.

[3] T. Huschka, "Ray Tracing Models for Indoor Environments and their Computational Complexity", 5th International Symposium on Personal, Indoor and Mobile Radio Communications (PIMRC '94), The Hague, The Netherlands, Sep. 1994.

[4] J. S. Hollis et al, "Microwave Antenna Measurements", Scientific Atlanta Inc., Atlanta, USA, 2nd edition, 1970.

[5] C. Ray Wylie and L. C. Barrett, "Advanced Engineering Mathematics", McGraw-Hill, International Student Edition, pp. 139-144, 5th edition, 1985.

Annex B

Reflection and Transmission Coefficients

1. Introduction

Propagation of radio signals in the atmosphere is rather complex to describe. However, when the wavelength is relatively small when compared with the surrounding obstacles of the propagation environment, the high frequency approximation for the wave front can be assumed. In other words, the wave front (Physical Optics) can be approximated by a ray (Geometric Optics).

The ray-tracing algorithm (presented in Annex A) is based on the high frequency approach. Typically the range of application of the algorithm is between 20 GHz and 80 GHz. The lowest limit is imposed by the diffraction phenomenon. The algorithm can still be valid if diffraction effects are taken into account. The highest limit is caused by the scattering phenomenon in rough surfaces. The algorithm traces possible rays between the transmitter and the receiver based on the Snell's law of reflection, which states that for each ray, the

angle of incidence is equal to the angle of reflection (see Figure B.1 where $\theta i=\theta r$). The reflection happens when the ray reaches a discontinuity in the propagation medium. That is to say, it reaches the border of two media with different electromagnetic properties, characterized by: ε - permittivity (F/m); μ - permeability (H/m); σ - conductivity (S/m); Z - impedance of medium (Ω); and η - index of refraction.

The characteristics of the reflecting surface are important for the explanation of how the energy is reflected, transmitted or absorbed. The type of material and if the surface can be considered smooth is determinant for the propagation characteristics. Smooth surfaces originate specular reflections. On the other hand, rough surfaces show many facets to the incident wave causing therefore a diffuse reflection and the energy scattering. A surface is smooth when its roughness is relatively small comparatively to the wavelength [1].

Due to its importance in the ray tracing algorithm, next sections presented the mathematical formulation related with the calculation of reflected and transmitted rays.

2. Derivation of the Reflection and Transmission Coefficients

The reflection and transmission coefficients are fundamental parameters to characterise how the electromagnetic energy is reflected or refracted by a certain medium and they relate the components of the incident ($\boldsymbol{E}_i$), transmitted ($\boldsymbol{E}_t$) and reflected ($\boldsymbol{E}_r$) electrical fields [2].

Figure B.1 shows an incident ray being reflected and refracted. In the figure only the electrical field is shown (parallel and perpendicular components to the plane of incidence), however, and assuming a TEM mode of propagation, the magnetic field is perpendicular to the electrical field and there is no component in the direction of propagation. Moreover, any arbitrary field can be resolved into perpendicular and parallel components, therefore each component will be addressed individually.

2.1 Perpendicularly polarised wave ($E_\perp$)

The reflection ($\rho_\perp$) and transmission ($\tau_\perp$) coefficients for a perpendicularly polarised wave are defined by (B.1) and (B.2).

$$\rho_{\perp} = \frac{E_{r\perp}}{E_{i\perp}} \tag{B.1}$$

$$\tau_{\perp} = \frac{E_{t\perp}}{E_{i\perp}} \tag{B.2}$$

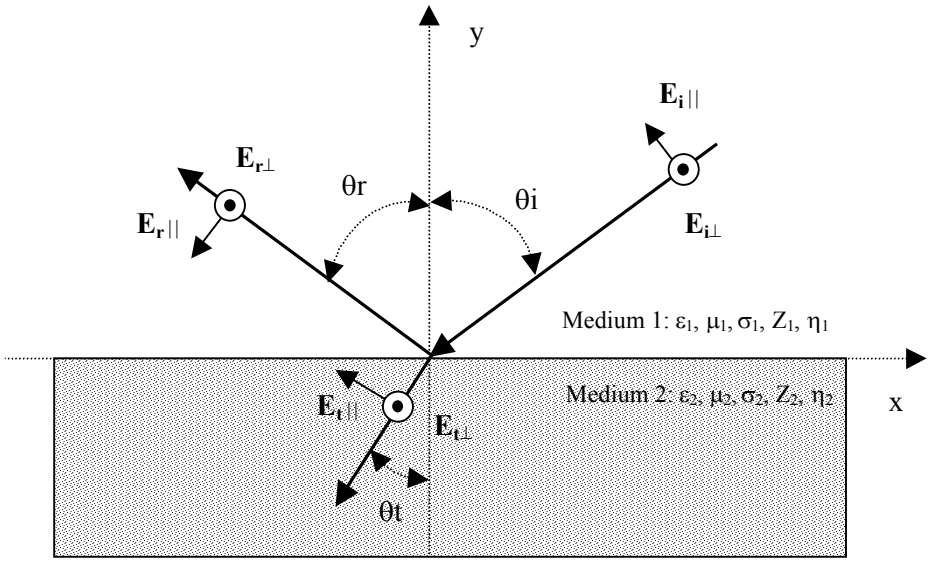

Figure B.1: Incident and reflected wave geometry in the incidence plane

$\boldsymbol{E}_{i\perp}$ is the perpendicular component of the incident electric field, $\boldsymbol{E}_{r\perp}$ the perpendicular component of the reflected electric field and $\boldsymbol{E}_{t\perp}$ the perpendicular component of the transmitted electric field, defined by (B.3), (B.4) and (B.5), respectively.

$$E_{i\perp} = \hat{z}\, E_0\, e^{j\gamma_1 (x\sin\theta i + y\cos\theta i)} \tag{B.3}$$

$$E_{r\perp} = \hat{z}\, \rho_{\perp} E_0\, e^{j\gamma_1 (x\sin\theta r - y\cos\theta r)} \tag{B.4}$$

$$E_{t\perp} = \hat{z}\, \tau_{\perp} E_0\, e^{j\gamma_2 (x\sin\theta t + y\cos\theta t)} \tag{B.5}$$

γ is the propagation coefficient of the medium and is given by (B.6).

$$\gamma = \sqrt{-w^2\mu\varepsilon + jw\mu\sigma} \tag{B.6}$$

The same type of relations can be derived for the magnetic field as shown in (B.7), (B.8) and (B.9).

$$H_{i\perp} = \left(-\hat{x}\cos\theta i + \hat{y}\sin\theta i\right)\frac{E_0}{Z_1} e^{j\gamma_1 (x\sin\theta i + y\cos\theta i)} \tag{B.7}$$

$$H_{r\perp} = \left(\hat{x}\cos\theta r + \hat{y}\sin\theta r\right)\rho_{\perp}\frac{E_0}{Z_1} e^{j\gamma_1 (x\sin\theta r - y\cos\theta r)} \tag{B.8}$$

$$H_{t\perp} = \left(-\hat{x}\cos\theta t + \hat{y}\sin\theta t\right)\tau_{\perp}\frac{E_0}{Z_2}e^{j\gamma_2(x\sin\theta t + y\cos\theta t)} \tag{B.9}$$

Based on the boundary conditions [2] applied for y=0 regarding the electric field, it can be concluded that θi=θr and

$$\sin\theta t = \frac{\gamma_1}{\gamma_2}\sin\theta i \tag{B.10}$$

regarding the magnetic field and again applying the boundary conditions for y=0,

$$\rho_{\perp} = \frac{Z_2\cos\theta i - Z_1\cos\theta t}{Z_2\cos\theta i + Z_1\cos\theta t} \tag{B.11}$$

Z is the impedance of the material (medium) and can be defined by (B.12). **ε** and **μ** can be complex figures.

$$Z = \sqrt{\frac{jw\boldsymbol{\mu}}{\sigma + jw\boldsymbol{\varepsilon}}} \tag{B.12}$$

If medium 2 is a perfect conductor, $Z_2 = 0$ and $\rho_{\perp} = -1$. For the case the medium is the free space $Z=Z_0=120\pi\ \Omega$.

(B.11) can be written in the following form ((B.13)) based on (B.6), (B.10) and (B.12).

$$\rho_{\perp} = \frac{\cos\theta i - \sqrt{\frac{\mu_1(\sigma_2 + jw\varepsilon_2)}{\mu_2(\sigma_1 + jw\varepsilon_1)}\left[1 - \left(\frac{jw\mu_1\sigma_1 - w^2\mu_1\varepsilon_1}{jw\mu_2\sigma_2 - w^2\mu_2\varepsilon_2}\right)\sin^2\theta i\right]}}{\cos\theta i + \sqrt{\frac{\mu_1(\sigma_2 + jw\varepsilon_2)}{\mu_2(\sigma_1 + jw\varepsilon_1)}\left[1 - \left(\frac{jw\mu_1\sigma_1 - w^2\mu_1\varepsilon_1}{jw\mu_2\sigma_2 - w^2\mu_2\varepsilon_2}\right)\sin^2\theta i\right]}} \tag{B.13}$$

(B.13) for two non-conducting media ($\sigma_1=0$ and $\sigma_2=0$) can be simplified to

$$\rho_{\perp} = \frac{\cos\theta i - \frac{\mu_1}{\mu_2}\sqrt{\frac{\mu_2\varepsilon_2}{\mu_1\varepsilon_1} - \sin^2\theta i}}{\cos\theta i + \frac{\mu_1}{\mu_2}\sqrt{\frac{\mu_2\varepsilon_2}{\mu_1\varepsilon_1} - \sin^2\theta i}} \tag{B.14}$$

and for loss-less non-magnetic dielectrics to

$$\rho_{\perp} = \frac{\cos\theta i - \sqrt{\frac{\varepsilon_2}{\varepsilon_1} - \sin^2\theta i}}{\cos\theta i + \sqrt{\frac{\varepsilon_2}{\varepsilon_1} - \sin^2\theta i}} \tag{B.15}$$

Considering medium 1 the free space, medium 2 a non-conducting medium and the complex permittivity ε given by the following equation:

$$\boldsymbol{\varepsilon} = \varepsilon_0\left(\varepsilon_r - j\frac{\sigma}{w\varepsilon_0}\right) = \varepsilon_0\varepsilon_r\left(1 - j\tan\delta\right) \tag{B.16}$$

(B.11) can be written in the following form

$$\rho_{\perp} = \frac{\cos\theta i - \sqrt{\varepsilon_r\left(1 - j\tan\delta\right) - \sin^2\theta i}}{\cos\theta i + \sqrt{\varepsilon_r\left(1 - j\tan\delta\right) - \sin^2\theta i}} \tag{B.17}$$

2.2 Parallel polarised wave ($E_{||}$)

The reflection ($\rho_{||}$) and transmission ($\tau_{||}$) coefficients for a parallel polarised wave are defined by (B.18) and (B.19).

$$\rho_{||} = \frac{E_{r||}}{E_{i||}} \tag{B.18}$$

$$\tau_{||} = \frac{E_{t||}}{E_{i||}} \tag{B.19}$$

$\boldsymbol{E}_{i//}$ is the parallel component of the incident electric field, $\boldsymbol{E}_{r//}$ the parallel component of the reflected electric field and $\boldsymbol{E}_{t//}$ the parallel component of the transmitted electric field, defined by (B.20), (B.21) and (B.22), respectively.

$$E_{i||} = \left(-\hat{x}\cos\theta i + \hat{y}\sin\theta i\right)E_0\, e^{j\gamma_1(x\sin\theta i + y\cos\theta i)} \tag{B.20}$$

$$E_{r||} = \left(-\hat{x}\cos\theta r + \hat{y}\sin\theta r\right)\rho_{||}E_0\, e^{j\gamma_1(x\sin\theta r - y\cos\theta r)} \tag{B.21}$$

$$E_{t||} = \left(-\hat{x}\cos\theta t + \hat{y}\sin\theta t\right)\tau_{||}E_0\, e^{j\gamma_2(x\sin\theta t + y\cos\theta t)} \tag{B.22}$$

The same type of relations can be derived for the magnetic field as shown in (B.23), (B.24) and (B.25).

$$H_{i||} = -\hat{z}\frac{E_0}{Z_1}e^{j\gamma_1(x\sin\theta i + y\cos\theta i)} \tag{B.23}$$

$$H_{r||} = \hat{z}\,\rho_{||}\frac{E_0}{Z_1}e^{j\gamma_1(x\sin\theta r - y\cos\theta r)} \tag{B.24}$$

$$H_{t||} = -\hat{z}\;\tau_{||}\frac{E_0}{Z_2}e^{j\gamma_2(x\sin\theta t + y\cos\theta t)} \tag{B.25}$$

Based on the boundary conditions [2] applied for y=0 regarding the electric field, it can be concluded that θi=θr and that the relation expressed by (B.10) remains valid. Regarding the magnetic field and again applying the boundary conditions for y=0,

$$\rho_{\parallel} = \frac{Z_2 \cos\theta t - Z_1 \cos\theta i}{Z_1 \cos\theta i + Z_2 \cos\theta t} \tag{B.26}$$

If the medium 2 is a perfect conductor $\rho_{\parallel} = -1$.

(B.26) can be written in the following form ((B.27)) based on (B.6), (B.10) and (B.12).

$$\rho_{\parallel} = \frac{-\cos\theta i + \sqrt{\frac{\mu_2(\sigma_1 + jw\varepsilon_1)}{\mu_1(\sigma_2 + jw\varepsilon_2)}\left[1 - \left(\frac{jw\mu_1\sigma_1 - w^2\mu_1\varepsilon_1}{jw\mu_2\sigma_2 - w^2\mu_2\varepsilon_2}\right)\sin^2\theta i\right]}}{\cos\theta i + \sqrt{\frac{\mu_2(\sigma_1 + jw\varepsilon_1)}{\mu_1(\sigma_2 + jw\varepsilon_2)}\left[1 - \left(\frac{jw\mu_1\sigma_1 - w^2\mu_1\varepsilon_1}{jw\mu_2\sigma_2 - w^2\mu_2\varepsilon_2}\right)\sin^2\theta i\right]}} \tag{B.27}$$

(B.27) for tow non-conducting media (σ_1=0 and σ_2=0) can be simplified to

$$\rho_{\parallel} = \frac{-\cos\theta i + \frac{\varepsilon_1}{\varepsilon_2}\sqrt{\frac{\mu_2\varepsilon_2}{\mu_1\varepsilon_1} - \sin^2\theta i}}{\cos\theta i + \frac{\varepsilon_1}{\varepsilon_2}\sqrt{\frac{\mu_2\varepsilon_2}{\mu_1\varepsilon_1} - \sin^2\theta i}} \tag{B.28}$$

and for loss-less non-magnetic dielectrics to

$$\rho_{\parallel} = \frac{-\cos\theta i + \sqrt{\frac{\varepsilon_2}{\varepsilon_1} - \sin^2\theta i}}{\cos\theta i + \sqrt{\frac{\varepsilon_2}{\varepsilon_1} - \sin^2\theta i}} \tag{B.29}$$

Considering medium 1 the free space, medium 2 a non-conducting medium and the complex permittivity ε, (B.27) can be further simplified in (B.30).

$$\rho_{\parallel} = \frac{-\varepsilon_r(1 - j\tan\delta)\cos\theta i + \sqrt{\varepsilon_r(1 - j\tan\delta) - \sin^2\theta i}}{\varepsilon_r(1 - j\tan\delta)\cos\theta i + \sqrt{\varepsilon_r(1 - j\tan\delta) - \sin^2\theta i}} \tag{B.30}$$

2.3 Other type of polarisations

As shown in Figure B.2, any electric field can be decomposed in its parallel and perpendicular components. The characterisation of any electric field that impinges a surface can be done by specifying the ε_r, tanδ, θi, and φ the polarisation angle of the incident wave.

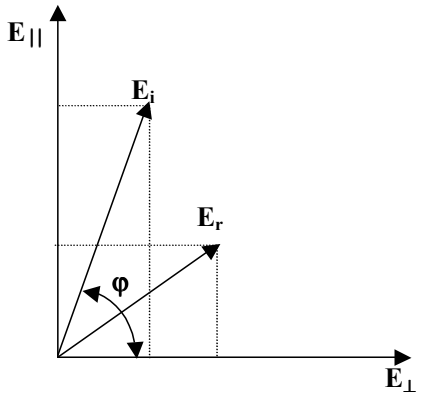

Figure B.2: Incident and reflected electrical field (TEM mode)

Based on Figure B.2, we can derive the following equation for the magnitude of the reflected electrical field:

$$|E_r(\varepsilon_r, \tan\delta, \theta i, \varphi)| = \sqrt{\left\|E_i\right|\rho_\perp(\varepsilon_r, \tan\delta, \theta i)\cos\varphi\Big|^2 + \left|E_i\right|\rho_\parallel\ (\varepsilon_r, \tan\delta, \theta i)\cos\varphi\Big|^2} \qquad \text{(B.31)}$$

The power reflection coefficient, being defined as the reflected over incident power ratio, can be written in the following form:

$$|\rho(\varepsilon_r, \tan\delta, \theta i, \varphi)|^2 = |\rho_\perp(\varepsilon_r, \tan\delta, \theta i)\cos\varphi|^2 + \left|\rho_\parallel\ (\varepsilon_r, \tan\delta, \theta i)\cos\varphi\right|^2 \qquad \text{(B.32)}$$

3. Reflection in Rough Surfaces

The above equations are only valid for smooth and infinite surfaces. To determine if a surface is smooth or rough we can use the Rayleigh criterion. This criterion sets the limit based on the wavelength and the angle of incidence of the radio wave. In expression (B.33) h represents the maximum height (rms of the surface irregularities) for a surface roughness to be considered smooth.

$$h < \frac{\lambda}{8\cos\theta i} \qquad \text{(B.33)}$$

The effects of the roughness, in the specular direction, can be taken into account by considering first the surface smooth and then multiplying the reflection coefficients by the Rayleigh factor defined by (B.34).

$$RF = e^{\left[-\frac{1}{2}\left(\frac{4\pi\sigma_h\cos\theta i}{\lambda}\right)\right]} \qquad \text{(B.34)}$$

σ_h represents the standard deviation of the surface roughness. When a surface is rough the energy is scattered.

4. References

[1] J. D. Parsons, "The Mobile Radio Propagation Channel", Prentech Press, London, 1992.

[2] John D. Kraus, "Electromagnetics", McGraw-Hill series in Electrical Engineering, 1984.